CONTENTS

AN INVESTIGATION INTO THE INFLUENCE OF B$_4$C REINFORCEMENT RATIO AND SINTERING TEMPERATURE ON THE PROPERTIES OF ALUMINUM METAL MATRIX COMPOSITES

*Ahmet KÖKEN [ID]

Kütahya Dumlupınar University, Kütahya Vocational School of Technical Sciences, Department of Machinery and Metal Technologies, Kütahya, TÜRKİYE
ahmet.koken@dpu.edu.tr

Highlights

- Mixing of powders in turbula device

- Compaction of mixing powders and sintering of block samples

- Bending strength of Al6061/B$_4$C composite

Graphical Abstract

Flowchart of the experimental process

*Corresponding Author: Ahmet KÖKEN, ahmet.koken@dpu.edu.tr
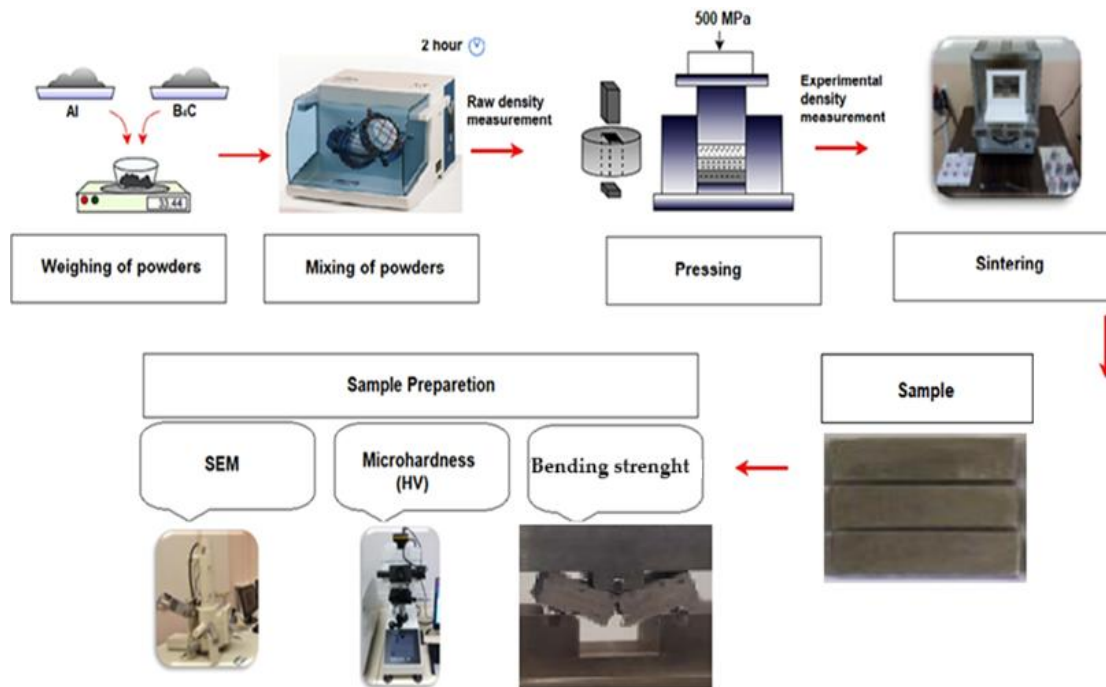
INVESTIGATION OF THE INFLUENCE OF B4C REINFORCEMENT RATIO AND SINTERING TEMPERATURE ON MECHANICAL AND MICROSTRUCTURAL PROPERTIES OF Al6061-BASED METAL MATRIX COMPOSITES

*Ahmet KÖKEN ^{iD}

Kütahya Dumlupınar University, Kütahya Vocational School of Technical Sciences, Department of Machinery and Metal Technologies, Kütahya, TÜRKİYE
ahmet.koken@dpu.edu.tr

ABSTRACT: In this study, aluminum alloy Al6061 matrix composites reinforced with boron carbide (B_4C) particles were fabricated using the powder metallurgy method. The effects of varying reinforcement ratios and sintering temperatures on the mechanical properties of the produced Al6061-based composites were investigated. Powder mixtures containing 10%, 20%, and 30% by weight of B_4C were blended using a turbo mixer. The mixed powders were compacted under a pressure of 500 MPa and then sintered in a tube furnace at temperatures of 575°C, 600°C, and 625°C for 3 hours under an argon atmosphere to produce metal matrix composite (MMC) samples. The density, hardness, and bending strength of the fabricated composites were determined. Microstructural and fracture surface analyses were conducted using scanning electron microscopy (SEM), and the resulting mechanical properties were discussed. The results indicated that the density of the samples decreased with increasing B_4C content but increased with higher sintering temperatures. Porosity levels were observed to rise with higher B_4C ratios, while increasing the sintering temperature reduced porosity. The lowest porosity, 2.17%, was found in the Al6061 sample sintered at 625°C. Across all sintering temperatures, an increase in B_4C reinforcement ratio led to higher hardness values but a reduction in bending strength. The highest bending strength of 118.32 MPa was achieved in the composite with 10% B_4C sintered at 575°C.

Keywords: Powder Metallurgy, Al6061-B_4C, Mmc_p, Sintering Temperature

1. INTRODUCTION

Technological advancements in the field of engineering have significantly increased the expectations for material performance, accelerating the development and utilization of composite materials. Composites, which are formed by combining two or more materials, have emerged as a promising alternative to meet these demands. Among them, metal matrix composites (MMCs), particularly those with aluminum matrices, stand out due to their ability to offer a combination of desirable mechanical and physical properties, such as high hardness, wear resistance, and low thermal expansion coefficients [1]. Aluminum matrix composites (AMCs) exhibit superior characteristics, including enhanced hardness, strength, toughness, and wear resistance, compared to conventional aluminum and its alloys, making them ideal for structural applications [2].

The production of these composites generally involves two primary approaches: liquid-phase methods and solid-state methods. In liquid-phase methods, solid reinforcement particles are added to molten aluminum. However, achieving a homogeneous distribution of the reinforcement within the matrix structure poses significant challenges. In contrast, powder metallurgy (PM), a solid-state method, offers distinct advantages in terms of achieving a more uniform distribution of reinforcement particles. This technique involves blending matrix and reinforcement powders, compacting the mixture under pressure, and subsequently sintering it. To optimize the properties of composites produced via powder metallurgy, critical parameters such as powder mixing ratios, distribution uniformity, compaction pressure, sintering temperature, and duration must be meticulously controlled [3].

*Corresponding Author: Ahmet KÖKEN, ahmet.koken@dpu.edu.tr

Powder metallurgy is preferred for several reasons, including high material utilization efficiency, the absence of melting losses, suitability for mass production, rapid fabrication of complex-shaped parts, controllable composition and microstructure, and its environmentally friendly nature. However, certain limitations exist, such as challenges in producing intricate components, high costs associated with low-volume production, and occasionally elevated powder costs, which can be considered disadvantages.

Aluminum's melting point is sufficiently high to meet the requirements of numerous applications, yet low enough to facilitate relatively straightforward composite processing. Additionally, aluminum can accommodate a variety of reinforcement materials. Commonly used reinforcements include B_4C [4], [5], [6], [7], [8], [9], TiB_2 [10], [11], Al_2O_3 [12], [13], SiC [14], [15], [16], [17], and TiC [18]. The primary purpose of incorporating reinforcement particles into the matrix is to enhance the hardness and thermal shock resistance of the composite material. In particle-reinforced powder metallurgy composites, the homogeneous distribution of reinforcement particles within the matrix is of critical importance, as uniform properties across the material directly influence its overall performance [11], [19], [20].

Today, particle-reinforced metal matrix composites (MMC_P) are widely used engineering materials due to their superior properties in various applications, and their development continues to be an active area of research. Several studies in the literature have explored these materials, with some notable examples as follows. Guleryuz et al. [8], in their study, investigated the microstructure and mechanical properties of Mg matrix composites reinforced with varying ratios of B_4C, fabricated using the powder metallurgy method. They aimed to determine the optimal reinforcement ratio to optimize hardness and flexural strength. Their findings revealed that the post-sintering density of the composites decreased with increasing B_4C content. They also observed that the hardness of B_4C-reinforced Mg matrix composites was higher compared to unreinforced Mg samples. XRD analyses indicated the formation of Al_2O_3, MgO, and MgB_2 phases in the composite structure. Compression tests demonstrated that the best results were obtained from composites with 3% reinforcement, attributing this to the weakening of interfacial bonds at higher reinforcement ratios. In the study conducted by Gürbüz [21], aluminum recovered from waste beverage cans was utilized as the matrix material. Initially, the cans were collected and subjected to a pre-melting process to remove paint and other contaminants. Although various methods exist for the production of aluminum matrix composites, the stir casting method was preferred in this particular study. Composites were fabricated with 3% and 6% SiC, 1%, 3%, and 6% B_4C, as well as 3% and 6% glass powder reinforcements. The produced specimens were subjected to hardness, density, bending, tensile, and wear tests. According to the experimental results, the highest hardness value observed in the SiC-reinforced composites was 81.08 Hv, and the maximum bending strength, achieved with 6% reinforcement, was measured as 302.329 MPa. For the B_4C-reinforced composites, the highest hardness value was found to be 86.08 Hv, while the glass powder-reinforced composites exhibited a maximum hardness of 77.47 Hv. Canakcı and Varol [22], in their study, explored the effects of mechanical alloying on the production of metal matrix composites. They milled Al2024 and Al2024-5% B_4C powders in a ball mill for durations of 0.5, 1, 2, 5, 7, and 10 hours. The mechanically alloyed powders were then subjected to uniaxial cold pressing at pressures of 300 and 500 MPa in a cylindrical mold. They found that longer milling times led to a more homogeneous distribution of B_4C and increased hardness. They concluded that mechanical alloying enhances composite properties by ensuring a uniform distribution of reinforcement particles. Ay et al. [23], in their study, investigated the influence of B_4C content on the hardness and wear properties of 7075Al-B_4C composites fabricated using the powder metallurgy technique. They added varying amounts of B_4C (3%, 6%, and 9%) to gas-atomized Al7075 powders, followed by homogenization, cold pressing, and sintering. They conducted metallographic examinations, SEM, XRD analyses, hardness measurements, and pin-on-disk wear tests. Their findings revealed that hardness increased with higher B_4C content, and the lowest weight loss was observed in composites containing 9% B_4C. They also noted that weight loss was directly proportional to sliding distance. Raja and Sahu [24], in their study, examined the cold pressing behavior and hardness variations of Al-B_4C composites produced via powder metallurgy at different reinforcement ratios (5%, 10%, 15%, and 20%). They found that composites with the highest reinforcement ratio, 20% B_4C,

exhibited the highest hardness values. Microstructural analyses revealed a uniform distribution and good bonding of reinforcement particles within the matrix. They reported that density values decreased with increasing B$_4$C content, which they attributed to the low density of B$_4$C. Additionally, they observed that hardness values increased with higher B$_4$C reinforcement ratios.

The primary objective of this study is to produce composite materials with enhanced mechanical properties by incorporating B$_4$C particles into Al6061 alloy, which is known for its excellent machinability, extrudability, and corrosion resistance. Within this scope, Al6061/B$_4$C composites were fabricated using the powder metallurgy (PM) process. Mechanical properties such as density, hardness, and bending strength were investigated, and fracture surfaces along with microstructures were evaluated and compared.

2. MATERIAL AND METHODS

In this study, Al6061 powders with an average particle size of 90.95 μm, produced via the gas atomization method and supplied from commercial firms, were used as the matrix material. Additionally, B$_4$C powders with an average particle size of 16 μm were utilized as the reinforcement material. The chemical composition of Al6061 is presented in Table 1. The flow chart of the experimental procedure applied in this study is illustrated in Figure 1.

Table 1. Chemical composition of Al6061 alloys

Element	Al	Mg	Zn	Cu	Si	Mn	Ti	Fe	Cr
Composition (%)	Balance	0,8-1,2	0,25	0,15-0,40	0,6-1,0	0,2-0,8	0,1	0,5	0,1
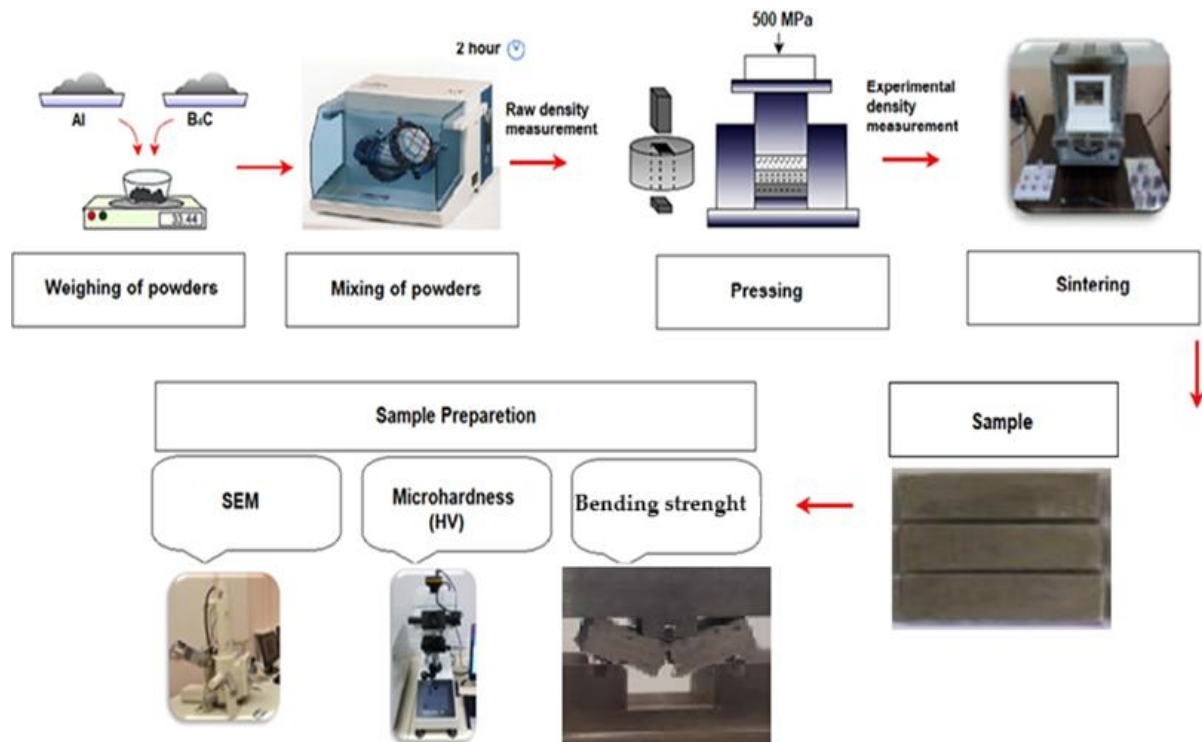
Figure 1. Flowchart of the experimental process

The weights of the samples to be produced were calculated using Equation 1. The theoretical densities of the powder mixtures were determined using Equation 2.

$$W = \rho . V \tag{1}$$

$$\rho mix = [(\%W)1 * \rho1] + [(\%W)2 * \rho2] + \cdots + [(\%W)n * \rho n] \tag{2}$$

Here, W denotes weight (g), V stands for volume (cm³), ρ represents density (g/cm³), ρ_{mix} is the theoretical density of the powder mixture (g/cm³), $(\%W)n$ indicates the weight percentage of the n component in the mixture, and ρ_n refers to the density of the n component (g/cm³).

The initial densities of Al6061-B$_4$C powder mixtures containing varying proportions of boron carbide are provided in Table 2.

Table 2. The bulk densities of the prepared powder mixtures

Sample	Mixture ratios (%)	Bulk density of powder mixture (g/cm³)
1	Al6061	2,7
2	Al6061-10% B$_4$C	2,682
3	Al6061-20% B$_4$C	2,664
4	Al6061-30% B$_4$C	2,646

Aluminum powder and boron carbide (B$_4$C) powders with weight ratios of 10%, 20%, and 30% were precisely weighed using a digital scale with a sensitivity of 0.1 mg and transferred to a mixing container. An equal weight of alumina (Al$_2$O$_3$) balls, relative to the powder weight, was added to the mixing container, ensuring that the total volume did not exceed two-thirds of the container's capacity. The mixture was homogenized in a turbo mixer for 2 hours. The mixing parameters (speed and duration) were optimized based on preliminary experiments.

A lubricant was prepared by adding 1 wt.% stearic acid to 50 ml of ethyl alcohol, intended for lubricating the mold walls during the pressing process. Prior to the pressing operation, a lubrication process was applied to the mold and punch surfaces to prevent adhesion. The compaction was carried out in a rigid die using a single-action press under a pressure of 500 MPa, producing samples with dimensions of 31.7x12.7x6.35 mm. A total of 50 samples were obtained, including 15 Al-B4C composite samples and 5 aluminum 6061 samples for each mixture.

The pressed samples were sintered at 575, 600, and 625°C for 3 hours in an argon atmosphere to achieve densification. The dimensions and weights of the samples were measured before and after sintering, and their densities were calculated. Argon gas was passed through a copper shavings purification unit to remove oxygen. The obtained density values were compared with the theoretical densities of the samples to evaluate the effectiveness of the sintering process.

The density of the produced composite was measured using the Archimedes' principle as defined in the ASTM B962-13 standard [25]. For this purpose, the weights of the samples in air (W_a) and in water (W_w) were first measured, and then the density (ρ) values were determined using Equation 3.

$$\rho_D = \left[\frac{W_a}{W_a - W_w}\right] * \rho_W \tag{3}$$

The percentage of porosity (P) was calculated using Equation 4.

$$\%P = \frac{\rho_{th} - \rho_{sin}}{\rho_{th}} \cdot 100 \tag{4}$$

Here, ρ_{th} denotes the theoretical density, while ρ_{sin} refers to the density of the sintered sample obtained experimentally.

After sintering, any potential oxide layers that may have formed on the sample surfaces were removed through grinding using sandpapers in the range of 320-1200 mesh, followed by polishing with diamond solutions of 6-3-1 microns in sequence. The microstructural characterization of the polished samples was conducted using a JEOL 5600LV scanning electron microscope (SEM). The distribution of boron carbide (B$_4$C) particles within the aluminum matrix and their microstructural features were

examined in the obtained images. For hardness characterization, a HVS-1000 digital microhardness tester was used, and Vickers hardness (HV) values were determined by averaging measurements taken from five different points on each sample.

The cross-breaking test was conducted using a Matest 2000 kN capacity device with a load increase rate of 0.04 kN/s. For the cross-breaking test, a setup compliant with the ASTM B-312 standard, as shown in Figure 2, was prepared. This setup included two support cylinders with a diameter of 3.1 mm and one loading cylinder on the upper block. The distance between the support cylinders was set to 25.4 mm. The pressing force at the moment of fracture was recorded for each loaded sample, and the bending strength value for each sample was calculated in N/mm² (MPa) using the standard formula provided in Equation (5).

$$S = \frac{(3PL)}{2bh^2} \tag{5}$$

Here S represents the bending strength (MPa), while P denotes the load measured at the point of specimen fracture (N), L signifies the span length (mm), h indicates the specimen height (6.35 mm), and b represents the specimen width (12.7 mm).
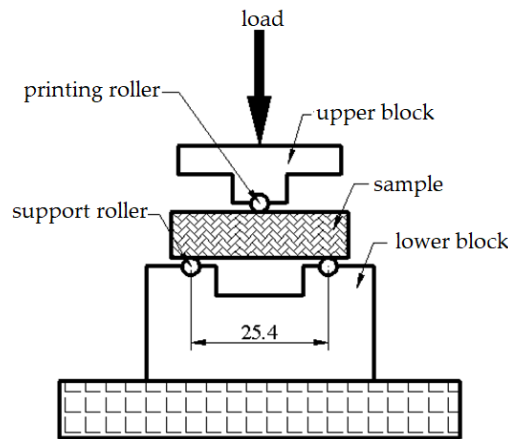
Figure 2. Schematic representation of the bending strength test setup

3. RESULTS AND DISCUSSION

It was observed that the densities of the produced samples decreased with an increase in the B₄C percentage, while they increased with higher sintering temperatures (Figures 3 and 4). The porosity rates (Figure 5) showed an increase with higher B₄C content, whereas porosity decreased with rising sintering temperatures. The lowest porosity was found to be 2.17% in Al6061 samples sintered at 625°C, while the highest porosity was 10.985% in composite samples with 30% B₄C sintered at 575°C. The increase in B₄C content negatively affected the compressibility of the samples. This is thought to be due to the difficulty in diffusion of Al around the increasing number of B₄C particles in the structure, leading to challenges in bonding these particles. Another reason for the increase in porosity with higher reinforcement content is the reduction in the overall compressibility of the composite, as the amount of hard and less compressible reinforcement particles in the structure increased.

In conclusion, it was determined that as the sintering temperature increased, porosity decreased, density increased, and the values approached the calculated theoretical densities. This can be interpreted as a weakening of compressibility and bonding with increasing reinforcement content, thereby increasing porosity. Similar findings were reported in studies by Guleryuz et al. [8], Ay et al. [23], and Raja and Sahu [24], where increasing reinforcement ratios led to a decrease in sample densities.
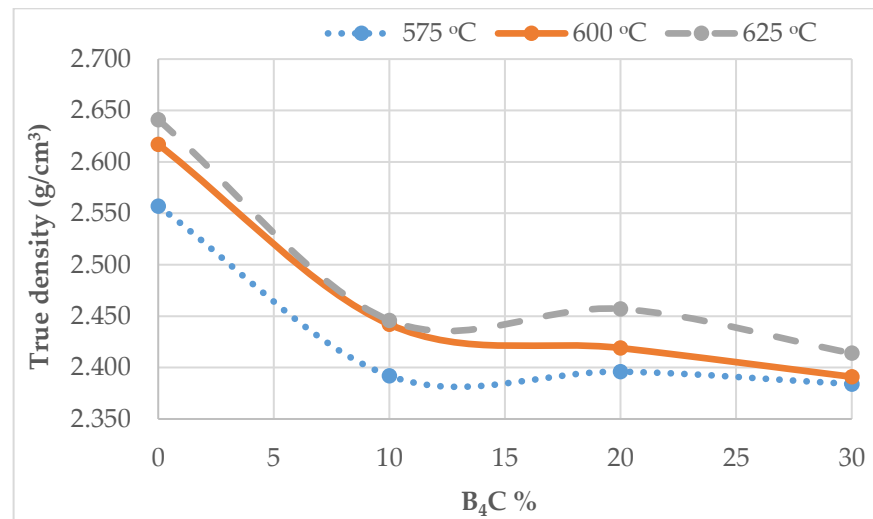
Figure 3. Variation of true density in composite samples depending on the reinforcement ratio
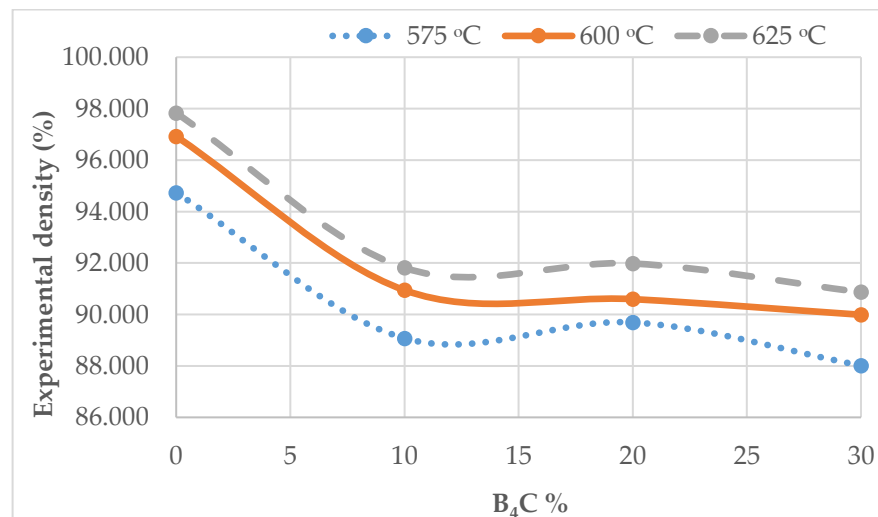
Figure 4. Variation of experimental density (%) in composite samples depending on the reinforcement ratio
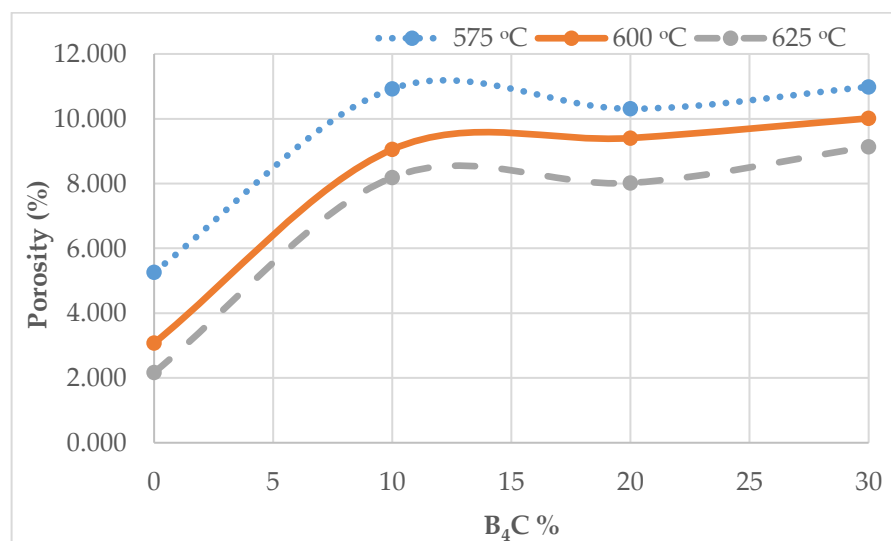
Figure 5. Variation of porosity in composite samples depending on the reinforcement ratio

SEM images of Al6061 and Al6061-B$_4$C composite samples with different mixing ratios are presented in Figure 6. Microstructural examinations of the samples were conducted to investigate the distribution of B$_4$C particles within the Al6061 matrix and the morphology of the pores. Upon analyzing the images, it was observed that the boron carbide particles were uniformly distributed, with no evidence of grain growth or agglomeration. The structure also exhibited gray and darker regions. The gray areas are associated with the formation of carbide structures, while the darker regions correspond to areas where porosity became more concentrated with increasing B$_4$C content.
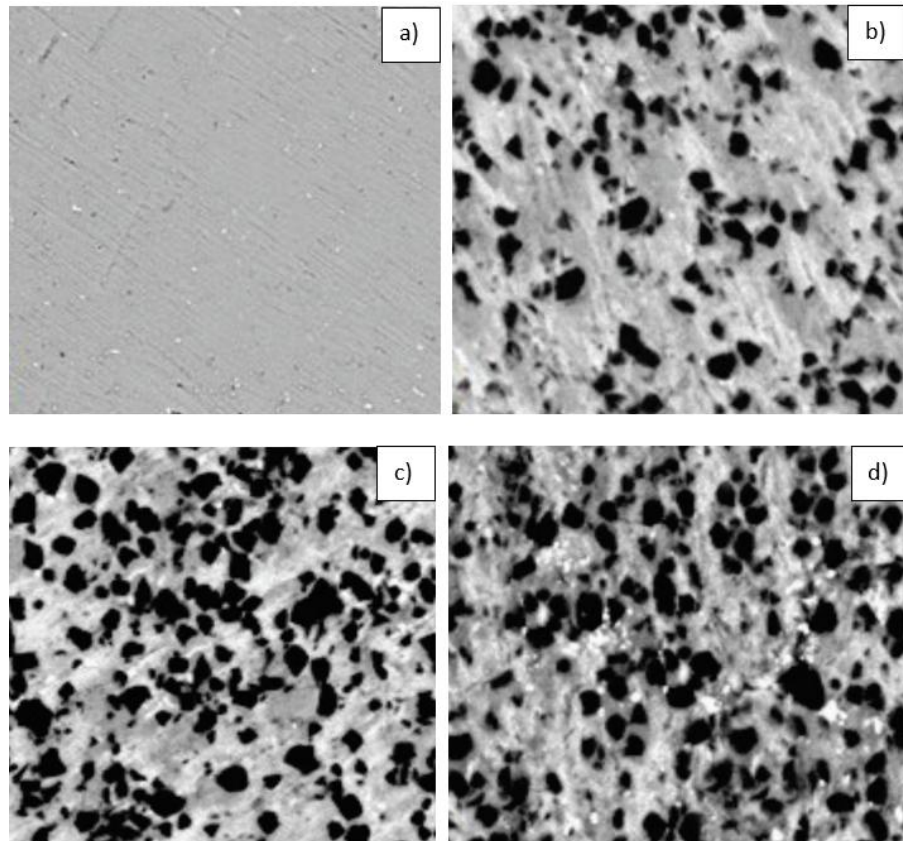
Figure 6. SEM images of the samples: a) 100% Al6061, b) Al6061-10% B$_4$C, c) Al6061-20% B$_4$C, d) Al6061-30% B$_4$C (x1000).

The Vickers hardness values of Al6061 and B$_4$C-reinforced composites are presented in Figure 7. According to the hardness measurement results, the reinforcement ratio and sintering temperature significantly influenced the hardness of the composite material. An increase in the B$_4$C percentage led to a linear rise in the hardness values of the composite material. The ductility of the composite continuously decreased with increasing B$_4$C content. Due to the high hardness of B$_4$C particles surrounded by a soft matrix, the hardness of the MMC (metal matrix composite) material was measured to be higher than that of the Al6061 matrix. The lowest hardness value was 40.25 HV for the unreinforced Al6061 sample sintered at 575°C, while the highest hardness value was 62.64 HV for the 30% B$_4$C-reinforced sample sintered at 625°C. The results demonstrated that the addition of B$_4$C and an increase in sintering temperature significantly improved the hardness. Similar findings were reported in studies by Ay et al. [23] and Raja and Sahu [24], where the hardness of composite materials increased with higher particle percentages.
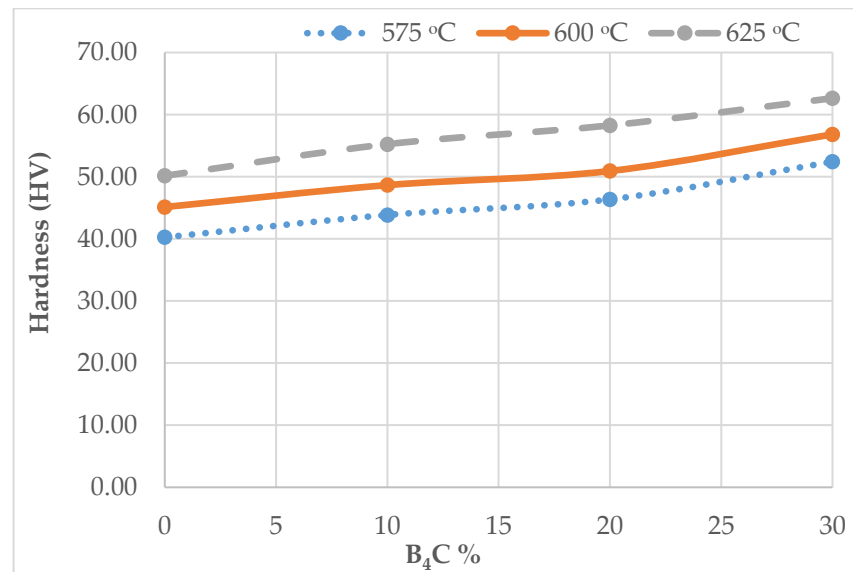
Figure 7. Variation of hardness in composite samples depending on reinforcement ratio and sintering temperature

In composites produced via the powder metallurgy method, a decrease in bending strength was observed with increasing B_4C reinforcement ratios, contrary to the expected increase (Figure 8). This decline can be attributed to microstructural issues such as the clustering of B_4C particles at high reinforcement ratios and the formation of voids at particle-particle and particle-matrix interfaces. These factors facilitated crack formation, increasing the brittleness of the composite and ultimately leading to a reduction in bending strength. The highest bending strength value was measured as 118.32 MPa for the 10% B_4C-reinforced sample sintered at 575°C, while the lowest bending strength value was 30.32 MPa for the unreinforced Al6061 sample sintered at 625°C. The decrease in bending strength with increasing reinforcement content can be explained by the weak interfacial bonds between the matrix and the reinforcement, as well as the inability of the increased B_4C content to provide the expected contribution to the load-bearing capacity of the composite. Excessive sintering temperatures can lead to a reduction in bending strength in Al6061-B_4C composites due to mechanisms such as phase transformations, grain growth, increased porosity, and internal stresses. Determining an optimal sintering temperature is critical for preserving the mechanical properties of the material.
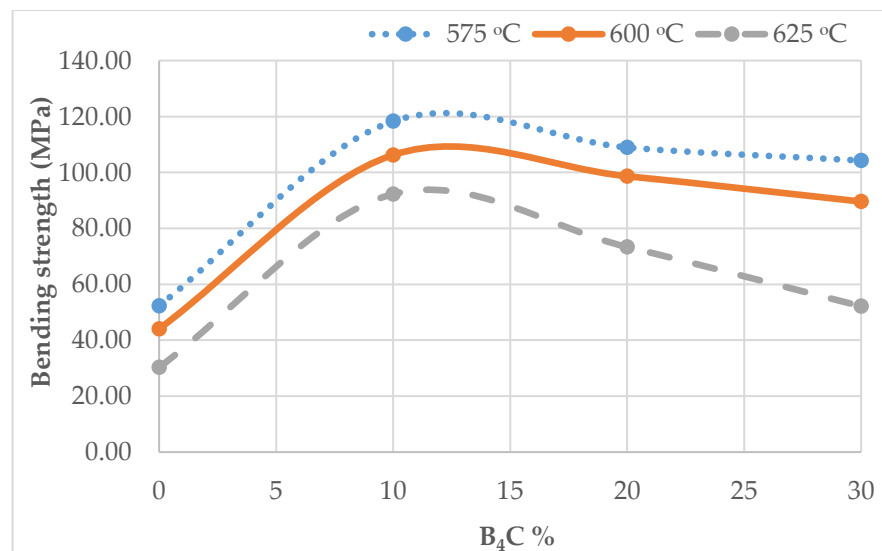
Figure 8. Results of the bending strength tests

The results of the fracture tests conducted on powder metallurgy samples produced from aluminum powder and a mixture containing 10% B_4C at different sintering temperatures are shown in Figure 9. In the cross-breaking test, the samples exhibited bending behavior under the applied load before fracturing. The ductile behavior and bending of the composite samples indicate good sintering within the material. The bending strength was measured as 118.32 MPa for the sample sintered at 575°C and 92.26 MPa for the sample sintered at 625°C.
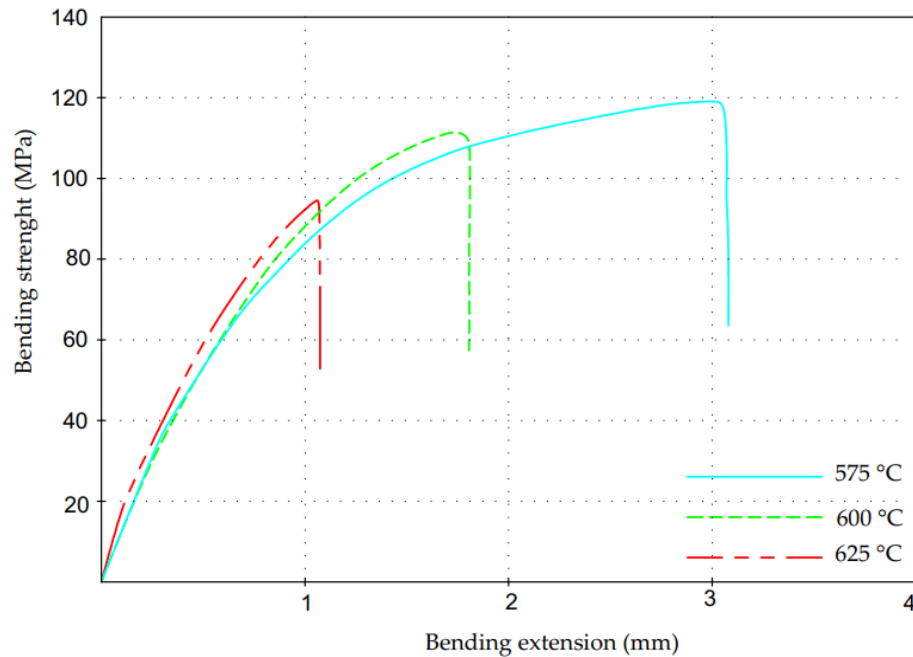
Figure 9. The effect of sintering temperature on bending strength

The SEM images of the fracture surfaces of the samples are presented in Figure 10. Upon examining the images, it is observed that the particles in the Al6061-10%B_4C reinforced sample are completely surrounded by the matrix, forming an interface free of voids. This excellent interfacial bonding enhances the adhesion between the matrix and particles, thereby improving the overall strength of the composite. Studies in the literature [26] also emphasize that interfacial bonding is one of the most critical parameters influencing the mechanical properties of composites.
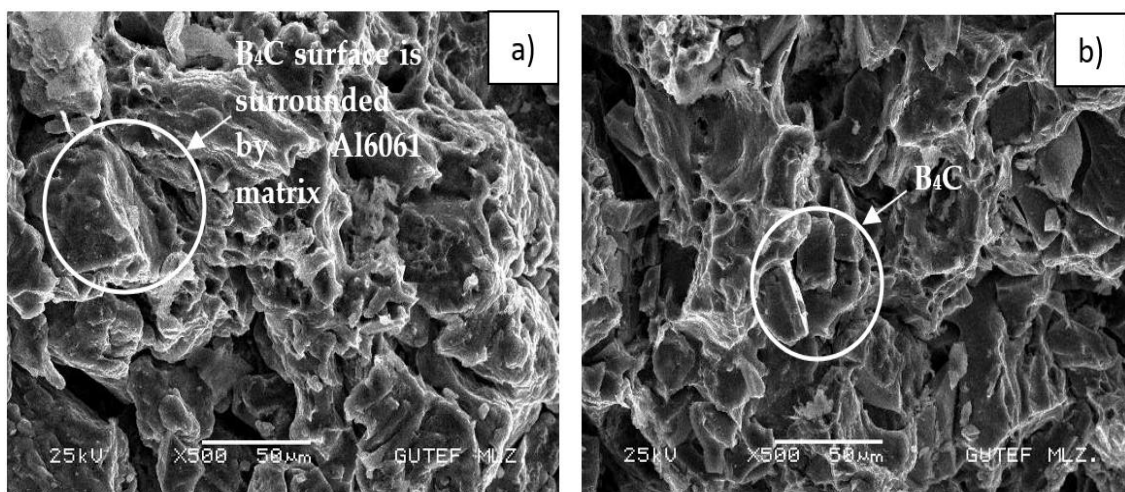
Figure 10. SEM images of the fracture surfaces of the samples: a) Al6061-10% B_4C, b) Al6061-30% B_4C

4. CONCLUSIONS

In this study, materials composed of Al6061 and 10%, 20%, and 30% by weight of B₄C were produced using the powder metallurgy method, and their density, hardness, and bending strength were investigated. Sintering temperatures of 575°C, 600°C, and 625°C were used as production parameters. The increase in the percentage of B_4C in the aluminum matrix and the sintering temperature values caused significant changes in the macro and micro properties of the composite. As a result of the experimental studies;

- It has been determined that Al6061 aluminum alloy can be successfully enhanced by reinforcing it with B_4C using the powder metallurgy technique.
- It was observed that the density of the produced samples continuously decreased with the increase in B_4C percentage, while it increased with the rise in sintering temperature. The porosity rates increased with the higher B_4C ratio but decreased with the increase in sintering temperature. The lowest porosity was determined to be 2.17% in the Al6061 sample sintered at 625°C.
- Microstructure analyses revealed that B_4C was uniformly distributed within the Al6061 matrix material, and the addition of B_4C led to the formation of micro-pores in the microstructure.
- The results obtained from hardness measurements demonstrated that the addition of B_4C and the increase in sintering temperature significantly improved the hardness. The lowest hardness value was determined as 40.25 HV in the unreinforced Al6061 sample sintered at 575°C, while the highest hardness value was recorded as 62.64 HV in the 30% B_4C reinforced sample sintered at 625°C.
- In the produced composites, a decrease in bending strength was observed with the increase in B_4C reinforcement ratio, contrary to the expected improvement. The highest bending strength value was determined as 118.32 MPa in the 10% B_4C reinforced sample sintered at 575°C, while the lowest bending strength value was recorded as 30.32 MPa in the unreinforced Al6061 sample sintered at 625°C.

Declaration of Ethical Standards

The author of this article declare that the materials and methods used in this study do not require ethical committee permission and/or legal-special permission.

Credit Authorship Contribution Statement

Ahmet KÖKEN: Researched and supplied experimental materials, conducted the experiments, wrote the article, and reviewed the manuscript.

Declaration of Competing Interest

Declaration of Competing Interest The authors declare that they have no known competing financial interests or personal relationships that could have appeared to influence the work reported in this paper.

Data Availability

Data will be made available on request.

REFERENCES

[1]   M. Rosso, "Ceramic and metal matrix composites: Routes and properties," *J Mater Process Technol*, vol. 175, no. 1–3, pp. 364–375, 2006, doi: 10.1016/j.jmatprotec.2005.04.038.

[2]   D. B. Miracle, "Metal matrix composites - From science to technological significance," *Compos Sci. Technol*, vol. 65, no. 15-16 SPEC. ISS., pp. 2526–2540, 2005, doi: 10.1016/j.compscitech.2005.05.027.

[3]   M. Kok, "Production and mechanical properties of Al_2O_3 particle-reinforced 2024 aluminium alloy composites," *J. Mater. Process Technol.*, vol. 161, no. 3, pp. 381–387, 2005, doi: 10.1016/j.jmatprotec.2004.07.068.

[4]   Z. Kovziridze, N. Nizharadze, G. Tabatadze, H. J. Heinrich, R. Goerke, H. Bornhoeft, and U. Kahnert, "Investigation of structural properties of hetero-module composite in the B_4C-BN-TiC-SiC-C system," presented at the 3rd Int. Congress on Ceramics (ICC3), Osaka, Japan, Nov. 14–18, 2010, in *IOP Conf. Ser.: Mater. Sci. Eng.*, vol. 18, no. 20, p. 202015, 2011, doi: 10.1088/1757-899X/18/20/202015.

[5]   A. Göçer and M. B. Karamis, "Production and mechanical characterization of steel/Al-B_4C layered circular hybrid composite materials," *Arab. J. Sci. Eng.*, vol. 49, no. 8, pp. 11717–11735, 2024, doi: 10.1007/s13369-024-08822-z.

[6]   A. Brillon et al., "Characterization of Al/B_4C composite materials fabricated by powder metallurgy process technique for nuclear applications," *Journal of Nuclear Materials*, vol. 565, p. 153724, 2022, doi: 10.1016/j.jnucmat.2022.153724.

[7]   Z. Guo, Q. Li, W. Liu, and G. Shu, "Evolution of microstructure and mechanical properties of Al-B4C composite after recycling," presented at the 3rd Int. Conf. on Manufacturing, Material and Metallurgical Engineering (ICMMME), Kuala Lumpur, Malaysia, Mar. 17–19, 2018, in *IOP Conf. Ser.: Mater. Sci. Eng.*, vol. 409, no. 1, p. 012005, 2018, doi: 10.1088/1757-899X/409/1/012005.

[8]   L. F. Güleryüz, S. Ozan, D. Uzunsoy, and R. Ipek, "An investigation of the microstructure and mechanical properties of B_4C reinforced PM magnesium matrix composites," *Powder Metallurgy and Metal Ceramics*, vol. 51, no. 7–8, pp. 456–462, 2012, doi: 10.1007/s11106-012-9455-9.

[9]   M. C. Şenel, Y. Kanca, and M. Gürbüz, "Reciprocating sliding wear properties of sintered Al-B_4C composites," *International Journal of Minerals, Metallurgy and Materials*, vol. 29, no. 6, pp. 1261–1269, 2022, doi: 10.1007/s12613-020-2243-5.

[10]   K. L. Tee, L. Lu, and M. O. Lai, "Wear performance of in-situ Al-TiB composite 2," *Wear*, vol. 240, no. 1-2, pp. 59-64, 2000. https://doi.org/10.1016/S0043-1648(00)00337-9.

[11]   C. M. Rao and K. M. Rao, "Abrasive wear behaviour of TiB_2 fabricated aluminum 6061," *Mater. Today Proc.*, vol. 5, no. 1, pp. 268-275, 2018. https://doi.org/10.1016/j.matpr.2017.11.082.

[12]   A. Kumar M.S., "Microstructural evaluation of Al-Al_2O_3 composites processed by stir casting technique," *Journal of Materials and Engineering*, vol. 2, no. 4, pp. 267–272, 2024, doi: 10.61552/JME.2024.04.004.

[13]   M. Zabihi, M. R. Toroghinejad, and A. Shafyei, "The production of Al/Al_2O_3 composite strips using a new method," presented at the Iran International Aluminum Conference (IIAC2012), Arak, Iran, May 15–16, 2012, doi: 10.13140/2.1.4312.9602.

[14]   Y. Li, Z. Wang, and Z. Guo, "Preparation of SiC/Al composite material by supergravity infiltration method and its properties," *Ceram Int*, vol. 50, no. 16, pp. 28025–28036, 2024, doi: 10.1016/j.ceramint.2024.05.100.

[15]   K. Mizuuchi et al., "Processing of Al/SiC composites in continuous solid-liquid co-existent state by SPS and their thermal properties," *Compos. Part B Eng.*, vol. 43, no. 4, pp. 2012–2019, 2012, doi: 10.1016/j.compositesb.2012.02.004.

[16]   K. Bravilin Jiju, G. Selvakumar, and S. Ram Prakash, "Study on preparation of Al–SiC metal matrix composites using powder metallurgy technique and its mechanical properties," *Materials Today: Proceedings*, vol. 27, no. 2, pp. 1843–1847, 2020, doi: 10.1016/j.matpr.2020.04.001.

[17] R. K. Behera, B. P. Samal, and S. C. Panigrahi, "Investigations into dry-sliding wear behaviour of a novel composite (aluminium-magnesium-silicon-copper-silicon carbide) produced by powder metallurgy route," *Mater. Sci. Eng. B*, vol. 52, no. 3, pp. 320–331, 2021, doi: 10.1002/mawe.202000140.

[18] R. Tyagi, "Synthesis and tribological characterization of in situ cast Al-TiC composites," *in Wear*, vol. 259, no. 1-6, pp. 569–576, 2005. doi: 10.1016/j.wear.2005.01.051.

[19] R. K. Singh, A. Telang, and S. Das, "High stress abrasive wear behaviour of aluminum allow and composite: A Review," *ARPN J. Eng. Appl. Sci.*, vol. 10, no. 18, pp. 8025-8037, 2015.

[20] G. N. Kumar, V. M. Reddy, Y. V. M. Reddy, and K. H. Reddy, "Study of abrasive wear behavior of AA6063/TiC$_P$ in-situ composites," *International Journal of Mechanical Engineering and Technology (IJMET)*, vol. 8, no. 5, pp. 42–52, 2017.

[21] F. T. Gürbüz, "Production of metal matrix from waste aluminum and investigation of mechanical properties in microparticle reinforced composites," M.S. thesis, Dept. Mech. Eng., Harran Univ., Şanlıurfa, Türkiye, 2023.

[22] A. Çanakçı and T. Varol, "Production and microstructure of AA2024-B$_4$C metal matrix composites by mechanical alloying method," *Usak Univ. J. Mater. Sci.*, vol. 1, no.1, pp. 15-22, 2012.

[23] H. Ay, D. Özyürek, M. Yıldırım, and B. Bostan, "The effects of B$_4$C amount on hardness and wear behaviours of 7075-B$_4$C composites produced by powder metallurgy method," *Acta Phys. Pol. A*, vol. 129, no. 4 pp. 565–568, 2016, doi: 10.12693/APhysPolA.129.565.

[24] T. Raja and O.P. Sahu, "Effects on microstructure and hardness of Al-B$_4$C metal matrix composite fabricated through powder metallurgy," *International Journal of Mechanical Engineering,* vol. 1, no. 1, pp. 1-5, 2014.

[25] M. B. N. Shaikh, S. Arif, T. Aziz, A. Waseem, M. A. N. Shaikh, and M. Ali, "Microstructural, mechanical and tribological behaviour of powder metallurgy processed SiC and RHA reinforced Al-based composites," *Surfaces and Interfaces*, vol. 15, pp. 166–179, 2019, doi: 10.1016/j.surfin.2019.03.002.

[26] A. K. Bodukuri, K. Eswaraiah, K. Rajendar, and V. Sampath, "Fabrication of Al–SiC–B$_4$C metal matrix composite by powder metallurgy technique and evaluating mechanical properties," *Perspect. Sci.*, vol. 8, pp. 428–431, 2016, doi: 10.1016/j.pisc.2016.04.096.

CAPACITY ANALYSIS IN ORTHOGONAL MULTIPLE ACCESS CELLULAR SYSTEMS

[1, *] Muhammed Furkan KOŞUM [iD] , [2]Ali Osman ÖZKAN [iD]

[1] *Baskent University, Kahramankazan Vocational School, Electronics and Automation Department, Ankara, TÜRKİYE*
[2] *Necmettin Erbakan University, Engineering Faculty, Electrical and Electronics Engineering Department, Konya, TÜRKİYE*
[1] mfurkankosum@baskent.edu.tr, [2] alozkan@erbakan.edu.tr

Highlights

- Determining the minimum physical distance required for a given link quality based on the receivers' SINR requirements.

- Assignment failure rate and blocking probability analysis of systems under the same traffic conditions according to the number of channels.

- Examining the maximum number of channels that can be provided per cell by the omnidirectional antenna scenario and the directional antenna scenario with the same communication conditions.

*Corresponding Author: Muhammed Furkan KOŞUM, mfurkankosum@baskent.edu.tr

CAPACITY ANALYSIS IN ORTHOGONAL MULTIPLE ACCESS CELLULAR SYSTEMS

[1], * Muhammed Furkan KOŞUM [ID] **, [2]Ali Osman ÖZKAN** [ID]

[1] *Baskent University, Kahramankazan Vocational School, Electronics and Automation Department, Ankara, TÜRKİYE*
[2] *Necmettin Erbakan University, Engineering Faculty, Electrical and Electronics Engineering Department, Konya, TÜRKİYE*
[1] mfurkankosum@baskent.edu.tr, [2] alozkan@erbakan.edu.tr

ABSTRACT: This paper provides a comprehensive analysis of capacity in orthogonal multiple access systems. In the coverage planning section, the focus is on cell radius and signal to noise ratio (SNR) at the cell boundary. The static channel allocation section examines capacity from the perspectives of signal to interference ratio (SIR), reuse distance, number of channels, cluster size, and group size. The guaranteed service-based capacity analysis section evaluates capacity based on signal to interference plus noise ratio (SINR) and cluster size, while the traffic-based capacity analysis section analyzes parameters such as relative traffic load, assignment failure rate, and blocking probability. The best-effort data services section assesses capacity in terms of data rates, and the interruption-based capacity analysis section looks at SINR and interruption probability. Finally, the directional antennas and sectorization section investigates capacity using directional antennas. These comprehensive analyses provide valuable insights into optimizing the performance of cellular systems and better understanding their capacity.

Keywords: *Assignment Failure Rate, Blocking Probability, Outage Probability, Reuse Distance, Static Channel Allocation*

1. INTRODUCTION

In orthogonal multiple access (OMA) systems, the overall signal bandwidth is divided into closely spaced narrow sub-channels. This process transforms the wideband frequency-selective fading channel into narrowband and relatively flat sub-channels that require simpler equalization. The orthogonality condition allows for the simultaneous transmission of subcarriers within a narrow frequency range without interfering with each other. At the receiver side, orthogonal signals can be separated using correlation techniques or conventional matched filters. This multiplexing technique offers several significant advantages, including high spectrum efficiency, robustness against multipath fading channels, resistance to multi-user interference, and simplified equalization [1] – [6].

Nevertheless, OMA enables users to use spectrum sources that are independent of each other, providing a powerful solution in terms of reliability and low complexity. Because of their traditional nature, static allocation methods are considered an important reference for resource management in terms of sharing available bandwidth and form the basis for more advanced planning. However, the limitations of the full use of spectrum resources limit the performance of OMA in certain scenarios. In this context, in addition to these advantages offered by OMA, alternative techniques such as non-orthogonal multiple access (NOMA) have been developed. NOMA aims to improve spectral efficiency by allowing the same spectrum sources to be shared by multiple users. However, this brings with it new challenges, such as interference management and increased processing load on the buyer's side [7] – [12]. In this article, the basic working principles and advantages of orthogonal multiple access systems are discussed; An in-depth analysis of interference interactions between different radio communication links that share the same radio spectrum is presented.

Focusing on capacity analysis in orthogonal multiple access systems, the paper examines various parameters to enhance the performance and efficiency of cellular networks. Key factors such as cell radius

*Corresponding Author: Muhammed Furkan KOŞUM, mfurkankosum@baskent.edu.tr

and signal-to-noise ratio (SNR) at the cell edge are evaluated, and the impact of these factors on network coverage is analyzed [13]. Capacity analysis is conducted based on technical parameters such as signal-to-interference ratio (SIR), reuse distance, number of channels, cluster size, and group sizes, aiming to optimize the spectrum efficiency and performance of cellular networks. Considering the signal-to-interference-plus-noise ratio (SINR) and cluster size, the capacity of the network to guarantee a certain quality of service is examined. Traffic management and capacity planning are conducted through performance indicators such as relative traffic load, assignment failure rate, and blocking probability. Capacity analysis is performed in terms of users' data rates, and the data transmission capacity of the network is evaluated. The relationship between SINR and outage probability is examined, focusing on the reliability and continuity of the network. Finally, the study explores how the use of directional antennas can enhance the capacity of cellular networks and make more efficient use of the spectrum. These comprehensive analyses provide strategic planning and optimization opportunities to maximize the capacity of cellular systems and improve network performance.

The aim of the article is to provide a comprehensive analysis of orthogonal multiple access systems, focusing on their working principles, advantages, and limitations in modern cellular networks. This study evaluates key parameters, including capacity, spectral efficiency, and network performance, while addressing challenges such as interference and coverage limitations. Additionally, the paper aims to highlight the importance of technical factors such as SINR, cluster size, and directional antennas in optimizing network performance. By examining these critical aspects, the study seeks to offer valuable insights and strategies for enhancing the efficiency and reliability of cellular systems, serving as a foundation for future research and advancements in radio access technologies.

2. MATERIAL AND METHODS

2.1. Coverage Area Planning

The service area covered by the base stations in a cellular system is called the coverage area. The coverage area can be divided into connection regions that each base station will serve. A base station's connection region is the geometric area where the signal strength received from that base station is greater than from other base stations and high enough to meet quality requirements. The connection region is the coverage area of the base station serving it. Each base station's coverage area is referred to as a cell. To ensure the same transmission quality across all cells, the cells must be of the same shape and size. Hexagonal cell grids are the most used cell model in wireless networks. A base station with an omnidirectional antenna is placed at the center of each cell grid [14] – [17]. An example of a hexagonal cell grid is shown in Figure 1.
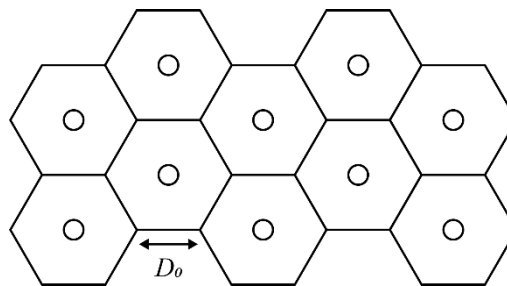
Figure 1. Cellular system coverage pattern

The planning of the coverage area is done by considering any cell. The radius of the considered cell is calculated in such a way that the signal quality is provided throughout the entire cell area. If the cell radius (D_0) satisfies the expression in Equation 1, the required received SNR (γ_0) at the cell boundary is achieved.

$$\frac{c_t P_t}{D_0^\alpha N} \geq \gamma_0 \rightsquigarrow D_0 \leq \left(\frac{c_t P_t}{\gamma_0 N}\right)^{1/\alpha} \tag{1}$$

In Equation 1, P_t is the transmitted power, N is the added noise power, and c_t is a constant containing the antenna gains and the path loss constant, and α is the propagation constant. According to Equation 1, once the radius of the cell is known, the number of cells that should be in the service area is found by dividing the total area by the area of one cell.

2.2. Static Channel Allocation

In modern wireless networks, the number of simultaneous connections within a service area exceeds the number of orthogonal waveforms. An effective way to manage the radio spectrum and provide more radio connections within the service area is to reuse the same frequency as often as possible within the service area. Thanks to the propagation characteristics of radio waves, it is possible to reuse this frequency. By reusing the same waveforms at different locations within the service area, with appropriate spatial separations, mutual interference can be kept quite low. The reuse of waveforms allows multiple connections to be established simultaneously, thereby increasing system capacity. The frequency of spectrum reuse is increased by the higher propagation loss as a function of distance, which is a paradox [12], [14], [18].

SINR constraints can be met by using short communication distances and keeping interfering users at a distance. As signal strength decreases with distance, terminals need to connect to the nearest base station to maximize the received SINR. The SINR (Γ_k) received from a specific mobile terminal in cell k, using the same waveform as N base stations within the service area, can be expressed as shown in Equation 2.

$$\Gamma_k = \frac{\frac{c_t P_k}{r^\alpha}}{\sum_{i=1, i \neq k}^{N} \left(\frac{c P_i}{D_{i,k}^\alpha}\right) + N} \geq \gamma_t \tag{2}$$

In Equation 2, P_i is the transmitter power of base station i and $D_{i,k}$ is the distance between base station i and mobile terminal k, and γ_t is the minimum SINR required for acceptable connection performance. With an appropriate selection of reuse distances $D_{i,k}$, good connection quality can be achieved for all active connections in different cells using the same frequencies. One goal in wireless network design is to achieve a system that allows the transmission of as much information as possible for a given bandwidth or supports as many simultaneous connections as possible.

The classic resource allocation scheme found in all old mobile phone systems is the static resource allocation scheme, also known as fixed channel allocation [19], [20]. In this scheme, a specific fixed number of channels is assigned to each access port. If the anticipated number of active terminals is consistent across all cells in the network, each access port should be allocated the same number of channels to ensure a uniform level of service throughout the system. This allocation is performed by dividing the available C channels into cluster sizes K of approximately equal size. Here, each access port is assigned a group. The group size is calculated as shown in Equation 3.

$$\eta = \left\lfloor \frac{C}{K} \right\rfloor \tag{3}$$

An access port has the right to freely use these channels to communicate with its terminals, but it cannot use any channels from another group. The group size (η) is a rough measure of the system's capacity, as it indicates the maximum number of simultaneous connections that can be supported in each cell.

Since the received power decreases monotonically with distance, the interference resulting from the repeated use of channels in the system depends on how far away the same channel is reused. To maintain

a sufficiently high SINR in base station-terminal connections, channels in one group cannot be reused in a cell that is too close to the first cell. A channel assignment is characterized by the minimum reuse distance (D) between two cells using the same channel. If many channel groups are used, the reuse distance will be large, and a relatively high SINR will be obtained. Such a procedure means that the number of channels available at each access port is reduced, resulting in lower system capacity. On the other hand, if a lower SINR can be tolerated, D can be made smaller. In this case, fewer channel groups are required, and the raw capacity (η) will be higher. There is a trade-off between transmission quality and transmission capacity [14].

Assuming that the K distinct waveform groups are numbered 1, 2, …, K, each cell is assigned one of these numbers. An effective allocation strategy should ensure symmetrical reuse across the service area while maximizing the minimum distance (D) between cells using the same channels. The allocation process then consists of forming a symmetric set of channel groups and repeating this set over the service area until it is fully covered [20] – [22]. Figure 2 illustrates several clusters of varying sizes for hexagonal cells.
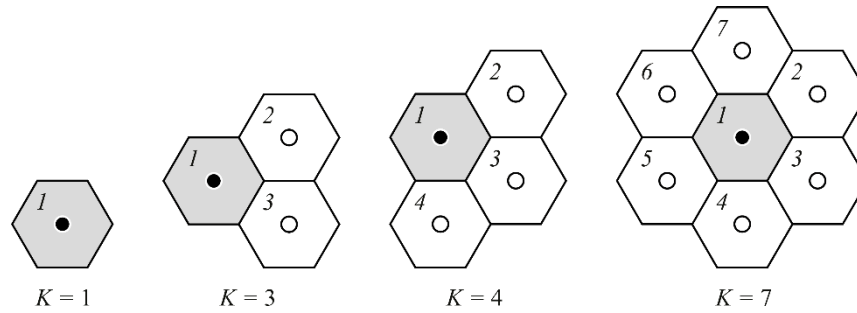
Figure 2. Examples of cluster sizes K = 1, 3, 4, 7 for hexagonal cells

The K values used in Figure 2 give a fully symmetric cell plan. Figure 3 shows the symmetric hexagonal cell plan for the case K = 7. These cell plans are characterized in that the patterns formed by cells with the same label are the same for all labels simply shifted. Furthermore, in such a cell plan, each cell has six nearest neighbors, all at the same distance D.
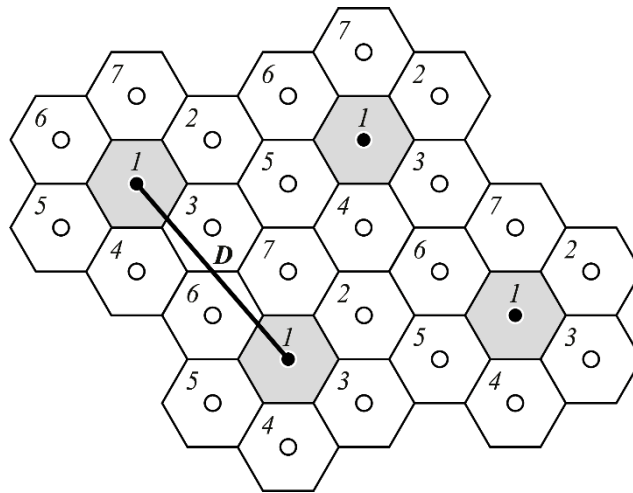
Figure 3. Examples of symmetric hexagonal cell plans

For fully symmetrical hexagonal cell layouts, the relationship between K and D is given $\Delta = D/D_0 = \sqrt{3K}$, where Δ is the normalized reuse distance. It is possible to show that fully symmetrical cell layouts exist for all integer values of K that can be written as $K = (i + j)^2 - ij$, where i,j = 0, 1, 2, 3, …. Therefore, the possible values for K are K = 1, 3, 4, 7, 9, 12, 13, … [23], [24]. Here, K = 1 corresponds to the trivial case

where all channels are used in all cells. These *K* values are valid only for hexagonal cell shapes. Other cell shapes, such as rectangular or triangular, have different valid values for the cluster size *K*. The principle of finding *K*, as previously mentioned, is to maintain symmetry in the cell layout.

2.3. Guaranteed Service-Based Capacity Analysis

In this section, some quite simplifying assumptions are made in the initial attempt to evaluate the capacity of a guaranteed service system based on static resource allocation [25]. The capacity of a wireless network can be measured as the average number of simultaneous radio connections supported by the system, $\eta = C/K$ users per cell. Considering the covered area, the area capacity is defined as $\eta_A = C/(KA_c)$ users per unit area, where A_c is the cell area. Therefore, calculating the capacity of a hexagonal cellular system is reduced to determining the cluster size *K*.

Assuming that a mobile phone system with a symmetrical hexagonal cell layout, as shown in Figure 4, uses a modulation scheme requiring a minimum SINR (γ_t) for acceptable connection performance, the system is examined for the downlink [26].
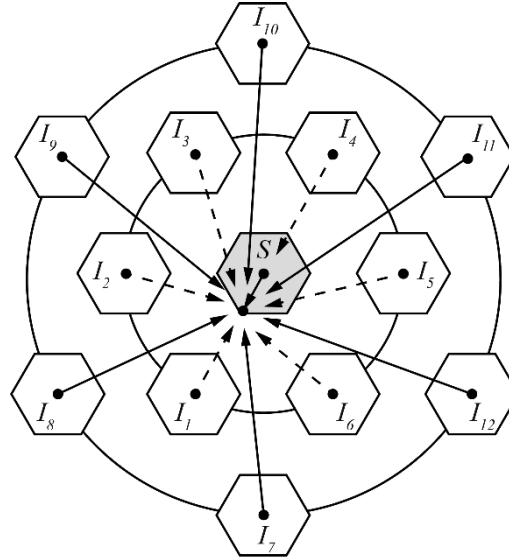
Figure 4. Common channel cell layers for downlink of hexagonal cellular systems

The transmitters use fixed transmit power *P*. Therefore, the SINR at a particular terminal in a cell using a particular channel is evaluated. To guarantee the minimum SINR for this terminal, the worst case where the channel is used in all these co-channel cells is considered. Also, the lowest SINR in the center cell is found when there is a terminal at the cell boundary, at one of the corners of the hexagon [14]. The SINR (Γ) at the mobile terminal is expressed as in Equation 4.

$$\Gamma = \frac{\frac{cP}{D_0^\alpha}}{\sum_k \left(\frac{cP}{D_k^\alpha}\right) + N} = \frac{1}{\sum_k \left(\frac{D_0}{D_k}\right)^\alpha + \frac{1}{\gamma_0}} \geq \gamma_t \tag{4}$$

In Equation 4, *N* is the noise power, *c* is an arbitrary propagation and antenna-related constant.

When considering this statement, two special cases can be distinguished:

Noise/Range-Limited Case: Interference is much smaller than thermal noise. In this situation, it can be said that access points are placed very sparsely due to low traffic demand, or the system is experiencing coverage issues. This is typically the case in a system first deployed in rural areas. In these systems, the problem is coverage, not capacity.

Interference-Limited Case: Interference is much stronger than thermal noise. The received signal

strength is high, and there are no coverage issues. This is typically the case in mature, heavily loaded systems in urban areas. In these systems, the focus is on capacity rather than coverage.

In a symmetrical hexagonal cell layout, each cell has exactly six co-channel neighbors at a distance D. Additionally, for all values of K given by the expression $K = (i + j)^2 - ij$, where $i,j = 0, 1, 2, 3, \ldots$, there are six additional co-channel cells at a distance of $\sqrt{3}D$, six at a distance of $\sqrt{4}D$, six at a distance of $\sqrt{7}D$, and six at a distance of $\sqrt{K}D$, and so on. It is also assumed that all interference sources in the same interference layer are at the same distance. While some interference sources may be closer than the nominal distance, and others farther away, this approach generally does not lead to significant errors unless very small reuse distances are used. Even with this approach, a closed-form expression for the SINR received at the mobile terminal is not obtained. Another approach that provides a closed-form expression is to visualize the co-channel interference sources as shown in Figure 5. Here, it can be assumed that there are six interference sources at a distance D from the cell of interest, 12 interference sources at a distance $2D$, and 18 interference sources at a distance $3D$.
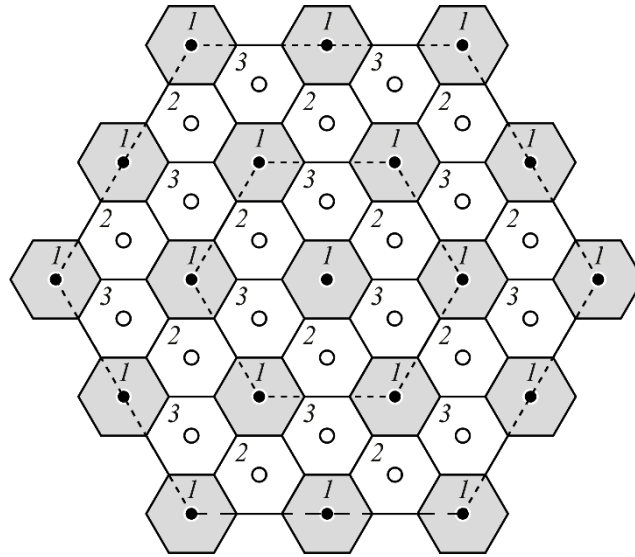
Figure 5. -channel interference layers plot when $K = 3$

Here, the received SINR Downlink (Γ_{DL}) is calculated as in Equation 5.

$$\Gamma_{DL} = \frac{1}{6 \sum_{n=1}^{+\infty} \dfrac{n}{\left(n\sqrt{3K}\right)^{\alpha}} + \dfrac{1}{\gamma_0}} = \frac{1}{\dfrac{6\zeta(\alpha - 1)}{\left(\sqrt{3K}\right)^{\alpha}} + \dfrac{1}{\gamma_0}} \geq \gamma_t \tag{5}$$

Here ζ is the Riemann zeta function. It is written as in Equation 6.

$$\zeta(\alpha - 1) = \sum_{n=1}^{+\infty} \left(\frac{1}{n^{\alpha-1}}\right) = \begin{cases} +\infty, & \alpha = 2 \\ 1.6449, & \alpha = 3 \\ 1.2021, & \alpha = 4 \\ 1.0823, & \alpha = 5 \end{cases} \tag{6}$$

For large values of α ($\alpha \geq 4$), it is noticed that the function $\zeta(\alpha - 1)$ converges to 1. This means that the co-channel interference is dominated by the six closest interference sources [14]. A similar analysis can be done for Uplink. The SINR Uplink (Γ_{UL}) received from the base station is calculated as in Equation 7.

$$\Gamma_{UL} = \frac{1}{6 \sum_{n=1}^{+\infty} \left(\dfrac{n}{\left(n\sqrt{3K} - 1\right)^{\alpha}}\right) + \dfrac{1}{\gamma_0}} \geq \gamma_t \tag{7}$$

In Equation 5 and Equation 7, γ_t represents the minimum SINR required for acceptable link performance, γ_0 represents the required received SNR achieved at the cell boundary, α is the propagation constant, K represents the cluster size of available channels divided into approximately equal sizes, and n represents an integer.

2.4. Traffic-Based Capacity Analysis

In this section, some simplifying assumptions are made in the initial attempt to evaluate the capacity of a guaranteed service system based on static resource allocation [25]. The number of channels at each access port is a rough but useful measure of capacity. It explains the ability to serve users from the operator's perspective but does not reflect user satisfaction. In general, the number of active users within a cell is not constant and changes over time. Calls in cellular networks are typically modeled as a Poisson process with the expected value of λ calls [27], [28]. The random number of mobile terminals in a particular cell during a given observation time interval is denoted by M_c and is obtained as $\Pr(M_c = k) = (\omega A_c)^k e^{-\omega A_c} /k!$. Here, ω is the number of calls per unit area (A_c), and $\lambda = E\{M_c\} = \omega A_c$ represents the expected number of calls [14].

A cellular system with η channels per cell faces a failure in assigning channels to users when the number of calls exceeds the available number of channels. The assignment failures within the cell are calculated as $Z = \max(0, M_c - \eta)$. Using this expression, the assignment failure rate (v_p) can be found as shown in Equation 8.

$$v_p = \frac{E\{Z\}}{E\{M_c\}} = \sum_{k=n}^{+\infty} (k - \eta) \frac{(\omega A_c)^{k-1}}{k!} e^{-\omega A_c} \qquad (8)$$

The relative traffic load is defined as $\varpi_\eta = \omega A_c/\eta = \omega A_c K/C$. Another way to express the traffic load is by considering the expected number of terminals per cell relative to the total number of channels in the entire system, which is defined as $\varpi_c = (\omega A_c)/C = \varpi_\eta/K$.

Systems that rely on static resource allocation can be analyzed relatively easily using the traditional telephony traffic model. Assuming limited terminal mobility (where terminals typically remain within a single cell for the duration of a call), call management in each cell can be modeled as independent M/M/η blocking systems. In this type of queuing system, incoming calls follow a Poisson process and are served by servers (η, the number of available channels per cell). If all channels are occupied, the calls are blocked and dropped. The classical metric used to evaluate this system is the blocking probability, which is the likelihood that a new incoming call encounters all channels busy and is refused service. The blocking probability (E_η) is calculated using the Erlang-B formula, as shown in Equation 9 [29].

$$E_\eta = \frac{\dfrac{\rho^\eta}{\eta!}}{\sum_{k=0}^{\eta} \dfrac{\rho^k}{k!}} \qquad (9)$$

Here ρ is the traffic load. The relative traffic load is defined as $\rho_\eta = \rho/\eta$. The traffic capacity is defined as $\rho_{max} = \max\{\rho | E_\eta < \rho_0\}$ erlang, like telephone channels. Here ρ_0 is the required blocking probability. The area traffic capacity is defined as $\rho_c = \rho_{max}/A_c$ erlang/unit area.

2.5. Best-Effort Data Services

Mobile data networks provide users with variable data rates. Therefore, the number of active users within a cell affects not the capacity of these systems but the peak and average data rates. This section attempts to relate the cell capacity of a mobile data system to adaptive data rates and the spectrum reuse

characteristics. Subsequently, a relationship is established between the cost and peak rates in the system to provide insight into how future systems should be deployed cost-effectively [30], [31]. The Downlink in a single circular cell is examined, where the expected received power decreases with the distance from the base station at the cell center by a power of α. It is assumed that the system is channelized as before, but the channel sizes may vary. The available bandwidth per cell is expressed as $W = W_s/K$, where W_s is the bandwidth allocated to the system. An ideal transmission system operating at the Shannon rate, aligned with the peak data rate R_{max} and using a TDMA access scheme, is assumed [14]. The SINR equation for a particular active user in the cell is written as $\Gamma_{DL}(D) = (cP_t/D^\alpha)/(\sum_k(cP_t/D_k^\alpha) + N)$.

By defining the normalized distance $\Delta = D/D_0$ (where $0 \leq \Delta \leq 1$), the SINR equation is rewritten as $\Gamma_{DL}(\Delta) = ((cP_t/D_0^\alpha)/(\sum_k((cP_t)/(D_k^\alpha)) + N))/\Delta^\alpha = \Gamma_{DL}(D_0)/\Delta^\alpha$.

The data rate R of the active user in the cell is written as in Equation 10.

$$R(\Delta) = min\left\{R_{max}, c_w W \ log_2\left(1 + \frac{\Gamma(D_0)}{\Delta^\alpha}\right)\right\} \tag{10}$$

Here c_w ($0 \leq c_w \leq 1$) is a constant describing the gap between the upper capacity limit (Shannon capacity) and the actual channel capacity. It is seen that the data rate at the center of the cell is limited by the peak data rate R_{max}. As we approach the cell boundary, the data rate decreases, and we have the edge data rate (R_{min}) at the cell edge ($\Delta = 1$) [14]. R_{min} is written as in Equation 11.

$$R_{min} = c_w W \ log_2\left(1 + \Gamma(D_0)\right) \tag{11}$$

Thus, the edge data rate is also defined by the cellular design and the edge SNR. The data rate in Equation 10 can also be expressed in terms of the minimum data rate as $R(d) = min\{R_{max}, c_w W \ log_2(1 + (2^{R_{min}/cW}/\Delta^\alpha)\}$.

Assuming that the users are uniformly distributed with a circular approach, the expected data rate for some randomly selected users is calculated as in Equation 12.

$$\bar{R} = E[R] = \int_0^1 R(x)2xdx \tag{12}$$

This expression gives the average data rate that a user will experience when equal amounts of resources are given to each user. Therefore, this expression can be called cell capacity.

2.6. Outage-Based Capacity Analysis

In real cellular systems, the received signal levels do not depend smoothly on the distance. On the contrary, the received signal can fluctuate significantly due to shadowing effects. A simple approach to address signal variation is to add a fading margin above the required minimum SINR. In practice, to guarantee that all terminals achieve a sufficient SINR in this way would require impractically large reuse distances and hence uninterestingly low capacities. Therefore, any real cellular system will abandon a small fraction of terminals that do not meet the SINR requirement for a higher capacity [14], [32] – [34].

To this end, this section begins by considering the stochastic variable Q, which represents the number of terminals assigned to a channel but cannot provide a sufficient SINR. From the user's perspective, there is no benefit to having taken a channel if the channel becomes useless. It is conceivable that fast-moving terminals can quickly switch to a more favorable state than slow-moving terminals. However, considering the latter case, it may not even be possible to distinguish between a traditional assignment error and a weak channel. In both cases, communication is not possible. The performance measure can now be generalized and the rate at which the system fails to assign useful channels is called the total assignment failure rate [14]. The total assignment failure rate is defined as in Equation 13.

$$v = \frac{E\{Z\} + E\{Q\}}{E\{M_c\}} = v_p + \chi \tag{13}$$

Therefore, the primitive assignment failure rate (v_p) is the assignment failure rate for a system design for conditions without co-channel interference. Here, the interference rate $\chi = E\{Q\}/(\omega A_c)$ is added to the new expression. This converges to the outage probability ω at moderate traffic loads as $\chi \approx \Pr(\Gamma < \gamma_t)$. Considering the hexagonal cellular system Uplink, the SINR equation received at base station i at distance r from the mobile terminal is written as $\Gamma_{\text{UL}} \approx 1/(\sum_{k=1}^{M}(X_k m_k P_k/m_i P_i)(r/D_k)^\alpha)$. Here, X_k, is the probability of activity at mobile terminal k. If mobile terminal k is active in the cell, $X_k = 1$, otherwise $X_k = 0$. The quantity in this equation is the sum of a random number of independent log-normally distributed random variables. It can be assumed that the channel assignments in different cells are independent. The number of terms in this sum is distributed binomially with the probability in Equation 14.

$$q = 1 - \sum_{k=0}^{\eta}\left(1 - \frac{k}{\eta}\right)\frac{(\omega A_c)^k}{k!}e^{-\omega A_c} = \varpi_\eta\left(1 - v_p\right) \tag{14}$$

Here q is the activity factor. It is proportional to the relative traffic load and the primitive assignment failure rate.

In most systems, the base station selection is such that the strongest base station is selected instantaneously. This may not be the base station geographically closest to the mobile terminal due to the shadowing effect. A distant terminal may create more damaging interference than a nearby terminal.

It is not possible to calculate the probability of outage precisely. It is necessary to resort to numerical integrations, approximations or computer simulations. The approximation is made by assuming that the interference is dominated by the strongest interference source. In addition, the six nearest interference sources are also considered, all of which are at approximately $D = D_0\sqrt{3}K$ from the receiver. For a certain number of active interference sources (l) and a certain distance (r), the outage probability can be estimated as $\Pr(\Gamma < \gamma_t | r, l) \approx 1 - [Q((10\alpha \log_{10}(r / D_0) - 10 \log_{10}((3K)^{\alpha/2} / \gamma_t)) /(\sigma\sqrt{2}))]^l$. Here, the same transmitter power is assumed for all active terminals. When averaged over the distance r, the average probability obtained for a certain number of interference sources is written as $\Pr(\Gamma < \gamma_t | l) \approx 1 - \int_0^1[Q((10\alpha \log_{10}(x) - 10 \log_{10}((3K)^{\alpha/2} / \gamma_t)) /(\sigma\sqrt{2}))]^l 2x dx$.

With the activity factor (q), the receiver is affected by the interference from the interference source (l) with the probability $v_l = (6 \quad l) q^l (1 - q)^{6-l}$. In this case, the average outage probability is written as $\Pr(\Gamma < \gamma_t) \approx 1 - \sum_{l=0}^{6} v_l \int_0^1[Q((10\alpha \log_{10}(x) - 10 \log_{10}((3K)^{\alpha/2} / \gamma_t)) /(\sigma\sqrt{2}))]^l 2x dx$.

When the cellular system is modeled as a finite waiting room, the total blocking probability (grade of service) including the effect of fading of channels is written as $\text{GoS} = E_\eta + \chi$ [14].

2.7. Directional Antennas and Sectorizations

All the systems analyzed in the previous sections use omnidirectional antennas. This is considered a common solution for good coverage of the service area. Because a radio access point usually has no information about where the mobile terminal is located. In addition to providing low antenna gain, omnidirectional antenna systems have the disadvantage of spreading the interference power of the access port in all directions, not just the desired direction. When using directional transmit antennas, the interference levels are significantly reduced. In addition, a directional receive antenna suppresses interference from unwanted directions. This results in lower reuse distances [14], [35].

Directional antennas tend to be quite bulky. Therefore, they are most used in radio access points. The antennas can be fixed or adaptable. Radio access points using fixed directional antennas usually require an array of antennas, each covering a sector with a peak at the radio access point. A mobile terminal connected to a radio access point moving in the service area is served by one of the directional antennas. As the mobile terminal moves, a transfer to a different antenna may be required. On the other hand, an

adaptive antenna array continuously monitors the mobile terminal. This has been shown to be a very effective tool for both mobile and fixed wireless systems. In this context in particular, the application of modern signal processing techniques to electronically steerable array antennas have proven useful in recent years. This section analyzes the simpler, fixed antenna case [14]. Let us assume that the base stations are equipped with ideal sector antennas with the relative density in the horizontal plane of the far field as given by Equation 15.

$$S(\phi) \approx \begin{cases} 2\pi/\phi_h &, |\phi| \leq \phi_h / 2 \\ 1/A_{sl} &, |\phi| > \phi_h / 2 \end{cases} \tag{15}$$

The antenna radiation diagram is characterized by the horizontal beamwidth ϕ_h and the side beam attenuation A_{sl}. An omnidirectional antenna is described by the horizontal beamwidth $\phi_h = 2\pi$. It is also assumed that the radio access point is in the center of the cell and directs one of its antennas in the direction $\phi = 0$. The SINR Uplink received from a particular mobile terminal within the cell $\phi = 0$ is now written as $\Gamma_{UL} = (c_t P_{k,0} S(\phi_0)/r^\alpha)/(\sum_{i=1}^{M}(X_i c_t P_{k,i} S(\phi_k)/(D_{k,i}^\alpha + N)))$.

The terminal communicating with the base station is assumed to be within the main beam of the antenna. The signals from the interfering mobile terminals using the same channel outside the main beam are greatly attenuated. However, the signals from the mobile terminals within the main beam are received with higher power than in the omnidirectional case. However, since the desired signal has the same antenna gain, the relative interference power of these latter terminals remains the same as in the omnidirectional case [14], [36].

When the side beam attenuation is large and the noise is neglected, the SINR equation is rewritten as $\Gamma_{UL} = (m_0 c P_0/r^\alpha)/(\sum_{k:|\phi_k|<\phi_h/2}(X_k m_k c P_k/D_k^\alpha) + N)$.

Compared to the omnidirectional case, the SINR increases at the same rate as the effective number of interfering terminals falling on the main beam. Approximately, it can be said that an antenna with a main beamwidth of $2\pi/N$ reduces the average interference power by a factor of N.

The use of directional antennas in practice is a great way to decrease the number of base station sites and reduce the system's infrastructure costs. Figure 6 illustrates the plan to put three base stations in the same place.
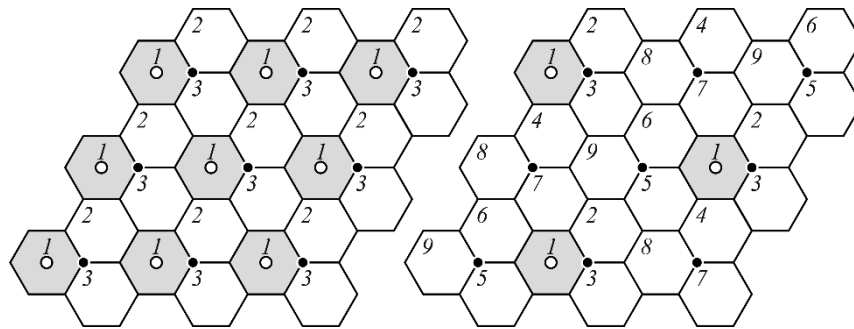
Figure 6. 120-degree field patterns for 1/3 and 3/9 reuse in hexagonal cellular system

The cluster is in the corner of three cells, where each base station uses 120° sector antennas to cover its cell. Otherwise, the cellular layout remains the same. Thanks to the directional antennas, only 1/3 of the interference is seen by the base station, reducing the interference power. It is shown that for reuse factors that are divisible by three, it is possible to find frequency assignments where the nearest common channel neighboring base stations do not face each other, thus avoiding the worst source of interference. Such reuse patterns are denoted as $x\sqrt{3x}$, where x is the reuse factor for the number of base stations. Common examples are 1/3, 3/9, and 4/12. In the 1/3 case, all base stations use all frequencies but divide the channels into three groups, one for each sector. On the other hand, placing the base station in the corner of the cell results in the terminal being twice as far from the base station as it is from the cell center [14], [37], [38].

3. RESULTS AND DISCUSSION

3.1. Reuse Distance

A mobile radio link scenario is established along a highway as shown in Figure 7. The transmitters use the same transmission power and the same waveforms. The modulation and detection schemes require that the SINR at the receivers be at least γ_t = 15 dB to achieve good link quality. It is assumed that the propagation loss is modeled as a power-law distance dependency. For propagation constants α = 4 and α = 2, the minimum distance D_{12} required for receiver M_2 to meet the SINR requirement is determined as follows.
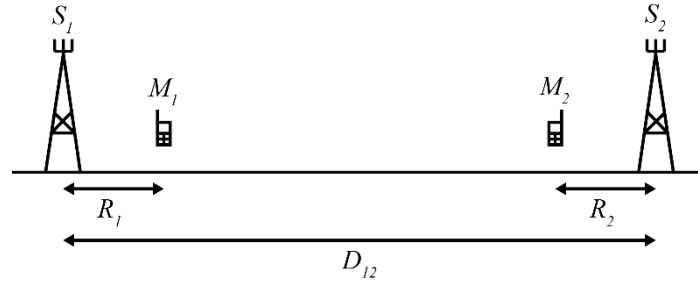
Figure 7. Mobile radio connection scenario

In this scenario, it is assumed that $D_0 = R_1 = R_2$ and $P_1 = P_2 = P_t$. In this case, according to Equation 2, the SIR received from receiver M_2 is written as $\Gamma_2 = 1/((D_0/(D_{12} - D_0))^\alpha + 1/\gamma_0) \geq \gamma_t$. From this equation, the separation distance and normalized reuse distance are obtained as in Equation 16.

$$\Delta \geq \left(1 + \frac{1}{\left(\frac{1}{\gamma_t} - \frac{1}{\gamma_0}\right)^{1/\alpha}}\right) \tag{16}$$

Figure 8, generated using Equation 16, shows the normalized reuse distance as a function of the average received SNR at the cell boundary.
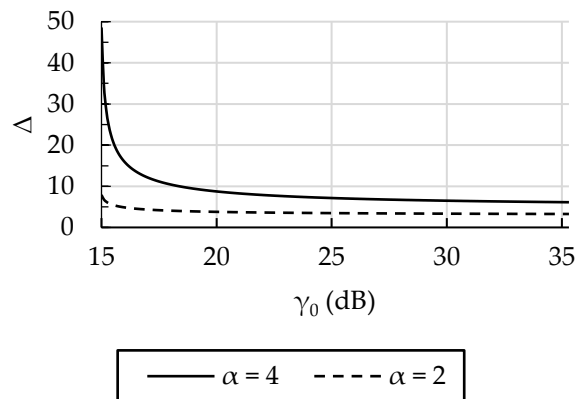
Figure 8. Normalized reuse distance as a function of average SNR at the cell boundary

As γ_0 increases, it is observed that the reuse distance reaches a minimum and the system becomes interference-limited (with N being negligible in the presence of interference). The received SINR is a deterministic quantity, and the SIR is always achieved when the above distance relationship is satisfied. In the case of shadowing effects, the received SINR becomes a random variable, and the reuse distance is

determined for a given outage probability

The minimum physical distance required between two transmitters using the same waveform to achieve a certain link quality is called the reuse distance. The inverse of this distance provides a rough measure of how many radio links per unit length can reuse the available bandwidth. As noted, the SINR rapidly increases with the increase of the D_{12} distance. It is observed that the SINR depends not on absolute distances but only on the ratio between D_{12} and R_2. This indicates that the system is scalable, allowing distance scales to be changed without affecting the SIR. However, this scaling cannot be pushed to extremes because, at very short distances, the propagation conditions approach line-of-sight conditions (α = 2). It is also noted that the reuse distance decreases as the propagation exponent α increases. Furthermore, the reuse distance depends on the required minimum SINR, which is related to the modulation and detection schemes used. Waveforms and detectors that are more resistant to interference will allow for more frequent reuse.

3.2. Cluster and Group Size

A mobile telephone system with $C = 120$ channels uses a modulation scheme that requires a minimum SIR of at least $\gamma_t = 15$ dB to achieve acceptable connection performance. It is assumed that the propagation loss depends only on the distance, increases with the fourth power of the distance ($\alpha = 4$), and the system is interference limited. The maximum number of channels that the system can provide per cell is calculated.

Assuming the uplink case and considering the six closest interference sources, SINR is calculated as $\Gamma = 1/(6/(\sqrt{3K} - 1)^4) \geq 15$ according to Equation 7. In this case, $K \geq 1/3 \, ((6 \times 15)^{1/4} + 1)^2 \approx 5.6$ is obtained. When we look at the situation in the $K = (i + j)^2 - ij$, where $i,j = 0, 1, 2, 3, \ldots$, it is seen that there is a symmetric cell plan for K values. According to the inequality $K \geq 5.6$, it requires the use of $K = 7$ for the reuse distance. As a result, using Equation 3, $\eta = \lfloor C/K \rfloor = \lfloor 120/7 \rfloor = 17$ is calculated as channel/cell.

3.3. Assignment Failure Rate

As observed in Equation 8, the assignment failure rate is a function that increases in ω and decreases in η. What is less obvious is that when we increase ω by the same amount, i.e., when we keep ϖ_η constant, the assignment failure rate decreases in η. In other words, a multi-channel system is more efficient than a low-channel system. This result is illustrated by the following mobile phone system scenario.

A mobile phone system designed for $K = 9$ channel groups is assumed to have a cell radius of 1 km. The system has $C = 720, 180$ and 45 channels. The maximum allowed assignment failure rate is given as 1%. The capacity of the system is calculated according to this scenario.

The area of the cell is calculated as $A_c = 1^2(3\sqrt{3})/2 \approx 2.6$ km². According to Equation 3, the available $\eta = \lfloor C/K \rfloor = 80, 20$ and 5 channels/cell are found.

When we look at the 1% assignment failure rate in Figure 9, which was created using Equation 8, it is found as $\varpi_\eta \approx 0.89, 0.72$ and 0.39.
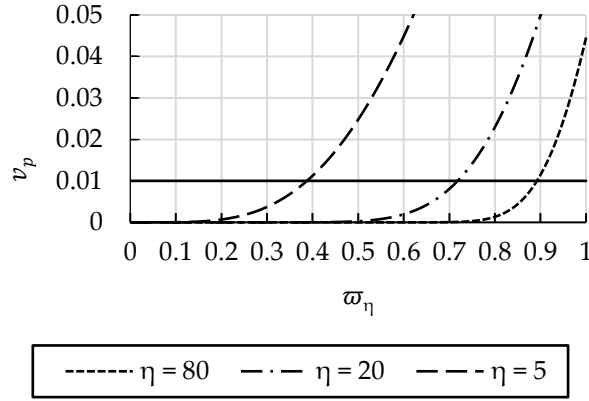
Figure 9. Channel assignment failure rate as a function of relative traffic load for η = 80, 20 and 5 channels/cell

According to these results, the capacity is calculated as $\omega = (\eta\varpi_\eta)/A_c \approx 27, 5.5$ and 0.75 calls/km². The number of channels/cells increases by 4 times between the three different cases. It is observed that the capacity increases by 7 and 5 times due to channel gain, respectively. It should be noted that the capacity depends primarily on η and A_c. When the last expression is rewritten, $\omega = \eta\varpi_\eta/A_c = C\varpi_\eta/KA_c$ is obtained. Using $\Delta = D/D_0 = \sqrt{3K}$, the approximation $K = \Delta^2/3 \approx c(\alpha)\gamma_t^{2/\alpha}$ is obtained. When these expressions are used together, $\omega \approx c'(\alpha)C\varpi_\eta/\gamma_t^{2/\alpha}A_c$ is obtained. This expression is written in dB as in Equation 17.

$$10log_{10}(\omega) \approx 10log_{10}\big(c'(\alpha)\big) + 10log_{10}(C) + 10log_{10}\big(\varpi_\eta\big) - \left(\frac{20}{\alpha}\right)log_{10}(\gamma_t) - 10log_{10}(A_c) \qquad (17)$$

As shown in Equation 17, there are three fundamental ways to increase the capacity of a wireless communication system:

Increase C: Expanding the available spectrum resources is often challenging.

Reduce γ_t: The required threshold can be lowered by utilizing modulation, detection, and channel coding schemes that are more resistant to interference. Since a decrease in K leads to a reduction in the cluster size K, the factor ϖ_η also decreases, effectively doubling the gain.

Reduce A_c: In practice, there is no strict limit to how much capacity can be increased by reducing the cell size. Smaller cells improve propagation conditions (with $\alpha = 2$ under line-of-sight conditions), which in turn slightly reduces the constant c'. However, this approach increases the number of cells per unit area. The capacity is roughly proportional to the total number of base stations in the system because A_c has an inverse correlation with the number of base stations.

Another observation is that system capacity increases under poor propagation conditions (as α increases).

3.4. Blocking Probability

As observed in Equation 9, the blocking probability is a function that increases in ρ and decreases in η. To put it differently, a system with numerous channels is more effective than one with few channels. This result is illustrated with the following mobile phone system scenario.

A mobile phone system designed for $K = 9$ channel groups is assumed to have a cell radius of 1 km. There are $C = 720, 180$ and 45 channels in the system. The maximum blocking probability is given as 2% erlang/km². According to this scenario, the area traffic capacity of the system is calculated.

The area of the cell is calculated as $A_c = 1^2(3\sqrt{3})/2 \approx 2.6$ km². According to Equation 3, the available $\eta = \lfloor C/K \rfloor = 80, 20$ and 5 channels/cell are found.

When we look at the 2% blocking probability in Figure 10, which was created using Equation 9, it is

found as $\rho_\eta \approx 0.87, 0.68$ and 0.33.
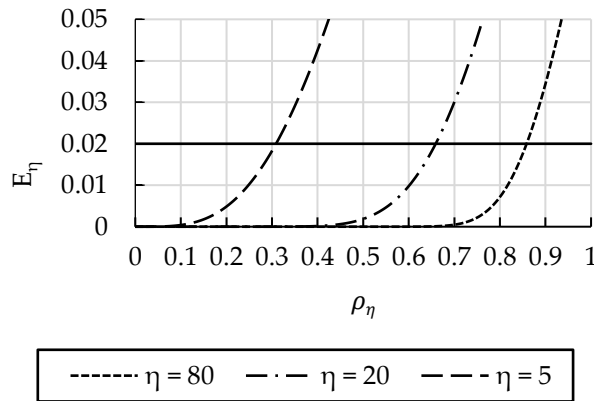
Figure 10. Blocking probability as a function of relative traffic density per channel and cell

According to these results, the area traffic capacity is calculated as $\rho_c = (\eta\rho_\eta)/A_c \approx 27, 5.2$ and 0.64 erlang/km². As can be seen, the capacity results obtained for the maximum assignment failure rate of 1% yield approximate values.

3.5. Data Rate

The following mobile phone system scenario illustrates a practical issue where data rates are adjusted in discrete steps rather than continuously.

Consider a mobile phone system designed for $K = 3$ channel groups with a total system bandwidth of 15 MHz. This system employs an adaptive modulation scheme operating with a discrete rate set $R = 1, 2, 4, 8,$ and 16 Mbps, and a threshold SNR $\gamma_0 = 4$ dB at the 50% Shannon limit ($c_w = 0.5$). The path loss exponent is $\alpha = 4$. The goal is to calculate the cell capacity per channel of the system.

By combining Equation 4 and Equation 5, the received SINR is calculated as $\Gamma(D_0) \approx 1/(6\zeta(\alpha\text{-}1)/(\sqrt{3K})^\alpha + 1/\gamma_0) = 1/((6 \times 1.2021)/(\sqrt{9})^4 + 1/4) \approx 3$.

The channel bandwidth is calculated as $W = W_s/K = 15/3 = 5$ MHz. The minimum edge data rate of the system is calculated as: $R_{min} = c_w W \log_2(1 + \Gamma(D_0)) = 2.5 \log_2(1 + 3) = 5$ Mbps. This indicates that the highest sustainable data rate at the cell edge from the discrete set is 4 Mbps.

As we move towards the cell center, SINR increases. The distance d_8 required to use the next data rate of 8 Mbps is calculated using Equation 10 in terms of R_{min} as $R(d_8) = c_w W \log_2(1 + \Gamma(D_0)/(d_8^\alpha)) \leadsto d_8 = (3/(2^{8/2.5}\text{-}1))^{1/4} \approx 0.78$. Similarly, the distance d_{16} required for the next data rate of 16 Mbps is calculated as $d_{16} = (3/(2^{16/2.5} - 1))^{1/4} \approx 0.44$.

Assuming a circular cell and considering that the proportion of users in each area is proportional to that area, the average data rate is calculated as $\bar{R} = E[R] = \int_0^1 R(x)2xdx = 16d_{16}^2 + 8 \times (d_8^2 - d_{16}^2) + 4 \times (1 - d_8^2) = 7.98$ Mbps.

The highest data rate ($R_{max} = 16$ Mbps) is used in only 44% of the cell radius, corresponding to about 19% of the users. If the highest data rate is disregarded, the average data rate decreases by less than 1 Mbps, a common scenario in noise-limited systems.

Considering the noise-limited case, and allowing W and R_{max} to approach infinity, the average data rate is calculated as shown in Equation 18.

$$\bar{R} = E[R] = \int_0^{\Delta_0} R(x)2xdx = (2\alpha - 3)R_{max}\left(\frac{R_{min}}{R_{max}}\right)^{2/\alpha} - (2\alpha - 4)R_{min} \tag{18}$$

In this case, the average data rate is not limited since R_{max} goes to infinity. This is of course to be

expected when infinite bandwidth is available.

3.6. Outage Probability

Consider a wireless network with 100 channels and an SINR threshold γ_t = 20 dB for good signal quality on the downlink. The path loss follows a log-normal distribution, with a standard deviation of σ = 6 dB and a log-mean proportional to $40\log_{10}(r)$, where r is the distance between the transmitter and the receiver. Additional noise is neglected.

Calculation of channel groups (cluster size, K) without fading effects: Neglecting fading effects (deterministic path loss), the number of channel groups under high traffic loads is calculated as $K \geq (6\gamma_t)^{2/\alpha}/3 = 120^{2/4}/3 \approx 3.7$ using Equation 5. Considering $K = (i + j)^2 - ij$, where i, j = 0, 1, 2, 3, …, it is determined that the cluster size K should be 4. Hence, the capacity per cell is calculated as $\eta = 100/4 \approx 25$ channels per cell.

Outage probability under high traffic loads: Given the cluster size (K) obtained in the deterministic case, the outage probability under high traffic loads is evaluated. According to Figure 11, the outage probability for K = 4 and γ_t = 20 dB is approximately 3%.

Required cluster size for maximum 5% outage probability: To achieve a maximum outage probability of 5% under high traffic conditions, Figure 11 indicates that the cluster size (K) needs to be 28. Therefore, the capacity per cell in this scenario is $\eta = 100/28 \approx 3$ channels per cell.

This represents an approximately eightfold decrease in capacity compared to the scenario without fading effects.
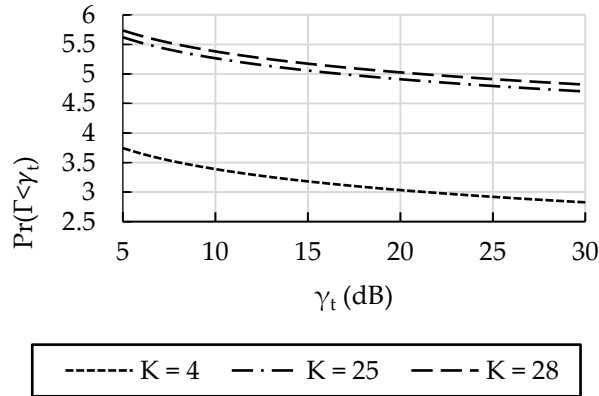
Figure 11. Outage probability of cellular system for different cluster sizes in shadowing effective channels

3.7. Group Size with Sector Antenna

In the following application, such a system is analyzed using simple analytical tools.

Consider a mobile phone system with 120 channels, where the radio access points use ideal 120° sector antennas placed at the corners of the cells. The system employs a modulation scheme requiring a minimum SIR threshold of γ_t = 15 dB to achieve acceptable connection performance. It is assumed that the path loss depends solely on distance, increasing with the fourth power of distance (α = 4), and that the system is interference limited. Additionally, it is assumed that all base stations using a particular channel group broadcast in the same direction within their cells. Without considering fading, the maximum number of channels per cell that the system can offer is calculated.

The worst-case interference scenario occurs when a terminal is located at the maximum distance from the radio access point, i.e., at $2D_0$. The 120° sector antennas experience interference from only two of the six nearest co-channel neighbors. Since all radio access point antennas are oriented in the same direction, both interfering sources must be located behind the serving radio access point terminal. The distance D

from the radio access point to the terminal under consideration is approximately calculated as follows. Considering only the first tier of interference, the SIR is given by $\Gamma \approx (cP/(2D_0)^4)/(2cP/D^4) = (\Delta/2)^4/2 > 15$. This equation simplifies to $\Delta > 2 \times 15^{1/4} \approx 3.94$. Given that $\Delta = \sqrt{3K}$, it follows that $\Delta^2/3 \approx 5$, leading to $K = 7$. Therefore, the number of channels per cell is $\eta = \lfloor C/K \rfloor = \lfloor 120/7 \rfloor = 17$ channels per cell.

This result is the same as the value of η obtained for omnidirectional antennas in the section on cluster and group size. However, the number of radio access points required is only 1/3 of the number used in the omnidirectional case.

4. CONCLUSIONS

This article examines the effects of important factors such as reuse distance, cluster and group size in mobile radio connection scenarios by performing capacity analysis in orthogonal multiple access systems. The findings clearly show the effects of various parameters on system performance.

In the reuse distance analysis, the minimum physical distance required for a certain connection quality is determined depending on the SINR requirements of the receivers. As shown in Table 1, it is observed that with the increase of this distance, the SINR increases rapidly, and the system has a scalable structure. In addition, waveforms that are more resistant to interference allow more frequent reuse.

Table 1. The reuse distance analysis results

$\gamma_t = 15$ (dB)	$\alpha = 2$	$\alpha = 4$
γ_0 (dB)	Δ (D/D₀)	Δ (D/D₀)
15	6.81	34.76
20	3.76	8.63
25	3.47	7.09
30	3.34	6.49
35	3.27	3.27

Cluster and group size studies are among the factors that directly affect the capacity of the mobile telephone system. As shown in Table 2, as a result of the calculations, it has been determined that the maximum number of channels per cell that the omnidirectional antenna scenario and the directional antenna scenario with the same communication conditions can offer are the same.

Table 2. Maximum number of channels analysis results according to the antenna scenario

Scenario	C	γ_t (dB)	α	K	η (channels/cell)
Omnidirectional	120	15	4	7	17
120° Sector	120	15	4	7	17

Assignment failure rate and blocking probability analyses revealed the efficiency of multi-channel systems. As shown in Table 3, it was determined that systems with fewer channels exhibit lower assignment failure rates and blocking probabilities under the same traffic conditions. This supports the idea that multi-channel systems offer a more efficient structure than systems with fewer channels.

Table 3. The assignment failure rate and blocking probability analysis results

K = 9		$v_p = \%1$		$E_\eta = \%2$	
C	η (channels/cell)	ϖ_η	ω (calls/km²)	ρ_η	ρ_c (erlang/km²)
720	80	0.89	27	0.87	27
180	20	0.72	5.5	0.68	5.2
45	5	0.39	0.75	0.33	0.64

In the data rate analysis, it was shown that the bandwidth of the mobile phone system can be optimized with discrete rate sets. As shown in Table 4, it was revealed that the average data rate was positively affected by increasing the performance of the system in noise-limited conditions.

Table 4. The data rate analysis results

W (MHz) = 5	$\bar{R}$ (Mbps) = 5	R_{min} (Mbps) = 7.98
R (Mbps)	d (%)	$Users$ (%)
1	175	100
2	142	100
4	110	100
8	78	61
16	44	19

As shown in Table 5, the outage probability analysis showed how the number of channel groups changes under high traffic loads. The calculation of the cluster size required to provide good signal quality was considered as a critical parameter to increase the efficiency of the system.

Table 5. The outage probability analysis results

C = 100	γ_t (dB) = 20	σ (dB) = 6	α = 4
Scenario	Pr (%)	K	η (channels/cell)
without fading effects	0	4	25
under high traffic loads	3	4	25
maximum %5 outage probability	5	28	3

In conclusion, this paper shows that the capacity analysis of orthogonal multiple access systems identifies important factors to be considered in the system design. The findings are a valuable reference for the optimization and performance enhancement of future mobile communication systems.

Declaration of Ethical Standards

The authors declare to comply with all ethical guidelines, including authorship, citation, data reporting, and original research publication.

Credit Authorship Contribution Statement

The authors declare that they have made equal contributions.

Declaration of Competing Interest

The authors declare no conflicts of interest.

Funding / Acknowledgements

No funding or research grant was received during the review, research or compilation of the article.

Data Availability

No data will be shared.

5. REFERENCES

[1]   T. Jiang, L. Song and Y. Zhang, (Ed.), *Orthogonal frequency division multiple access fundamentals and applications*, CRC Press, 2010, doi: 10.1201/9781420088250.

[2]   P. Wang, J. Xiao and L. Ping, "Comparison of orthogonal and non-orthogonal approaches to future wireless cellular systems," in *IEEE Vehicular Technology Magazine*, vol. 1, no. 3, pp. 4-11, Sept. 2006, doi: 10.1109/MVT.2006.307294.

[3]   A. F. M. S. Shah, A. N. Qasim, M. A. Karabulut, H. Ilhan and M. B. Islam, "Survey and Performance Evaluation of Multiple Access Schemes for Next-Generation Wireless Communication Systems," in *IEEE Access*, vol. 9, pp. 113428-113442, 2021, doi: 10.1109/ACCESS.2021.3104509.

[4]   W. K. New, K. -K. Wong, H. Xu, K. -F. Tong, C. -B. Chae and Y. Zhang, "Fluid Antenna System Enhancing Orthogonal and Non-Orthogonal Multiple Access," in *IEEE Communications Letters*, vol. 28, no. 1, pp. 218-222, Jan. 2024, doi: 10.1109/LCOMM.2023.3333313.

[5]   Y. Al-Eryani and E. Hossain, "The D-OMA Method for Massive Multiple Access in 6G: Performance, Security, and Challenges," in IEEE Vehicular Technology Magazine, vol. 14, no. 3, pp. 92-99, Sept. 2019, doi: 10.1109/MVT.2019.2919279.

[6]   F. Ayvenli and Ç. Kurnaz, "OFDM Sistemlerinde Kanal Kestirimi İçin Yeni Bir Uyarlamalı Pilot Yerleşim Algoritması", *KONJES*, vol. 9, no. 4, pp. 943-964, 2021, doi: 10.36306/konjes.866310.

[7]   H. Kaya and F. Kara, "Dikgen Olmayan Çoklu Erişim NOMA : Gelecek Nesil Radyo Erişim Ağlarında Kitlesel Erişimin ve Spektral Verimliliğin Sağlanması için Çözüm", *Karaelmas Fen ve Mühendislik Dergisi*, vol. 9, no. 1, pp. 152-165, 2019, doi: 10.7212/zkufbd.v9i1.1305.

[8]   B. Demiral and Ö. Ertuğ, "Aşağı-hat MIMO-NOMA sistemlerinin max-max-max ve max-min-max anten seçim algoritmaları ile rayleigh kanallarda performans analizi", *GUMMFD*, vol. 38, no. 3, pp. 1675-1688, 2023, doi: 10.17341/gazimmfd.1031507.

[9]   A. Maatouk, M. Assaad and A. Ephremides, "Minimizing The Age of Information: NOMA or OMA?", *IEEE INFOCOM 2019 - IEEE Conference on Computer Communications Workshops (INFOCOM WKSHPS)*, Paris, France, pp. 102-108, 2019, doi: 10.1109/INFCOMW.2019.8845254.

[10]   H. Liang et al., "Orthogonal Model Division Multiple Access," in *IEEE Transactions on Wireless Communications*, vol. 23, no. 9, pp. 11693-11707, Sept. 2024, doi: 10.1109/TWC.2024.3384421.

[11]   C. Wu, X. Mu, Y. Liu, X. Gu and X. Wang, "Resource Allocation in STAR-RIS-Aided Networks: OMA and NOMA," in *IEEE Transactions on Wireless Communications*, vol. 21, no. 9, pp. 7653-7667, Sept. 2022, doi: 10.1109/TWC.2022.3160151.

[12]   K. Wang, F. Fang, D. B. D. Costa and Z. Ding, "Sub-Channel Scheduling, Task Assignment, and Power Allocation for OMA-Based and NOMA-Based MEC Systems," in *IEEE Transactions on Communications*, vol. 69, no. 4, pp. 2692-2708, April 2021, doi: 10.1109/TCOMM.2020.3047440.

[13]   C. Altuntaş and N. Tunalıoğlu, "Retrieving the SNR metrics with different antenna configurations for GNSS-IR", *TUJE*, vol. 6, no. 1, pp. 87-94, 2022, doi: 10.31127/tuje.870620.

[14]   G. Miao, J. Zander, K. W. Sung, and S. Ben Slimane, "Principles of cellular systems," in *Fundamentals of Mobile Data Networks*, Cambridge: Cambridge University Press, pp. 95-145, 2016, doi: 10.1017/CBO9781316534298.

[15]   G. L. Stüber, *Principles of Mobile Communication*, Springer, New York, NY, 2011, doi: 10.1007/978-1-4614-0364-7.

[16]   R. Pattuelli and V. Zingarelli, "Precision of the estimation of area coverage by planning tools in cellular systems," in *IEEE Personal Communications*, vol. 7, no. 3, pp. 50-53, June 2000, doi: 10.1109/98.847923.

[17]   J. Boccuzzi, "Introduction to Cellular Mobile Communications," in M. Vaezi, Z. Ding and H. Poor, (Ed.), *Multiple Access Techniques for 5G Wireless Networks and Beyond*, Springer, Cham, 2019, doi: 10.1007/978-3-319-92090-0_1.

[18]   M. P. Mishra and P. C. Saxena, "Survey of channel allocation algorithms research for cellular systems," *International Journal of Networks and Communications*, 2(5), 75-104, 2012, doi: 10.5923/j.ijnc.20120205.02.

[19]   D. Cox, "Cochannel Interference Considerations in Frequency Reuse Small-Coverage-Area Radio Systems," in *IEEE Transactions on Communications*, vol. 30, no. 1, pp. 135-142, January 1982, doi: 10.1109/TCOM.1982.1095385.

[20]   V. H. M. Donald, "Advanced mobile phone service: The cellular concept," in *The Bell System Technical Journal*, vol. 58, no. 1, pp. 15-41, Jan. 1979, doi: 10.1002/j.1538-7305.1979.tb02209.x.

[21]   I. Katzela and M. Naghshineh, "Channel assignment schemes for cellular mobile telecommunication systems: a comprehensive survey," in *IEEE Personal Communications*, vol. 3, no. 3, pp. 10-31, June 1996, doi: 10.1109/98.511762.

[22]   P. Subrahmanya and A. Farajidana, "5G and Beyond: Physical Layer Guiding Principles and Realization," *Journal of the Indian Institute of Science*, 100, 263-279, 2020, doi: 10.1007/s41745-020-00172-7.

[23]   S. Sousa, F. J. Velez and J. M. Peha, "Impact of propagation model on capacity in small-cell networks," *2017 International Symposium on Performance Evaluation of Computer and Telecommunication Systems (SPECTS)*, Seattle, WA, USA, pp. 1-8, 2017, doi: 10.23919/SPECTS.2017.8046782.

[24]   Y. Liang and A. Goldsmith, "Adaptive Channel Reuse in Cellular Systems," *2007 IEEE International Conference on Communications*, Glasgow, UK, pp. 857-862, 2007, doi: 10.1109/ICC.2007.146.

[25]   W. C. Lee, *Mobile communications design fundamentals*, John Wiley and Sons, 2010, doi: 10.1002/9780470930427

[26]   S. Wang and C. Ran, "Rethinking cellular network planning and optimization," in *IEEE Wireless Communications*, vol. 23, no. 2, pp. 118-125, April 2016, doi: 10.1109/MWC.2016.7462493.

[27]   M. Ghorbanzadeh, A. Abdelhadi and C. Clancy, "Cellular communications systems in congested environments," *Switzerland: Springer International Publishing*, 21-36, 2017, doi: 10.1007/978-3-319-46267-7

[28]   M. A. Habib *et al.*, "Transformer-Based Wireless Traffic Prediction and Network Optimization in O-RAN," *2024 IEEE International Conference on Communications Workshops (ICC Workshops)*, Denver, CO, USA, pp. 1-6, 2024, doi: 10.1109/ICCWorkshops59551.2024.10615438.

[29]   W. S. Kim and V. K. Prabhu, "Enhanced capacity in CDMA systems with alternate frequency planning," *ICC '98. 1998 IEEE International Conference on Communications. Conference Record. Affiliated with SUPERCOMM'98 (Cat. No.98CH36220)*, Atlanta, GA, USA, vol.2, pp. 973-978, 1998, doi: 10.1109/ICC.1998.685157.

[30]   E. -C. Park, M. Kim and K. -J. Park, "Analysis and Design of Best-Effort Broadcasting Services in Cellular Networks," in *IEEE Transactions on Vehicular Technology*, vol. 62, no. 8, pp. 3953-3963, Oct. 2013, doi: 10.1109/TVT.2013.2259272.

[31]   H. Xia, Y. Zhao and Z. Zeng, "Best effort spectrum allocation scheme for femtocell networks in dense deployment," in *China Communications*, vol. 11, no. 8, pp. 109-116, Aug. 2014, doi: 10.1109/CC.2014.6911092.

[32]   R. Giuliano and F. Mazzenga, "Exponential effective SINR approximations for OFDM/OFDMA-based cellular system planning," in *IEEE Transactions on Wireless Communications*, vol. 8, no. 9, pp. 4434-4439, September 2009, doi: 10.1109/TWC.2009.081403.

[33]   A. Limmanee, S. Dey and J. S. Evans, "Service-Outage Capacity Maximization in Cognitive Radio for Parallel Fading Channels," in *IEEE Transactions on Communications*, vol. 61, no. 2, pp. 507-520, February 2013, doi: 10.1109/TCOMM.2012.101812.110747.

[34]   S. K. Singh, K. Agrawal, K. Singh and C. -P. Li, "Outage Probability and Throughput Analysis of UAV-Assisted Rate-Splitting Multiple Access," in *IEEE Wireless Communications Letters*, vol. 10, no. 11, pp. 2528-2532, Nov. 2021, doi: 10.1109/LWC.2021.3106456.

[35]   S. Gurung and N. Pradhan, *Antenna system in cellular mobile Communication*, Kathamandu University, Nepal, July 2004.

[36]   I. Riedel, P. Rost, P. Marsch and G. Fettweis, "Creating Desirable Interference by Optimized

Sectorization in Cellular Systems," *2010 IEEE Global Telecommunications Conference GLOBECOM 2010*, Miami, FL, USA, pp. 1-5, 2010, doi: 10.1109/GLOCOM.2010.5683456.

[37]   A. Negi, *Analysis of Relay-based Cellular Systems*, Portland State University, 2006, doi: 10.15760/etd.2666.

[38]   K. Bechta, J. M. Kelner, C. Ziółkowski and L. Nowosielski, "Inter-Beam Co-Channel Downlink and Uplink Interference for 5G New Radio in mm-Wave Bands." *Sensors*, 21, 793, 2021, doi: 10.3390/s21030793.

A COUPLED MCST-FEM INVESTIGATION OF SIZE-DEPENDENT BUCKLING OF PERFORATED NANOBEAMS ON WINKLER-PASTERNAK FOUNDATION

* **Uğur KAFKAS** (iD)

Kütahya Dumlupınar University, Vocational School of Technical Science, Construction Technology Department, Kütahya, TÜRKİYE
ugur.kafkas@dpu.edu.tr

Highlights

- Increasing Winkler and Pasternak foundation parameters enhances the critical buckling load

- Higher MCST length scale improves nanobeam stability, demonstrating nanoscale effects

- More holes reduce the critical buckling load by weakening structural stiffness

- Longer beams exhibit lower critical buckling loads even with a greater number of holes

- Nanoscale effects captured by MCST provide stability beyond classical beam theories

*Corresponding Author: Uğur KAFKAS, ugur.kafkas@dpu.edu.tr

A COUPLED MCST-FEM INVESTIGATION OF SIZE-DEPENDENT BUCKLING OF PERFORATED NANOBEAMS ON WINKLER-PASTERNAK FOUNDATION

* Uğur KAFKAS ⓘD

Kütahya Dumlupınar University, Vocational School of Technical Science, Construction Technology Department, Kütahya, TÜRKİYE
ugur.kafkas@dpu.edu.tr

ABSTRACT: The buckling behavior of perforated nanobeams on elastic foundations has become increasingly important, mainly due to their widespread use in nanostructures and nanotechnology systems. This study investigates the buckling behavior of perforated nanobeams resting on Winkler-Pasternak elastic foundations using Modified Couple Stress Theory (MCST) and the Finite Element Method (FEM). The analysis examines the effects of various parameters, including foundation elasticity, MCST internal length scale, perforation properties, and beam length, on critical buckling loads. Results indicate that increasing both Winkler and Pasternak foundation parameters enhances the critical buckling load, with the Pasternak parameter showing a more pronounced effect due to its incorporation of shear effects. The MCST internal length scale parameter significantly influences nano-beam stability, highlighting the importance of size effects at nanoscale dimensions. Higher filling ratios correlate directly with increased buckling resistance, while a greater number of holes reduces overall structural stiffness and decreases the critical buckling load. Beam length exhibits an inverse relationship with buckling strength; longer beams demonstrate lower critical buckling loads than shorter beams, regardless of the number of holes present.

Keywords: *Buckling Analysis, Finite Element Method, Modified Couple Stress Theory, Perforated Nanobeam, Winkler-Pasternak Foundation*

1. INTRODUCTION

Nanobeams are important nanostructures with many applications, including nanosystems, sensors, and micro/nano-electro-mechanical systems (MEMS-NEMS) [1]. The increasing use of perforated nanobeams, particularly when weight reduction or functional requirements necessitate structural modifications, has made it crucial to understand their mechanical behavior and study the effects of the number of holes, filling ratio, and small-scale impact on these behaviors [2]. These structures often interact with elastic foundations in engineering applications, and their mechanical behavior varies accordingly.

Classical beam theories (CTs) may be inadequate for analyzing nanoscale structures due to their inability to account for size-dependent effects [3]. Many higher-order elasticity theories have been proposed in the literature to overcome these deficiencies. One such theory is the Modified Couple Stress Theory (MCST) developed by Yang et al. [4]. This theory was introduced to capture these size effects by incorporating an intrinsic length scale parameter into the analysis. In recent years, many studies have been conducted to analyze the mechanical behavior of nanostructures using MCST [5] - [12].

The stability of beams on elastic foundations has been studied using various foundation models. The Winkler elastic foundation (WEF) model, widely used due to its simplicity, models the interaction between the foundation and the beam with springs [13], [14]. The Winkler-Pasternak elastic foundation (W-PEF) model improved the WEF model by including the shear interactions between the spring elements [15], [16]. There have been many studies investigating the mechanical behavior of nanostructures using elastic foundation models and MCST [17] - [21]. Togun and Bağdatlı [18] developed an MCST-based model to analyze the free vibration behavior of simply supported (S-S) nanobeams resting on a WEF. By employing Hamilton's principle and the multiple scale method, their study demonstrates that the incorporation of a

---

*Corresponding Author: Uğur KAFKAS, ugur.kafkas@dpu.edu.tr

material length scale parameter effectively captures significant size effects—yielding higher fundamental frequencies than those predicted by classical Euler–Bernoulli theory—and that an increased non-dimensional Winkler foundation parameter enhances system stiffness. Akgöz ve Civalek [18] investigated the free vibration behavior of single-layered graphene sheets on a Pasternak-type elastic matrix using MCST and an analytical thin plate model. Their analytical results demonstrate that the material length scale parameter significantly affects the vibration frequencies—especially for smaller geometries and higher vibration modes—with its influence diminishing as the Winkler and shear modulus parameters increase. Şimşek [21] developed a non-classical beam model for the static and nonlinear vibration analysis of microbeams on a three-layered nonlinear elastic foundation by integrating MCST with Euler–Bernoulli beam theory and incorporating von-Kármán's geometric nonlinearity. The study reveals that the inclusion of a length scale parameter and nonlinear foundation stiffness coefficients significantly influences both the static deflection and the nonlinear frequency ratio, with the derived closed-form expressions being validated through extensive numerical comparisons.

Perforated nanobeams are nanostructures with modified stiffness properties created using various techniques and must be modeled appropriately [22]. Luschi and Pieri [23] proposed a local model for the micromechanical properties of microscale perforated beams. Although many researchers have studied either perforated macro/nano beams [24] - [35] or nanobeams on elastic foundations [36] - [44], the effects of hole patterns and elastic foundation interactions on nanobeam buckling behavior have not been sufficiently investigated. Abdelrahman et al. [36] modeled the buckling behavior of perforated nanobeams in a piezoelectric sandwich structure, considering elasticity and dimensional effects. Almitani et al. [37] performed the stability analysis of perforated nanorods, considering the surface energy effect. Abdelrahman and Eltaher [2] investigated the bending and buckling responses of perforated nanobeams, examining the effects of surface energy on different beam theories. Eltaher et al. [38] analytically investigated the static bending and buckling behavior of perforated nanobeams according to Euler-Bernoulli and Timoshenko theories, considering nonlocal effects. Kafkas et al. [22] proposed an analytical solution by considering non-local effects and deformable boundary conditions while investigating the buckling behavior of perforated nano/microbeams on an elastic foundation.

This study makes a novel contribution to the field of nanostructure mechanics by integrating MCST with FEM for analyzing the buckling behavior of perforated nanobeams on W-PEF. Unlike traditional analyses based solely on classical continuum theories, this study explicitly accounts for nanoscale size effects through the incorporation of an intrinsic length scale parameter. A comprehensive literature review indicates that no previous work has addressed the buckling behavior of perforated nanobeams on W-PEF using MCST, either analytically or numerically. These contributions not only extend the theoretical framework for understanding nanoscale buckling phenomena but also offer guidance for designing and optimizing advanced nanostructured materials.

2. MATERIAL AND METHODS

The geometrical configuration of a S-S perforated nanobeam loaded by an axial force P, defined by the presence of holes of dimensions L, b and h in the cross-sectional region, is shown in Figure 1.
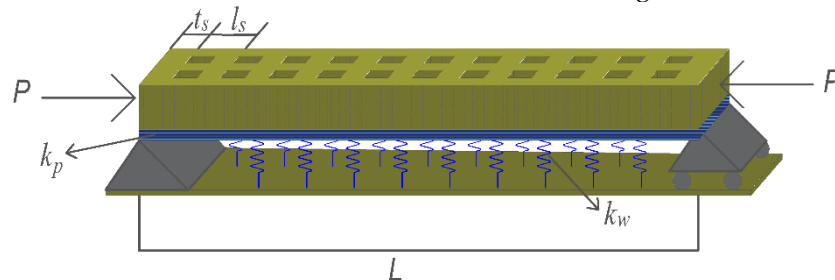
Figure 1. Perforated nanobeam resting on a W-PEF

To effectively analyze the mechanical response of perforated structures, it is essential to consider the

periodic arrangement of the cut-out holes. Luschi and Pieri [23] presented analytical solutions for equivalent geometric and material properties of perforated beams. Let l_s and t_s denote the spatial period and period length, respectively, and the filling ratio α can be represented as follows [23]:

$$\alpha = \frac{t_s}{l_s}, \quad 0 < \alpha \leq 1 \tag{1}$$

The critical point to note here is that in the case of $\alpha = 1$, the nanobeam represents a fully filled solid beam, while $\alpha < 1$ refers to the case with holes [29]. N indicates the number of holes along the cross-section, the equivalent bending stiffness and shear stiffness of the perforated beam compared to the solid beam can be expressed as follows [23], [38] - [40]:

$$\frac{(EI)_p}{EI} = \frac{\alpha(N+1)(N^2 + 2N + \alpha^2)}{(1 - \alpha^2 + \alpha^3)N^3 + 3\alpha N^2 + (3\alpha^2 + 2\alpha^3 - 3\alpha^4 + \alpha^5)N + \alpha^3} \tag{2}$$

$$\frac{(GA)_p}{EA} = \frac{\alpha^3(N+1)}{2N} \tag{3}$$

where E and G represent the modulus of elasticity and shear, A and I represent the cross-sectional area and moment of inertia of the filled beam, respectively, and $A = bh$. The sub-index p represents the perforated nano-beam.

2.1. Modified Couple Stress Theory

MCST, first proposed by Yang et al. [4], accounts for the small size effects observed in micro- and nanoscale structures by incorporating a material length scale parameter into its equations. According to MCST, for a solid nano-beam resting on a W-PEF, the governing equation for the buckling problem can be represented as follows [41], [42]:

$$EI\frac{\partial^4 w}{\partial x^4} + GAl_m^2\frac{\partial^4 w}{\partial x^4} + P\frac{\partial^2 w}{\partial x^2} - k_p\frac{\partial^2 w}{\partial x^2} + k_w w = 0 \tag{4}$$

where EI and GA are the bending and shear stiffnesses of the solid beam, respectively, l_m is the material length scale parameter, k_w and k_p are the WEF and W-PEF parameters, respectively, and w is the transverse displacement. If the bending and shear stiffnesses of the perforated nano-beam given in Equations (2) and (3) are substituted in Equation (4), the governing equation can be shown as follows:

$$[(EI)_P + (GA)_P l_m^2]\frac{\partial^4 w}{\partial x^4} + [P - k_p]\frac{\partial^2 w}{\partial x^2} + k_w w = 0 \tag{5}$$

2.2. Finite Element Method

To examine the buckling behavior of a nanobeam resting on a W-PEF via the FEM and to determine the critical buckling loads by accounting for the size effect using the MCST, the nanobeam is discretized into more minor beam elements.

2.2.1 Finite element discretization process

The nanobeam is discretized into N^e finite elements, each consisting of two nodes with four degrees of freedom (DOF) per element—two translational (w_1, w_2) and two rotational (θ_1, θ_2) DOFs. The shape functions ξ are employed to interpolate the displacement field within each element based on nodal values. The governing differential equation, incorporating MCST effects, is formulated in its weak form to

facilitate FEM implementation. The nodal displacement vector, $\mathbf{w}$, represents the displacements and rotations at both ends of the beam element and is shown as follows [43]:

$$\mathbf{w} = [w_1 \quad \theta_1 \quad w_2 \quad \theta_2] \tag{6}$$

where w_1 and θ_1 represent the transverse displacement and rotation at node 1 and w_2 and θ_2 represent the transverse displacement and rotation at node 2, respectively.

The shape functions can be given as follows [44]:

$$\boldsymbol{\xi} = \begin{bmatrix} \xi_1 \\ \xi_2 \\ \xi_3 \\ \xi_4 \end{bmatrix} \tag{7}$$

Both the displacement and rotation of the nanobeam at each nodal point can be represented by the shape functions as follows:

$$w = w_1\xi_1 + \theta_1\xi_2 + w_2\xi_3 + \theta_2\xi_4 \tag{8}$$

Given the length L_e of each beam segment, the elements of the shape function vector can be defined as follows [44]:

$$\boldsymbol{\xi} = \begin{bmatrix} \xi_1 \\ \xi_2 \\ \xi_3 \\ \xi_4 \end{bmatrix} = \begin{bmatrix} 1 - \dfrac{3x^2}{L_e^2} + \dfrac{2x^3}{L_e^3} \\ x - \dfrac{2x^2}{L_e} + \dfrac{x^3}{L_e^2} \\ \dfrac{3x^2}{L_e^2} - \dfrac{2x^3}{L_e^3} \\ -\dfrac{x^2}{L_e} + \dfrac{x^3}{L_e^2} \end{bmatrix} \tag{9}$$

According to the MCST with a small-scale effect, to obtain the weak form of the governing differential equation for buckling of a nanobeam on a W-PEF, shape functions can be chosen as weighting functions, and the differential equation can be formulated in weighted integral form. This requires multiplying the residual R by the weighting functions and integrating the result over the entire length of the nanobeam:

$$R = [(EI)_P + (GA)_P l_m^2]\frac{\partial^4 w}{\partial x^4} + [P - k_p]\frac{\partial^2 w}{\partial x^2} + k_w w \tag{10}$$

$$\int_0^L \left([(EI)_P + (GA)_P l_m^2]\boldsymbol{\xi}\frac{\partial^4 w}{\partial x^4} + [P - k_p]\boldsymbol{\xi}\frac{\partial^2 w}{\partial x^2} + k_w \boldsymbol{\xi} w \right) dx = 0 \tag{11}$$

Parts integrate equation (11), and the chain rule is used to obtain the general form:

$$\int_0^L \left([(EI)_P + (GA)_P l_m^2]\frac{d^2\boldsymbol{\xi}}{dx^2}\frac{d^2\boldsymbol{\xi}^T}{dx^2} + [P - k_p]\frac{d\boldsymbol{\xi}}{dx}\frac{d\boldsymbol{\xi}^T}{dx} + k_w \boldsymbol{\xi}\boldsymbol{\xi}^T \right) dx = 0 \tag{12}$$

2.2.2 Solution steps in the FEM approach

To determine the critical buckling load of the perforated nanobeam using FEM, the following solution procedure is applied:

1. Discretization: The nanobeam is divided into N^e elements, each modeled using two-node beam elements that incorporate transverse displacement and rotation.
2. Shape Function Definition: The displacement field is approximated using Hermite cubic shape functions, ensuring continuity in displacement and rotation.
3. Weak Formulation: The governing equation is rewritten in weighted residual form, where shape functions serve as weighting functions, allowing the formulation of the stiffness matrix K and load matrix B.
4. Stiffness and Load Matrix Computation: The global system matrices are assembled based on element contributions.
5. Eigenvalue Problem Solving: The characteristic equation $|K - \lambda B| = 0$ is solved to determine the critical buckling load, where $\lambda = P_{cr}/P$ represents the eigenvalue.

To derive the global system matrices; the stiffness, elastic foundation and axial load matrices of the nanobeam, the shape functions in Equation (9) are substituted in Equation (12), and integrals are performed term by term. The resulting matrices are defined below:

$$K_L = (EI)_P \int_0^{L_e} \begin{Bmatrix} \xi_1'' \\ \xi_2'' \\ \xi_3'' \\ \xi_4'' \end{Bmatrix} \{\xi_1'' \ \xi_2'' \ \xi_3'' \ \xi_4''\} dx = \frac{(EI)_P}{L_e^3} \begin{bmatrix} 12 & 6L_e & -12 & 6L_e \\ 6L_e & 4L_e^2 & -6L_e & 2L_e^2 \\ -12 & -6L_e & 12 & -6L_e \\ 6L_e & 2L_e^2 & -6L_e & 4L_e^2 \end{bmatrix} \tag{13}$$

$$K_M = (GA)_P l_m^2 \int_0^{L_e} \begin{Bmatrix} \xi_1'' \\ \xi_2'' \\ \xi_3'' \\ \xi_4'' \end{Bmatrix} \{\xi_1'' \ \xi_2'' \ \xi_3'' \ \xi_4''\} dx = \frac{(GA)_P l_m^2}{L_e^3} \begin{bmatrix} 12 & 6L_e & -12 & 6L_e \\ 6L_e & 4L_e^2 & -6L_e & 2L_e^2 \\ -12 & -6L_e & 12 & -6L_e \\ 6L_e & 2L_e^2 & -6L_e & 4L_e^2 \end{bmatrix} \tag{14}$$

$$K_W = k_W \int_0^{l_e} \begin{Bmatrix} \xi_1 \\ \xi_2 \\ \xi_3 \\ \xi_4 \end{Bmatrix} \{\xi_1 \ \xi_2 \ \xi_3 \ \xi_4\} dx = \frac{k_w}{420} \begin{bmatrix} 156L_e & 22L_e & 54L_e & -13L_e^2 \\ 22L_e^2 & 4L_e^3 & 13L_e^2 & -3L_e^3 \\ 54L_e & 13L_e^2 & 156L_e & -22L_e^2 \\ -13L_e^2 & -3L_e^3 & -22L_e^2 & 4L_e^3 \end{bmatrix} \tag{15}$$

$$K_P = k_p \int_0^{L_e} \begin{Bmatrix} \xi_1' \\ \xi_2' \\ \xi_3' \\ \xi_4' \end{Bmatrix} \{\xi_1' \ \xi_2' \ \xi_3' \ \xi_4'\} dx = \frac{k_p}{30L_e} \begin{bmatrix} 36 & 3L_e & -36 & 3L_e \\ 3L_e & 4L_e^2 & -3L_e & -L_e^2 \\ -36 & -3L_e & 36 & -3L_e \\ 3L_e & -L_e^2 & -3L_e & 4L_e^2 \end{bmatrix} \tag{16}$$

$$B_A = P \int_0^{l_e} \begin{Bmatrix} \xi_1' \\ \xi_2' \\ \xi_3' \\ \xi_4' \end{Bmatrix} \{\xi_1' \ \xi_2' \ \xi_3' \ \xi_4'\} dx = \frac{P}{420} \begin{bmatrix} 156L_e & 22L_e & 54L_e & -13L_e^2 \\ 22L_e^2 & 4L_e^3 & 13L_e^2 & -3L_e^3 \\ 54L_e & 13L_e^2 & 156L_e & -22L_e^2 \\ -13L_e^2 & -3L_e^3 & -22L_e^2 & 4L_e^3 \end{bmatrix} \tag{17}$$

In these equations, K_L is the matrix derived from the CT (local), K_M is the matrix related to MCST, which also takes into account the effect of small size by means of the material length scale parameter. If the K_M matrix is neglected, the finite element solution reduces to the Euler-Bernoulli beam theory based on classical mechanics. The K_W and K_P matrices are due to the WEF parameter and the Pasternak shear layer effect, respectively, while the B_A matrix is the matrix due to the axial load. From the K_W and K_P matrices, if the K_P matrix is neglected, buckling analysis to MCST can be performed for the nano-beam resting on a WEF, while if both K_W and K_P are neglected, the buckling behavior of the nano-beam not resting on an elastic foundation is analyzed.

The buckling loads of a nanobeam resting on the W-PEF can be calculated according to MCST using the total stiffness and load matrices as follows [45]:

$$|K - \lambda B| = 0 \tag{18}$$

where λ eigenvalue represents the ratio of the critical buckling load (P_{cr}) to the applied axial load (P), K is the sum of the stiffness matrices, and B is the sum of the matrices resulting from the axial load and is shown as:

$$\lambda = \frac{P_{cr}}{P} \tag{19}$$

$$[K] = [K_L] + [K_M] + [K_W] + [K_P] \tag{20}$$

$$[B] = [B_A] \tag{21}$$

3. RESULTS AND DISCUSSION

This chapter examines the critical buckling loads of nanobeams resting on a W-PEF using numerical results based on the MCST, considering the effects of size and elastic foundation. The study provides a FEM-based solution, and analyses are conducted to validate the results and to explore the influence of various parameters on the buckling behavior of nanobeams. For these analyses, as well as the presentation of figures and tables, the following dimensionless quantities are employed:

$$K^w = \frac{k_w L^4}{EI} \tag{22}$$

$$K^p = \frac{k_p L^2}{EI} \tag{23}$$

A comparison study to verify the accuracy of the FEM model is presented in this section. The analytical solution of critical buckling loads according to MCST for a S-S solid nanobeam resting on the W-PEF is given by Mercan et al. [41] as follows:

$$\overline{P(n)} = (EI + GAl_m^2)\frac{n^2\pi^2}{L^2} + \frac{k_w L^2}{n^2\pi^2} + k_p \tag{24}$$

where n is the mode number of the buckling.

By substituting the equivalent bending stiffness and shear stiffness of the perforated beams, derived from Equations (2) and (3), into Equation (24), the critical buckling loads according to the MCST for a S-S perforated nanobeam resting on a W-PEF can be analytically determined. In Equation (24), the smallest load ($n = 1$) is called the critical buckling load [46] and can be calculated as follows:

$$P_{cr} = [(EI)_P + (GA)_P l_m^2]\frac{\pi^2}{L^2} + \frac{k_w L^2}{\pi^2} + k_p \tag{25}$$

The analytically calculated critical buckling loads, along with the results obtained from the FEM model for varying element numbers, are presented in Table 1. The geometrical and material properties of the perforated nanobeam are given as follows in Table 1 and in the rest of the study unless otherwise stated: $E = 1$ TPa, $h = 2$ nm, $b = 4$ nm, $K^w = 100$, $K^p = 5$, $N = 5$, $\alpha = 0.5$, and $l_m = 0.5$. Comparisons are made for different values of L and N^e.

Table 1. Comparison of critical buckling loads (P_{cr}) obtained from Equation (25) and FEM for different values of L and N^e

L (nm)	P_{cr} (nN)					
	Eq. 25	FEM				
		$N^e = 10$	$N^e = 15$	$N^e = 20$	$N^e = 25$	$N^e = 30$
10	602.3807	602.3834	602.3812	602.3809	602.3808	602.3807
20	150.5952	150.5958	150.5953	150.5952	150.5952	150.5952
30	66.9312	66.9315	66.9312	66.9312	66.9312	66.9312
40	37.6488	37.6490	37.6488	37.6488	37.6488	37.6488
50	24.0952	24.0953	24.0952	24.0952	24.0952	24.0952

From Table 1, the analytical solution given in Equation (25) closely matches the solution provided by the FEM. For all other L lengths except $L = 10$ nm, the $N^e = 20$ case gives exact results up to four digits after the integer. In the case of $L = 10$, the exact result is obtained at $N^e = 30$. In the analyses performed throughout the study, $N^e = 30$ was chosen considering this situation, and all analyses were performed according to this value.

Figure 2 compares the critical buckling loads of a perforated nanobeam resting on a W-PEF as predicted by CT and MCST. The numerical values employed in this figure are consistent with those listed in Table 1. Two different length-scale parameters are selected for MCST: $l_m = 1$ nm. and $l_m = 2$ nm.
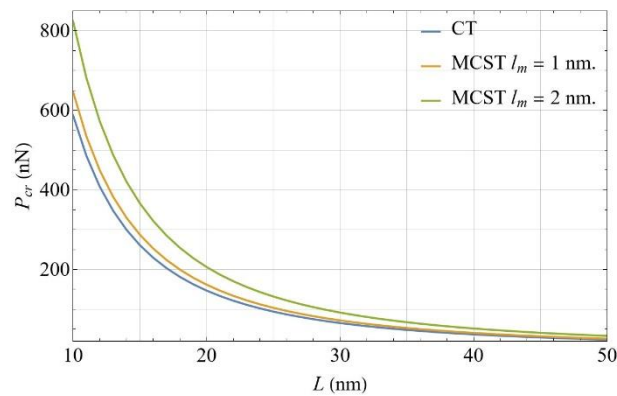
Figure 2. Comparison of the critical buckling loads for CT and MCST

In applying the MCST, the length scale parameter is typically determined by comparing experimentally measured size-dependent mechanical responses—such as bending stiffness, natural frequencies, or related behaviors at micro/nano scales—with theoretical predictions from MCST. Yang et al. [4] have outlined methodological approaches whereby experimental micro-scale data are modeled under the MCST framework to obtain the corresponding material length scale. Similarly, Park and Gao [47] employed variational methods to derive closed-form solutions, thereby highlighting the importance of calibrating l_m based on the bending and vibration responses of micro-beams. Their findings indicate that l_m is closely tied to the microstructural characteristics of the material, such as grain size, crystal structure, or atomic-level regularity. Due to the scarcity of comprehensive nano-scale experimental data— often stemming from the high costs and complexities of conducting such experiments—the range $0 < l_m/h \leq 1$ is frequently adopted in the literature [26], [41], [48]. This practical choice captures a broad spectrum of microstructural effects without requiring exhaustive experimental calibration for every specific material. As seen in Figure 2, MCST yields consistently higher critical buckling loads than the CT, demonstrating the enhanced stiffness arising from material microstructure effects.

Figure 3 demonstrates the effects of the elastic foundation on the critical buckling load. The analysis uses previously mentioned material and geometrical properties with $L = 30$ nm. The figure presents critical buckling loads for various values of K^w and K^p.
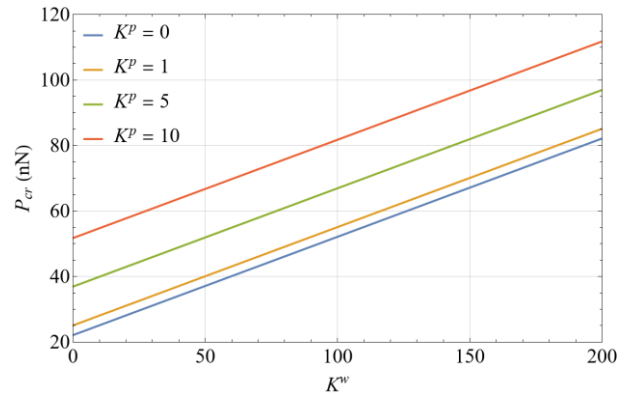
Figure 3. The critical buckling loads for different values of dimensionless elastic foundation parameters

The results show that critical buckling load values increase continuously as the dimensionless WEF parameter (K^w) increases, indicating more vital interaction between the nanobeam and foundation, thereby growing stiffness. The WEF model simulates foundation resistance using a spring analogy - as this resistance increases, the beam's buckling resistance also increases. This linear relationship shows that K^w's effect on critical buckling load is consistent across all values, meaning the beam's buckling stability is directly proportional to foundation stiffness. Figure 3 displays four curves representing different dimensionless Pasternak parameter (K^p) values (0, 1, 5, 10). The critical buckling load increases with K^p, similar to K^w. The Pasternak parameter enhances foundation stiffness by incorporating shear deformations, making the nanobeam more resistant to buckling. Even when $K^p = 0$, the buckling load increases with K^w, and this trend becomes more pronounced when K^p is included in the analysis. This demonstrates that the beam achieves greater stability when the foundation is modeled using both the spring analogy (Winkler) and shear effects (Pasternak). Each curve in Figure 3 corresponds to a specific K^p value, showing P_{cr} increasing with K^w. Higher K^p values yield greater P_{cr} values for equivalent K^w values. Notably, K^p has a significantly greater effect on the nanobeam's P_{cr} value than K^w. For instance, when $K^p = 0$, increasing K^w from 0 to 100 results in approximately 135% increase in P_{cr}. Similarly, when $K^w = 0$, increasing K^p from 0 to 10 produces a comparable percentage increase in P_{cr}, demonstrating how shear effects substantially strengthen the beam's buckling capacity. To further elucidate the combined effects of the K^w and K^p foundation parameters on the critical buckling load, Figure 4 has been added. This figure offers a comprehensive visualization of the interaction between K^w, K^p, and P_{cr}, clearly depicting how simultaneous variations in both foundation parameters influence buckling behavior.
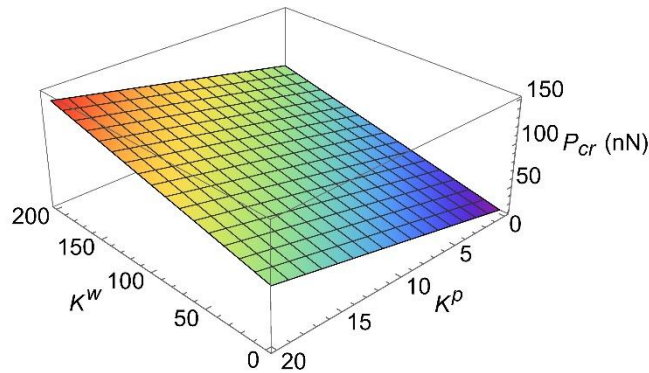
Figure 4. Variation of the critical buckling loads depending on K^w and K^p

Figures 5 and 6 illustrate how P_{cr} varies with the filling ratio and hole number while also revealing the effect of MCST's length scale parameter. The analysis uses $K^w = 100$ and $K^p = 5$, with $l_m = 0.1$ in Figure 5 and $l_m = 2$ in Figure 6, allowing examination of cases where MCST's effect is minimal and

maximal, respectively.
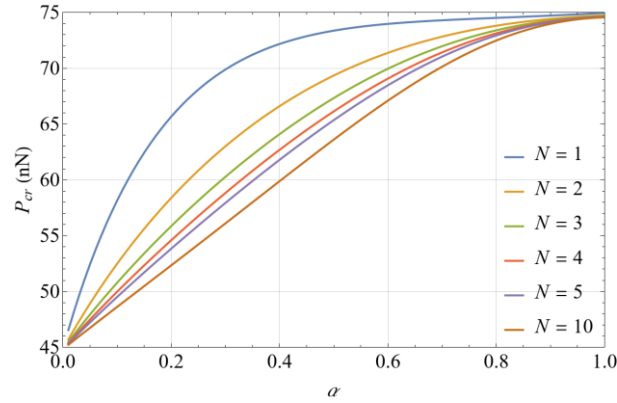
Figure 5. Variation of the critical buckling loads depending on α and N ($l_m = 0.1$)
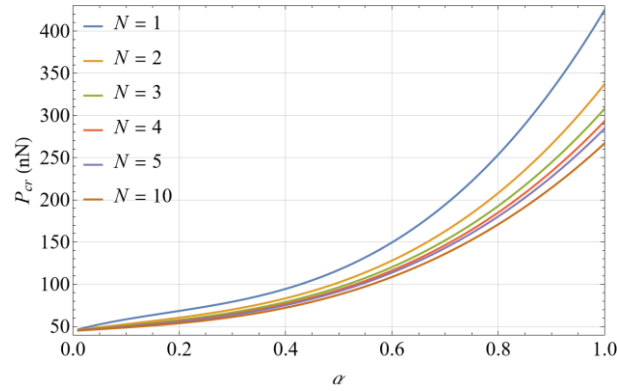
Figure 6. Variation of the critical buckling loads depending on α and N ($l_m = 2$)

Figures 5 and 6 illustrate the relationship between the critical buckling load, the filling ratio, and the number of holes in perforated nanobeams. The results indicate that P_{cr} increases significantly as α approaches 1, meaning that a fully filled beam exhibits higher buckling resistance. For a given α, an increase in N leads to a decrease in P_{cr}, as more perforations reduce the overall stiffness, thereby diminishing the buckling resistance. When $N = 1$, the nanobeam retains the highest P_{cr}, confirming that fewer perforations contribute to greater structural rigidity. Conversely, when $N = 10$, the increased number of perforations weakens the structure, leading to lower P_{cr} values. A key observation is the influence of the internal length scale parameter on buckling resistance. Comparing different cases ($l_m = 0.1$ versus $l_m = 2$) reveals that a larger l_m significantly increases P_{cr}, demonstrating that MCST accounts for microscale effects that enhance the beam's stiffness.

This effect is particularly evident in Figures 5 and 6, where the $N = 1$ curve consistently exhibits the highest P_{cr} values. The difference between Figures 5 and 6 is attributed solely to the variation in l_m. This discrepancy can be explained by examining the role of shear stiffness, which is influenced by l_m. As seen in the governing equation, the term $(GA)_P l_m^2$ contributes directly to P_{cr}. When l_m is small, $(GA)_P$ has a limited effect, leading to a concave downward trend in Figure 5. However, when l_m is large, the influence of $(GA)_P$ becomes more pronounced, smoothing out the increase in P_{cr} as α increases, resulting in a convex upward trend in Figure 6. This finding reveals the role of micro-scale shear effects in determining the buckling response of perforated nanobeams. Furthermore, the relationship between α and N indicates that although Pcr generally increases with α, this effect diminishes as N increases. In other words, when a nanobeam has a high number of perforations, increasing the filling ratio has a limited impact on its buckling strength. This suggests that the structural weakening effect caused by perforations depends not only on α but also on N and lm, demonstrating the necessity of incorporating non-classical continuum theories for accurate stability predictions in nanoscale beams.

Figure 7 provides a detailed examination of MCST's length scale parameter effect, showing P_{cr} variation as a function of l_m and N.
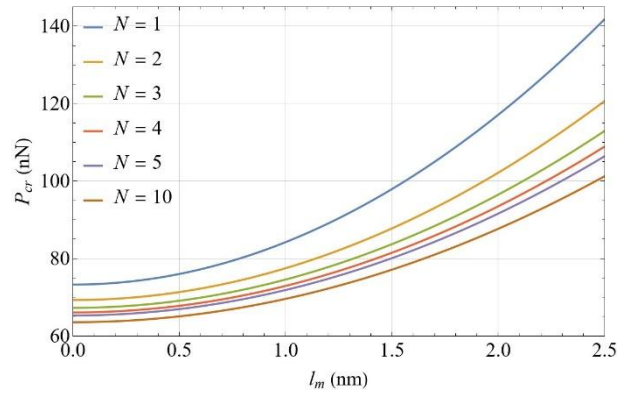
Figure 7. Variation of the critical buckling loads depending on l_m and N

The results clearly demonstrate increasing P_{cr} values with higher l_m values, indicating how the MCST's l_m parameter contributes to beam stiffness at nanoscale dimensions. This shows that size effects, significant at nano dimensions, enhance stiffness and buckling resistance. P_{cr} decreases with increasing N, and this effect becomes more pronounced at higher l_m values. The P_{cr} difference between $N = 1$ and $N = 10$ is approximately 13.25% at $l_m = 0.02$ nm, increasing to 28.60% at $l_m = 2.5$ nm. However, higher l_m values mitigate the holes' weakening effect on the beam. For instance, the P_{cr} value for $N = 1$ and $l_m = 0$ (CT) is lower than for $N = 10$ and $l_m = 1.3$ nm. This demonstrates how l_m's positive contribution to nanobeam stability can match or exceed P_{cr} values even with more holes. These findings indicate that the internal length parameter counterbalances hole-induced structural weakening by increasing stiffness in nano-sized structures. Consequently, with higher l_m parameter values, critical buckling load can remain high despite increased hole numbers.

Figure 8 analyzes the relationship between critical buckling loads and nanobeam length for varying numbers of holes.
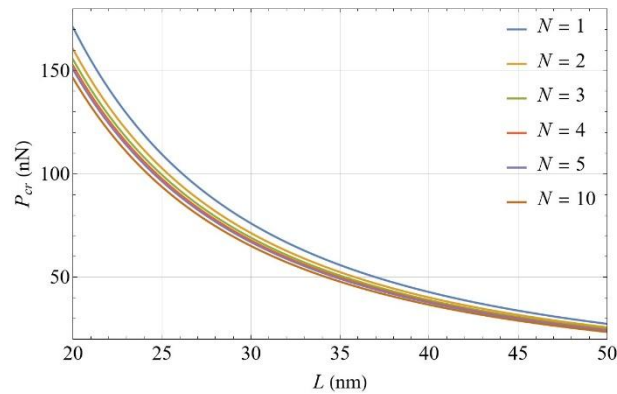
Figure 8. Variation of the critical buckling loads depending on L and N

The analysis demonstrates that critical buckling load decreases as beam length increases, confirming that longer beams have lower buckling resistance. This trend is consistent across all hole configurations. Beams with fewer holes maintain higher critical buckling load values even as length increases, indicating that structural stiffness decreases significantly with both increased hole numbers and the nanobeam length. Comparing configurations from $N = 1$ to $N = 10$ reveals that a higher number of holes substantially reduces critical buckling load. This reduction occurs because holes diminish the beam's overall structural stiffness, lowering its buckling resistance. The $N = 10$ configuration yields the lowest critical buckling load values, demonstrating the negative impact of multiple holes on structural stability.

Figures 9 through 12 examine elastic foundation effects on critical buckling load. Figures 9 and 11 plot

results for $K^p = 5$ with varying K^w values, while Figures 10 and 12 show results for $K^w = 100$ with varying K^p values. Figures 9 and 10 analyze effects relative to the number of holes, while Figures 11 and 12 examine effects relative to the filling ratio.
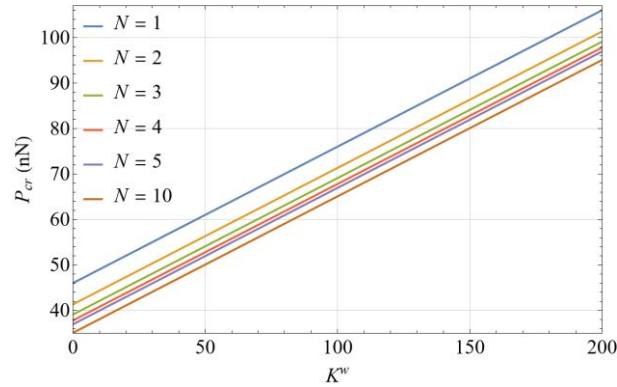
Figure 9. Variation of the critical buckling loads depending on K^w and N ($K^p = 5$)
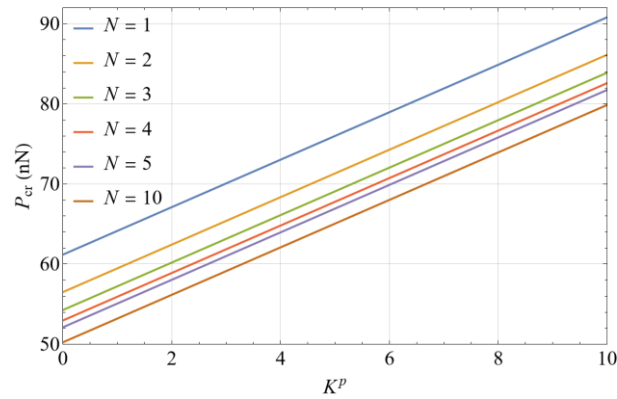
Figure 10. Variation of the critical buckling loads depending on K^p and N ($K^w = 100$)

Figure 9 demonstrates that critical buckling load increases with higher WEF parameter values. However, increasing the number of holes (from $N = 1$ to $N = 10$) significantly reduces critical buckling load. The holes weaken structural stiffness, diminishing the foundation stiffness's positive effect on critical buckling load. Beams with fewer holes ($N = 1$) exhibit higher buckling loads, indicating that foundation stiffness more effectively enhances structural stability in these cases. Similarly, Figure 10 shows that the critical buckling load increases with higher Pasternak foundation parameter values. The Pasternak foundation model's incorporation of shear effects enhances beam stiffness, improving buckling resistance. While critical buckling load still decreases with increased hole numbers, higher K^p values partially compensate for hole-induced weakening through increased foundation shear stiffness. Nevertheless, configurations with more holes ($N = 10$) maintain lower critical buckling loads, indicating that hole-induced weakening dominates despite increased foundation stiffness. Both figures demonstrate that critical buckling load increases with higher K^w and K^p parameters due to enhanced elastic foundation support, though increased hole numbers consistently reduce critical buckling load.
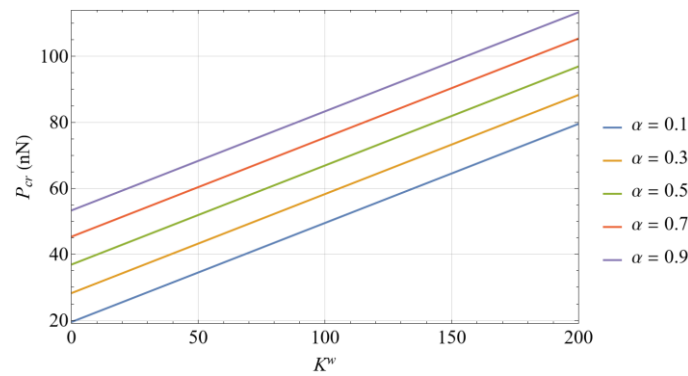
Figure 11. Variation of the critical buckling loads depending on K^w and α ($K^p = 5$)
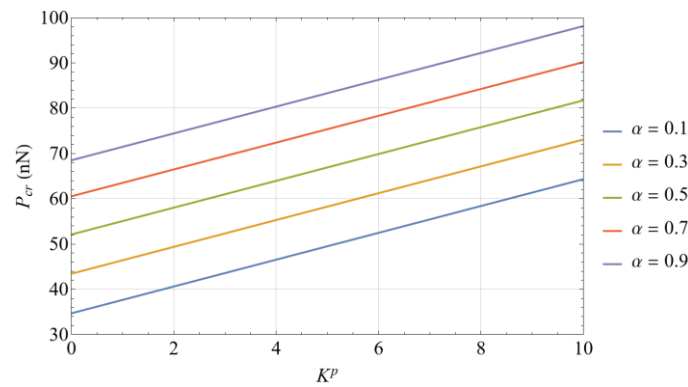
Figure 12. Variation of the critical buckling loads depending on K^p and α ($K^w = 100$)

Figures 11 and 12 reveal that critical buckling load increases significantly with higher filling ratios, indicating enhanced structural stiffness and buckling resistance. Both foundation parameters (K^w and K^p) positively affect P_{cr}. Figure 11 clearly shows P_{cr} increasing with K^w, demonstrating enhanced buckling resistance as foundation support strengthens. Additionally, P_{cr} increases linearly with the filling ratio (as α increases from 0.1 to 0.9). Figure 12 shows that similar P_{cr} increases with higher K^p values. P_{cr} consistently increases with α for each K^p value, demonstrating that higher filling ratios combined with foundation shear stiffness provide enhanced buckling resistance.

4. CONCLUSIONS

This study contributes to the field of nanostructure mechanics by investigating the buckling behavior of perforated nanobeams resting on W-PEF using MCST and FEM. This analysis significantly extends previous work on nanoscale buckling by incorporating size effects through MCST—an approach not previously applied to perforated nanobeams on W-PEF. The results demonstrate several key findings that advance the understanding of nanoscale mechanical behavior:

- Both Winkler and Pasternak foundation parameters substantially increase critical buckling loads, with the Pasternak foundation demonstrating superior influence due to its incorporation of shear effects. This finding aligns with previous research [16], [18] - [20], on beam–foundation interaction but extends the literature by examining perforated nanobeams at the nanoscale.
- The inclusion of the internal length scale parameter increases the predicted buckling capacity, emphasizing the need to account for size-dependent microstructural effects. These results support previous MCST-based studies on nano-beams without holes [41] - [43], but additionally demonstrate the interaction between holes and microstructural stiffness.
- Higher fill ratios are associated with increased buckling resistance, while additional holes reduce structural stability. Unlike macro-scale studies that treat holes as simple mass

reduction, this analysis also reveals the interactions between holes, size effects and foundation properties at the nanoscale.

- Beam length exhibits an inverse relationship with buckling resistance, particularly pronounced in highly perforated configurations, indicating a heightened sensitivity to geometric parameters at the nanoscale.

These findings provide practical guidance for nanostructured material design, particularly for applications requiring optimized buckling resistance. Future research directions should include:

- Investigating temperature effects on perforated nanobeam stability, particularly for applications in extreme thermal environments.
- Exploring different nanomaterials (e.g., graphene, carbon nanotubes) with their respective size-dependent properties.
- Examining dynamic loading conditions and vibration response.
- Incorporating multi-physics coupling effects (electro-mechanical, thermo-mechanical) relevant to next-generation nano-devices.

The methodology developed in this study provides a framework for future investigations into complex nanostructure behavior where classical theories prove inadequate.

Declaration of Ethical Standards

The author(s) declare that they have carried out this completely original study by adhering to all ethical rules including authorship, citation and data reporting.

Credit Authorship Contribution Statement

Uğur Kafkas conceived and designed the study, analyzed the data and wrote the manuscript.

Declaration of Competing Interest

The author(s) declare that they have no known competing financial interests or personal relationships that could have appeared to influence the work reported in this paper.

Funding / Acknowledgements

The author(s) received no financial support for the research.

Data Availability

This study does not contain usable data.

REFERENCES

[1]   M. A. Eltaher, A. Khairy, A. M. Sadoun, and F.-A. Omar, "Static and buckling analysis of functionally graded Timoshenko nanobeams," *Appl Math Comput*, vol. 229, pp. 283–295, Feb. 2014, doi: 10.1016/j.amc.2013.12.072.

[2]   A. A. Abdelrahman and M. A. Eltaher, "On bending and buckling responses of perforated nanobeams including surface energy for different beams theories," *Eng Comput*, vol. 38, no. 3, pp. 2385–2411, Jun. 2022, doi: 10.1007/s00366-020-01211-8.

[3]   M. Ö. Yaylı, "Stability analysis of a rotationally restrained microbar embedded in an elastic matrix using strain gradient elasticity," *Curved and Layered Structures*, vol. 6, no. 1, pp. 1–10, Jan. 2019, doi: 10.1515/cls-2019-0001.

[4]   F. Yang, A. C. M. Chong, D. C. C. Lam, and P. Tong, "Couple stress based strain gradient theory for elasticity," *Int J Solids Struct*, vol. 39, no. 10, pp. 2731–2743, May 2002, doi: 10.1016/S0020-7683(02)00152-X.

[5]   M. Ö. Yaylı, "Torsional vibrations of restrained nanotubes using modified couple stress theory," *Microsystem Technologies*, vol. 24, no. 8, pp. 3425–3435, Aug. 2018, doi: 10.1007/s00542-018-3735-3.

[6]   S. K. Park and X.-L. Gao, "Bernoulli–Euler beam model based on a modified couple stress theory," *Journal of Micromechanics and Microengineering*, vol. 16, no. 11, pp. 2355–2359, Nov. 2006, doi: 10.1088/0960-1317/16/11/015.

[7]   S. C. Polat and S. M. Bağdatlı, "Investigation of stepped microbeam vibration motions according to modified couple stress theory," *Zeitschrift für Naturforschung A*, vol. 78, no. 5, pp. 379–393, May 2023, doi: 10.1515/zna-2022-0286.

[8]   B. Uzun and M. Ö. Yaylı, "Porosity dependent torsional vibrations of restrained FG nanotubes using modified couple stress theory," *Mater Today Commun*, vol. 32, p. 103969, Aug. 2022, doi: 10.1016/j.mtcomm.2022.103969.

[9]   B. Uzun and M. Ö. Yaylı, "A Finite Element Solution for Bending Analysis of a Nanoframe using Modified Couple Stress Theory," *International Journal of Engineering and Applied Sciences*, vol. 14, no. 1, pp. 1–14, Sep. 2022, doi: 10.24107/ijeas.1064690.

[10]   B. Uzun and M. Ö. Yaylı, "A Unified Technique for Stability Analysis of an Embedded FG Porous Nano/Microbeam Via Modified Couple Stress Theory," *Nano*, Jul. 2024, doi: 10.1142/S1793292024500723.

[11]   B. Akgöz and Ö. Civalek, "Strain gradient elasticity and modified couple stress models for buckling analysis of axially loaded micro-scaled beams," *Int J Eng Sci*, vol. 49, no. 11, pp. 1268–1280, Nov. 2011, doi: 10.1016/j.ijengsci.2010.12.009.

[12]   B. Uzun, U. Kafkas, and M. Ö. Yaylı, "Free vibration analysis of nanotube based sensors including rotary inertia based on the Rayleigh beam and modified couple stress theories," *Microsystem Technologies*, vol. 27, no. 5, pp. 1913–1923, May 2021, doi: 10.1007/s00542-020-04961-z.

[13]   S. C. Pradhan and G. K. Reddy, "Buckling analysis of single walled carbon nanotube on Winkler foundation using nonlocal elasticity theory and DTM," *Comput Mater Sci*, vol. 50, no. 3, pp. 1052–1056, Jan. 2011, doi: 10.1016/J.COMMATSCI.2010.11.001.

[14]   B. Uzun, Ö. Civalek, and M. Ö. Yaylı, "Vibration of FG nano-sized beams embedded in Winkler elastic foundation and with various boundary conditions," *Mechanics Based Design of Structures and Machines*, vol. 51, no. 1, pp. 481–500, Jan. 2023, doi: 10.1080/15397734.2020.1846560.

[15]   N. Togun and S. Bağdatlı, "Nonlinear Vibration of a Nanobeam on a Pasternak Elastic Foundation Based on Non-Local Euler-Bernoulli Beam Theory," *Mathematical and Computational Applications*, vol. 21, no. 1, p. 3, Mar. 2016, doi: 10.3390/mca21010003.

[16]   B. Uzun and M. Ö. Yaylı, "Porosity and Deformable Boundary Effects on the Dynamic of Nonlocal Sigmoid and Power-Law FG Nanobeams Embedded in the Winkler–Pasternak Medium," *Journal of Vibration Engineering & Technologies*, vol. 12, no. 3, pp. 3193–3212, Mar. 2024, doi: 10.1007/s42417-023-01039-8.

[17]   W.-T. Park, S.-C. Han, W.-Y. Jung, and W.-H. Lee, "Dynamic instability analysis for S-FGM plates embedded in Pasternak elastic medium using the modified couple stress theory," *Steel and Composite Structures*, vol. 22, no. 6, pp. 1239–1259, Dec. 2016, doi: 10.12989/scs.2016.22.6.1239.

[18]   N. Togun and S. M. Bağdatli, "The vibration of nanobeam resting on elastic foundation using modified couple stress theory," *Tehnički glasnik*, vol. 12, no. 4, pp. 221–225, Dec. 2018, doi: 10.31803/tg-20180214212115.

[19]   B. Akgöz and Ö. Civalek, "Free vibration analysis for single-layered graphene sheets in an elastic matrix via modified couple stress theory," *Mater Des*, vol. 42, pp. 164–171, Dec. 2012, doi: 10.1016/j.matdes.2012.06.002.

[20]   B. Akgöz and Ö. Civalek, "Modeling and analysis of micro-sized plates resting on elastic medium using the modified couple stress theory," *Meccanica*, vol. 48, no. 4, pp. 863–873, May 2013, doi: 10.1007/s11012-012-9639-x.

[21]   M. Şimşek, "Nonlinear static and free vibration analysis of microbeams based on the nonlinear elastic foundation using modified couple stress theory and He's variational method," *Compos Struct*, vol. 112, pp. 264–272, Jun. 2014, doi: 10.1016/j.compstruct.2014.02.010.

[22]   U. Kafkas, Y. Ünal, M. Ö. Yaylı, and B. Uzun, "Buckling analysis of perforated nano/microbeams with deformable boundary conditions via nonlocal strain gradient elasticity," *Adv Nano Res*, vol. 15, no. 4, pp. 339–353, 2023, doi: 10.12989/anr.2023.15.4.339.

[23]   L. Luschi and F. Pieri, "An analytical model for the determination of resonance frequencies of perforated beams," *Journal of Micromechanics and Microengineering*, vol. 24, no. 5, p. 055004, May 2014, doi: 10.1088/0960-1317/24/5/055004.

[24]   U. Kafkas, "On the free vibration of a perforated Rayleigh beam with deformable ends," *Engineering Science and Technology, an International Journal*, vol. 56, p. 101787, Aug. 2024, doi: 10.1016/J.JESTCH.2024.101787.

[25]   A. A. Abdelrahman, M. A. Eltaher, A. M. Kabeel, A. M. Abdraboh, and A. A. Hendi, "Free and forced analysis of perforated beams," *Steel and Composite Structures*, vol. 31, no. 5, p. 489, 2019.

[26]   B. Uzun and M. Ö. Yaylı, "Bending Analysis of A Perforated Microbeam With Laplace Transform," *Konya Journal of Engineering Sciences*, vol. 11, pp. 23–31, Dec. 2023, doi: 10.36306/konjes.1384835.

[27]   A. Assie, Ş. D. Akbaş, A. H. Bashiri, A. A. Abdelrahman, and M. A. Eltaher, "Vibration response of perforated thick beam under moving load," *The European Physical Journal Plus*, vol. 136, no. 3, p. 283, Mar. 2021, doi: 10.1140/epjp/s13360-021-01224-2.

[28]   M. A. Eltaher, R. A. Shanab, and N. A. Mohamed, "Analytical solution of free vibration of viscoelastic perforated nanobeam," *Archive of Applied Mechanics*, vol. 93, no. 1, pp. 221–243, Jan. 2023, doi: 10.1007/s00419-022-02184-4.

[29]   U. Kafkas, B. Uzun, M. Ö. Yaylı, and G. Güçlü, "Thermal vibration of perforated nanobeams with deformable boundary conditions via nonlocal strain gradient theory," *Zeitschrift für Naturforschung A*, vol. 0, no. 0, Jun. 2023, doi: 10.1515/zna-2023-0088.

[30]   Ö. Civalek, B. Uzun, and M. Ö. Yaylı, "Size-dependent nonlinear stability response of perforated nano/microbeams via Fourier series," *Archive of Applied Mechanics*, vol. 93, no. 12, pp. 4425–4443, Dec. 2023, doi: 10.1007/s00419-023-02501-5.

[31]   B. Uzun, Ö. Civalek, and M. Ö. Yaylı, "Critical buckling loads of embedded perforated microbeams with arbitrary boundary conditions via an efficient solution method," *Zeitschrift für Naturforschung A*, vol. 78, no. 2, pp. 195–207, Feb. 2023, doi: 10.1515/zna-2022-0230.

[32]   T. Küpeli, Y. H. Çavuş, B. Uzun, and M. Ö. Yaylı, "Free Vibration Response of a Steel Liquid Storage Tank with Porous and Perforated Columns via an Exact Continuum Method," *Gazi University Journal of Science*, vol. 36, no. 2, pp. 555–571, Jun. 2023, doi: 10.35378/gujs.1047479.

[33]   M. A. Koç, M. Eroğlu, and İ. Esen, "Dynamic analysis of high-speed train moving on perforated Timoshenko and Euler–Bernoulli beams," *International Journal of Mechanics and Materials in Design*, vol. 18, no. 4, pp. 893–917, Dec. 2022, doi: 10.1007/s10999-022-09610-z.

[34]   A. A. Abdelrahman, I. Esen, C. Özarpa, and M. A. Eltaher, "Dynamics of perforated nanobeams subject to moving mass using the nonlocal strain gradient theory," *Appl Math Model*, vol. 96, pp. 215–235, Aug. 2021, doi: 10.1016/j.apm.2021.03.008.

[35]   A. A. Abdelrahman, I. Esen, C. Özarpa, R. Shaltout, M. A. Eltaher, and A. E. Assie, "Dynamics of perforated higher order nanobeams subject to moving load using the nonlocal strain gradient theory," *Smart Struct Syst*, vol. 28, no. 4, pp. 515–53, Oct. 2021, doi: 10.12989/sss.2021.28.4.515.

[36]   A. A. Abdelrahman, H. E. Abdel-Mottaleb, A. Aljabri, E. R. I. Mahmoud, and M. A. Eltaher, "Modeling of size dependent buckling behavior of piezoelectric sandwich perforated nanobeams

rested on elastic foundation with flexoelectricity," *Mechanics Based Design of Structures and Machines*, pp. 1–27, Jun. 2024, doi: 10.1080/15397734.2024.2365918.

[37]   K. H. Almitani, A. A. Abdelrahman, and M. A. Eltaher, "Stability of perforated nanobeams incorporating surface energy effects," *Steel and Composite Structures, An International Journal*, vol. 35, no. 4, pp. 555–566, 2020.

[38]   M. A. Eltaher, A. M. Kabeel, K. H. Almitani, and A. M. Abdraboh, "Static bending and buckling of perforated nonlocal size-dependent nanobeams," *Microsystem Technologies*, vol. 24, no. 12, pp. 4881–4893, Dec. 2018, doi: 10.1007/s00542-018-3905-3.

[39]   I. Esen, A. A. Abdelrahman, and M. A. Eltaher, "Dynamics analysis of timoshenko perforated microbeams under moving loads," *Eng Comput*, vol. 38, no. 3, pp. 2413–2429, Jun. 2022, doi: 10.1007/s00366-020-01212-7.

[40]   M. A. Eltaher, A. M. Abdraboh, and K. H. Almitani, "Resonance frequencies of size dependent perforated nonlocal nanobeam," *Microsystem Technologies*, vol. 24, no. 9, pp. 3925–3937, Sep. 2018, doi: 10.1007/s00542-018-3910-6.

[41]   K. Mercan, H. M. Numanoglu, B. Akgöz, C. Demir, and Ö. Civalek, "Higher-order continuum theories for buckling response of silicon carbide nanowires (SiCNWs) on elastic matrix," *Archive of Applied Mechanics*, vol. 87, no. 11, pp. 1797–1814, Nov. 2017, doi: 10.1007/s00419-017-1288-z.

[42]   Ö. Civalek, H. Numanoğlu, and K. Mercan, "Finite Element Model and Size Dependent Stability Analysis of Boron Nitride and Silicon Carbide Nanowires/Nanotubes," *Scientia Iranica*, vol. 0, no. 0, pp. 0–0, Apr. 2019, doi: 10.24200/sci.2019.52517.2754.

[43]   Ç. Demir and Ö. Civalek, "A new nonlocal FEM via Hermitian cubic shape functions for thermal vibration of nano beams surrounded by an elastic matrix," *Compos Struct*, vol. 168, pp. 872–884, May 2017, doi: 10.1016/J.COMPSTRUCT.2017.02.091.

[44]   J. N. Reddy, *Energy Principles and Variational Methods in Applied Mechanics* , 2. New York: John Wiley and Sons, 2002.

[45]   J. K. Phadikar and S. C. Pradhan, "Variational formulation and finite element analysis for nonlocal elastic nanobeams and nanoplates," *Comput Mater Sci*, vol. 49, no. 3, pp. 492–499, Sep. 2010, doi: 10.1016/j.commatsci.2010.05.040.

[46]   M. Şimşek, "Some closed-form solutions for static, buckling, free and forced vibration of functionally graded (FG) nanobeams using nonlocal strain gradient theory," *Compos Struct*, vol. 224, p. 111041, Sep. 2019, doi: 10.1016/j.compstruct.2019.111041.

[47]   S. K. Park and X.-L. Gao, "Variational formulation of a modified couple stress theory and its application to a simple shear problem", *Zeitschrift für angewandte Mathematik und Physik*, 59:904–917, 2008, doi: 10.1007/s00033-006-6073-8.

[48]   J. N. Reddy, "Microstructure-dependent couple stress theories of functionally graded beams", *J Mech Phys Solids*, 59:2382–2399, 2011, doi: 10.1016/j.jmps.2011.06.008.

PHOTODYNAMIC THERAPY FOR PERI-IMPLANTITIS: COMPARATIVE ANALYSES ON *IN VITRO* MODELS

[1] Ebru SARAÇ ID **, [2] Eylül Sena CEYLAN** ID **, [3, *] Mustafa Kemal RUHİ** ID

[1, 3] *Boğaziçi University, Institute of Biomedical Engineering, Istanbul, TURKIYE*
[2] *Izmir Katip Çelebi University, Department of Biomedical Engineering, İzmir, TURKIYE*
[1] ebru.sarac@std.bogazici.edu.tr, [2] 190402015@ogr.ikcu.edu.tr, [3] kemal.ruhi@bogazici.edu.tr

Highlights

- Sandblasting one side of the titanium discs increases the clustered and surface-associated bacteria.

- *S. aureus* shows less sensitivity to Ce6-mediated aPDT than MB-mediated aPDT in planktonic conditions.

- Ce6-mediated aPDT performs comparably to MB-mediated aPDT in the adhered bacteria model, however, both treatments resulted in less than a 1-log reduction in bacterial load

- Despite Ce6's lower dark toxicity compared to MB, MB-mediated aPDT remains the preferred option for peri-implantitis treatment due to its lower cost.

Graphical Abstract

In this study, planktonic bacteria and bacteria grown on sandblasted titanium discs were used to model the disease peri-implantitis, which is defined as the microbial complication characterized by soft tissue inflammation and progressive bone loss around a dental implant due to bacterial infection. The treatment methods that are compared are aPDT using 660 nm light source and two photosensitizers, Ce6 and MB.

*Corresponding Author: Mustafa Kemal RUHİ, kemal.ruhi@bogazici.edu.tr

PHOTODYNAMIC THERAPY FOR PERI-IMPLANTITIS: COMPARATIVE ANALYSES ON *IN VITRO* MODELS

[1] Ebru SARAÇ ID **, [2] Eylül Sena CEYLAN** ID **, [3, *] Mustafa Kemal RUHİ** ID

[1, 3] *Boğaziçi University, Institute of Biomedical Engineering, Istanbul, TÜRKİYE*
[2] *Izmir Katip Çelebi University, Department of Biomedical Engineering, İzmir, TÜRKİYE*
[1] ebru.sarac@std.bogazici.edu.tr, [2] 190402015@ogr.ikcu.edu.tr, [3] kemal.ruhi@bogazici.edu.tr

ABSTRACT: Chlorin e6 (Ce6) is a Food and Drug Administration-approved photosensitizer that is promising with its low cytotoxicity and effective generation of reactive oxygen species for PDT of bacterial infections. Although the eradication of bacteria by Ce6-mediated antibacterial photodynamic therapy (aPDT) was previously investigated, no previous study has systematically analyzed this treatment method using distinct experimental models in the context of peri-implantitis. This study aims to compare the effectiveness of Ce6-mediated antibacterial aPDT by comparing the outcomes with methylene blue (MB)-mediated protocol as a standard for aPDT in oral applications using two different experimental models. By evaluating these treatments across different conditions, this study intended to provide new insights into their relative efficacy. Additionally, this study investigated the differences in bacterial susceptibility between planktonic and surface-attached states, highlighting how attachment alone may influence treatment resistance. Planktonic *Staphylococcus aureus (S. aureus)* and *S. aureus* adhered to roughened titanium discs were treated with non-toxic concentrations of Ce6 and MB, followed by the irradiation using a 660 nm light source at 100 mW/cm^2 power density. The treatment outcomes were evaluated using the serial dilution method. Ce6-mediated aPDT could achieve less than a log decrease in normalized colony forming unit (CFU) in planktonic bacteria, while the reduction in normalized CFU in MB-mediated protocol was about 4-log. In the titanium-adhered infection model, the reduction after both protocols was below 1-log, representing a relatively low bactericidal efficacy. In conclusion, Ce6-mediated aPDT is as efficient as the MB-mediated protocol on bacteria adhered to titanium discs. However, both protocols exhibited limited efficacy. These results emphasize the challenge of effectively targeting adhered bacterial populations and suggest the need for optimizing aPDT protocols.

Keywords: Peri-Implantitis, Photodynamic Therapy, Chlorin E6, Methylene Blue

1. INTRODUCTION

Titanium is one of the most popular biomaterials used in dental implants [1]. The implant surface is usually roughened to increase new bone formation around the implant, also known as osseointegration [2]. However, rough surfaces can promote bacterial adhesion on implants, potentially leading to peri-implantitis, an infectious condition that causes bone loss around dental implants [2], [3], [4]. The treatment methods for peri-implantitis include antibiotics, resective surgery, mechanical debridement, and applying certain chemicals for decontamination. Although surgery is an effective treatment for peri-implantitis, this invasive procedure can cause pain and discomfort due to prolonged healing [5]. Antibiotic treatment may not be effective on resistant bacteria [6]. Mechanical debridement may alter the surface properties of the implant, and chemicals should be used with caution due to their high toxicity [5]. Overall, adjuvant treatments are generally needed for successful treatment outcomes [7].

Antibacterial PDT (aPDT) is a non-invasive method that relies on the administration of a chemical called photosensitizer, followed by irradiation of the infected area with light at a specific wavelength to create reactive oxygen species (ROS), toxic to bacteria [8], [9], [10]. Due to this distinct mechanism, aPDT can be an effective treatment method for the inactivation of antibiotic-resistant bacteria [11], [12]. aPDT was evaluated by many research groups as individual or adjuvant therapy for peri-implantitis. For

*Corresponding Author: Mustafa Kemal RUHİ, kemal.ruhi@bogazici.edu.tr

example, Dörtbudak *et al.* investigated the antimicrobial effect of toluidine blue-mediated aPDT on patients with peri-implantitis by irradiating the implant surfaces with a 690 nm light source for one minute [13]. The result of the study showed that toluidine blue-mediated aPDT reduced the average bacterial counts by 2 logs. A case report from Carvalho *et al.* showed that aPDT using methylene blue (MB) and 660 nm light together with surgery resulted in adequate cleaning of the infection and promoted bone regeneration after a 6-month follow-up [14]. Ghanem *et al.,* however, reported that the role of aPDT as an adjunct to mechanical curettage is debatable in the review article they analyzed five clinical and four experimental studies [15]. The literature search reveals that studies that exploit aPDT for peri-implantitis most commonly prefer MB and toluidine blue as photosensitizers [14]. Although many effective studies have been reported, the therapeutic window (the condition for a photodynamic inactivation that ensures bacteria are effectively eliminated without causing harm to other cells) of these photosensitizers could not be precisely determined [16], [17], [18].

The photosensitizer that was suggested for the current study, chlorin e6 (Ce6), has been studied extensively in cancer studies due to its favorable properties, such as low dark toxicity, high absorption at near-infrared wavelengths of the electromagnetic spectrum, and effective generation of ROS upon excitation by light [19], [20]. However, there are limited studies evaluating Ce6 for aPDT. In a study that compares the aPDT efficiency of MB and Ce6 on *Streptococcus mutans (S. mutans)* biofilms, Nie *et al.* demonstrated that both Ce6 and MB were efficient in removing biofilms, although Ce6-mediated aPDT was more effective than MB at higher photosensitizer concentrations [21]. Another study of the same group examined the synergistic antibacterial effect of Ce6 and hydrogen peroxide on multi-species biofilms [22]. Their results showed that 50 μM Ce6 with 5 minutes of irradiation led to an approximately 0.8-log CFU reduction. The addition of 33.3 mM hydrogen peroxide enhanced this effect, increasing the reduction to 2.1-log CFU. Avşar et al. investigated the antibacterial efficacy of Ce6-mediated PDT in the presence of 20% ethanol against methicillin-resistant *Staphylococcus aureus* (MRSA) [23]. All PDT-treated groups demonstrated strong antibacterial efficacy, which was further increased by the addition of ethanol. Bishoff et al. explored the efficacy of Ce6-mediated aPDT on various multidrug-resistant *S. aureus* strains by increasing both incubation and irradiation times [24]. The authors assessed 1, 5, and 10-minute irradiation at a power density of 30.6 mW/cm². At 512 μM Ce6 with a total fluence of 18.60 J/cm², the bacterial load was reduced by 3-log (99.9% killing rate). Similarly, at lower Ce6 concentrations (32 and 64 μM), approximately a 0.7-log reduction was observed. Park et al. investigated the effect of Ce6-mediated PDT on *S. aureus Xen29*, a bioluminescent strain derived from *S. aureus* ATCC 25923, in biofilms [25]. A significant reduction in biofilm formation was achieved using 10 μM Ce6 irradiated at 10 J/cm².

This study hypothesizes that Ce6-mediated aPDT will be an efficient method for the treatment of peri-implantitis. *In vitro* aPDT studies generally utilize glassware or well plates to examine aPDT efficacy, although the implants are typically made from titanium. Using more realistic *in vitro* models is necessary to mimic the physical and mechanical environment that may affect the behavior and treatment response of bacteria [26], [27], [28]. Therefore, in this study, our research group aimed to compare the efficacy of Ce6-mediated aPDT with MB-mediated protocol on both planktonic bacteria and bacteria adhered to titanium discs as *in vitro* peri-implantitis models. While both the experimental models and the peri-implantitis treatment methods evaluated in this study have been previously investigated, no study to date has systematically compared their outcomes across different models. By applying these treatments to two distinct experimental systems, our study provides new insights into how model selection may influence treatment efficacy, offering a more comprehensive understanding of their potential clinical relevance.
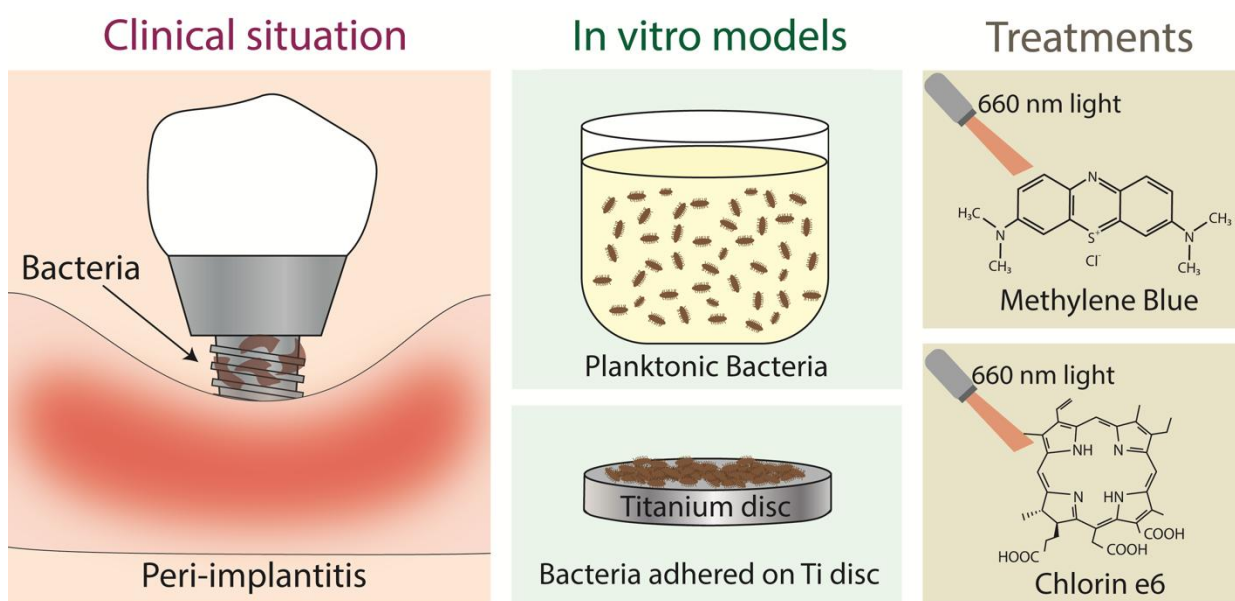
Graphical Abstract. In this study, planktonic bacteria and bacteria grown on sandblasted titanium discs were used to model the disease peri-implantitis, which is defined as the microbial complication characterized by soft tissue inflammation and progressive bone loss around a dental implant due to bacterial infection. The treatment methods that are compared are aPDT using 660 nm light source and two photosensitizers, Ce6 and MB.

2.   MATERIAL AND METHODS

This study first fabricated and characterized the *in vitro* peri-implantitis model. Then, the dark toxicities of the photosensitizers on bacteria and mouse fibroblast cells were evaluated. Subsequently, the aPDT efficacy of the two photosensitizers was assessed on two different infection models. The details of the methods are given below.

2.1. Bacterial strain and assessment of the treatment outcomes

This study utilized bacterial cultures, which do not involve human or animal subjects. Therefore, ethics approval and informed consent were not required for this research. ATCC 25923 *S. aureus* from -80°C frozen stock was used to obtain single colonies by a streaking method on a tryptic soy agar plate. A single colony was inoculated with the tryptic soy broth (TSB) and cultured overnight (18-20 hours) at 37°C in a shaking incubator at 200 rpm. 1 ml of overnight culture was centrifuged at 3000 rpm for 10 minutes, and the supernatant was discarded. The pellet was washed two times and resuspended in phosphate-buffered saline (PBS) to a final concentration of 10^{7}-10^{8} colony-forming units (CFU) per milliliter (CFU/ml). After the experiments, all groups were diluted by using the serial dilution method. 30 μL of aliquots of diluted suspensions were spread on tryptic soy agar plates and incubated for 24 hours at 37°C. CFUs were counted and multiplied by the dilution factor to assess the efficacy of the treatments.

2.2. Cell culturing and assessment of cytotoxicity

The cytotoxicity study was conducted using L929 mouse fibroblast cells. These cells were grown in RPMI 1640 medium with 10% fetal bovine serum (FBS) and 1% penicillin/streptomycin and maintained at 37°C in a 5% CO_2 environment. On the first day, 10,000 cells were placed in each well of a 96-well plate and allowed to incubate overnight. The next day, the cells were exposed to specified concentrations of photosensitizers in for 15 minutes. After the exposure, the medium was replaced with fresh RPMI, and the cells were incubated overnight. The cytotoxicity of the photosensitizers on L929 cells was evaluated

using the MTT assay.

2.3. Preparation of rough titanium discs

One side of the grade-2 titanium discs was treated with sandblasting to increase bacteria adhesion. Untreated sides of the discs were covered with polydimethylsiloxane to prevent bacterial adhesion and to adhere discs to the well surface. 9 discs with 15 mm diameter and 2 mm thickness were used throughout the experiments. Before each experiment, the discs were ultrasonically cleaned with acetone and absolute ethanol, then rinsed with distilled water and autoclaved for 15 minutes at 121°C.

2.4. Roughness measurement of titanium discs

Roughness values were measured before and after the experiments using a Hirox, KH-8700 3D digital microscope. Arithmetic mean deviation of the assessed profile (Ra), maximum height of profile (Rz), and ten-point mean roughness (Rzjis, average of the absolute values of the five highest peaks and the five deepest valleys) were analyzed by the software of the device.

2.5. Culturing bacteria on titanium discs

S. aureus was grown in TSB overnight at 37°C in a shaking incubator at 200 rpm. The culture was diluted in fresh TSB to a final concentration of 10^7-10^8 CFU/ml supplemented with 200 µl of 50% glucose. Titanium disks were placed into wells of a 12 well-plate, and 1.5 ml of TSB culture was dispensed into the wells. After the first 24 hours, 500 ml of fresh TSB was added into each well and bacteria were grown for another 24 hours at 37°C. Before aPDT applications, the discs were washed 2 times with 1 ml PBS to remove the planktonic or loosely adherent bacterial cells.

2.6. Optical setup and absorption spectra of the photosensitizers

A Thorlabs M660L4-C1 660 nm collimated LED light source was used throughout the experiments. The power density of the light source was adjusted to 100 mW/cm^2 using a power meter before each aPDT application. 30 J/cm^2 and 60 J/cm^2 energy densities were applied to the wells by setting the irradiation times to 5 and 10 minutes. The absorption spectra of the photosensitizers (Ce6: 25 µM, MB: 5 µM) were acquired before and after irradiations (Ce6: 60 J/cm^2, MB: 30 J/cm^2) using a Nanodrop 2000c UV-visible spectrophotometer.

2.7. Photodynamic therapy

The stock solutions of Ce6 and MB were prepared in PBS from powder and stored in the refrigerator at 4°C. On the first day of experiments, 1 ml aliquots of bacterial suspension were transferred into wells. In the "no treatment," "only laser" and "only photosensitizer" groups, bacterial suspensions were mixed with the same amount of PBS. Different PDT parameters were chosen in this study based on the dark toxicity and preliminary phototoxicity results, as shown in Table 1. In the aPDT groups, 1 ml of Ce6 (25 µM) and MB (5 µM) solutions were added to the wells and mixed with bacterial suspension in the dark. The wells were incubated for 15 minutes at 37°C and then exposed to light (5 minutes for 30 J/cm^2, 10 minutes for 60 J/cm^2). For the experiments conducted on titanium discs, the discs covered with bacteria were placed on new 12-well plates and incubated with 1 ml of 25 µM Ce6 and 5 µM MB solutions for 15 minutes at 37°C. After the incubation period, the photosensitizer solutions were replaced with fresh PBS to minimize non-specific phototoxicity. Subsequently, the disks were exposed to light at 100 mW/cm^2 for 5 or 10 minutes. A summary of the PDT parameters is shown in Table 1.

Table 1. Summary of the PDT experiment parameters

	Photosensitizer concentration (μM)	Excitation duration (s)	Power density (mW/cm²)	Energy density (J/cm²)
Ce6-mediated PDT	25	600	100	60
MB-mediated PDT	5	300	100	30

To disaggregate the clusters of bacteria, disks were placed in 1 ml PBS and cleaned in an ultrasonic bath for 15 minutes, then vortexed for 1 minute. Bacterial suspensions were serially diluted and CFUs were determined as described in the assessment of the treatment outcomes. The experiments were performed at least three times.

2.8. Scanning electron microscope (SEM) analysis

The bacteria on titanium discs were imaged using a Philips XL30 ESEM FEG instrument. Before imaging, specimens were fixed in 2.5% glutaraldehyde overnight at 4°C and then dehydrated through 25%, 50%, 75%, and 100% ethanol. Finally, hexamethyldisilazane solution was applied to each disc, and discs were stored overnight in a hood.

2.9. Statistical analysis

The treatment outcomes were assessed by counting and normalizing the CFU to the respective no-treatment control. The normalized data were analyzed using analysis of variance (ANOVA) and Dunnett's multiple comparison test. The groups that are statistically significantly different ($p < 0.05$) were marked with a star (*). The data generated and analyzed during this study are available from the corresponding author upon request.

3. RESULTS

3.1. Dark toxicity of Ce6 and MB

The dark toxicities of the photosensitizers were evaluated at 5, 10, 25, and 50 μM concentrations. According to the results, the dark toxicity of Ce6 was lower than that of MB. For example, the normalized CFU for 25 μM Ce6 was 90.0%. On the other hand, the same concentration of MB decreased the normalized CFU to around 6.5% (Figure 1). Based on the results represented in Figure 1, the concentrations of Ce6 and MB that did not cause significant toxicity on *S. aureus* were determined as 25 μM and 5 μM, respectively.
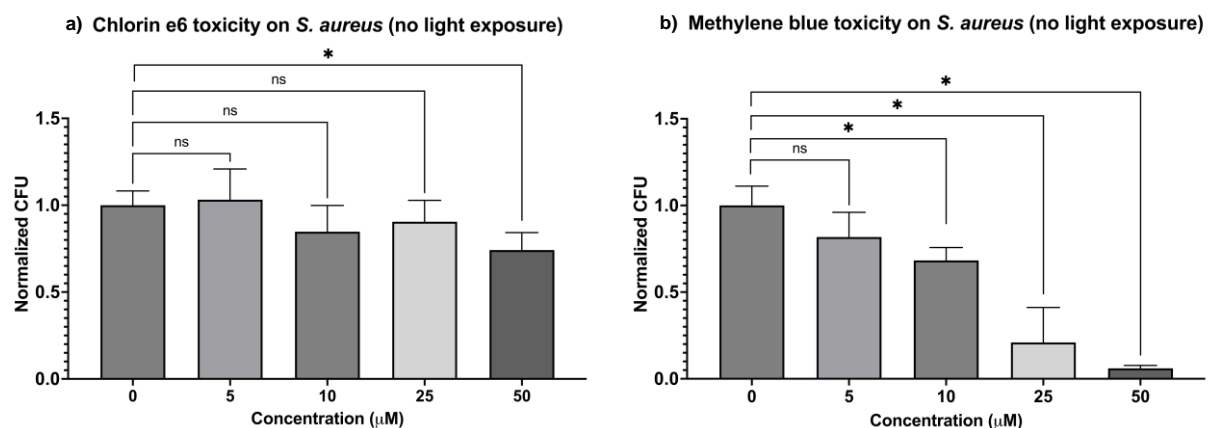
Figure 1. Dark toxicity of (a) Ce6 and (b) MB on *S. aureus* at varying concentrations. The groups that included photosensitizers were normalized to respective 0 mM controls. (ns: Not significant, *: p<0.05).

Additionally, the cytotoxicity of these concentrations on L929 mouse fibroblast cells was investigated, and the results revealed that the specified concentrations do not cause any significant toxicity on fibroblast cells (Figure 2)
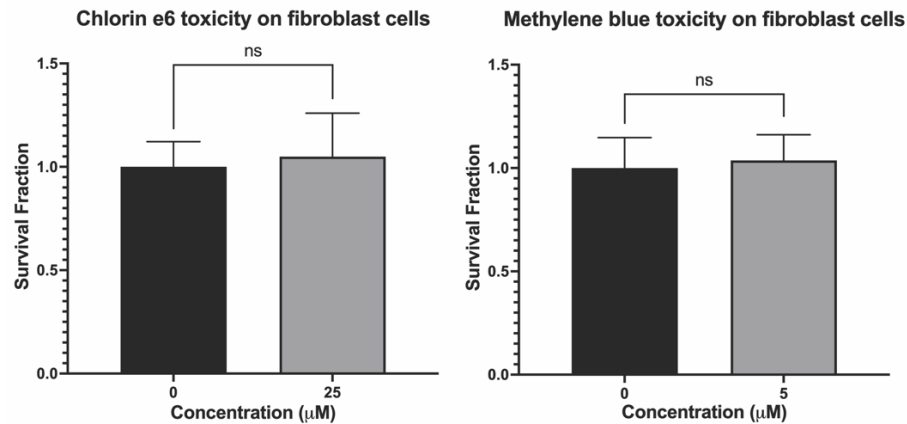
Figure 2. Dark toxicity of (a) Ce6 and (b) MB on L929 mouse fibroblast cells at specified concentrations (ns: Not significant).

3.2. Absorption spectra of the photosensitizers and the effect of 660 nm light on *S. aureus*

The absorption spectra of the photosensitizers shown in Supplementary Figure 1a reveal that both photosensitizers have absorptions around 660 nm. To determine the effect of 660 nm LED irradiation at 100 mW/cm^2 power density on bacteria, this power density was applied to the bacterial cultures for 5 and 10 minutes to achieve energy densities of 30 and 60 J/cm^2, respectively. The results have shown that light irradiation at these parameters does not cause any significant decrease in CFU (Supplementary Figure 1b).

3.3. Roughness of polished and sandblasted titanium discs

The roughness measurements shown in Table 2 revealed that both the arithmetic mean deviation and maximum height of the profile in sandblasted titanium discs are higher than in polished titanium discs, which was expected to increase the clustered and surface-associated bacteria number. The digital microscope images that correspond to the data in Table 2 are presented in Supplementary Figure 2.

Table 2. Titanium discs roughness values

	Polished Sample	Rough Sample 1	Rough Sample 2	Rough Sample 3
Ra, arithmetic mean deviation of the assessed profile (μm)	0.587	2.063	1.868	2.154
Rz, maximum height of the profile(μm)	1.173	4.612	4.262	4.688
Rzjis, ten-point mean roughness (μm)	0.911	3.737	3.372	3.754

3.4. Comparison of Ce6- and MB-mediated aPDT on planktonic bacteria and bacteria adhered to titanium discs

Ce6-mediated aPDT was first tested on planktonic bacteria using 30 and 60 J/cm^2 energy densities. Since the CFU decreased with increasing light energy density, the higher light energy density, 60 J/cm^2, was determined as the energy density to be used for further Ce6-mediated aPDT experiments (Supplementary Figure 3a). Unlike the Ce6-mediated application, aPDT using 5 μM MB and 30 J/cm^2 light

energy density was highly efficient, causing more than a 4-log decrease in the CFU (Supplementary Figure 3b). Therefore, no further experiment using a higher energy density was conducted, and 30 J/cm² was determined as the energy density to be used for further MB-mediated aPDT experiments.

The results shown in Figure 3 revealed that Ce6-mediated aPDT protocol (25 μM photosensitizer and 60 J/cm² energy density), which was drastically less efficient than MB-mediated protocol in the planktonic model, was as efficient as MB-mediated aPDT protocol (5 μM photosensitizer and 30 J/cm² energy density) on bacteria adhered to titanium discs.
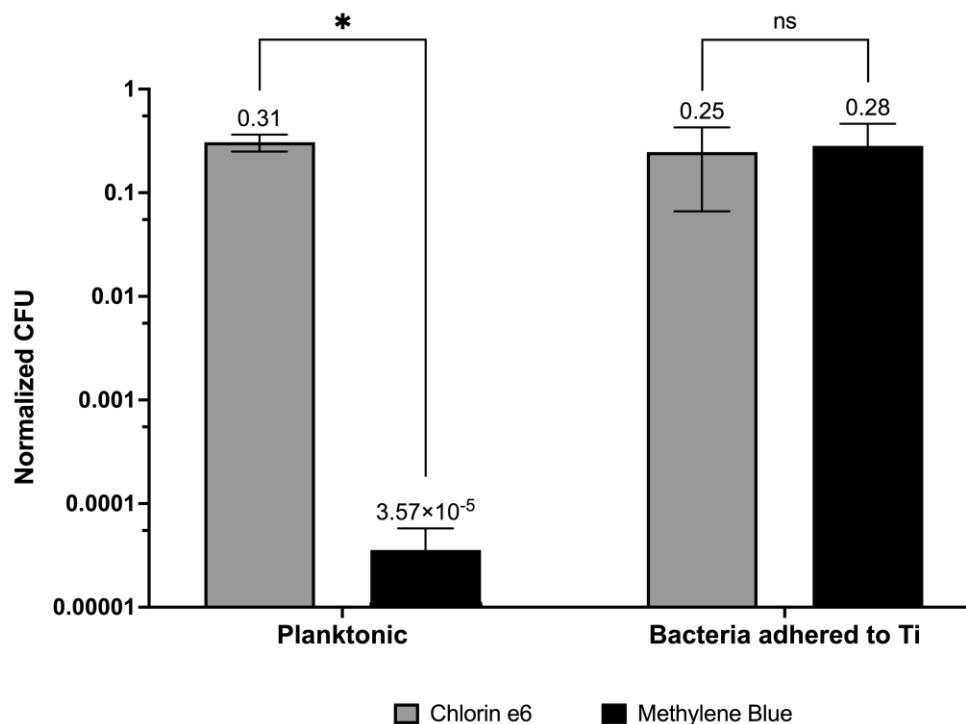
Figure 3. The change in the number of CFU after Ce6- and MB-mediated aPDT on two *in vitro* models: planktonic bacteria and bacteria adhered to titanium discs. Treatment groups were normalized to respective no-treatment controls. (Ce6-mediated aPDT: 25 μM Ce6 and 60 J/cm² energy density, MB-mediated aPDT: 5 μM MB and 30 J/cm² energy density, ns: Not significant, *: $p < 0.05$).

3.5. SEM examination of titanium discs with or without applications

The SEM images revealed the successful roughening of titanium discs, as well as the formation of clusters of bacteria. As shown in Figure 4, there are very few bacteria attached to the polished titanium disc; however, sandblasted titanium discs are covered with bacteria clusters. A visual examination of the images in Figure 4 suggests that both Ce6- and MB-mediated aPDT, had fewer bacteria on the surface of the discs compared to the control group. The full image set can be found in Supplementary Figure 4.

	Polished titanium No treatment	Sandblasted titanium No treatment	Chlorin e6-mediated photodynamic therapy	Methylene blue-mediated photodynamic therapy
Without KCl				
With KCl				
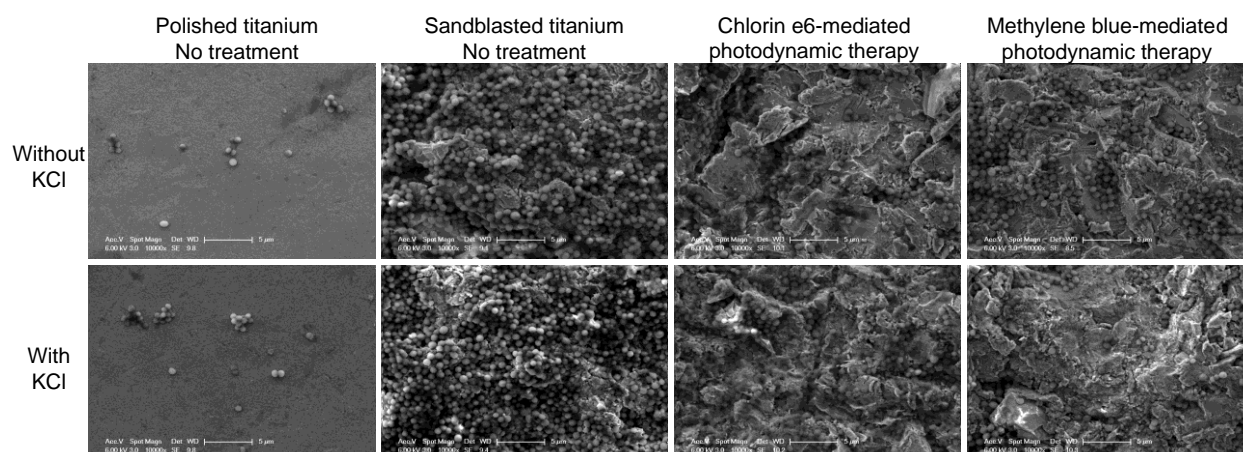
Figure 4. SEM images of bacteria clusters on titanium discs. (Scale bar: 5 μm, Ce6-mediated aPDT: 25 μM Ce6 and 60 J/cm² energy density, MB-mediated aPDT: 5 μM MB and 30 J/cm² energy density).

4. DISCUSSION

The treatment of peri-implantitis is challenging, therefore, alternative or complementary approaches to antibiotics and mechanical debridement are needed. aPDT is a promising treatment method for peri-implantitis, which was mostly researched using MB and TB. This study aimed to evaluate Ce6-mediated aPDT for peri-implantitis by comparing the results with MB-mediated protocol as a standard, in two different *in vitro* models. The first part of this study aimed to assess the dark toxicity of Ce6 and MB on planktonic bacteria and mouse fibroblast cells. According to our results, the concentrations of Ce6 and MB that did not cause significant toxicity on bacteria and fibroblast cells were determined as 25 μM and 5 μM, respectively. This difference is likely due to inherent variations in their chemical composition, mode of action, or interactions with cells, which was not investigated here but could be explored in future studies. A similar difference in cytotoxicity was also stated in the study of Nie *et al.*, however, the optimal concentrations of Ce6 and MB that we found were around five times less than what Nie *et al.* It should be kept in mind that Nie *et al.* evaluated the dark toxicity of these photosensitizers on *S. mutans* biofilms [21]. The second part of this study aimed to create a biofilm-like layer on a titanium surface that mimics the structure of a moderately rough dental implant surface because when investigating implant-associated infections, it is essential to study surface-adherent bacteria rather than planktonic suspensions, as bacteria attached to a surface exhibit different physiological characteristics and responses to treatments. In contrast to free-floating bacteria, surface-adherent populations can demonstrate increased tolerance to antibiotics and host immune responses, which may contribute to the persistence of infections [29], [30]. Therefore, studying bacteria in this adhered state provides a more clinically relevant understanding of how infections develop on biomaterials and allows for more effective evaluation of antimicrobial strategies. The literature focusing on bacterial adhesion suggests that the degree of bacterial adhesion depends on multiple factors, including chemical composition, wettability, and roughness of the surface [31]. While some reports suggest that surface roughness does not influence bacterial retention capacity [32], [33]; there are also studies reporting that rough surfaces enhance bacterial adhesion by providing a larger surface area. For example, İnan et al. reported that *Candida albicans* and *Staphylococcus epidermidis* adhesion varied significantly among PMMA and CO-Cr alloy substrates, with rougher surfaces exhibiting significantly higher bacterial load compared to smoother ones [34]. A study by Yoda et al. investigated the adherence of *Staphylococcus epidermidis* on five different kinds of surfaces, including stainless steel and pure titanium, and they grouped them as fine and coarse based on their surface roughness [35]. According to the results of the study, bacterial adhesion was significantly greater in the coarse groups. Here, we successfully roughened the surface by sandblasting the titanium discs to increase the number of clustered and surface-associated bacteria. Figure 4 reveals that bacteria adhered to the sandblasted samples instead of the polished samples. Therefore, our results are in accordance with the studies that suggest that increased

surface roughness promotes bacterial adhesion.

In the following step, the bacteria were treated with aPDT. According to the results shown in Figure 3, *S. aureus* was less sensitive to Ce6-mediated aPDT than MB-mediated aPDT in planktonic conditions. This finding is consistent with some studies in the literature while differing from others. For instance, a study by Çağan et al. evaluating Ce6-mediated PDT on *Pseudomonas aeruginosa* and the potentiation of bacterial eradication using ethanol also demonstrated that Ce6, when used with light energy densities and photosensitizer concentrations similar to our study, was ineffective [36]. However, Avşar et al. reported that Ce6-mediated PDT achieved a 99.99% bacterial reduction in MRSA at 20 μM with 25 J/cm² irradiation, which does not align with our results [23]. Also, Park et al. demonstrated a significant reduction in *S. aureus* biofilms at 10 μM Ce6 with 10 J/cm² [25]. These discrepancies could be attributed to differences in experimental conditions, such as incubation time, irradiation parameters, and bacterial strains. In the second *in vitro* model, however, surface-attached bacteria exhibited greater resistance to MB-mediated PDT compared to their planktonic counterparts. This increased resistance may result from physiological and metabolic changes that occur upon attachment. Surface-associated bacteria may exhibit altered gene expression, and local environmental factors, such as limited diffusion of the photosensitizer molecules, may further influence bacterial susceptibility. A noteworthy result in this study is that Ce6-mediated aPDT on bacteria adhered to titanium discs was as effective as on planktonic bacteria. In other words, the efficacy of Ce6-mediated aPDT was not negatively affected due to the cluster formation and surface adhesion of bacteria. The same light source was used to excite both photosensitizers, however, the energy densities, as well as the photosensitizer concentrations were higher in Ce6-mediated experiments. Differences in the chemical structures of the two photosensitizers may also have affected the interaction of these photosensitizers with bacteria in two different models. It should also be kept in mind that the two photosensitizers have different absorption characteristics at a wavelength of 660 nm (Supplementary Figure 1a and 1b). Further evaluation of Figure 3 also reveals that aPDT did not cause a log-level decrease in CFU when applied to bacteria adhered to titanium discs, therefore the efficacy of aPDT remained low compared to similar studies in the literature. However, it should be noted that other studies applied aPDT on well plates or by disassociating the bacteria instead of conducting aPDT directly on bacteria-adhered titanium surfaces [21], [37].

An important limitation of this study is the use of a mono-species model, which does not fully reflect the complexity of real peri-implantitis (PI) conditions. According to the literature, in the early stages of peri-implantitis, facultative anaerobic bacteria such as *Streptococcus* and *Actinomyces* species initially adhere to the implant surface [38], [39]. These early colonizers create a microbial ecosystem that facilitates the attachment of more complex and pathogenic bacteria, including difficult-to-treat gram-negative bacteria, further increasing resistance to conventional therapies [40], [41]. Therefore, incorporating a representative Gram-negative bacterium would provide a more comprehensive evaluation of the proposed treatments' efficacy.

Overall, this study provides insights into the differential efficacy of Ce6 and MB in aPDT across varying *in vitro* models. The results of the study reveal how results can differ from one *in vitro* model to another, which emphasizes the challenge in translating laboratory findings into real-world applications. Furthermore, the limited effectiveness observed in the adhered bacteria using the two researched aPDT protocols underscores the need for further optimization of aPDT for infection and, more specifically, for peri-implantitis. Future research should explore combination therapies or alternative photosensitizers to enhance aPDT outcomes in more clinically relevant models.

5. CONCLUSIONS

This study aimed to evaluate Ce6-mediated aPDT for peri-implantitis by comparing its efficacy to a standard protocol using both simple and complex *in vitro* models. The findings indicated that Ce6-mediated aPDT performed comparably to MB-mediated aPDT in the adhered bacteria model. However, both treatments resulted in less than a 1-log reduction in bacterial load. According to these results, despite Ce6's lower dark toxicity compared to MB, MB-mediated aPDT remains the preferred option for peri-

implantitis treatment due to its lower cost. Future research will focus on testing these protocols on implants retrieved from peri-implantitis cases and employing *in vivo* peri-implantitis models. Additionally, the potential of sequential aPDT applications, combination therapies, or alternative photosensitizers will be explored to enhance treatment efficacy.

Declaration of Ethical Standards

The authors declare that this study was conducted in compliance with all applicable laws, regulations, and institutional guidelines. All procedures were carried out in accordance with ethical standards.

Credit Authorship Contribution Statement

- **Ebru Saraç**: Conducted the experiments, analyzed the data, and contributed to the writing of the manuscript.

- **Eylül Sena Ceylan**: Conducted fibroblast cell culturing and cytotoxicity experiments.

- **Dr. Mustafa Kemal Ruhi**: Planned the study, provided resources, contributed to the writing of the manuscript, and performed manuscript editing.

Declaration of Competing Interest

The authors declare that they have no known competing financial interests or personal relationships that could have appeared to influence the work reported in this paper.

Funding / Acknowledgements

Data Availability

The data supporting this article's findings can be provided upon request.

REFERENCES

[1] H. Tschernitschek, L. Borchers, and W. Geurtsen, "Nonalloyed titanium as a bioinert metal--a review," *Quintessence Int*, vol. 36, no. 7-8, pp. 523-30, Jul-Aug 2005. [Online]. Available: https://www.ncbi.nlm.nih.gov/pubmed/15997933.

[2] W. Orapiriyakul, P. S. Young, L. Damiati, and P. M. Tsimbouri, "Antibacterial surface modification of titanium implants in orthopaedics," *J Tissue Eng*, vol. 9, p. 2041731418789838, Jan-Dec 2018, doi: 10.1177/2041731418789838.

[3] B. Klinge, M. Hultin, and T. Berglundh, "Peri-implantitis," *Dent Clin North Am*, vol. 49, no. 3, pp. 661-76, vii-viii, Jul 2005, doi: 10.1016/j.cden.2005.03.007.

[4] P. Diaz, E. Gonzalo, L. J. G. Villagra, B. Miegimolle, and M. J. Suarez, "What is the prevalence of peri-implantitis? A systematic review and meta-analysis," *BMC Oral Health*, vol. 22, no. 1, p. 449, Oct 19 2022, doi: 10.1186/s12903-022-02493-8.

[5] D. Rokaya, V. Srimaneepong, W. Wisitrasameewon, M. Humagain, and P. Thunyakitpisal, "Peri-implantitis Update: Risk Indicators, Diagnosis, and Treatment," *Eur J Dent*, vol. 14, no. 4, pp. 672-682, Oct 2020, doi: 10.1055/s-0040-1715779.

[6]   A. J. van Winkelhoff, "Antibiotics in the treatment of peri-implantitis," *Eur J Oral Implantol,* vol. 5 Suppl, pp. S43-50, 2012. [Online]. Available: https://www.ncbi.nlm.nih.gov/pubmed/22834393.

[7]   O. Unursaikhan *et al.*, "Comparative evaluation of roughness of titanium surfaces treated by different hygiene instruments," *J Periodontal Implant Sci,* vol. 42, no. 3, pp. 88-94, Jun 2012, doi: 10.5051/jpis.2012.42.3.88.

[8]   F. Cieplik *et al.*, "Antimicrobial photodynamic therapy - what we know and what we don't," *Crit Rev Microbiol,* vol. 44, no. 5, pp. 571-589, Sep 2018, doi: 10.1080/1040841X.2018.1467876.

[9]   Y. Feng, C. Coradi Tonon, S. Ashraf, and T. Hasan, "Photodynamic and antibiotic therapy in combination against bacterial infections: efficacy, determinants, mechanisms, and future perspectives," *Adv Drug Deliv Rev,* vol. 177, p. 113941, Oct 2021, doi: 10.1016/j.addr.2021.113941.

[10]   R. Youf *et al.*, "Antimicrobial Photodynamic Therapy: Latest Developments with a Focus on Combinatory Strategies," *Pharmaceutics,* vol. 13, no. 12, Nov 24 2021, doi: 10.3390/pharmaceutics13121995.

[11]   S. Rajesh, E. Koshi, K. Philip, and A. Mohan, "Antimicrobial photodynamic therapy: An overview," *J Indian Soc Periodontol,* vol. 15, no. 4, pp. 323-7, Oct 2011, doi: 10.4103/0972-124X.92563.

[12]   S. K. Sharma *et al.*, "Drug discovery of antimicrobial photosensitizers using animal models," *Curr Pharm Des,* vol. 17, no. 13, pp. 1303-19, 2011, doi: 10.2174/138161211795703735.

[13]   O. Dortbudak, R. Haas, T. Bernhart, and G. Mailath-Pokorny, "Lethal photosensitization for decontamination of implant surfaces in the treatment of peri-implantitis," *Clin Oral Implants Res,* vol. 12, no. 2, pp. 104-8, Apr 2001, doi: 10.1034/j.1600-0501.2001.012002104.x.

[14]   G. Garcia de Carvalho, J. C. Sanchez-Puetate, N. Casalle, E. Marcantonio Junior, and D. Leal Zandim-Barcelos, "Antimicrobial photodynamic therapy associated with bone regeneration for peri-implantitis treatment: A case report," *Photodiagnosis Photodyn Ther,* vol. 30, p. 101705, Jun 2020, doi: 10.1016/j.pdpdt.2020.101705.

[15]   A. Ghanem *et al.*, "Is mechanical curettage with adjunct photodynamic therapy more effective in the treatment of peri-implantitis than mechanical curettage alone?," *Photodiagnosis Photodyn Ther,* vol. 15, pp. 191-6, Sep 2016, doi: 10.1016/j.pdpdt.2016.06.007.

[16]   M. Tim, "Strategies to optimize photosensitizers for photodynamic inactivation of bacteria," *J Photochem Photobiol B,* vol. 150, pp. 2-10, Sep 2015, doi: 10.1016/j.jphotobiol.2015.05.010.

[17]   J. Yu, C. H. Hsu, C. C. Huang, and P. Y. Chang, "Development of therapeutic Au-methylene blue nanoparticles for targeted photodynamic therapy of cervical cancer cells," *ACS Appl Mater Interfaces,* vol. 7, no. 1, pp. 432-41, Jan 14 2015, doi: 10.1021/am5064298.

[18]   Y. Y. Huang, A. Wintner, P. C. Seed, T. Brauns, J. A. Gelfand, and M. R. Hamblin, "Antimicrobial photodynamic therapy mediated by methylene blue and potassium iodide to treat urinary tract infection in a female rat model," *Sci Rep,* vol. 8, no. 1, p. 7257, May 8 2018, doi: 10.1038/s41598-018-25365-0.

[19]   T. E. Kim and J. E. Chang, "Recent Studies in Photodynamic Therapy for Cancer Treatment: From Basic Research to Clinical Trials," *Pharmaceutics,* vol. 15, no. 9, Aug 31 2023, doi: 10.3390/pharmaceutics15092257.

[20]   A. Hak, M. S. Ali, S. A. Sankaranarayanan, V. R. Shinde, and A. K. Rengan, "Chlorin e6: A Promising Photosensitizer in Photo-Based Cancer Nanomedicine," *ACS Appl Bio Mater,* vol. 6, no. 2, pp. 349-364, Feb 20 2023, doi: 10.1021/acsabm.2c00891.

[21]   M. Nie *et al.*, "Photodynamic inactivation mediated by methylene blue or chlorin e6 against Streptococcus mutans biofilm," *Photodiagnosis Photodyn Ther,* vol. 31, p. 101817, Sep 2020, doi: 10.1016/j.pdpdt.2020.101817.

[22]   M. Nie *et al.*, "Synergetic antimicrobial effect of chlorin e6 and hydrogen peroxide on multi-species biofilms," *Biofouling,* vol. 37, no. 6, pp. 656-665, Jul 2021, doi: 10.1080/08927014.2021.1954169.

[23]   N. Topaloğlu Avşar, E. Bakay, and A. Kolkıran, "Photodynamic action of chlorin e6 against methicillin resistant staphylococcus aureus with the aid of ethanol," (in en), *Archives of Clinical and Experimental Medicine,* vol. 5, no. 3, pp. 100-105, December 2020, doi: 10.25000/acem.740365.

[24]   K. Winkler *et al.*, "Photodynamic inactivation of multidrug-resistant Staphylococcus aureus by chlorin e6 and red light (lambda=670nm)," *J Photochem Photobiol B,* vol. 162, pp. 340-347, Sep 2016, doi: 10.1016/j.jphotobiol.2016.07.007.

[25]   J. H. Park *et al.*, "In vitro and in vivo antimicrobial effect of photodynamic therapy using a highly pure chlorin e6 against Staphylococcus aureus Xen29," *Biol Pharm Bull,* vol. 35, no. 4, pp. 509-14, 2012, doi: 10.1248/bpb.35.509.

[26]   V. D. Gordon and L. Wang, "Bacterial mechanosensing: the force will be with you, always," *J Cell Sci,* vol. 132, no. 7, Apr 3 2019, doi: 10.1242/jcs.227694.

[27]   F. Camacho-Alonso, J. Salinas, M. Sanchez-Siles, J. Pato-Mourelo, B. D. Cotrina-Veizaga, and N. Ortega, "Synergistic antimicrobial effect of photodynamic therapy and chitosan on the titanium-adherent biofilms of Staphylococcus aureus, Escherichia coli, and Pseudomonas aeruginosa: An in vitro study," *J Periodontol,* vol. 93, no. 6, pp. e104-e115, Jun 2022, doi: 10.1002/JPER.21-0306.

[28]   M. Giannelli *et al.*, "Effects of photodynamic laser and violet-blue led irradiation on Staphylococcus aureus biofilm and Escherichia coli lipopolysaccharide attached to moderately rough titanium surface: in vitro study," *Lasers Med Sci,* vol. 32, no. 4, pp. 857-864, May 2017, doi: 10.1007/s10103-017-2185-y.

[29]   L. Cegelski, C. L. Smith, and S. J. Hultgren, "Adhesion, Microbial," in *Encyclopedia of Microbiology (Third Edition),* M. Schaechter Ed. Oxford: Academic Press, 2009, pp. 1-10.

[30]   P. Shree, C. K. Singh, K. K. Sodhi, J. N. Surya, and D. K. Singh, "Biofilms: Understanding the structure and contribution towards bacterial resistance in antibiotics," *Medicine in Microecology,* vol. 16, p. 100084, 2023/06/01/ 2023, doi: https://doi.org/10.1016/j.medmic.2023.100084.

[31]   W. Teughels, N. Van Assche, I. Sliepen, and M. Quirynen, "Effect of material characteristics and/or surface topography on biofilm development," *Clin Oral Implants Res,* vol. 17 Suppl 2, pp. 68-81, Oct 2006, doi: 10.1111/j.1600-0501.2006.01353.x.

[32]   T. Wassmann, S. Kreis, M. Behr, and R. Buergers, "The influence of surface texture and wettability on initial bacterial adhesion on titanium and zirconium oxide dental implants," *Int J Implant Dent,* vol. 3, no. 1, p. 32, Dec 2017, doi: 10.1186/s40729-017-0093-3.

[33]   Y. Wu, J. P. Zitelli, K. S. TenHuisen, X. Yu, and M. R. Libera, "Differential response of Staphylococci and osteoblasts to varying titanium surface roughness," *Biomaterials,* vol. 32, no. 4, pp. 951-60, Feb 2011, doi: 10.1016/j.biomaterials.2010.10.001.

[34]   S. T. Hale İnan, Evșen Tamam, Bora Bağıs, "Farklı kaide materyallerine mikrobiyal tutunmanın değerlendirilmesi," (in tr), *Cumhuriyet Dental Journal,* vol. 17, no. 2, pp. 151-158, May 2014, doi: 10.7126/cdj.58140.1008002313.

[35]   I. Yoda *et al.*, "Effect of surface roughness of biomaterials on Staphylococcus epidermidis adhesion," *BMC Microbiol,* vol. 14, p. 234, Sep 2 2014, doi: 10.1186/s12866-014-0234-2.

[36]   M. Çağan, A. Kolkiran, and N. Topaloğlu, "The effect of ethanol on photoinactivation of pseudomonas aeruginosa with chlorin e6 as an adjuvant therapy," in *2017 Medical Technologies National Congress (TIPTEKNO),* 12-14 Oct. 2017 2017, pp. 1-4, doi: 10.1109/TIPTEKNO.2017.8238123.

[37]   A. Widodo, D. Spratt, V. Sousa, A. Petrie, and N. Donos, "An in vitro study on disinfection of titanium surfaces," *Clin Oral Implants Res,* vol. 27, no. 10, pp. 1227-1232, Oct 2016, doi: 10.1111/clr.12733.

[38]   N. de Campos Kajimoto, Y. de Paiva Buischi, M. Mohamadzadeh, and P. Loomer, "The Oral Microbiome of Peri-Implant Health and Disease: A Narrative Review," *Dent J (Basel),* vol. 12, no. 10, Sep 24 2024, doi: 10.3390/dj12100299.

[39]   S. Dieckow *et al.*, "Structure and composition of early biofilms formed on dental implants are complex, diverse, subject-specific and dynamic," *NPJ Biofilms Microbiomes,* vol. 10, no. 1, p. 155, Dec 24 2024, doi: 10.1038/s41522-024-00624-3.

[40]   P. S. Kumar, M. R. Mason, M. R. Brooker, and K. O'Brien, "Pyrosequencing reveals unique microbial signatures associated with healthy and failing dental implants," *J Clin Periodontol*, vol. 39, no. 5, pp. 425-33, May 2012, doi: 10.1111/j.1600-051X.2012.01856.x.

[41]   F. Schwarz, J. Derks, A. Monje, and H. L. Wang, "Peri-implantitis," *J Periodontol*, vol. 89 Suppl 1, pp. S267-S290, Jun 2018, doi: 10.1002/JPER.16-0350.

EFFICIENT PRETREATMENT OF CORN STRAW AND SORGHUM WITH LTTM FOR ENHANCED BIO-CONVERSION

[1] **Ahmet ÇATALOLUK** (ID) **,** [2] **Harun DEMİRLİ** (ID) **,** [3] **Berna NİŞ** (ID) **,** [4, *] **Burçak KAYA ÖZSEL** (ID)

Bursa Technical University, Department of Chemistry, Bursa, TURKIYE
[1] ahmetcataloluk72@gmail.com, [2] hdemirli52@gmail.com, [3] berna.nis@btu.edu.tr, [4] burcak.kaya@btu.edu.tr

Highlights

- Optimized LTTM pretreatment conditions maximize yields of xylose, glucose, and sucrose.

- LTTM pretreatment significantly enhances biomass conversion to 5-HMF and levulinic acid.

- LTTMs present a sustainable and effective approach for biomass pretreatment

*Corresponding Author: Burçak KAYA ÖZSEL, burcak.kaya@btu.edu.tr

EFFICIENT PRETREATMENT OF CORN STRAW AND SORGHUM WITH LTTM FOR ENHANCED BIO-CONVERSION

[1] **Ahmet ÇATALOLUK** (ID) , [2] **Harun DEMİRLİ** (ID) , [3] **Berna NİŞ** (ID) , [4, *] **Burçak KAYA ÖZSEL** (ID)

Bursa Technical University, Department of Chemistry, Bursa, TÜRKİYE
[1] ahmetcataloluk72@gmail.com, [2] hdemirli52@gmail.com, [3] berna.nis@btu.edu.tr, [4] burcak.kaya@btu.edu.tr

ABSTRACT: This study explores using a low transition temperature mixture (LTTM), containing sulfamic acid and ethylene glycol for the pretreatment of corn straw and sorghum biomass, aimed to improve the efficiency of converting biomass into platform chemicals. We first optimized the pretreatment conditions (solid-liquid ratio, temperature, and time) and assessed the conversion of pretreated biomass into 5-hydroxymethylfurfural (5-HMF) and levulinic acid (LA) using the catalyst Amberlyst-15. Optimal pretreatment conditions were found to be a solid-liquid ratio of 1:5 (w/w), a temperature of 40 °C, and a duration of 4 hours, which resulted in the highest yields of sugars; xylose, glucose, and sucrose. In the catalytic conversion of sorghum and corn straw pretreated with LTTM at 200 °C in the presence of Amberlyst-15, 801.2 ppm glucose and 1967.3 ppm levulinic acid were obtained from sorghum, while 663.9 ppm glucose and 1936.3 ppm levulinic acid were produced from corn straw. The study demonstrates that LTTMs offer effective and sustainable biomass pretreatment, improving the accessibility of lignocellulosic structure to catalysts, leading to higher yields of desired products like glucose and levulinic acid.

Keywords: Biomass, 5-Hydroxymethylfurfural, Levulinic Acid, LTTM, Pretreatment

1. INTRODUCTION

The utilization of renewable biomass in chemical production is not only significant for green chemistry but also plays a crucial role in sustainability. One of the biomass resources used for this purpose is lignocellulosic biomass. It primarily comprises lignin, cellulose, and hemicellulose, along with minor amounts of volatile oils and inorganic components [1]. The main target when producing chemicals from lignocellulosic biomass is the hydrolysis of cellulose and hemicellulose into their monosaccharides. Monosaccharides can be converted into several chemical products through other reactions like hydrolysis, dehydration, hydrogenation, oxidation, etc., under proper conditions for example, in either acid or base media [2], [3], [4]. The main goal of biomass pretreatment is to break down the complex structure of lignocellulosic biomass through the removing of lignin to make the cellulose and hemicellulose more accessible for subsequent processes like hydrolysis. Lignin provides mechanical strength to the cell wall via covalent cross-linking with the hemicellulosic structure and binding of the cellulose fibers [5], [6].

Biomass pretreatment methods can be classified into four main groups: physical, chemical, biological, and physicochemical pretreatments [7]. It is well-established that chemical pretreatment effectively removes lignin and hemicellulose from the structure. Various chemical pretreatment methods include dilute acid hydrolysis, strong acid hydrolysis, alkaline hydrolysis, organosolv processes, oxidative delignification, and more innovative approaches such as using ionic liquids, deep eutectic solvents (DES), or low transition temperature mixtures (LTTM) to enhance the accessibility of cellulose and hemicellulose for further processing [8]. Ionic liquids (ILs) are unconventional, primarily non-volatile ionic organic solvents, typically composed of an organic cation and an organic or inorganic anion, with melting points generally below 100 °C [9]. While ILs are known to be highly effective in the pretreatment of biomass, their use is limited due to several issues such as high costs, energy-intensive recovery processes, toxicity, and environmental concerns regarding their biodegradability [10]. To address these challenges, subsequent research has favored the use of deep eutectic solvents (DES), which are low-cost, easier to synthesize, have lower toxicity, higher biodegradability, and offer easier and more cost-effective recovery

*Corresponding Author: Burçak KAYA ÖZSEL, burcak.kaya@btu.edu.tr

and reuse compared to ILs [11]. Low transition temperature mixtures (LTTMs), classified as a subgroup of deep eutectic solvents (DESs), are unique in that they do not have a distinct melting point but instead display a glass transition temperature [12]. Although LTTMs show similar characteristics to DESs, they stand out as appealing solvents due to their wide availability of starting materials, biodegradability, biocompatibility, low toxicity, and straightforward preparation methods [13].

LTTMs have been often used in the literature for the removal of lignin. The degradation of the hard lignin-carbohydrate structure through the pretreatment increases the accessibility to the cellulosic/hemicellulosic structure, thus facilitating the breakdown of the biomass in hydrolysis or conversion. In a work focused on the preparation of LTTMs using L-malic acid/sucrose and monosodium glutamate, the effective solubility of grinded empty fruit bunches (EFBs) from an oil palm mill in LTTM was investigated [14]. Another study demonstrates that low LTTMs combining choline derivatives and glycerol effectively enhance cellulose content and lignin removal in corncob pretreatment. According to the results, corncob exhibited highly efficient pretreatment, with a 153% increase in cellulose content and a 27% lignin removal by using microwave irradiation heating at 90 °C and 150 °C, with residence times of 5 and 10 min. [15]. Lim et al. used an LTTM (choline chloride: malic acid) for the hydrolysis of bamboo to produce 5-HMF [16]. Through microwave heating, which is faster and more energy-efficient compared to traditional methods, they demonstrated that 5-HMF could be obtained with a yield of 10.8% under optimal conditions (120 °C, 10 minutes of reaction time). In this study, a new low transition temperature mixture (LTTM) composed of sulfamic acid and ethylene glycol, which was previously developed and characterized by our research group [17], was utilized for lignocellulosic biomass (corn straw and sorghum) pretreatment for hydrolysis and bio-conversion process. The pretreatment process aims to enhance the efficiency of subsequent catalytic conversions, a crucial step in the valorization of biomass. After subjecting the biomass to the optimized pretreatment conditions, the conversion of the treated corn straw and sorghum into valuable platform chemicals, including 5-hydroxymethylfurfural (5-HMF) and levulinic acid (LA), were investigated using the commercial solid acid catalyst Amberlyst-15. These chemicals serve as key intermediates for the production of biofuels, bioplastics, and other high-value chemicals, making this research significant in the context of sustainable chemical production. This study plays a significant role in filling the gap in the literature regarding the use of newly emerging LTTMs in biomass pretreatment. Demonstrating the efficacy of LTTMs in enhancing biomass conversion yields will facilitate to have more sustainable and cost-effective processes for producing renewable chemicals.

2. MATERIAL AND METHODS

2.1. Materials

The corn straw and sweet sorghum used as biomass in this study were obtained from local sales points in the Adana region of Turkey. Characterization of biomass materials was conducted in terms of cellulose [18], hemicellulose [19], and lignin [20]. The cellulose content of corn straw and sorghum was 51% and 49%, respectively, with hemicellulose fractions of 15.5% and 14.8%, and lignin contents of 15.2% and 15.5%. Ethylene glycol ($C_2H_6O_2$, ≥99 %), D-glucose ($C_6H_{12}O_6$), 5-Hydroxymethylfurfural (5-HMF), levulinic acid and D-xylose ($C_5H_{10}O_5$) were procured from Sigma-Aldrich. Sulfamic acid (amidosulfonic acid, H_3NSO_3, for analysis), sucrose ($C_{12}H_{22}O_{11}$), phosphoric acid (85%), and acetonitrile (HPLC grade) were provided by Merck.

2.2. Preparation of Low-Transition Temperature Mixture (LTTM)

As previously described in our earlier work, vacuum-dried sulfamic acid (0.04 mol) and ethylene glycol (0.12 mol) were weighed in a 1:3 molar ratio and placed into a 50 mL flask. The mixture was stirred in a 90 °C oil bath until a homogeneous solution was obtained [17].

2.3. Determination of Pretreatment Conditions

In the pretreatment of biomass with LTTM, the reaction conditions were first optimized. Specifically, 1 g of biomass was weighed to evaluate the effects of solid-liquid ratio (1:5, 1:10, and 1:20 w/w), pretreatment temperature (room temperature (rt.), 40 °C, 60 °C, and 100 °C), and pretreatment duration (4, 8, and 12 hours) on hydrolysis. Following pretreatment under desired conditions, the biomass was separated from the LTTM by a simple filtration, washed with distilled water until the pH was neutral, and then dried in an oven at 110 °C. Biomass recovery is determined by the following formula;

$$Recovery\ (\%) = \left({}^{m}/_{1} \right) * 100 \tag{1}$$

where m represents the sample washed and dried after pretreatment.

2.4. Hydrolysis and Conversion of Pretreated Biomass

0.25 g of the dried pretreated biomass sample was taken in a bench-type reactor (Parr Model 4590 HP/HT, Parr Instrument Co, USA), 20 mL of water was added, and conversion was carried out at two different temperatures (180 and 200 °C) for 1 hour (Figure 1). In the catalytic conversion step, the same procedure was followed, with the addition of 0.125 g of the commercial catalyst Amberlyst-15 to the reaction medium. The reaction was terminated with an ice bath, and the solid-liquid mixture was separated with filtration. In the optimization step, the simple sugar content in the liquid product was measured after hydrolysis to determine the most effective pretreatment conditions. In the conversion step, both the sugar content and the amount of 5-HMF and LA were analyzed in a hydrolysis solution.
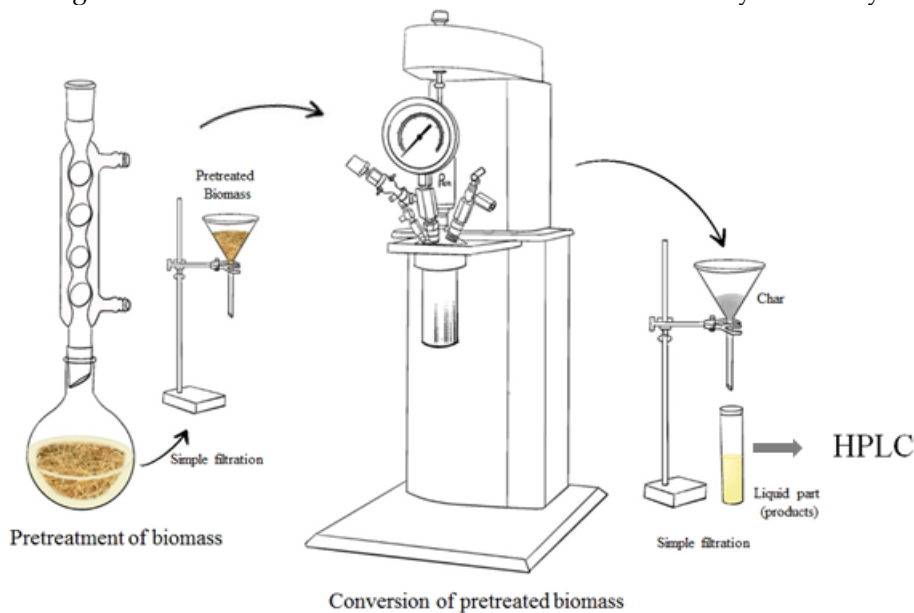
Figure 1. Schematic representation of the experimental setup

2.5. Liquid Phase Analysis

The sugar content in the hydrolysate solution was analyzed using high-performance liquid chromatography (HPLC) system (Agilent 1200 Series, USA) equipped with a refractive index detector and an Inert-Sustain-NH$_2$ column (250 x 4.6 mm). The column temperature was maintained at 35 °C. An isocratic mobile phase consisted of a 75:25 (v/v) acetonitrile-water was used at a flow rate of 1 mL/min. The injection volume was 20 µL and ran for 15 min. The analysis of 5-HMF and LA was performed using

a high-performance liquid chromatography (HPLC) system (Agilent 1200 Series, USA) equipped with an ACE C18 column (250 × 4.6 mm) and a multiple wavelength detector. The detection wavelengths were set at 280 nm for 5-HMF and at 210 nm for LA. The oven temperature was kept at 25 °C. A gradient elution method was employed with 0.001% phosphoric acid (H_3PO_4)-methanol mobile phase at a flow rate of 0.5 mL/min. The injection volume was 5 μL and ran for 30 min. All samples were filtered through a 0.2 μm filter prior to analysis.

2.6. FT-IR Analysis of Biomass Samples

The FT-IR spectra of the biomass and pretreated biomass were obtained using a Spectrum Two FT-IR/ATR system. The analysis was conducted over a wavenumber range of 4000-400 cm^{-1}, with each spectrum acquired after four scans.

3. RESULTS AND DISCUSSION

3.1. FT-IR Analysis of Biomass and Pretreated Biomass

Upon examining the FT-IR spectra of both biomass samples in Figure 2, it is clear that while partial changes were observed in the corn straw, the alterations in the spectrum of the pretreated sorghum biomass were more pronounced. The disappearance of the bands in the 2900-2800 cm^{-1} region following pretreatment was attributed to the removal of methoxy groups within the lignin structure. The slight decrease in the band at 1730 cm^{-1} was associated with the removal of the ester bond between lignin and hemicellulose groups in sorghum spectra. Additionally, the decrease in the intensity of the band at 1605 cm^{-1} was linked to the reduction of lignin content and the diminished aromatic ring vibrations. The disappearance of the bands in the 780-850 cm^{-1} region was attributed to the loss of the syringyl structure within lignin [21], [22]. However, when considering the biomass recovery data presented in Table 1, it is observed that sorghum pretreatment under the same conditions exhibits a lower recovery percentage compared to corn straw, suggesting that a greater amount of lignin may have been removed. This difference in lignin removal could explain the observed variations in the FT-IR spectra.
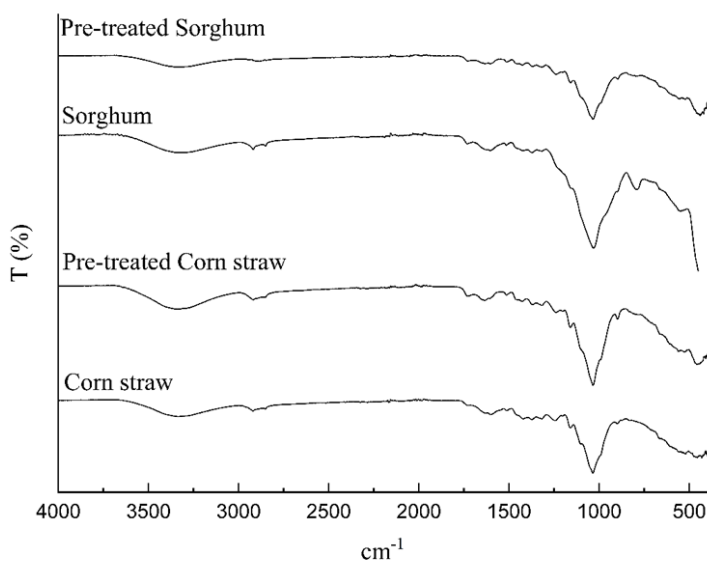
Figure 2. The FT-IR spectra of untreated and pretreated biomass samples

3.2. The Influence of Pretreatment Conditions (Solid-Liquid Ratio, Temperature, Time) on Hydrolysis Efficiency

The primary objective of pretreatment in biomass hydrolysis is to remove lignin from the structure and thereby enhance the accessibility of sugar units in cellulose and hemicellulose polymers. Deep eutectic solvents (DES) and low-transition temperature mixtures (LTTMs) provide cost-effective solutions in this context by enabling pretreatment under lower temperature and pressure conditions. Moreover, these solvents are generally biodegradable and exhibit low toxicity, making them aligned with environmentally sustainable practices. Also, LTTMs generally exhibit low cellulose solubility, which enables selective removal of lignin from the biomass without any degradation in the cellulose regions [13]. The key aim in optimizing the pretreatment process is to maximize the yield of accessible sugar units while minimizing the consumption of chemicals and reducing cost-intensive factors such as temperature and time.

The optimal solid-liquid ratio in pretreatment is crucial for effective biomass hydrolysis. A very low solid-liquid ratio may result in incomplete saturation of biomass samples by LTTM, whereas a very high ratio can lead to excessive biomass degradation and reduce recovery. Moreover, a high solid-liquid ratio can also result in solvent wastage, increased energy consumption, and elevated pretreatment costs. In the study, the solid-liquid ratios of 1:5, 1:10, and 1:20 (w/w) were used taking the literature into consideration [23]. When working with a 1:5 solid-liquid ratio, the biomass recovery was higher, and this value slightly decreased as the solid-liquid ratio increased to 1:20 (Table 1). However, in Figure 3a it can be seen that, the sugar content of hydrolysate solution pretreated with a 1:5 ratio was higher than compared to other ratios. The highest xylose and glucose yield, due to further hydrolysis of hemicellulose, was achieved with treated biomass sample at a ratio of 1:5 (Figure 3a). Thus, pretreatment was conducted at a solid-liquid ratio of 1:5, which produced the highest sugar yields.

Table 1. Effect of the solid-liquid ratio, temperature, and time on the recovery percentage of preprocessed biomass

Biomass	Solid/Liquid (w/w)	Temperature(°C)	Time (h)	Recovery (%)
Corn straw	1:5	60	4	83.9
Corn straw	1:10	60	4	82.1
Corn straw	1:20	60	4	81.8
Corn straw	1:5	rt.	4	83.0
Corn straw	1:5	40	4	83.3
Corn straw	1:5	100	4	68.5
Corn straw	1:5	40	8	75.5
Corn straw	1:5	40	12	78.0
Sorghum	1:5	40	4	77.0

The biomass sample was pretreated with LTTM at different temperatures at a 1:5 solid-liquid ratio and the resulting sugar concentration of hydrolysates was presented in Figure 3b to illustrate the effect of temperature on sugar yield. Although the highest xylose concentration was achieved through the hydrolysis of biomass pretreated at 60 °C, it is clear that the hydrolysis performed after pretreatment at 40 °C resulted in both a higher total sugar concentration and a higher sugar variety in the solution. When the pretreatment was performed at 100 °C, the concentration of glucose and sucrose slightly increased, while

the amount of xylose significantly decreased likely due to excessive biomass degradation. This is supported by the drop in recovery from 83.9% at 60 °C to 68.5% at 100 °C (Table 1). According to Figure 3b, the highest amount of glucose and sucrose was obtained from biomass pretreated at 40 °C, indicating 40 °C as the most effective pretreatment temperature.

The effect of the pretreatment time at 40 °C on the sugar content in the hydrolysate after biomass hydrolysis was shown in Figure 3c. The highest concentrations of xylose, glucose, and sucrose were achieved after 4 h of pretreatment. However, extending the pretreatment time from 4 to 8 hours resulted in an 8% decrease in biomass recovery (Table 1). This suggests that the decrease in xylose content may indicate the removal of not only lignin but also some xylan from the structure during pretreatment. Extending the pretreatment time to 12 hours has not result in a significant change in recovery, indicating that the corn straw reached saturation after 8 hours of pretreatment.

3.3. The Effect of Hydrolysis Temperature and Different Biomass Types on the Hydrolysis and Conversion of Biomass Pretreated with LTTM

In the first part of the present study, pretreatment conditions (solid-liquid ratio, temperature, and time) of corn straw have been optimized for effective hydrolysis of biomass by the design of some experiments. After the optimum pretreatment conditions were determined, the effects of different temperatures and different types of biomass on the hydrolysis process were investigated. In addition to corn straw, hydrolysis experiments were also conducted with pretreated sorghum, and hydrolysis was performed at 200 °C in addition to 180 °C. Moreover, the sugar content and amount of 5-HMF and LA were observed using Amberlyst-15 as a solid acid catalyst for the conversion of pretreated biomass samples. Amberlyst-15 can provide high selectivity in LA production and it acts as a strong acidic catalyst due to the sulfonic acid ($-SO_3H$) groups. These groups enhance the hydrolysis of biomass to release sugars and facilitate the subsequent conversion of these sugars into levulinic acid and byproducts. By optimizing reaction conditions, such as temperature and duration, the formation of undesirable byproducts can be minimized, thereby improving LA yield. In the literature, Amberlyst-15 is frequently used for the conversion of simple sugars. For instance, in a study on the dehydration of fructose to LA using Amberlyst-15, a high yield (>50%) was achieved with at 120 °C in water [24]. A modified Amberlyst-15 catalyst was evaluated for its performance in the conversion of glucose. The results demonstrated its ability to catalyze both the isomerization of glucose and the dehydration of fructose in a single one-pot reaction. This process achieved a 68% yield of 5-hydroxymethylfurfural (HMF) in an H_2O/THF biphasic system [25].

In the hydrolysis of pretreated corn straw at 200 °C, the sugar concentrations in the hydrolysate solution showed a significant decrease compared to 180 °C, probable progression of different conversion reactions at the higher temperature (Figure 4). On the other hand, in the catalyzed hydrolysis at 180°C, the xylose concentration increased from 876.4 to 1081.9 ppm, and the glucose concentration increased from 249.6 to 637.8 ppm, while sucrose was completely degraded and could not be detected (Figure 4).

When corn straw was hydrolyzed at 200°C with Amberlyst-15, the glucose concentration remained almost the same compared to the catalyzed hydrolysis conducted at 180 °C, while the xylose concentration sharply decreased from 1081.9 to 25.5 ppm. However, as can be seen from Figure 5, at 200 °C the levulinic acid content of the liquid corn straw hydrolysate increased sharply. If levulinic acid is the target product in the conversion of pretreated corn and sorghum biomass, it is clear that a higher temperature in an acidic reaction medium is necessary.
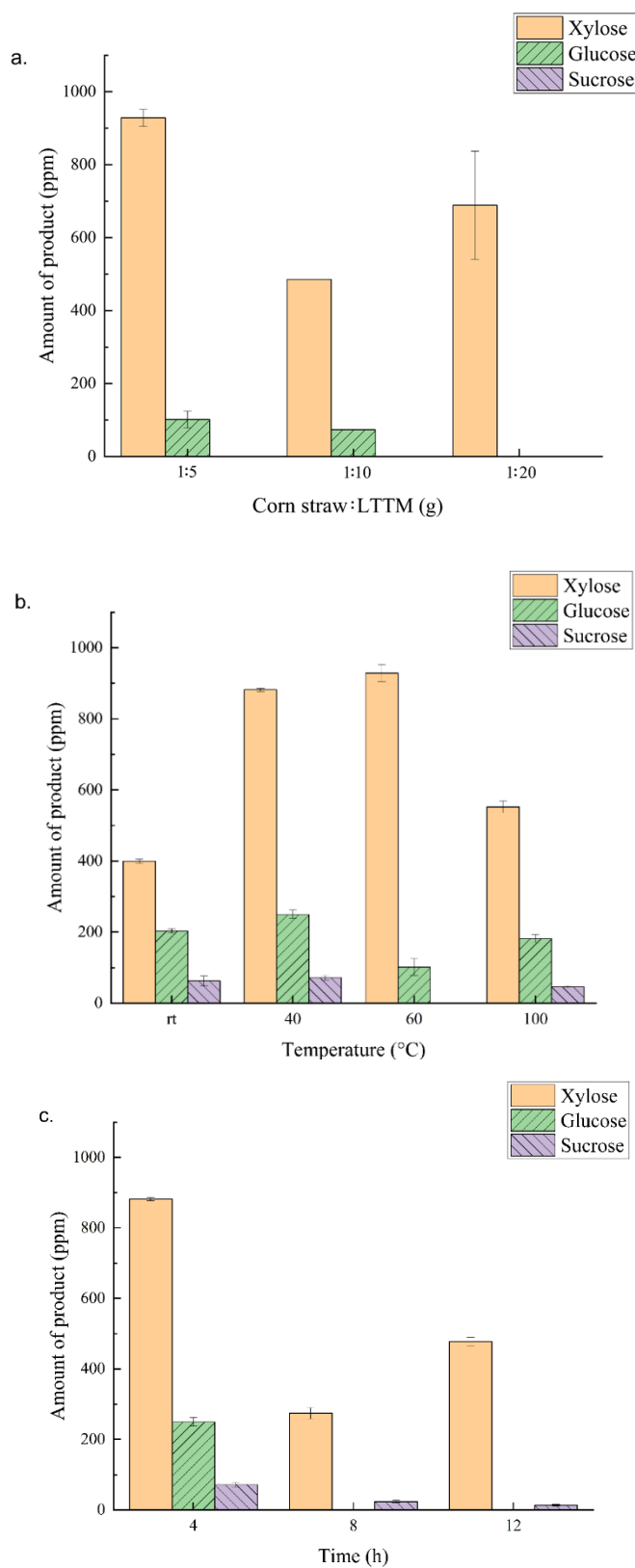
Figure 3. Amounts of sugars obtained from the hydrolysis of corn straw after the pretreatment process; optimization of **a.** the solid-liquid ratio **b.** temperature and **c.** time

During the catalytic conversion of pretreated sorghum at 200 °C, the amount of 5-HMF slightly decreased, while the amount of LA increased from zero to 1967.3 ppm. The amount of LA obtained from

the conversion of pretreated sorghum is slightly higher than the amount obtained from pretreated corn straw with Amberlyst-15 at 200 °C. In the hydrolysis of sorghum at 200 °C without a catalyst, the amounts of xylose and glucose were high, while sucrose is nearly the same compared to corn straw. Chemical pretreatment with LTTM can enhance sugar release, thereby enabling sorghum known to has high sugar content to support more efficient production of platform chemicals.
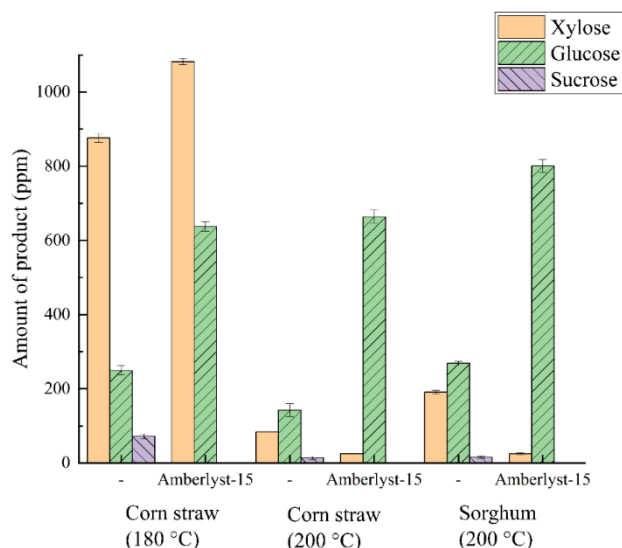
Figure 4. Amounts of sugars obtained from the hydrolysis of pretreated corn straw and sorghum at different temperatures
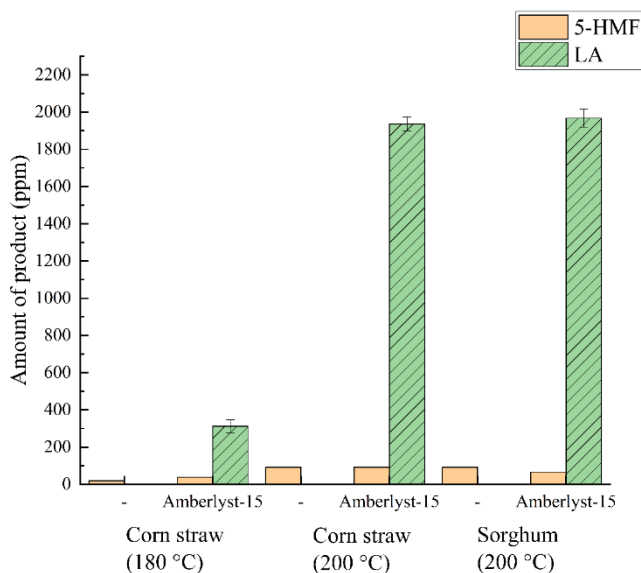
Figure 5. Amounts of 5-HMF and LA obtained from the hydrolysis of pretreated corn straw and sorghum at different temperatures

4. CONCLUSIONS

This study highlights the effectiveness of using a low transition temperature mixture (LTTM) containing sulfamic acid and ethylene glycol for the pretreatment of corn straw and sorghum biomass before bio-conversion. The optimal conditions, which included a solid-liquid ratio of 1:5, a pretreatment temperature of 40 °C, and a pretreatment duration of 4 hours, achieved the highest sugar yields after the

hydrolysis of biomass. By optimizing pretreatment conditions, we demonstrated that LTTMs can significantly enhance the conversion efficiency of biomass into valuable platform chemicals like 5-HMF and LA. The use of LTTM offered advantages such as lower temperature and pressure requirements, reduced chemical consumption, and alignment with environmentally sustainable practices. The addition of Amberlyst-15, a commercial catalyst, further enhanced xylose and glucose yields while decreasing sucrose levels, demonstrating its role in breaking down sucrose along with hemicellulose and cellulose. Additionally, the catalyst promoted conversion reactions, resulting in increase formation of levulinic acid from 5-HMF. Overall, optimizing LTTM pretreatment conditions and utilizing an effective solid acid catalyst significantly improve biomass hydrolysis and conversion efficiency.

Declaration of Ethical Standards

Authors declare to comply with all ethical guidelines including authorship, citation, data reporting, and publishing original research.

Credit Authorship Contribution Statement

A.C: Experimental Section, Data Curation, Investigation, Writing–original draft. H.D: Experimental Section, Data Curation, Investigation, Writing–original draft. B.N: Methodology, Investigation Conceptualization, Resources, Writing – original draft, B.K.O: Methodology, Conceptualization, Resources, Writing -review & editing, Supervision

Declaration of Competing Interest

The authors declare that they have no known competing financial interests or personal relationships that could have appeared to influence the work reported in this paper.

Funding / Acknowledgements

No funding is available for this research.

Data Availability

Data will be made available on request.

REFERENCES

[1]   A. Barhoum et al., "Plant celluloses, hemicelluloses, lignins, and volatile oils for the synthesis of nanoparticles and nanostructured materials," *Nanoscale*, vol. 12, no. 45, Nov., pp. 22845–22890, 2020.

[2]   P. A. Lazaridis, S. Karakoulia, A. Delimitis, S. M. Coman, V. I. Parvulescu, and K. S. Triantafyllidis, "d-Glucose hydrogenation/hydrogenolysis reactions on noble metal (Ru, Pt)/activated carbon supported catalysts," *Catalysis Today*, vol. 257, no. 2, Nov., pp. 281–290, 2015.

[3]   W. Deng, R. Lobo, W. Setthapun, S. T. Christensen, J. W. Elam, and C. L. Marshall, "Oxidative hydrolysis of cellobiose to glucose," *Catalysis Letters*, vol. 141, no. 4, Apr., pp. 498–506, 2011.

[4]   J. N. Chheda and J. A. Dumesic, "An overview of dehydration, aldol-condensation and hydrogenation processes for production of liquid alkanes from biomass-derived carbohydrates," *Catalysis Today*, vol. 123, no. 1–4, May, pp. 59–70, 2007.

[5]   R. Rinaldi and F. Schüth, "Design of solid catalysts for the conversion of biomass," *Energy and Environmental Science*, vol. 2, no. 6, Jun., pp. 610–626, 2009.

[6]   Z. Yinghuai, K. T. Yuanting, and N. S. Hosmane, "Applications of ionic liquids in lignin chemistry," in *Ionic Liquids: New Aspects for the Future*, J. Kadokawa Ed. London: InTech, 2013, pp-315-346.

[7]   V. B. Agbor, N. Cicek, R. Sparling, A. Berlin, and D. B. Levin, "Biomass pretreatment: Fundamentals toward application," *Biotechnology Advances*, vol. 29, no. 6, Nov., pp. 675–685, 2011.

[8]   M. N. F. Norrrahim, R. A. Ilyas, N. M. Nurazzi, M. S. A. Rani, M. S. N. Atikah, and S. S. Shazleen, "Chemical pretreatment of lignocellulosic biomass for the production of bioproducts: An overview," *Applied Science and Engineering Progress*, vol. 14, no. 4, Oct., pp. 588–605, 2021.

[9]   Y. Dai, J. Van Spronsen, G. J. Witkamp, R. Verpoorte, and Y. H. Choi, "Ionic liquids and deep eutectic solvents in natural products research: Mixtures of solids as extraction solvents," *Journal of Natural Products*, vol. 76, no. 11, Nov., pp. 2162–2173, 2013.

[10]   S. Xia, G. A. Baker, H. Li, S. Ravula, and H. Zhao, "Aqueous ionic liquids and deep eutectic solvents for cellulosic biomass pretreatment and saccharification," *RSC Advances*, vol. 4, no. 21, Feb., pp. 10586–10596, 2014.

[11]   A. Satlewal, R. Agrawal, S. Bhagia, J. Sangoro, and A. J. Ragauskas, "Natural deep eutectic solvents for lignocellulosic biomass pretreatment: Recent developments, challenges and novel opportunities," *Biotechnology Advances*, vol. 36, no. 8, Dec., pp. 2032-2050, 2018.

[12]   M. Francisco, A. Van Den Bruinhorst, and M. C. Kroon, "New natural and renewable low transition temperature mixtures (LTTMs): screening as solvents for lignocellulosic biomass processing," *Green Chemistry*, vol. 14, no. 8, Jun., pp. 2153–2157, 2012.

[13]   J. L. Wong, S. N. B. A. Khadaroo, J. L. Y. Cheng, J. J. Chew, D. S. Khaerudini, and J. Sunarso, "Green solvent for lignocellulosic biomass pretreatment: An overview of the performance of low transition temperature mixtures for enhanced bio-conversion," *Next Materials*, vol. 1, no. 2, Jun., p. 100012, 2023.

[14]   C. L. Yiin, A. T. Quitain, S. Yusup, M. Sasaki, Y. Uemura, and T. Kida, "Characterization of natural low transition temperature mixtures (LTTMs): Green solvents for biomass delignification," *Bioresource Technology*, vol. 199, Jan., pp. 258–264, 2016.

[15]   S. Phromphithak, T. Katongtung, P. Pholchan, and N. Tippayawong, "Microwave-heated pretreatment of corncob, Giant Juncao grass, and hemp using choline derivatives with glycerol," *BioEnergy Research*, vol. 18, no. 1, Dec., pp. 1–12, 2025.

[16]   H. Y. Lim, N. A. Rashidi, K. W. Cheah, and A. S. A. Manaf, "One step microwave synthesis of 5-hydroxymethylfurfural from bamboo in presence of low transition temperature mixture," *Chemcal Engneering Transactions*, vol. 106, Dec., pp. 127–132, 2023.

[17]   B. Nis, B. Kaya Ozsel, and Y. Kaya, "A DES or LTTM: Eco-friendly solvent mediums for conversion of biomass to levulinic acid as a key chemical," *Journal of Molecular Liquids*, vol. 409, Sep., p. 125462, 2024.

[18]   T. Foyle, L. Jennings, and P. Mulcahy, "Compositional analysis of lignocellulosic materials: Evaluation of methods used for sugar analysis of waste paper and straw," *Bioresource Technology*, vol. 98, no. 16, Nov., pp. 3026–3036, 2007.

[19]   R. C. Sun and J. Tomkinson, "Characterization of hemicelluloses obtained by classical and ultrasonically assisted extractions from wheat straw," *Carbohydrate Polymers*, vol. 50, no. 3, Nov., pp. 263-271, 2002.

[20]   *Standard Test Method for Determination of Acid-Insoluble Residue in Biomass*, E1721 − 01(2015), ASTM, 2015.

[21]   D. Haldar and M. K. Purkait, "Thermochemical pretreatment enhanced bioconversion of elephant grass (Pennisetum purpureum): insight on the production of sugars and lignin," *Biomass Conversion and Biorefinery*, vol. 12, no. 4, Apr., pp. 1125–1138, 2022.

[22]   A. H. Ab Rahim, Z. Man, A. Sarwono, W. S. Wan Hamzah, N. M. Yunus, and C. D. Wilfred, "Extraction and comparative analysis of lignin extract from alkali and ionic liquid pretreatment," *Journal of Physics Conference Series*, vol. 1123, no. 1, Nov., p. 012052, 2018.

[23]   H. Xu et al., "Key process parameters for deep eutectic solvents pretreatment of lignocellulosic biomass materials: A review," *Bioresource Technology*, vol. 310, Aug., p. 123416, 2020.

[24]   P. A. Son, S. Nishimura, and K. Ebitani, "Synthesis of levulinic acid from fructose using Amberlyst-

15 as a solid acid catalyst," *Reaction Kinetics, Mechanism and Catalysis*, vol. 106, no. 1, Mar., pp. 185–192, 2012.

[25]   S. Xu et al., "Efficient conversion of glucose into 5-hydroxymethylfurfural using a bifunctional Fe3+ modified Amberlyst-15 catalyst," *Sustainable Energy Fuels*, vol. 3, no. 2, Jan., pp. 390–395, 2019.

OPTIMIZATION OF 3D PRINTING PARAMETERS FOR PLA/PCL FILAMENT USING THE TAGUCHI METHOD: EFFECTS ON MECHANICAL PROPERTIES AND SHAPE MEMORY PERFORMANCE

[1,]* **Meltem ERYILDIZ**[ID], [2] **Bekir Kağan KUTLUHAN**[ID], [3] **Mihrigül EKŞİ ALTAN**[ID]

[1,2] *Istanbul Beykent University, Mechanical Engineering Department, Istanbul, TÜRKİYE*
[3] *Yildiz Technical University, Mechanical Engineering Department, Istanbul, TÜRKİYE*
[1]meltemeryildiz@beykent.edu.tr, [2]2003040039@student.beykent.edu.tr, [3]meksi@yildiz.edu.tr

Highlights

- Taguchi method optimized 3D printing parameters for PLA/PCL blends.

- Lines infill pattern achieved 83% shape recovery rate at 185°C, 40 mm/s.

- Print speed of 40 mm/s and 185°C optimized mechanical and shape memory performance.

- Regression and ANOVA validated effects on mechanical and shape memory properties.

Graphical Abstract (Optional)

Flowchart of the proposed method

***Corresponding Author:** Meltem ERYILDIZ, meltemeryildiz@beykent.edu.tr*

OPTIMIZATION OF 3D PRINTING PARAMETERS FOR PLA/PCL FILAMENT USING THE TAGUCHI METHOD: EFFECTS ON MECHANICAL PROPERTIES AND SHAPE MEMORY PERFORMANCE

[1], * Meltem ERYILDIZ [iD], [2] Bekir Kağan KUTLUHAN [iD], [3] Mihrigül EKŞİ ALTAN [iD]

[1,2] *Istanbul Beykent University, Mechanical Engineering Department, Istanbul, TÜRKİYE*
[3] *Yildiz Technical University, Mechanical Engineering Department, Istanbul, TÜRKİYE*
[1]meltemeryildiz@beykent.edu.tr, [2]2003040039@student.beykent.edu.tr, [3]meksi@yildiz.edu.tr

ABSTRACT: This study investigates the optimization of 3D printing process parameters for PLA/PCL filament using the Taguchi method. A Taguchi L9 orthogonal array design was employed to explore the effects of print speed (40, 60, 80 mm/s), temperature (185,190,200°C), and infill pattern (the Lines, Gyroid, Triangle) on both mechanical and shape memory properties of the printed parts. The experiments were conducted using a Fused Deposition Modeling (FDM) 3D printer. The mechanical properties, including tensile strength, and shape memory properties such as shape recovery ratio, were evaluated for each combination of process parameters. The experiments revealed that a print speed of 40 mm/s, a nozzle temperature of 185°C, and the Lines infill pattern produced the best shape memory performance, achieving the shape recovery rate of 78.60% and the recovery time of 69 seconds. For tensile strength, the optimal conditions were found to be 40 mm/s, 185°C, and the Gyroid infill pattern, resulting in the highest tensile strength of 21.985 MPa. However, for simplicity and faster production, the Lines infill pattern is preferred. This research provides valuable insights for optimizing the 3D printing process of PLA/PCL filament and enhancing its mechanical and shape memory performance, which is crucial for various applications in biomedical, textile, and packaging industries.

Keywords: 3D Printing, Mechanical Properties, PLA/PCL Filament, Shape Memory Properties, Taguchi Method

1. INTRODUCTION

Additive manufacturing, commonly known as 3D printing, produces three-dimensional objects by layering material step by step, following a digital design. The advent of 3D printing technology has revolutionized various industries, particularly in the medical field, where it enables the production of patient-specific models, prosthetics, and implants with unparalleled precision and customization. This cutting-edge technology offers the ability to create complex geometries tailored to individual patient needs, enhancing surgical planning and improving overall healthcare outcomes [1].

Of the many materials utilized in 3D printing, Polylactic Acid (PLA) and Polycaprolactone (PCL) have garnered significant attention due to their biodegradability, biocompatibility, and simplicity of processing. PLA, a thermoplastic derived from renewable resources such as corn starch, is widely appreciated for its mechanical properties and environmental friendliness, and it is commonly applied in biomedical fields because of its biodegradability, biocompatibility, and ability to support tissue regeneration and drug delivery systems [2]. PCL, similarly, is a biodegradable polyester known for its reduced melting point, high flexibility, and biocompatibility, making it suitable for various medical and industrial applications [3]. A key drawback of PLA is its brittleness and limited impact resistance, which may limit its application in certain functional parts. Combining PLA with PCL is a good option to overcome these limitations, as PCL's flexibility and low melting point enhance the toughness and durability of the resulting material [4].

Fused deposition modeling (FDM) is an additive manufacturing technique commonly employed to produce geometrically intricate prototypes and components. FDM works by melting thermoplastic filament and forcing it through a heated nozzle layer by layer onto a build platform, where each layer

*Corresponding Author: Meltem ERYILDIZ, meltemeryildiz@beykent.edu.tr

solidifies to form a three-dimensional object [5]. While it reduces cycle time and eliminates the need for expensive tools.

Optimizing FDM 3D printing parameters for PLA/PCL material is crucial for achieving high-quality prints with precise dimensions, superior surface finish, and desired mechanical properties, ensuring efficiency and reliability in additive manufacturing processes. The Taguchi method has been widely applied in various fields, including 3D printing and electrospinning, to optimize process parameters and enhance material properties. By employing a systematic design of experiments (DOE) approach, the Taguchi method enables efficient parameter selection while minimizing experimental effort. Hasdiansah et al. [7] optimized FDM 3D printing parameters for TPU using the Taguchi method, identifying layer thickness as the most significant factor affecting surface roughness. Singh et al. [8] optimized FDM 3D printing parameters for PLA-nanographene composites using the Taguchi method, identifying composition as the most significant factor influencing wear resistance. Meyva-Zeybek et al. [9] applied the Taguchi method to optimize electrospinning parameters for PLA and PLA/POSS nanofibers, demonstrating that using a Taguchi L9 orthogonal array significantly reduced the number of experiments while effectively determining the optimal conditions. Nazir et al. [10] applied the Taguchi method to optimize PA-6 nanofiber electrospinning, identifying polymer concentration as the key factor influencing fiber diameter and determining optimal conditions for minimal diameter and variation.

Process parameters like nozzle temperature, print speed, infill pattern, infill density, and layer height influence the final product's dimensional precision, surface quality, and mechanical strength [10]. However, the interplay between these parameters is complex, necessitating a systematic approach to identify the optimal settings. Researchers have extensively investigated the impact of these parameters on part characteristics and explored process parameter optimization, focusing primarily on neat thermoplastic polymers such as PLA, PCL, or ABS. Mohamed et al. [11] examined how factors such as raster angle, layer thickness, build orientation, air gap, road width, and number of contours affect material consumption, build time, and dynamic flexural modulus in FDM. Vidakis et al. [12] explored how six essential 3D printing parameters influence key quality metrics such as surface finish, dimensional precision, and porosity in material extrusion (MEX) additive manufacturing, utilizing robust experimental methods and predictive regression models to optimize part quality and performance. Le et al. [13] studied the optimization of mechanical properties and print time for PLA using FDM, emphasizing the balance between print speed and ultimate strength by varying parameters such as number of outer shells, nozzle diameter, nozzle temperature, infill pattern and infill density through DOE and ANOVA. Despite significant progress, further research in this field remains essential, particularly as each newly developed material in additive manufacturing requires tailored process parameters to optimize its performance characteristics. Understanding how key FDM parameters influence the shape recovery rate is crucial for advancing the practical applications of shape memory materials. Liu et al. [14] focused primarily on investigating the thermoresponsive shape memory effects and material characteristics of PLA/PCL blends, rather than conducting an in-depth study of the FDM process conditions. Qui et al. [15] aimed to produce a PLA/PCL filament, investigating the influence of PCL content on filament geometry, dimensions, surface roughness, and ultimate tensile strength. However, they did not extensively study specific FDM process parameters in their research.

Shape memory properties are also crucial aspects to optimize, as they significantly influence the functionality and responsiveness of the printed structures. Saptaji et al. [16] investigated the activation and shape recovery properties of 3D printed PLA samples, examining the effects of various printing parameters such as thickness, infill density, printing speed, deformation temperature, and recovery temperature, with results showing that the highest recovery ratio of 0.784 was achieved under specific conditions, and the thickness parameter was identified as the most significant factor influencing shape memory behavior. Hosseinzadeh et al. [17] examined the impact of deformation temperature, recovery temperature, and heating rate on the shape recovery of PLA, finding that the optimal conditions (deformation temperature of 53.31°C, recovery temperature of 59.94°C, and heating rate of 8.05°C/min) improved shape recovery from 93.03% to 98.14% in 3D-printed rounded rectangle structures, and

enhanced recovery in diamond and honeycomb structures as well. Eryildiz [18] investigated the effects of 4D printing process parameters, including sample thickness, nozzle temperature, deformation temperature, and holding time, on the shape recovery of PLA, finding that sample thickness had the greatest impact and that increasing deformation, holding, and nozzle temperatures enhanced shape recovery, while greater sample thickness negatively affected it. While various studies have explored the effects of different process parameters on shape memory and recovery of PLA in 4D printing, further research is needed to optimize process parameters for various geometries and applications to enhance the functionality and performance of 4D printed PLA/PCL structures.

In this study, the objective is to optimize the 3D printing process parameters for PLA/PCL filament using the Taguchi method. The Taguchi method, a robust statistical tool for optimizing process parameters, offers an efficient approach to address this challenge. By employing a designed set of experiments, the Taguchi method helps in understanding how various factors impact the quality of 3D-printed objects. This method not only simplifies the optimization process but also enhances the reproducibility and reliability of the results [19]. By systematically analyzing the effects of key parameters, we seek to identify the optimal conditions that yield high-quality prints with improved mechanical properties and shape memory characteristics. Additionally, statistical analyses, including ANOVA and regression modeling, were employed to validate the influence of the selected process parameters on the observed properties. This research will contribute to the growing body of knowledge in the field of additive manufacturing, especially in medical and 4D printing applications, enriching our understanding and capabilities in these cutting-edge fields.

2. MATERIAL AND METHODS

2.1. Materials

PLA (Natureworks Ingeo® 4043D from Resinex, Turkey), exhibits a melt flow index (MFI) of 6 g/10 min (at 210°C, 2.16 kg), a density of 1.24 g/cm³, and a melting point ranging from 145 to 160 °C. PCL, obtained as Perstorp Capa 6500 pellets from Biesterfeld, Turkey has a melt flow index (MFI) of 5.9–7.9 g/10 min (measured at 160°C with a 2.16 kg load), a density of 1.1 g/cm3, and a melting point range of 58–60°C. Both PLA and PCL pellets were dried at 40°C for 24 hours in a NÜVE MF 106 oven prior to melt-blending.

2.2. Fabrication of PLA/PCL Filament

The PLA/PCL blend (80:20 ratio by weight) was processed using a twin-screw extruder (Rondol, England, L/D=10) at 60 rpm, with the temperature profile from die to feeder set at 150°C, 185°C, 175°C, 165°C, and 80°C. Post-extrusion, the blend was pelletized and dried overnight at 40°C in a NÜVE MF 106 oven. 1.75 mm diameter filament was extruded using a Filament Maker-Composer 350 (3devo, Turkey) at temperatures between 150°C to 170°C, ensuring a filament thickness deviation of only 5 μm.

2.3. 3D Printing Process

The blended PLA/PCL filament was loaded into a desktop FDM 3D printer (Flashforge Creator 3 Pro, Turkey) to produce the samples. The printer parameters, such as layer height, bed temperature, infill density, and cooling fan speed, were chosen based on established literature and are listed as fixed parameters in Table 1 [14-15].

Table 1. 3D printing parameters for sample fabrication

Printing Parameters	Settings
Nozzle diameter	0.4 mm
Bed temperature	50°C
Layer thickness	0.18 mm
Infill density	60%
Number of shells	3
Top and bottom layers	0
Wall thickness	1.2 mm

Optimization of print speed, nozzle temperature, and infill pattern was conducted using a Taguchi experimental design to enhance mechanical and shape memory properties. Print speed, nozzle temperature, and infill pattern are critical parameters in FDM 3D printing that directly influence mechanical characteristics and shape memory performance of printed parts. Optimizing these parameters ensures that the prints achieve desired levels of strength, dimensional accuracy, and shape retention, crucial for applications in fields such as medicine and advanced manufacturing [20]. Infill patterns are critical for shaping the mechanical properties and shape recovery capabilities in 4D printing. The specific arrangement and geometry of infill patterns within printed parts directly influence factors such as structural strength, flexibility, and the ability to achieve desired shape transformations. Optimizing infill patterns ensures that 4D-printed objects exhibit reliable performance and functionality tailored to their intended applications [21]. The temperature of the nozzle greatly affects both the process and mechanical properties of printed objects. It dictates the material flow dynamics and layer adhesion during deposition, crucial for ensuring structural integrity and dimensional accuracy. Moreover, temperature settings play a pivotal role in activating shape memory effects in responsive materials, enabling the printed parts to undergo programmable transformations over time. Thus, optimizing nozzle temperature is essential for achieving robust mechanical properties and reliable shape-changing capabilities in 4D-printed components [22]. Printing speed is also a critical parameter that impacts both the mechanical properties of the printed objects and the efficiency of the printing process. Optimizing print speed ensures precise deposition of material layers, which is crucial for maintaining dimensional accuracy and structural integrity. Moreover, the rate at which material is deposited influences the bonding between layers, affecting the overall strength, durability, and surface finish of the printed parts. Print speed influences shape recovery in 4D printing by affecting the material's cooling rate and layer adhesion, crucial for controlling the activation and efficacy of shape memory properties [23].

The print speed, nozzle temperature, and infill patterns were selected based on a combination of established literature, preliminary trials, and the technical limitations of the FDM printer used in this study. The print speed range of 40, 60, and 80 mm/s was chosen to explore low, medium, and high-speed settings, balancing the effects on mechanical and shape memory properties while avoiding excessively low speeds that increase print times or high speeds that compromise interlayer adhesion. Similarly, the nozzle temperature range of 185°C, 190°C, and 200°C was determined based on the thermal behavior of PLA and PCL, ensuring optimal material flow and interlayer bonding without thermal degradation or insufficient bonding. The selected infill patterns—Lines, Gyroid, and Triangle—were included to study their distinct mechanical and structural characteristics. Lines were chosen for simplicity and efficiency, Gyroid for isotropic mechanical properties, and Triangle for its rigidity, allowing for a comprehensive analysis of their effects on the mechanical and shape memory behavior of the PLA/PCL blends.

2.4. Characterization

Mechanical characteristics like tensile strength and elongation at break, were evaluated using standard ASTM methods. Tensile tests on the 3D-printed samples were conducted using a Zwick Roell 8497 tensile testing machine equipped with a 20 kN load cell at room temperature, with a crosshead speed of 5 mm/min. Samples were shaped in a dog bone configuration following ASTM D638 Type IV

specifications (Figure 1).
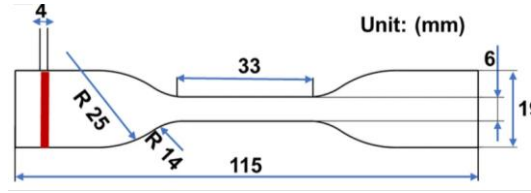
Figure 1. Tensile test specimen conforming to ASTM D638 Type IV standards

Differential scanning calorimetry (DSC) was employed with a Perkin Elmer DSC6000 device in a nitrogen atmosphere at a rate of 10°C/min to characterize the melting behavior of the PLA/PCL material. The glass transition temperature of the material was determined for conducting shape memory tests. The shape recovery characteristics of samples printed with FDM were analyzed by programming a temporary shape: heating the sample beyond its glass transition temperature (Tg) to set the temporary shape, cooling it below Tg to fix this shape with a constraint, releasing the constraint upon cooling to allow temporary shape recovery, and heating above Tg to return to the permanent shape, maintaining stability until reprogramming [18].
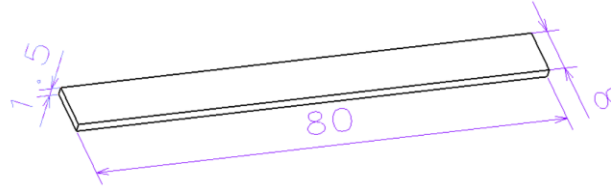
Figure 2. Shape memory sample dimensions (units in mm)

During the programming step, shape recovery samples (Figure 2) were exposed to heat in a water bath at the glass transition temperature. The samples were then bent to 90° (θu) and held in place for a specified duration. After cooling to 25°C, the external force was removed, allowing the specimen to deform freely due to internal stress (θf). Upon reheating to Tg, the recovery angle θr was recorded (Figure 3). The shape recovery ratio (Rr) was determined using Equation (1) [24]:

$$R_r\,(\%) \ = [(\theta_f - \theta_r)/\theta_f]\;x\;100 \tag{1}$$
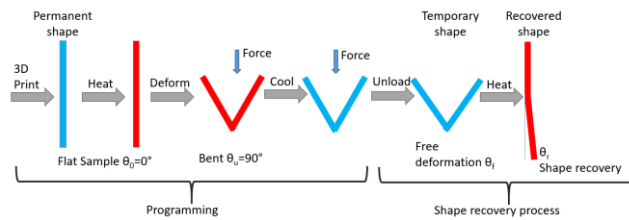
Figure 3. The sequential steps of shape-memory-based 4D printing.

Figure 4. Experimental setup and workflow of the study

Figure 4 provides a comprehensive visual representation of the experimental procedures and applications conducted in this study.

2.5. Methodology

In this experimental study, the Taguchi method using Minitab R16 software was utilized, incorporating print speed, nozzle temperature, and infill pattern as control factors, while tensile strength and shape recovery rate were chosen as the response variables. Each factor was tested at three levels, as specified in Table 2, and the experimental design was structured using an L9 factorial design as depicted in Table 3. Additionally, statistical analyses including ANOVA, regression modeling, and probability plots were performed to evaluate the significance and influence of the selected parameters on the observed mechanical and shape memory properties, ensuring a comprehensive understanding of the process optimization.

Table 2. Control factor levels.

Symbol	Control Factor	Level 1	Level 2	Level 3
A	Print Speed (mm/s)	40	60	80
B	Nozzle Temperature (°C)	185	190	200
C	Infill Pattern	Lines	Gyroid	Triangle

The 'larger is better' criterion was used in the Taguchi method to identify optimal process conditions aimed at achieving the highest tensile strength and shape recovery ratio.

Table 3. L9 Orthogonal Array Used in the Experimental Study.

No	Print Speed (mm/s) (A)	Nozzle Temperature (°C) (B)	Infill Pattern (C)
1	40	185	Lines
2	40	190	Gyroid
3	40	200	Triangle
4	60	185	Gyroid
5	60	190	Triangle
6	60	200	Lines
7	80	185	Triangle
8	80	190	Lines
9	80	200	Gyroid

3. RESULTS AND DISCUSSION

3.1. Thermal Behavior of PLA/PCL Blend

Figure 5 displays the differential scanning calorimetry (DSC) results for the PLA/PCL blend, showing values for the glass transition temperature (Tg), cold crystallization temperature (Tc), melting temperature (Tm), and melting enthalpy (ΔHm) as 46.57°C, 122.90°C, 150.67°C, and 66.519 J/g, respectively.
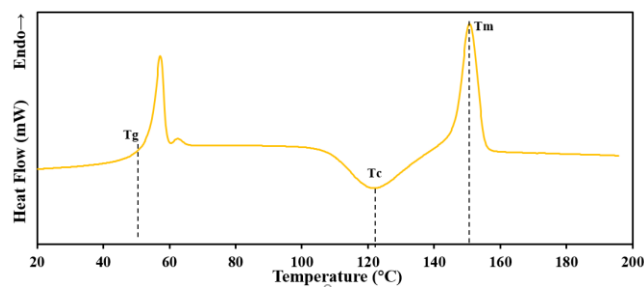
Figure 5. Second heating DSC thermogram for the PLA/PCL filament

The glass transition temperature (Tg) of neat PLA was 48.40°C, which decreased to 46.57°C with the addition of 20% PCL by weight resulting in improved flexibility and altered thermal characteristics of the PLA/PCL blend [25-26]. In 4D printing processes, Tg is critical as it affects molecular stability under deformation conditions [18]. The Tg derived from DSC data was determined to guide shape recovery and deformation temperatures.

3.2. Analysis of Mean

The Taguchi method is a reliable statistical approach for optimizing process parameters to achieve the best possible performance with minimal variability. This method employs an orthogonal array to systematically vary the levels of each factor and evaluate their effects on the desired outcomes [27]. In this study, the Taguchi L9 factorial design was utilized to optimize the 3D printing parameters for PLA/PCL filament, focusing on print speed, nozzle temperature, and infill pattern. The objective was to enhance the tensile strength of the printed parts, with the optimization process guided by the Signal-to-Noise (SN) ratio using the 'larger is better' criterion. The primary factors investigated were print speed (A), nozzle temperature (B), and infill pattern (C). The tensile stress and shape recover rate measurements for each experimental run are summarized in Table 4.

Table 4. Tensile stress and shape recovery rate measurements for each experimental run

No	Print Speed (mm/s) (A)	Nozzle Temperature (°C) (B)	Infill Pattern (C)	Tensile Stress (MPa)	Recovery Rate (%)	Time (s)
1	40	185	Lines	20.596	78.60	69
2	40	190	Gyroid	21.678	58.22	43
3	40	200	Triangle	18.196	79.66	53
4	60	185	Gyroid	21.985	70.56	29
5	60	190	Triangle	17.849	61.07	44
6	60	200	Lines	19.572	83.00	43
7	80	185	Triangle	17.563	73.18	75
8	80	190	Lines	20.429	73.89	100
9	80	200	Gyroid	21.724	55.85	120

The Signal-to-Noise (SN) ratio has an essential role in determining the optimal parameter settings, particularly when applying the 'larger is better' criterion to optimize a response variable, such as tensile strength and shape memory rate. Based on the SN ratios calculated for each experimental run (Figure 6), the optimal parameter combinations were identified as A1B1C2—where A1 corresponds to a print speed of 40 mm/s, B1 to a nozzle temperature of 185°C, and C2 to the Gyroid infill pattern for mechanical test results—and A1B1C1—where C1 is the Lines infill pattern—for shape recovery test results. These combinations yielded the highest SN ratios, indicating the most favorable conditions for maximizing tensile strength and shape recovery.
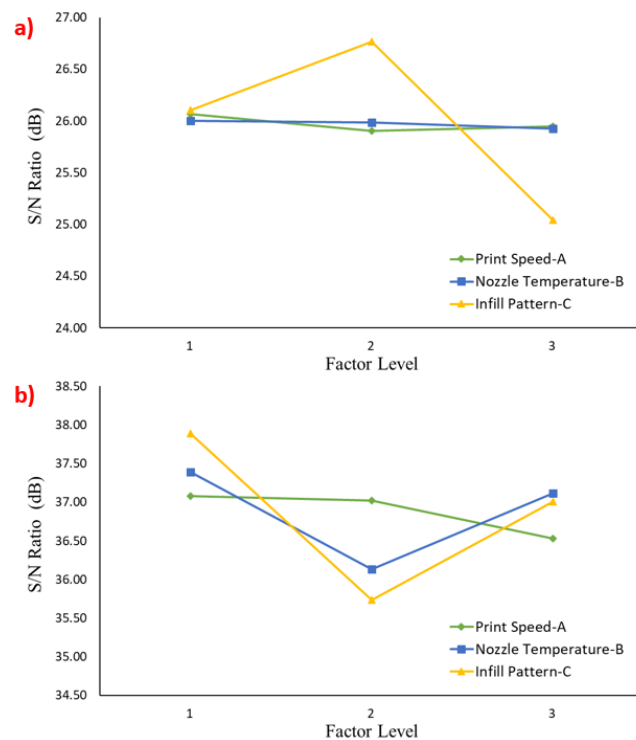
Figure 6. SN ratios for a) tensile test, b) shape recovery rate.

3.3. Mechanical properties optimization

3.3.1. Impact of print speed on tensile mechanical properties

The print speed did not show a significant effect on the tensile strength of the printed samples. Lower print speeds, particularly at 40 mm/s, generally resulted in higher tensile stress values. For instance, Run 2 (40 mm/s, 190°C, Gyroid) achieved a tensile stress of 21.678 MPa, whereas Run 7 (80 mm/s, 185°C, Triangle) registered 17.563 MPa (Figure 7, Table 4).

A slower print speed allows the extruded filament more time to fuse with the preceding layers, enhancing interlayer adhesion [28]. Enhanced adhesion contributes to improved mechanical properties, as evidenced by the higher tensile stress values. Conversely, higher print speeds can result in inadequate bonding due to rapid deposition, which can lead to weaker mechanical performance [29].
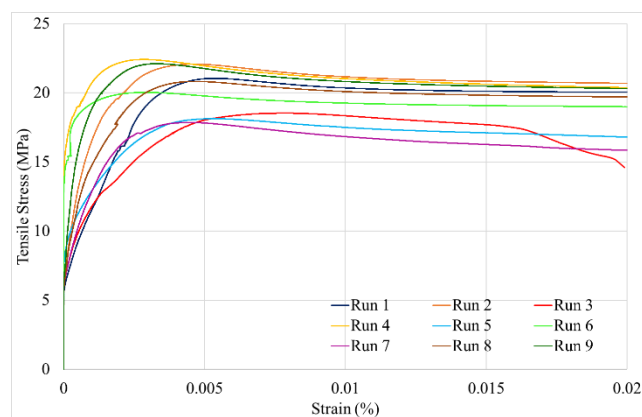
Figure 7. Stress-strain curves of printed PLA/PCL blends for each experimental run.

3.3.2. Impact of Nozzle Temperature on Tensile Mechanical Properties

Nozzle temperature affects the viscosity of the extruded filament, the degree of layer adhesion, and the overall print quality. In this study, nozzle temperature (185°C, 190°C, and 200°C) did not show a significant effect on the tensile strength of the printed PLA/PCL parts.

A lower nozzle temperature of 185°C was identified as optimal for achieving higher tensile strength. This is because at 185°C, the PCL in the blend, which has a lower melting point, is sufficiently melted to enhance flexibility and interlayer adhesion without degrading its structural integrity. This temperature allows the PLA to bond effectively while maintaining the elastic properties provided by the PCL, resulting in superior mechanical performance. For example, at 185°C, combined with a print speed of 60 mm/s and a Gyroid infill pattern, the tensile strength reached 21.985 MPa. This suggests that the balance between PLA's rigidity and PCL's flexibility is best maintained at this temperature, leading to improved tensile properties [30].

At higher temperatures, such as 200°C, the tensile strength decreased. The increased temperature improves the flow and bonding of PLA but may lead to thermal degradation of PCL, reducing the overall mechanical performance of the blend. The study found that higher temperatures tend to weaken the material's mechanical properties, as evidenced by a tensile strength of only 17.849 MPa at 200°C.

3.3.3. Impact of Infill Pattern on Tensile Mechanical Properties

The infill pattern is a vital factor in 3D printing that greatly affects the tensile mechanical properties of the printed parts. Different infill patterns distribute stress and strain differently throughout the printed structure, affecting the overall strength and durability of the part. In this study, three infill patterns—Lines, Gyroid, and Triangle—were analyzed to assess their impact on the tensile strength of PLA/PCL

blends.

The lines infill pattern emerged as one of the most effective for maximizing tensile strength. This pattern, consisting of straight lines oriented at alternating angles in each layer, provides a uniform distribution of stress along the primary loading direction. The simplicity of this pattern reduces print time while ensuring sufficient interlayer bonding. At a print speed of 40 mm/s and a nozzle temperature of 185°C, the Lines pattern achieved a tensile strength of 20.596 MPa, indicating its effectiveness in enhancing mechanical properties without compromising print efficiency. In accordance with our study, Mishra et al. [31] demonstrated that the Lines infill pattern provided maximum mechanical properties, highlighting its effectiveness in enhancing impact resistance and overall structural integrity in 3D-printed components.

The Lines infill pattern is often favored for its simplicity and efficiency. It consists of straight lines printed at alternating angles in each layer. This pattern is not only quick to print but also provides decent mechanical strength, particularly in one direction (usually the direction of the lines). The alternating pattern of the lines helps distribute stress more evenly across the part, enhancing its ability to withstand tensile forces. Compared to more intricate infill patterns like the Gyroid or the Triangle, the Lines infill pattern may not offer multidirectional strength, but in this specific case, it likely provided sufficient strength in the direction where it was most needed, contributing to the highest tensile stress observed. Additionally, the simplicity of the Lines pattern means less print head movement, which can reduce the risk of defects and inconsistencies, further improving print quality [32, 33].

The Gyroid infill pattern, known for its complex 3D structure, provided the highest tensile strength in certain configurations. The continuous, curved surfaces of the Gyroid pattern allow for isotropic stress distribution, reducing stress concentration points and improving overall mechanical performance [34]. For example, when printed at 60 mm/s and 185°C, the Gyroid pattern produced a tensile strength of 21.985 MPa, the highest observed in this study (Figure 7, Table 4). This pattern is particularly beneficial in applications requiring balanced mechanical properties in multiple directions. The best parameter combination to maximize the tensile strength of PLA/PCL 3D-printed parts, as determined by the Taguchi optimization, is a print speed of 40 mm/s, a nozzle temperature of 185°C, and the Gyroid infill pattern. This setup achieved the highest tensile strength, demonstrating optimal conditions for creating strong, durable parts with consistent mechanical properties. Kadhum et al. [35] also found that the Gyroid infill pattern delivered the best mechanical performance, consistent with our findings that it enhances tensile strength and durability. Similarly, Birosz et al. [36] showed that the Gyroid infill patterns excel in mechanical resistance, supporting our results on their effectiveness in enhancing tensile strength.

The Triangle infill pattern, while structurally robust, did not perform as well as the Lines or Gyroid infill patterns in terms of tensile strength. The angular geometry of this pattern can lead to localized stress concentrations, which may contribute to lower mechanical strength under tensile loads, a similar observation made by Jasim et al. [37].

3.4. Shape Memory Properties Optimization

3.4.1. Impact of Print Speed on Shape Recovery Rate

The shape recovery rate varied significantly with changes in print speed. Print speed directly affects the material deposition rate and cooling dynamics during the FDM printing process [38]. Based on the Taguchi optimization, the optimal parameter combination (A1B1C1: 40 mm/s, 185°C, Lines pattern) yielded a high shape recovery rate of 78.60%, reinforcing the importance of lower print speeds in achieving better shape recovery performance.

As seen in Table 4 and Figure 8, at 40 mm/s (Runs 1–3), the shape recovery rates varied depending on the infill pattern and nozzle temperature. The highest recovery rate at this speed was 79.66% (Run 3, 200°C, Triangle pattern), while the lowest was 58.22% (Run 2, 190°C, Gyroid pattern). This indicates that lower print speeds generally enhance layer bonding and reduce residual stress, but the influence of other parameters, such as infill pattern and nozzle temperature, remains significant. At a lower print speed, the extruded material has more time to cool and bond properly between layers, leading to stronger interlayer

adhesion and less residual stress within the printed part. This stronger bonding is crucial for the shape memory effect, as it allows the material to store and release elastic energy more efficiently when undergoing shape transformations. Similar observations were reported by Şahin and Mardini [39] who found that interlayer adhesion depends heavily on printing speed and interlayer interval time, which significantly influence the mechanical characteristics of 3D-printed structures. Additionally, Weng et al. [40] observed that printing speed, along with factors such as superplasticizer dosage and curing conditions, plays a crucial role in enhancing bond strength between layers in extrusion-based 3D printing processes, further emphasizing the importance of controlling these parameters to enhance the structural integrity of printed components.

At a moderate print speed of 60 mm/s (Runs 4–6), the highest overall shape recovery rate (83.00%) was achieved in Run 6 (200°C, Lines pattern), likely due to a balanced material consistency, thermal history, and interlayer bonding. Additionally, Run 4 (185°C, Gyroid pattern) recorded the fastest shape recovery time (29 seconds), suggesting that moderate speeds allow for efficient elastic energy storage and rapid shape recovery.

At higher print speeds (80 mm/s, Runs 7–9), recovery times increased, and shape recovery rates generally declined. The lowest shape recovery rate (55.85%) was observed in Run 9 (200°C, Gyroid pattern), while Run 8 (190°C, Lines pattern) achieved 73.89%, maintaining a relatively stable performance. This decline at higher speeds is likely due to insufficient cooling time between layers, weaker interlayer adhesion, and increased porosity, which introduce residual stresses that hinder shape recovery. Yang et al. (2020) have demonstrated that lower print speeds can enhance mechanical properties and shape memory performance because of better layer fusion and reduced thermal gradients in the printed part, supporting the findings in this study [41].

These findings confirm that lower to moderate print speeds (40–60 mm/s) yield better shape recovery performance, while higher speeds (80 mm/s) introduce structural inconsistencies. The Taguchi analysis identified 40 mm/s as the optimal print speed, reinforcing previous studies that highlight the importance of deposition rate in controlling shape memory behavior. Achieving an optimal balance between structural integrity and recovery efficiency requires careful parameter selection, particularly in applications where precise shape recovery is critical.

The shape recovery rate is significantly influenced by print speed, as seen in Table 4, where variations in recovery rates align with changes in deposition speed. The highest recovery rate (83.00%) was observed in Run 6 (60 mm/s, 200°C, Lines pattern), while the lowest (55.85%) occurred in Run 9 (80 mm/s, 200°C, Gyroid pattern). However, a single high recovery rate does not necessarily indicate optimal conditions; instead, the overall trend must be considered. The optimal parameter combination (A1B1C1: 40 mm/s, 185°C, Lines) yielded a high recovery rate (78.60%), reinforcing the importance of lower print speeds in achieving better shape memory performance. At higher print speeds (60 mm/s and 80 mm/s), the rapid deposition reduces cooling time between layers, potentially weakening interlayer adhesion and introducing residual stress, which negatively impacts the material's ability to recover its original shape. In contrast, at lower print speeds (40 mm/s), the extended cooling time promotes stronger bonding and better layer fusion, leading to more efficient shape recovery. These findings align with previous studies that highlight the critical role of deposition rate in shape memory behavior, emphasizing that moderate print speeds offer the best balance between structural integrity and recovery efficiency [39,40].

3.4.2. Impact of Nozzle Temperature on Shape Recovery Rate

As shown in Table 4, nozzle temperature significantly influences the shape recovery rate by affecting material viscosity, interlayer bonding, and internal stress distribution during printing. The Taguchi analysis identifies the optimal parameter combination as A1B1C1 (40 mm/s print speed, 185°C nozzle temperature, and Lines infill pattern), meaning that the highest shape recovery rate is not necessarily achieved in a single run but rather through the optimal balance of all parameters.
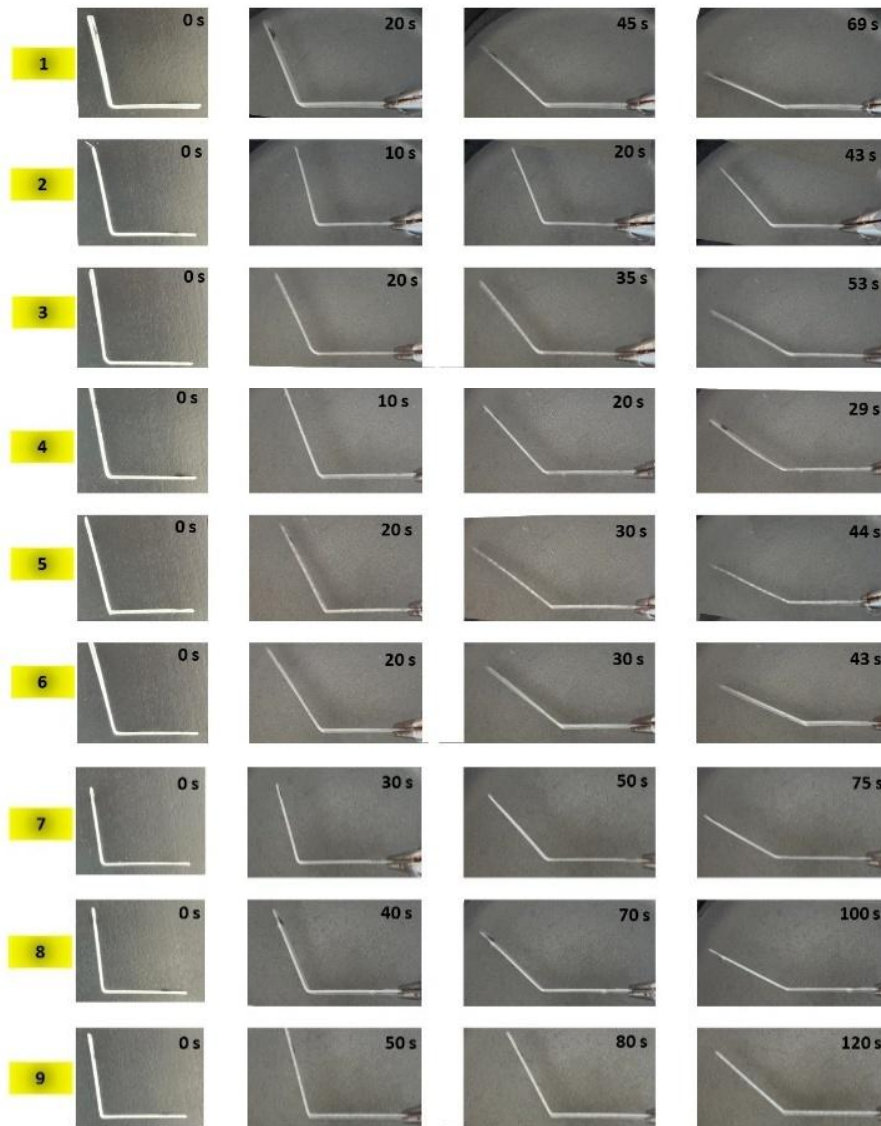
Figure 8. Shape recovery rates for all nine experimental runs.

Across the tested conditions, higher nozzle temperatures (200°C) showed inconsistent recovery results, where Run 6 (200°C) exhibited the highest individual recovery rate (83.00%), but Run 9 (200°C) had the lowest (55.85%). This suggests that while increased temperature can improve layer bonding and polymer chain mobility, it may also lead to thermal degradation or excessive fluidity at higher speeds, reducing overall recovery performance. The inconsistency in shape recovery rate at 200°C can be attributed to the combined effects of polymer chain mobility, thermal degradation, and print speed. At this higher temperature, polymer chains gain increased mobility, which can enhance interlayer diffusion [42] and improve shape recovery, as observed in Run 6 (200°C, 60 mm/s, Lines, 83.00%). However, excessive heat can also lead to thermal degradation, causing polymer chain scission and reducing molecular weight [43], which weakens the material's ability to recover its original shape. This effect is particularly pronounced when combined with high print speeds, as seen in Run 9 (200°C, 80 mm/s, Gyroid, 55.85%), where rapid extrusion may have resulted in poor layer adhesion, internal defects, and increased residual stresses that hindered shape recovery. Additionally, at high temperatures, excessive material fluidity can lead to poor layer deposition and structural inconsistencies, further affecting the recovery performance. The infill pattern also plays a role, as the Lines pattern in Run 6 may have facilitated better thermal distribution, while the Gyroid pattern in Run 9 could have contributed to localized stress

concentrations, reducing recovery efficiency. These findings suggest that while a higher nozzle temperature can improve layer bonding, it must be carefully optimized in conjunction with print speed and infill pattern to prevent excessive softening and degradation, ensuring consistent shape memory performance.

Nozzle temperature is crucial in determining the viscosity of the extruded material and its adhesion between layers during the FDM printing process [44]. At the optimal nozzle temperature of 185°C (Runs 1, 4, and 7), the recovery rates remained relatively stable, with Run 1 (40 mm/s, 185°C, Lines) achieving 78.60% and Run 4 (60 mm/s, 185°C, Gyroid) reaching 70.56%. This indicates that 185°C maintains good molecular integrity and adhesion, supporting efficient shape recovery without excessive softening or degradation. The PLA/PCL blend achieves a balance where the material flow is smooth enough to ensure strong interlayer bonding but not so high that it leads to overheating or thermal degradation [45]. This balance is essential for effective shape recovery, as it allows the material to maintain its integrity and undergo elastic deformation, enabling it to revert to its original form when the temperature exceeds its glass transition point. Issabayeva and Shishkovsky [46] observed similar effects, noting that lower temperatures improved shape recovery of PLA by reducing residual stress.

For 190°C (Runs 2, 5, and 8), recovery rates showed more variability, ranging from 58.22% (Run 2, 40 mm/s, Gyroid) to 73.89% (Run 8, 80 mm/s, Lines). This suggests that 190°C may not always provide consistent benefits for shape memory performance, especially when combined with infill patterns that do not optimize thermal diffusion. At higher nozzle temperatures (200°C), the material may become overly fluid, causing poor layer deposition and potential sagging, which can weaken the part's overall structure. This weakened structure negatively impacts the shape recovery rate, as internal defects and weakened bonds hinder the material's capacity to revert to its initial shape [46-47].

The shape recovery rate and time are influenced by nozzle temperature. At 185°C (Runs 1, 4, and 7), recovery rates remained stable (70.56%–78.60%) with moderate recovery times (29–75 s), indicating optimal viscosity and strong interlayer bonding. At 190°C (Runs 2, 5, and 8), recovery rates varied more (58.22%–73.89%) with longer times in some cases (up to 100 s), likely due to increased fluidity affecting layer adhesion. At 200°C (Runs 3, 6, and 9), results were inconsistent—Run 6 achieved the highest recovery rate (83.00%) in 43 s, while Run 9 had the lowest (55.85%) with the longest recovery time (120 s), suggesting that excessive heat can enhance chain mobility [48] but also lead to thermal degradation or weak structural integrity. These findings highlight 185°C as the most stable temperature, while higher temperatures require careful optimization to avoid excessive softening and prolonged recovery times.

3.4.3. Effect of Infill Pattern on The Shape Recovery Rate

The infill pattern plays a crucial role in determining the shape recovery rate, as it influences internal stress distribution, energy storage, and deformation behavior. As seen in Table 4, the Lines, Gyroid, and Triangle patterns exhibited varying recovery performances under different conditions, highlighting the importance of selecting the appropriate infill structure. The infill pattern determines the internal geometry and distribution of material within a printed part, affecting its mechanical properties and shape recovery capabilities [46].

Among the tested patterns, the Lines pattern demonstrated the most consistent and favorable results, particularly in Run 6 (60 mm/s, 200°C, Lines) where the highest individual shape recovery rate of 83.00% was observed. Additionally, Run 1 (40 mm/s, 185°C, Lines) achieved a recovery rate of 78.60%, further supporting the effectiveness of this pattern. The superior performance of the Lines pattern can be attributed to its uniform stress distribution and efficient load transfer, which enhances elastic energy storage and release during shape recovery.

The Lines infill pattern creates a continuous path of material that allows for consistent stress distribution and efficient storage and release of elastic energy. This uniform stress distribution is crucial for effective shape recovery, as it minimizes internal stress concentrations that could hinder the material's capacity to revert to its initial shape. Aloyaydi et al. [49] found similar effects in their study, highlighting that optimized infill strategies contribute to enhanced mechanical performance and shape memory

behavior by ensuring even stress distribution and reducing potential deformation-induced stress concentrations.

More complex patterns like the Gyroid and the Triangle may introduce more variability in internal stress distribution, leading to areas of high stress concentration that can adversely affect shape recovery performance. The study by Liu et al. (2020) indicated that simpler infill patterns, such as the Lines, tend to perform better in shape memory applications due to their predictable internal structure and consistent bonding characteristics [21]. The Gyroid pattern, while known for its excellent mechanical stability, showed more variability in recovery performance. In Run 9 (80 mm/s, 200°C, Gyroid), the lowest recovery rate (55.85%) was recorded, whereas Run 4 (60 mm/s, 185°C, Gyroid) achieved a moderate recovery rate of 70.56%. The reduced performance in certain cases may be due to inconsistent energy storage within the complex, curved structure of the Gyroid pattern, which can lead to localized stress concentrations and hinder full shape recovery. The Triangle pattern exhibited intermediate recovery rates, with Run 3 (40 mm/s, 200°C, Triangle) achieving 79.66%, while Run 5 (60 mm/s, 190°C, Triangle) showed a lower recovery rate of 61.07%. The performance variability suggests that while the Triangle pattern provides good structural support, it may not allow for optimal elastic energy release, affecting the efficiency of shape memory behavior.

The shape recovery time varies significantly across different experimental runs, highlighting the influence of processing parameters on the recovery dynamics of the printed structures. As seen in Table 4, the shortest recovery time was observed in Run 4 (29 seconds, 70.56% recovery rate), while the longest was in Run 9 (120 seconds, 55.85% recovery rate). Generally, shorter recovery times indicate faster energy release and efficient structural recovery, whereas longer times suggest delayed response due to weaker interlayer bonding or internal stresses. The optimal combination (A1B1C1: 40 mm/s, 185°C, Lines) not only yielded a high shape recovery rate but also maintained a moderate recovery time (69 seconds), balancing structural integrity and response efficiency. Notably, longer recovery times in Runs 8 and 9 (100s and 120s, respectively) may be attributed to weaker adhesion or increased internal resistance to shape change, further reinforcing the importance of optimized print parameters for enhanced shape memory performance.

3.5. Statistical Analysis

To understand the statistical significance of the selected 3D printing parameters on the mechanical and shape memory properties of the PLA/PCL blends, an Analysis of Variance (ANOVA) was performed. The evaluated parameters included print speed (A), nozzle temperature (B), and infill pattern (C), with tensile strength and shape recovery rate chosen as response variables. The results of the ANOVA are summarized in Table 6 and Table 7.

Regression analysis was also conducted to further understand the influence of print speed, nozzle temperature, and infill pattern on tensile stress and shape recovery rate. The regression models provide a quantitative representation of the contributions of these factors to the observed properties of the PLA/PCL blends.

3.5.1. Tensile Strength

The ANOVA results for tensile strength, presented in Table 6, indicate that the infill pattern (C) was the most significant factor affecting the tensile properties, with a p-value < 0.05. This suggests that the geometric arrangement of the infill pattern plays a critical role in determining the mechanical strength of the printed parts. In contrast, print speed (A) and nozzle temperature (B) exhibited less significant effects (p > 0.05). The results align with previous studies [50], where infill patterns significantly influenced stress distribution and interlayer adhesion.

Table 5. ANOVA results for tensile strength

Control factor	DF	Sum of Squares	Mean Square	F-Value	p-value	Contribution (%)
Print speed (mm/s) [A]	2	0.1994	0.0997	0.34	0.746	0.82
Nozzle temperature (°C) [B]	2	0.0751	0.0375	0.13	0.886	0.31
Infill pattern [C]	2	23.3980	11.6990	40.01	0.024	96.45
Error	2	0.5847	0.2924			2.41
Total	8	24.2572				

The relationship between tensile stress and the 3D printing parameters was further explored through regression analysis, as shown in Equation (2):

$$\text{Tensile Stress (MPa)} = 22.8 - 0.126A - 0.109B - 1.16C \tag{2}$$

where A represents print speed, B represents nozzle temperature, and C represents infill pattern.

The regression analysis highlights that the infill pattern (C) exerts the most significant influence on tensile stress, consistent with the ANOVA results where it was found to be statistically significant ($p < 0.05$). The coefficients for print speed (*A*) and nozzle temperature (B) are smaller, indicating their relatively lower impact on tensile stress within the studied parameter ranges. The coefficient of determination (R^2) was found to be 84.6%, indicating that the model explains a substantial portion of the variation in tensile stress. This suggests that the model provides a reasonably good fit for predicting tensile stress based on the selected process parameters. Infill pattern (C) contributes the most (96.45%) to tensile strength, making it the dominant factor, as shown in Table 7. Print speed (A) and nozzle temperature (B) have minimal contributions (0.82% and 0.31%), indicating that they do not significantly influence tensile strength. The error contribution is low (2.41%), meaning the model explains almost all of the variability in the data.
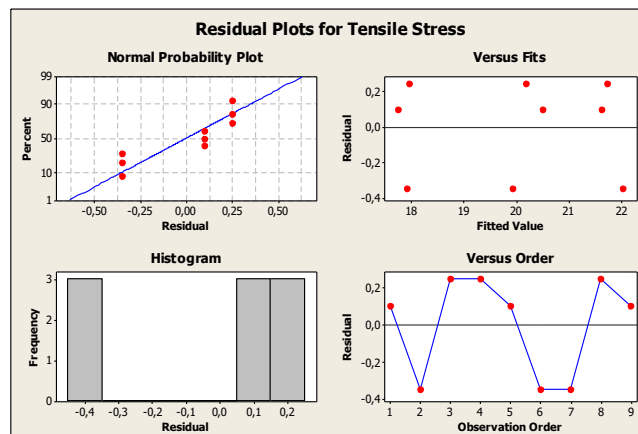
Figure 9. The residual plots for tensile stress

The residual plots for tensile stress, as shown in Figure 9, provide a graphical evaluation of the regression model's assumptions and the quality of the fit. The normal probability plot indicates that the residuals follow an approximately linear trend, suggesting that the normality assumption is reasonably satisfied. The residuals versus fitted values plot shows a random scatter with no discernible patterns, indicating that the variance of the residuals is constant and there is no evidence of heteroscedasticity. The histogram of residuals appears symmetric, further supporting the assumption of normality. Lastly, the residuals versus order plot shows no significant trends or patterns, suggesting that the residuals are independent and do not exhibit autocorrelation. These observations confirm that the regression model assumptions are adequately met, and the results can be considered reliable within the tested parameter range.

3.5.2. Shape Recovery Rate

The ANOVA analysis for shape recovery (Table 7) indicates that the three studied parameters—print speed, nozzle temperature, and infill pattern—each contribute to variations in the shape recovery rate. Among these, the infill pattern shows a relatively stronger influence, with nozzle temperature also contributing moderately, compared to print speed. While none of the parameters demonstrated a statistically significant effect ($p > 0.05$), their contributions highlight trends that can guide optimization efforts. These results suggest that shape memory performance is influenced by a combination of parameters, and additional factors, such as material composition or layer height, may further enhance optimization strategies for achieving improved recovery rates.

Table 6. ANOVA results for shape recovery rate

Control factor	DF	Sum of Squares	Mean Square	F-Value	p-value	Contribution (%)
Print speed (mm/s) [A]	2	36.02	18.01	0.26	0.796	4.63
Nozzle temperature (°C) [B]	2	167.37	83.68	1.19	0.457	21.49
Infill pattern [C]	2	434.53	217.27	3.09	0.245	55.79
Error	2	140.85	70.43			18.09
Total	8	778.78				

The regression equation for shape recovery rate (SRR) is shown in Equation (3):

$$\text{SRR (\%)} = 83.4 - 2.26A - 0.64B - 3.60C \tag{3}$$

where A represents the print speed in millimeters per second (mm/s), B represents the nozzle temperature in degrees Celsius (°C), and C represents the infill pattern used during 3D printing.

The regression analysis indicates that the infill pattern (C) has the most noticeable effect on shape recovery rate, as reflected in its coefficient magnitude (-3.60). Print speed (A) and nozzle temperature (B) also influence the shape recovery rate, but their effects are smaller, as indicated by their respective coefficients of -2.26 and -0.64. The coefficient of determination (R^2) was found to be 62.3%, indicating that the model provides a moderate fit for predicting the shape recovery rate based on the selected process parameters. These results indicate that the selected 3D printing parameters have varying impacts on shape memory performance. The infill pattern (C) is the most influential factor, contributing 55.79% to shape recovery, followed by nozzle temperature (B) with 21.49%, indicating a moderate effect. Print speed (A) has a lower impact at 4.63%. The error term accounts for 18.09%, suggesting some variability that may be influenced by additional factors not considered in the model.

The residual plots for shape recovery rate, as presented in Figure 10, offer insights into the adequacy of the regression model. The normal probability plot shows an approximate linear trend, indicating that the residuals are reasonably normally distributed. The residuals versus fitted values plot exhibits a random dispersion, with no evident patterns or systematic bias, suggesting that the assumption of homoscedasticity is met. The histogram of residuals displays a roughly balanced distribution, supporting the normality of residuals. The residuals versus order plot does not show any consistent trends or repetitive patterns, indicating that the residuals are independent over the sequence of observations. These results suggest that the regression model appropriately fits the shape recovery rate data and fulfills the underlying assumptions, providing confidence in the analysis within the tested parameter range.
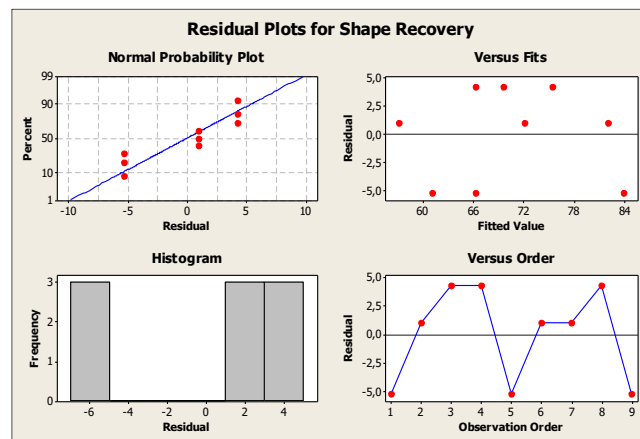
Figure 10. The residual plots for tensile stress
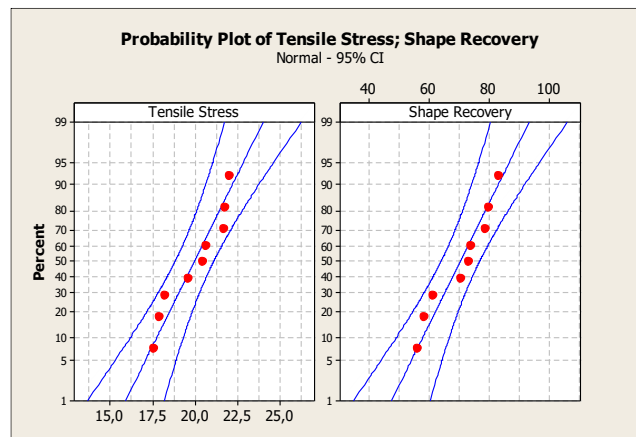
Figure 11. The residual plots for tensile stress and shape recovery ratio

The probability plots for tensile stress and shape recovery, as shown in Figure 11, illustrate how well the data follow a normal distribution. For tensile stress, the mean value is 19.95 MPa with a standard deviation of 1.741 MPa, while for shape recovery, the mean is 70.45% with a standard deviation of 9.866%. The Anderson-Darling (AD) test results for tensile stress (AD = 0.408, p = 0.272) and shape recovery (AD = 0.352, p = 0.379) confirm that the residuals for both responses align well with the normal distribution, as the p-values are greater than 0.05. The red data points in both plots fall within the confidence intervals, further validating the assumption of normality. These results suggest that the models for tensile stress and shape recovery are statistically sound, and the residuals do not exhibit significant deviations from normality, supporting the reliability of the analyses.

4. CONCLUSIONS

In this study 3D printing process parameters such as print speed, nozzle temperature, and infill pattern were successfully optimized using the Taguchi method to enhance the mechanical and shape memory properties of PLA/PCL blends printed via Fused Deposition Modeling (FDM). The results indicate that the infill pattern was the most influential factor for tensile strength, while both infill pattern and nozzle temperature had a greater impact on shape recovery rate. In contrast, print speed showed a relatively lower effect on both responses. These findings provide valuable insights for optimizing material performance in applications such as biomedical devices, textiles, and aerospace.

The optimal combination for maximizing shape recovery performance was identified as a print speed of 40 mm/s, a nozzle temperature of 185°C, and a Lines infill pattern. Under these conditions, the shape recovery rate of 78.60% and the recovery time of 69 s were achieved, demonstrating the importance of slower print speeds, optimal thermal control, and simpler infill geometries for enhanced shape memory

capabilities. Conversely, higher nozzle temperatures (190°C and 200°C) and more complex infill patterns, such as the Gyroid, resulted in lower recovery rates and longer recovery times due to weakened interlayer bonding and increased internal stresses.

For mechanical properties, the study revealed that a lower print speed and a nozzle temperature of 185°C, along with a Gyroid infill pattern, resulted in the greatest tensile strength. However, for simplicity and faster production, the Lines infill pattern could be preferred over the Gyroid, as it offers sufficient tensile strength while reducing print time and complexity.

Statistical analysis, including ANOVA and regression modeling, validated the influence of the studied parameters on both tensile strength and shape memory performance. The ANOVA results identified the infill pattern as the most significant factor for tensile strength, while regression analysis quantified the impact of print speed, nozzle temperature, and infill pattern. Residual and probability plots confirmed the reliability of the models, ensuring their accuracy in predicting PLA/PCL blend performance under different 3D printing conditions.

These findings contribute valuable insights into optimizing FDM parameters for PLA/PCL blends, supporting the development of advanced materials for biomedical and 4D printing applications. The Taguchi method proved effective in identifying optimal print parameter combinations, enhancing reproducibility and reliability in process optimization.

Declaration of Ethical Standards

The authors declare to comply with all ethical guidelines, including authorship, citation, data reporting, and original research publication.

Credit Authorship Contribution Statement

All authors made equal contributions to this study.

Declaration of Competing Interest

The authors declare that they have no conflict of interest.

Funding / Acknowledgements

Data Availability

Data available on request from the authors

REFERENCES

[1]   O. Öztürk, M. A. Şen, and M. Aydın, "The influence of fused filament fabrication parameters on the fracture behavior of PLA specimens considering energy consumption," *Konya Journal of Engineering Sciences*, vol. 12, no. 2, pp. 451–464, 2024.

[2]   S. Solechan, A. Suprihanto, S.A. Widyanto, J. Triyono, D. F. itriyana, J. P. Siregar, and T. Cionita, "Investigating the effect of PCL concentrations on the characterization of PLA polymeric blends for biomaterial applications," *Materials*, vol. 15, no. 20, Art. no. 7396, 2022.

[3]   T. C. Mokhena, M. B. Chabalala, S. Mapukata, A. Mtibe, L. Hlekelele, Z. Cele, and K. Shingange. "Electrospun PCL-based materials for health-care applications: an overview," *Macromolecular Materials and Engineering*, vol. 309, no. 8. Art. no. 2300388, 2024.

[4]   T. Patrício, M. Domingos, A. Gloria, U. D'Amora, J.F. Coelho, and P.J. Bártolo, "Fabrication and

characterisation of PCL and PCL/PLA scaffolds for tissue engineering," *Rapid Prototyping Journal*, vol. 20, no. 2, pp. 145-156, 2014.

[5]   A. Alafaghani and A. Qattawi, "Investigating the effect of fused deposition modeling processing parameters using Taguchi design of experiment method," *Journal of Manufacturing Processes*, vol. 36, Dec., pp. 164-174, 2018.

[6]   H. Hasdiansah, R. I. Yaqin, P. Pristiansyah, M. L. Umar, and B. H. Priyambodo, "FDM-3D printing parameter optimization using taguchi approach on surface roughness of thermoplastic polyurethane parts," *International Journal on Interactive Design and Manufacturing (IJIDeM)*, vol. 17, no. 6, pp. 3011-3024, 2023.

[7]   S. Singh, R.K. Attri, and S. Trivedi, "Optimization of FDM 3D printing process parameters for improving wear characteristics of PLA-nGr composite using taguchi DOE". *Journal of Materials Engineering and Performance*, Oct., pp. 1-9. 2024.

[8]   Y. Meyva-Zeybek and C. Kaynak, "Electrospinning of PLA and PLA/POSS nanofibers: use of taguchi optimization for process parameters," *Journal of Applied Polymer Science*, vol. 138, no.3, Art. no. 49685, 2021.

[9]   A. Nazir, N. Khenoussi, L. Schacher, T. Hussain, D. Adolphe, and A.H. Hekmati, "Using the taguchi method to investigate the effect of different parameters on mean diameter and variation in PA-6 nanofibres produced by needleless electrospinning," *RSC Advances*, vol. 5, no.94, pp. 76892-76897, 2015.

[10]   A. Dey and N. Yodo, "A systematic survey of FDM process parameter optimization and their influence on part characteristics," *Journal of Manufacturing and Materials Processing*, vol. 3, no. 3, Art. no. 64, 2019.

[11]   O.A. Mohamed, S.H. Masood, and J.L. Bhowmik, "Mathematical modeling and FDM process parameters optimization using response surface methodology based on Q-optimal design," *Applied Mathematical Modelling*, vol. 40, no. 23-24, pp. 10052–10073, 2016.

[12]   N. Vidakis, C. David, M. Petousis, D. Sagris, N. Mountakis, and A. Moutsopoulou, "The effect of six key process control parameters on the surface roughness, dimensional accuracy, and porosity in material extrusion 3D printing of polylactic acid: prediction models and optimization supported by robust design analysis," *Advances in Industrial and Manufacturing Engineering*, vol. 5, Nov., Art. no. 100104, 2022.

[13]   L. Le, M. A. Rabsatt, H. Eisazadeh, and M. Torabizadeh, "Reducing print time while minimizing loss in mechanical properties in consumer FDM parts," *International Journal of Lightweight Materials and Manufacture*, vol. 5, no. 2, pp. 197-212, 2022.

[14]   H. Liu, H. He, and B. Huang, "Favorable thermoresponsive shape memory effects of 3D printed poly (lactic acid)/poly (ε-caprolactone) blends fabricated by fused deposition modeling". *Macromolecular Materials and Engineering*, vol. 305, no. 11, Art. no. 2000295, 2020.

[15]   H. M. Qiu, K. W. Hou, J. P. Zhou, W. J. Liu, J. B. Wen, and Q. F. Gu, "Preparation of biodegradable PLA/PCL composite filaments: effect of PLA content on strength," *IOP Conference Series: Materials Science and Engineering*, vol. 770, no. 1, Art. no. 012059, 2020.

[16]   K. Saptaji, C. O. Rochmad, O. A. Juniasih, G. K. Sunnardianto, F. Triawan, A. I. Ramadhan, and A. Azhari, "Enhancing shape-recovery ratio of 4D printed polylactic acid (PLA) structures through processing parameter optimization," *Progress in Additive Manufacturing*, vol. 9, no. 6, pp. 1869-1881, 2024.

[17]   M. Hosseinzadeh, M. Ghoreishi, and K. Narooei, "An investigation into the effect of thermal variables on the 3D printed shape memory polymer structures with different geometries," *Journal of Intelligent Material Systems and Structures*, vol. 33, no. 5, pp. 715-726, 2022.

[18]   M. Eryildiz, "Influence of process parameters on the shape recovery properties of 4D-printed polylactic acid parts produced by fused deposition modeling," *Journal of Materials Engineering and Performance*, vol. 32, no. 9, pp. 4258-4269, 2023.

[19]   P. Kumar, P. B. Barua, J. L. Gaindhar, "Quality optimization (multi-characteristics) through

Taguchi's technique and utility concept," *Quality and Reliability Engineering International*, vol. 16, no. 6, pp. 475-485, 2000.

[20] D. Syrlybayev, B. Zharylkassyn, A. Seisekulova, M. Akhmetov, A. Perveen, and D. Talamona, "Optimisation of strength properties of FDM printed parts—A critical review," *Polymers*, vol. 13, no. 10, Art. no. 1587, 2021.

[21] T. Liu, L. Liu, C. Zeng, Y. Liu, and J. Leng, "4D printed anisotropic structures with tailored mechanical behaviors and shape memory effects," *Composites Science and Technology*, vol. 186, Jan., Art. no. 107935, 2020.

[22] J. Wang, Z. Wang, Z. Song, L. Ren, Q. Liu, and L. Ren, "Programming multistage shape memory and variable recovery force with 4D printing parameters," *Advanced Materials Technologies*, vol. 4, no. 11, Art. no. 1900535, 2019.

[23] Y. S. Alshebly, and M. Nafea, "Effects of printing parameters on 4D-printed PLA actuators," *Smart Materials and Structures*, vol. 32, no. 6, Art. no. 064008, 2023.

[24] D. Kong, A. Guo, H. Wu, X. Li, J. Wu, Y. Hu, and S. Guo, "Four-dimensional printing of polymer-derived ceramics with high-resolution, reconfigurability, and shape memory effects," *Additive Manufacturing*, vol. 83, Mar., Art. no. 104050, 2024.

[25] S. Ma, Z. Jiang, M. Wang, L. Zhang, Y. Liang, Z. Zhang, and L. Ren, "4D printing of PLA/PCL shape memory composites with controllable sequential deformation," *Bio-Design and Manufacturing*, vol. 4, Jul., pp. 867-878, 2021.

[26] P. Kiani, M. Sedighi, M. Kasaeian-Naeini, and A. H. Jabbari, "High cycle fatigue behavior and thermal properties of PLA/PCL blends produced by fused deposition modeling," *Journal of Polymer Research*, vol. 30, no. 7, Art. no. 264, 2023.

[27] C. Hamzaçebi, P. Li, P.A.P. Pereira, and H. Navas, "Taguchi method as a robust design tool. Quality Control-Intelligent Manufacturing," in *Quality Control - Intelligent Manufacturing, Robust Design and Charts*, P. Li, P. A. R. Pereira, and H. Navas, Eds. London: IntechOpen, Mar., pp. 1-19, 2020.

[28] S. H. Ahn, M. Montero, D. Odell, S. Roundy, and P. K. Wright, "Anisotropic material properties of fused deposition modeling ABS," *Rapid prototyping journal*, vol. 8, no. 4, pp. 248-257, 2002.

[29] M. Domingo-Espin, J. M. Puigoriol-Forcada, A. A. Garcia-Granada, J. Llumà, S. Borros, and G. Reyes, "Mechanical property characterization and simulation of fused deposition modeling polycarbonate parts," *Materials & Design*, vol. 83, Oct., pp. 670-677, 2015.

[30] A. Li, X. G. Chen, L. Y. Zhang, and Y. F. Zhang, "Temperature and infill density effects on thermal, mechanical and shape memory properties of polylactic acid/poly (ε-caprolactone) blends for 4d printing," *Materials*, vol. 15, no. 24, Art. No. 8838, 2022.

[31] P. K. Mishra, P. Senthil, S. Adarsh, M. S. Anoop, "An investigation to study the combined effect of different infill pattern and infill density on the impact strength of 3D printed polylactic acid parts," *Composites Communications*, vol. 24, Apr., Art. No. 100605, 2021.

[32] T. S. Tamir, G. Xiong, Q. Fang, X. Dong, Z. Shen, and F. Y. Wang, "A feedback-based print quality improving strategy for FDM 3D printing: an optimal design approach," *The International Journal of Advanced Manufacturing Technology*, vol. 120, no. 3, pp. 2777-2791, 2022.

[33] A. R. Avdeev, A. A. Shvets, and I. S. Torubarov, "Investigation of kinematics of 3D printer print head moving systems," *Proceedings of the 5th International Conference on Industrial Engineering (ICIE 2019)*, vol. I5, Dec., pp. 461-471, 2020.

[34] G. Chouhan and G. Bala Murali, "Designs, advancements, and applications of three-dimensional printed gyroid structures: A review," *Proceedings of the Institution of Mechanical Engineers, Part E: Journal of Process Mechanical Engineering*, vol. 238, no. 2, pp. 965-987, 2024.

[35] A. H. Kadhum, S. Al-Zubaidi, and S. S. Abdulkareem, "Effect of the infill patterns on the mechanical and surface characteristics of 3D printing of PLA, PLA+ and PETG materials," *ChemEngineering*, vol. 7, no. 3, Art. no. 46, 2023.

[36] M. T. Birosz, D. Ledenyak, and M. Ando, "Effect of FDM infill patterns on mechanical properties".

Polymer Testing, vol. 113, Sep., Art. no. 107654, 2022.

[37]   M. F. Jasim, T. F. Abbas, and A. F. Huayier, "The effect of infill pattern on tensile strength of PLA material in fused deposition modeling (FDM) process," *Engineering and Technology Journal*, vol. 40, no. 21, pp. 1723-1730, 2022.

[38]   A. Chalgham, A. Ehrmann, I. Wickenkamp, "Mechanical properties of FDM printed PLA parts before and after thermal treatment," *Polymers*, vol. 13, no. 8, Art. no. 1239, 2021.

[39]   H. G. Şahin and A. Mardani, "Mechanical properties, durability performance and interlayer adhesion of 3DPC mixtures: a state-of-the-art review," *Structural Concrete*, vol. 24, no. 4, pp. 5481-5505, 2023.

[40]   Y. Weng, M. Li, D. Zhang, M. Tan, and S. Qian, "Investigation of interlayer adhesion of 3D printable cementitious material from the aspect of printing process," *Cement and Concrete Research*, vol. 143, May., Art. no. 106386, 2021.

[41]   T. Yang and C. Yeh, "Morphology and mechanical properties of 3D printed wood fiber/polylactic acid composite parts using fused deposition modeling (FDM): the effects of printing speed," *Polymers*, vol. 12, no. 6, Art. no. 1334, 2020.

[42]   S. Mani and R. Khare, "Effect of chain flexibility and interlayer interactions on the local dynamics of layered polymer systems," *Macromolecules*, vol. 51, no. 2, pp. 576-588, 2018.

[43]   J. Yoon, H. Jin, I. Chin, C. Kim, and M. Kim, "Theoretical prediction of weight loss and molecular weight during random chain scission degradation of polymers," *Polymer*, vol. 38, no. 14, pp. 3573-3579, 1997.

[44]   Y. Lyu, H. Zhao, X. Wen, L. Lin, A. Schlarb, and X. Shi, "Optimization of 3D printing parameters for high-performance biodegradable materials," *Journal of Applied Polymer Science*, vol. 138, no. 32, Art. no. 50782, 2021.

[45]   K. Elhattab, S. Bhaduri, and P. Sikder, "Influence of fused deposition modelling nozzle temperature on the rheology and mechanical properties of 3D printed β-tricalcium phosphate (TCP)/polylactic acid (PLA) composite," Polymers, vol. 14, no. 6, Art. no. 1222, 2022.

[46]   Z. Issabayeva and I. Shishkovsky, "Prediction of the mechanical behavior of polylactic acid parts with shape memory effect fabricated by FDM," *Polymers*, vol. 15, no. 5, Art. no. 1162, 2023.

[47]   M. Barletta, A. Gisario, and M. Mehrpouya, "4D printing of shape memory polylactic acid (PLA) components: investigating the role of the operational parameters in fused deposition modelling (FDM)," *Journal of Manufacturing Processes*, vol. 61, Jan., pp. 473-480, 2021.

[48]   S. J. Zhen, "The effect of chain flexibility and chain mobility on radiation crosslinking of polymers," *Radiation Physics and Chemistry*, vol. 60, no. 4-5, pp. 445-451, 2001.

[49]   B. Aloyaydi, S. Sivasankaran, and A. Mustafa, "Investigation of infill-patterns on mechanical response of 3D printed poly-lactic-acid," *Polymer Testing*, vol. 87, Jul., Art. no. 106557, 2020.

[50]   M. Othmani, K. Zarbane, and A. Chouaf, "Effect of infill and density pattern on the mechanical behaviour of ABS parts manufactured by FDM using Taguchi and ANOVA approach," *Archives of Materials Science and Engineering*, vol. 111, no. 2, pp. 66-77, 2021.

A DYNAMIC ANALYSIS OF AN INDUSTRIAL C-TYPE ECCENTRIC PRESS THROUGH MODELING, SIMULATION, AND EXPERIMENTAL TESTING

[1],*Ahmet KÖKEN [ID] , **[2]Abdurrahman KARABULUT** [ID]

[1]Kütahya Dumlupınar University, Kütahya Vocational School of Technical Sciences, Machinery and Metal Technologies Department, Kütahya, TÜRKİYE
[2]Afyon Kocatepe University, Technology Faculty, Mechanical Engineering Department, Afyonkarahisar, TÜRKİYE
[1] ahmet.koken@dpu.edu.tr, [2] akarabulut@aku.edu.tr

Highlights

- MATLAB/Simulink modeling and analysis of the press-ground system
- A dynamic model was developed to analyze two mass impact load responses
- Stiffness and damping optimization of vibration isolator systems

Graphical Abstract
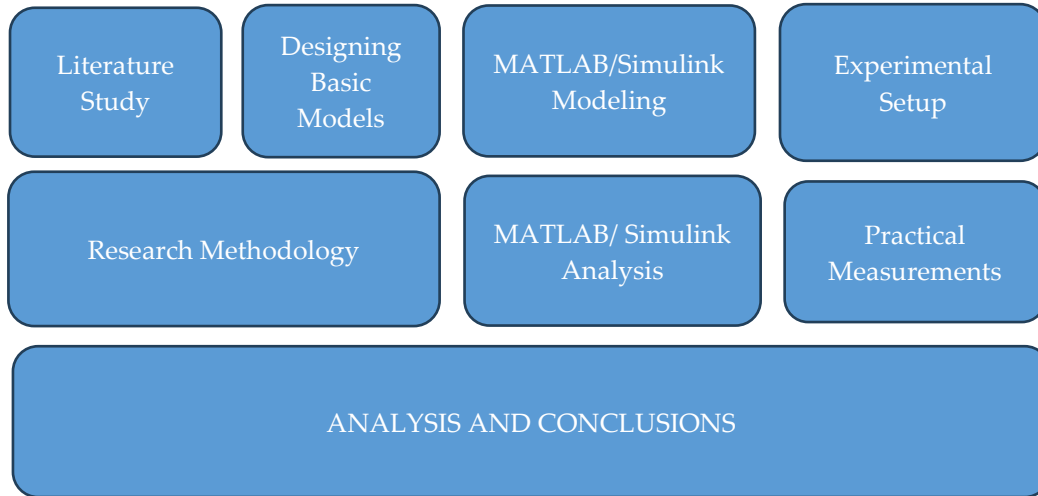
Literature Study	Designing Basic Models	MATLAB/Simulink Modeling	Experimental Setup
Research Methodology		MATLAB/ Simulink Analysis	Practical Measurements
ANALYSIS AND CONCLUSIONS			

Flowchart of the proposed method

*Corresponding Author: Ahmet KÖKEN, ahmet.koken@dpu.edu.tr

A DYNAMIC ANALYSIS OF AN INDUSTRIAL C-TYPE ECCENTRIC PRESS THROUGH MODELING, SIMULATION, AND EXPERIMENTAL TESTING

1, *Ahmet KÖKEN [ID] , **2Abdurrahman KARABULUT** [ID]

1Kütahya Dumlupınar University, Kütahya Vocational School of Technical Sciences, Machinery and Metal Technologies Department, Kütahya, TÜRKİYE
2Afyon Kocatepe University, Technology Faculty, Mechanical Engineering Department, Afyonkarahisar, TÜRKİYE
1 ahmet.koken@dpu.edu.tr, 2 akarabulut@aku.edu.tr

ABSTRACT: This study provides a comprehensive analysis of the dynamic behavior, modeling, simulation, and experimental validation of industrial C-type eccentric presses, offering critical insights into the optimization of press ground vibration. Through detailed modeling, the forces and vibrations experienced during operation were mathematically characterized, while simulations effectively demonstrated the system's behavior under varying operational conditions, and experimental studies confirmed the reliability of these models. The investigation also examined the impact of dynamic loads on machine foundations, analyzing single and double mass-spring systems using MATLAB simulations and analytical solutions to assess the influence of ground-foundation characteristics on the press's dynamic response. Prior to vibration isolation, the average peak ground displacement (PGD) was measured at 5.075×10^{-2} mm, which decreased to 3.46×10^{-2} mm and 2.7×10^{-2} mm with the application of VI-1 and VI-3 isolators, respectively. The VI-3 isolator proved most effective, reducing transmitted dynamic forces to 2.57×10^4 N. Parametric analyses highlighted the system's sensitivity to isolator stiffness and damping ratios, with a stiffness ratio of 0.01 between the isolator and ground reducing foundation vibrations by approximately 46.8%. This research emphasizes the importance of dynamic modeling in designing and optimizing vibration isolation systems, making a significant contribution to enhancing vibration control in industrial applications.

Keywords: Eccentric Press, Vibration Isolator, 2-DOF Modeling, Dynamic Response

1. INTRODUCTION

Press foundations undergo significant dynamic excitation due to short-duration impulsive loads experienced during normal operation. These dynamic effects, originating from the interface between the upper and lower press modules, often manifest as excessive vibrations that can compromise the press system's performance and disrupt the surrounding environment. The primary design goals for blocking foundations of press systems are to ensure stability and to mitigate vibration amplitudes and transmitted forces to minimize environmental disturbance. Non-linear dry friction mounting systems are commonly employed to support press systems to achieve these objectives. The presence of these systems significantly modifies the foundation system's dynamic response, particularly in terms of natural frequency and damping, when subjected to impulsive loads. Hence, developing a non-linear dry friction mounted block foundation model is crucial [1].

Press foundations can be categorized into two principal types: inertial block foundations (Figure 1(a)) and block foundations equipped with non-linear dry friction isolation systems (Figure 1(b) and 1(c)). When a press is rigidly coupled to an inertial block anchored in the ground, as depicted in Figure 1(a), the foundation system can be idealized as a single-degree-of-freedom system in the vertical axis. The foundation arrangements illustrated in Figures 1(b) and 1(c) can be represented as two-degree-of-freedom systems [1].

---

*Corresponding Author: Ahmet KÖKEN, ahmet.koken@dpu.edu.tr
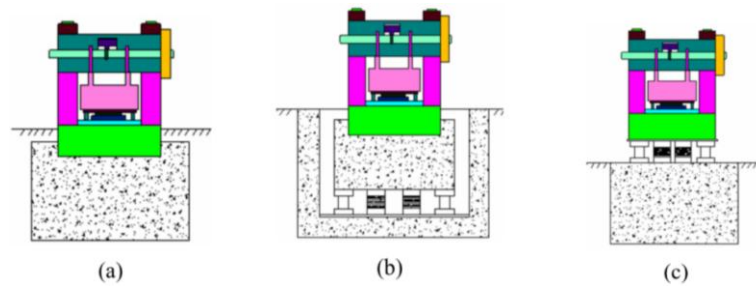
Figure 1. Schematic representations of press foundation configurations: (a) single-degree-of-freedom foundation system and (b, c) two-degree-of-freedom foundation systems with non-linear dry friction isolation [1].

The dynamic precision and reliability of high-speed, high-precision presses depend on effective vibration isolation. Minimizing press vibration is paramount for achieving high-precision stamping operations. Although commonly employed linear vibration isolators are effective in attenuating low-frequency vibrations, their performance is constrained at higher frequencies.

Vibration analysis has gained significant prominence in engineering disciplines, particularly in research and development endeavors, driven by the increasing demand for medium to high-frequency analysis [2]. Given the high dynamic loads and substantial vibration amplitudes generated by equipment such as presses, specialized isolation systems are imperative. The objective of these systems is to attenuate equipment-induced vibrations and minimize their environmental impact [3]. Drawing upon experimental investigations and computational modeling, various isolation systems tailored for presses have been developed [4], [5].

A comprehensive body of research has emerged in recent years focusing on vibration isolation techniques for impact machinery. Some of the studies conducted in the literature are as follows: Zheng et al. [4] presented a dynamic model for analyzing the dynamic performance of a closed-loop high-speed press system in their research. Jia et al. [6] studied the dynamic analysis of a closed-loop high-speed precision press using 2-DOF and 3-DOF models, including modeling, simulation, and experimental validation under periodic impact loads. Jancarczyk et al. [7] performed an in-depth investigation into vibration monitoring within hydraulic presses, employing cutting-edge measurement systems incorporating accelerometers. The suggested system, consisting of a three-axis accelerometer, a data acquisition device, and dedicated measurement software, was shown to streamline accurate vibration tracking and evaluation. They examined the impact of sensor positioning and sampling rate on the measurement outcomes. Temporal and spectral analyses were conducted on the collected data. The findings revealed a link between vibration magnitudes and diverse production variables, including the concurrent output of multiple parts and press force. These results emphasized the significance of vibration measurement as a vital factor in regulating production parameter configurations. Dal and Baklacı [8] placed vibration isolation rubber pads under the workbench legs in their study to reduce vibration-induced noise. After repeated measurements and analyses under the same conditions, they reported a significant decrease in noise and vibration levels of the polishing machine. In their study, Wang et al. [9] proposed a nonlinear vibration isolation platform with a nonlinear isolation system to mitigate ground vibrations from mechanical equipment. They investigated the effects of flexible foundations and isolator parameters on the platform's performance. Saberi et al. [10] carried out a comprehensive study involving both theoretical modeling and experimental testing to analyze the mechanical vibrations occurring during the hot forging process. Kekeç and Ghiloufi [11] investigated the propagation of ground vibrations induced by explosions within a medium of loose, dry sand, encompassing both surface and subsurface scenarios. The study involved the monitoring of particle velocities and the determination of dominant frequency components within the artificially generated vibration field. Chehab et al. [12] presented a rigorous investigation into the design of isolation foundations for forging equipment. Utilizing fundamental soil mechanics principles, the authors conducted a parametric study to evaluate the performance of various vibration reduction configurations

and subsequently optimized the design parameters. Avcı and Yazgan [13] presented a comprehensive analysis of displacement rates in structures supported by sandy soils. The study employed nonlinear equivalent single-degree-of-freedom systems to model the dynamic behavior of the soil-structure system. Tekeci et al. [14] presented a comprehensive analysis of the fatigue life of the mounting connection in a shock absorber system. A finite element model, corroborated by modal testing, was utilized to predict the fatigue life. Vibration tests further substantiated the model's accuracy and facilitated the quantification of damping ratios. Köken [15] conducted a study to evaluate the efficacy of vibration isolators in reducing ground vibrations transmitted from press machines. The findings of the study demonstrated that vibration isolators can substantially attenuate ground vibrations. Wang et al. [16] presented a design optimization framework for low-impact transmission foundations tailored to forging hammer applications. The study demonstrated that a viscous spring isolator mounting system, when optimized, can effectively attenuate shock and vibration transmission, leading to a reduction in the overall foundation size. A case study involving a 3-ton forging hammer validated the superiority of the proposed optimization method over conventional design approaches in terms of impact and vibration isolation performance. Hızarcı and Kıral [17] investigated the vibration response of an engineering structure to harmonic ground excitation and explored the potential of air jet actuators for vibration control. Alhuhydan et al. [18] presented an investigation into the reduction of excessive vibration generated by a model. The study focused on the implementation of suitable vibration control strategies. Zhu et al. [19] conducted an analysis of a two-mass vibration system characterized by nonlinear stiffness and damping. Their study demonstrated that significant vibration suppression can be achieved by tuning system parameters and excitation frequency. Lang et al. [20] conducted an evaluation of the impact of nonlinear viscous damping on the performance of single-degree-of-freedom vibration isolators. They developed a frequency response function to characterize the relationship between damping and the transmissibility of vibrations. Ping et al. [21] formulated a mathematical model for a nonlinearly coupled isolator characterized by quadratic, viscous, and Coulomb damping, and a nonlinear spring force. The dynamic transmissibility of the system subjected to deterministic excitation was derived analytically. Kunadharaju and Borthakur [22] presented a study investigating the application of elastomeric dampers and spring vibration isolators beneath the anvil and foundation of forging hammers for vibration reduction. Through analytical and finite element modeling, they developed an isolation system that effectively meets current environmental vibration standards. Guo et al. [23] presented an investigation into the application of a vibration isolation system to reduce vibration transmission between a machine and its foundation. The results demonstrated the efficacy of the proposed system in mitigating unwanted shocks and vibrations. Kumar and Boora [24] experimentally analyzed the dynamic behavior of a machine foundation. They investigated the effects of two distinct combinations of a spring mounting base and a rubber pad interposed between the machine base and the concrete foundation block. In their studies, Köken et al. [25], [26] and Karabulut et al. [27] experimentally investigated the use of vibration isolators for the ground isolation of machine tools and emphasized that the use of vibration isolators has a significant effect on reducing ground vibrations. Abd-Elhamed et al. [28] analyzed the dynamic response of machine foundations under harmonic and impulsive loading conditions. They obtained closed-form solutions for the displacement, velocity, and acceleration time histories resulting from two distinct types of impulsive loads. Kam et al. [29], [30] it has been emphasized that controlling vibrations in systems is crucial, as excessive vibration amplitudes can lead to inefficiency and system failures.

To ensure satisfactory performance of the machine, the mounting system and/or foundation should be designed such that vibration amplitudes do not exceed 1.2 mm [31]. In the study, the dynamic behavior of an industrial C-type eccentric press was investigated using both MATLAB simulations and experimental analysis. Three vibration isolators (VI-1, VI-2, VI-3) with different stiffness and damping properties were comparatively analyzed, and their performances were examined in detail. It was found that the VI-3 isolator could reduce ground vibrations by up to 46.8% and was the most effective solution. The stiffness ratio (0.01) of the mounting system was determined to have a significant effect on

vibrations and was found to considerably reduce vibration levels. The comparison of field measurements with simulation results demonstrated that the model accurately represents real operating conditions. The study provides a practical guide for the optimization of vibration isolation systems in industrial machinery. Unlike similar studies in the literature, the performances of different isolator types were compared, and the effect of a specific stiffness ratio was examined in detail.

2. MATERIAL AND METHODS

2.1. Mathematical Models

Press foundations are modeled as lumped mass systems. The foundation systems are commonly modeled as single or two-mass systems, contingent upon the foundation's configuration.

A press foundation devoid of a vibration isolator can be idealized as a single-mass system (Figure 2). In this idealized model, k_0 and c_0 denote the stiffness and damping coefficients of the soil, m_1 represents the mass of the press, m_2 represents the mass of the foundation block, and m_t denotes the total mass of the system. F_t is the impulsive force exerted on the foundation block, and $x(t)$ represents the resulting response of the foundation block.
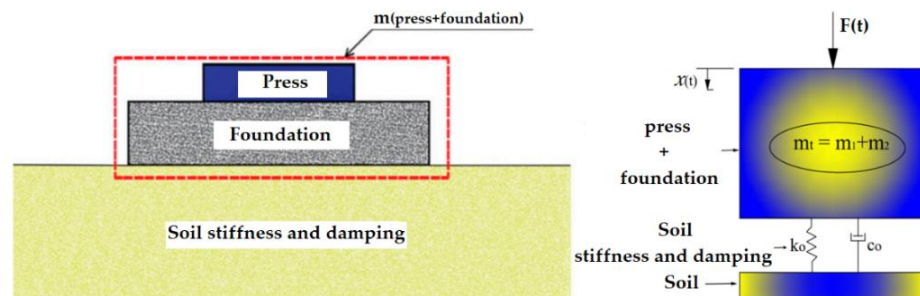
Figure 2. Actual system

A press foundation incorporating a vibration isolator can be idealized as a two-mass system (Figure 3). In this idealized model, k_1 and c_1 denote the stiffness and damping coefficients of the vibration isolator, and k_0 and c_0 denote the stiffness and damping coefficients of the soil. m_1 represents the mass of the press, and m_2 represents the mass of the foundation block. When subjected to dynamic excitation, the press and the foundation block exhibit a characteristic response. This response is contingent upon the magnitude, duration, and frequency of the excitation, as well as the system properties, such as mass, stiffness, and damping. $x_1(t)$ and $x_2(t)$ represent the displacements of the press and the foundation block, respectively.
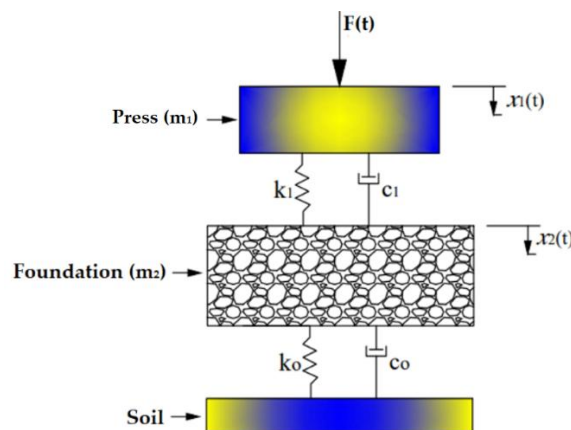
Figure 3. Idealized press- foundation- soil system

2.2. Impact Load

The impact loads resulting from strikes can take various forms. The differences between these loads arise from factors such as the size and shape of the material, its temperature and mechanical properties, the elastic properties of the materials constituting the press system components, the contact surface geometry, and the impact energy. The presence of numerous factors influencing the time-dependent variation of press forces makes it quite challenging to determine these forces theoretically. Therefore, these forces are determined through experimental methods. For theoretical investigations, the real and nonlinear time-dependent variation curves of impact loads are approximated using various methods, such as straight lines or trigonometric functions (Figure 4) [31].
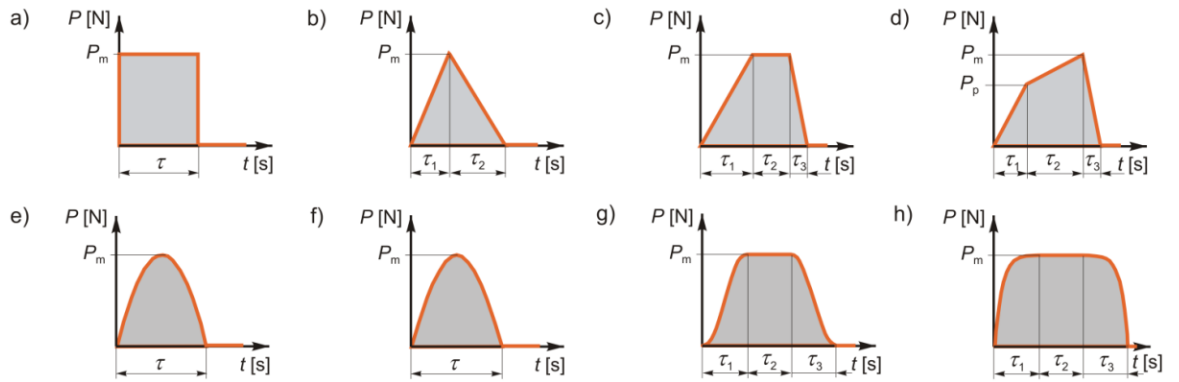
Figure 4. Shapes of impact loads: a) rectangular, b) triangular, c) trapezoidal, d) triangular-trapezoidal, e) parabolic, f) half-sine, g) inverted sine-rectangular, h) exponential-rectangular [31].

The time-varying nature of the impact was simplified by assuming a rectangular pulse shape, where the force is constant over the duration of the impact and then drops abruptly to zero.

$$f(t) = \begin{cases} p_m = \dfrac{S}{t_p} = \dfrac{(1+R)\sqrt{2 \cdot U \cdot m_B}}{t_p} & 0 \le t \le t_p \\ 0 & t > 0 \end{cases} \tag{1}$$

Here, p_m maximum impact force, S magnitude of the impact load, t_p loading duration, R coefficient of restitution, U total energy of the press, m_B mass of the ram.

2.3. Analysis Method

To investigate the dynamic characteristics of single and dual-mass systems, equations of motion have been developed based on d'Alembert's principle. The derived equations serve as a mathematical model for describing the force-motion relationship within the system.

Equation (2) provides a mathematical representation of the single-mass system.

$$m_t \ddot{x} + c_0 \dot{x} + k_0 x = F(t) \tag{2}$$

Here, k_0 stiffness, c_0 damping coefficient, m_t total mass and $x(t)$ foundation displacement.

Equations (3) and (4) provide a mathematical representation of the two-mass system.

$$m_1 \ddot{x}_1 + c_1(\dot{x}_1 - \dot{x}_2) + k_1(x_1 - x_2) = F(t) \tag{3}$$

$$m_2 \ddot{x}_2 - c_1(\dot{x}_1 - \dot{x}_2) - k_1(x_1 - x_2) + c_0 \dot{x}_2 + k_0 x_2 = 0 \tag{4}$$

Matrix form,

$$[m]\{\ddot{x}\} + [c]\{\dot{x}\} + [k]\{x\} = \{F(t)\} \tag{5}$$

$$\begin{bmatrix} m_1 & 0 \\ 0 & m_2 \end{bmatrix} \begin{Bmatrix} \ddot{x}_1 \\ \ddot{x}_2 \end{Bmatrix} + \begin{bmatrix} c_1 & -c_1 \\ -c_1 & c_1 + c_0 \end{bmatrix} \begin{Bmatrix} \dot{x}_1 \\ \dot{x}_2 \end{Bmatrix} + \begin{bmatrix} k_1 & -k_1 \\ -k_1 & k_1 + k_0 \end{bmatrix} \begin{Bmatrix} x_1 \\ x_2 \end{Bmatrix} = \begin{Bmatrix} F(t) \\ 0 \end{Bmatrix} \tag{6}$$

The force passing through the assembly system can be calculated using equation (7).

$$f_a(t) = k_1(x_1 - x_2) + c_1(\dot{x}_1 - \dot{x}_2) \tag{7}$$

The force transmitted to the ground can be calculated using equation (8).

$$f_b(t) = k_0 x_2 + c_0 \dot{x}_2 \tag{8}$$

The response of a single-degree-of-freedom system to harmonic excitation has been mathematically investigated by Rao [32]. Figure 5 shows the variation of force transmission ratio (Tr) with the frequency ratio $r = \omega/\omega_n$ and damping ratio (ζ). For successful isolation, the transmitted force to the foundation must be lower than the applied excitation force. The graph shows that for frequency ratios up to ($\sqrt{2}$), increasing damping decreases the force transmission ratio, but for frequency ratios greater than ($\sqrt{2}$), the force transmission ratio increases again with increasing damping [33]. This finding indicates the necessity of an adjustable damping mechanism in the design of suspension systems.
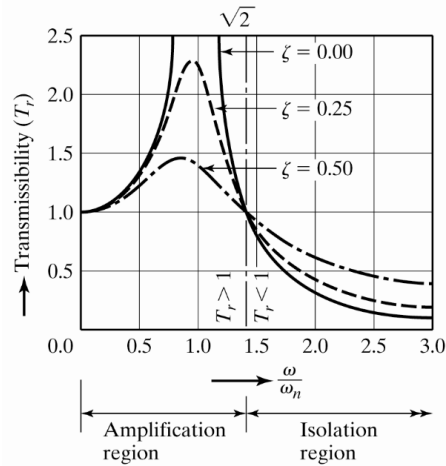
Figure 5. Variation of transmission ratio (T_r) with ω [32].

The transmissibility of a system subjected to harmonic motion is described by equation (9).

$$T_r = \sqrt{\left(\frac{k^2 + \omega^2 c^2}{[(k - m\omega^2)^2 + \omega^2 c^2]} \right)} \tag{9}$$

Equation (10) defines the relationship between transmissibility (T_r), damping ratio (ζ), and frequency ratio (r) of a system.

$$T_r = \sqrt{\frac{1 + (2\zeta r)^2}{(1 - r^2)^2 + (2\zeta r)^2}} \tag{10}$$

The frequency ratio (r) and the damping ratio (ζ) are determined by equations (11) and (12), respectively.

$$r = \frac{\omega}{\omega_n} \tag{11}$$

$$\zeta = \frac{c}{2m\omega_n} \tag{12}$$

2.4. MATLAB/Simulink Modeling

Simulink simulations are based on the numerical solution of sets of ordinary differential equations that describe the dynamic behavior of a system. When considering the steady-state conditions of the model, the variable-step, fourth-order Runge-Kutta method, which is Simulink's default solver, ensures accurate capture of all dynamic characteristics of the system. This allows for precise determination of the parameters necessary for the design of systems such as vibration isolators and presses. The numerical solution of the differential motion equations in the MATLAB program is illustrated in Figures 6, 7, and 8, which show the visualized simulation models of the press system created in MATLAB Simulink.
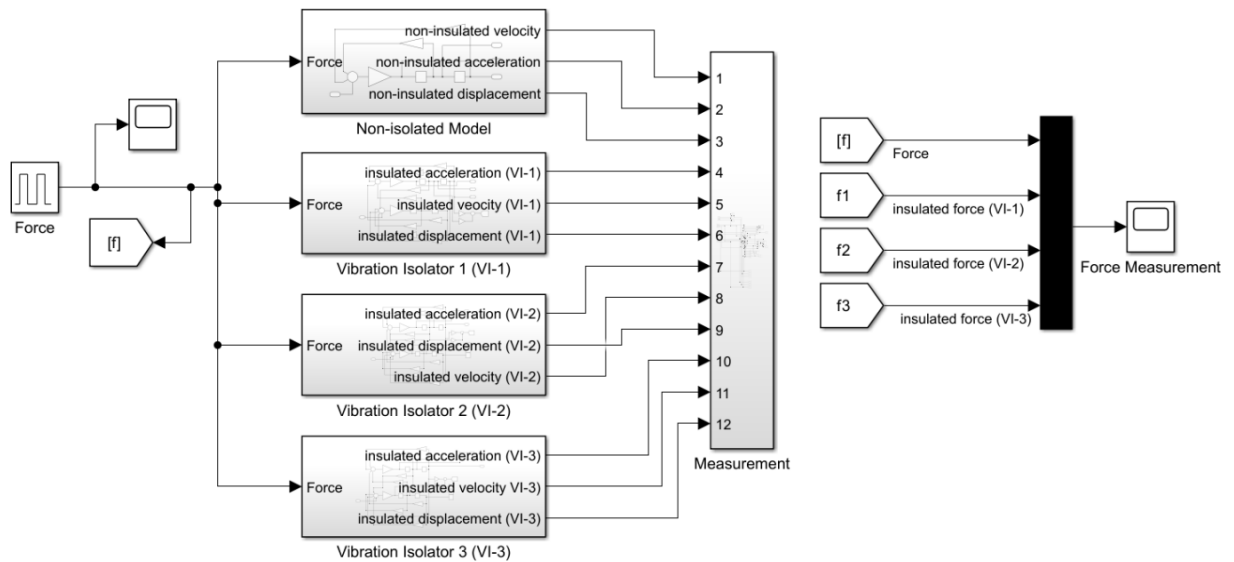
Figure 6. A Simulink-based simulation model of a press system
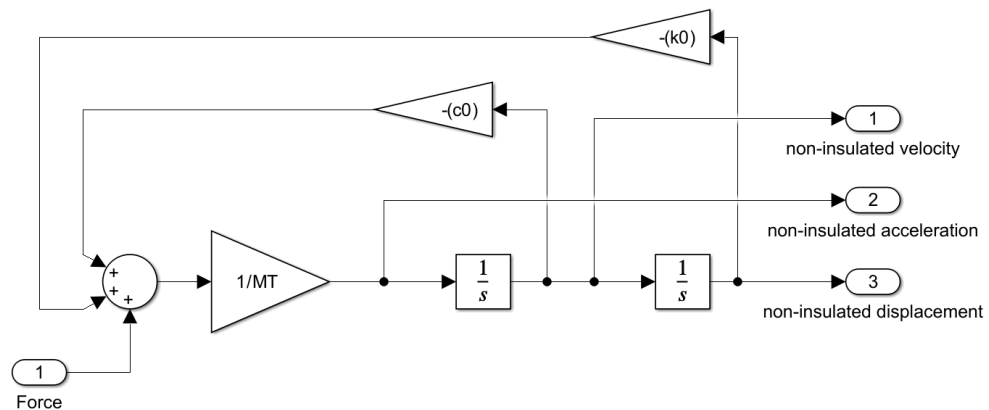
Figure 7. Simulink simulation model without isolation
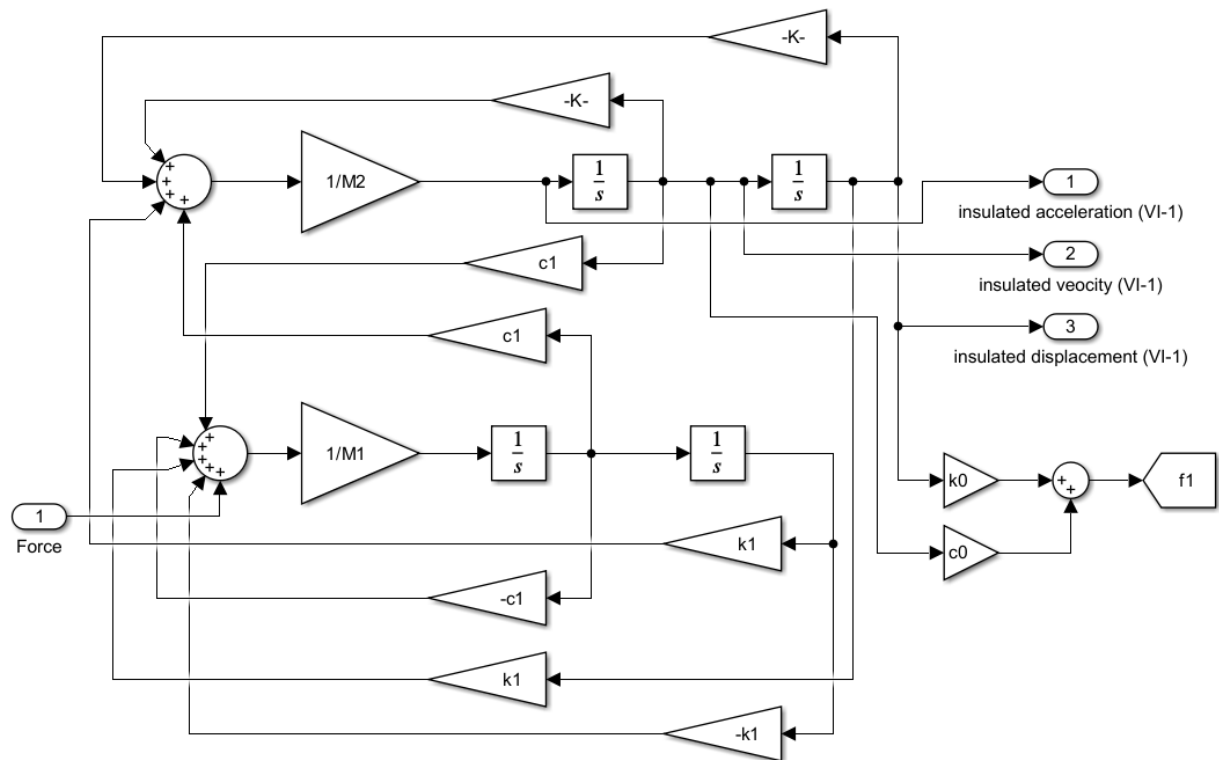
Figure 8. Simulink simulation model with isolation

The parameters used in the simulation model were determined based on the characteristic properties of the type C eccentric press and the actual foundation system. Based on the preliminary design results for stability and settlement, the foundation dimensions were determined to be 4m x 4m x 2m. The masses of the press and foundation block are presented in Table 1, while the stiffness and damping values of the soil and vibration isolators are given in Table 2. The stiffness ratio, defined as the ratio of the isolator stiffness to the soil stiffness, was selected as 0.01.

Table 1. Mass parameters of the press and foundation system

Parameters	Unit	Symbol	Value
Press	kg	m_1	6 000
Foundation	kg	m_2	40 000
Total mass	kg	m_t	46 000

Tablo 2. Stiffness and damping values

	Parameters	Unit	Symbol	Value
Soil	Stiffness	(N/m)	k_0	8.11×10^8
	Damping	(N.s/m)	c_0	1.13×10^7
Vibration Isolator 1 (VI-1)	Stiffness	(N/m)	k_1	8.11×10^6
	Damping	(N.s/m)	c_1	5.65×10^5
Vibration Isolator 1 (VI-2)	Stiffness	(N/m)	k_1	8.11×10^6
	Damping	(N.s/m)	c_1	3.36×10^5
Vibration Isolator 1 (VI-3)	Stiffness	(N/m)	k_1	8.11×10^6
	Damping	(N.s/m)	c_1	1.12×10^5

2.5. Experimental Study

An experimental study was undertaken to analyze the dynamic response of the system, a press machine, vibration isolator, and vibration test rig. In this study, the Solid 3D view (Figure 9) illustrating the details of the Type C eccentric press machine subjected to vibration isolation, along with its technical specifications (Table 3), are presented below. Vibration isolators with optimized stiffness and damping characteristics were chosen to mitigate vibration transmission.
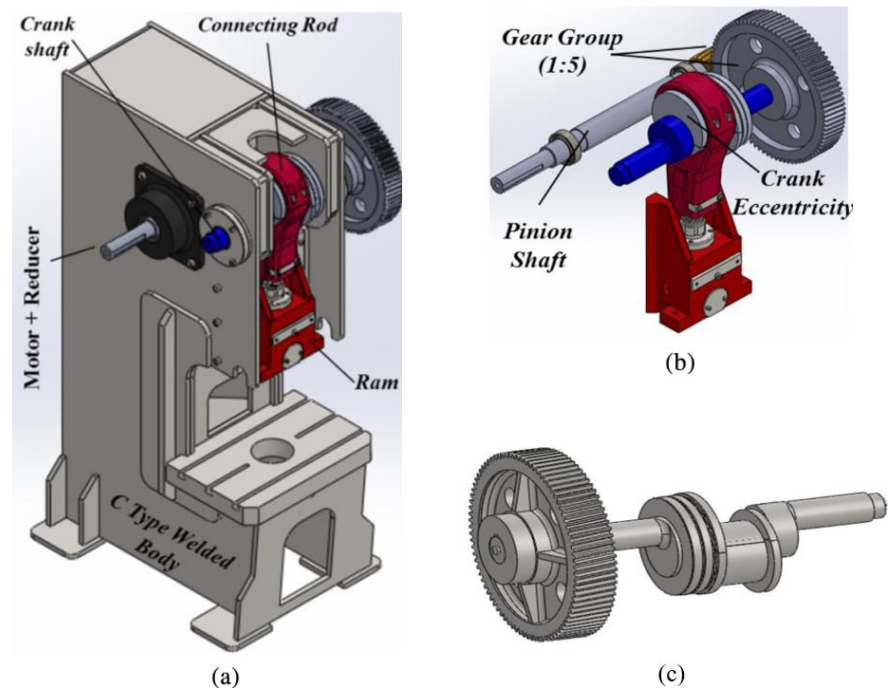
Figure 9. Solid model of the press: (a) complete assembly, (b) transmission mechanism, (c) solid CAD model of the crank assembly [34].

Tablo 3. Technical specifications of a press machine

Parameters	Unit	Value
Pressure	ton	100
Transfer	rpm	55
Stroke adjustment	mm	10-130
Connected max. mold height	mm	320
Table-ram distance	mm	450
Regulation setting	mm	80
Table size	mm	900x650
Engine power	kW	7,5
Engine speed	rpm	1450

2.5.1 Experimental setup and vibration analysis

To evaluate the performance of vibration isolators on a C-type eccentric press machine, an experimental setup, as shown in Figure 10, was established. Initially, the press was operated without isolators (Figure 10(a)) to measure baseline vibration values. Subsequently, vibration isolators were installed under the machine feet (Figure 10(b)), and the measurements were repeated. The vibrations generated during the cutting process of a 2 mm thick St 37 black sheet metal material in a cutting-bending compound die, as shown in Figure 10(c), were analyzed. Vibration measurements were

conducted using the EXTECH VB500 – a four-channel vibration measurement and recording device, the technical specifications of which are provided in Table 4. In order to determine the effects of vibrations generated during the operation of the press machine on the operator and the surrounding environment, vibration data were measured from a reference point located 30 cm away from the press machine on the ground, representing the vibration level to which the operator is exposed. Throughout the experiments, care was taken to maintain a constant force on the machine. The experimental data were compared with the results of the theoretical model to gain a deeper understanding of the vibrations occurring during the cutting process.
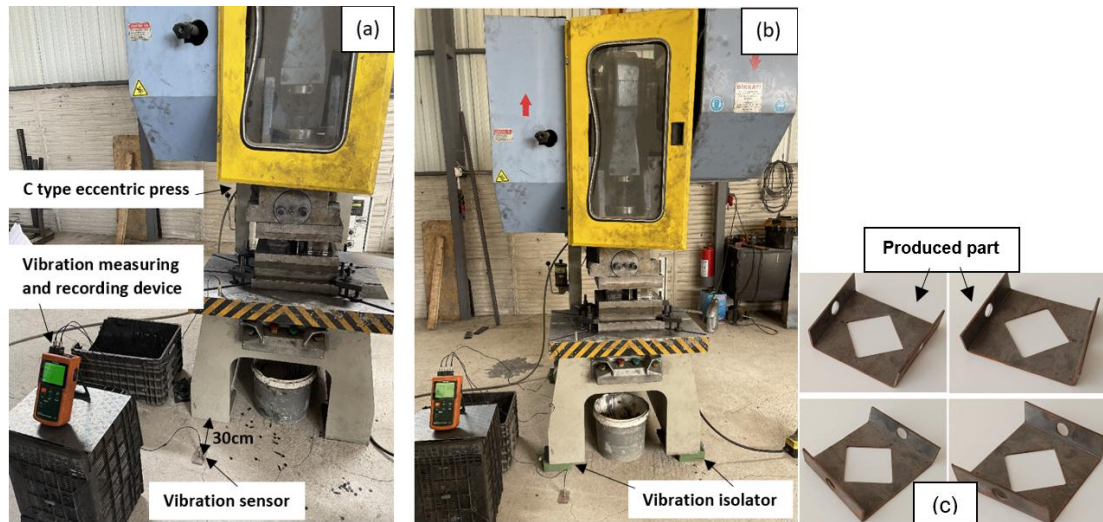
Figure 10. Vibration isolation of a type C eccentric press; (a) non-isolated, (b) isolated, (c) produced part

Table 4. Technical specifications of EXTECH VB500

Specifications	
Acceleration	656ft/s², 200m/s², 20.39g (peak)
Velocity	7.87in/s, 200mm/s, 19.99cm/s (peak)
Displacement	0.078in, 2mm (peak-to-peak)
Resolution	1ft/s2, 0.1m/s², 0.01g; 0.01in/s, 0.1mm/s, 0.01cm/s; 0.001in, 0.001mm
Basic accuracy	± (5%+2 digits)
Memory	20M data records using 2G SD card
Dimensions	8 x 3 x 1.5" (203 x 76 x 38mm)
Weight	1.13lbs (515g)

3. RESULTS AND DISCUSSION

3.1. Simulation of press using MATLAB/Simulink

The dynamic response of a press to a single impact load was investigated parametrically by varying the type of vibration isolator. The soil properties were assumed to be linear and characterized by stiffness and damping coefficients of k_0 = 8.11 x 10⁸ N/m and c_0 = 1.13 x 10⁷ N.s/m, respectively [1]. The impact duration, coefficient of restitution, and maximum force were defined based on. The effectiveness of isolation systems in mitigating ground vibrations was assessed by evaluating the maximum displacement, velocity, acceleration and force of the system.

Figure 11 illustrates the ground motion displacement values. The average peak ground displacement (PGD) in the uninsulated condition was measured to be 5.075 x 10⁻² mm. When isolation was applied, the maximum PGD was reduced to 3.46 x 10⁻² mm using isolator VI-1, and further reduced to 2.7 x 10⁻² mm with isolator VI-3. The results indicate that VI-3 was most effective in mitigating ground

vibrations. The parametric study revealed that the dynamic response of the system is highly sensitive to variations in the mass, stiffness, and damping ratio of the vibration isolator. This implies that vibration isolators provide a means to tailor the system response by adjusting critical parameters such as stiffness and damping to achieve the desired level of vibration isolation. These findings emphasize the significance of damping in enhancing the performance of vibration isolation systems.
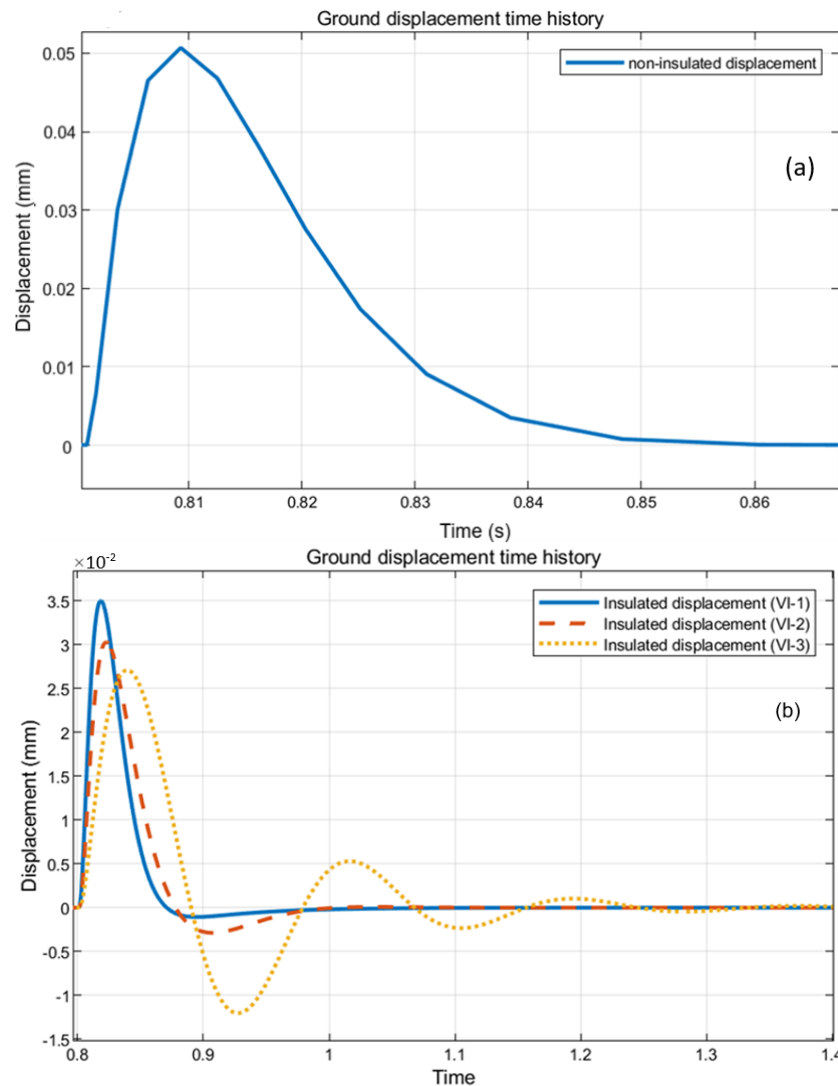
Figure 11. Time history of ground displacement: (a) without isolation, (b) with isolation

The velocity-time graph presented in Figure 12 demonstrates the effects of different vibration isolators (VI-1, VI-2, VI-3) on ground velocity variations. When the VI-1 vibration isolator was used, the maximum velocity was measured as 3.5×10^{-3} m/s. This indicates that the isolator reduces vibrations to a certain level but results in a higher velocity value compared to the other isolators. With the VI-2 vibration isolator, the maximum velocity was determined to be 2.45×10^{-3} m/s. This shows that it provides more effective vibration isolation than VI-1 and further reduces ground velocity. For the VI-3 vibration isolator, the maximum velocity was measured as 1.22×10^{-3} m/s. This demonstrates that it is the most effective among the three isolators, reducing ground velocity the most and controlling vibrations optimally. In conclusion, the graph reveals that the performance of vibration isolators varies depending on the type of isolator, with VI-3 being the most effective solution. This information can provide significant guidance in selecting the most suitable isolator for vibration control.
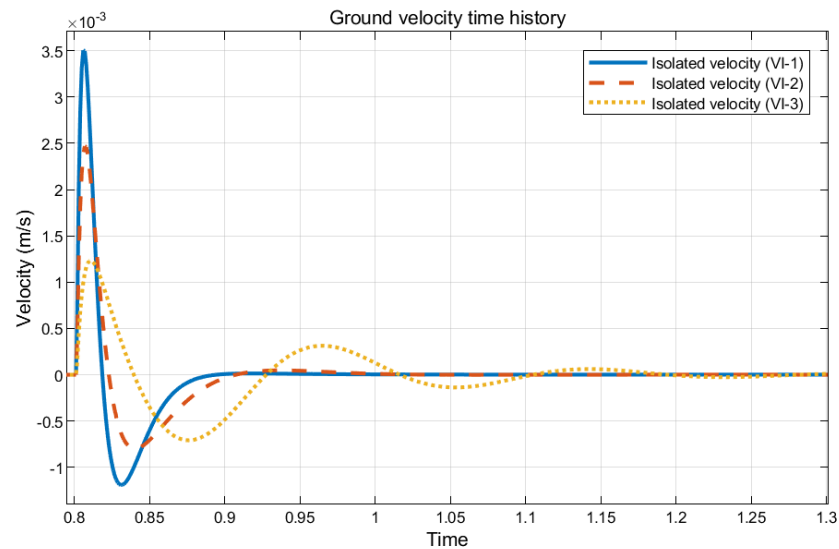
Figure 12. Time history of ground velocity

The graph presented in Figure 13 comparatively shows the ground vibration acceleration values of the press machine after the application of isolation. When examining the effects of isolation applications on vibration acceleration, the average peak value of ground vibration acceleration was measured as 1.62 m/s² when VI-1 was used. Although this value represents a significant improvement compared to the pre-isolation condition, even more effective results were achieved with VI-2 and VI-3. In the application using VI-2, the vibration acceleration decreased to 0.98 m/s², showing a noticeable reduction compared to VI-1. When VI-3 was used, the vibration acceleration was measured as 0.35 m/s², representing the lowest value among the vibration acceleration results. These results demonstrate that VI-3 is the most effective isolator for vibration control and can provide significant performance improvements in industrial applications. The trends in the graphs further support this improvement and highlight the success of isolation techniques in reducing vibration acceleration. Such isolators can both extend the lifespan of machinery and significantly reduce environmental vibration-related issues. In future studies, research on different operating conditions and isolator designs could be conducted to establish a broader database for vibration control. Such studies will contribute significantly to achieving more effective vibration control in industrial applications.
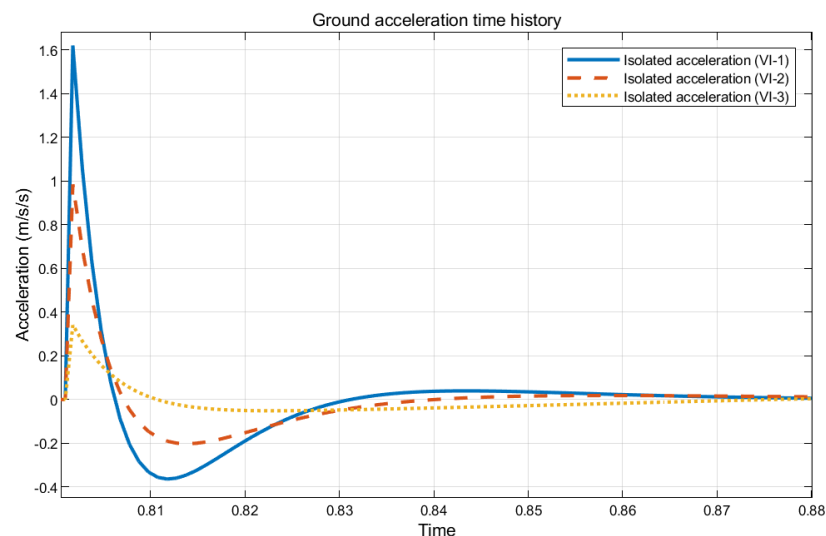
Figure 13. Time history of ground acceleration

Figure 14 illustrates the dynamic forces transmitted to the ground after the implementation of vibration isolation systems on a 100-ton press. The results indicate that the maximum average peak dynamic force transmitted to the ground was 5.14×10^4 N for VI-1, whereas the minimum was 2.57×10^4 N for VI-3. The lowest dynamic load on the ground was observed for the VI-3 type isolator. The parametric study demonstrated that selecting a stiffness ratio of 0.01 between the isolator and the soil can significantly reduce foundation vibrations. A decrease in the stiffness ratio results in a reduction in both the transmitted force and foundation response. However, this may lead to excessive vibration amplitudes of the press, compromising the performance. Conversely, an increase in the stiffness ratio will reduce the press vibration amplitude but may increase the foundation response and transmitted force.
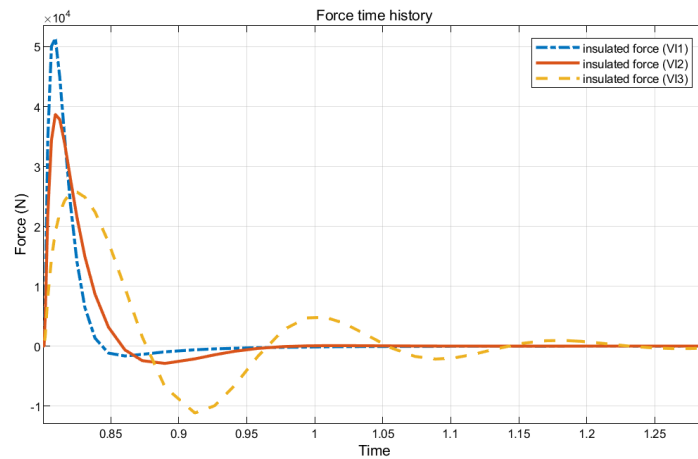
Figure 14. Time history of dynamic loads transmitted to the foundation

3.2. Comparison of simulation and experimental results

A comparative analysis of simulated and experimental dynamic responses of the press foundation is presented in Figure 15. For the isolated case with VI-3, the simulated average peak ground displacement was found to be 2.7×10^{-2} mm, which shows excellent agreement with the experimentally measured value of 2.5×10^{-2} mm. The high level of correlation between the numerical and experimental results provides strong evidence for the validity of the proposed dynamic model in capturing the actual behavior of the press under operating conditions. These findings emphasize the crucial role of dynamic modeling in the design and selection of appropriate vibration isolation systems.
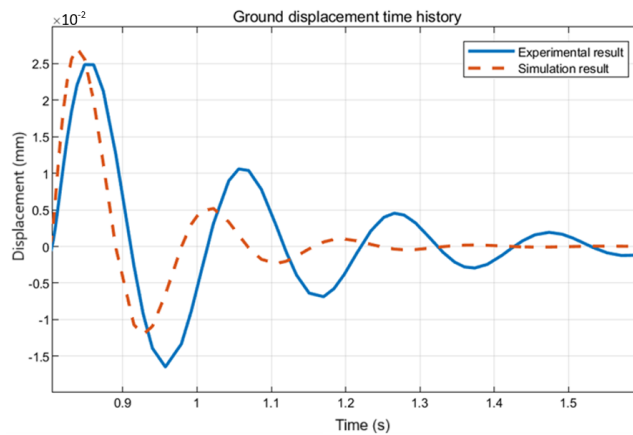
Figure 15. Comparison of simulated and experimental ground displacements

4. CONCLUSIONS

This study investigated the dynamic behavior of industrial C-type eccentric presses using MATLAB/Simulink modeling and simulation. The effectiveness of vibration isolators (VI-1, VI-2, VI-3) in reducing ground vibrations was evaluated under impact loading conditions. The results demonstrated that VI-3 was the most effective isolator, reducing peak ground displacement (PGD) from 5.075×10^{-2} mm (uninsulated) to 2.7×10^{-2} mm. Similarly, ground velocity and acceleration were minimized to 1.22×10^{-3} m/s and 0.35 m/s^2, respectively, using VI-3. The dynamic forces transmitted to the ground were also lowest with VI-3 (2.57×10^4 N), highlighting its superior performance.

A parametric study revealed that the system's dynamic response is highly sensitive to isolator stiffness and damping. A stiffness ratio of 0.01 between the isolator and soil reduced foundation vibrations by approximately 46.8%. However, optimizing this ratio is critical to balance press vibration amplitudes and foundation response.

The simulation results showed excellent agreement with experimental data, validating the proposed dynamic model. For VI-3, the simulated PGD (2.7×10^{-2} mm) closely matched the experimental value (2.5×10^{-2} mm), confirming the model's accuracy.

These findings underscore the importance of dynamic modeling in designing effective vibration isolation systems. VI-3 emerged as the optimal solution for minimizing vibrations and enhancing press performance. Future studies should explore additional isolator designs and operating conditions to further improve vibration control in industrial applications.

Declaration of Ethical Standards

The authors of this article declare that the materials and methods used in this study do not require ethical committee permission and/or legal-special permission.

Credit Authorship Contribution Statement

Ahmet KÖKEN: Researched and supplied experimental materials, conducted the experiments, drafted the article, and wrote and reviewed the manuscript.

Abdurrahman KARABULUT: Conducted the experiments, reviewed the manuscript.

Declaration of Competing Interest

Declaration of Competing Interest The authors declare that they have no known competing financial interests or personal relationships that could have appeared to influence the work reported in this paper.

Funding / Acknowledgements

Data Availability

Data will be made available on request.

REFERENCES

[1]   E. Zheng, X. Zhou, and S. Zhu, "Dynamic response analysis of block foundations with nonlinear dry friction mounting system to impact loads," *Journal of Mechanical Science and Technology*, vol. 28, no. 7, pp. 2535–2548, 2014, doi: 10.1007/s12206-014-0611-7.

[2]   Y. Kara and H. Akbulut, "Mechanical behavior of helical springs made of carbon nanotube additive epoxy composite reinforced with carbon fiber," *Journal of the Faculty of Engineering and Architecture of Gazi University*, vol. 32, no. 2, pp. 417–427, 2017, doi: 10.17341/gazimmfd.322166.

[3]   A. G. Chehab, M. Hesham, and E. Naggar, "Design of efficient base isolation for hammers and presses." *Soil Dynamics and Earthquake Engineering*, vol. 23, no. 2, pp. 127-141, 2003.

[4]   E. Zheng, F. Jia, Z. Zhang, and J. Shi, "Dynamic modelling and response analysis of closed high-speed press system," *Proceedings of the Institution of Mechanical Engineers, Part K: Journal of Multibody Dynamics*, vol. 226, no. 4, pp. 315–330, 2012, doi: 10.1177/1464419312445008.

[5]   M. Heidari and M. H. El Naggar, "Using reinforced soil systems in hammer foundations," *Proceedings of the Institution of Civil Engineers: Ground Improvement*, vol. 163, no. 2, pp. 121–132, 2010, doi: 10.1680/grim.2010.163.2.121.

[6]   F. Jia and F. Xu, "Dynamic analysis of closed high-speed precision press: Modeling, simulation and experiments," *Proc Inst Mech Eng C J Mech Eng Sci*, vol. 228, no. 13, pp. 2383–2401, 2014, doi: 10.1177/0954406213517093.

[7]   D. Jancarczyk, I. Wróbel, P. Danielczyk, and M. Sidzina, "Enhancing vibration analysis in hydraulic presses: A case study evaluation," *Applied Sciences (Switzerland)*, vol. 14, no. 7, 2024, doi: 10.3390/app14073097.

[8]   H. Dal and M. Baklacı, "Noise and vibration abatement study on a fabric polishing machine," *Gazi Journal of Engineering Sciences*, vol. 7, no. 2, pp. 121–133, 2021, doi: 10.30855/gmbd.2021.02.05.

[9]   F. Wang *et al.*, "Research and application of vibration isolation platform based on nonlinear vibration isolation system," *J Sens.*, vol. 2023, 2023, doi: 10.1155/2023/9967142.

[10]   S. Saberi, J. Fischer, M. Stockinger, R. Tikal, and R. Afsharnia, "Theoretical and experimental investigations of mechanical vibrations of hot hammer forging", *The International Journal of Advanced Manufacturing Technology*, vol. 114, pp. 3037-3045, 2021, doi: 10.1007/s00170-021-07061-y/Published.

[11]   B. Kekeç and D. Ghiloufi, "Propagation characteristics of surface and in-depth vibrations in sand grounds: a comparative analysis," *Konya Journal of Engineering Sciences*, vol. 10, no. 1, pp. 1–17, 2022, doi: 10.36306/konjes.884110.

[12]   A. G. Chehab and M. H. El Naggar, "Response of block foundations to impact loads," *J. Sound Vib.*, vol. 276, no. 1–2, pp. 293–310, 2004, doi: 10.1016/j.jsv.2003.07.028.

[13]   Y. Avcı and U. Yazgan, "Maximum inelastic displacement ratio for systems with soil-structure interaction," *Journal of the Faculty of Engineering and Architecture of Gazi University*, vol. 34, no. 3, pp. 1527–1537, 2019, doi: 10.17341/gazimmfd.460502.

[14]   U. Tekeci and B. Yıldırım, "Predicting fatigue life of a mount of a device with shock absorber," *Journal of Polytechnic*, vol. 27, no. 3, pp. 1005-1015, 2024, doi: 10.2339/politeknik.1210934.

[15]   A. Köken, "A research on reduction of vibrations at foundation of press workbench using vibration isolator," *PhD thesis, Afyon Kocatepe University, Institute of Science and Technology*, 2023.

[16]   G. Wang and Z. Dong, "Design optimization of low impact transmission foundation for forging hammers," *Engineering Computations (Swansea, Wales)*, vol. 23, no. 2, pp. 166–186, 2006, doi: 10.1108/02644400610644531.

[17]   B. Hızarcı and Z. Kıral, "Active vibration control of engineering structures using air jet pulses," *Konya Journal of Engineering Sciences*, vol. 7, pp. 933–947, 2019, doi: 10.36306/konjes.624373.

[18]   K. Alluhydan, A. T. El-Sayed, and F. T. El-Bahrawy, "The effect of proportional, proportional-integral, and proportional-integral-derivative controllers on improving the performance of torsional vibrations on a dynamical system," *Computation*, vol. 12, no. 8, 2024, doi: 10.3390/computation12080157.

[19]   S. J. Zhu, Y. F. Zheng, and Y. M. Fu, "Analysis of non-linear dynamics of a two-degree-of-freedom vibration system with non-linear damping and non-linear spring," *J. Sound Vib.*, vol. 271, no. 1–2, pp. 15–24, 2004, doi: 10.1016/S0022-460X (03)00249-9.

[20]   Z. Q. Lang, X. J. Jing, S. A. Billings, G. R. Tomlinson, and Z. K. Peng, "Theoretical study of the effects of nonlinear viscous damping on vibration isolation of sdof systems," *J. Sound Vib.*, vol. 323, no. 1–2, pp. 352–365, 2009, doi: 10.1016/j.jsv.2009.01.001.

[21]   Y. Ping, Y. Jianming, and D. Jianning, "Dynamic transmissibility of a complex nonlinear coupling isolator," *Tsinghua Science and Technology*, vol. 11, no. 5, pp. 538-542, 2006.

[22]   R. R. Kunadharaju and A. Borthakur, "Analysis and design of foundation systems to control the vibrations due to forging impact hammer," *Journal of Structural Engineering*, vol. 44, no. 5, pp. 404-413, 2017.

[23]   M. Guo, B. Li, J. Yang, W. Li, and S. Y. Liang, "Active piezoelectric vibration isolation system of machine tools," in *Proc. 2015 Int. Conf. Electrical, Electronics and Mechatronics*, Atlantis Press, 2015, pp. 169–172. doi: 10.2991/iceem-15.2015.42.

[24]   J. Kumar and V. Boora, "Dynamic response of a machine foundation in combination with spring mounting base and rubber pad," *Geotechnical and Geological Engineering*, vol. 27, no. 3, pp. 379–389, 2009, doi: 10.1007/s10706-008-9239-7.

[25]   A. Köken and A. Karabulut, "The effect of vibration isolator on the dynamic response of machine tools," *Pamukkale University Journal of Engineering Sciences*, vol. 29, no. 1, pp. 104–109, 2023, doi: 10.5505/pajes.2022.68327.

[26]   A. Köken and A. Karabulut, "Reducing the force transmitted to the ground by using vibration damper in machine tools", *Journal of Polytechnic*, vol. 25, no. 1, pp. 399-404, 2022. doi: 10.2339/politeknik.881839.

[27]   A. Karabulut and A. Köken, "Investigation of the effect of the vibration wedge on the vibration isolation of the guillotine shears machine," *Gazi Journal of Engineering Sciences*, vol. 6, no. 3, pp. 210–216, 2020, doi: 10.30855/gmbd.2020.03.04.

[28]   A. Abd-Elhamed, S. Alkhatib, and M. A. Dagher, "Closed-form solutions to investigate the nonlinear response of foundations supporting operating machines under blast loads," *Journal of Low Frequency Noise Vibration and Active Control*, vol. 42, no. 3, pp. 1162–1187, 2023, doi: 10.1177/14613484231174856.

[29]   M. Kam and H. Saruhan, "Vibration damping capacity of deep cryogenic treated AISI 4140 steel shaft supported by rolling element bearings," *Materials Testing*, vol. 63, no. 8, pp. 742–747, 2021, doi: 10.1515/mt-2020-0118.

[30]   M. Kam, H. Saruhan, U. Kabasakaloglu, and T. Guney, "Vibration damping capacity of a rotating shaft heat treated by various procedures," *Materials Testing*, vol. 63, no. 10, pp. 966–969, 2021, doi: 10.1515/mt-2021-0026.

[31]   A. Trabka, "Effect of pulse shape and duration on dynamic response of a forging system," *Acta Mechanica et Automatica*, vol. 13, no. 4, pp. 226–232, 2020, doi: 10.2478/ama-2019-0030.

[32]   S. S. Rao, *Mechanical Vibrations*, 5th ed., Prentice Hall, 2011.

[33]   E. Kılıç and B. Kuşcu, "Vehicle suspension control with magnetic force," *Journal of the Faculty of Engineering and Architecture of Gazi University*, vol. 39, no. 1, pp. 649–664, 2023, doi: 10.17341/gazimmfd.1173153.

[34]   R. Halicioglu, L. C. Dulger, A. T. Bozdana, "Structural design and analysis of a servo crank press," *Engineering Science and Technology, an International Journal* vol. 19, no. 4, pp. 2060–2072, 2016, http://dx.doi.org/10.1016/j.jestch.2016.08.008.

EFFECT OF NANOPARTICLE DOPE ON ELECTRICAL AND THERMAL CONDUCTIVITY OF PVA NANOFIBERS

[1] Fevzi KURUL [ID], **[2] *İbrahim ÜLKE** [ID]

[1] *Kırıkkale University, Kırıkkale Vocational School, Kırıkkale, TÜRKİYE*
[2] *Gazi University, Engineering Faculty, Mechanical Engineering Department, Ankara, TÜRKİYE*
[1]fevzikurul@kku.edu.tr, [2]ibrahimulke@gazi.edu.tr

Highlights

- Ag and Pt doping significantly increased PVA nanofiber electrical conductivity.

- Ag doping improved thermal conductivity by 28%, while Pt caused a 43% decrease.

- Ag-doped fibers showed superior power and current densities compared to pure PVA.

Graphical Abstract

PEM fuel cell performance of 5 wt% Ag nanoparticle doped PVA nanofiber
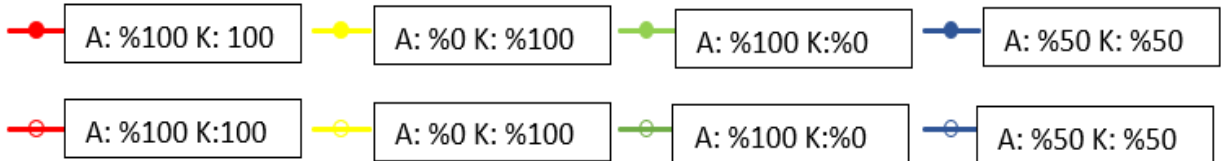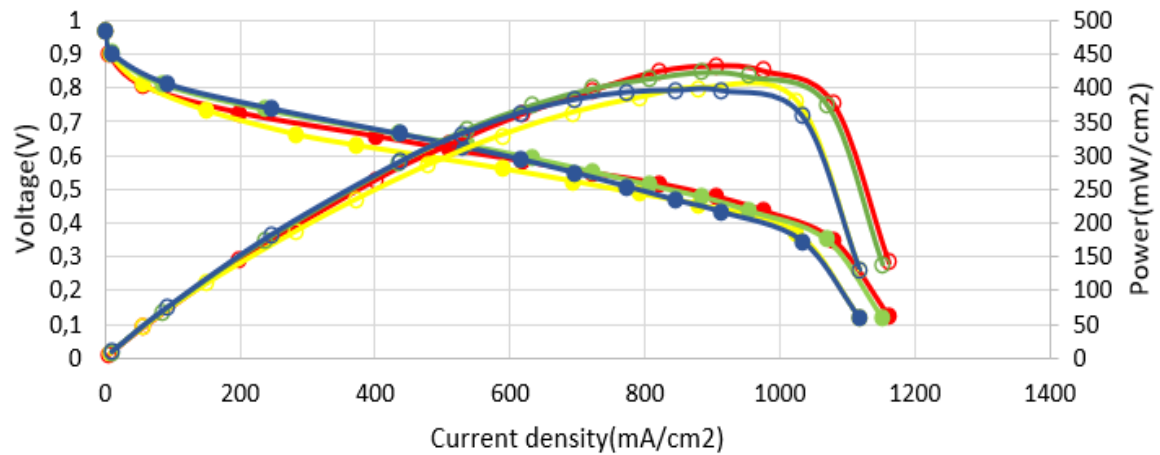
*Corresponding Author: İbrahim ÜLKE, ibrahimulke@gazi.edu.tr

EFFECT OF NANOPARTICLE DOPE ON ELECTRICAL AND THERMAL CONDUCTIVITY OF PVA NANOFIBERS

¹ Fevzi KURUL 🆔 **, ² *İbrahim ÜLKE** 🆔

¹ Kırıkkale University, Kırıkkale Vocational School, Kırıkkale, TÜRKİYE
² Gazi University, Engineering Faculty, Mechanical Engineering Department, Ankara, TÜRKİYE
¹fevzikurul@kku.edu.tr, ²ibrahimulke@gazi.edu.tr

ABSTRACT: PVA nanofiber materials are widely utilized in energy applications, particularly in PEM fuel cells. In this study, Ag- and Pt-doped PVA nanofibers were fabricated via the electrospinning method at different weight ratios and compared with pure PVA nanofibers. The thermal and electrical conductivities, PEM fuel cell performances, and morphological structures of the nanofibers were investigated. The results demonstrated that the highest electrical conductivity (16.80 S/cm) was achieved with the addition of 5% Ag nanoparticles, while Pt nanoparticle doping also improved electrical conductivity but to a lesser extent (14.90 S/cm). In terms of thermal conductivity, Ag nanoparticle doping increased the Thermal Conductivity Coefficient by approximately 28%, whereas Pt nanoparticle doping had the opposite effect, reducing it by 43%. Additionally, the hydrophilicity of the nanofibers increased with increasing nanoparticle content. The PEM fuel cell tests indicated that Ag-doped PVA nanofibers exhibited superior performance compared to pure PVA nanofibers, making them a promising material for energy applications.

Keywords: PEM Fuel Cell, PVA Nanofiber, Design of Experiment, Nanoparticle

1. INTRODUCTION

Materials have different properties at the nanometer size compared to their other states. When the particles are small enough and can be characterized as nanoparticles, their mechanical properties change accordingly. Nanoscale materials may have better strength and thermal or electrical properties than bulk materials. PVA nanofibers are solid fibers with nano diameters developed for particular purposes. PVA nanofibers are fibers with submicron diameters developed for specific purposes. Although there are many ways to produce nanofibers, the electrospinning method is considered a very effective and widely used technique [1]. In this technique, PVA nanofibers are produced by applying a strong electric field and converting the polymeric material solution into continuous nano-sized fibers [2]. Ultra-high draw rates caused by extensional flow enable the development of a continuous nanofiber. In this way, fibers can be easily collected into non-woven fabrics [3]. Although PVA nanofibers are widely used in their pure form, they are also used in special applications by adding various properties. Wali et al. studied the effect of silver addition to PVA nanofibers on antibacterial activity using bacteria [4]. In a similar study, silver nanoparticle-doped nanofibers were investigated, and their positive effects were determined in terms of developing antimicrobial wound dressings that can solve the difficulties associated with chronic wounds and provide infection control and wound healing support [5]. Khaleel et al. investigated the antimicrobial effect of ZnO nanoparticle-reinforced PVA nanomaterial [6]. In another study, PVA samples prepared using the electrospinning technique of silver nanoparticles were examined, and it was determined that silver nanoparticles increased thermal stability and electrical conductivity [7]. Besides medical fields, the energy sector is another area of usage for nanoparticle-doped PVA nanofibers.

PEM fuel cells are electrochemical systems that convert hydrogen into electrical energy, whereas other fuel cell types, such as DMFC and SOFC, can utilize alternative fuels like methanol, biogas, or coal. In the fuel cell, electric current is obtained by combining hydrogen with oxygen through electrochemical processes [8]. Since there is no combustion, no exhaust gas is formed. As a result, fuel cells are a clean

*Corresponding Author: İbrahim ÜLKE, ibrahimulke@gazi.edu.tr

and environmentally friendly energy production source that does not pollute the environment [9, 10]. Although the electrochemical reaction in PEM fuel cells does not involve moving parts, auxiliary components such as compressors, cooling systems, and fans can impact system efficiency and may require maintenance over time [11]. They can reach maximum efficiency at low power levels, and efficiency decreases linearly with increasing power [12]. After discovering high-performance polymers, PEM fuel cells were developed for application in space studies [13, 14] and unique military systems [15]. Compared to efficiency, PEM fuel cells operate more efficiently than thermal energy systems. In addition, unlike thermal systems, fuel cells are unaffected by the Carnot cycle criteria. [16]. PVA nanofibers are critical materials for PEM fuel cells. Adding various nano-sized additives to this critical material can improve its essential properties. Yanılmaz et al. examined the electrical properties of PVA-based B, N, and F-doped carbon nanofiber material and found that the cycle numbers of batteries from this material increased [17]. The amount of power obtained from PEM fuel cells varies depending on the number of cells and the limitations of the fuel cell model. Model constraints rely on the design of the parts that make up the PEM fuel cell, the material properties of these parts, and the fuel and oxidizer used.

Surface contact angle and hydrophilicity significantly influence the efficiency of Proton Exchange Membrane (PEM) fuel cells by affecting gas diffusion, water management, and proton conductivity. A lower contact angle corresponds to higher hydrophilicity, which enhances water management and improves proton conductivity, ultimately increasing fuel cell efficiency. Conversely, a higher contact angle indicates a more hydrophobic surface, which can lead to water accumulation or inadequate hydration, negatively impacting overall performance. Hydrophilic surfaces facilitate effective water removal from the electrode surface while promoting proton transport, thus optimizing cell performance. However, excessive hydrophilicity may result in excessive water retention, potentially obstructing gas diffusion. In contrast, hydrophobic surfaces prevent water accumulation but may reduce proton conductivity if insufficient water is retained within the membrane. Nanofibers are produced using Ag and Pt nanoparticles with various materials other than PVA. For example, Wanwong et al. developed a multifunctional air filter made of Ag-doped nanofiber material [18]. In their studies, Sakthivel et al. used Ni-Pt nanoparticles and carbon nanofibers as catalysts [19]. In another study, Electrospun Ag/TiO2 heterostructured nanofibers were produced for photoelectrochemical applications. Photoelectrochemical performances of the samples were investigated under full spectrum light illumination. Study results showed that Ag nanoparticles enhanced photocatalytic activity compared to pure nanofibers [20]. Similar to this study, there are many studies examining carbon-based nanofibers produced using titanium dioxide [21], nitrogen [22-25], or some other additive materials [26-28]. Few studies in literature examine Ag or Pt nanoparticle-doped PVA nanofiber materials. This study examined the electrical and thermal effects of Ag and Pt nanoparticle-doped PVA nanofibers produced by the electrospinning method. Experimental studies were conducted to produce homogeneous PVA nanofiber by considering the concentration ratio, voltage, feeding amount, and distance. SEM analyses of the produced nanofibers were performed, and parameter optimization was performed by considering the average nanofiber diameter. After finding the ideal parameters, nanofiber production was carried out using Ag and Pt nanoparticles in various ratios.

This study aims to investigate the impact of Ag and Pt nanoparticle doping on the electrical and thermal properties of PVA nanofibers produced via the electrospinning method. By optimizing doping ratios and production parameters, the research seeks to enhance the performance of these nanofibers, particularly for applications in PEM fuel cells. The findings are expected to contribute to the development of advanced energy materials with improved conductivity and tailored thermal properties, offering potential benefits in clean energy technologies.

2. MATERIAL AND METHODS

2.1. Solution Preparation

PVA, sodium dodecyl sulfate (SDS), Ag nanoparticle, Pt nanoparticle, Dimethyl Formamide (DMF), Acetone, and Chloroform were used to produce Ag or Pt-doped PVA nanofibers. 98-99% Hydrolyzed, high molecular weight (average 88,000-97,000 g/mol) PVA polymer was used in the study, and Sodium Dodecyl Sulfate ($C_{12}H_{25}NaO_4S$) was used to lower the surface tension of the solution. Ag (silver) nanoparticles (99.995%, 18 nm) and Pt (platinum) used in the study were used as additives to PVA nanofibers with the best structure. Dimethylformamide (DMF), Chloroform ($CHCl_3$), and Acetone (C_3H_6O) were used to determine the solvent of PVA in the experiments.

2.2. Electrospinning And Characterization Setup

In this study, for the production of Ag and Pt doped PVA nanofibers, an electrospinning device, SEM device, Thermal Conductivity measurement device, static surface contact, angle measurement device, transmission electron microscope (TEM), four-point electrical conductivity measurement device were used. The nanofibers' diameters were analyzed with a Zeiss Evo LS10 microscope (SEM). Crystal structure examinations and XRD analysis of the samples were performed using a D8 Advance brand diffractometer. To determine the thermal conductivity coefficients of PVA nanofibers doped with Ag or Pt a P.A. Hilton H-940 brand thermal conductivity measuring device was used.

Temperature values measured from 6 different points were recorded depending on the 6, 8, and 10-watt power values supplied to the system. The probes on the device are connected to TC1, TC2, TC3, TC7, TC8, TC9. While the Th value was found by interpolating from T1-T3 values, the Tc value was found from T7-T9 values. The nanofibers whose thermal conductivity coefficient was desired to be measured were cut to 25 mm in diameter and placed between the cold and hot ends. The resulting temperature values were made and recorded separately for each sample. The hydrophobic and hydrophilic properties of the produced fibers were determined using the Dataphysics instruments GmbH O.C.A. 15EC device. The mixtures with PVA, Ag nanoparticles, Pt nanoparticles, and SDS were mixed in an ultrasonic mixer until they became homogeneous. A four-point electrical conductivity measuring device made resistance measurements of thin materials.

2.3. PVA Nanofiber Production to Determine Optimum Parameters

At the beginning of the experimental studies, PVA + pure water solution was mixed in an ultrasonic mixer until a homogeneous mixture was obtained. After this, as the mixed solution heated up, it was allowed to cool to room temperature. SDS solution with a concentration of 1% by weight was added to each gram of solution by syringe, and the solution was mixed in the magnetic stirrer for another 20 minutes. The solution was then cooled at low speed to room temperature. 2 mL of the solution was drawn into a syringe and placed in the teflon apparatus of the electrospin device. After the solution drawn into the syringe was connected to the device, the positive and negative polarization tips were attached to the needle at the end of the syringe and the collector. The distance between the syringe needle and the collector was adjusted according to the distance value determined in Table 1, and the needle tip was aligned in the middle of the collector.

In Proton Exchange Membrane (PEM) fuel cells, system efficiency is influenced by several factors, including electrical connections and conductivity, electrode and catalyst efficiency, hydrogen supply and purity, as well as auxiliary components such as compressors and cooling systems. In this study, the PEM fuel cell performance of the nanofiber with the highest electrical conductivity among the produced Ag- or Pt-doped PVA nanofibers was investigated. The performance measurements were conducted at the Fuel Cell Technologies Laboratory of TÜBİTAK Marmara Research Center (MAM) Energy Institute. For these experiments, Toray 120 was used as the gas diffusion layer (GDL), a widely utilized

component in PEM fuel cells. The primary role of the GDL is to ensure uniform gas distribution to the electrode surface while simultaneously contributing to electrical conductivity and water management. Toray 120's effectiveness in gas distribution, electrical conductivity, and water regulation significantly impacts overall fuel cell efficiency. By optimizing gas flow and water control, high-quality GDLs such as Toray 120 enhance PEM fuel cell performance.

SEM analysis confirmed the production of homogeneous PVA nanofibers, and optimized electrospinning parameters were determined accordingly. Using these parameters, Ag and Pt nanoparticle-doped PVA nanofibers were synthesized with weight ratios of 1%, 3%, and 5%. Initially, PVA nanofibers were prepared, and the solution was allowed to cool to room temperature. Then, Ag and Pt nanoparticles were added at the specified weight ratios and stirred magnetically for an extended period to ensure homogeneity. After cooling to room temperature, the mixture was processed. Although no additional analysis such as Dynamic Light Scattering (DLS) was conducted to verify aggregation, the extended stirring process aimed to promote uniform nanoparticle dispersion.

Table 1. Production parameters and average diameters of PVA nanofibers.

Number	Coding	Concentration Rate (%Weight)	Voltage (kV)	Feed Quantity (mL/h)	Distance (cm)	Average Nanofiber Diameter (nm)
1	FİBER-1	8	15	1	11	516.14 ± 35.4
2	FİBER-2	8	20	1.5	13	442.36 ± 41.6
3	FİBER-3	8	25	2	15	331.82 ± 35.7
4	FİBER-4	10	15	1.5	15	320.66 ± 55.3
5	FİBER-5	10	20	2	11	325.36 ± 42.4
6	FİBER-6	10	25	1	13	633.38 ± 53.6
7	FİBER-7	12	15	2	13	315.88 ± 41.1
8	FİBER-8	12	20	1	15	534.12 ± 52.5
9	FİBER-9	12	25	1.5	11	667.55 ± 51.7

3. RESULTS AND DISCUSSION

Figure 1 presents SEM images of the produced PVA nanofibers, highlighting the influence of process parameters on fiber formation, morphology, and diameter distribution. The nanofiber structure is significantly affected by key electrospinning parameters, including concentration ratio, applied voltage, feed rate, and the distance between the needle tip and the collector. As seen in Figure 1, increasing the polymer concentration results in thicker nanofibers with more uniform structures. At lower concentrations, the nanofibers exhibit a bead-like morphology due to insufficient polymer chain entanglement. As the concentration increases, the fibers become smoother and more continuous. Applied voltage plays a critical role in fiber formation. At lower voltages (e.g., 15 kV), the nanofibers tend to have larger diameters and irregular structures due to weaker electrostatic forces. When the voltage is increased to 25 kV, the nanofibers exhibit finer diameters and more uniform structures, as the higher electric field strength promotes better stretching of the polymer jet.

The feed rate directly influences fiber diameter and uniformity. A lower feed rate (e.g., 1 mL/h) leads to thinner fibers, while a higher feed rate (e.g., 2 mL/h) results in thicker fibers with a more irregular distribution. At excessively high feed rates, the solution does not have enough time to evaporate completely, leading to defects such as beading and fiber fusion.
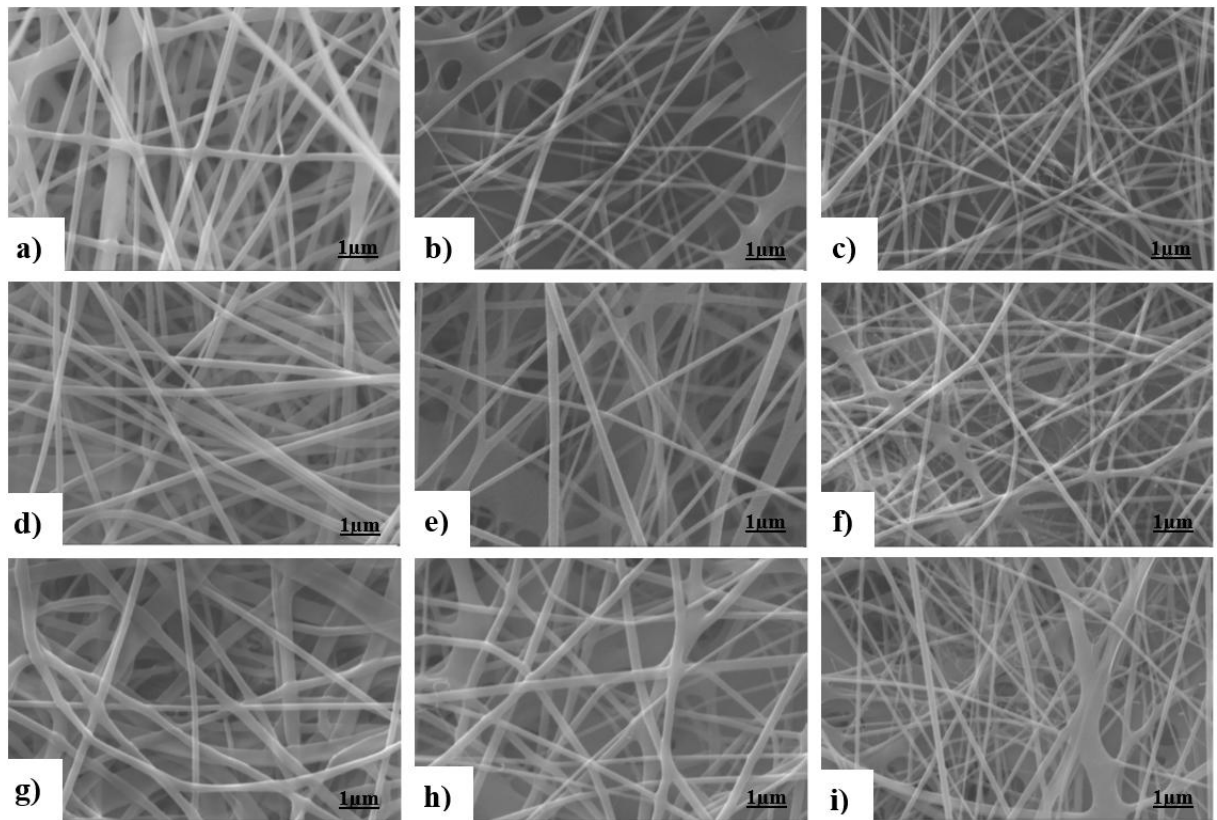
Figure 1. Produced PVA nanofibers (a) Fiber-1 b) Fiber-2 (c) Fiber-3 (d) Fiber-4 (e) Fiber-5 (f) Fiber-6 (g) Fiber-7 (h) Fiber-8 (i) Fiber-9
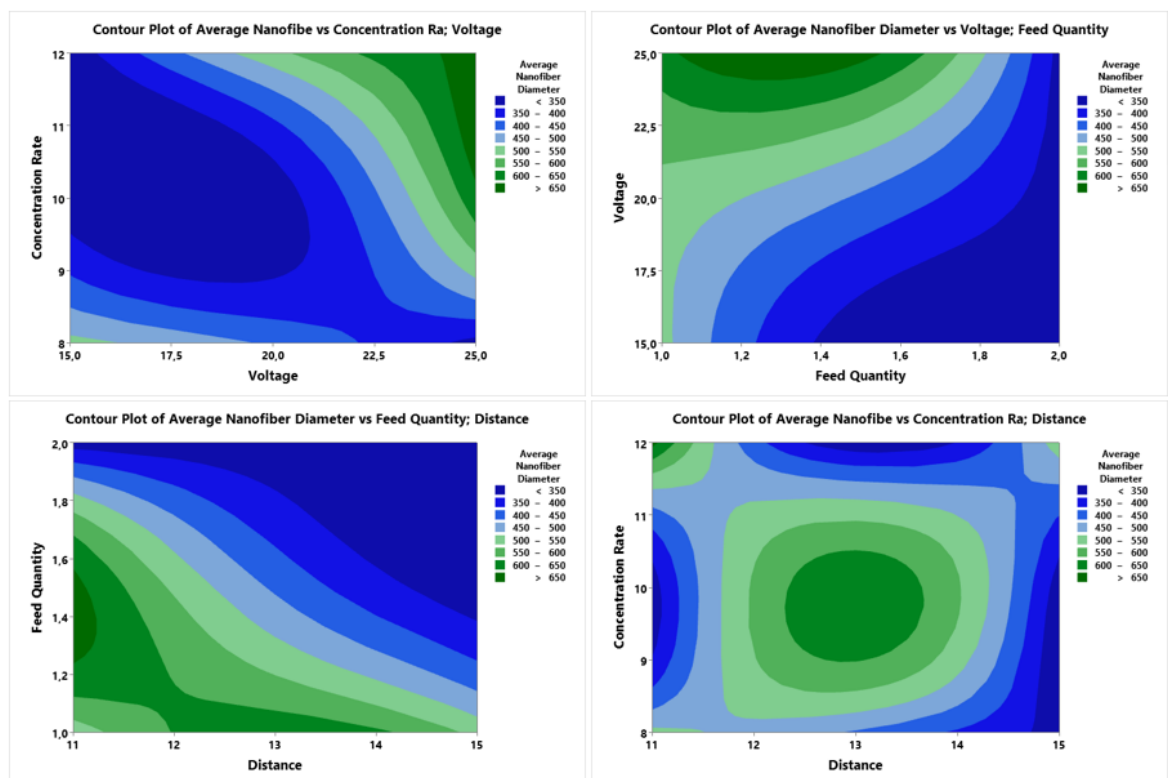
Figure 2. Relationship between variables and nanofiber diameter

According to Figure 2, the relationship between concentration ratio, voltage, and nanofiber diameter is nonlinear. While an increase in concentration generally led to larger nanofiber diameters, other parameters such as voltage and feed rate also influenced the final morphology. The lowest average nanofiber diameter was measured as 315.88±41 nm, whereas the highest reached 667.55±51.7 nm (Table 1). The results indicate that optimizing the processing parameters is crucial to controlling nanofiber dimensions effectively. The distance between the needle tip and the collector affects solvent evaporation and fiber solidification. When the distance is too short (e.g., 11 cm), fibers tend to be thicker and may exhibit incomplete solvent evaporation. In contrast, increasing the distance (e.g., 15 cm) allows for better stretching and thinner fibers but can also lead to fiber breakage if the distance is too large. Overall, Figure 1 illustrates that optimizing electrospinning parameters is crucial for achieving smooth, defect-free nanofibers with controlled diameters. The fiber diameter distribution observed in Table 1 confirms that these parameters must be carefully balanced to obtain uniform nanofibers with desirable properties.

3.2. Production and SEM Analysis of Ag and Pt Nanoparticle-Doped PVA Nanofibers

Optimization was made by considering the average nanofiber diameters obtained from SEM results, and ideal production parameters were determined. Accordingly, the production parameters of Ag and Pt nanoparticle-doped PVA nanofibers were determined as voltage 18 kV, feeding amount 1.8 mL/hour, and distance between the needle tip and collector 14 cm. Considering these parameters, 1, 3, and 5% nanoparticles by weight were added to PVA manufactured in homogeneous structures, and PVA nanofibers with Ag and Pt nanoparticles were produced.

The PEM membranes were fabricated using both pure PVA and Ag-Pt doped PVA nanofibers. The production process involved electrospinning the nanofiber mats followed by a crosslinking and stabilization step to enhance membrane durability and performance. The impregnation method used was solution casting and thermal annealing, ensuring the homogeneous distribution of Ag and Pt nanoparticles within the PVA matrix. During the process, PVA solutions containing Ag and Pt nanoparticles were electrospun onto a collector to form a uniform fibrous membrane. Subsequently, the membranes were subjected to chemical crosslinking with glutaraldehyde vapor to improve mechanical stability and water resistance. After crosslinking, the membranes were thermally annealed at controlled temperatures to optimize their structural properties and enhance ionic conductivity. The final membranes were tested for their proton conductivity and mechanical integrity before integration into PEM fuel cells.

According to the SEM analysis results in Figure 3, pure PVA nanofiber's average diameter was 271.47±16.3 nm. When 1% Ag nanoparticle by weight was added to the PVA solution, the average nanofiber diameter was 280.75±25.1 nm; when 3% Ag nanoparticle was added, it was 292.40±12.9 nm; and when 5% Ag nanoparticle was added, the average diameter is 297.62±23.8 nm and also increased when the amount of Ag nanoparticles increased. The average diameter of the nanofiber obtained by adding 1% Pt was found to be 220.10±13.9 nm. It was determined that the average diameter of the nanofiber produced by adding 3% Pt nanoparticles was 196.24±23.1 nm, and it was 5% Pt nanoparticles was 144.30±10.9 nm. As a result, it was determined that nanofiber diameters decreased as the amount of Pt nanoparticles increased.
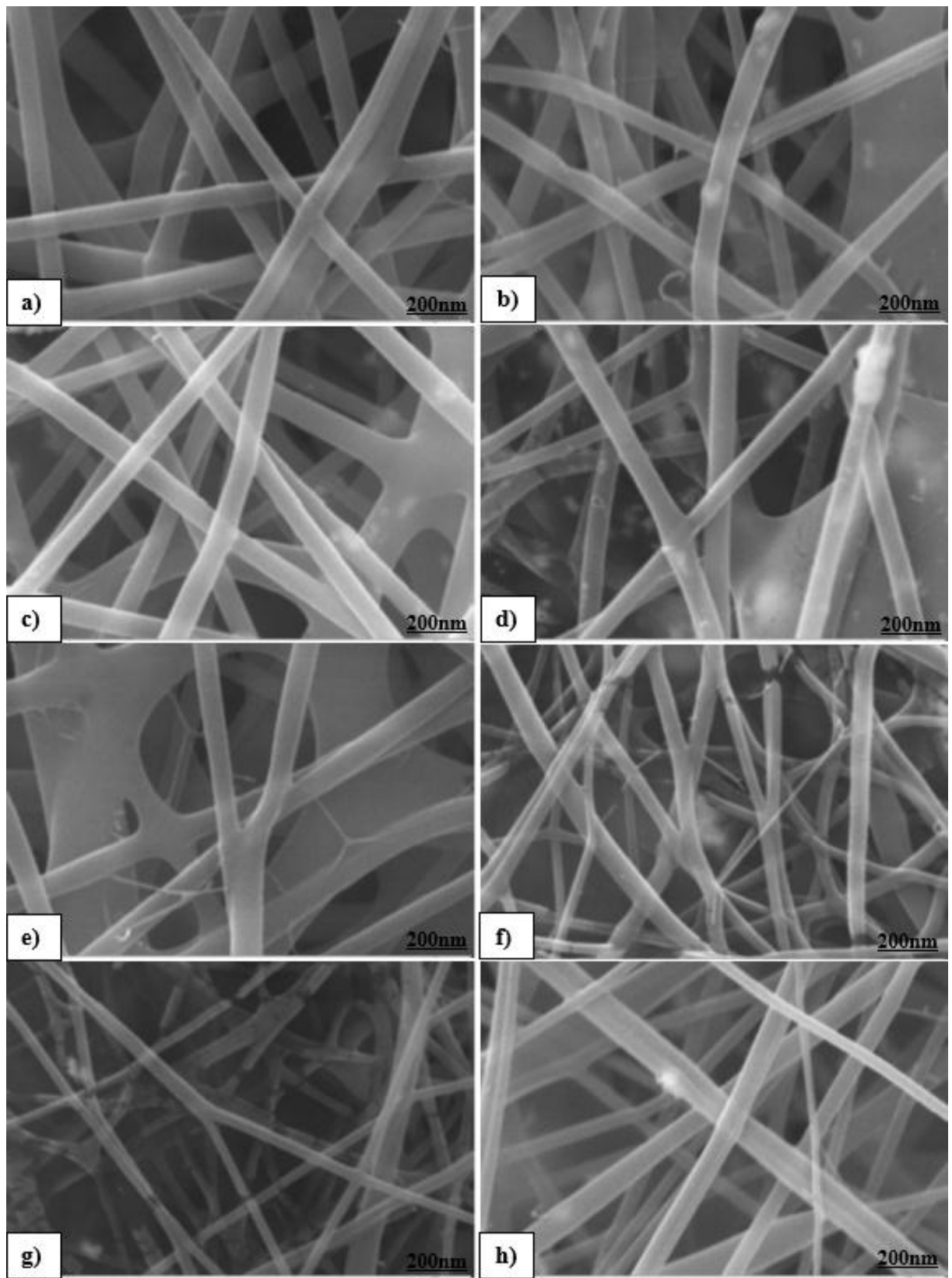
Figure 3. SEM images of pure and doped nanofibers (a) Pure PVA nanofibers for Ag nanoparticle doping (b) 1% Ag-Doped (c) 3% Ag-doped (d) 5% Ag-doped (e) Pure PVA nanofibers for Pt nanoparticle doping (f) 1% Pt doped (g) 3% Pt doped (h) 5% Pt doped

3.3. Physical Characteristics of Ag/Pt Nanoparticle Doped PVA Nanofibers

The highest conductivity values in PVA nanofibers doped with Ag nanoparticles and Pt nanoparticles were determined with a 5% Ag/Pt contribution by weight. These are, respectively, the electrical conductivity of Ag nanoparticle-doped PVA nanofiber is 16.80 S/cm and Pt nanoparticle-doped PVA nanofiber is 14.90 S/cm. In this study, the highest Electrical Conductivity is 16.80 S/cm. This value belongs to PVA nanofiber with Ag nanoparticle doping of 5% by weight. Therefore, the Gas Diffusion Layer prepared for the PEM fuel cell performance test was prepared based on 5% Ag-doped PVA nanofiber.

Table 2. Physical characteristics of Ag/Pt nanoparticle doped PVA nanofibers

Contribution Rate and Material	Average Nanofiber Diameter (nm)	Electrical Conductivity (S/cm)	Thermal Conductivity (W/mK)	Maximum Static Surface Contact Angle (°)
Pure nanofibers for Ag-doped	271.47±16.3	12.60	1.198	37.32
1% Ag	280.75±25.1	15.50	1.238	36.96
3% Ag	292.40±12.9	16.10	1.450	35.69
5% Ag	297.62±23.8	16.80	1.535	34.24
Pure nanofibers for Pt-doped	315.88±20.4	12.90	1.182	76.38
1% Pt	220.10±13.9	13.80	1.053	43.09
3% Pt	196.24±23.1	14.80	0.706	26.29
5% Pt	144.30±10.9	14.90	0.670	25.27

When evaluated regarding Thermal Conduction, it was determined that the Thermal Conductivity Coefficient decreased as the amount of Pt nanoparticles added by weight increased. If the Thermal Conductivity Coefficient of 5% Pt nanoparticle added PVA nanofiber is compared with the Thermal Conductivity Coefficient of pure PVA nanofiber, 5% Pt nanoparticle added PVA nanofiber reduced the Thermal Conductivity Coefficient of pure PVA nanofiber by 43.32%. Additionally, as seen in Table 2 and Figure 5, it was determined that as Ag/Pt nanoparticles were added to PVA, its Hydrophilicity Was Enhanced.

a) Pure PVA for Ag doped   b) 1% Ag doped   c) 3% Ag doped   d) 5% Ag doped

e) Pure PVA for Pt doped   f) 1% Pt doped   g) 3% Pt doped   h) 5% Pt doped
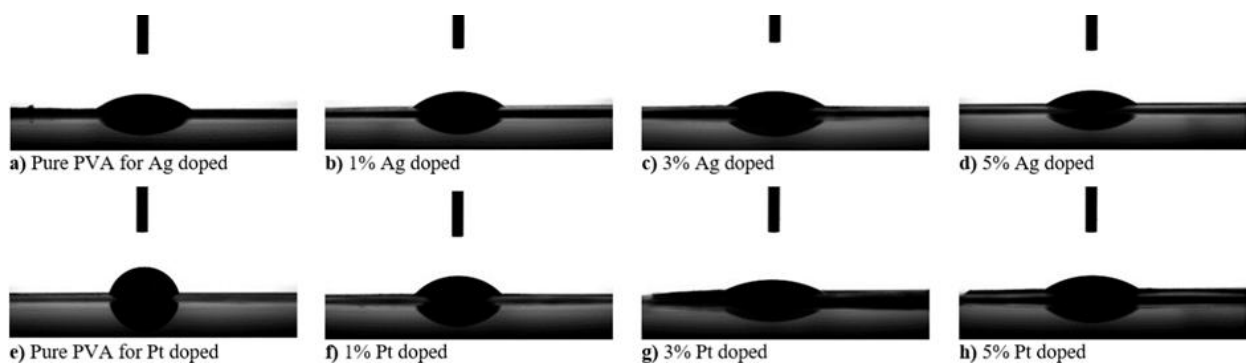
Figure 4. Static surface contact angles of pure, Ag/Pt-doped PVA drops

3.4. Pem Fuel Cell Performance of the 5% Ag-Doped Nanofiber

Pure PVA nanofiber (for Ag) without any additives and 5% Ag nanoparticle doped, which has the highest electrical conductivity (16.80 S/cm) among all the produced samples, PVA nanofiber is used on the anode side of the gas diffusion layer in the PEM fuel cell, with or without Ag additives. PEM fuel cell

performances of PVA nanofibers were examined. In these tests, a 0.6 mg/cm2 Pt-loaded electrode was used on the anode side of the fuel cell, while a 0.6 mg/cm2 Pt-loaded electrode was used on the cathode side. Toray 120 was chosen as the gas diffusion layer. In the experiments, hydrogen was given at 0.21 liters per minute and oxygen at 0.18 liters per minute.
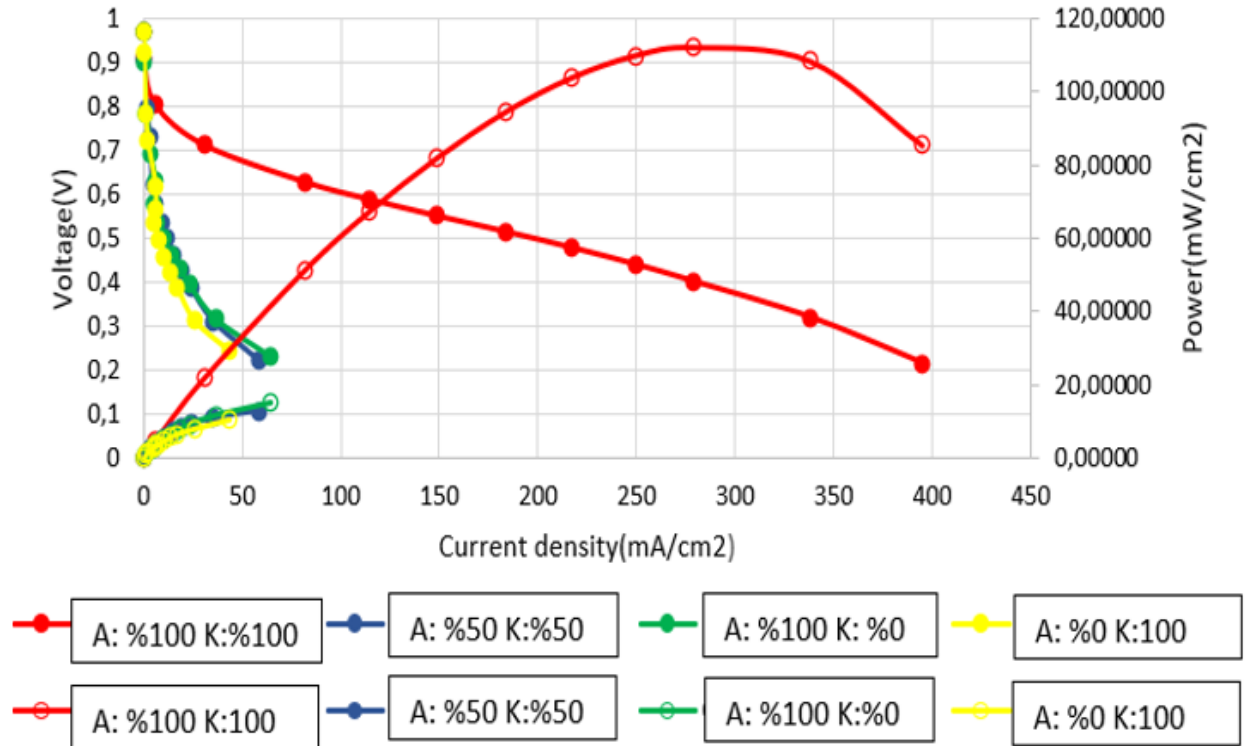
Figure 5. PEM fuel cell performance of pure PVA nanofiber (for Ag)
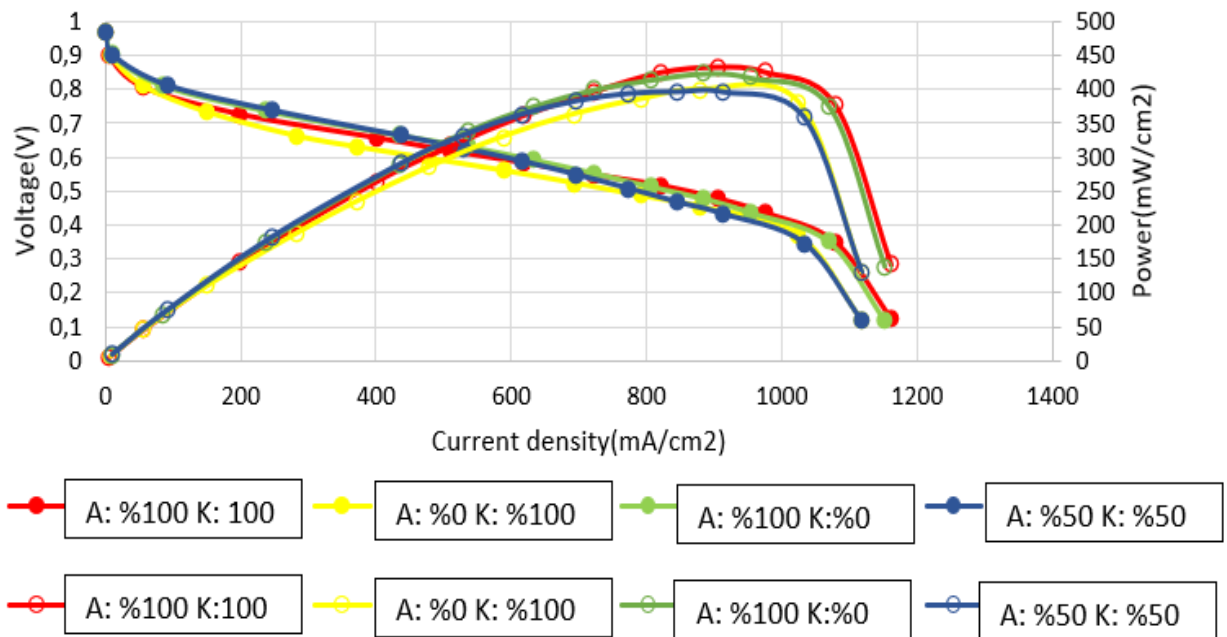
Figure 6. PEM fuel cell performance of 5 wt% Ag nanoparticle doped PVA nanofiber

The experiments were carried out at 60 °C temperature and with different humidity conditions (anode and cathode 100% humidity; anode and cathode 50% humidity; anode dry, cathode 100%

humidity; anode 100%, cathode dry), and the results of the experiments are shown in Figure 5 and Figure 6 presented. The highest power and current density values occurred in the tests at 60 °C and when the anode and cathode were 100% humid. As the amount of Ag nanoparticles in the structure increases, the power density of 5% Ag nanoparticle-doped PVA nanofiber rises according to the current density compared to pure PVA nanofiber. This is because Ag is a material with high electrical conductivity.

The increase in power density of the fuel cell cannot be solely attributed to the enhancement of electrical conductivity. Several other critical factors influence fuel cell performance, including operating pressure, membrane compression, water management, reactant gas flow rates, and temperature control. Operating pressure affects the reaction kinetics and gas diffusion within the cell, while membrane compression influences proton conductivity and mechanical stability. Proper compression ensures optimal contact between the membrane and electrodes, reducing interfacial resistance and improving overall efficiency. Additionally, effective water management is crucial to prevent membrane dehydration or excessive water accumulation, both of which can negatively impact power output. Therefore, while electrical conductivity plays a significant role, these additional parameters must be considered when evaluating fuel cell performance.

3.5. EDS and TEM Analysis of Pure and 5%Ag Nanoparticle Doped PVA Nanofibers

EDS and TEM analyses were conducted to thoroughly investigate the effects of Ag nanoparticle doping on the elemental composition and structural properties of PVA nanofibers. Figure 7 and Figure 8 illustrate the comparative analysis of pure PVA nanofibers and those doped with 5% Ag nanoparticles, which exhibited the highest electrical conductivity among all the tested samples. The results revealed that the addition of silver nanoparticles led to a noticeable reduction in the percentages of carbon and oxygen within the nanofibers. This reduction indicates a successful integration of Ag nanoparticles into the polymer matrix, which altered the chemical composition and contributed to the improved properties of the nanofibers. Furthermore, TEM analysis provided clear evidence of the effective interaction between Ag nanoparticles and the PVA structure.

Element	Weight [%]	Atom [%]
Carbon	43.32	50.34
Nitrogen	2.97	2.96
Oxygen	53.19	46.40
Sodium	0.34	0.21
Aluminium	0.02	0.01
Silicon	0.16	0.08
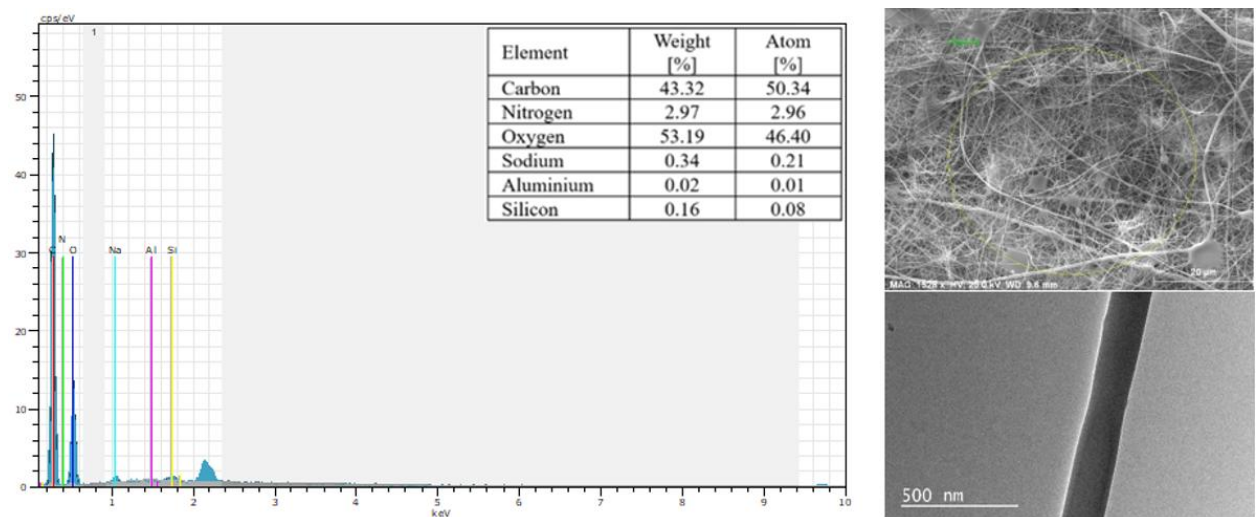
Figure 7. EDS and TEM analysis of pure PVA Nanofibers

Although platinum (Pt) is a metal with high intrinsic thermal conductivity, its addition to PVA nanofibers does not necessarily enhance thermal conductivity due to several factors. The dispersion of Pt nanoparticles within the polymer matrix plays a crucial role; if the nanoparticles are not homogeneously distributed or tend to agglomerate, phonon scattering increases, leading to higher interfacial thermal resistance and limiting heat transfer efficiency. Additionally, Pt nanoparticles can alter the molecular

interactions within the PVA matrix, disrupting phonon transport since heat conduction in polymer-based systems primarily occurs through phonon interactions rather than electron movement, as in bulk metals. Structural and morphological changes introduced by Pt, such as modifications in fiber compactness and potential void formation, can further reduce effective thermal conductivity. Furthermore, the presence of Pt nanoparticles may affect the viscosity and solidification behavior of the polymer solution, influencing fiber morphology and reducing thermal transport efficiency. As a result, while Pt is thermally conductive in bulk form, its nanoscale incorporation into PVA nanofibers can lead to increased phonon scattering, interfacial resistance, and structural alterations, ultimately decreasing effective thermal conductivity.
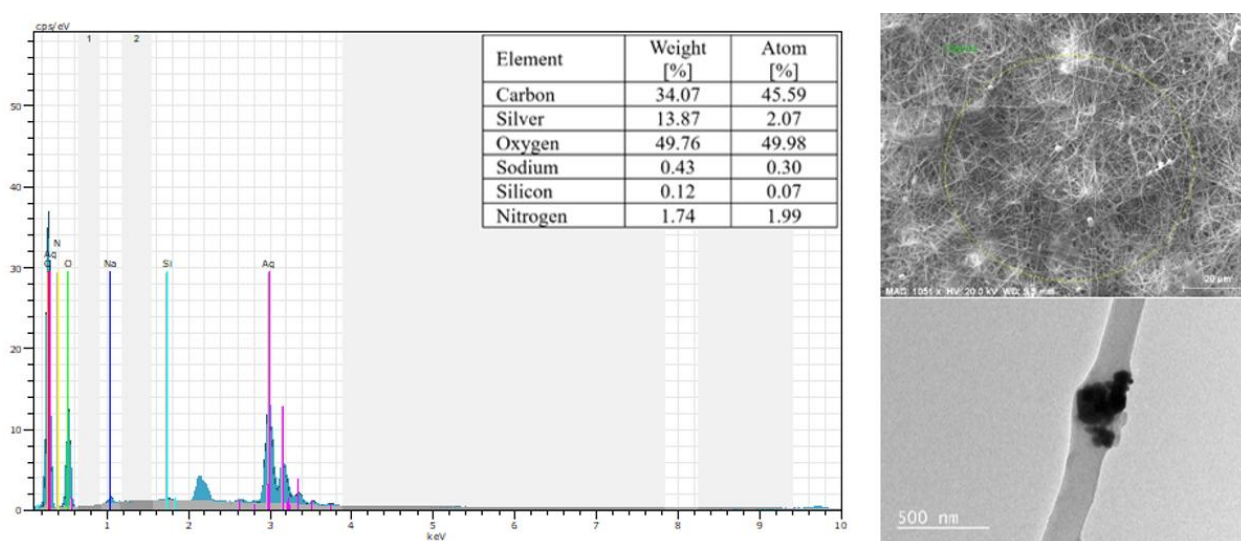
Figure 8. EDS and TEM analysis of 5%Ag-doped PVA Nanofibers

The uniformly distributed silver particles within the nanofibers played a significant role in enhancing their electrical properties. The increase in electrical conductivity was attributed to the high intrinsic conductivity of silver, which facilitated better charge transport within the nanofiber matrix. Similarly, the thermal conductivity of the nanofibers improved due to the efficient heat transfer facilitated by the Ag nanoparticles. These findings highlight the dual role of Ag doping in enhancing both electrical and thermal properties, making the nanofibers suitable for advanced applications, such as in PEM fuel cells and other energy systems. The results underscore the importance of nanoparticle distribution and interaction within the polymeric structure, as these factors directly influence the overall performance and potential applications of the material.

4. RESULTS AND DISCUSSION

This study focused on the effects of Ag and Pt nanoparticle doping on the thermal and electrical properties of PVA nanofibers produced using the electrospinning method. The experimental results revealed that doping PVA nanofibers with Ag nanoparticles significantly increased electrical conductivity, with the highest value achieved at a 5% doping ratio. Additionally, the thermal conductivity of Ag-doped nanofibers was enhanced, making them promising candidates for energy-related applications. In contrast, Pt nanoparticle doping improved electrical conductivity but caused a notable decrease in thermal conductivity. This indicates that the choice of nanoparticle plays a critical role in tailoring the properties of PVA nanofibers for specific applications.

The addition of Ag nanoparticles to the PVA solution can influence the solution viscosity. If Ag nanoparticles increase viscosity, the solution becomes less fluid, leading to the formation of thicker nanofibers during electrospinning. Generally, well-dispersed Ag nanoparticles contribute to higher viscosity, which affects fiber morphology by reducing jet stretching and resulting in larger fiber

diameters. In contrast, Pt nanoparticle addition appears to have the opposite effect, leading to a decrease in fiber diameter. One possible explanation is that Pt nanoparticles may influence the solidification dynamics of the PVA solution, promoting faster fiber formation. This accelerated solidification can restrict fiber elongation during electrospinning, resulting in thinner fibers.

Ag-doped nanofibers exhibited superior performance in PEM fuel cell tests, demonstrating higher power density and current density compared to pure PVA nanofibers. The improved electrical and thermal properties of Ag-doped fibers are attributed to the inherent high conductivity and optimal dispersion of Ag nanoparticles. SEM, EDS, and TEM analyses confirmed the structural and compositional changes induced by the nanoparticle doping, further validating the observed enhancements.

The study underscores the potential of nanoparticle-doped PVA nanofibers, particularly Ag-doped variants, in advancing PEM fuel cell technology and other energy-related applications. Future research aims to expand on these findings by optimizing production parameters, experimenting with additional nanoparticle types, and evaluating the long-term stability and scalability of these nanofibers. Moreover, testing on advanced computational and experimental setups may provide deeper insights into their behavior under varied operational conditions.

4. CONCLUSIONS

This study demonstrated the significant impact of Ag and Pt nanoparticle doping on the electrical and thermal properties of PVA nanofibers. Ag-doped nanofibers, especially at a 5% doping ratio, exhibited superior electrical conductivity and enhanced thermal performance, making them ideal candidates for energy-related applications such as PEM fuel cells. Conversely, Pt-doped nanofibers improved electrical conductivity but reduced thermal conductivity, highlighting the importance of nanoparticle selection based on specific application requirements. The results underline the potential of nanoparticle-doped PVA nanofibers in advancing clean energy technologies. Future work will focus on optimizing production parameters, exploring additional nanoparticle types, and assessing the long-term stability and scalability of these materials for broader industrial applications.

Declaration of Ethical Standards

The authors declare that they have no known competing financial interests or personal relationships that could have appeared to influence the work reported in this paper.

Credit Authorship Contribution Statement

Author 1: Conceptualization, Formal analysis, Investigation, Methodology, Resources, Software, Writing – original draft, Visualization **Author 2:** Methodology, Supervision, Validation, Writing – review & editing

Declaration of Competing Interest

The authors declare that they have no known competing financial interests or personal relationships that could have appeared to influence the work reported in this paper.

Funding / Acknowledgements

The authors declare that there is no financial support.

Data Availability

All data generated or analyzed during this study are included in this published article.

REFERENCES

[1]   Malara, A., "Environmental concerns on the use of the electrospinning technique for the production of polymeric micro/nanofibers", Scientific Reports, 14(1):8293, 2024.

[2]   Mowafi, S. and H. El-Sayed, "Production and utilization of keratin and sericin-based electrospun nanofibers: A comprehensive review", Journal of Natural Fibers, 20(1):2192544, 2023.

[3]   Habis, C., et al., "Specific role of Al in the synthesis of electrospun Al: ZnO nanofibers: Thermal and elemental analysis", Materials Today Communications, 38:108196, 2024.

[4]   Wali, A., et al., "Silver nanoparticles in electrospun ethyl hydroxy ethyl cellulose-PVA Nanofiber: Synthesis, characterization and wound dressing applications", Carbohydrate Polymer Technologies and Applications, 7:100477, 2024.

[5]   George, N., et al., "Incorporating silver nanoparticles into electrospun nanofibers of casein/polyvinyl alcohol to develop scaffolds for tissue engineering", International Journal of Biological Macromolecules, 131501, 2024.

[6]   Khaleel, M.R., F.S. Hashim, and A.H.O. Alkhayatt, "Preparation, characterization, and the antimicrobial activity of PVA-PVP/ZnO nanofiber films via indigenous electrospinning setup", Journal of Molecular Structure, 138325, 2024.

[7]   Krishna, K., et al., "Fabrication and conductivity study of silver nanoparticles loaded polyvinyl alcohol (PVA-AgNPs) nanofibers", Materials Today: Proceedings, 42:515-520, 2021.

[8]   Wang, Y., et al., "PEM Fuel cell and electrolysis cell technologies and hydrogen infrastructure development–a review", Energy & Environmental Science, 15(6):2288-2328, 2022.

[9]   Abdelkareem, M.A., et al., "Environmental aspects of fuel cells: A review", Science of The Total Environment, 752:141803, 2021.

[10]   Sharma, S., S. Agarwal, and A. Jain, "Significance of hydrogen as economic and environmentally friendly fuel", Energies, 14(21):7389, 2021.

[11]   Patil, V., et al., "Degradation mechanisms in PEM fuel cells: A brief review", Materials Today: Proceedings, 2023.

[12]   Karanfil, G., "Importance and applications of DOE/optimization methods in PEM fuel cells: A review", International Journal of Energy Research, 44(1):4-25, 2020.

[13]   Singh, R., A.S. Oberoi, and T. Singh, "Heat pipes for PEM fuel cell cooling: State of the art review", Materials Today: Proceedings, 2023.

[14]   Datta, A., "PEM Fuel Cell MODEL for conceptual design of hydrogen eVTOL aircraft", 2021.

[15]   Ormsby, S., "Modelling and design of PEM fuel cell electric military armoured vehicles using a new real-world operation profile model", 2021.

[16]   Athanasaki, G., A. Jayakumar, and A. Kannan, "Gas diffusion layers for PEM fuel cells: Materials, properties and manufacturing–A review", International Journal of Hydrogen Energy, 48(6):2294-2313, 2023.

[17]   Yanilmaz, M., et al., "Centrifugally spun PVA/PVP based B, N, F doped carbon nanofiber electrodes for sodium ion batteries", Polymers, 14(24):5541, 2022.

[18]   Yoon, H., et al., "Adaptive Epidermal Bioelectronics by Highly Breathable and Stretchable Metal Nanowire Bioelectrodes on Electrospun Nanofiber Membrane", Advanced Functional Materials, 2313504, 2024.

[19]   Sakthivel, P., et al., "Low content of Ni-Pt nanoparticles decorated carbon nanofibers as efficient electrocatalyst for hydrogen evolution reaction", Journal of Chemical Technology & Biotechnology, 2024.

[20]   Yu, H., M. Zhang, and T. Jin, "Electrospun Ag/TiO2 Heterostructured Nanofibers for Photoelectrochemical Applications", Russian Journal of Physical Chemistry A, 97(12):2786-2791, 2023.

[21]   Wang, C., et al., "Controllable growth of silver nanoparticles on titanium dioxide/nitrogen-doped carbon nanofiber/molybdenum disulfide: Toward enhanced photocatalytic-activating peroxymonosulfate performance and "memory catalysis"", Chemical Engineering Journal, 479:

147752, 2024.

[22]   Gao, M., et al., "Flexible nitrogen-doped carbon nanofiber-reinforced hierarchical hollow iron oxide nanorods as a binder-free electrode for efficient capacitive deionization", Desalination, 549:116360, 2023.

[23]   Sharma, G.K. and N.R. James, "Flexible N-doped carbon nanofiber-polydimethylsiloxane composite containing La0. 85Sr0. 15CoO3− δ nanoparticles for green EMI shielding", ACS Applied Nano Materials, 6(7):6024-6035, 2023.

[24]   Guan, J., et al., "Integrating RuCo alloy in N-doped carbon nanofiber for efficient hydrogen evolution in alkaline media", Journal of Alloys and Compounds, 942:168941, 2023.

[25]   Chen, F., et al., "Hierarchical N-doped carbon nanofiber-loaded NiCo alloy nanocrystals with enhanced methanol electrooxidation for alkaline direct methanol fuel cells", Journal of Colloid and Interface Science, 646:43-53, 2023.

[26]   Yang, T., et al., "Oxygen-doped carbon nanofiber nonwovens as an effective interlayer towards accelerating electrochemical kinetics for lithium-sulfur battery", Applied Surface Science, 611:155690, 2023.

[27]   Wang, F., et al., "Sulfur doped hollow carbon nanofiber anodes for fast-charging potassium-ion storage", Applied Surface Science, 614:156149, 2023.

[28]   Zhang, L., et al., "Rapid quantitative detection of luteolin using an electrochemical sensor based on electrospinning of carbon nanofibers doped with single-walled carbon nanoangles", Analytical Methods, 15(25):3073-3083, 2023.

A COMPARISON OF ACTUAL AND SIMULATED DATA TO DETERMINE THE EFFECT OF LOSS PARAMETERS ON THE PERFORMANCE OF BUILDING-INTEGRATED PHOTOVOLTAIC SYSTEMS

[1,] *Selçuk SAYIN [iD], [2] Fatma YETGİN [iD]

[1] *Konya Technical University, Architecture and Design Faculty, Department of Architecture, Konya, TÜRKİYE*
[2] *Yetgin Mimarlık, Dalyan Mah. Atatürk Cad. No:17/A-210, Beyşehir, Konya, TÜRKİYE*
[1]ssayin@ktun.edu.tr, [2] fatmaytg_94@hotmail.com

Highlights

- Photovoltaic system simulation with PVsyst 7.2.14

- Comparison of simulation and actual data of a building integrated photovoltaic system

- Determining the effect of loss parameters to system performance

Graphical Abstract
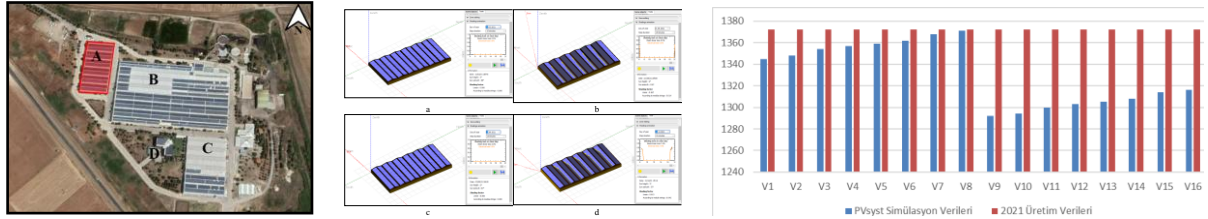
Figure Simulation and comparison phases

*Corresponding Author: Selçuk SAYIN, ssayin@ktun.edu.tr

A COMPARISON OF ACTUAL AND SIMULATED DATA TO DETERMINE THE EFFECT OF LOSS PARAMETERS ON THE PERFORMANCE OF BUILDING-INTEGRATED PHOTOVOLTAIC SYSTEMS

1, *Selçuk SAYIN [iD] **, 2 Fatma YETGİN** [iD]

1 *Konya Technical University, Architecture and Design Faculty, Department of Architecture, Konya, TÜRKİYE*
2 *Yetgin Mimarlık, Dalyan Mah. Atatürk Cad. No:17/A-210, Beyşehir, Konya, TÜRKİYE*
1ssayin@ktun.edu.tr, 2 fatmaytg_94@hotmail.com

ABSTRACT: The efficiency of photovoltaic systems is not very high, but the initial investment costs are high. Simulation programmes are used to determine the efficiency of the photovoltaic system to be installed and to calculate the energy production values. However, there are differences between the simulation data of the photovoltaic system and the actual production data. The aim of this study is to compare the actual production data and simulation data of a photovoltaic system in use. For this comparison, a factory building in Beyşehir, Konya, which has a photovoltaic system integrated on its roof, is analysed. PVsyst 7.2.14 tool was used for the simulation of the photovoltaic system. The simulation data obtained from the PVsyst tool of the photovoltaic system were compared with the actual production data of 2021. While the actual production data of the system in 2021 is 1372,2 Mwh, the production data obtained from the simulation is 1345,1 Mwh. In order to determine the reason for this difference, the effect of dusting loss, temperature loss, module mismatch loss and aging loss parameters on energy production was analysed through different variations.

Keywords: Solar Energy, Simulation, Building Integrated Photovoltaic Systems, Loss Parameters

1. INTRODUCTION

In the last 20 years, a return to renewable energy has started due to its favourable characteristics such as environmentally friendly, inexhaustible, abundant and widely available resource infrastructure. In addition to these, factors such as technological developments and favourable policies have also helped the rapid development of renewable energy [1]. In 2020, energy generation from photovoltaic systems, which accounted for 3.2% of global electricity generation, increased by 156 TWh compared to 2019 and reached 821 TWh. This corresponds to a growth of 23% [2].

Buildings have a big role in world total energy consumption. Looking at 2019 total energy consumption data by sectors, the building sectors, including residential, commercial and public buildings, is responsible for 29% of energy use in the world [3]. Buildings, which account for almost one-third of the world's energy consumption, are also major cause of carbon dioxide (CO_2) emissions. Looking at CO_2 emissions by sectors in 2019 in the world, the construction sector is responsible for 8%. In Turkey, this rate is 16% [4]. Energy efficient designs have emerged with the development of technologies that use energy consciously in buildings. Research has found that it is possible to reduce the energy consumption of a building by 30% to 50% by using existing technologies [5].

The effective use of solar energy in buildings is realised in the form of energy generation from photovoltaic panels mounted on the roof and facade of the building as a surface covering element, shading element or skylight [6]. Recently, attempts have been made to install photovoltaic systems on the roofs of office buildings, houses, institutions and industrial buildings to overcome the crisis arising from the increase in energy consumption. These attempts will not only solve the energy crisis but also reduce the harmful effects of greenhouse gas emissions from fossil fuels [7]. In recent years, the increase in grid-connected building integrated photovoltaic systems has also led to an increase in installed power

---

*Corresponding Author: Selçuk SAYIN, ssayin@ktun.edu.tr

photovoltaic systems. The term building integrated refers to photovoltaic systems mounted on the roof or facade of buildings. In order to get the highest level of energy production data, the installation area and the system must be utilized very well [8].

Photovoltaic systems have high initial investment costs and not very high efficiency. For this reason, various simulation tools are used to define the energy production potential and efficiency of the system before the photovoltaic systems are installed. Thus, a feasibility study is carried out before the photovoltaic system investment is made. However, there are differences between the actual energy production data of each system and simulation data. The aim of this study is to compare the simulation data and actual energy production data of a photovoltaic system integrated into the building and put into operation. There are many parameters that affect the efficiency of the photovoltaic system such as climate data, solar radiation, dusting, shading, cable losses, inverter losses, mismatch losses etc. The research question is: How do these parameters affect the efficiency of the building integrated photovoltaics? The problem of the study is to determine the effect of loss parameters on the performance of building integrated photovoltaic systems through the comparison of actual energy production data and simulation data. The study is limited to the effect of temperature loss, module mismatch loss, dusting and aging loss on system performance.

2. LITERATURE SURVEY

2.1. Photovoltaic System Losses

Performance ratio is a significant parameter which measures the photovoltaic system's efficiency. The performance ratio is the ratio of the energy produced in the photovoltaic system to the highest theoretically possible energy production and reveals the quality of the system. The lower the losses, the higher the performance ratio of the photovoltaic system. The performance ratio is independent of the orientation of the system and the instantaneous solar radiation [9, 10].

The performance of photovoltaic systems is affected by environmental factors related to local conditions such as temperature, dusting and snow. Factors such as shading, direct current (DC) and alternating current (AC) cable losses are related to system design. Incompatibilities between modules and inverter losses are related to the quality of the materials in the system [10]. There are many parameters such as losses of the photovoltaic system due to panel tilt angle, radiation losses in the modules, inverter losses, structural losses of photovoltaic components and losses due to the environment. The characteristic values of the system components, geographical location, surrounding structures and system failures affect the energy produced. The losses occurring in the photovoltaic system are mostly caused by shading and the least loss is caused by AC cable losses. The performance ratio, which reveals the quality of the system, is important in the evaluation of losses [9].

The angles at which the sun rays fall on the earth and the annual insolation values of the location of the building vary from region to region affect the energy to be obtained from the panel in the design of the building integrated photovoltaic system. The decrease in solar radiation intensity also decreases the panel power. [11]. Another factor affecting the efficiency of photovoltaic panels is shading. Factors such as buildings, tree branches, chimneys that cast shadows on the panel, reduce the efficiency of the system. For this reason, while designing the system, attention should be paid to the elements that create shadow on the panels [12]. In land or roof applied installations, the shadowing of the photovoltaic arrays on the trestles affects the efficiency. For this reason, attention should be paid to the distance to be left between the photovoltaic arrays. [13]. Another important parameter affecting the panel efficiency is temperature. The relationship between panel temperature and panel power is inversely proportional. This shows that the increase in temperature decreases the power of photovoltaic modules. The efficiency of the panels decreases by 1% for every 10°C temperature increase. Providing air flow on the back side of the panels minimises the heating of the photovoltaic modules [9, 14]. Cable losses are the losses occurring in the cables used for energy transmission in photovoltaic systems, also called ohmic losses. Cable losses are of great importance in roof integrated photovoltaic systems. In order to minimise the loss, the cable cross-

sections should be increased [15].

Yet another important losses in photovoltaic systems are mismatch losses. The difference in the energy produced by two or more arrays causes mismatch losses in the modules. This difference is caused by factors such as partial shading, dusting, different operating temperatures, different irradiance values or solar panel power tolerance. The severity of mismatch losses increases or decreases depending on the differences between the power tolerances of the modules connected in series in the array [10, 16]. Panel losses are the losses that occur in solar panels due to ageing and power tolerance. In photovoltaic systems, losses due to aging increase as the years of use of the panels increase. Solar panel manufacturers provide a 25-year performance power guarantee. In addition, since the use of panels with high power tolerance in photovoltaic systems will further increase the mismatch losses, solar panels with low power tolerance should be preferred [17]. Inverter losses occur during the conversion of DC to AC and as a result of not calculating the inverter power correctly. The maximum power that solar panels can produce and the inverter power should be selected to be equal or higher. The ratio of the rated module power to the rated AC output power of the inverter under standard test conditions (STC) affects the inverter efficiency. This may prevent the inverter from transferring all of the generated power to the grid. [10, 17]. Dusting and snowing losses are the losses caused by the contamination of the surfaces of photovoltaic modules, which reduces the amount of radiation reaching the modules. Industrial air pollution, road dust, meteorological dust transport, exhaust fumes, bird droppings are the factors that cause pollution. Dusting causes power loss in solar collectors. Losses due to dusting reach up to 15% in regions with low rainfall. If the angle of the panel with the horizontal is more than 15°, it is supposed that rain can clean the panel and the efficiency loss due to dusting is limited to 0,5%. If the panel angle is less than 15° and the region where the system is installed receives little rainfall, the efficiency loss rate exceeds these values. According to the researches, losses due to dusting rarely exceed 4%. In regions where snowfall is frequent, 2% snow loss can be assumed in roof systems [10]. It is possible to give values such as 1% when the photovoltaic systems are outside the city centre, 2% when they are in the city centre, and 3% when they are in the industrial zone and city centre [18]. While some of the radiation coming to the photovoltaic modules is absorbed by the cells, the module surface reflects some of it. Losses due to reflected radiation are called reflection losses. The glass on the surface of the photovoltaic modules has a tempered structure to maximise absorption and minimise losses due to reflection. The cells are coated with an anti-reflection coating to prevent light reflection [16].

2.2. Photovoltaic System Simulation and Comparison Studies

Kandasamy et al. [19] used PVsyst 5.59 tool and simulated a 1 MW grid connected photovoltaic solar PV system. By comparing the energy production, performance ratio, efficiency and cost, the feasibility of grid connected photovoltaic system in the southern region of Tamil Nadu is discussed. Kumar et al. [20] simulated 100 kWp grid connected photovoltaic system using PVsyst 6.52 tool. Temperature and solar radiation values were taken from Meteonorm 7.1, the database of the simulation programme, and a system was installed to meet the energy needs of the campus. They concluded that the performance capacity of the system is 80%. Sadikoglu [21] examined the dusting effect on the performance of a 1 MWp photovoltaic system installed in Konya Organised Industrial Zone. The 1-year energy production values of the panel groups with and without cleaning in the same climatic conditions and location were observed, and it was concluded that panel cleaning contributed 3,92% to the performance. The effect of the performance increase is estimated to increase to 5,65% if the whole system is cleaned.

Sharma et al. [22] analysed the performance of a 190 kWp photovoltaic system installed in India. The average annual performance rate of the photovoltaic system is 74%, the capacity factor is 9,27% and the system efficiency is 8,3%. Measured solar radiation data of the power plant were entered using PVsyst tool and the system was simulated. In 2011, the plant provided 154,43 MWh of energy, while the annual energy output given by PVsyst is 156,40 MWh. PVsyst simulation results were compared with the results of the photovoltaic system. The estimated energy yield from the simulation result is close to the monitored

result with a difference of 1,4%. Okello et al. [23] compared the actual production data of a 3,2 kWp grid-connected photovoltaic system at the Outdoor Research Facility at the Nelson Mandela Metropolitan University in South Africa with simulated performance data using PVsyst tool. In 2013, the photovoltaic system produced 5757 kWh/year, while 5754,5771 kWh/year was obtained for the simulation performed using measured and weather variables obtained from Meteonorm. Despite the similar simulation results, it was observed that the simulation result using in-situ measured climate data was closer to the measured monthly energy data.

Özerdem et al. [24] evaluated the 1,2 MW Serhatköy power plant's performance, the first grid-connected photovoltaic system in Northern Cyprus. Serhatköy photovoltaic power plant was simulated using PVsyst tool and the annual energy given to the grid was 2145 MWh. When the simulation results of the power plant and the results obtained from the actual plant production were compared, it was found that in 2012, the power plant produced 1985,21 MWh of energy, 7,47% less than the simulation data, and in 2013, the power plant produced 2152,36 MWh of energy, 0,32% more than the simulation data. Haydaroğlu and Gümüş [25] simulated the 250 kWp solar power plant installed at Dicle University Faculty of Engineering with PVsyst 6.39 simulation tool and analysed its compliance with the performance criteria specified in the standards. They also compared the simulation results with the actual production data between December 2015 and April 2016. It was determined that the actual production data was higher than the simulation data except January.

Şimşek [15] calculated the performance parameters and factors affecting the efficiency of solar power plants located in Torbalı and Gölbaşı. Modelling and simulation of the field was performed in PVsyst tool. Actual energy production data and simulation data were evaluated and compared over the parameters. It was found that the results were similar. It was observed that the most loss was caused by temperature. Other losses were caused by dusting, reflection and array mismatch loss. Keskin [26] simulated a 1 MW solar power plant installed in Niğde using PVsyst tool. The actual production data of the power plant and PVsyst simulation results are compared. The actual energy production data was 1,72% higher than the simulation data. Atlım [13] compared the effect of panel tilt angle on the system efficiency of 2 different power plants in Balıkesir Bandırma. Simulations of both plants were performed in PVsyst 6.7.6 tool. The energy production data of the plants were compared with the simulation results and it was determined that the panel tilt angle for Balıkesir would be between 28°-30° in the south direction. Bolat et al. [27] entered the information of the grid-connected Lebit Energy Solar Power Plant (SPP) with an installed power of 200 kWp into PVsyst tool and simulated the plant in the light of the data obtained from the database. The actual energy production data of Lebit Energy SPP and PVsyst simulation data were compared. The simulation data was 0,56% higher than the actual production data. Vidal et al. [28] simulated a grid-connected 8,2 kWp photovoltaic system installed in Punta Arenas (Chile) in 2018 using PVsyst tool. The annual and monthly performance of the system is evaluated and compared. A comparison between the results measured in the photovoltaic system and the results simulated in PVsyst tool made. As a result of the comparison, it is observed that the photovoltaic system produces more energy than the simulated photovoltaic model in PVsyst.

Çınaroğlu and Nalbantoğlu [29] analysed three solar power plants located in Kilis by modelling in PVsyst 7.1. tool. The three-year energy production data of the power plants and the production data in the PVsyst 7.1. simulation report were compared. As a result of the comparison, it was observed that the data obtained were close to each other, but the power plant energy production data were less. It was determined that the differences may be caused by factors such as weather events, cloudy days, changing air temperature, dust and snow accumulated on the panel. Srivastava et al. [30] conducted a one-year performance evaluation of a university park integrated grid-connected photovoltaic system located in the north of India. Partial shading photovoltaic power plant was simulated by creating a real 3D environment in PVsyst and PV*SOL tools. The results of the real plant and the results obtained from these two tools are compared, and it is seen that the simulation results do not match the real system results due to the effect of shading.

There are studies in the literature in the field of comparing the actual energy production data of

photovoltaic systems with the energy data estimated using PVsyst simulation tool. The novelty of this study is to determine the possible differences that may arise as a result of the comparison of actual energy production data and simulated energy data through independent variables by giving different values to the loss parameters.

3. MATERIAL AND METHOD

3.1. Material

Approximately 30% of the energy requirement of the facility with an installed capacity of 4788,72 kWp operating in Beyşehir district of Konya province, which is examined in this study, is met by the grid-connected photovoltaic system. The actual energy production data of the photovoltaic system integrated into the building between 1 January 2021 and 31 December 2021 and the PVsyst 7.2.14 tool were used as material.

Simulation programs analyse the operating behaviour of photovoltaic systems and can predict energy production data. By using simulation programs, the placement direction, angle, position and shadow falling on the panels can be analysed and designed as 3D in the program [31]. There are many paid or free simulation programmes used for photovoltaic system and performance worldwide. The most widely used among these programmes are PV*SOL, RETScreen, TRNSYS, HOMER, INSEL, PVSYST [32]. PVsyst tool contains location, meteorological data and photovoltaic system elements in its infrastructure, the losses in photovoltaic systems can be transferred to the system in detail, shading losses can be analysed with 3D drawing feature and feasibility cost analysis can be done [27]. In this study, PVsyst tool was preferred for 3D modelling. PVsyst has a wide meteorological database for different areas for the whole world. It also allows manual addition of data for sites not registered in the tool [33]. It gives the results as a full report with specific tables and graphs, and allows the export of the data to be used in other softwares. To get the results, some input to the tool is required [34]. PVsyst is the most widely used analysis programme in the world and is also known as the most trusted programme because it contains many parameters in its database. The database contains details such as location, meteorological data, panel angle and orientation, panel and inverter specifications, annual power reduction rates of panels, detailed solar radiation values, shading analyses, regional pollution rates, ground reflection rates (albedo), grid specifications, cable distances [35].

A grid-connected photovoltaic system was installed on the roof of the factory located at 37°45' north latitude and 31°40' east longitude in Beyşehir district of Konya province, with an area of 315304,79 m² and consisting of 4 different buildings named as A, B, C, D in this study. Building D in the facility, whose Google Earth image is given in Figure 1, started energy production for the first time in August 2018, and the system of the other buildings started energy production in August 2020.

The system is designed with panels integrated into the roof with a 12° slope in two different directions by limiting the roof areas of the buildings. The facility consists of a total of 17736 domestic production Gazioglu Solar Energy brand polycrystalline panels with a total installed power of 4778,72 kWp and a total of 74 Huawei brand inverters. 72 of the inverters are 60 kW and 2 of them are 30 kW. Building A was used in this study since the entire roof surface of building A was covered with photovoltaic panels (Figure 2) and energy production data of the building was obtained.

Meteorological data for the location of the factory building is not available in the database of PVsyst tool. The meteorological data of the location was synthetically generated from the data obtained from satellites between 2003-2013 via Meteonorm 8.0. Monthly irradiance values and sunshine hours of the region obtained from the Solar Energy Potential Atlas of the Enerji İşleri Genel Müdürlüğü (EİGM) were analysed. When the annual averages of the data are compared, the value of 4.76 kWh/m²/day in the Meteonorm database is 4,48 kWh/m²/day in the EİGM data. It is seen that there is not much difference between the meteorological data provided by the simulation tool and the data provided by EİGM.

Figure 1. Google Earth Image of the Factory

Figure 2. Building Integrated PVs on the roof of Building A

In the photovoltaic system of building A, 3480 pieces 270 Wp polycrystalline panels of Gazioglu Solar Energy brand were used. Table 1 shows the electrical characteristics, mechanical data and thermal characteristics of this panel under STC.

Since the module of Gazioglu Solar Enerji brand is not included in the database of PVsyst tool, the specifications given in Table 1 were defined to the system. Photovoltaic modules were placed on the 12° sloping sandwich panel roof surface of building A, whose dimensions are 62 m*123 m. A total of 3480 modules on 12 surfaces with a gap of 10 cm between the roof and the module, 5*58=290 modules were placed in the vertical direction on each surface.

In the photovoltaic system of building A; Huawei brand 14 inverters with 60 kW power and 1 inverter with 30 kW power were used. The specifications of 30 kW and 60 kW inverters are given in Table 2. Since the Huawei brand inverter was not included in the database of PVsyst software, the specifications given in Table 2 were defined to the system. A total of 240 panels (20 series 12 parallel) were connected to a 60 kW inverter and a total of 120 panels (20 series 6 parallel) were connected to a 30 kW inverter.

Table 1. Gazioğlu Solar Enerji 270 Wp panel specifications [36]

ELECTRICAL CHARACTERISTICS (STC)			
Maximum Power (Pmax)		270 Wp	
Open Circuit Voltage (Voc)		38,8 V	
Short Circuit Current (Isc)		9,21 A	
Mpp Voltage (Vmpp)		31,3 V	
Mpp Current (Impp)		8,63 A	
Efficiency (%)		%16,62	
MATERIAL AND DIMENSIONS		**THERMAL CHARACTERISTICS**	
Cell Type	Polycrystalline	Nominal Operating Cell Temperature (NOCT)	46 °C
Number of Cells	60	Pmax	-0,43%/K
Length	1647 mm	Voc	-0,31 %/K
Width	992 mm	Isc	0,073 %/K
Height	40 mm		
Weight	17,2 kg		

Table 2. Huawei 30 kW and 60 kW invertor specifications [37, 38]

	HUAWEI 30 kW	HUAWEI 60 kW
INPUT		
Max. DC Power	33900 W	67400 W
Max. Input Voltage	1100 V	1100 V
Max. Current per MPPT	22 A	22 A
Max. Short Circuit Current per MPPT	30 A	30 A
Start Voltage	200 V	200 V
MPPT Operating Voltage Range	200 V-1000 V	200 V-1000 V
Rated Input Voltage	400V	380/400V
Number of Inputs	8	12
Number of MPPT Trackers	4	6
OUTPUT		
Rated AC Active Power	30 kW	60 kW
Max. AC Apparent Power	33 kVA	66 kVA
Rated Output Voltage	230 V/ 400 V	230V / 400V
Rated Output Current	@400V	79.4A @480V
Max. Output Current	48.A@400V	95.3A @400V
Rated AC Grid Frequency	50/60 Hz	50/60 Hz
Weight	62 kg	74 kg

3.2. Method

In the method of the study, the electrical and technical information of the factory building was entered into the PVsyst 7.2.14 simulation programme, the building was modelled and simulated in 3D. The one-year energy production data of the factory building and the simulation data obtained in PVsyst 7.2.14 software were compared and the differences and the factors that may cause the differences were analysed. In addition, the performance analysis of the system was also performed. The International Energy Agency (IEA) developed performance parameters within the scope of IEC 61724 [39] standard to analyse the grid connected photovoltaic system's performance.

In PVsyst tool, the close shading analysis of the building is made according to the position of the sun as 3D design. According to the shading factor table obtained as a result of the simulation of the factory building, it is observed that shadow is formed in the system when the sun height is 10° and below. The angle of incidence of the sun's rays on the earth varies from day to day and time of day. Sun rays make a

higher angle with the horizontal surface at noon in summer compared to winter months. Radiations coming steeply in summer fall at a narrower angle in winter. For this reason, performing the shading analysis on December 21 (the day with the lowest solar elevation angle) gives the best results. The shading scenes on March 21, June 21, September 23 and December 21 according to the orientation of the building and the placement of the photovoltaic modules are shown in Figure 3.

After defining all the necessary information for the photovoltaic system, detailed losses related to the system were entered and detailed loss parameters affecting the system performance were defined. If the temperature measurement values of the photovoltaic system components are not available, the PVsyst temperature loss parameter can be taken as 29 W/m²K for free-standing systems with air circulation on all sides of the PVsyst temperature loss parameter, 15 W/m²K if there is no heat exchange at the back of the modules when the wind blows and the modules receive the wind in a limited way, and 20 W/m²K if the modules receive the wind through air ducts when the wind blows [40]. In this study, since there are no temperature measurement values in the roof integrated photovoltaic system design, the temperature loss parameter is assumed to be 20 W/m²K assuming that the modules receive the wind through air ducts. If detailed information such as the average length of the DC cables between the modules, the cross-section and length of the cables between the module and the inverter, and the length between the module and the DC collection box are known, the percentage of DC ohmic loss can be calculated in detail [26]. According to PVsyst, the default power loss rate is 1,5%. Since detailed information about the cable cross-sections and lengths of the factory building was not available, the default value of 1,5% DC ohmic loss was accepted.

| a-March 21 | b-June 21 |
| c-September 23 | d-December 21 |
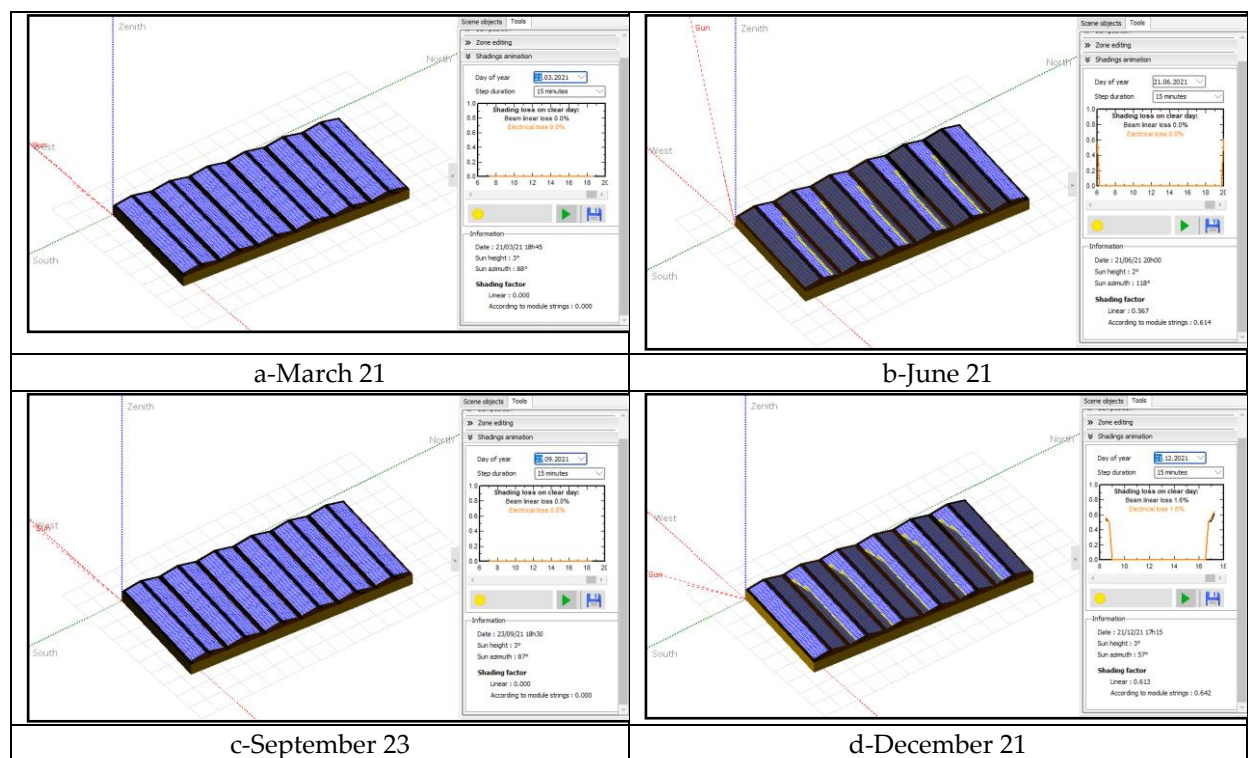
Figure 3. Shadow analysis of building A

The AC losses are also not defined as detailed information is not available. For module quality loss PVsyst selects one quarter of the difference between the values according to the tolerance of the photovoltaic module manufacturer. The mismatch loss is due to the fact that in an array of modules, the lowest current drives the current of the entire array. By default, the PVsyst programme assumes a loss of 2% for power losses and 2.5% for constant voltage uses [40]. Since the tolerance value of the modules used in the factory building in this study is -0/+5 Wp, one quarter of the difference between the tolerance values-1.25% is determined as the module quality loss value. Module mismatch loss default value of 2%, constant

voltage loss of 2.5% and string voltage mismatch default value of 0,1% were accepted.

In order for the solar panels to work efficiently and healthily, maintenance instructions are applied at certain time intervals in the factory. Cleaning and maintenance of the panels are carried out; once a month in December, January, February, March and once every 2 weeks in other months. The surface of all panels is cleaned with water with the help of an equipment in a way to remove dust and any substance that will reduce efficiency. While cleaning, damage controls of the panels, cables of the panels and socket places are also carried out. In addition, the energy values produced by the panel groups are also checked at regular intervals and fault detection is carried out. These controls ensure the continuity of the energy production of the system. In PVsyst tool, dusting loss can be entered monthly or annually. Since the facility is located outside the city centre and cleaning is carried out regularly, dusting loss is accepted as 1% per year. The radiation that reaches to the surface of the photovoltaic cells decreases due to reflections. In PVsyst tool, the annual reflection loss value was calculated with fresnel-normal glass technique and the default value was accepted. Aging in photovoltaic systems causes gradual loss of efficiency. Gazioglu Solar Energy provides 25 years linear performance guarantee for the panels. PVsyst defines an average degradation rate. Since the facility was commissioned in August 2020, the aging factor was assumed to be 0,20% for 1 year in the simulation. Losses caused by the cessation of production due to malfunction and maintenance in the photovoltaic system are unavailability losses. Since the periods when the system could not produce could not be determined, no value was defined in the PVsyst tool.

4. RESULTS AND DISCUSSION

4.1. Photovoltaic System Simulation Results

As a result of the simulation of the photovoltaic system of the existing factory, monthly and annual energy production data of the system, energy loss percentages, the amount of radiation on the panel surface, average temperature values were received. In addition, according to standard of IEC 61724 [39], the performance parameters of the system were obtained and performance analysis was performed. The annual loss diagram obtained as a result of the simulation is given in Figure 4. In the diagram, it can be seen that the annual global irradiation to the horizontal plane is 1737 kWh/m². Photovoltaic panels were placed 12° angled depending on the roof slope of the building. The amount of radiation on the surface of the panel decreased by 1,2%. According to the modelling, the loss due to shadowing on the panels was recorded as 0,2%. The loss due to reflection was 4,4% and the loss due to dusting and snowing was 1%. When these losses, which can be defined as optical losses in general, are summed up, the effective radiation to the panel surface at the selected geographical location is 1621 kWh/m² per year. The efficiency of the panel used in the photovoltaic system under STC is 16,53%. In relation to the panel efficiency, 16,53% of the energy that could be produced was converted to photovoltaic and as a result, the nominal energy in the panel array was determined as 1524 MWh.

Losses due to photovoltaic panel characteristics are defined as array losses. After 1 year, module degradation loss is 0,2%, irradiation loss is 0,7%, thermal loss is 7,6%, array mismatch loss is 2,1%, DC ohmic loss is 1,1%. As a result of 11,7% total array losses, the amount of energy at the array output, defined as the assumed array energy, was determined as 1368 MWh. Losses related to the inverter and grid connections are defined as system losses. Inverter losses are calculated as 1,7%. The available energy at the inverter output was determined as 1345 MWh. As a result of all losses, the simulation gives that 1345 MWh of energy can be produced from the photovoltaic system in 1 year. The performance parameters for comparison of PVsyst simulation results; reference yield (Y_R), array yield (Y_A), final yield (Y_F) and performance ratio (PR) are given in Table 3.
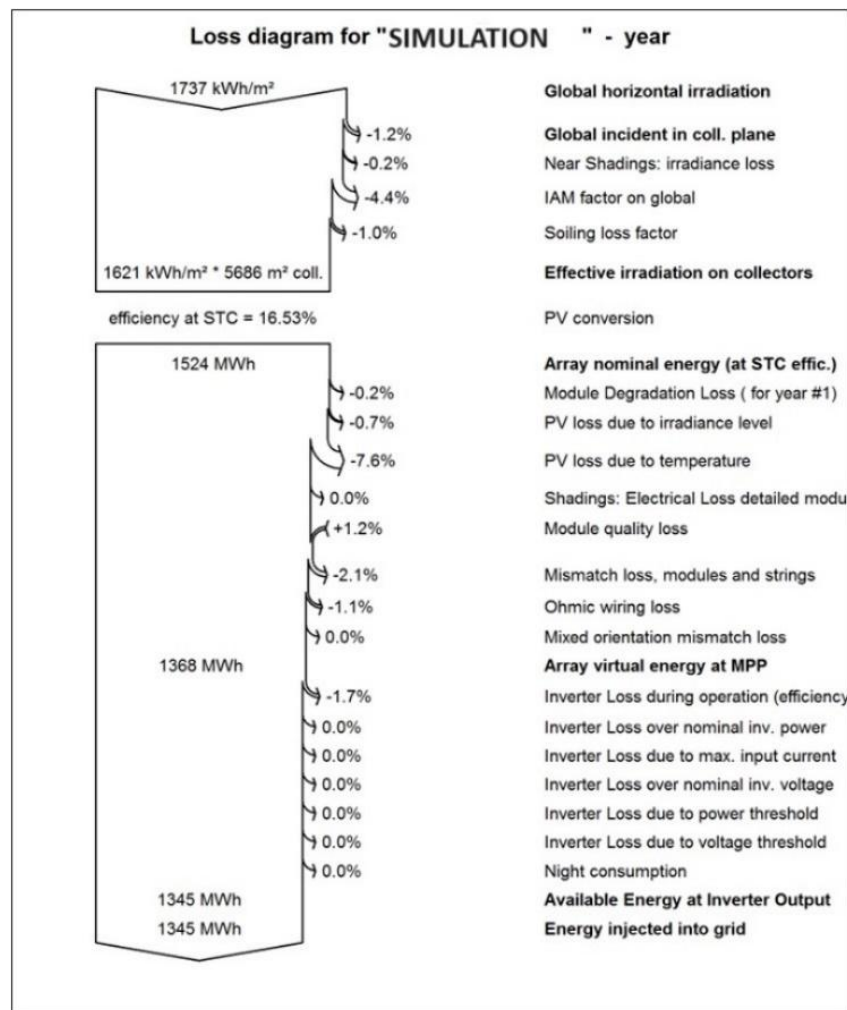
Figure 4. Yearly loss diagramme derived from PVsyst

According to Table 3, the highest performance rate was 89,6% in February and the lowest was 79,0% in July. The annual performance ratio is 83,4%. Depending on the temperature increase, system performance decreases in summer months and increases in winter months. The actual energy production data of the factory building and the simulation data obtained using PVsyst tool are given in Table 4. When the table is analysed; it is predicted that the factory building can produce a total of 1345,1 MWh of energy in 1 year according to PVsyst simulation results, while the factory building produces 1372,2 MWh of energy in total for 1 year. There is a difference of 27,1 MWh between actual energy production data and simulation data. Thus, the 2021 energy production data of the factory is 2% higher than the PVsyst simulation data. This shows that the factory building realises a higher performance than the predicted production data.

Table 3. PVsyst monthly performance parameters

	Reference yield Y_R (kWh/m²/day)	Array yield Y_A (kWh/m²/day)	Final yield Y_F (kWh/m²/day)	Performance rate PR (Y_F/Y_R)
January	2,14	1,92	1,88	0,883
February	2,96	2,70	2,65	0,896
March	4,06	3,64	3,58	0,881
April	5,38	4,73	4,65	0,864
May	6,67	5,69	5,59	0,839
June	7,42	6,12	6,01	0,810
July	7,47	6,01	5,90	0,790
August	6,62	5,36	5,26	0,796
September	5,48	4,55	4,48	0,817
October	3,65	3,14	3,09	0,845
November	2,58	2,26	2,22	0,858
December	1,92	1,70	1,67	0,871
Average	4,70	3,99	3,92	0,834

Table 4. Real production data of factory building in 2021 and PVsyst simulation data

	PVsyst Simulation Data (kWh)	Real Production Data of 2021 (kWh)	Realisation Rate %
January	54902	48148	%87,69
February	69843	80966	%115,92
March	104216	95611	%91,74
April	131161	134995	%102,92
May	162912	174954	%107,39
June	169456	165612	%97,73
July	171990	182800	%106,28
August	153321	159199	%103,83
September	126175	124143	%98,38
October	89885	107230	%119,29
November	62523	67969	%108,71
December	48684	30586	%62,82
TOTAL	1345068	1372213	%102,01

When the actual generation data and simulation data are compared, it is seen that in February, April, May, July, August, October and November, the actual generation data is higher than the simulation data, while in January, March, June, September and December, the simulation data is higher than the actual generation data of the factory building. The highest generation in the factory building was in July with 182,800 MW and the lowest generation was in December with 30,586 MW. The reason for this situation is that the highest radiation is obtained in July and the lowest radiation is obtained in December. The difference between the production data of the factory building and the simulation data was the lowest in September and the highest in December. This difference in December may be due to the harsh climatic conditions of the region and the snow falling on the panels for a long time.

4.2. Determination of the Effect of Loss Parameters to Photovoltaic System Performance

There are various approaches to determine the effect of parameters on system performance. The simplest and most widely used method is the "one at a time (OAT)" approach, where one parameter at a time is varied by a certain percentage while keeping the others constant. With this method, the effective parameters in the variation of the result can be obtained. This type of analysis is one of the "local" sensitivity analysis methods, as it deals only with sensitivity with respect to selected point estimates and not for the entire parameter distribution [41]. Sensitivity analysis is the study of how the variation in the model result can be qualitatively or quantitatively allocated to different sources of variation in the model input. Many sources of uncertainty such as measurement errors, lack of information or misunderstanding

of mechanisms constitute the input factor in sensitivity analysis [42]. Sensitivity analysis is necessary to identify the input parameters that contribute the most variability in the output, the unimportant parameters and the parameters that interact with each other [43].

Within the scope of this study, the effect of temperature, module mismatch, dusting and aging loss parameters on the result is evaluated with the "one at a time" method of the difference arising as a result of the comparison of 1-year energy production data and simulation data of the photovoltaic system. The system was simulated by taking the temperature loss value of 15 W/m^{2}K as an independent variable and new data were obtained. The default value recommended by PVsyst for mismatch losses was set as 1% in previous versions and twice as 2% for constant voltage uses. However, it is reported in PVsyst documentation that there is no absolute value for mismatch losses [40]. In this study, module mismatch losses were simulated by defining 2% as recommended by PVsyst 7.2.14 as default and 2,5% for constant voltage usage. However, since detailed calculation of mismatch losses was not performed, the simulation data were obtained again by defining the mismatch loss value of 1% and 2% for constant voltage usage as an independent variable while examining the effect of the parameters on the system performance. Since the factory building is located outside the settlement boundaries, the annual pollution loss was defined as 1% and simulated according to this value. However, since there is no device to measure the annual pollution loss of the modules, this loss percentage is not precise. Based on the information that the modules are cleaned once a month in the winter months and twice a month in the other months, the dusting loss was entered as 1% in December, January, February, March and 0% in the other months. The annual dusting loss of the system was defined as 0,3% as an independent variable. Since the installation of the photovoltaic system was completed in August 2020, the aging loss was defined as 0,2% for 1 year. Since the system has not yet completed one year in the one-year total energy data used in this study, the annual aging loss of the system is defined as 0% as an independent variable. In the simulation, the results and performance ratios of 16 different variations obtained by giving 2 different values to 4 independent variables determined to evaluate the effect of loss parameters are given in Table 5. "15-20" for temperature loss, "2/2.5%-1/2%" for module mismatch loss, "1%-0,3%" for dusting loss and "0,2-0%" for aging loss alternative values are used. V1 variation is the result obtained according to the loss values defined in the PVsyst tool according to the default values.

Table 5. Given values to independent variables and acquired energy production data

	Temperature Losses (W/m2K)	Mismatch Losses %	Dusting Losses %	Aging Loss %	Energy Production (MWh)	Performance Ratio (PR) %
V1	20	%2 / %2,5	%1	1 year %0,20	1345	%83,4
V2	20	%2 / %2,5	%1	0	1348	%83,5
V3	20	%2 / %2,5	%0,3	1 year %0,20	1354	%84
V4	20	%2 / %2,5	%0,3	0	1357	%84,1
V5	20	%1 / %2	%1	1 year %0,20	1359	%84,2
V6	20	%1 / %2	%1	0	1362	%84,4
V7	20	%1 / %2	%0,3	1 year %0,20	1368	%84,8
V8	20	%1 / %2	%0,3	0	1371	%85
V9	15	%2 / %2,5	%1	1 year %0,20	1292	%80,1
V10	15	%2 / %2,5	%1	0	1294	%80,2
V11	15	%2 / %2,5	%0,3	1 year %0.20	1300	%80,6
V12	15	%2 / %2,5	%0,3	0	1303	%80,8
V13	15	%1 / %2	%1	1 year %0,20	1305	%80,9
V14	15	%1 / %2	%1	0	1308	%81,1
V15	15	%1 / %2	%0,3	1 year %0,20	1314	%81,4
V16	15	%1 / %2	%0,3	0	1316	%81,6

It was previously stated that there was a difference of 2% between the simulation result and the actual production data. When the ratios given in Table 5 are analysed, the closest to the actual production data is V8 variation with 0,07% and the furthest is V9 variation with 6,19%.

4.3. Discussion

When the loss parameters occurring in the system as a result of the simulation are analysed, it is seen that the highest loss is due to temperature. The temperature loss value is 7,6%. Temperature loss is one of the important parameters affecting the efficiency. Temperature loss is followed by reflection loss, array mismatch loss, inverter loss, DC ohmic wiring loss and dusting loss. Shading is one of the important parameters affecting the efficiency of photovoltaic panels. The fact that the factory surroundings are open and there are no shading factors such as buildings, trees, chimneys, electricity poles on the panel positively affects the efficiency. Panels facing north also experience shading at certain time intervals. The dusting loss of the system is 1%. The analysis of the results show that the realisation rate is the lowest in December with 62,18% and the highest in October with 119,29%.

Okello et al. [23], Haydaroğlu and Gümüş [25], Keskin [26], Vidal et al. [28], Bolat et al. [27], Çınaroğlu and Nalbantoğlu [29], compared the production data of the installed photovoltaic system with the data obtained from the PVsyst tool in their studies. In the studies of Bolat et al. and Çınaroğlu and Nalbantoğlu, the simulation data were higher than the actual production data. In other studies, real data were higher than simulation data. Comments have been made about the reasons for the difference between real data and simulation data, but no study has been carried out on this subject. This study, which examines the effect of loss parameters on photovoltaic system performance in detail, contributes to this gap in the literature.

5. CONCLUSION

In this study, the actual values and characteristics of the photovoltaic system, which was integrated on the roof of an existing facility and whose production data has been recorded since August 2020, were defined and simulated in the PVsyst 7.2.14 simulation program. In the simulation results, energy production data, loss data and performance parameters defined and IEC 61724 standard used to analyse the performance of the system.

As can be seen from the results, there are differences between the simulation data and the production data of the factory building in 2021 due to environmental factors. Since there is no on-site measurement data for factors such as temperature, radiation, wind, dusting, snow, shading, etc., the values provided by the programme for some loss parameters in the simulation study were accepted as default. Therefore, simulation results and actual production results do not exactly coincide. In general, when the annual production results are evaluated, it is observed that there are close results. Since there is no climate data for 2021 for the location of the facility, simulation was performed by taking the average of 10-year climate data obtained from the Meteonorm database. The possibility that the 2021 climate data may be different from the 10-year forecast may differentiate the simulation results from the actual production data. In addition, the OAT method of changing one variable at a time by a certain percentage was used to determine which parameters may cause the difference between actual production data and simulation data.

In this study, the importance of renewable energy source sun and photovoltaic systems is emphasised. It is aimed to contribute to the widespread use of energy production by using photovoltaic systems for Turkey with high solar energy potential. The realistic results of the simulation tool PVsyst, which is used to simulate the energy production potential and efficiency of the system before photovoltaic system designs, are mentioned. The fact that PVsyst tool produces results close to reality, shows that it is a reliable programme. Although there is a difference between the one year real production data of the photovoltaic system and the annual total production data of the PVsyst tool, close results can be obtained. However, differences may occur in monthly energy production results. These differences are due to the fact that the losses in the system cannot be fully calculated. In order to estimate the monthly production data closer to reality, as much data as possible about the temperature, radiation, wind direction, wind speed and dust parameters of the region where the system is installed are needed. In order to determine the irradiance, temperature, wind speed and dust parameters that affect the efficiency of the photovoltaic system, it is

necessary to set up a device. In order to measure the amount of irradiance, a pyranometer can be connected to the output of the photovoltaic modules. In order to minimise temperature loss, temperature monitoring sensors can be installed on the modules to prevent temperature-related failures. The effect of dusting can be detected if two modules with the same characteristics are periodically cleaned at a certain time interval, one of them is periodically cleaned and the other is not cleaned and energy measurement values are recorded.

Calculation and determination of the panel optimum tilt angle value of the photovoltaic system will increase the efficiency of the system. The optimum tilt angle of the panels varies between 35°-40° depending on the latitude in Turkey. It is thought that the module tilt angle of the factory building will increase the amount of energy produced. For high performance photovoltaic systems, regular monitoring of the factors affecting the performance and efficiency of the system is required.

Declaration of Ethical Standards

The authors of this article declare that the materials and methods used in this study do not require ethical committee permission and/or legal-special permission.

Credit Authorship Contribution Statement

Selçuk SAYIN: Conceptualization, evaluation of results, writing
Fatma YETGİN: Data collection and simulation

Declaration of Competing Interest

The authors declare that they have no known competing financial interests or personal relationships that could have appeared to influence the work reported in this paper.

Data Availability

Due to the nature of this study, no statistical or formula-based data were utilized.

Symbols

A	Ampere	kWp	Kilowatt peak
°C	Celsius degree	mm	Millimetre
GW	Gigawatt	m²	Square meter
Hz	Hertz	MPPT	Maximum Power Point Tracking
K	Kelvin	MW	Megawatt
kVA	Kilo volt ampere	MWp	Megawatt-Peak
kg	Kilogram	MWh	Megawatt hour
kW	Kilowatt	TWh	Terawatt hour
kWh	Kilowatt hour	V	Volt
kWh/m²	Kilowatt hour / square meter	W	Watt
kWh/m²/day	Kilowatt hour / square meter / day	W/m²K	Watt / square meter Kelvin
kWh/year	Kilowatt hour / year	Wp	Watt peak

REFERENCES

[1]   Y. Liu, M. Li, X. Ji, X. Luo, M. Wang, Y. Zhang, "A comparative study of the maximum power

point tracking methods for PV systems," *Energy Conversion and Management*, vol. 85, pp. 809-816, 2014, https://doi.org/10.1016/j.enconman.2014.01.049

[2] https://www.iea.org/reports/solar-pv, [Accessed January 9, 2022].

[3] https://www.iea.org/data-and-statistics/data-browser/?country= WORLD&fuel=Energy%20consumption&indicator=CO2Industry, [Accessed March 9, 2022].

[4] :https://www.iea.org/data-and-statistics/data-browser?country= TURKEY&fuel=CO2%20emissions&indicator=CO2BySector, [Accessed March 9, 2022].

[5] J. Pellegrino, A. Fanney, A. Persily, P. Domanski, W. Healy, S. Bushby, "Measurement science roadmap for net-zero energy buildings," Technical Note (NIST TN), National Institute of Standards and Technology, Gaithersburg, MD, 2010.

[6] Ç. Oluklulu, "Güneş enerjisinden etkin olarak yararlanmada kullanılan fotovoltaik modüller, boyutlandırılmaları ve mimaride kullanım olanakları üzerine bir araştırma," Msc Thesis, Gazi University Graduate School of Natural and Applied Sciences, 2001.

[7] R. Sharma, S. Goel, 2017, "Performance analysis of a 11.2 kWp roof top grid-connected PV system in Eastern India," *Energy Reports,* vol. 3, pp. 76-84, 2017, https://doi.org/10.1016/j.egyr.2017.05.001

[8] G. Makrides, B. Zinsser, M. Norton, G. E. Georghiou, M. Schubert, J. H. Werner, "Potential of photovoltaic systems in countries with high solar irradiation," *Renewable and Sustainable Energy Reviews*, vol. 14. No. 2, pp. 754-762, 2010, https://doi.org/10.1016/j.rser.2009.07.021

[9] M. E. Bilgili, M. Dağtekin, "Fotovoltaik piller ile elektrik üretiminde uygun eğim açısının ve yıllık oluşan enerji farkının belirlenmesi," *Gaziosmanpaşa Bilimsel Araştırma Dergisi*, vol. 6, pp. 156-167, 2017.

[10] E. Deniz, "Güneş enerjisi santrallerinde kayıplar," *III. Elektrik Tesisat Ulusal Kongre ve Sergisi Bildirileri*, İzmir, 2013.

[11] S. Turhan, İ. Çetiner, "Fotovoltaik Sistemlerde Performans Değerlendirmesi," *6. Ulusal Çatı & Cephe Sempozyumu*, Bursa, 2012.

[12] B. G. Çelik, "Fotovoltaik modüllerin mimaride uygulama olanakları-Eskişehir için bir örnek çalışma," Msc Thesis, Anadolu University Graduate School of Natural and Applied Sciences, 2002.

[13] F. Atlım, "Balıkesir ilindeki PV sistemlerin analizi," Msc Thesis, Balıkesir University, Institute of Science, 2019.

[14] B. Alaçakır, "Didim'de kurulan şebeke bağlantılı güneş pili sisteminin tanıtılması ve performansının incelenmesi," *Güneş Günü Sempozyumu*, Kayseri, 1999.

[15] S. Şimşek, "Fotovoltaik sistemlerde verimliliği etkileyen faktörlerin incelenmesi," Msc Thesis, Hacettepe University Graduate School of Natural and Applied Sciences, 2018.

[16] M. A. Köprü, "Fotovoltaik Sistemlerde Kablo Kayıplarının İncelenmesi," Msc Thesis, Fırat University Graduate School of Natural and Applied Sciences, 2016.

[17] H. K. Demiryürek, "200 kwp kurulu güçteki lebit enerji güneş santralinin pvsyst ile tasarımı ve üretim değerleri ile simülasyon değerlerinin karşılaştırılması," Msc Thesis, Sakarya University Graduate School of Natural and Applied Sciences, 2018.

[18] B. Mutluay, "Bir fotovoltaik güç santrali tasarımının sistem simülasyonu ve tekno ekonomik fizibilitesi," Msc Thesis, Fırat University Graduate School of Natural and Applied Sciences, 2016.

[19] C. P. Kandasamy, P. Prabu, K. Niruba, "Solar potential assessment using PVSYST software," *International Conference on Green Computing, Communication and Conservation of Energy (ICGCE)*, Chennai, pp. 667-672, 2013, DOI:10.1109/ICGCE.2013.6823519

[20] N. M. Kumar, M. R. Kumar, P. R. Rejoice, M. Mathew, "Performance analysis of 100 kWp grid connected Si-poly photovoltaic system using PVsyst simulation tool," *Energy Procedia*, vol. 117, pp. 180-189, 2017, https://doi.org/10.1016/j.egypro.2017.05.121

[21] F. Sadıkoğlu, 2018, "1 MWp şebekeye bağlı güneş enerjisi santrali performans analizi," Msc Thesis, Necmettin Erbakan University Graduate School of Natural and Applied Sciences, 2018.

[22] V. Sharma, A. Kumar, O. S. Sastry, S. S. Chandel, "Performance assessment of different solar photovoltaic technologies under similar outdoor conditions," *Energy,* vol. 58, pp. 511-518, 2013,

https://doi.org/10.1016/j.energy.2013.05.068

[23]   D. Okello, E. E. Van Dyk, F. J. Vorster, "Analysis of measured and simulated performance data of a 3.2 kWp grid-connected PV system in Port Elizabeth, South Africa," *Energy Conversion and Management*, vol. 100, pp. 10–15, 2015, https://doi.org/10.1016/j.enconman.2015.04.064

[24]   Ö. C. Özerdem, S. Tackie, S. Biricik, "Performance Evaluation of Serhatköy (1.2 MW) PV Power Plant", *9th International Conference on Electrical and Electronics Engineering (ELECO)*, Bursa, pp. 398-402, 2015, 10.1109/ELECO.2015.7394510

[25]   C. Haydaroğlu, B. Gümüş, "Dicle Üniversitesi güneş enerjisi santralinin PVsyst ile simülasyonu ve performans parametrelerinin değerlendirilmesi," *Dicle Üniversitesi Mühendislik Fakültesi Mühendislik Dergisi*, vol. *7, no.* 3, pp. 491–500, 2016.

[26]   A. Keskin, "Niğde ili güneş enerji santrali modellemesi ve performans parametreleri değerlendirmesi," Msc Thesis, Gazi University Graduate School of Natural and Applied Sciences, 2019.

[27]   M. Bolat, U. Arifoğlu, H. K. Demiryürek, "Lebit enerji güneş santralinin PVsyst programı ile analizi," *BEU Journal of Science*, vol. 9, no. 3, pp. 1351-1363, 2020, https://doi.org/10.17798/bitlisfen.650786

[28]   H. Vidal, M. Rivera, P. Wheeler, N. Vicencio, "The analysis performance of a grid-connected 8.2 kwp photovoltaic system in the patagonia region," *Sustainability*, vol. 12, no. 21, pp. 1-16, 2020, https://doi.org/10.3390/su12219227

[29]   M. S. Çınaroğlu, M. Nalbantoğlu, "Şebekeye bağlı üç adet fotovoltaik enerji santralinin PVsyst programı ile analizi; Kilis örneği," *El-Cezerî Journal of Science and Engineering*, vol. 8, no. 2, pp. 675-687, 2021, DOI:10.31202/ecjse.865649

[30]   R. Srivastava, A. N. Tiwari, V. K. Giri, "Performance evaluation of parking integrated grid-connected photovoltaic system located in Northem India," *Environment Development and Sustainability*, vol. 23, pp. 5756-5775, 2021, https://doi.org/10.1007/s10668-020-00845-4

[31]   O. Ceylan, "Fotovoltaik programlarının simülasyon sonuçlarının doğruluğunun incelenmesi," Msc Thesis, Süleyman Demirel University Graduate School of Natural and Applied Sciences, 2017.

[32]   C. C. Tutaşı, "Güneş enerjisinden ısı ve elektrik eldesinin tekno-ekonomik simülasyonu: örnek bir uygulama," Msc Thesis, Başkent University Institute of Science Engineering, 2018.

[33]   F. Yetgin, "Binaya Entegre Fotovoltaik (PV) Panellerin Simülasyon ve Gerçek Üretim Verilerinin Karşılaştırılması," Msc Thesis, Konya Technic University Institute of Graduate Studies, 2022.

[34]   P. Yadav, N. Kumar, S. S. Chandel, "Simulation and performance analysis of a 1kWp photovoltaic system using PVsyst", *International Conference on Computation of Power, Energy, Information and Communication (ICCPEIC)*, Chennai, pp. 358-363, 2015, 10.1109/ICCPEIC.2015.7259481

[35]   M. H. Girgin, "Bir fotovoltaik güneş enerjisi santralinin fizibilitesi, Karaman bölgesinde 5 MW'lık güneş enerjisi santrali için enerji üretim değerlendirmesi ve ekonomik analizi," Msc Thesis, İstanbul Technical University Energy Institute, 2011.

[36]   Gazioğlu Solar Enerji, 270 W panel, http://www.gazioglusolar.com.tr/pdf/gse_poly_60_5BB_265_280.pdf., [Accessed March 27, 2022].

[37]   Huawei 30 kW invertör, https://www.3de3enerji.com.tr/wp-content/uploads/2019/08/huawei-SUN2000-33KTL-A-trifaze-inverter.pdf., [Accessed March 27, 2022].

[38]   Huawei 60 kW invertör, https://www.3de3enerji.com.tr/wp-content/uploads/2019/10/huawei-SUN2000-60KTL-M0-trifaze-inverter.pdf., [Accessed March 27, 2022].

[39]   IEC 61724, "Photovoltaic system performance monitoring – Guidelines for measurement, data exchange and analysis," International Electrotechnical Commission, 1998.

[40]   https://www.pvsyst.com/help/, PVsyst 7.2 Help Manuel, [Accessed April 20, 2022].

[41]   D. M. Hamby, "A review of techniques for parameter sensitivity analysis of environmental models," *Enviromental Monitoring and Assessment*, vol. 32, pp. 135-154, 1994, https://doi.org/10.1007/BF00547132

[42]   G.U. Harputlugil, J. Hensen, G. Çelebi, "A prospect to develop thermally robust outline design and to explore its applicability to the different climate necessities of Turkey," *International Journal of Low-Carbon Technologies*, vol. 6, no.1, pp. 76-85, 2011, https://doi.org/10.1093/ijlct/ctq050

[43]   G. L. Mountford, P. M. Atkinson, J. Dash, T. Lankaster, S. Hubbard, "Sensitivity of vegetation phenological parameters: from satellite sensors to spatial resolution and temporal compositing period," in *Sensitivity Analysis in Earth Observation Modelling*, Petropoulos G. P., Srivastava P. K., Eds. Elsevier, Amsterdam, 2017, pp. 75-90.

ADVANCED MODELING FOR SEA LEVEL PRESSURE PREDICTION: A COMPARATIVE EVALUATION OF ANN AND ANFIS TECHNIQUES

*Erman ÖZER [iD]

Recep Tayyip Erdoğan University, Computer Engineering Department, Rize, TÜRKİYE
erman.ozer@erdogan.edu.tr

Highlights

- The study compares the performance of ANN and ANFIS for forecasting SLP forecasting.

- The ANFIS surpasses ANN in accuracy, with lower RMSE and higher R²,proving more reliable.

- ANFIS emerges as the better choice for SLP due to improved accuracy and performance.

- Improved SLP forecasts support disaster management and infrastructure planning.

*Corresponding Author: Erman ÖZER, erman.ozer@erdogan.edu.tr

ADVANCED MODELING FOR SEA LEVEL PRESSURE PREDICTION: A COMPARATIVE EVALUATION OF ANN AND ANFIS TECHNIQUES

* Erman ÖZER ⁰

Recep Tayyip Erdoğan University, Computer Engineering Department, Rize, TÜRKİYE
erman.ozer@erdogan.edu.tr

ABSTRACT: Pressure forecast plays a crucial role in weather forecasting, and this has a direct effect on the many fields including disaster management, agriculture, energy systems etc. The goal of this study is to compare the performances between ANN and ANFIS-based models for predicting around distribution over a range of different sea-level pressure values using various meteorological attributes as inputs. This study focuses on air temperature, wind speed, and humidity data sourced from the Macau Meteorological and Geophysical Office. We populated the dataset with missing values and performance metrics were used to train and test both models (RMSE, MAPE, R^2). Overall results show that both models are good for Prediction but in accuracy, we can say that ANFIS is performing better of all the ANN types at RMSE and R^2 than others for Sea Level Pressure Forecasting. This increased accuracy can help in a wide variety of fields, from weather-related risk management and infrastructure planning to agricultural yield forecasting.

Keywords: Artificial Neural Networks, ANFIS, Sea Level Pressure Forecasting

1. INTRODUCTION

Pressure forecasting is one of the major challenges in weather data analysis research. Weather modeling is a widely utilized application of machine learning algorithms, extensively employed in scientific research. The algorithms allows to handle high-dimension and non-linear datasets such as atmospheric data. Weather forecasting can be performed with higher accuracy levels using machine learning models than using typical statistical methods.

Definition of Artificial Neural Network(ANN)[1] is that a learning model designed on the basis of how human brain works. This model also works by training it with your data, and keeps adjusting the weights in each neuron throughout so as to process the data and make the predictions. This new ANN has been trained on a bunch of data and learns from for example (new) videos it analyses, to make predictions on previously unseen new data. ANN models are widely utilized for analyzing complex meteorological datasets, including Sea Level Pressure (SLP) forecasting. ANN can learn non-linear relationships and handle missing records efficiently.

ANFIS(Adaptive-Network Based Fuzzy Inference Systems)[2] is described as a mix of networks and fuzzy logic systems that works to grasp the intricate connections, within data and offer predictions by translating human expertise into fuzzy logic rules effectively. Furthermore. In addition to making deductions based on specified rules[3,4]. ANFIS improves prediction accuracy by refining its rule optimization strategies. This methodology enhances SLP forecasting by analyzing meteorological scenarios to produce precise predictions.

ANN effectively addresses challenges and processes incomplete data with robustness [5]. Yet figuring out the network setup usually involves some trial and error work. The performance of ANN is heavily dependent on the quality and relevance of the training data. On the other hand, ANFIS is known for its ability to automatically learn logic rules. By doing it can better capture how intricate systems behave. Provide a more adaptable framework. However tuning the parameters in an ANFIS model can be a time consuming task. Moreover dealing with datasets may lead to increased costs and longer processing times according to sources [6,7].

*Corresponding Author: Erman ÖZER, erman.ozer@erdogan.edu.tr

A comparative analysis of these models aids in identifying the most accurate approach for SLP forecasting. Meteorological studies such as pressure forecasting rely on machine learning techniques such as ANN and ANFIS to obtain accurate and reliable results. These techniques improve the accuracy of weather forecasts, enabling precautions to be taken against future weather conditions.

2. LITERATURE REVIEW

Accurate weather forecasting is crucial as it enables individuals and organizations to make informed decisions. It impacts people's clothing choices, company logistics, and government planning. It also plays a vital role in transportation, agriculture, and many other sectors[8,9]. Flash floods are sudden rises in water levels due to intense precipitation, posing risks to life and property[10-12]. Extreme weather events in 2015 alone caused over 7.9 billion dollars in damages, highlighting the impact on the economy[13]. Protecting the population and infrastructure from flooding and extreme temperatures is a major concern. Critical infrastructure is essential for society's functioning[14,15]. Rising humidity and temperatures from global warming can lead to hazardous events like glacier melting[16].

SLP is crucial for weather forecasting. It influences air mass movement and weather system formation. Accurate forecasts improve overall weather prediction accuracy and disaster preparedness[17]. Pressure variations are key in large storm development, like tropical cyclones. Forecasting helps anticipate and mitigate damage from storms, hurricanes, and tsunamis. The agricultural sector benefits from precise pressure forecasts for better planning of irrigation, planting, and harvesting, boosting productivity. SLP also impacts energy generation in wind and hydroelectric power plants[18].

Accurate SLP forecasts in certain areas can have a significant impact on daily life. They can help reduce the impact of natural disasters, increase agricultural productivity, improve energy efficiency, and make daily life easier. Table 1[19] shows the relationship between pressure and other weather factors on mortality rates in 12 cities[19].

Table 1. Effect of Weather on Mortality at 12 Locations

Cities	Population	Number of Deaths	Average Temperature	Average Humidity	Pressure
Atlanta	1.642.533	36,2	17,1	67,0	736
Birmingham	651.525	19,1	16,9	70,5	747
Canton	367.585	9,9	10,0	73,7	729
Chicago	5.105.067	133,4	10,1	70,8	744
Colorado	397.014	6,0	9,5	51,0	610
Detroit	2.111.687	59,7	10,5	69,2	744
Houston	2.818.199	47,0	20,3	75,0	760
Minneapolis	1.518.196	32,3	7,9	68,7	739
New Haven	804.219	20,4	10,7	66,8	760
Pittsburgh	1.336.449	42,4	11,2	69,3	732
Seattle	1.507.319	29,3	11,4	77,0	752
Spokane	361.364	8,7	8,8	68,0	699

Literature reviews show extensive research on weather forecasting. Zhou et al. used ANN and SVM for power forecasting, showing that ANN performed well but required significant computational tuning. Our study supports this finding, as ANN needed hyperparameter optimization to improve accuracy [20]. They used SVM, PCC, and ANN to predict sunny, cloudy, or rainy weather, aiming to enhance power generation forecasts. ANN was specifically used to optimize energy systems. Additionally, Aris Pujud Kurniawan et al. developed a weather forecasting model using fuzzy logic for

agricultural automation [21]. This model uses weather, humidity, and temperature data to automate irrigation decisions, determining when crops require watering.

Ahmad Yusuf Ardiansyah et al. developed a rain sensing system that predicts weather levels using a Mamdani Fuzzy Inference System. The system integrates humidity and temperature sensors with the Arduino platform to predict rain intensity using fuzzy logic [22].

Setyaningrum et al. developed an ANFIS-based weather prediction system and found that ANFIS outperformed traditional regression methods. Our results align with this, showing ANFIS's superior ability in handling meteorological data[23]. ANFIS: It is the fuzzy logic and ANN combined to forecast complex weather fields. Munandar et al. compared ANFIS and linear regression for rainfall prediction, concluding that ANFIS had higher accuracy in non-linear systems. This supports our findings that ANFIS better captures the complex relationships in sea level pressure data [24].

Gopi Krishna et al. introduce an IoT and ANN based weather monitoring & forecasting system [25]. It uses a IoT-based ESP32 microcontroller to monitor temperature, humidity and soil moisture. This data is being processed in an ANN that provides the ability to carry out agricultural activities in a better manner. Another study using Deep Learning models for weather forecasting is conducted by Bala Maheswari [26]. Models such as CNN, LSTM, and GRU give better results in weather prediction as they can work efficiently with meteorological data.

Prediction of SLP is a primary goal in this study, such floors dimensions with variables like air temperature, wind intensity and humidity using ANN and ANFIS. We will evaluate the models on three different aspects RMSE (Root Mean Squared Error), MAPE (Mean Absolute Percentage Error) and R^2 (Determination Coefficient) to find out which model is performing well. Such forecasts can help greatly in terms of energy and infrastructure planning as far as the government is concerned, and also help with decisions there. Unlike previous studies that primarily focused on general weather forecasting, this research is among the first to specifically compare ANN and ANFIS for sea level pressure prediction. While many studies utilize ANN for weather prediction, few explore the impact of data preprocessing techniques and hyperparameter tuning, which we address in detail. Additionally, we enhance the robustness of our findings by validating results through statistical significance tests, an aspect often overlooked in prior ANN vs. ANFIS comparisons.

3. ANN AND ANFIS

3.1. ANN

Inputs are the data coming into the neural cell, and these data can be provided from the outside world or from other neural cells. In a neural network, neurons are interconnected through weighted links, where the weights encode input information used by the network to solve problems.
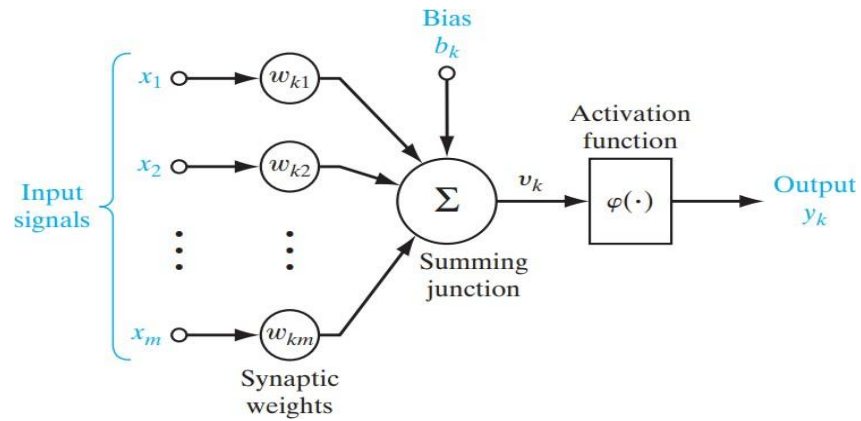
Figure 1. Artificial Neural Network

Inputs are processed by multiplying them by weights before they reach the kernel, so that the impact of inputs on outputs can be adjusted.

$$net_{input} = x_1 w_1 + x_2 w_2 \tag{1}$$

The summation function is an operation utilized to compute the net input to the neural network, usually the sum of the weights. The cell's net input is computed by summing all the input values and the product of the weights of these inputs.

$$u_k = \sum_{j=1}^{m} w_{kj} x_j \tag{2}$$

The activation function determines the output the cell will produce by processing the net input and can be calculated by various formulas; some models require the derivative of this function.

$$y_k = \varphi(u_k + b_k) \tag{3}$$

The cell's output, determined by the activation function, can either serve as the neural network's output or be fed back as input to the cell itself.

$$y = f\left(net_{input}\right) \tag{4}$$

2.2. ANFIS

The ANFIS combines the advantages of two machine learning techniques. These are fuzzy logic and ANN. Systems with established input and output values can be analyzed using fuzzy logic. This allows you to optimize the modeling rule set and membership function parameters. The optimization process is performed using the ANN learning method.
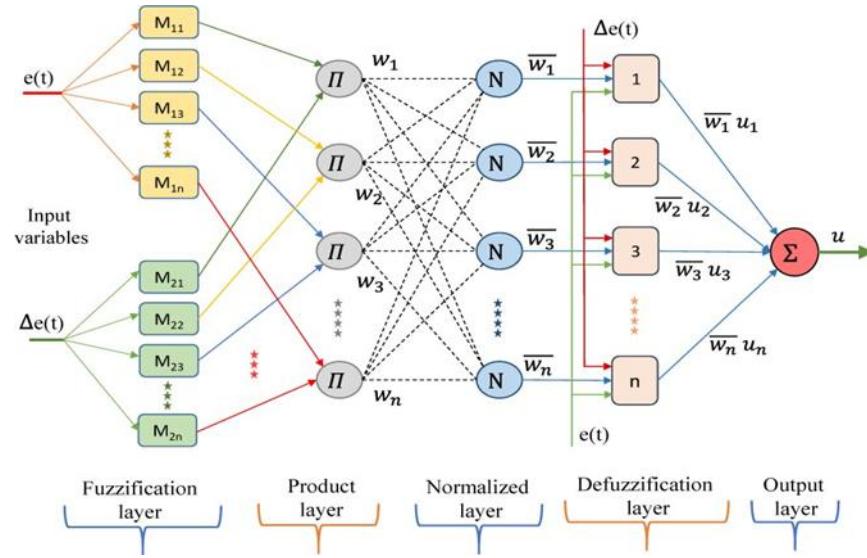
Figure 2. ANFIS

The ANFIS method utilizes input-output data to implement a fuzzy inference system, typically optimized via backpropagation or a combination of least squares and membership function parameters. During the training process, parameter optimization is typically achieved using a hybrid algorithm that combines least squares estimation with gradient descent. The parameters optimized by ANFIS are the basic parameters that determine the shape of the membership parameters.

As seen in Figure 2, the layers found are as follows respectively: In the Fuzzification layer, each node generates the membership degrees corresponding to the linguistically defined labels. The Product layer nodes multiply the membership degrees associated with the antecedent parts of the fuzzy logic rules, thereby determining the firing strength of each rule. The Normalization layer subsequently normalizes this firing strength, calculating the ratio of each rule's firing strength to the total firing strengths across all rules. The Defuzzification layer's nodes assess the contribution of each rule to the overall output, while a single node in the Output layer computes the overall output by summing the contributions from all rules.

4. DATASET

The dataset contains weather information accessed on a daily basis and published by the Macau Meteorology and Geophysics Office[27]. Based on the analysis of historical weather data, the general distribution of weather pressures is presented in the Table 2. Each feature plays an important role in forecasting weather conditions. These features provide information in fields such as climatology and meteorology.

Table 2. Definition of Variables

Variable	Description
Mean_MSL_Pressure	Average SLP
Air_Temperature_Max	Maximum air temperature
Air_Temperature_Mean	Average air temperature
Air_Temperature_Min	Minimum air temperature
Mean_Dew_Point	Average dew point
Mean_Relative_Humidity	Average relative humidity
Insolation_Duration	Duration of solar radiation
Wind_Prevailing_Direction	Prevailing wind direction
Wind_Mean_Speed	Average wind speed
Total_Precipitation	Total rainfall

Mean_MSL_Pressure is the average weight of gases in the atmosphere at sea level, used in weather forecasts. Air_Temperature_Max is the highest temperature in a time period, while Air_Temperature_Mean is the average temperature to analyze climate trends. Air_Temperature_Min is the lowest temperature for understanding cold weather and plant growth. Mean_Dew_Point measures moisture in the air. Mean_Relative_Humidity is the average humidity over time for climate understanding. Insolation_Duration is the sun's visible time influencing energy production and photosynthesis. Wind_Prevailing_Direction shows the general wind direction. Wind_Mean_Speed is the average wind speed. Total_Precipitation indicates total rainfall in a period, crucial for water management, flood risk analysis, and drought monitoring.eviews show extensive research on weather forecasting. Zhipeng Zhou et al. created a power forecasting model for photovoltaic plants based on weather conditions[20]. They used SVM, PCC, and ANN to predict sunny, cloudy, or rainy weather, aiming to enhance power generation forecasts. ANN was specifically used to optimize energy systems. Additionally, Aris Pujud Kurniawan et al. developed a weather forecasting model using fuzzy logic for agricultural automation[21]. This model uses weather, humidity, and temperature data to automate irrigation decisions, determining when crops require watering.

A statistical overview of the dataset is provided in the table below, including key variables used in the study:

Table 3. Summary Statistics of the Dataset

Variable	Mean	Standard Deviation	Min	Max
Sea Level Pressure	1012.4	3.5	1005	1020
Air Temperature	26.1	4.2	18.3	33.5
Wind Speed	3.8	1.5	0.5	7.2
Humidity	78.6	6.8	60.2	95.3

The dataset, collected from the Macau Meteorological and Geophysical Office, includes key meteorological variables such as Sea Level Pressure (SLP), Air Temperature, Wind Speed, and Humidity. The mean SLP is 1012.4 hPa with a standard deviation of 3.5, indicating minimal fluctuation in pressure levels. Air temperature averages 26.1°C, but a 4.2°C standard deviation suggests noticeable variations across different days. Wind speeds are generally low, averaging 3.8 m/s, with occasional stronger winds reaching 7.2 m/s. Humidity levels are high, with a mean of 78.6% and a maximum of 95.3%, reflecting the region's humid climate. These summary statistics help in understanding the dataset's distribution and variability, which is crucial for improving the accuracy of sea level pressure prediction models.

5. METRICS

5.1. Root Mean Squared Error (RMSE)

The RMSE is a measure that calculates the difference between model predictions and actual values. It indicates the spread of prediction errors around the regression line.

$$RMSE = \sqrt{\frac{1}{n}\sum_{i=1}^{n}(y_i - \hat{y}_i)^2}$$

(5)

The RMSE can be biased by large errors when assessing performance based on the mean of squared errors. Utilizing median or absolute error values can offer a more reliable evaluation of model performance.

5.2. Mean Absolute Percentage Error (MAPE)

The MAPE is a common metric for evaluating the accuracy of regression and time series models. It is expressed as a percentage, with lower values indicating higher accuracy. However, MAPE cannot be calculated if there is a zero between the true values, as this results in a division by zero error.

$$MAPE = \frac{1}{n}\sum_{i=1}^{n}\left|\frac{y_i - \hat{y}_i}{y_i}\right| *100$$

(6)

5.3. Determination Coefficient (R²)

The R² Value which is used for evaluation of prediction performance of the model. If the R² value is 0, then the model's prediction performance will be at it worst with all prediction values being equal to the mean of the actual dependent variable values. However, if the R² is less than zero — suggesting that our predictions perform worse on average than the mean — and those prediction values stray further from the mean, you might want to reconsider your analysis. This measure is between 0 and 1, and when the forecasts align exactly with the actual values, $R^2 = 1$. When R² equals 1, the model might simply have memorized our training data and it will performs very bad on other data. Thus, R² near 1 will tell you that your model is very good for some value of "good".You can include R² in your decision criteria if and only if you balance it out with other stuff. A negative R² hints that the predictions are probably worse than simply working incorrectly, which may suggest fundamental problems with the analysis.

$$R^2 = \frac{\sum_{i=1}^{n}(y_i - \hat{y}_i)^2}{\sum_{i=1}^{n}(y_i - \bar{y})^2}$$

(6)

6. RESULTS AND DISCUSSION

The dataset was divided into 80% for training and 20% for testing. The Artificial Neural Network (ANN) model used in this study consists of an input layer with three neurons representing air temperature, wind speed, and humidity. It includes two hidden layers, each containing ten neurons, utilizing the Rectified Linear Unit (ReLU) activation function. The output layer comprises a single neuron for predicting sea level pressure, employing a linear activation function. The model is optimized using the Adam optimizer with a learning rate of 0.001 . Training is conducted over 100 epochs with a

batch size of 32 to ensure effective learning and generalization.

To ensure balanced input data, Min-Max Scaling was applied to all numerical variables:

$$X^I = \frac{X - X_{min}}{X_{max} - X_{min}} \tag{7}$$

This transformation scales all values between 0 and 1, preventing larger numerical values (e.g., wind speed vs. humidity) from dominating the learning process.

The result is by the ANN program, which creates an ANN model and prints them out as what can be seen in Figure 3 Word output. Usually, this is the plot used to assess how well a model did in terms of predicted SLP values compared with observed data. The variation in cost over epochs, gradients and learning rate. The first gradient was equal to 3.19e+03, and our lambda reached a stopping threshold of 1.96 after epoch 35 This visualization helps to understand how the model is converging and how stable is the training process. It also gives insight into error distribution which errors are frequent and how big in size, is the errors random or any kind of bias inbuilt present in the model as well as overfitting tendency. The error histogram presented in Figure 5 shows this analysis.

Training Progress

Unit	Initial Value	Stopped Value	Target Value
Epoch	0	35	1000
Elapsed Time	-	00:00:00	-
Performance	841	7.57	0
Gradient	3.19e+03	1.96	1e-07
Mu	0.001	0.001	1e+10
Validation Checks	0	6	6

Figure 3. Visualization of ANN model predictions compared to actual Sea Level Pressure values
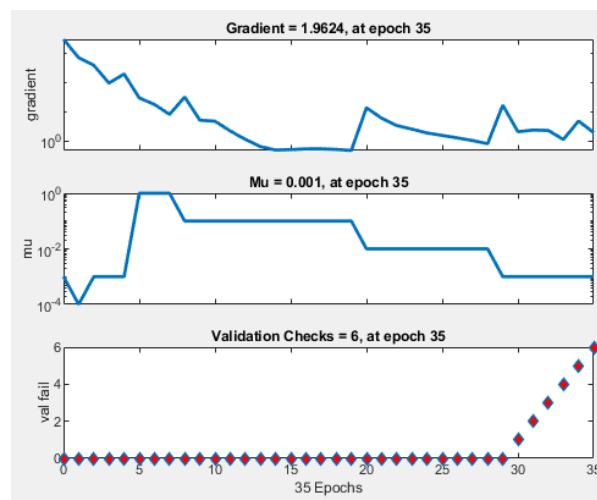
Figure 4. "Traning State" Output
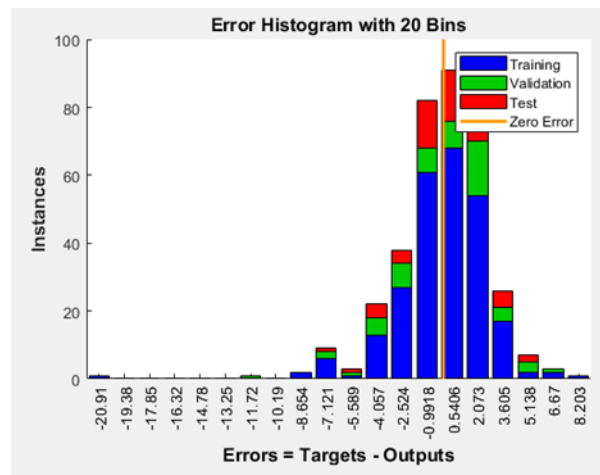
Figure 5. Distribution of prediction errors for the ANN model, showing error spread and frequency.

Figure 6 shows the performance of the ANN model on the validation set. It indicates the lowest validation error achieved at epoch 29, which is important for determining optimal model parameters. The best validation performance was 10.8. The regression output evaluates the relationship between predicted and actual target values, usually shown in regression plots with an R^2 value indicating the goodness-of-fit, demonstrating how well the model's predictions match the actual data.
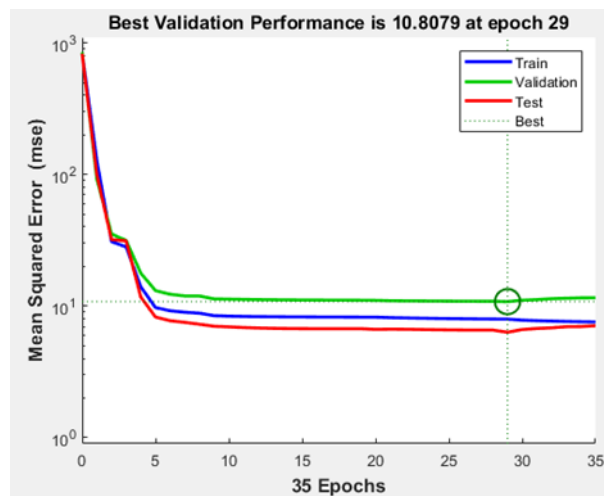
Figure 6. "Best Validation Performance" Output
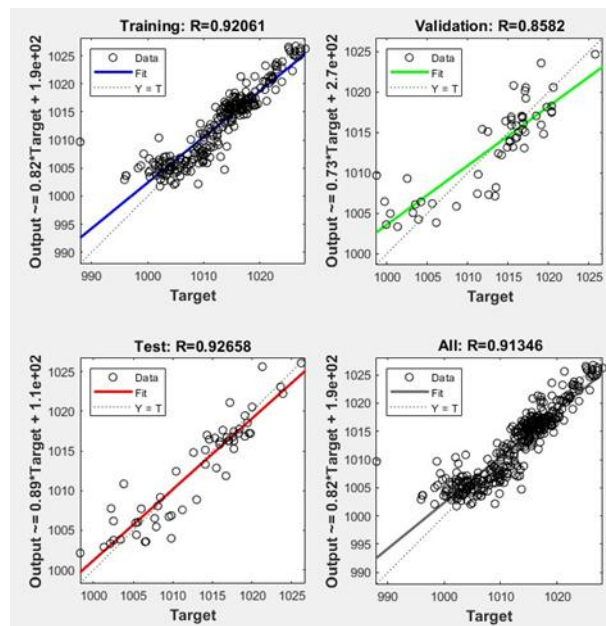
Figure 7. "Regression" Output

Figure 8 shows a comparison of error metrics (RMSE, MAPE, and R^2) for the ANN and ANFIS models, making it easier to evaluate their performance and determine the better model.

Table 3. Comparison of ANN and ANFIS Metrics

	RMSE	MAPE	R^2
ANN	2,8531	0,2024	0,8531
ANFIS	2,2181	0,1414	0,8997
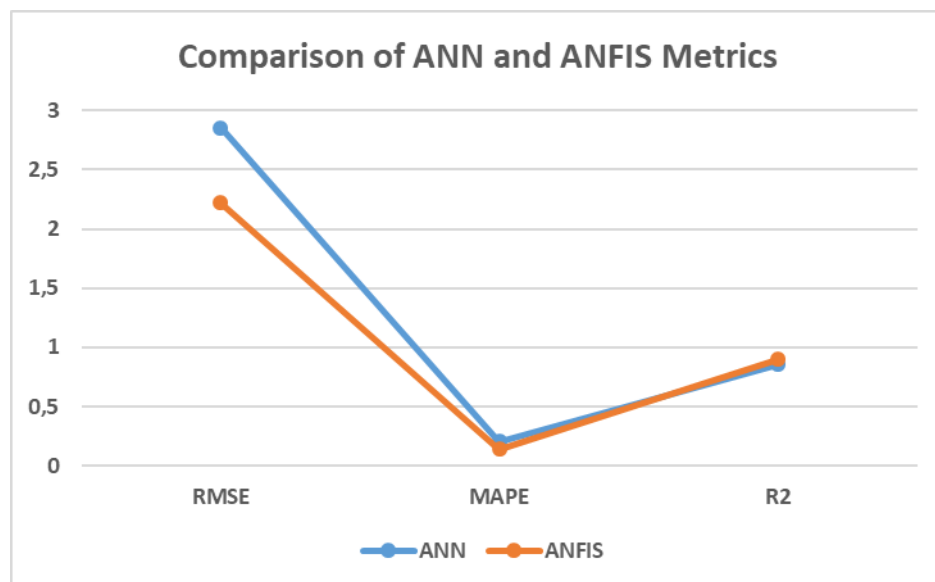
Figure 8. Comparison of RMSE, MAPE, and R^2 values for ANN and ANFIS models

To validate the performance differences between ANN and ANFIS, a paired t-test was conducted on the RMSE values. The results indicated that the performance improvement of ANFIS over ANN was statistically significant ($p < 0.05$), confirming that ANFIS provides more accurate predictions.

A detailed error analysis reveals that ANFIS outperforms ANN in sea level pressure prediction, as evidenced by a lower RMSE (2.2181) compared to ANN (2.8531), indicating higher precision. The

MAPE further supports ANFIS's superior generalization across various meteorological conditions. Additionally, the residual distribution analysis, shown in the error histogram (Figure 5), demonstrates that ANN exhibits a wider spread of errors, whereas ANFIS errors are more concentrated and smaller, highlighting its superior consistency and reliability.

Despite their advantages, both ANN and ANFIS have certain limitations. ANN is prone to overfitting, especially when training data is limited, and requires extensive hyperparameter tuning to achieve optimal performance. On the other hand, ANFIS is computationally expensive due to the complexity of fuzzy rule generation and experiences a decline in performance when handling extremely large datasets. These challenges highlight the need for careful model selection and optimization based on the specific requirements of sea level pressure prediction.

7. CONCLUSIONS AND FUTURE WORK

In this paper, the performance of ANN and ANFIS algorithms is compared for predicting SLP in Macau based on using the metrics RMSE, MAPE, and R^2. ANFIS outperforms in RMSE and R^2, while ANN and ANFIS have similar performances in MAPE. Therefore, ANFIS is the most efficient in predicting the SLP of Macau. RMSE calculates the magnitude of error that happened due to prediction. Its value of RMSE will be low for better performance. R^2 decides goodness of fit. The value of R^2 will be high for better fitting with true values. On the contrary, MAPE gives the exact measure of error than RMSE. The present study identifies the potentiality of such models in enhancing the capability of weather forecasting, disaster management, and preparedness. Techniques of ANN and ANFIS could be useful in future research for the forecast of other weather conditions.

The results of this research which investigated sea level pressure prediction in Macau using ANN and ANFIS models show potential applications beyond Macau itself. The models presented in this study can be employed in various coastal and inland regions after regional tailoring since meteorological factors affect atmospheric pressure similarly throughout different locations.The methods used in the study offer a basis for forecasting other weather components, such as temperature variations, wind patterns, and precipitation levels, which facilitates future application in climate analysis while enhancing energy management and preparedness for disasters. To ascertain these models' efficacy globally, future research should examine how well they function in diverse climatic conditions.

Declaration of Ethical Standards

The author declare compliance with all ethical standards in conducting the paper.

Credit Authorship Contribution Statement

The author was solely responsible for the conceptualization, methodology, data analysis, writing, and final approval of the manuscript.

Declaration of Competing Interest

The author declares no competing interests relevant to the content of this article.

Funding / Acknowledgements

The author declares that there is no financial support.

Data Availability

All data generated or analyzed during this study are included in the published article and are available at: https://www.smg.gov.mo/en/subpage/345/embed-path/p/query-weather-e_panel.

REFERENCES

[1]   Haykin, Simon Neural networks and learning machines / Simon Haykin. —3rd ed. p. cm. Rev. ed of: Neural networks. 2nd ed., 1999. Includes bibliographical references and index. ISBN-13: 978-0-13-147139-9

[2]   J. . -S. R. Jang, "ANFIS: adaptive-network-based fuzzy inference system," in IEEE Transactions on Systems, Man, and Cybernetics, vol. 23, no. 3, pp. 665-685, May-June 1993, doi: 10.1109/21.256541

[3]   Walia, Navneet & Singh, Harsukhpreet & Sharma, Anurag. (2015). ANFIS: Adaptive Neuro-Fuzzy Inference System- A Survey. International Journal of Computer Applications. 123. 32-38. 10.5120/ijca2015905635.

[4]   E. Özer, N. Sevinçkan and E. Demiroğlu, "Comparative Analysis of Computational Intelligence Techniques in Financial Forecasting: A Case Study on ANN and ANFIS Models," 2024 32nd Signal Processing and Communications Applications Conference (SIU), Mersin, Turkey, 2024, pp. 1-4, doi: 10.1109/SIU61531.2024.10600769.

[5]   E. Özer, "Thyroid Disease Diagnosis: A Study on the Efficacy of Feature Reduction and Biomarker Selection in Artificial Neural Network Models", IJMSIT, c. 8, sy. 2, ss. 59–62, 2024.

[6]   M. Elsisi, M. -Q. Tran, K. Mahmoud, M. Lehtonen and M. M. F. Darwish, "Robust Design of ANFIS-Based Blade Pitch Controller for Wind Energy Conversion Systems Against Wind Speed Fluctuations," in IEEE Access, vol. 9, pp. 37894-37904, 2021, doi: 10.1109/ACCESS.2021.3063053.

[7]   J. . -S. R. Jang, "Input selection for ANFIS learning," Proceedings of IEEE 5th International Fuzzy Systems, New Orleans, LA, USA, 1996, pp. 1493-1499 vol.2, doi: 10.1109/FUZZY.1996.552396

[8]   Teruko Tamura, Clothing as a Mobile Environment for Human Beings, Journal of the Human-Environment System, 2007, Volume 10, Issue 1, Pages 1-6, Released on J-STAGE December 20, 2007, Online ISSN 1349-7723, Print ISSN 1345-1324, https://doi.org/10.1618/jhes.10.1,

[9]   Betsill, M. M. (2001). Mitigating Climate Change in US Cities: Opportunities and obstacles. Local Environment, 6(4), 393–406. https://doi.org/10.1080/13549830120091699

[10]   Valdivieso, P., Andersson, K.P. & Villena-Roldán, B. Institutional drivers of adaptation in local government decision-making: evidence from Chile. Climatic Change 143, 157–171 (2017). https://doi.org/10.1007/s10584-017-1961-9

[11]   Q. Fu, D. Niu, Z. Zang, J. Huang and L. Diao, "Multi-Stations' Weather Prediction Based on Hybrid Model Using 1D CNN and Bi-LSTM," 2019 Chinese Control Conference (CCC), Guangzhou, China, 2019, pp. 3771-3775, doi: 10.23919/ChiCC.2019.8866496.

[12]   Information guide of prediction and warning service of Czech Hydrometeorological Institute for water managers: Flash floods and possibilities of their prediction - Formation of flash floods [online],Available:http://portal.chmi.cz/files/portal/docs/poboc/CB/pruvodce/pruvodce_vodohos podari_ffg. html. [Accessed: 01-Nov-2024].

[13]   Flash Flood Guidance, Flood Forecast Service of Czech Hydrometeorological Institute. Available : http://hydro.chmi.cz/hpps/main_rain.php?mt=ffg. [Accessed: 10-Nov-2024].

[14]   Mcgovern, Amy & Elmore, Kimberly & Gagne, David & Haupt, Sue & Karstens, Christopher & Lagerquist, Ryan & Smith, Travis & Williams, John. (2017). Using Artificial Intelligence to Improve Real-Time Decision-Making for High-Impact Weather. Bulletin of the American Meteorological Society. 98. 10.1175/BAMS-D-16-0123.1.

[15]   IPCC AR4 WG1, Technical Summary, section TS 5.3. 1997-2017 Available at: https://wg1.ipcc.ch/publications/wg1-ar4/ar4-wg1-ts.pdf. [Accessed: 15-Nov-2024].

[16]   Bernauer, Thomas, "Climate Change Politics",Annual Review of Political Science, 2013, doi.org/10.1146/annurev-polisci-062011-154926

[17]   J. Lu, G. Vecchi, A., and T. Reichler, "Expansion of the Hadley cell under global warming". Geophysical Research Letters. 2007, 34 (6). DOI:10.1029/2006GL028443.

[18]   Bhaskaran K, Hajat S, Haines A, Herrett E, Wilkinson P, Smeeth L. Effects of ambient temperature on the incidence of myocardial infarction. Heart. 2009 Nov;95(21):1760-9. doi:

10.1136/hrt.2009.175000. Epub 2009 Jul 26. PMID: 19635724.

[19]   Wichmann, J., Ketzel, M., Ellermann, T. et al. Apparent temperature and acute myocardial infarction hospital admissions in Copenhagen, Denmark: a case-crossover study. Environ Health 11, 19 (2012). https://doi.org/10.1186/1476-069X-11-19

[20]   Z. Zhou, L. Liu and N. Y. Dai, "Day-ahead Power Forecasting Model for a Photovoltaic Plant in Macao Based on Weather Classification Using SVM/PCC/LM-ANN," 2021 IEEE Sustainable Power and Energy Conference (iSPEC), Nanjing, China, 2021, pp. 775-780, doi: 10.1109/iSPEC53008.2021.9735777.

[21]   A. P. Kurniawan, A. N. Jati, and F. Azmi, 'Weather prediction based on fuzzy logic algorithm for supporting general farming automation system', in 2017 5th International Conference on Instrumentation, Control, and Automation (ICA), 2017, pp. 152–157.

[22]   A. Y. Ardiansyah, R. Sarno and O. Giandi, "Rain detection system for estimate weather level using Mamdani fuzzy inference system," 2018 International Conference on Information and Communications Technology (ICOIACT), Yogyakarta, Indonesia, 2018, pp. 848-854, doi: 10.1109/ICOIACT.2018.8350711.

[23]   A. H. Setyaningrum and P. M. Swarinata, "Weather prediction application based on ANFIS (Adaptive neural fuzzy inference system) method in West Jakarta region," 2014 International Conference on Cyber and IT Service Management (CITSM), South Tangerang, Indonesia, 2014, pp. 113-118, doi: 10.1109/CITSM.2014.7042187.

[24]   D. Munandar, "Optimization weather parameters influencing rainfall prediction using Adaptive Network-Based Fuzzy Inference Systems (ANFIS) and linier regression," 2015 International Conference on Data and Software Engineering (ICoDSE), Yogyakarta, Indonesia, 2015, pp. 1-6, doi: 10.1109/ICODSE.2015.7436990.

[25]   P. G. Krishna, K. Chandra Bhanu, S. A. Ahamed, M. Umesh Chandra, N. Prudhvi and N. Apoorva, "Artificial Neural Network (ANN) Enabled Weather Monitoring and Prediction System using IoT," 2023 International Conference on Intelligent Data Communication Technologies and Internet of Things (IDCIoT), Bengaluru, India, 2023, pp. 46-51, doi: 10.1109/IDCIoT56793.2023.10053534.

[26]   K. B. Maheswari and S. Gomathi, "Analyzing the Performance of Diverse Deep Learning Architectures for Weather Prediction," 2023 5th International Conference on Inventive Research in Computing Applications (ICIRCA), Coimbatore, India, 2023, pp. 738-746, doi: 10.1109/ICIRCA57980.2023.10220887.

[27]   Macao Meteorological and Geophysical Bureau. (2021, Jan.) Query observation data. [Online]. Available: https://www.smg.gov.mo/en/subpage/345/embed-path/p/query-weather-e_panel. [Accessed: 17-Nov-2024].

EFFECT OF GRAPHITE AND MAX PHASE ON THE THERMAL AND DIELECTRIC PROPERTIES OF N-VINYL CARBAZOLE AND BENZYL METHACRYLATE COPOLYMER

1, * Esra BARIM [iD] , **2 Emrah GUNDOGDU** [iD]

1 Munzur University, Vocational School of Tunceli, Tunceli, TÜRKİYE
2 Munzur University, Munzur University Institute of Sciences, Tunceli, TÜRKİYE
[1]esrabarim@munzur.edu.tr, [2]emrahgundogdu62@gmail.com

Highlights

- A copolymer containing NVC and BZMA monomers was synthesized and its composites with graphite/Ti_3AlC_2 (MAX phase) were made and characterized.

- The effects of graphite/MAX phase on the thermal and electrical behaviour of the copolymer were investigated.

- The glass transition temperature of the copolymer increased in direct proportion to the doped graphite/MAX phase content.

- .Two of the composites were evidenced to be semiconductors by their electrical behaviour.

- The dielectric performance of copolymer was improved with graphite/MAX phase for use as functional components in energy storage devices

Graphical Abtract

*Corresponding Author: Esra BARIM, esrabarim@munzur.edu.tr

EFFECT OF GRAPHITE AND MAX PHASE ON THE THERMAL AND DIELECTRIC PROPERTIES OF N-VINYL CARBAZOLE AND BENZYL METHACRYLATE COPOLYMER

[1], * Esra BARIM [ID], [2] Emrah GUNDOGDU [ID]

[1] *Munzur University, Vocational School of Tunceli, Tunceli, TÜRKİYE*
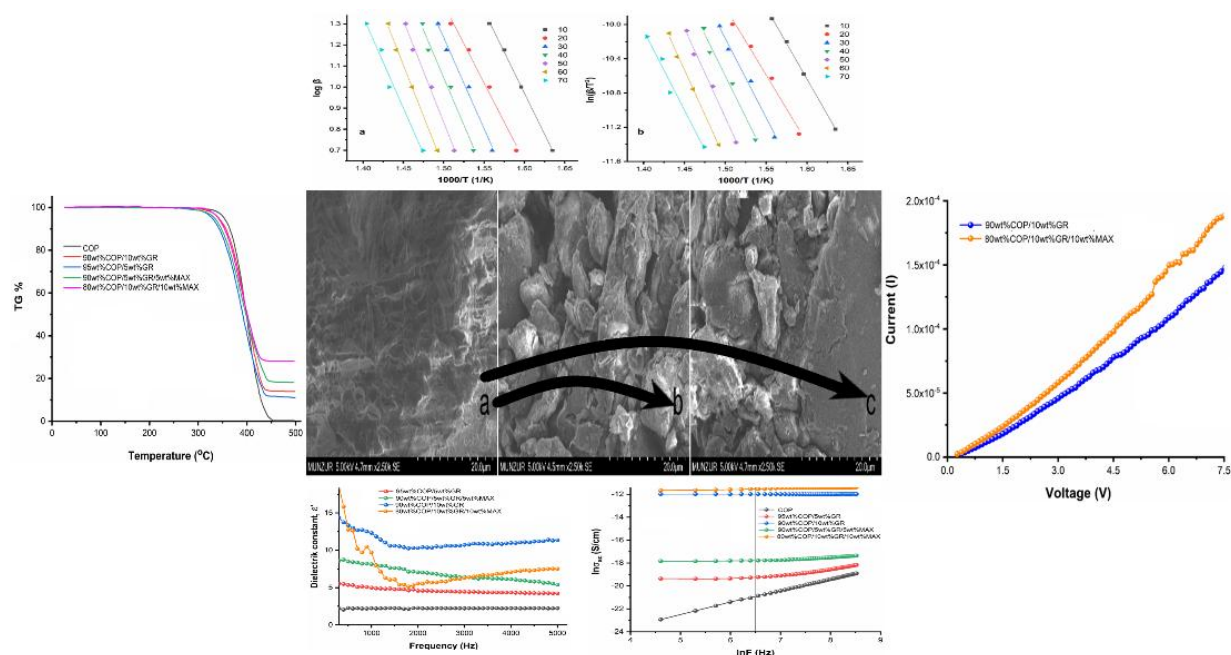[2] *Munzur University, Munzur University Institute of Sciences, Tunceli, TÜRKİYE*
[1]esrabarim@munzur.edu.tr, [2]emrahgundogdu62@gmail.com

ABSTRACT: In this study, the P(N-vinyl carbazole-co-benzyl methacrylate) copolymer was synthesized, characterized by FT-IR/^{1}H-NMR spectroscopic methods, and its composition was calculated from ^{1}H NMR spectra. Composites of the copolymer with four different ratios of graphite (GR) and MAX phase (Ti_3AlC_2) by weight were prepared to obtain functional and novel electronic components for energy storage applications. Scanning electron microscopy, X-ray diffraction analyses were performed for some samples. Differential scanning calorimetry, thermogravimetric analysis curves were used to determine the thermal behavior of the materials. It was concluded that the composite with the highest glass transition temperatures and thermal stability was the composite with 10wt%GR/10wt%MAX additive. The thermal degradation kinetics of the copolymer and the composite containing 10wt%GR/10wt%MAX were investigated by applying the Flynn-Wall-Ozawa (FWO), Kissinger-Akahira-Sunose (KAS) methods and it was found that the thermal degradation activation energy of the composite was lower than that of the polymer. The dielectric properties of the materials were investigated at room temperature and between 0.1 kHz and 5 kHz. At 1 kHz the dielectric constants of the copolymer and 10wt%GR-doped composite were found to be 2.22 and 12.31, respectively. The composites doped with 10wt%GR and 10wt%GR/10wt%MAX were confirmed to be semiconductors.

Keywords: N-Vinylcarbazole, Benzyl Methacrylate, Graphite, MAX, Composite, Activation Energy, Dielectric

1. INTRODUCTION

Polymers, as cornerstones of materials science, have facilitated innovations that touch every aspect of our lives at all times. The use of polymers in combination with other organic and inorganic materials to improve the properties of the materials has led to the growth of composite studies. Composite materials are the focus of much scientific research due to their outstanding properties such as thermal resistance and conductivity [1-3]. Polymer composites are materials consisting of a polymer matrix reinforced with other materials known as fillers or reinforcing materials. The polymer matrix provides a stable structure, while the reinforcements offer specific mechanical, thermal, or electrical properties. These composites have found applications in optoelectronic devices, energy storage applications, the chemical industry, and many other sectors [4-8].

N-vinyl carbazole (NVC) and benzyl methacrylate (BZMA) monomers are frequently used in copolymerization and composite studies due to their unique properties. NVC, valued for its molecular ordering, is a significant monomer in materials science. It enables the synthesis of novel and functional polymers through addition polymerization with compatible monomers. The carbazole ring in the structure of NVC promotes π-conjugation within the polymer, enhancing its optical and electronic properties. P(NVC), the polymer derived from this monomer, has broad applications in organic solar cells, coatings, lenses, sensors, photovoltaic devices, and electroluminescent devices within the polymer industry as a result of its photophysical properties [9, 10]. Despite its widespread use, P(NVC) has limitations that affect its suitability for certain applications. Its low dielectric constant of approximately 3 [11-13] restricts its potential in energy storage applications, while its high glass transition temperature (Tg) of about 227 °C [14] limits its processability. These characteristics are significant drawbacks preventing

Corresponding Author: Esra BARIM, esrabarim@munzur.edu.tr

P(NVC) from broader use as a polymeric material [11, 14]. The dielectric properties of materials can be suitable for some applications and limiting for others. For example, In general materials with low dielectric constants are used for electronic packaging systems and materials with high dielectric constants are used for energy storage devices [15, 16]. The dielectric properties strongly depend on ambient properties such as temperature, frequency, etc., as well as the percentage of the composition of the copolymer [17]. To address these limitations of P(NVC), which is notable for its thermal stability and optical and dielectric properties [18, 19], researchers have explored various copolymers and composites. For example, Bilbao et al. synthesized NVC copolymers with different acrylate and methacrylate monomers [20], Haldar et al. developed P(NVC)/Fe3O4 composites [21], Sonone et al. investigated P(NVC)/TiO2 composite films [22], and Goumri et al. studied P(NVC)/graphene oxide composites [23]. Recently, Muntaser et al. reported that P(NVC)/polyvinyl chloride (PVC)/ZnO nanocomposite films exhibited enhanced thermal stability and dielectric-conductivity properties [24]. Duran et al. examined P(NVC)/TiO2 composites and reported their suitability as corrosion-resistant coating materials [25]. Research on P(NVC) is ongoing [26-28]. The BZMA monomer is a methacrylic monomer containing a phenyl group in its structure. Although widely applied in various fields [29-32], BZMA has primarily been used in copolymerization studies to impart thermal functionality [33]. For instance, Xie et al. synthesized copolymers with varying BZMA and MMA compositions in microsphere form, highlighting that properties such as thermal stability and glass transition temperature (Tg) can be adjusted based on the monomer's composition [29]. Demirelli et al. reported that the dielectric constant of P(BZMA) was 3.22, with a Tg of 73 °C at 1 kHz at room temperature. They prepared composites of BZMA with lactone end groups and graphene, observing that the composite's thermal stability increased while Tg decreased in parallel with the amount of graphene added [33, 34].

Graphite (GR), a widely preferred reinforcement material in recent polymer composite studies, is an allotrope of carbon known for its excellent electrical conductivity due to delocalized electrons within its structure. Graphite's durability in terms of thermal properties also makes it suitable for various industrial applications [35]. Consequently, it is often chosen in composite studies to enhance the dielectric, electrical, and thermal properties of materials [36-38]. Another reinforcement material gaining popularity in recent years is the MAX phase. The MAX phase is a three-layered compound with the general formula Mn+1AXn, where M is a transition metal, A is a group A element, X is carbon or nitrogen, and n ranges from 1 to 3. MAX phases are named based on the value of n; for example, Ti3AlC2 is referred to as a 312 MAX phase [39]. MAX phases are ideal for various structural applications in industry due to their resistance to high temperatures and corrosion. Additionally, their metallic conductivity makes them suitable for electrical contacts, sensors, and electronic devices [40-44].

This study aimed to develop functional semiconducting polymer composite systems with enhanced thermal stability, processability, and specific dielectric and electrical properties suitable for energy storage applications in various devices. For this purpose, a copolymer was synthesized from NVC-BZMA monomers. Composites of this polymer with reinforcement materials, namely GR and/or a MAX phase (Ti3AlC2), were prepared in four different weight ratios. The thermal, dielectric, and electrical properties of the polymer and its composites were then investigated. The results indicated that the reinforcing materials had a substantial thermal impact on the polymer system and significantly improved its dielectric and electrical properties.

2. MATERIALS AND METHODS

The monomers used for copolymer synthesis were N-vinyl carbazole (193.244 g/mol) and benzyl methacrylate (176 g/mol), with azobisisobutyronitrile (AIBN) as the initiator for the polymerization reaction. All reagents were obtained from Sigma-Aldrich. N-vinyl carbazole was purified by crystallization in methanol and used. Benzyl methacrylate was purified by washing with sodium hydroxide, and AIBN was purified by crystallization in chloroform. Analytically pure solvents including 1,4-dioxane (Sigma-Aldrich), dichloromethane (Merck), and ethyl alcohol (Sigma-Aldrich) were used in the study. Nitrogen gas was introduced during the polymerization reaction to eliminate oxygen radicals,

while graphite (GR; <20 μm Sigma Aldrich) and the MAX phase (Ti₃AlC₂; ≤100 μm particle size, Sigma-Aldrich) were used as reinforcement materials in the composite preparation stage. For sonication during composite preparation, an FY-US-01 FYtronix digital ultrasonic homogenizer was employed. Fourier transform infrared (FT-IR) spectra were obtained using a PerkinElmer Spectrum 100 model FT-IR spectrophotometer and ^{1}H NMR spectra was recorded on a Bruker Avance 300 MHz NMR instrument in CDCl₃ solvent. X-ray diffraction (XRD) data were acquired in the range of 10–90° at 2θ using a Rigaku Miniflex600 X-ray diffractometer device and scanning electron microscopy (SEM) images were captured with a Hitachi SU3500 device. TGA curves for the copolymer and composites were obtained by heating from room temperature to 500 °C in aluminum containers at a rate of 10 °C/min in a nitrogen gas atmosphere using a Shimadzu TGA-50 device. DSC analysis of the polymer and composites was conducted using a Shimadzu DSC-60A device in the range of 25 °C to 250 °C. For dielectric measurements, a QuadTech 7600 LRC impedance analyzer was used.

2.1. Synthesis of the Copolymer

The P(N-vinyl carbazole-co-benzyl methacrylate) copolymer was synthesized via the free radical polymerization method. 6 mmol NVC and 4 mmol BZMA monomers were placed in a polymerization tube together with AIBN at a rate of 1% of the total weight of the monomers, dissolved in 1,4-dioxane solvent. The solution in the polymer tube was passed through nitrogen gas for five minutes and then the cap was closed. The polymerization reaction was conducted in an oil bath at 70 °C for 12 hours. Ethyl alcohol was used to precipitate the resulting polymer and this process was repeated three times to ensure complete removal of any residual monomer. The final product was obtained as a white solid. The P(N-vinyl carbazole-co-benzyl methacrylate) copolymer, designated as COP, was then dried in a vacuum oven at 40 °C for 24 hours. FT-IR and ^{1}H NMR spectroscopy were used for structural characterization. The synthesis scheme of the copolymer is shown in Figure 1.
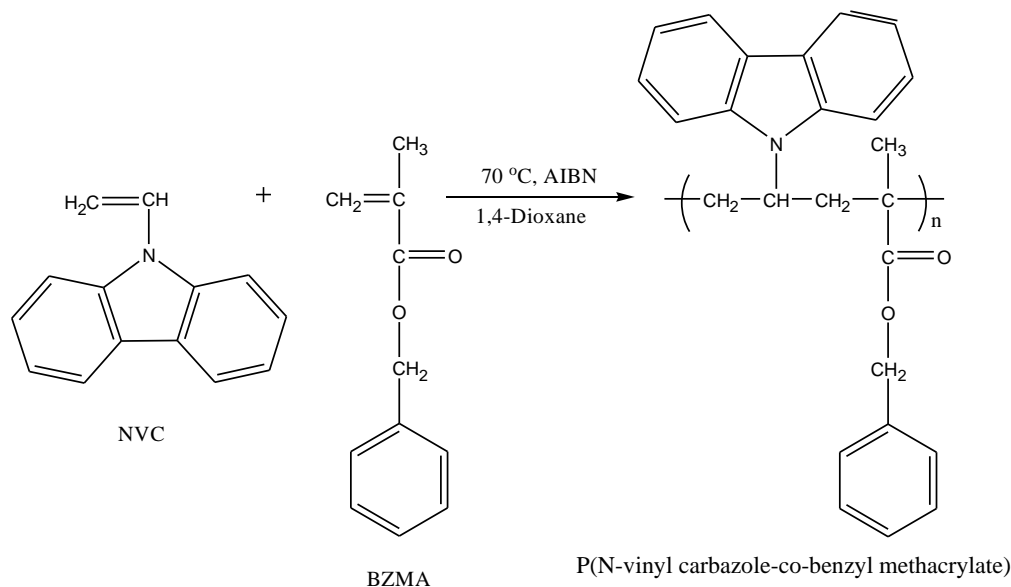
Figure 1. Synthesis scheme of P(N-vinyl carbazole-co-benzyl methacrylate) (COP) copolymer

2.2. Preparation of COP/Graphite/MAX Composites

All composites were prepared by the solvent casting method in three steps using dichloromethane as the solvent. COP was used as the polymer matrix, while graphite (GR) and MAX (Ti₃AlC₂) served as the reinforcement materials. In the first step, the specified amount of copolymer was dissolved in a beaker

containing solvent. In the second step, the reinforcement material, weighed at a specific ratio relative to the polymer matrix, was dispersed in a separate beaker with solvent for 1 hour. In the final step, the dispersed reinforcement material was added to the polymer solution, and the solvent was removed using an evaporator. The resulting composite materials were first air-dried and then placed in a vacuum oven at 40 °C until they reached a constant weight. The composites were designated as 95wt%COP/5wt%GR, 90wt%COP/10wt%GR, 90wt%COP/5wt%GR/5wt%MAX, and 80wt%COP/10wt% GR/10wt% MAX. This nomenclature is based on the amount of material used by weight when preparing the composites. For example, the first sample was prepared using 95 mg copolymer and 5 mg graphite.

3. FINDINGS AND DISCUSSION

3.1. FT-IR analysis

In the FT-IR spectrum of the COP polymer shown in Figure 2, peaks at 3032 and 3064 cm^{-1} correspond to aromatic C-H stretching vibrations, while peaks at 2937–2978 cm^{-1} correspond to aliphatic C-H stretching vibrations. The 1721 cm^{-1} peak indicates the ester carbonyl group, the 1450 cm^{-1} peak is associated with C=C stretching vibrations in the aromatic ring, the 1331 cm^{-1} peak is attributed to vinylidene, and the 1158–1220 cm^{-1} peaks correspond to the (-C=O)-O-C group. The 694 cm^{-1} peak is attributed to C-H stretching vibrations of monosubstituted benzene rings [45-47]. No functional groups related to graphite were observed in the FT-IR spectrum [48]. Additionally, the absence of a peak around 1635 cm^{-1} corresponding to the CH$_2$=CH- structure from the monomers confirms the formation of the copolymer. The FT-IR spectra of the composites exhibit all the peaks observed in the copolymer spectrum. However, in the composite spectra, the copolymer peaks show a shift to lower wave numbers and are broadened due to the influence of the reinforcing materials. This may be due to the interactions between the polymer matrix and the reinforcing material graphite. This shift indicates successful doping of the composite [36, 49, 50].
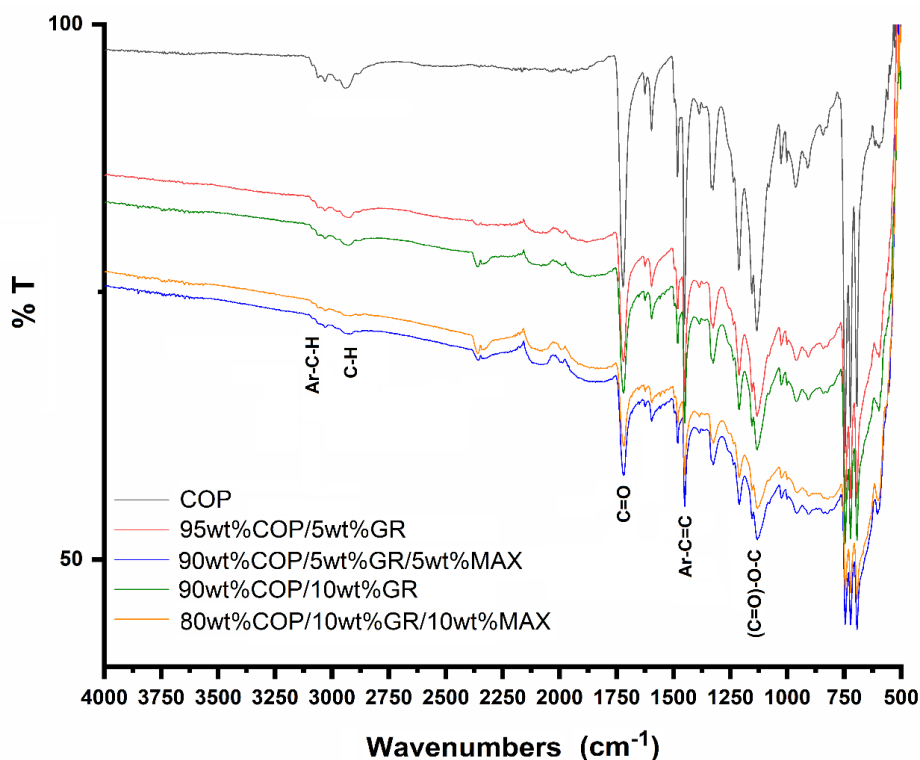
Figure 2. FT-IR spectrum of COP and its composites

3.2. ¹H NMR analysis and composition determination of the COP copolymer

In the ¹H NMR spectrum of the copolymer shown in Figure 3, the peaks between 0.3 and 1.6 ppm correspond to the -CH$_3$ and -CH$_2$ protons in the polymer chain, the peak at 4.8 ppm represents the -O-CH$_2$ protons of the BZMA monomer, and the peaks between 6.5 and 8 ppm indicate protons associated with the aromatic rings of the NVC and BZMA monomers [45]. The presence of signals characteristic of the copolymer structure and the absence of signals for vinylic protons at 6.5 and 5.5 ppm confirm the successful synthesis of the copolymer.
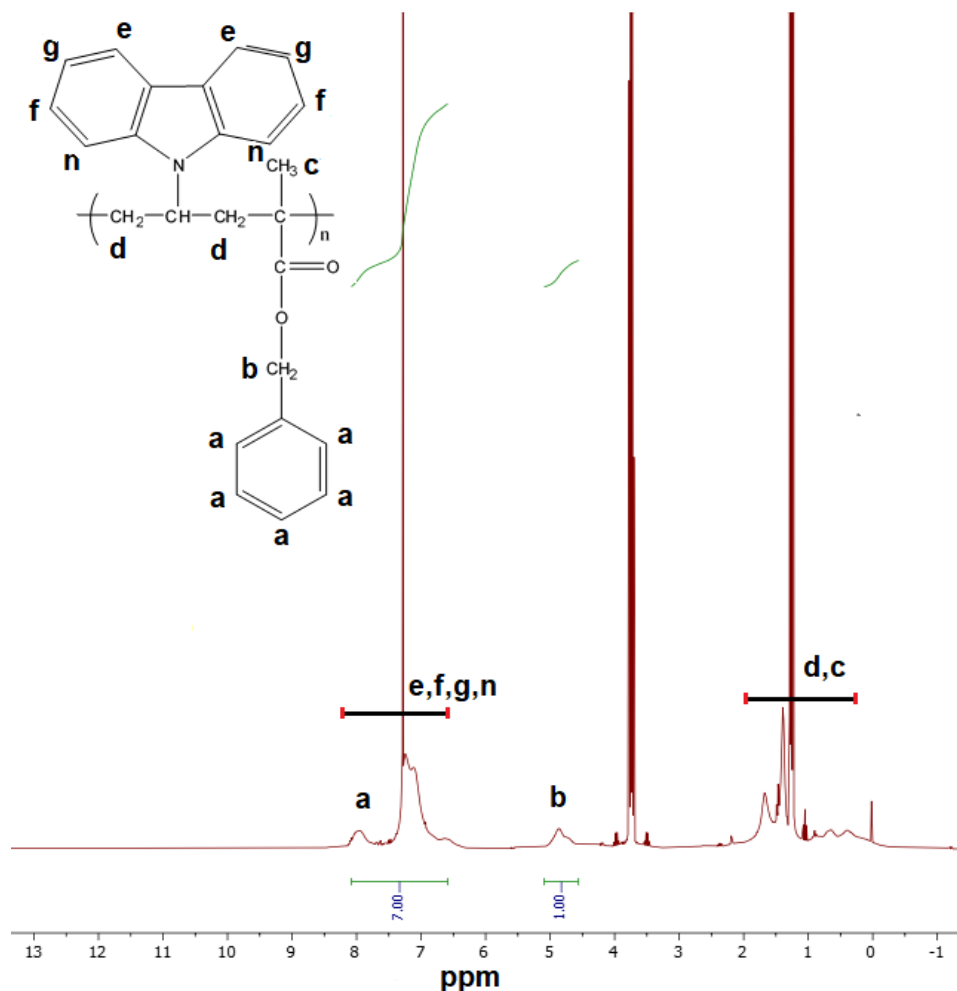
Figure 3. ¹H NMR spectrum of COP polymer

The percentage composition of the copolymer was determined based on the ¹H NMR spectrum. Integral heights of the aromatic ring protons of the NVC and BZMA units, as well as the O-CH$_2$ protons of the BZMA units in the copolymer, were used in the calculation. Equations 1 and 2 were applied to calculate the copolymer composition.

$$\frac{Integral\ height\ of\ aromatic\ protons}{Integral\ height\ of\ OCH_2\ protons} = \frac{8m_1 + 5m_2}{2m_2} = \frac{7}{1} \tag{1}$$

$$m_1 + m_2 = 1 \tag{2}$$

Here, m_1 is the mole fraction of NVC units in the copolymer and m_2 is the mole fraction of BZMA units. According to the calculations, the composition of the COP copolymer consisted of 53% NVC units and 47% BZMA units.

3.3. XRD analysis

XRD analyses of the 90wt%COP/10wt%GR and 80wt%COP/10wt%GR/10wt%MAX composites shown in Figure 4. In the spectrum of the 90wt%COP/10wt%GR composite in Figure 4a, graphite (Card number, 9011577) produced a signal at 2θ = 54.45° (001) with the strongest signal at 2θ = 26.5° (002) [51]. Figure 4b displays the XRD spectrum of the 80wt%COP/10wt%GR/10wt%MAX composite, with signals observed at 2θ = 9.50° (002), 19.08° (004), 26.5°(002), 33.9° (101), 36.6° (103), 38.9° (104), 41.6° (105), 54.7° (004), 60.04° (110), 65.32° (1011), 73.76° (118). At 26.5° the signal correspond to graphite (Card number, 9012230), while the MAX phase (Card number 7221324) gives its most characteristic signal at 38.9° [52, 53]. The broad signal in the range of 19.08° to 28.79° is due to the amorphous structure of the polymer [54].
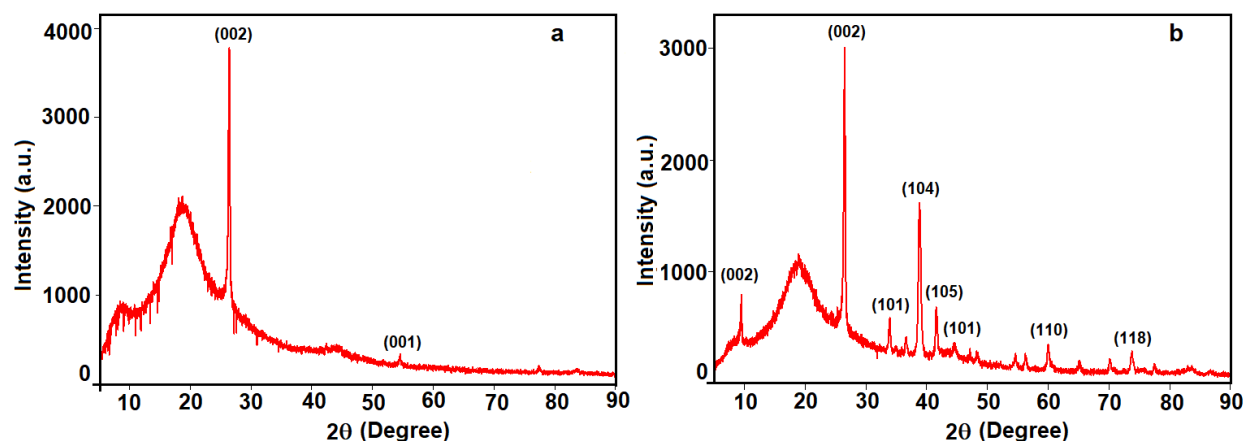
Figure 4. XRD spectra of a) 90wt%COP/10wt%GR b) 80wt%COP/10wt%GR/10wt%MAX

3.4. SEM analysis

SEM images of the surface morphologys of pure polymer and some of its composites of the surface morphologys were showed in Figure 5. It was observed that the copolymer, which initially exhibited a surface that appeared as if it had pores, lost this appearance after doping and generally turned into a rough, tightly packed structure [52]. Comparing the surface morphologies of the composites with the SEM images of the copolymer reveals significant changes, indicating successful doping.
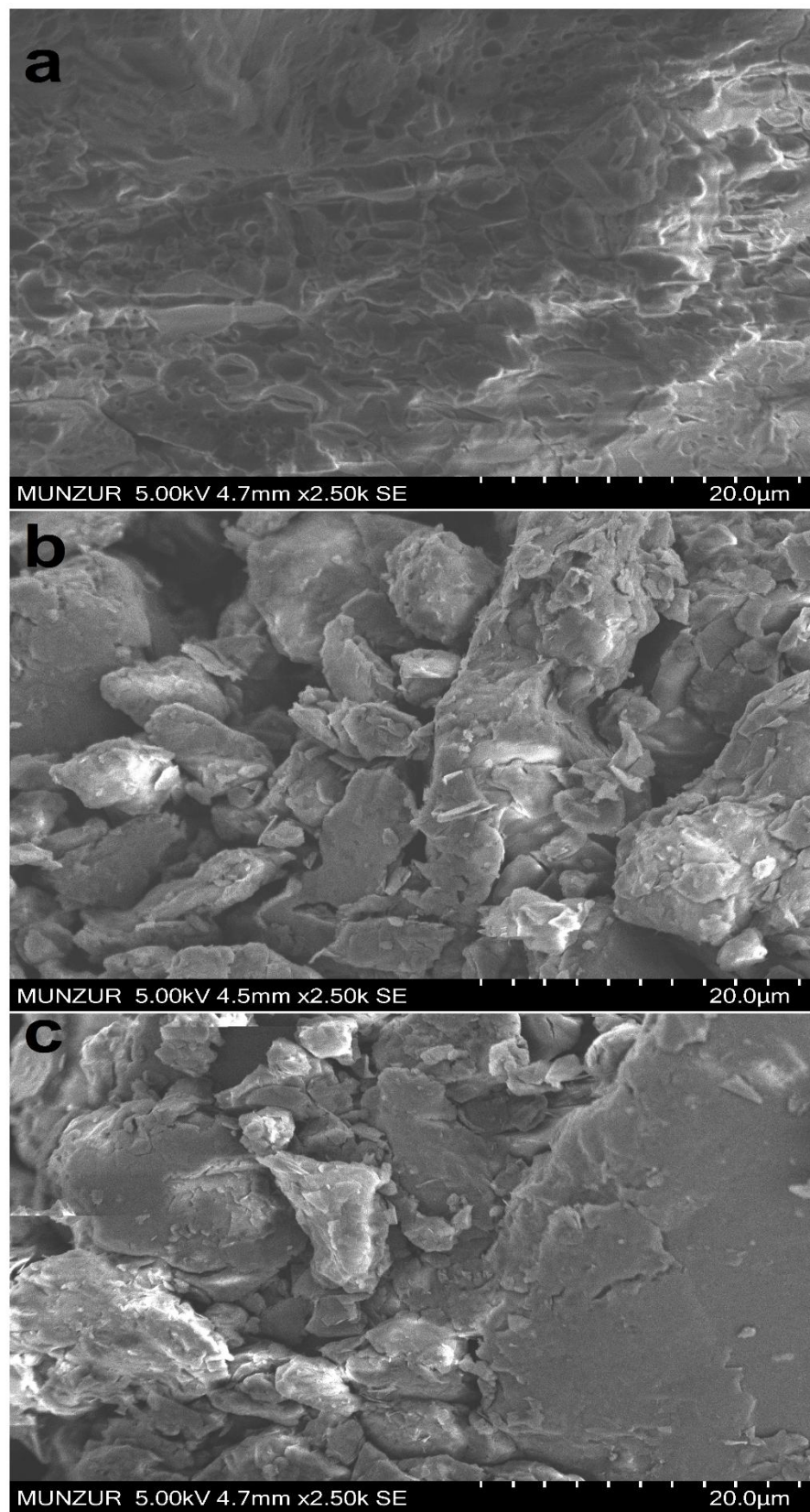
Figure 5. SEM micrographs of a) COP, b) 90wt%PCOP/10wt%GR, and c)
80wt%COP/10wt%GR/10wt%MAX

3.5. Thermal Analysis

3.5.1. DSC analysis

DSC analysis of the polymer and composites shown in Figure 6. Glass transition temperatures (Tg) are provided in Table 1. The Tg values of the polymer and composites whose DSC curves are displayed in Figure 6 fall within the Tg range of P(NVC) (227 °C) and P(BZMA) homopolymers (73 °C). The Tg value of COP polymer is 101.74 °C. It was observed that the Tg values of the composites increased by approximately 2 °C compared to the polymer alone. These increases in Tg were noted to occur with progressively higher concentrations of GR and/or MAX. While 5 wt%GR doping raised the Tg value of the polymer by 0.37 °C, both GR and MAX phase doping resulted in an increase exceeding 1.7 °C. Changes in Tg values in amorphous polymers are associated with the mobility or flexibility of polymer chains [55]. The higher Tg values observed in composites compared to polymer are attributed to the influence of reinforcement materials on the polymer chain. This effect is due to the reinforcement materials restricting polymer chain mobility, thereby reducing the polymer's free volume and raising the glass transition temperatures [56].
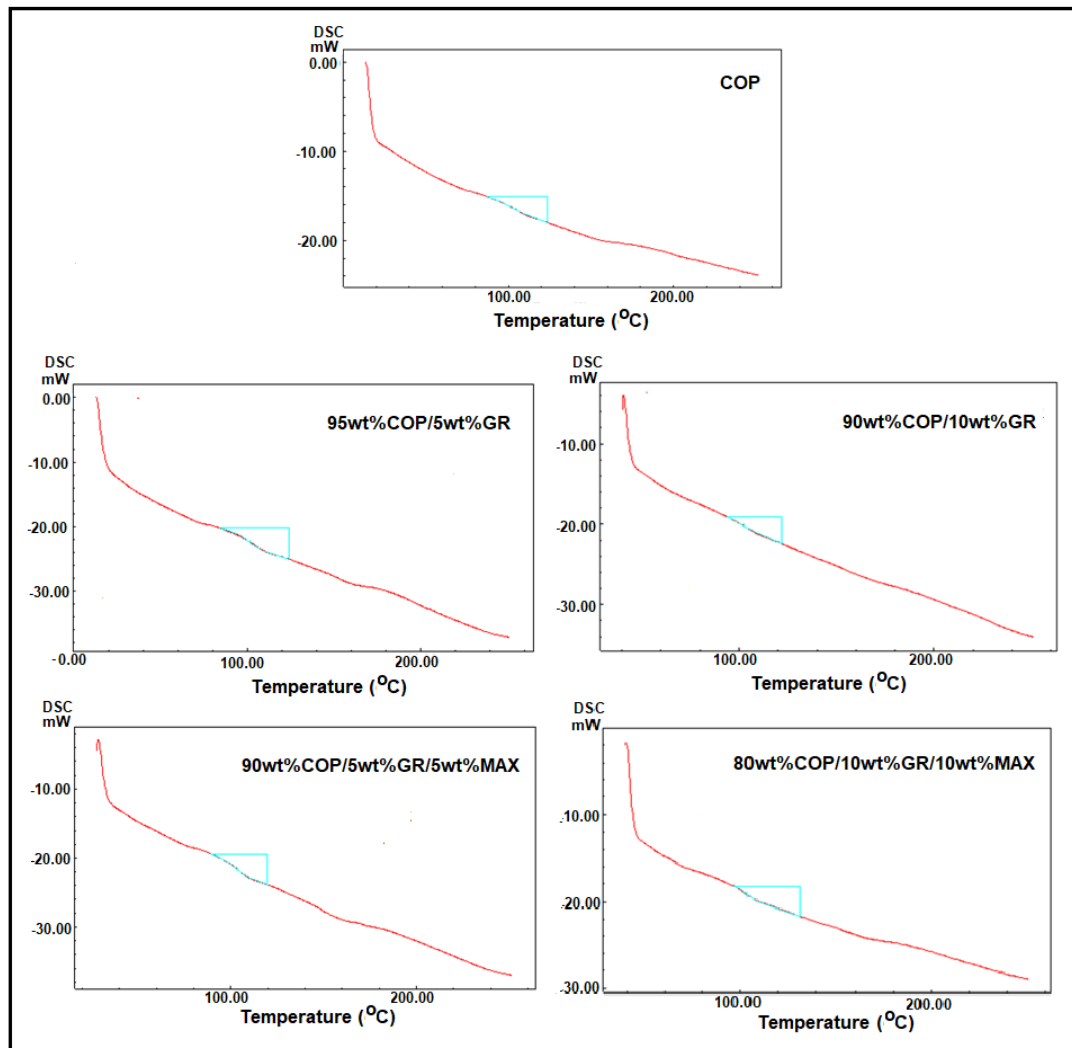
Figure 6. DSC curves of COP and composites

Table 1. Tg values of polymer and composites

Polymers and composites	Tg (°C)
COP	101.74
95wt%COP/5wt%GR	102.11
90wt%COP/10wt%GR	102.72
90wt%COP/5wt%GR/5wt%MAX	103.50
80wt%COP/10wt%GR/10wt%MAX	103.70

3.5.2. TGA analysis

TGA curves for the copolymer and composites shown in Figure 7. Thermal data calculated from the TGA thermograms are presented in Table 2. The initial decomposition temperature of the copolymer was 330 °C, while it decreased across all composites. Adding 5wt%GR to the polymer reduced the initial decomposition temperature by 39 °C, and the inclusion of 10wt%GR and 10wt%MAX lowered it by 12 °C. Generally, to assess the thermal stability of polymeric materials, temperature values indicating 50% weight loss are examined [57]. Doping of 10wt%GR and 10wt%GR/10wt%MAX improved the thermal stability of the polymer by 0.5 °C and 3 °C, respectively. These increases may have resulted from strong interfacial interactions of GR and MAX with the polymer matrix [58]. The composite with the highest thermal stability (401.5 °C) was the one doped with 10wt%GR and 10wt%MAX. Furthermore, the residue content of the composites increased with higher amounts of GR and MAX, both of which are highly resistant to heat, indicating that the composite with the highest GR and MAX content also had the greatest residual weight.
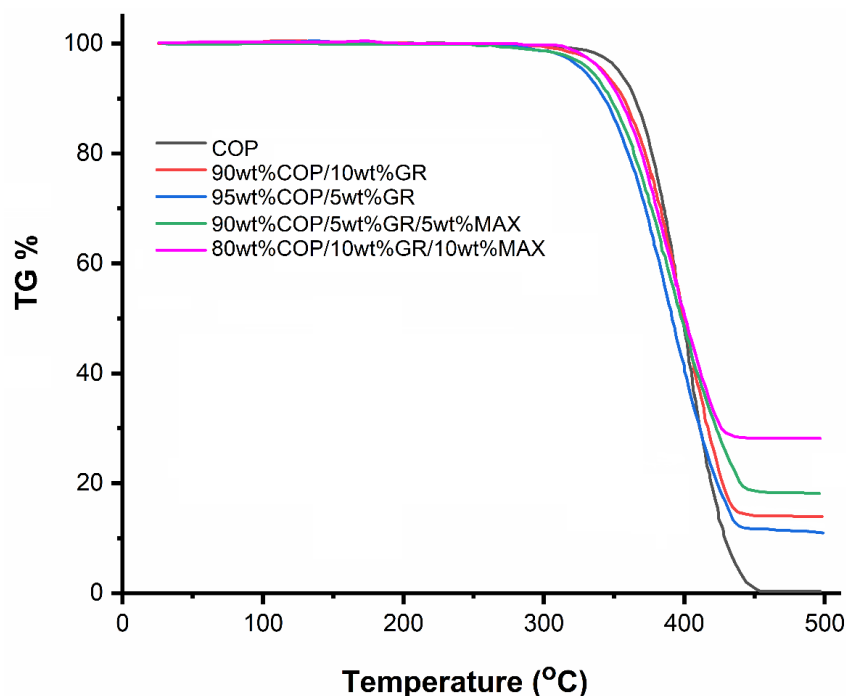
Figure 7. TGA curves of polymer and composites at 10 °C/min

Table 2. Thermal data of polymer and composites at 10 °C/min heating rate

Polymer and Composites	T_{int} (°C)	%10	%30	%50	%70	%90	% Residue at 500 °C
COP	330	365.0	386.0	398.5	411.0	424.0	-
95wt%COP/5wt%GR	291	343.5	372.0	390.5	411.0	-	11.56
90wt%COP/10wt%GR	307	357.0	383.0	399.0	418.0	-	13.76
90wt%COP/5wt%GR/5wt%MAX	293	347.0	377.0	397.5	422.5	-	17.88
80wt%COP/10wt%GR/10wt%MAX	318	354.5	380.0	401.5	427.0	-	27.6

T_{int}: Initial decomposition temperature

3.5.3. Thermal Degradation Kinetics of COP and 80wt%COP/10wt%GR/10wt%MAX

Thermal degradation kinetic data for polymers are essential parameters that aid in understanding the thermal degradation process of these materials. One commonly used method for investigating polymer thermal degradation kinetics is calculating thermal degradation activation energies by analyzing thermogravimetric analysis (TGA) data. Thermal decomposition is closely related to the heating rate, with characteristic temperature points changing in TGA curves taken at different heating rates for the same material [59, 60].

All kinetic studies operate under the assumption that the isothermal rate of conversion, $d\alpha/dt$, is a linear function of k (T) (the temperature-dependent rate constant) and $f(\alpha)$ (a function of the non-temperature-dependent conversion), as shown in Equation 3 [61, 62].

$$\frac{d\alpha}{dt} = \beta \frac{d\alpha}{dt} = k(T)f(\alpha) \tag{3}$$

$$\alpha = \frac{m_0 - m_t}{m_0 - mf} \tag{4}$$

In these equations, m_o represents the initial mass of the sample, m_t is the instantaneous mass, and m_f is the final mass. α denotes the degree of transformation, which is determined from TGA data. t is the time and T is the temperature. The constant heating rate is denoted by β (where $\beta = dT/dt$) and k (T) is the rate constant. The result is expressed with the Arrhenius equation, as shown in Equation 5.

$$k(T) = Ae^{-E_a/RT} \tag{5}$$

In Equation 5, A is the exponential factor (K^{-1}), E_a is the activation energy (kJ/mol), T is the absolute temperature (°C), and R is the universal gas constant (R = 8.314 J/mol K). When these equations are combined, Equation 6 can be written [63].

$$\frac{d\alpha}{dt} = Ae^{-E_a/RT}f(\alpha) \tag{6}$$

Some kinetic methods recommended by the International Confederation for Thermal Analysis and Calorimetry (ICTAC) are available in the literature [64]. Among these, the Flynn-Wall-Ozawa (FWO) and Kissinger-Akahira-Sunose (KAS) models are frequently used to calculate the activation energy of polymer thermal degradation [50]. Both methods are integral methods that are independent of reaction order. In the FWO method, parallel curves are obtained by plotting log β against 1000/T at varying heating rates. E_a is calculated by determining the slope of these curves. Equation 7 is used for the FWO method [65, 66].

$$log(\beta) = log\left[\frac{AEa}{g(a)R}\right] - 2.315 - \frac{0.457\,Ea}{RT} \tag{7}$$

In the above equation, (α) is an unknown function of the conversion. According to this equation, the activation energy ($-0.457\ E_a/RT$) is calculated using the slope of the log $\beta^{-1}/T(K^{-1})$ plot.

When applying the KAS method to calculate the activation energy, ln (β/T^2) is plotted against $1/T(K^{-1})$. The value of E_a is calculated from the slope of the linear lines obtained from this graph. The equation for the KAS method is defined in Equation 8 [67].

$$ln\left(\frac{\beta}{T^2}\right) = ln\left(\frac{AR}{g(\alpha)Ea}\right) - \frac{Ea}{RT} \tag{8}$$

In this context, to calculate the E_a values, TGA thermograms of the polymer and its composite containing 10 wt.% GR/10 wt.% MAX were recorded with heating from 30 °C to 500 °C under a nitrogen atmosphere at heating rates of 5, 10, 15, and 20 °C/min, as shown in Figures 8a and 8b. The graphs for COP, where the FWO and KAS methods were applied, are presented in Figures 9a and 9b.
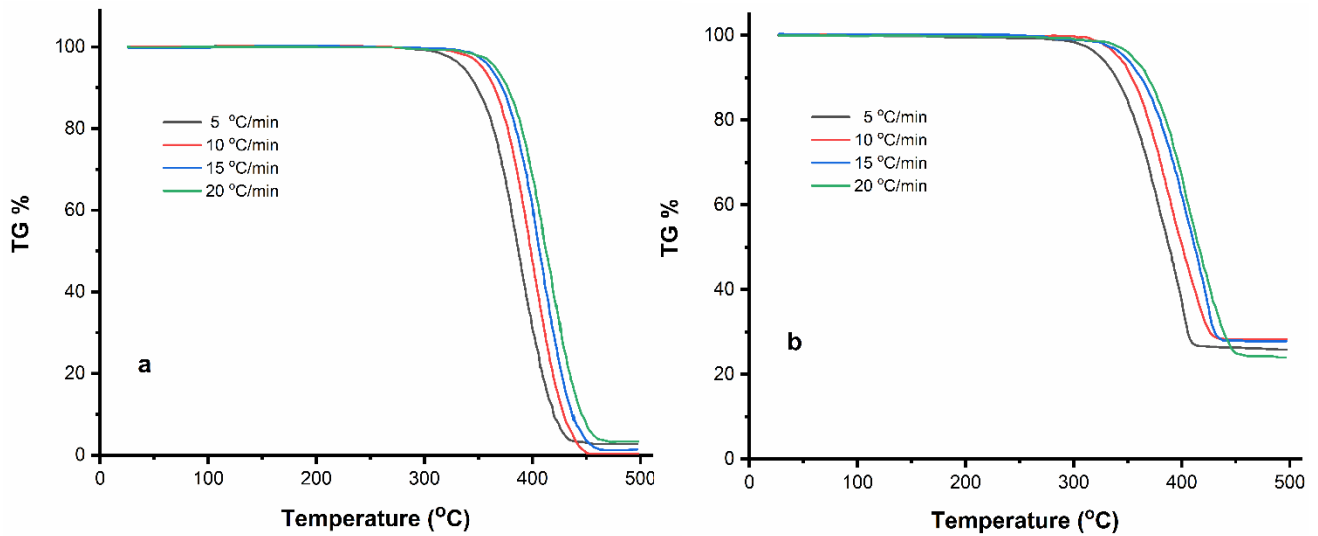
Figure 8. TGA curves of (a) polymer and (b) composite at different heating rates
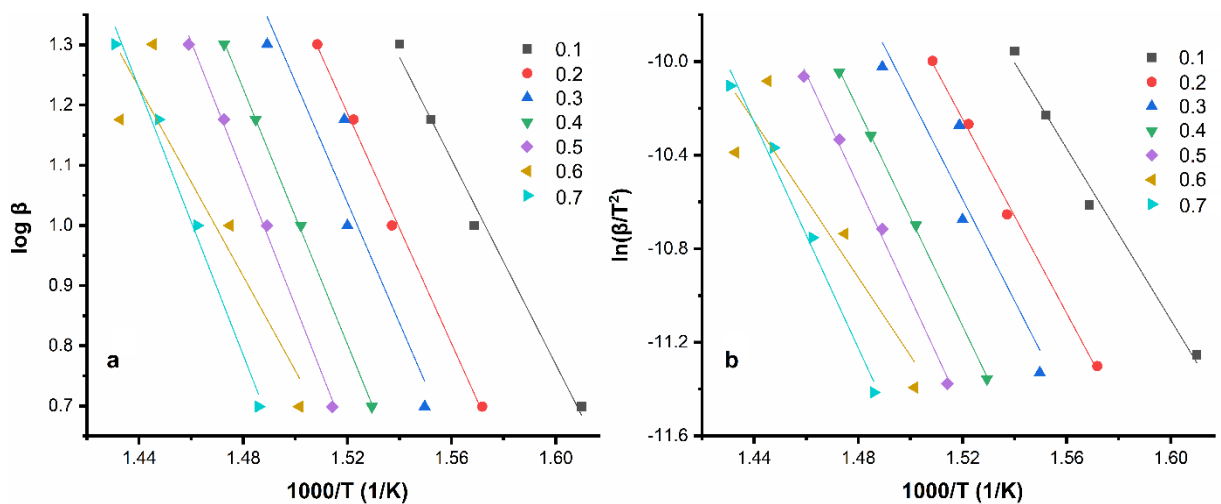
Figure 9. Kinetic curves of thermal degradation of copolymer at different conversion rates: (a) FWO method, (b) KAS method

To understand the effect of doping materials GR and MAX on the polymer's degradation process, the thermal degradation activation energy of the composite containing 10wt%GR/10wt%MAX was analyzed,

with the activation energy determined in the same way as for the copolymer. The composite's graphs according to the FWO and KAS methods are shown in Figures 10a and 10b.
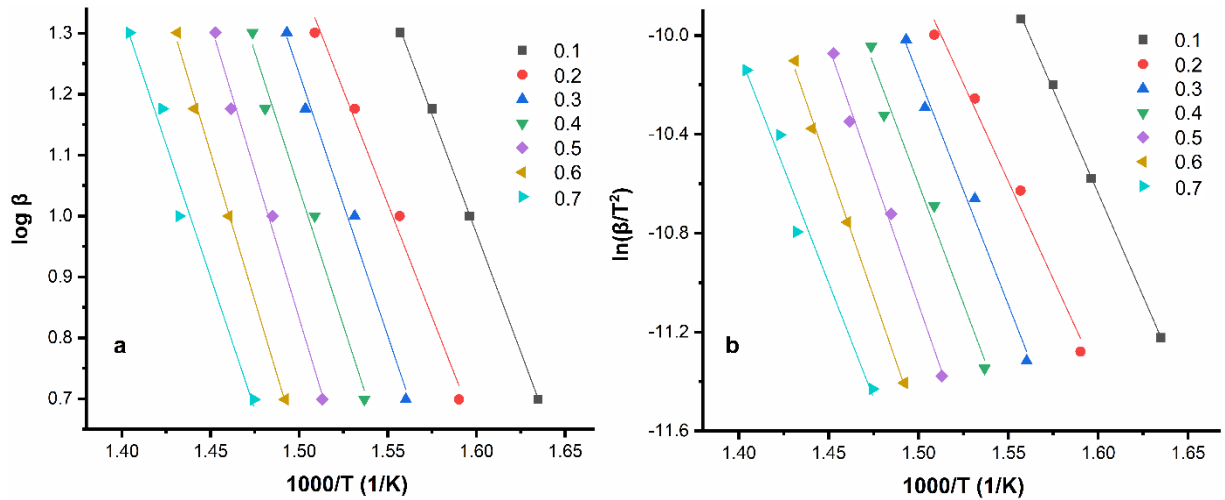
Figure 10. Kinetic curves of thermal degradation of 80wt%COP/10wt%GR/10wt%MAX composite at different conversion rates: (a) FWO method, (b) KAS method

The thermal degradation activation energies of the polymer and its composite, calculated from the FWO and KAS graphs for conversions from 0.1 to 0.7, are presented in Table 3. As shown in Table 3, the activation energy of the polymer increased from 0.1 to 0.6, decreased at 0.6, and then increased again at 0.7. The lines are nearly parallel across all conversions, with the exception of the non-parallel line at 0.6, attributed to the complexity of the dissociation mechanism [63]. In the composite, the activation energy increased up to 0.7 before decreasing at this point. The increasing E_a values of the composite at conversions above 0.1 are due to the significant impact of GR and MAX on the polymer. The thermal degradation activation energies for the polymer were determined as 178.3 kJ/mol and 176.6 kJ/mol according to the FWO and KAS methods, respectively. For the composite, the values were 158.2 kJ/mol according to the FWO method and 155.5 kJ/mol according to the KAS method. In both systems, the E_a values were closest at a conversion value of 0.3. The composite's E_a values were lower than those of the polymer, indicating the notable effect of GR and MAX on the polymer's degradation process. The strong interfacial interactions between the reinforcing materials GR and MAX and the polymer matrix in the composite system increase the thermal stability of the polymer, as shown in Figure 6, while simultaneously accelerating the thermal degradation process. The growing tendency of the reinforcements to aggregate within the polymer matrix made the polymer susceptible to faster degradation.

Table 3. Thermal degradation activation energy values of COP and its composite calculated according to FWO and KAS methods

Conversion	COP		Composites	
	FWO	KAS	FWO	KAS
(α)	Ea (kj/mol)	Ea (kj/mol)	Ea (kj/mol)	Ea (kj/mol)
0.1	154.7	152.3	141.7	138.7
0.2	174.2	172.1	135.1	131.5
0.3	182.2	180.8	156.7	154.0
0.4	192.9	191.9	163.4	160.9
0.5	199.9	199.7	175.7	173.7
0.6	142.6	138.7	176.8	174.7
0.7	201.6	200.8	158.0	154.7
Avarage	**178.3**	**176.6**	**158.2**	**155.5**

The average activation energy conversion plots for both the polymer and the composite are shown in Figures 11a and 11b, respectively. During the thermal degradation of the composite, activation energy increased with conversion. This rise in activation energy can be attributed to the barrier effect of the reinforcement materials, which protect the polymer as it undergoes thermal degradation at higher temperatures. As previously discussed, reinforcement materials GR and MAX play a substantial role in the thermal degradation stages of the polymer [68].
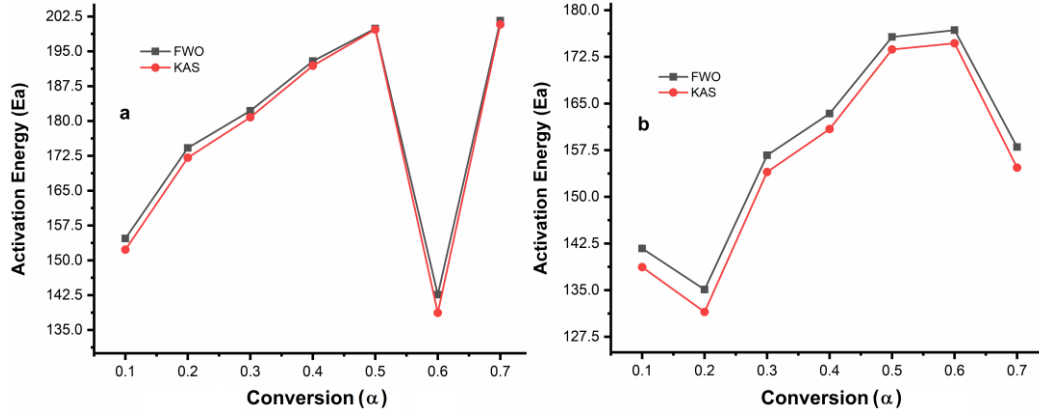
Figure 11. Activation energy conversion graph of a) COP and b) composite

3.6. Dielectric Measurements of Polymer and Composites

Dielectric measurements for the polymer and its composites were conducted at room temperature over a frequency range of 100 Hz to 5 kHz. Initially, pellets of the materials were prepared under four tons of pressure and their thickness was measured, and then dielectric measurements were performed. The dielectric constants of the materials were calculated from Equation 9 using capacitance (C_p).

$$\varepsilon^* = \varepsilon' + \varepsilon'' \tag{9}$$

In Equation 9, ε' represents the real part of the dielectric constant and ε'' is the imaginary part of the dielectric constant. The real part of the dielectric constant can be expressed by Equation 10.

$$\varepsilon' = \frac{C_p \cdot d}{\varepsilon_0 A} \tag{10}$$

Here, ε_0 is the dielectric constant of the vacuum (8.854×10^{-12}), d is the thickness (m) and A is the surface area (m²) of the sample, C_p is the parallel capacitance (F), and Df is the dielectric loss factor. For the imaginary part, Equation 11 can be written as follows [69, 70].

$$\varepsilon'' = \varepsilon' Df \tag{11}$$

The dielectric constant (ε')-frequency plot of the materials is presented in Figure 12 and the dielectric loss (ε'')-frequency plot is shown in Figure 13. The pure polymer exhibited a dielectric constant of 2.2 at 1 kHz at room temperature; however, the dielectric constant increased across all composites. The dielectric constants for 95wt%COP/5wt%GR, 90wt%COP/10wt%GR, 90wt%COP/5wt%GR/5wt%MAX, and 80wt%COP/10wt%GR/10wt%MAX composites were measured as 4.98, 12.31, 8.13, and 9.71, respectively. Among these, the smallest increase in the dielectric constant occurred with the addition of 5wt%GR, yet even this amount yielded a 2.26-fold increase. The dielectric constant increased 3.66-fold in the composite with 5wt%GR and 5wt%MAX and 4.41-fold in the composite containing 10wt%GR and 10wt%MAX. The composite with 10wt%GR achieved the highest dielectric constant at 12.31, marking the maximum increase observed. Additionally, while the dielectric loss of the pure polymer was –0.061 under identical

conditions, an increase was observed in all composites. Notably, composites containing 10% GR exhibited substantial increases in dielectric loss. The observed increases in dielectric properties suggest that the composites become highly polarized at low frequencies in alignment with the applied electric field. This can be attributed to charge accumulation at interfaces and interface polarization. As the concentration of reinforcing material in the composites rises, aggregation occurs, leading to greater polarization and elevated dielectric values. Additionally, both the dielectric constants and dielectric losses of the composites tend to decrease with increasing frequency. This reduction is due to the shorter time available for interface dipoles to orient in response to the alternating field, a common characteristic in conductor-insulator systems [71-73]. At higher frequencies, the almost constant values of ε' and ε'' reflect the reduced efficiency of orientation and interface polarization, which is generally more effective at low frequencies [74].
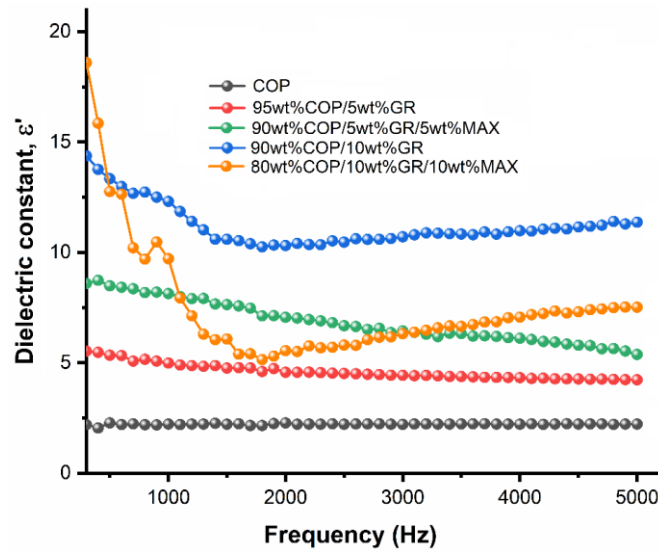
Figure 12. Plot of dielectric constants of COP and composites with frequency
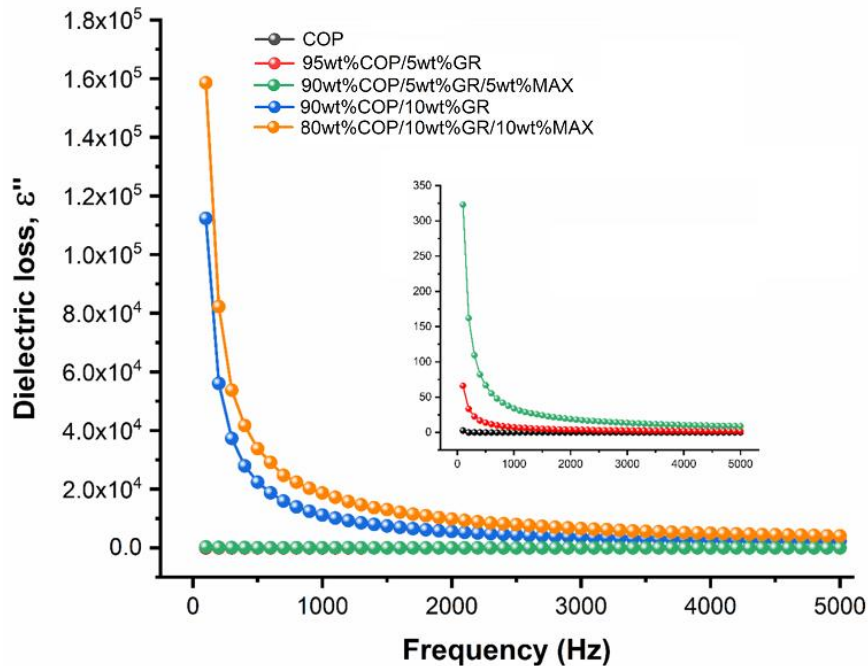
Figure 13. Variation of dielectric loss of COP and its composites with frequency

G_p (conductivity) values of polymer and composites were measured with an impedance analyzer device in the range of 100 Hz to 5 kHz. Conductivity (σ) (AC conductivity) values were calculated using Equation 12 [75].

$$\sigma = G_p \frac{d}{A} \tag{12}$$

When the conductivity-frequency plot given in Figure 14 is examined, it is observed that DC conductivity increases in composites compared to the pure polymer in Region I. GR and MAX, used as reinforcing materials in polymer composites, possess good semiconducting properties. The homogeneous distribution of these materials within the polymer matrix and the formation of a conductive path in the insulating matrix resulted in an increase in conductivity, particularly due to higher amounts of GR and MAX doping [75, 76].
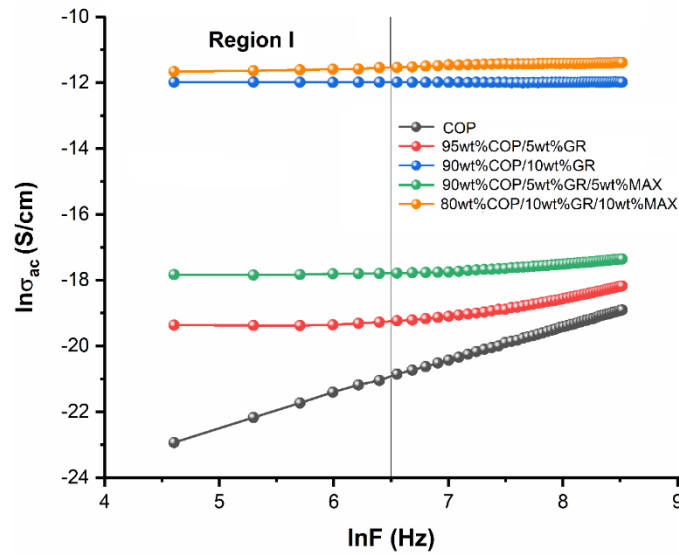
Figure 14. Variation of conductivity of COP and composites with frequency

When the current (I)-voltage (V) graphs of 90wt%COP/10wt%GR and 80wt%COP/10wt%GR/10wt%MAX composites, given in Figure 15, are examined, it is seen that the current increases with increasing voltage and these composites have semiconductor properties.
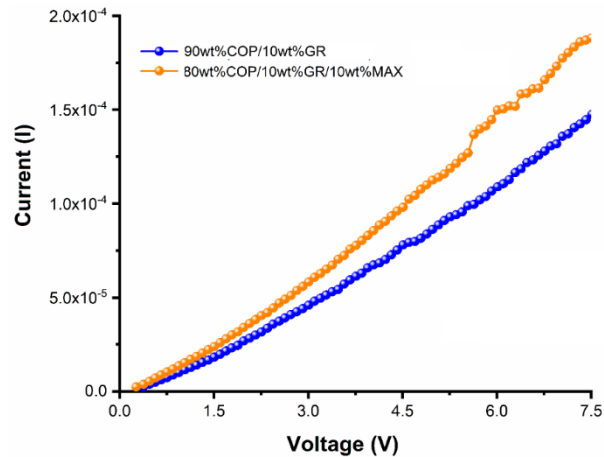
Figure 15. Current (I)-voltage (V) plot of 90wt%COP/10wt%GR and 80wt%COP/10wt%GR/10wt% MAX composites

4. CONCLUSION

In this study, the processability, thermal stability, and dielectric and electrical properties of the COP copolymer and its composites doped with different weight ratios of GR and/or MAX phase (Ti_3AlC_2) were investigated. With the synthesized copolymer, the Tg value, which limits the processability of P(NVC), decreased from 227 °C to 101.74 °C and increased by approximately 2 °C in the composites. However, the results of thermogravimetric analysis revealed that in 10wt%GR and 10wt%GR/10wt%MAX-filled copolymer composites, GR and MAX limited thermal diffusion, thereby increasing the thermal stability of the composites compared to the polymer. This increase in thermal stability may allow the composites to be used at high temperatures or in applications requiring thermal insulation. The composite with 10wt%GR/10wt%MAX-doped polymer exhibited the highest thermal stability at 401.5 °C. A comparison of the thermal degradation activation energy values of the polymer and the 80wt%COP/10wt%GR/10wt%MAX composite, calculated according to the FWO and KAS methods, showed that GR and MAX had a significant effect on the polymer, accelerating the degradation process and reducing the E_a value of the polymer. The investigated dielectric properties of the copolymer and its composites showed that doping improved the dielectric properties of the polymer. With 10wt%GR doping, the dielectric constant of the polymer increased by a factor of 5.5. These increases were also observed in dielectric loss. As the proportion of graphite and MAX in the composites increased, both the dielectric constant and dielectric loss showed further increases. These enhancements in dielectric properties indicate that the composites are well polarized at low frequencies in the direction of the applied electric field. Among the composites, it was observed that conductivity increased with higher GR and MAX concentrations, with the 90wt%COP/10wt%GR and 80wt%COP/10wt%GR/10wt%MAX composites demonstrating semiconducting properties. As a result, the studied materials could be considered for applications requiring both thermal stability and processability, and given their dielectric-conductivity properties, they hold potential for use as functional components in energy storage devices.

Declaration of Ethical **Standards**

Authors declare to comply with all ethical guidelines including authorship, citation, data reporting, and publishing original research

Credit Authorship Contribution Statement

E.BARIM: Investigation, Experimental Section, Writing-review and editing, Resources, Supervision
E.GUNDOGDU: Investigation, Experimental Section, Resources.

Declaration of Competing Interest

The authors declare that they have no known competing financial interests or personal relationships that could have appeared to influence the work reported in this paper.

Funding / Acknowledgements

This study was not funded by any institution

Data Availability

The data that support the findings of this study are available from the corresponding author.

REFERENCES

[1]   S. Demirezen, M. Ulusoy, H. Durmus, H. Cavusoglu, K. Yılmaz and S. Altındal, "Electrical and

photodetector characteristics of schottky structures interlaid with P (EHA) and P (EHA-co-AA) functional polymers by the iCVD method", *ACS omega*, vol 8, no. 49, pp. 46499-46512, 2023.

[2]   K. Demirelli, E. Barım, H. Tuncer, G. Barım and A. M. Abubakar, "Synthesis and characterization of N-(2-acetyl benzofuran-3-yl) methacryl amide and ethyl methacrylate copolymer/graphite oxide composites and study of their kinetic and electrical properties", *Polymer Bulletin*, vol 79, no. 7, pp. 4721-4743, 2022.

[3]   G. Barim, C. A. Canbay, O. Karaduman and C. Ahmedova, "Synthesis and electrical, thermal and structural characterization of polyaniline doped with Ho_2S_3-In_2S_3", *Journal of Materials and Electronic Devices*, vol 1, no. 1, pp. 49-54, 2019.

[4]   S. M. Mousavi, S. A. Hashemi, M. Y. Kalashgrani, A. Gholami, Y. Mazaheri, M. Riazi, D. Kurniawan, M. Arjmand, O. Madkhali, M. D. Aljabri, M. M. Rahman, and W. H. Chiang, "Bioresource Polymer Composite for Energy Generation and Storage: Developments and Trends", *The Chemical Record*, vol 24, no. 1, pp. e202200266, 2024.

[5]   A. M. El-naggar, N. Alhaqbani, A. A. Alsaleh, A. M. Kamal, A. A. Albassam and A. M. Aldhafiri, "Structural, optical characteristics, and Poole–Frenkel emission in PMMA/PVAc/TBAI/milled MWCNTs polymer composites for optoelectronic applications", *Optical and Quantum Electronics*, vol 56, no. 8, pp. 1281, 2024.

[6]   B. Ates, S. Koytepe, A. Ulu, C. Gurses and V. K. Thakur, "Chemistry, structures, and advanced applications of nanocomposites from biorenewable resources", *Chemical Reviews*, vol 120, no. 17, pp. 9304-9362, 2020.

[7]   N. Karthi, K. Kumaresan, S. Sathish, S. Gokulkumar, L. Prabhu and N. Vigneshkumar, "An overview: Natural fiber reinforced hybrid composites, chemical treatments and application areas", *Materials today: proceedings*, vol 27, no.3, pp. 2828-2834, 2020.

[8]   D. G. Atinafu, Y. S. Ok, H. W. Kua and S. Kim, "Thermal properties of composite organic phase change materials (PCMs): A critical review on their engineering chemistry", *Applied thermal engineering*, vol 181, no. Aug., pp. 115960, 2020.

[9]   D. Das, P. Gopikrishna, R. Narasimhan, A. Singh, A. Dey, P. K. Iyer, "White polymer light emitting diodes based on PVK: the effect of the electron injection barrier on transport properties, electroluminescence and controlling the electroplex formation", *Physical Chemistry Chemical Physics*, vol 18, no. 48, pp. 33077-33084, 2016.

[10]   S. Wang, S. Yang, C. Yang, Z. Li, J. Wang, W. Ge, "Poly (Nvinylcarbazole)(PVK) photoconductivity enhancement induced by doping with CdS nanocrystals through chemical hybridization", *The Journal of Physical Chemistry B*, vol 104, no. 50, pp. 11853-11858, 2000.

[11]   J. M. Pearson, *Concise Encyclopaedia of Polymer Science and Engineering*. NY: Wiley Interscience Publications, 1990.

[12]   R. C. Penwell, B. N. Ganguly and T. W. Smith, "Poly (N-vinylcarbazole): A selective review of its polymerization, structure, properties, and electrical characteristics", *Journal of Polymer Science: Macromolecular Reviews*, vol 13, no. 1, pp. 63-160, 1978.

[13]   D. Ghosh, P.S. Sardar, M. Biswas, A. Mondal and N. Mukherjee, "Dielectric characteristics of poly (N-vinylcarbazole) and its nanocomposites with ZnO and acetylene black", *Materials Chemistry and Physics*, vol 123, no. 1, pp. 9-12, 2010.

[14]   J. M. Pearson and M. Stolka, *Poly(N-vinylcarbazole), (Polymer Monographs)*. NY: Gordon and Breach, 1981.

[15]   K. Maex, M. R. Baklanov, S. H. Brongersma and Z. S. Yanovitskaya, "Low dielectric constant materials for microelectronics", *Journal Applied Physics*. vol 93, no. 11, pp. 8793-8841, 2003.

[16]   K. Yang, X. Huang, Y. Huang, L. Xie and P. Jiang, "Fluoro-polymer@$BaTiO_3$ hybrid nanoparticles prepared via RAFT polymerization: toward ferroelectric polymer nanocomposites with high dielectric constant and low dielectric loss for energy storage application", *Chemistry of Materials*, vol 25, no. 11, pp. 2327-2338, 2013.

[17]   F. Biryan and K. Demirelli, "Copolymerization of benzyl methacrylate and a methacrylate bearing

benzophenoxy and hydroxyl side groups: Monomer reactivity ratios, thermal studies and dielectric measurements'', *Fibers and Polymers*, vol 18, no. 9, pp. 1629-1637, 2017.

[18]   S. Tazuke and S. Okamura, *Encyclopedia of Polymer Science and Technology*. NY: Wiley, 1971.

[19]   A. Ryttel, "Thermomechanical and dielectrical properties of alkyl methacrylate with N-vinyl carbazole copolymers", *Journal of Macromolecular Science, Part A*, vol 34, no. 1, pp. 211-219, 1997.

[20]   E. Bilbao, M. Laza, J. L. Vilas, M. T. Garay, M. Rodríguez and L. M. León, "Thermal Degradation of Copolymers of N-Vinylcarbazole with Acrylic and Methacrylic Monomers", *Journal of Macromolecular Science, Part A*, vol 43, no. 7, pp. 1029-1041, 2006.

[21]   I. Haldar, A. Kundu, M. Biswas, and A. Nayak, "Preparation and evaluation of a poly (N-vinylcarbazole)–Fe_3O_4 (PNVC–Fe_3O_4) nanocomposite", *Materials Chemistry and Physics*, vol 128, no. 1-2, pp. 256-264, 2011.

[22]   R. S. Sonone, V. M. Raut and G. H. Murhekar, "Structural and electroluminescence properties of pure PVK and doped TiO_2 polymer thin films", *International Journal of Advanced Research in Chemical Scienceis*, vol 1, no. 1, pp. 87-94, 2014.

[23]   M. Goumri, R. Hatel, B. Ratier and M. Baitoul, "Optical and electrical properties of poly (N-vinylcarbazole)/grapheneoxide nanocomposites for organic semiconductor devices", *Applied Physics A*, vol 126, no. 8, pp. 647, 2020.

[24]   A. A. Al-Muntaser, E. Banoqitah, M. A. Morsi, A. Y. Madkhli, J. M. Abdulwahed, R. Alwafi, A. F. Al Naim and A. Saeed, "Fabrication and characterizations of nanocomposite flexible films of ZnO and polyvinyl chloride/poly (N-vinyl carbazole) polymers for dielectric capacitors", *Arabian Journal of Chemistry*, vol 16, no. 10, pp. 105171, 2023.

[25]   B. Duran and E. Şimşek, "Poly (N-vinyl carbazole)-TiO_2 composite coating for protection of steel", *Journal of Adhesion Science and Technology*, vol 37, no. 20, pp. 2781-2794, 2023.

[26]   A. G. Al Lafi, S. Mousa and G. Alssayes, "A description of the physical ageing and annealing processes in poly (N-vinyl carbazole) using differential scanning calorimetry and two-dimensional correlation mapping analysis", *Journal of Thermal Analysis and Calorimetry*, vol 149, no. 17, pp. 9275-9284, 2024.

[27]   Y. Mu, J. Fan, B. Chu, S. Zhong and Y. Cheng, "Synthesis of n-vinyl carbazole from acetylene by a continuous high-pressure liquid-phase process with Inherent safety", *Chemical Engineering Journal*, vol 493, no. Aug., pp. 152642, 2024.

[28]   C. C. Sorensen, A. Y. Bello and F. A. Leibfarth, "Stereoselective Polymerization of 3, 6-Disubstituted N-Vinylcarbazoles", *ACS Macro Letters*, vol 13, no. 5, pp. 614-620, 2024.

[29]   M. Xie, F. Chen, J. Liu, T. Yang, S. Yin, H. Lin, Y. Xue and S. Han, "Synthesis and evaluation of benzyl methacrylate-methacrylate copolymers as pour point depressant in diesel fuel", *Fuel*, vol 255, no. Nov., pp. 115880, 2019.

[30]   K. Ueno, "Soft materials based on colloidal self-assembly in ionic liquids", *Polymer Journal*, vol 50, no. 10, pp. 951-958, 2018.

[31]   C. Yoon, H. S. Kwon, J. S. Yoo, H. Y. Lee, J. H. Bae and J. H. Choi, "Preparation of thermally stable dyes derived from diketopyrrolopyrrole pigment by polymerisation with polyisocyanate binder", *Coloration Technology*, vol 131, no. 1, pp. 2-8, 2015.

[32]   M. Worzakowska, "Starch-g-poly (benzyl methacrylate) copolymers: characterization and thermal properties", *Journal of Thermal Analysis and Calorimetry*, vol 124, no. Feb., pp. 1309-1318, 2016.

[33]   K. Demirelli, M. Coskun and E. Kaya, "Polymers based on benzyl methacrylate: Synthesis via atom transfer radical polymerization, characterization, and thermal stabilities", *Journal of Polymer Science Part A: Polymer Chemistry*, vol 42, no. 23, pp. 5964-5973, 2004.

[34]   X. Liu, X. Dai, W. Boyko, A. S. Fleischer and G. Feng, "Surfactant-mediated synthesis of monodisperse Poly (benzyl methacrylate)-based copolymer microspheres", *Colloids and Surfaces A: Physicochemical and Engineering Aspects*, vol 633, no. 2, pp. 127870, 2022.

[35]   D. D. L. Chung, "Review graphite", *Journal of materials science*, vol 37, no. 8, pp. 1475-1489, 2002.

[36] F. Biryan and K. Demirelli, ''Thermal decomposition, kinetics and electrical measurements of Poly (3-Acetamidopropyl Methacrylate)/graphite composites'', *Ferroelectrics*, vol 550, no. 1, 51-75, 2019.

[37] S. Maletić, N. Jović Orsini, M. Milić, J. Dojčilović and A. Montone, "Dielectric properties of epoxy/graphite flakes composites: Influence of loading and surface treatment", *Journal of Applied Polymer Science*, vol 141, no. 5, pp. e54881, 2024.

[38] C. Tu, F. Zhang, J. Zheng, Y. Zhang, Y. Liang, J. Cao, F. Kong, Y. Yang, N Lin, N. Zhang, X. Chen, F. Wang and W. Zhou, "Interfacial insight into elevated dielectric properties in graphite nanosheets reinforced PVDF composites via engineering TiO_2 shell as an interlayer", *Journal of Polymer Research*, vol 31, no. 2, pp. 31, 2024.

[39] M. W. Barsoum, "The MN+ 1AXN phases: A new class of solids: Thermodynamically stable nanolaminates", *Progress in solid state chemistry*, vol 28, no. 1-4, pp. 201-281, 2000.

[40] M.W. Barsoum, D. Brodkin and T. El-Raghy, "Layered Machinable Ceramics for High Temperature Applications", *Scripta Materialia*, vol 36, no. 5, 1997.

[41] M.W. Barsoum and T. El-Raghy, "The MAX Phases: unique New Carbide and Nitride Materials Ternary ceramics turn out to be surprisingly soft and machinable, yet also heat-tolerant, strong and lightweight", *American Scientist*, vol 89, no. 4, pp. 33443, 2001.

[42] P. Eklund, M. Beckers, U. Jansson, H. Högberg and L. Hultman, "The Mn+ 1AXn phases: materials science and thin-film processing", *Thin Solid Films*, vol 518, no. 8, 1851-1878, 2010.

[43] J. Zhang, K. Chen and X. Sun, MAX phase ceramics/composites with complex shapes, *ACS Applied Materials & Interfaces*, vol 13, no. 4, 5645-5651, 2021.

[44] K. Dash and A. Dash, "In-situ formation of 2D-TiCx in Cu-Ti$_2$AlC composites: an interface reaction study", *Materials Letters*, vol 284, no. 2, 128935, 2021.

[45] E. Barım, "Synthesis, Characterization, Optical and Thermal Properties of P (NVC-co-BZMA) Copolymer and Its ZnO Composites", *Gazi University Journal of Science Part A: Engineering and Innovation*, vol 9, no. 4, 526-536, 2022.

[46] I. Haldar, A. Kundu, M. Biswas and A. Nayak, "Preparation and evaluation of a poly(N-vinylcarbazole)–Fe_3O_4 (PNVC–Fe_3O_4) nanocomposite", *Materials Chemistry and Physics*, vol 128, no. 1-2, 256-264, 2011.

[47] S. Bashir, M. S. Awan, M. A. Farrukh, R. Naidu, S. A. Khan, N. Rafique, S. Ali, I. Hayat, I. Hussain and M. Z. Khan, "In-vivo (Albino Mice) and in-vitro Assimilation and Toxicity of Zinc Oxide Nanoparticles in Food Materials", *International Journal of Nanomedicine*, vol 17, no. Sep., 4073-4085, 2022.

[48] S. A. El-Khodary, G. M. El-Enany, M. El-Okr and M. Ibrahim, "Preparation and characterization of microwave reduced graphite oxide for high-performance supercapacitors", *Electrochimica Acta*, vol 150, no. Dec., 269-278, 2014.

[49] K. M. Rehan, B. Anbarasu, P. M. Ashfaque, S. M. Safiullah and K. A. Basha, ''Synthesis and characterization of poly (vinyl carbazole-co-ethoxy ethyl methacrylate) and its nanocomposites'', *Materials Today: Proceedings*, vol 50, no. 3, 325-330, 2022.

[50] K. Demirelli, A. M. Abubakar, A. A. Ahmad and E. Bagcı, "The effect of end group and graphene on dielectric properties and thermal degradation of poly(benzyl methacrylate) prepared by ATRP method", *Polymer Bulletin*, vol 80, no. 1, pp. 279-307, 2022.

[51] M. Akshay, S. Jyothilakshmi, Y. S. Lee, V. Aravindan, ''CuS modified graphite from spent Li-ion batteries towards building high energy Na-ion capacitors via solvent-co-intercalation process'', *Chemical Engineering Journal*, vol 498, no. 1, 155462, 2024.

[52] M. Mahmood, A. Rasheed, I. Ayman, T. Rasheed, S. Munir, S. Ajmal, P. O. Agboola, M. F. Warsi, and M. Shahid, "Synthesis of Ultrathin MnO_2 Nanowire-Intercalated 2D-MXenes for High-Performance Hybrid Supercapacitors", *Energy & Fuels*, vol 35, no. 4, 3469-3478, 2021.

[53] A. Syuy, D. Shtarev, A. Lembikov, M. Gurin, R. Kevorkyants, G. Tselikov, A. Arsenin and V. Volkov, ''Effective Method for the Determination of the Unit Cell Parameters of New MXenes. Materials'', *Materials*, vol 15, no. 24, 8798, 2022.

[54]   E. Marimuthu and V. Murugesan, ''Influence of ultrasound on multi-site phase transfer catalyzed polymerization of N-vinyl carbazole in two phase system'', *SN Applied Sciences*, vol 1, no. 6, 638, 2019.

[55]   Z. Mao and J. Zhang, "Toughening effect of CPE on ASA/SAN binary blends at different temperatures", *Journal of Applied Polymer Science*, vol 133, no. 20, pp. 43353, 2016.

[56]   D. Kapusuz, "Production and structural analysis of Ti₃AlC₂/Ti₃C₂ incorporated epoxy composites", *Konya Journal of Engineering Sciences*, vol 7, no. 3, pp. 632-644, 2019.

[57]   M. Coskun, G. Barim and K. Demirelli, "Thermal stabilities of poly(n-acryloyl-n'-methylpiperazine), its blends with poly(methyl methacrylate), and poly(n-acryloyl-n'-methylpiperazine-co-methyl methacrylate)", *Journal of Macromolecular Science, Part A*, vol 43, no. 1, 83-93, 2006.

[58]   D. Liu, L. Hentschel, G. Lin, C. Kukla, S. Schuschnigg, N. Ma, C. Wallis, V. Momeni, M. Kitzmantel and G. Sui, "Multifunctional Ti₃AlC₂-Based Composites via Fused Filament Fabrication and 3D Printing Technology", *Journal of Materials Engineering and Performance*, vol 32, no. 20, pp. 9174-9181, 2023.

[59]   S. Vyazovkin, A. K. Burnham, J. M. Criado, L.A. Pérez-Maqueda, C. Popescu and N. Sbirrazzuoli, "ICTAC Kinetics Committee recommendations for performing kinetic computations on thermal analysis data", *Thermochim Acta,* vol 520, no. 1, 1-19, 2011.

[60]   D. N. Waters and J. L. Paddy, "Equations for isothermal differential scanning calorimetric curves", *Analytical Chemistry*, vol 60, no. 1, pp. 53-57, 1988.

[61]   D. S. Achilias, E. Panayotidou and I. Zuburtikudis, "Thermal degradation kinetics and isoconversional analysis of biodegradable poly (3-hydroxybutyrate)/ organomodified montmorillonite nanocomposites", *Thermochimica Acta*, vol 514, no. 1, pp. 58-66, 2011.

[62]   S. Ceylan and Y. Topçu, "Pyrolysis kinetics of hazelnut husk using thermogravimetric analysis", *Bioresource Technology*, vol 156, no. 182, 182-188, 2014.

[63]   S. Bano, N. Ramzan, T. Iqbal, H. Mahmood and F. Saeed, "Study of thermal degradation behavior and kinetics of ABS/PC blend", *Polish Journal of Chemical Technology*, vol 22, no. 3, pp. 64-69, 2020.

[64]   S. Vyazovkin, K. Chrissafis, M. L. Di Lorenzo, N. Koga, M. Pijolat, B. Roduit, N. Sbirrazzuoli and J. J. Sunol, "ICTAC Kinetics Committee recommendations for collecting experimental thermal analysis data for kinetic computations", *Thermochimica Acta*, vol 590, no. Aug., pp. 1-23, 2014.

[65]   J. H. Flynn and L. A. Wall, "General treatment of the thermogravimetry of polymers", *Journal of Research of the National Bureau of Standards*, vol 70, no. A6, pp. 487-523, 1966.

[66]   T. Ozawa, "A new method of analyzing thermogravimetric data", *Bulletin of the Chemical Society of Japan*, vol 38, no. 11, pp. 1881-1886, 1965.

[67]   H. E. Kissinger, "Reaction Kinetics in Differential Thermal Analysis", *Analytical Chemistry*, vol 29, no. 11, pp. 1702-1706, 1957.

[68]   K. Chrissafis, "Kinetics of thermal degradation of polymers: complementary use of isoconversional and model-fitting methods", *Journal of Thermal Analysis and Calorimetry*. Vol 95, no. 1, pp. 273-283, 2008.

[69]   P. Seven, , M. Coskun and K. Demirelli, "Synthesis and characterization of two-armed graft copolymers prepared with acrylate and methacrylate using atom transfer radical polymerization", *Reactive and Functional Polymers*, vol 68, no. 5, pp. 922–930, 2008.

[70]   S. Rajendran and M. Ramesh Prabhu, "Effect of different plasticizer on structural and electrical properties of PEMA-based polymer electrolytes", *Journal of Applied Electrochemistry*, vol 40, no. 2, pp. 327-332, 2010.

[71]   K. W. Wagner, "Erklärung der dielektrischen Nachwirkungsvorgänge auf Grund Maxwellscher Vorstellungen" *Archiv für Elektrotechnik*, vol 2, no. 9, 371-387, 1914.

[72]   L. K. H. Van Beek, "Progress in Dielectrics", J. B. Birks ed., Heywood, London, vol 7, no. 71, pp. 69-113, 1967.

[73]   W. J. Wang, C. W. Li and K. P. Chen, "Electrical, dielectric and mechanical properties of a novel

Ti$_3$AlC$_2$/epoxy resin conductive composites", *Materials Letters*, vol 110, no. Nov., pp. 61-64, 2013.

[74]   S. Ningaraju, , N. H. Vinayakaprasanna, , A. P. Gnana Prakash and H. B. Ravikumar, "Free volume dependence on electrical properties of Poly (styrene co-acrylonitrile)/Nickel oxide polymer nanocomposites", *Chemical Physics Letters*, vol 698, no. Apr., pp. 24-35, 2018.

[75]   E. Jayamani, T. C. Peng, M. K. B. Bakri and A. Kakar, "Comparative Analysis on Dielectric Properties of Polymer Composites Reinforced With Synthetic and Natural Fibers", *Journal of Vinyl & Additive Technology,* vol 24, no. S1, pp. E201-E216, 2018.

[76]   H. Li, Z. Chen, L. Liu, J. Chen, M. Jiang and C. Xiong, "Poly(vinylpyrrolidone)-coated graphene/poly(vinylidene fluoride) composite films with high dielectric permittivity and low loss", *Composites Science and Technology*, vol 121, no. Dec., pp. 49-55, 2015.

STATIC ANALYSIS OF AXISYMMETRIC THIN CYLINDRICAL SHELL USING THE COMPLEMENTARY FUNCTIONS METHOD

[1, *] Osman AYAZ [ID], [2] Ahmad Reshad NOORI [ID], [3] Burkay SİVRİ [ID], [4] Beytullah TEMEL [ID]

[1,3,4] *Cukurova University, Engineering Faculty, Civil Engineering Department, Adana, TÜRKİYE*
[2] *Istanbul Gelisim University, Engineering Faculty, Civil Engineering Department, Istanbul, TÜRKİYE*
[1] osmanayaz1302@gmail.com, [2] arnoori@gelisim.edu.tr, [3] bsivri@cu.edu.tr, [4] btemel@cu.edu.tr

Highlights

- Static analysis of thin axisymmetric cylidrical shells under various loading types is performed by the Complementary Functions Method (CFM).

- Thin shell theory is used, and the effects of shear deformation are ignored.

- Solution of initial value problems is performed using the Runge-Kutta 5 (RK5) numerical procedure.

- Parametric studies have been carried out for uniform and parabolic loads.

- A computer program is coded in Wolfram Mathematica.

*Corresponding Author: Osman AYAZ, osmanayaz1302@gmail.com

STATIC ANALYSIS OF AXISYMMETRIC THIN CYLINDRICAL SHELL USING THE COMPLEMENTARY FUNCTIONS METHOD

[1], * Osman AYAZ , **[2] Ahmad Reshad NOORI** ,**[3] Burkay SİVRİ** ,**[4] Beytullah TEMEL**

[1,3,4] Cukurova University, Engineering Faculty, Civil Engineering Department, Adana, TÜRKİYE
[2] Istanbul Gelisim University, Engineering Faculty, Civil Engineering Department, Istanbul, TÜRKİYE
[1] osmanayaz1302@gmail.com, [2] arnoori@gelisim.edu.tr, [3] bsivri@cu.edu.tr, [4] btemel@cu.edu.tr

ABSTRACT: The analysis of thin cylindrical shells is essential for a wide range of engineering applications, making it critical to understand their static behavior under various loading conditions. In this study, the static analysis of axisymmetric thin cylindrical shells is performed using the Complementary Functions Method (CFM). The research focuses on examining the static behavior of cylindrical shells made of homogeneous, isotropic, and linear elastic materials under various loading conditions. The governing differential equations for the static response of these structural elements are derived based on thin shell theory, utilizing the principle of minimum total potential energy. These equations are solved using CFM, an efficient numerical solution method. In this context, the CFM is coded in Wolfram Mathematica. To validate the accuracy and reliability of the proposed solution method, the results are compared with existing studies in the literature, demonstrating a high degree of consistency and confirming the effectiveness of the method. It has been observed that the type of loading significantly impacts the behavior of the shell.

Keywords: Axisymmetric Structures, Complementary Functions Method (CFM), Cylindrical Shell, Thin Shell Theory

1. INTRODUCTION

The analysis of cylindrical shells, widely encountered in different engineering fields such as civil, storage, mechanical, aerospace, marine, and transportation,–plays a significant role in contemporary engineering problems. Axisymmetric cylindrical shells are commonly found in structures like vaults, pipes, water and steam boilers, tanks, and the fuselages of missiles and aircraft. In engineering studies, one of the most frequently encountered difficulties in the design of axisymmetric cylindrical shells is static analysis under symmetrical loads. The differential equations that govern the static behavior of shells subjected to external loads can be solved through various analytical methods. For differential equations that are unsolvable or difficult to solve analytically, advancements in computer technology now ~~allow~~ enables rapid and efficient solutions using numerical methods. Studies on axisymmetric shells and plates which date back to 19th century can be found in the literature. The analysis of axisymmetric shells using the direct stiffness method [1], the free vibration analysis of conical shells using the Rayleigh-Ritz method [2], the development of mixed formulations with two- and three-node elements based on the finite element method, as well as dynamic analyses of axially symmetric shells under different loading conditions using approaches such as the direct integration method, Hamilton's principle, and the Galerkin method [3-6]. Free vibration analyses of axially symmetric cylindrical, hyperbolic, and conical shells and plates with varying thicknesses inspired by the beam-on-elastic-foundation analogy [7-9], optimization with free vibration [10,11] dynamic analyses in Laplace space [12], and theoretical analyses of axially symmetric shells and plates using different numerical methods [13], [14] can be cited to the related subject. [15] conducted a comprehensive examination of the thermo-mechanical behavior of axisymmetric cylinders, with a particular focus on the boundary conditions. The study employed numerical models developed using the Finite Element Method (FEM) and Finite Difference Method (FDM) to assess the accuracy of the applied analytical method. [16] Proposed a

*Corresponding Author: Osman AYAZ, osmanayaz1302@gmail.com

unified solution method for investigation of elasticity and thermo-elasticity problems of axisymmetric solid cylinders. [17] Used the Galerkin method to investigate the torsional stability of non-homogeneous composite cylindrical shells under mixed boundary conditions. [18] Examined the first- layer failure strength and the three-dimensional elastic response of a cylindrical shell under axisymmetric loading. Additionally, they conducted experimental tests to verify the validity and applicability of the proposed theory for initial layer failure strength. [19] Investigated the static bending response of pressurized axisymmetric cylindrical shell based on Higher Order Shear Deformation Theory (HOSDT). [20] Extended the meshless approach to analyze the static and dynamic behavior of a circular cylindrical shell composed of a material model derived from the combination of Neo-Hookean and Fung materials. [21] Examined the static bending response of a circular cylindrical shell made of isotropic material under static loading. Their research determined that incorporating transverse effects in the present solution results in increased displacement values in moderately thick cylindrical shells; however, this effect diminishes as the length-to-radius of curvature ratio (l/a) increases.

In this study, the static behavior of axisymmetric cylindrical shells under various loading types is investigated. The canonical equations governing the behavior of the cylindrical shells under consideration are derived based on thin shell theory using the principle of minimum total potential energy, and numerical and parametric studies were conducted. For this purpose, the Complementary Functions Method (CFM), which has been effectively applied in the numerical solution of various mechanical problems [22-28]. The key advantage of this efficient approach lies in transforming the two-point boundary value problem into a system of Initial Value Problems (IVP), which can be readily solved using well-established numerical techniques available in the literature. The fifth-order Runge-Kutta (RK5) scheme is preferred to be used with the CFM for the numerical solution of the set of IVPs.

2. MATERIAL AND METHODS

This study considers a two-dimensional axisymmetric thin cylindrical shell composed of homogeneous, isotropic, and linear elastic material. The equations governing the static behavior of the thin cylindrical shell with a rotational symmetry axis are derived using the principle of minimum total potential energy, based on the assumptions of thin shell theory. The derived equations are then solved numerically by using the Complementary Functions Method (CFM). Due to axial symmetry, displacements exist only in the x and y directions, as expressed by the following equation.
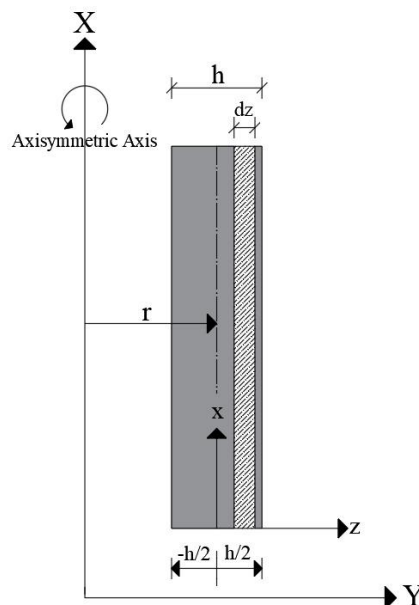
Figure 1. Axisymmetric cylindrical shell

$$U_x = u(x) \tag{1}$$
$$U_y = w(x) \tag{2}$$

U_x represents the displacement in the meridional direction, while U_y denotes the displacements in the direction normal to the shell. Here, u indicates deformation (elongation or shortening) in the meridional direction, and w represents the displacement (deflection) along the normal axis. The strains and curvatures in the meridional and circumferential directions are given as follows [29].

$$\varepsilon_x = \frac{du}{dx} \tag{3}$$

$$\varepsilon_\theta = \frac{w}{r} \tag{4}$$

$$\chi_x = \chi' \tag{5}$$
$$\chi_\theta = 0 \tag{6}$$

The strain-stress relationship is provided by the following equations.

$$\sigma_x = \frac{E}{1 - v^2} \left(\varepsilon_x + v\varepsilon_\theta + z\chi_x \right) \tag{7}$$

$$\sigma_\theta = \frac{E}{1 - v^2} \left(\varepsilon_\theta + v\varepsilon_x + z\,v\,\chi_x \right) \tag{8}$$

Here σ_x and σ_θ represent the normal stresses in the meridional and circumferential directions respectively, E denotes the modulus of elasticity, v is the Poisson ratio and χ_x is the curvature in the meridional direction.

In the following equations, derivatives are defined as $\frac{d(\cdot)}{dx} = (\cdot)'$. The membrane forces in the meridional and circumferential directions of the shell are obtained as follows

$$N_x = D(\varepsilon_x + v\varepsilon_\theta) \tag{9}$$
$$N_\theta = D(\varepsilon_\theta + v\,\varepsilon_x) \tag{10}$$

In the equations (9-10) D, is the material rigidity constant and has the $D = \frac{Eh}{(1-v^2)}$ value.

The total potential energy equation for the axisymmetric thin cylindrical shell is given by the following equation.

$$\Pi_t = \int_0^X \int_0^{2\pi} \left[\left(N_x u' + N_\theta \frac{w}{r} + M_x \chi' + 2Q\,(\chi - w') \right) - (p_x\,u + p_z\,w) \right] r\,d\theta\,dx \tag{11}$$

In this equation, p_x and p_z represent the external forces in the meridional and circumferential directions, respectively. By taking the derivatives of the required quantities in this equation, six canonical differential equations governing the static behavior of the axisymmetric thin cylindrical shell are obtained.

$$w' = \chi \tag{12}$$

$$\chi' = \frac{1}{K} M_x \tag{13}$$

$$u' = \frac{1}{D} N_x - v\frac{w}{r} \tag{14}$$

$$N_x' = -p_x \tag{15}$$
$$M_x' = Q \tag{16}$$

$$Q' = -\frac{v}{r} N_x - \frac{D}{r^2}(1 - v^2)\,w + p_z \tag{17}$$

In these equations, w represents the deflection in the normal direction to the shell, χ denotes the rotation, u is the displacement in the meridional direction, N_x is the axial force, M_x is the bending moment, and Q is the shear force acting on the unit width. The resulting set of equations (12-17) is written in matrix form as shown in equation (18).

$$\frac{d\{\Psi(x)\}}{dx} = [A(x)]\{\Psi(x)\} + \{\phi(x)\} \tag{18}$$

This equation stands for a two-point boundary value problem. In the equation, $[A(x)]$ denotes the differential transition matrix, $\{\Psi(x)\}$ is the state vector, and similarly, $\{\phi(x)\}$ represents the load vector.

In this study, the solution of equation (18) is obtained using the (CFM), an effective numerical

technique. With the CFM, the solution is to be performed by transforming the two-point boundary value problem into an Initial Value Problems (IVP).

The general solution for the preceding set of canonical equations (12-17) is:

$$\{\boldsymbol{\Psi}\} = \sum_{m=1}^{6} C_m \left[U^{(m)}\right] + \{\boldsymbol{\phi}\} \tag{19}$$

C_m are the constants to be acquired from the boundary conditions given at the beginning and end of the solution interval. $U^{(m)}$ are the linearly independent complementary solutions where for IVPs the component mth is equal to 1 wherease all others are equal to 0.

$$\frac{dU^{(m)}}{dx} = [A]\{U^{(m)}\} \quad (m = 1, \dots, n) \tag{20}$$

$\{\boldsymbol{\phi}\}$ is the particular solution with all 0 initial conditions [30].

$$\frac{d\{\boldsymbol{\phi}\}}{dx} = [A]\{\boldsymbol{\phi}\} + \{F\} \tag{21}$$

In the above equation the column vector $\{F\}$ represents loading conditions.

For numerical solutions, the fifth-order Runge-Kutta (RK5) algorithm [31] is employed. This numerical scheme is preferred due its high accuracy and easy application. The results obtained from RK5 is equivalent to the 7th order Taylor series [18]. For this purpose, a computer program based on the RK5 algorithm for the static analysis of thin axisymmetric cylindrical shells using CFM is coded in Wolfram Mathematica [32] software which is a powerful computational tool widely used in scientific research, engineering, and mathematical modeling. With its advanced symbolic and numerical computation capabilities, it provides an efficient environment for solving differential equations, performing data analysis, and visualizing complex mathematical functions.

3. RESULTS AND DISCUSSION

In this study, to validate the proposed method, a constant-thickness water tank problem from the literature is solved numerically using the CFM, and the results are compared on Tables (1-2) and Figures (2-6). Subsequently, the static behavior of an axisymmetric thin cylindrical shell with wall thickness of $h = 0.16\,m$, height of $H = 5m$ and radius of $12\,m$ under various loading conditions is examined parametrically. The Poisson ratio is $v = 1/6 = 0.16666$ and modulus of elasticity $E = 2.1 * 10^5\,MPa$. The geometric and material properties are supposed to be the same in all applications.

To further investigate the static response of an axisymmetric cylindrical shell, this study examines the considered problem under Parabolically Distributed Loading (PDL) and Uniformly Distributed Loading (UDL). PDL conditions are commonly encountered in silos of grains, corn, seeds, sand, cement, chemicals, coal or crushed rocks, while UDL scenarios are relevant to structures like nuclear reactor containment vessels, reactors in chemical plants and etc. This study parametrically analyzes the influence of PDL and UDL on the static behavior of the structure. To achieve this, the shell element is discretized into 10 equal segments and analyzed using the CFM

Application 1.

The static behavior of the constant-thickness cylindrical shell, shown in Figure 2 with specified boundary conditions, material, and geometric properties, has been investigated. The obtained results are presented in a comparative form on Tables (1-2) and Figures (3-7) for clamped-Free boundary supports.
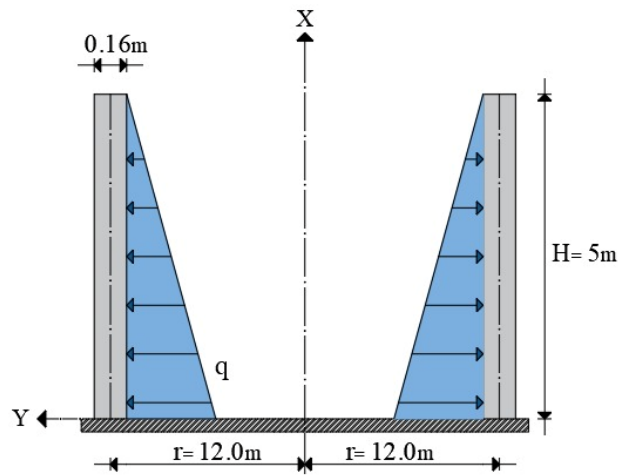
Figure 2. Constant thickness cylindrical water tank

Boundary conditions at the fixed and free ends:

$$x = 0 \Rightarrow \begin{cases} w = 0 \\ \chi = 0 \\ u = 0 \end{cases} \tag{22}$$

$$x = H \Rightarrow \begin{cases} N_x = 0 \\ M_x = 0 \\ Q = 0 \end{cases} \tag{23}$$

$$q = q_0 (H - x) , \qquad q_0 = 1 \, MPa \tag{24}$$

Table 1. Comparison of the nodal displacements and rotations

$x(m)$	$w \, (mm) \cdot 10^3$		$\chi \, (Rad) \cdot 10^3$		$u \, (mm) \cdot 10^3$	
	Present Study	**[29]**	**Present Study**	**[29]**	**Present Study**	**[29]**
0	0.0000	0.000	0.0000	0.000	0.0000	0.000
0.5	-0.2587	-0.258	0.8343	0.834	-0.0007	-0.000
1	-0.6923	-0.692	0.8091	0.809	-0.0040	-0.003
1.5	-1.0145	-1.014	0.4565	0.456	-0.0100	-0.010
2	-1.1448	-1.144	0.0743	0.074	-0.0176	-0.017
2.5	-1.1051	-1.105	-0.2135	-0.213	-0.0255	-0.025
3	-0.9508	-0.950	-0.3858	-0.385	-0.0327	-0.032
3.5	-0.7344	-0.734	-0.4678	-0.467	-0.0386	-0.038
4	-0.4911	-0.491	-0.4960	-0.495	-0.0428	-0.042
4.5	-0.2422	-0.242	-0.5011	-0.501	-0.0454	-0.045
5	0.0084	0.008	-0.5012	-0.501	-0.0462	-0.046

Table 2. Comparison of the cross-sectional forces

$x(m)$	N_x (N)		M_x (Nm)		Q (N)	
	Present Study	[29]	Present Study	[29]	Present Study	29]
0	0.000	0.000	2.2147	2.214	-4.7385	-4.738
0.5	0.000	0.000	0.4348	0.434	-2.4745	-2.474
1	0.000	0.000	-0.3786	-0.378	-0.9059	-0.905
1.5	0.000	0.000	-0.5900	-0.589	-0.0439	-0.043
2	0.000	0.000	-0.5085	-0.508	0.3028	0.302
2.5	0.000	0.000	-0.3365	-0.336	0.3514	0.351
3	0.000	0.000	-0.1787	-0.178	0.2687	0.268
3.5	0.000	0.000	-0.0725	-0.072	0.1567	0.156
4	0.000	0.000	-0.0184	-0.018	0.0649	0.064
4.5	0.000	0.000	-0.0011	-0.001	0.0114	0.011
5	0.000	0.000	0.0000	0.000	0.0000	0.000
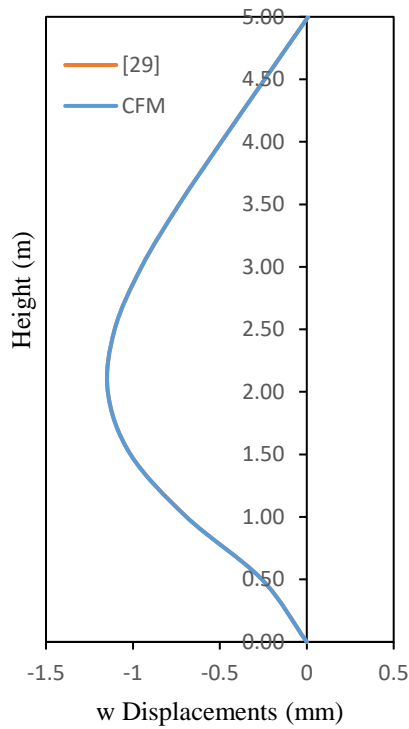
Figure 3. Comparison of w displacements
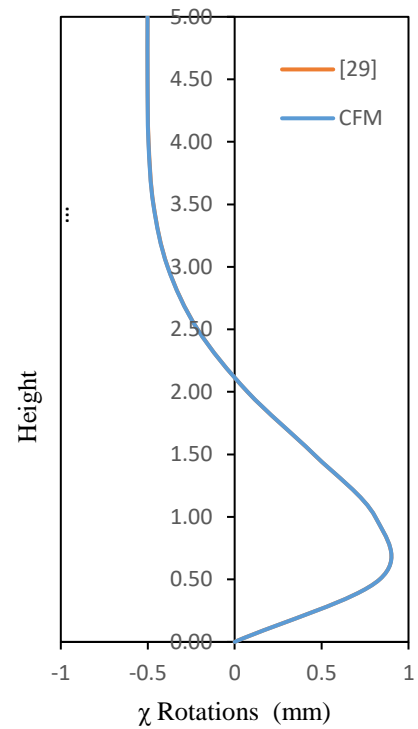
Figure 4. Comparison of χ rotations
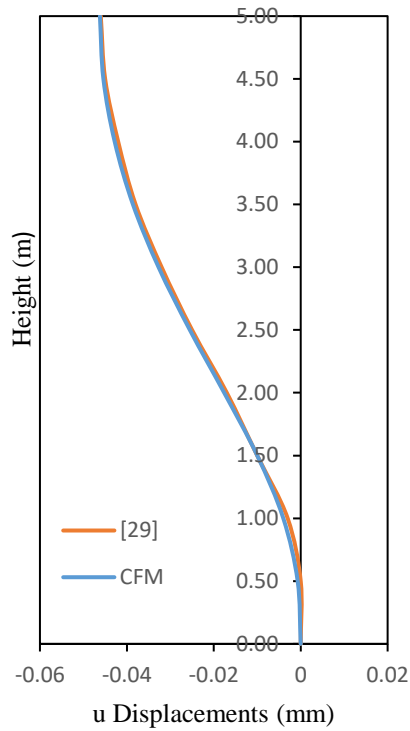
Figure 5. Comparison of u displacements
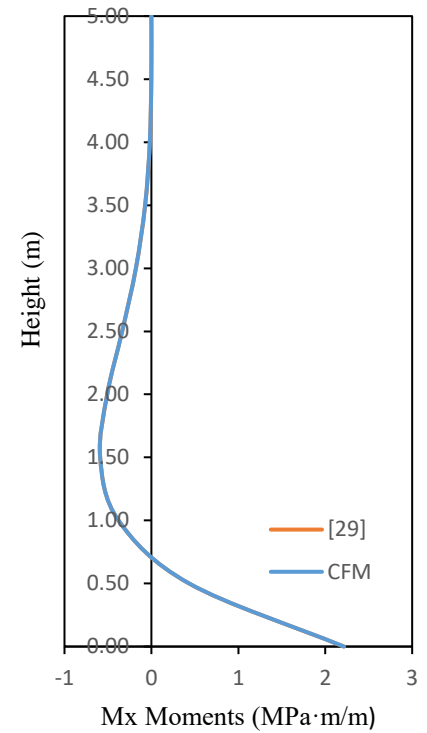
Figure 6. Comparison of bending moments
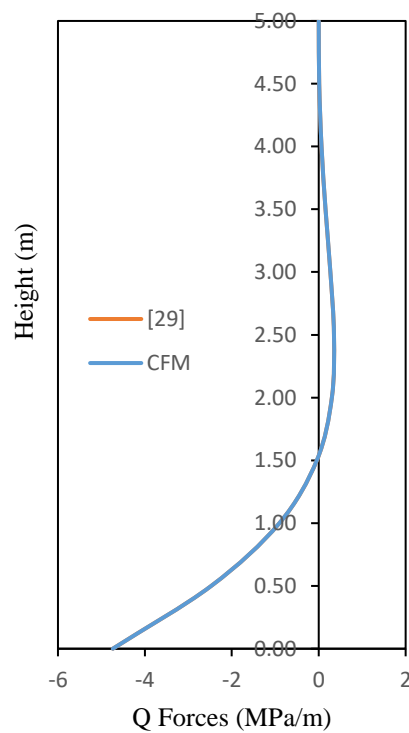
Figure 7. Comparison of shear forces

An analysis of the figures and the values presented in the tables indicates that the results obtained from CFM. demonstrate a high degree of accuracy, with errors predominantly remaining below 1%, thereby validating the reliability of the present study and confirming the robustness of the proposed methodology for further analysis. The maximum transverse displacement value is observed as

$-1.1448\ mm$ at $x = 2$, the maximum rotation value is $0.8343\ rad$ at $x = 0.5$ and the maximum meridional displacement value is -0.0462 at $x = 5$

Application 2.

The static behavior of the constant-thickness cylindrical shell, whose geometry is shown in Figure 8, is analyzed under parabolic loading. The boundary conditions defined by the equations (22-23) are applied for this problem. The value of q_0 is considered as $1\ MPa$.

$$q = q_0 \left(1 - \frac{x^2}{H^2} \right)$$
(25)
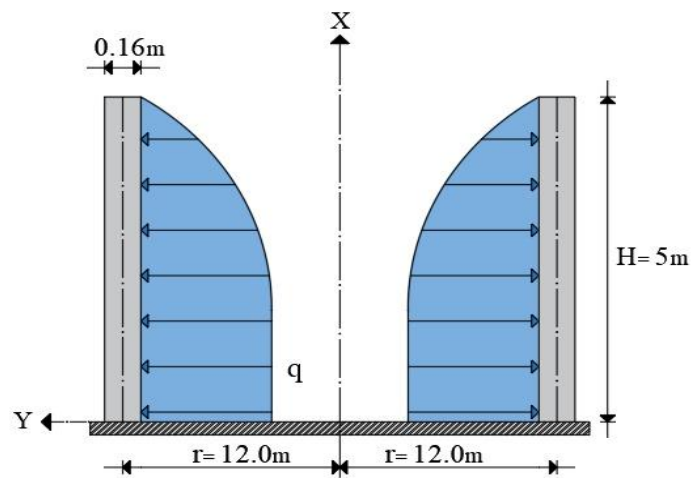
Figure 8. Cylindrical shell under parabolic pressure

Table 3. Displacements and rotation values for parabolic pressure

x(m)	$w(mm) \cdot 10^3$	$\chi\ (Rad) \cdot 10^3$	$u\ (mm) \cdot 10^3$
0	0.0000	0.0000	0.0000
0.5	0.0645	-0.2119	0.0002
1	0.1782	-0.2201	0.0010
1.5	0.2704	-0.1416	0.0026
2	0.3172	-0.0464	0.0047
2.5	0.3195	0.0336	0.0069
3	0.2877	0.0896	0.0090
3.5	0.2336	0.1236	0.0108
4	0.1667	0.1415	0.0122
4.5	0.0939	0.1485	0.0131
5	0.0192	0.1496	0.0135

Table 4. Cross sectional forces for parabolic pressure

x (m)	N_x (N)	M_x (Nm)	Q (N)
0	0.0000	-40.4770	79.9965
0.5	0.0000	-9.6151	44.4940
1	0.0000	5.6223	18.3270
1.5	0.0000	10.5457	3.0382
2	0.0000	10.0703	-3.8143
2.5	0.0000	7.5800	-5.5515
3	0.0000	4.9096	-4.9082
3.5	0.0000	2.7774	-3.5995
4	0.0000	1.2894	-2.3913
4.5	0.0000	0.3582	-1.3341
5	0.0000	0.0000	0.0000

(a)   (b)   (c)
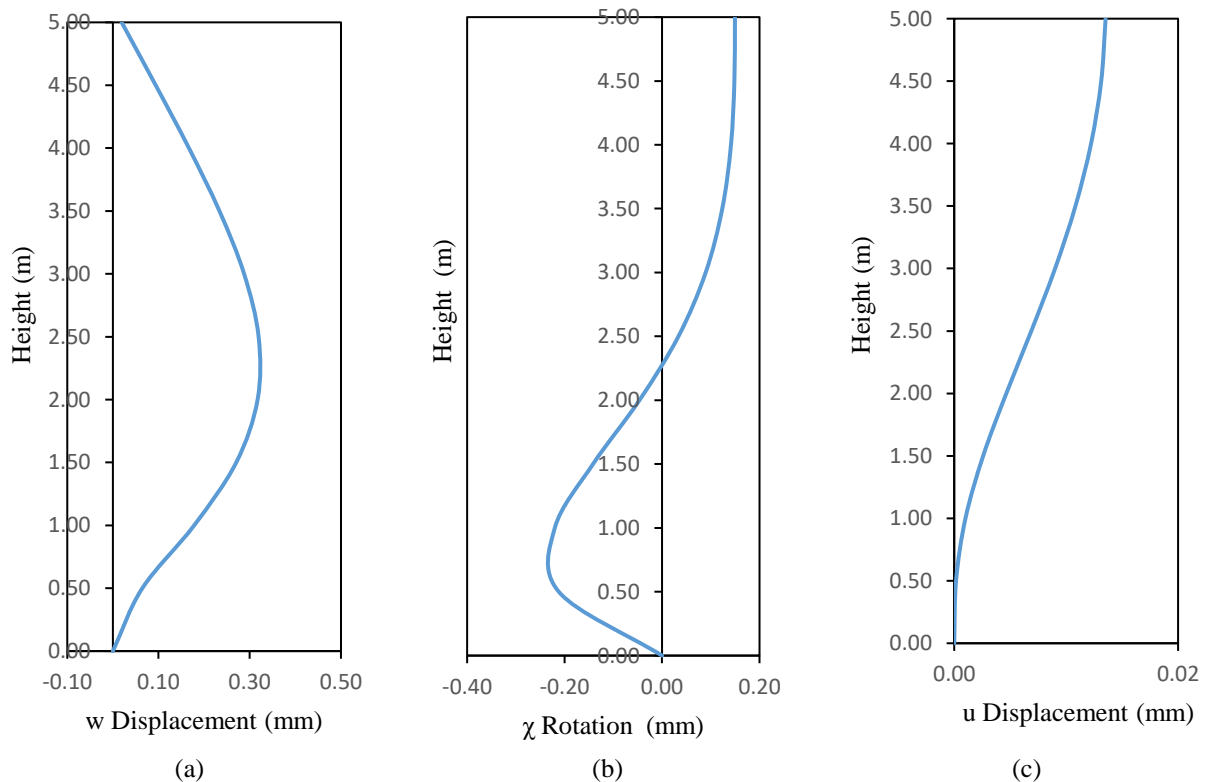
Figure 9. Transverse Displacement, Rotation and axial displacement of Cylindrical shell under parabolic pressure

The system described is subjected to parabolic pressure, which induces varying displacement and rotation along its length. Given the conditions, parabolic pressure likely influences the displacements and rotations in a nonlinear manner, as evidenced by the fluctuations shown in Fig. 9. As observed in Table 3 and Fig. 9(a), the transverse displacement w starts at 0 and increases, with the maximum deflection reaching $0.3195\ mm$ at $x = 2.5\ m$. Beyond $x = 2.5\ m$, the value of w decreases, reaching $0.0192\ mm$ at $x = 5\ m$. From Fig. 9 (b) it is seen that the rotation (χ) changes sign, indicating a change in the bending direction. The maximum value of rotation is obtained as $-0.2201\ rad$ at $x = 1$. The displacement u demonstrates an increasing elongation along the height of the shell. As shown in fig. 9 (c) the maximum meridional displacement happens at the top end of the structure obtained as $0.0135\ mm$.

Application 3.

The static behavior of the constant-thickness cylindrical shell, with geometric properties shown in Figure 10, has been analyzed for uniform distributed load. The boundary conditions and material properties specified by the equations (22-23) is used in the analysis.

$$q_0 = 1 \; MPa$$
$$q = q_0 \tag{26}$$
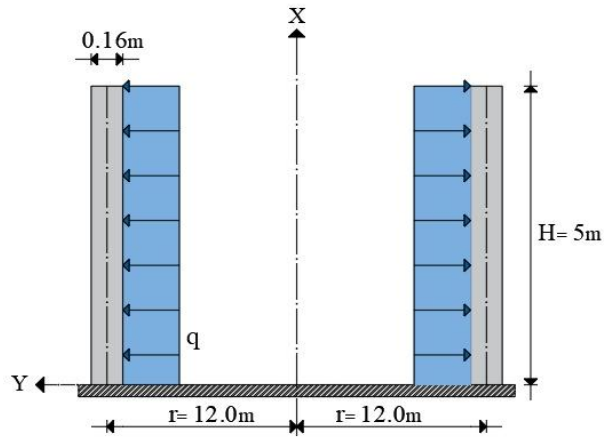
Figure 10. Axisymmetric cylindrical shell under uniform distributed loading

Table 5. Variation of displacements and rotation with respect to height

$x(m)$	$w(mm) \cdot 10^3$	$\chi \, (Rad) \cdot 10^3$	$u \, (mm) \cdot 10^3$
0	0	0	0
0.5	0.068833	-0.2292	0.000173
1	0.19552	-0.25491	0.001085
1.5	0.30963	-0.1943	0.002856
2	0.38724	-0.11693	0.005299
2.5	0.43414	-0.04476	0.008152
3	0.44562	-0.015	0.011201
3.5	0.44683	0.005007	0.014928
4	0.44267	0.012638	0.017400
4.5	0.43577	0.014476	0.020451
5	0.42852	0.014523	0.023452

Table 6. Variation of the cross-sectional forces with respect to height

x (m)	N_x (N)	M_x (Nm)	Q (N)
0	0.0000	-42.3830	79.9320
0.5	0.0000	-11.5530	44.4300
1	0.0000	5.2832	18.2710
1.5	0.0000	8.5558	3.0159
2	0.0000	8.0886	-3.7476
2.5	0.0000	5.6713	-5.3092
3	0.0000	3.1875	-4.3881
3.5	0.0000	1.4004	-3.0711
4	0.0000	0.4199	-1.2577
4.5	0.0000	0.0521	-0.3148
5	0.0000	0.0000	0.0000
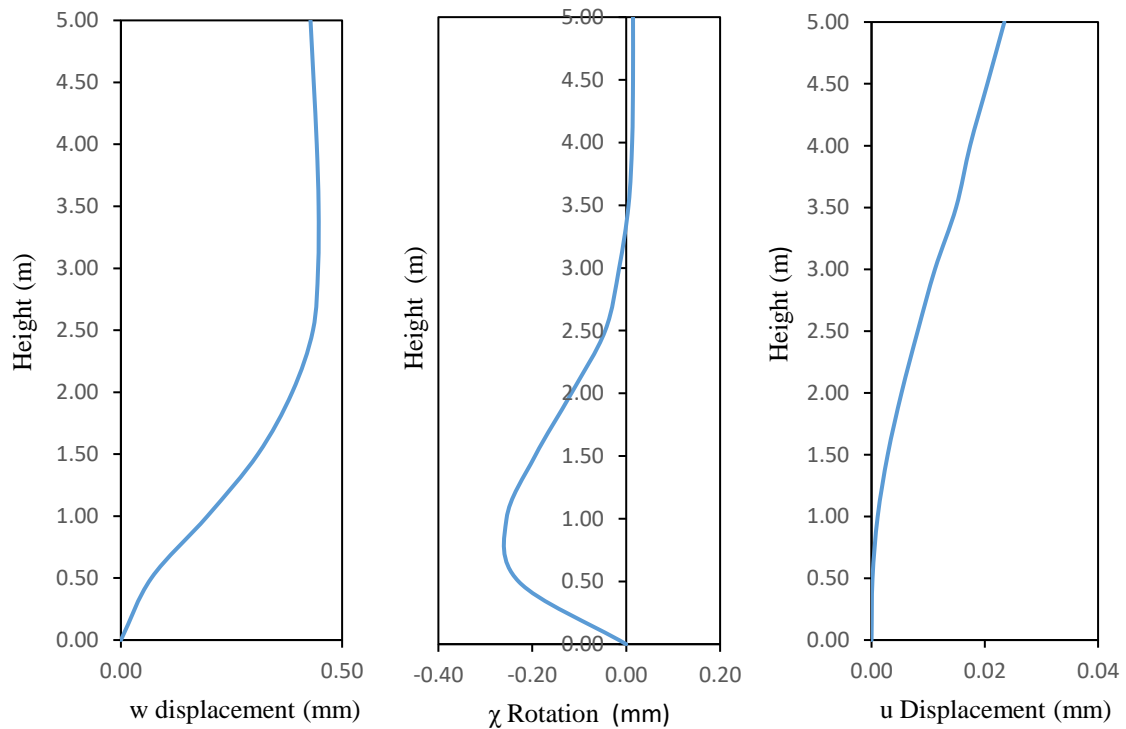
Figure 11. Transverse Displacement, Rotation and axial displacement of Cylindrical shell under UDL

The transverse displacement along the height of the shell increases gradually as x increases where the maximum transverse displacement value is observed as $0.44562 mm$ at $x = 3m$. Rotation demonstrates a non-linear change where maximum rotation is observed as -0.25491 at $x = 1m$. The meridional displacement increases smoothly as x increases where the highest value for meridional displacement is observed as $0.023452\ mm$ at the height of $x = 5\ m$.

4. CONCLUSIONS

In this study, the static behavior of axisymmetric thin cylindrical shells made of homogeneous, isotropic, and linear elastic material under various loads has been numerically investigated using the Complementary Functions Method (CFM). The RK5 algorithm is preferred for solving the IVP.

A computer program for the static analysis of cylindrical shells using CFM has been developed in Wolfram Mathematica. The results of the coded program are compared with those of the literature and

demonstrated convenient agreement. For better understanding of the behavior of the axisymmetric cylindrical shell, parametric analyses are conducted under parabolic and uniformly distributed loading types.

Analysis reveals that loading types significantly influences the behavior of the shell structure, as distinct loading conditions yield different response magnitudes. Based on the results presented in tables 1-6 and figures 3-7, 9 and 11 the following key observations can be highlighted:

- The maximum lateral deflection values under hydrostatically, parabolically and uniformly distributed loading conditions are found to be $-1.1448 \cdot 10^3 mm$, $0.3195 \cdot 10^3\ mm$ and $0.44562 \cdot 10^3\ mm$ respectively.
- The maximum rotation values under hydrostatically, parabolically and uniformly distributed loading conditions are obtained as $0.8343 \cdot 10^3 rad$, $-0.2201 \cdot 10^3\ rad$ and $-0.25491 \cdot 10^3\ rad$ respectively.
- The maximum meridional deflection values under hydrostatically, parabolically and uniformly distributed loading conditions are obtained as $-0.0462 \cdot 10^3 mm$, $0.0135 \cdot 10^3\ mm$,$0.023452 \cdot 10^3 mm$ respectively.

These findings indicate that hydrostatic pressure loading produces the most significant deflections. Therefore, considering hydrostatic pressure for designing purposes would enhance structural safety and reliability than the other loading scenarios.

Declaration of Ethical Standards

The authors declare that they have carried out this completely original study by adhering to all ethical rules including authorship, citation and data reporting. .

Credit Authorship Contribution Statement

O. AYAZ: Methodology, Conceptualization, Resources, Investigation, Analyzing Writing, Review & Editing.
A. R. NOORI: Methodology, Conceptualization, Resources, Review, Supervision.
B. SİVRİ: Resources, Modeling, Writing -review & editing.
B. TEMEL: Methodology, Conceptualization, Review, Supervision. .

Declaration of Competing Interest

The authors declared that they have no conflict of interest .

Funding / Acknowledgements

Data Availability

Data supporting the findings of this study can be obtained from the corresponding author with reasonable requests to assist in scientific studies.

REFERENCES

[1]   P. E. Grafton and D. R. Strome, "Analysis of axisymmetrical shells by the direct stiffness method," *AIAA Journal*, vol. 1, no. 10, pp. 2342–2347, 1963, doi: 10.2514/3.2064.

[2]   Garnet, H and J. Kempner, "Axisymmetric Free Vibrations of Conical Shells," *AIAA Journal*, vol. 2, no. 3, pp. 458–466, 1964.

[3]   D. A. Godfrey and M. M. Moussa, "Dynamic analysis of axisymmetric shells under arbitrary transient pressures," *Nuclear Engineering and Design*, vol. 23, no. 2, pp. 187–194, 1972.

[4]   A. Tessler, "An efficient, conforming axisymmetric shell element including transverse shear and rotary inertia," *Computers & Structures*, vol. 15, no. 5, pp. 567–574, 1982.

[5]   B. Suarez, M. Canet, and E. Onate, "Free vibration analysis of plates, bridges and axisymmetric shells using a thick finite strip method," *Engineering Computations*, vol. 5, no. 3, pp. 123–130, 1988, doi: 10.1108/eb023734

[6]   A. F. Loula, I. Miranda, T. J. Hughes, and L. P. Franca, "On mixed finite element methods for axisymmetric shell analysis," Computer Methods Appl. Mech. Eng., vol. 72, no. 2, pp. 201–231, 1989.

[7]   D. P. Thambiratnam, "A simple finite element analysis of hyperboloidal shell structures," *Computers & Structures*, vol. 48, no. 2, pp. 249–254, Jul. 1993, doi: 10.1016/0045-7949(93)90417-C.

[8]   D. P. Thambiratnam and V. Thevendran, "Axisymmetric free vibration analysis of cylindrical shell structures using BEF analogy," *Computers & Structures*, vol. 43, no. 1, pp. 145–150, 1992.

[9]   D. P. Thambiratnam and Y. Zhuge, "Axisymmetric free vibration analysis of conical shells," *Engineering Structure*, vol. 15, no. 2, 1993.

[10]   M. Ozakqa and E. Hinton, "Free vibration analysis and optimisation of axisymmetric plates and shells—I. Finite element formulation," *Computers & Structures*, vol. 52, no. 6, pp. 1181–1197, 1994.

[11]   M. Özakça and E. Hinton, "Free vibration analysis and optimisation of axisymmetric plates and shells—II. Shape optimisation," *Computers & Structures*, vol. 52, no. 6, pp. 1199–1211, 1994.

[12]   A. R. Noori and B. Temel, "Dynamic analysis of axisymmetric shells in the Laplace domain," in *Proc. 1st Int. Mediterranean Science and Engineering Congress (IMSEC)*, Adana, Turkey, Oct. 2016. [Online]. Available: https://www.researchgate.net/publication/316922251

[13]   A. Filippidis and A. J. Sadowski, "Modern analysis of axisymmetric shells with AQUINAS: A MATLAB finite element toolbox," *SoftwareX*, vol. 23, 101434, 2023.

[14]   H. Guo and H. Zheng, "The linear analysis of thin shell problems using the numerical manifold method," *Thin-Walled Structures*, vol. 124, pp. 366–383, 2018, doi: 10.1016/j.tws.2017.12.027.

[15]   P. Das, M. A. Islam, S. Somadder, and M. A. Hasib, "Analytical and numerical analysis of functionally graded (FGM) axisymmetric cylinders under thermo-mechanical loadings," *Materials Today: Communications*, vol. 33, 104405, 2022, doi: 10.1016/j.mtcomm.2022.104405.

[16]   Y. V. Tokovyy, "Integration of the equations of plane axisymmetric problems of the theory of elasticity and thermoelasticity for layered solid cylinders," *Journal of Mathematical Sciences*, vol. 282, no. 5, pp. 769–779, 2024, doi: 10.1007/s10958-024-07215-9.

[17]   A. H. Sofiyev, A. Deniz, M. Avcar, P. Özyigit, and M. H. Omurtag, "Effects of the non-homogeneity and elastic medium on the critical torsional load of the orthotropic cylindrical shell," *Acta Physica Polonica A*, vol. 123, no. 4, pp. 728–730, 2013, doi: 10.12693/APhysPolA.123.728.

[18]   F. Gu et al., "Theoretical study on 3D elastic response and first layer failure strength of composite cylinders subjected to axisymmetric loadings," *International Journal of Pressure Vessels and Piping*, vol. 210, 105245 , 2024, doi: 10.1016/j.ijpvp.2024.105245.

[19]   M. H. Samadzadeh, M. Arefi, and A. Loghman, "Static bending analysis of pressurized cylindrical shell made of graphene origami auxetic metamaterials based on higher-order shear deformation theory," *Heliyon*, vol. 10, no. 16, 2024, doi: 10.1016/j.heliyon.2024.e36319.

[20]   I. D. Breslavsky, M. Amabili, and M. Legrand, "Static and dynamic behavior of circular cylindrical shell made of hyperelastic arterial material," *Journal of Applied Mechanics*, vol. 83, no. 5, 051002 , 2016, doi: 10.1115/1.4032549.

[21]   C. U. Nwoji, D. G. Ani, O. A. Oguaghamba, and V. T. Ibeabuchi, "Static bending of isotropic circular cylindrical shells based on the higher order shear deformation theory of Reddy and

Liu," *International Journal of Applied Mechanics and Engineering*, vol. 26, no. 3, pp. 141–162, 2021, doi: 10.2478/ijame-2021-0041.

[22] B. Temel, S. Yildirim, and N. Tutuncu, "Elastic and viscoelastic response of heterogeneous annular structures under arbitrary transient pressure," *International Journal of Mechanical Sciences*, vol. 89, pp. 78–83, 2014, doi: 10.1016/j.ijmecsci.2014.08.021.

[23] S. Yildirim and N. Tutuncu, "Radial vibration analysis of heterogeneous and non-uniform disks via complementary functions method," *Journal of Strain Analysis for Engineering Design*, vol. 53, no. 5, pp. 332–337, 2018, doi: 10.1177/0309324718765006.

[24] A. R. Noori and B. Temel, "On the vibration analysis of laminated composite parabolic arches with variable cross-section of various ply stacking sequences," *Mechanics of Advanced Materials and Structures*, vol. 27, no. 19, pp. 1658–1672, 2020, doi: 10.1080/15376494.2018.1524949.

[25] B. Temel, T. A. Aslan, and A. R. Noori, "In-plane vibration analysis of parabolic arches having a variable thickness," *International Journal of Dynamics and Control*, vol. 9, no. 3, pp. 910–921, 2021, doi: 10.1007/s40435-020-00727-7.

[26] A. R. Noori, T. A. Aslan, and B. Temel, "Dynamic analysis of functionally graded porous beams using complementary functions method in the Laplace domain," *Composite Structures*, vol. 256, 113094, 2021, doi: 10.1016/j.compstruct.2020.113094.

[27] B. Temel, T. A. Aslan, and A. R. Noori, "An efficient dynamic analysis of planar arches," *European Mechanical Science, 1(3), 82-88*, 2017.

[28] T. A. Aslan, A. R. Noori, and B. Temel, "Dynamic response of viscoelastic tapered cycloidal rods," *Mechanics Research Communications*, vol. 92, pp. 8–14, 2018, doi: 10.1016/j.mechrescom.2018.06.006.

[29] K. Sayar, "Dönel kabuk sistemlerin diferansiyel geçiş matrisleriyle çözümü," *Doçentlik Tezi*, 1970.

[30] Y. Mengi, *Numerical Methods in Engineering*, Adana, Turkey: Çukurova University, 1993.

[31] S. Chapra and R. Canale, *Numerical Methods for Engineers*, 7th ed., 2011.

[32] Wolfram Research Inc., *Mathematica*, Wolfram Research, Inc., 2024.

LIMESTONE AND NATURAL POZZOLAN BLENDED CEMENTS: EVALUATING SULFATE RESISTANCE FOR SUSTAINABLE CONSTRUCTION

[1] **Ahmet YİĞİT** [ID] **, [2, *] Furkan TÜRK** [ID] **,[3] Ülkü Sultan KESKİN** [ID]

Konya Technical University, Engineering and Natural Science Faculty, Civil Engineering Department, Konya, TÜRKİYE
[1] yigitahmet@hotmail.com, [2] fturk@ktun.edu.tr, [3] uskeskin@ktun.edu.tr

Highlights

- Blended Cements for Sustainability: Limestone and pozzolan cements as alternatives.

- Sulfate Resistance Comparison: Limestone cements resist sulfate better than pozzolan.

- Long-Term Durability: Blended cements last 360 days under sulfate exposure.

*Corresponding Author: Furkan TÜRK, fturk@ktun.edu.tr

LIMESTONE AND NATURAL POZZOLAN BLENDED CEMENTS: EVALUATING SULFATE RESISTANCE FOR SUSTAINABLE CONSTRUCTION

¹ Ahmet YİĞİT ID **, ², * Furkan TÜRK** ID **,³ Ülkü Sultan KESKİN** ID

Konya Technical University, Engineering and Natural Science Faculty, Civil Engineering Department, Konya, TÜRKİYE
¹ yigitahmet@hotmail.com, ² fturk@ktun.edu.tr, ³ uskeskin@ktun.edu.tr

ABSTRACT: This study aims to compare the behavior of ordinary Portland cement, sulfate resistant cement, natural pozzolan blended cement and limestone blended cement, produced in the same strength class as Portland clinker, under the influence of sulfate. For this purpose, five different cements were produced in Konya Cement production facilities. Characterization and sulfate tests were carried out on the cements. The strengths of the cements blended with limestone and natural pozzolan were determined in different sulfate environments and under normal curing conditions, and their behavior under sulfate effect was observed during a 360-day monitoring period. The experimental results revealed that the sulfate resistant cement with the lowest C_3A content had the highest sulfate resistance. Moreover, the limestone blended cement showed a superior performance compared to the natural pozzolan blended cement. The compressive strength of the natural pozzolana blended cement was 50.1 MPa at 28 days and decreased by about 6% to 47.1 MPa after 360 days of sulfate exposure. On the other hand, the 28-day compressive strength of the limestone blended cement was 49.8 MPa, while it remained almost unchanged at 50 MPa after 360 days of sulfate exposure. These results show that limestone and natural pozzolan blended cements have the potential for widespread use in construction applications in line with environmental sustainability goals.

Keywords: Blended Cements, Limestone, Natural Pozzolan, Sulfate Resistance

1. INTRODUCTION

Concrete, a material that is utilized extensively across various construction projects and architectural endeavors on a global scale, is recognized as one of the most prevalent building substances in existence. Notably, beyond the numerous advantages that concrete possesses, which include remarkable compressive strength, cost-effectiveness, and the versatility to be molded into an array of desired shapes and forms, it is also imperative to acknowledge that it is not devoid of certain inherent disadvantages. Concrete elements must be durable to extreme environmental conditions. Various measures are taken to ensure the durability of concrete structures, especially in environments rich in aggressive chemicals (acid, base, salt, etc.). With external protection, aggressive chemicals can be prevented from reaching concrete structures, but this is not possible in every case. In addition to external protection, the durability of the elements can be increased by optimizing the concrete or cement components. Factors such as soil, groundwater, and seawater that can come into contact with various concrete elements can contain high levels of sulfate The incorporation of cement replacement materials (CRM) such as fly ash, blast furnace slag, calcined clay, and natural pozzolans in concrete mixtures can enhance the longevity of concrete components, especially their resistance to sulfate attack [1], [2], [3], [4]. Moreover, the use of SCMs in mixtures does not only provide durability, but also helps to reduce the maintenance and repair needs and the carbon footprint of the cement and concrete industry by reducing the amount of clinker. In addition to traditional CRMs, additives such as anti-sulfate inhibitors, hydrophobic agents, various waste powders, nanomaterials, etc. are the subject of various research in the literature to increase the impermeability and sulfate resistance of concrete [5], [6], [7].

With increasing environmental concerns, there is a growing interest in using recycled materials [8],

*Corresponding Author: Furkan TÜRK, fturk@ktun.edu.tr

reducing greenhouse gas emissions in cement production and reducing the clinker/cement ratio. Various academic and industry studies on topics such as limestone calcined clay cement (LC3), blended cement and geopolymer concrete are progressing with determination [9], [10], [11], [12], [13]. The most important consideration in these studies, which support global sustainability initiatives, should be both maintaining performance standards and minimizing environmental impact. Binders with reduced clinker to cement ratios are candidates to become widespread in traditional construction applications and replace ordinary Portland cement. However, a comparative study of the behavior of blended cements produced with various mineral additives that meet certain performance standards under aggressive conditions is required. This is essential to facilitate the selection of cements for long-term applications and to ensure that they meet the demands of modern construction practices.

Considering the environmental impacts, various innovation efforts in the cement and concrete industry are continuing to increase rapidly. Recently, studies have been carried out on the production of cement with different contents without compromising performance. Reducing the amount of clinker, which is responsible for high greenhouse gas emissions, per unit of cement is the basis of these studies [14]. In studies where cement or clinker is substituted with various mineral additives, the main priority is to reduce the amount of cement as much as possible without losing performance. Cement and/or concrete production methods that show the same performance compared to the reference sample and have a lower carbon footprint are considered acceptable within the scope of emission reduction studies. Although specimens substituted with various additives show sufficient strength in the short term, various durability studies are also needed. While reducing clinker content can reduce carbon emissions, it can also affect the performance of concrete if not managed properly [15]. In particular, substituting clinker or cement with materials such as limestone and natural pozzolana can improve durability parameters such as freeze-thaw, alkaline silica reaction, chloride resistance as well as environmental advantages [16], [17], [18]. However, it is important to design the mix carefully to avoid problems such as low early strength and workability. In addition, although it can be inferred from life cycle analysis studies in the literature which cement is more environmentally friendly, it is worth investigating which cement performs better against specific durability problems. This study is based on investigating the sulfate resistance of cements containing different proportions of clinker but belonging to the same class.

The aim of this study is to compare the sulfate resistance of limestone blended, natural pozzolan blended and ordinary cements produced with Portland clinker of the same strength class. For regions containing sulphate groundwater and regions with sulphate content in the soil structure, it would be appropriate to use a sustainable cement type with easy accessibility, high sulphate resistance and low cost. For this reason, it was decided to investigate the effect of limestone blended cements with low fineness and high Blaine values on sulfate resistance with the hypothesis that the filling effect of limestone will increase the filling effect and impermeability. Various properties of the blended and ordinary cements produced were defined and their behavior under the effect of sulfate was compared.

2. MATERIAL AND METHODS

In this study, five different cements were produced to investigate the behavior of different cements under sulfate effect. To be used in this study, ordinary Portland cement (CEM I 42.5), limestone (CEM II/A/L 42.5), natural pozzolan (CEM II/A/P 42.5) and limestone-natural pozzolan blended (CEM II/A 42.5) cements and sulphate resistant cement (CEM I SR-5 42.5) were produced at Konya Cement production facilities. The additive ratios of the produced cements were determined considering the condition of belonging to the same strength class (42.5). The physical properties, compressive strengths and performance of the cements produced within the scope of the study were examined after sulfate effect.

2.1. Material

2.1.1. Clinker substitutes

In Central Anatolia and especially around Konya region, it is difficult to access additives such as blast furnace slag, fly ash, silica fume in terms of cost and sustainability. Due to the abundance of limestone and natural pozzolana resources in this region [19], limestone and natural pozzolana are more advantageous than other additives in terms of access and cost. Considering these issues, natural pozzolana and limestone were preferred as clinker replacement materials in this study. Detailed analysis of limestone (LS) and natural pozzolan (NP) used in the study is presented in Table 1.

Table 1. Analysis of limestone and natural pozzolan used as additives in cements produced

Chemical and physical content		Limestone	Natural pozzolan
SiO_2	%	1.04	64.64
Al_2O_3	%	0.42	16.93
Fe_2O_3	%	0.11	5.33
CaO	%	53.93	4.64
MgO	%	0.30	1.08
SO_3	%	0.09	0.00
K_2O	%	0.02	3.42
Na_2O	%	0.02	3.00
Cl	%	0.018	0.002
Loss of ignition	%	44.67	2.64
Moisture	%	1.86	13.0
Pozzolanic activity	MPa		5.7
Reactive SiO_2	%		28.1

2.1.2. Cement composition

The compositions and 28-day compressive strengths of different cements produced in Konya Cement production facilities within the scope of this study are presented in Table 2. All cements produced are in the same class (42.5) according to TS EN 197-1.

Table 2. Cement compositions and 28-day compressive strengths

Sample	Short name	Clinker (%)	Gypsum (%)	Natural Pozzolan (%)	Limestone (%)	Comp.Str. (MPa)
CEM II/A M (P-L) 42.5 R	CEM II/A	78.05	5.89	8.70	7.36	47.0
CEM I 42.5 R	CEM I	88.13	5.14	0.0	6.44	46.0
CEM I 42.5 R SR-5	SR-5	88.75	4.42	0.0	6.43	48.6
CEM II/A (L) 42.5 R	CEM II A/L	77.21	5.89	0.0	14.64	46.7
CEM II/A (P) 42.5 R	CEM II A/P	78.56	5.11	15.56	0.77	45.1

2.2. Method

2.2.1. Determination of physical, chemical and mechanical properties of cement

The cements produced within the scope of this study were tested for insoluble residue (IR) according to TS EN 196-2, Blaine surface area and sieve residue according to TS EN 196-6, normal consistency and setting time according to TS EN 196-3, elemental composition by XRF and compressive strength on days 2, 7 and 28 according to TS EN 196-1. With these analyzes, the basic parameters that are decisive in the

identification of cement were determined

2.2.2. Preparation of mortar mixtures and tests

Standard mortar mixtures were prepared in accordance with TS EN 196-1 with the cements produced within the scope of this study and whose basic properties were defined. The prepared mixtures were placed in 40x40x160 mm molds and kept in the mold for 24 hours. After 24 hours, the specimens were removed from the mold and cured in lime-saturated water until the test day.

The compressive strengths of the hardened mortar specimens cured in lime-saturated water were determined at 28, 40, 90, 150 and 360 days of age. In addition, standard mortar mixtures were prepared from the cements produced to be used in sulfate resistance tests. After 28 days of normal curing, the age of the specimens was considered zero and they were placed in 3% magnesium sulfate ($MgSO_4$) solution. The compressive strengths of the specimens kept in sulfate solution were similarly determined at 28, 40, 90, 150 and 360 days of age and compared with the specimens kept in normal curing. The work flow diagram of the study is presented in Figure 1 and photos of some of the prepared and tested samples are presented in Figure 2.
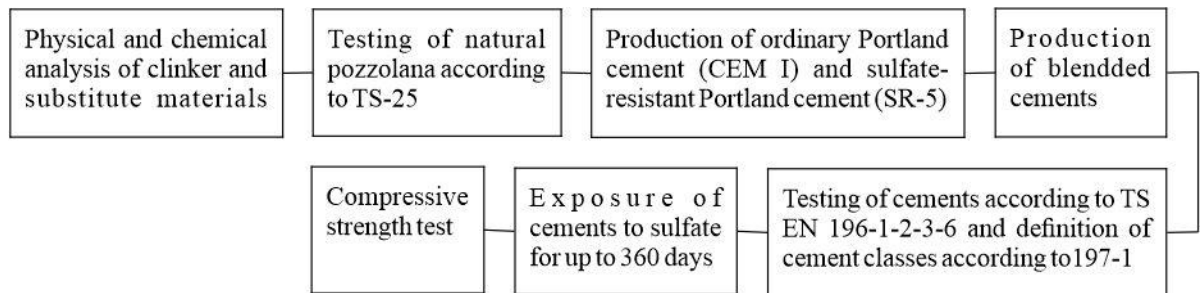
Figure 1. The flow chart
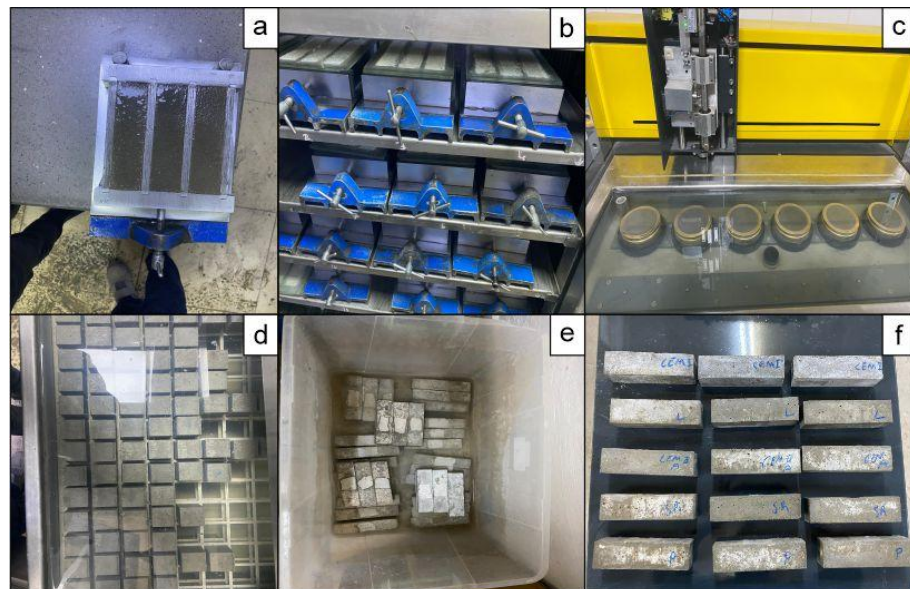
Figure 2. Molded fresh mortar (a), specimens kept in curing cabinet (b,d), setting time determination test (c), samples kept in $MgSO_4$ solution (e,f)

3. RESULTS AND DISCUSSION

3.1. Physical, chemical and mechanical properties of cements

The chemical and physical properties of the produced cements are presented in Table 3 and Table 4, respectively. According to the chemical analysis results, the lowest amount of C_3A was found in SR-5 cement and the highest amount of C_3A was found in CEM II A/P cement.

Table 3. Chemical composition of cement

Content (%)	CEM II/A M (P-L) 42.5 R	CEM I 42.5 R	CEM I 42.5 R SR-5	CEM II/A (L) 42.5 R	CEM II/A (P) 42.5 R
SiO_2	21.26	18.6	19.38	17.97	24.86
Al_2O_3	5.12	4.52	4.35	4.38	6.13
Fe_2O_3	4.44	4.16	4.54	3.96	5.51
CaO	58.52	61.36	61.71	62.34	53.61
MgO	1.06	1.1	1.15	0.97	1.18
SO_3	3.55	3.21	2.89	3.55	3.2
K_2O	0.88	0.69	0.61	0.74	1.03
Na_2O	0.49	0.33	0.32	0.36	0.63
Cl	0.0177	0.00203	0.0182	0.0179	0.0165
C_3A	6.06	4.94	3.85	4.91	6.92
C_4AF	13.51	12.66	13.82	12.05	16.77

Table 4. Physical properties of cement

Sample	CEM II/A M (P-L) 42.5 R	CEM I 42.5 R	CEM I 42.5 R SR-5	CEM II/A (L) 42.5 R	CEM II/A (P) 42.5 R
Bf (cm^2/g)	4228	3721	3689	4713	4046
32 μm (%)	6.9	-	-	5.5	9.2
45 μm (%)	2.5	5.6	3.0	1.7	4.1
IR (%)	7.68	0.45	0.54	2.14	13.58
Standard consistency (%)	29.0	27.8	28.3	28.3	29.3
Initial set (min.)	140	150	155	150	255
Final set (min.)	220	220	230	220	345

When the Blaine fineness and sieve residue values of the cements were analyzed, the cement with the highest Blaine fineness was found to be CEM II/A/L. The cement with the lowest Blaine fineness is SR-5. In addition, the 32 μm sieve residue of LS-blended cement is 5.5%. Both sieve residue and Blaine fineness values indicate that LS-blended cement is the most finely ground type among the cements to be compared. The standard consistency of the cement types containing NP is slightly higher than the other cement types. When the physical and chemical analyzes were examined, it was seen that all cement types prepared for use in the experiment fulfilled the requirements of TS EN 197-1 standard.

The 2,7 and 28-day strength results of the cements used in the study are given in Figure 3. All cement types used belong to 42.5 MPa strength class. In addition, it was determined that the 2-day early strength values, which is a requirement of TS EN 197-1 standard, were above 20 MPa in all cement types.
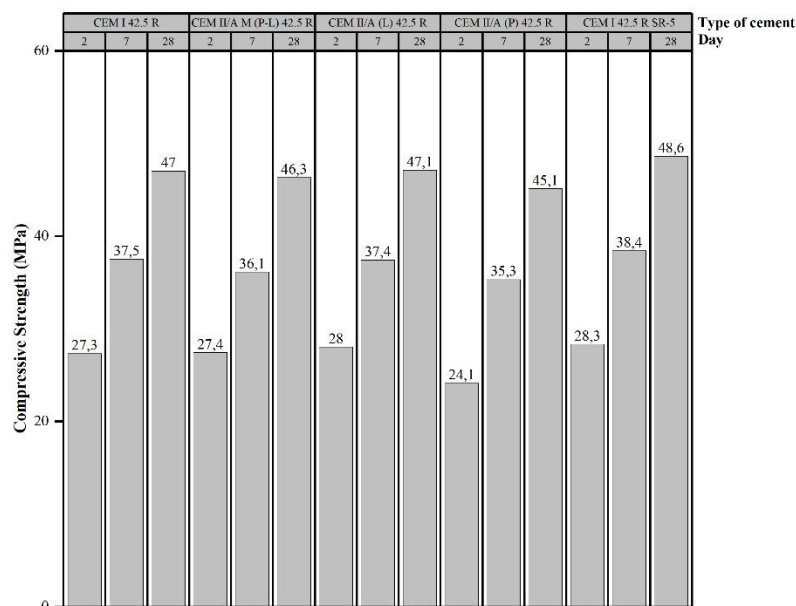
Figure 3. Compressive strength results of cements

All cements belong to the same strength class. Replacing clinker with various additives can often result in strength reduction, depending on pozzolanic activity and substitution rate [20]. However, the component ratios and Blaine fineness of the cements were optimized in this study so that the cements belonged to the same strength class. SR-5 cement (88.75%) with the highest clinker content has the lowest Blaine fineness, while CEM II A/L cement (77.21%) with the lowest clinker content has the highest Blaine fineness. It is know that cement in which some of the clinker has been replaced with inert LS would need to be ground finer to perform as well as cement with higher clinker content [21]. However, not only the fineness but also the type and amounts of components affect the strength [22]. Compared to other cements, the setting time of NP-blended cement was slightly delayed and the early strength was slightly lower. This is related to the slow progression of pozzolanic reactions and their effectiveness at later ages. The better early strength and setting time of cement with LS and NP (CEM II/A) compared to cement with NP alone (CEM II A/P) may be related to the fineness. The strength and setting time results of CEM II/A cement, which contains less pozzolanic material but has higher Blaine fineness, showed that the cement fineness can prevent pozzolanic reactions at early age. In addition, the pozzolanic activity of the natural pozzolan used in the experiment was determined to be 5.7 MPa and the reactive SiO_2 content was determined to be 28.1% according to TS-25. Although the natural pozzolan used meets TS-25 requirements, the reactive silica content is low.

According to TS EN 197-1 and TS-25, the limits that Portland cements should meet and the information showing the properties of the cements produced within the scope of the study are presented in Table 5.

3.2. Sulfate tests

After determining that the cements produced in the first stage were in compliance with the standards and belonged to the same strength class, 120 samples were prepared for each cement type in the second stage and 60 of them were kept in magnesium sulfate solution and 60 of them were kept in a standard curing pool. The compressive strengths of the specimens kept under different curing conditions were determined at 28, 90, 150, and 360 days. The compressive strength results of the mortar mixtures prepared with the cements used in the experiment are presented in Figure 4.

Table 5. Limits of TS EN 197-1 and TS-25

	Limits of TS EN 197-1					Cement within the scope of this study				
Cement type	Early strength (2-days MPa)	Strength (28-days MPa)	SO$_3$ (%)	C$_3$A (%)	Initial setting (min.)	Early strength (2-days MPa)	Strength (28-days MPa)	SO$_3$ (%)	C$_3$A (%)	Initial setting (min.)
CEM I 42.5 R	≥ 20	$62.5 \geq X \geq 42.5$	≤ 4	-	≥ 60	27.3	47	3.21	4.94	150
CEM I 42.5-R-SR5	≥ 20	$62.5 \geq X \geq 42.5$	≤ 4	< 5	≥ 60	28.3	48.6	2.89	3.85	155
CEM II/A (L) 42.5 R	≥ 20	$62.5 \geq X \geq 42.5$	≤ 4	-	≥ 60	28	47.1	3.55	4.91	150
CEM II/A (P) 42.5 R	≥ 20	$62.5 \geq X \geq 42.5$	≤ 4	-	≥ 60	24.1	45.0	3.2	6.92	255
CEM II/A M (P-L) 42.5 R	≥ 20	$62.5 \geq X \geq 42.5$	≤ 4	-	≥ 60	27.4	46.3	3.55	6.06	140
	Limits of TS 25					Pozzolan within the scope of this study				
Type	Reactive silica (%)	SiO$_2$+Al$_2$O$_3$+Fe$_2$O$_3$ (%)	SO$_3$ (%)	Cl (%)	Pozzolanic activity (MPa)	Reactive silica	SiO$_2$+Al$_2$O$_3$+Fe$_2$O$_3$	SO$_3$ (%)	Cl (%)	Pozzolanic activity (Mpa)
Natural pozzolan	≥ 25	≥ 70	≤ 3	≤ 0.1	≥ 4	28.1	81.57	0	0.002	5.7
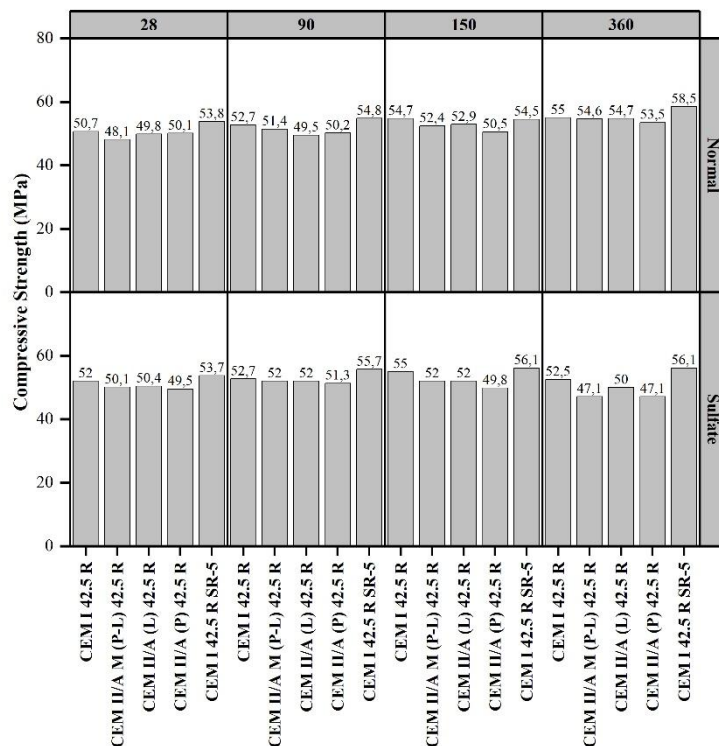
Figure 4. Compressive strength results of cements in sulphate and normal curing

All tests were carried out after a normal curing period of 28 days, assuming the specimen age to be zero. According to the test results, an increase in strength was observed for all cement types up to day 150, including the specimens in sulfate solution. An increase in strength is expected in the initial periods. The reason why the strength decrease could not be detected within 150 days is that magnesium sulfate reacts very slowly with the calcium-silica-hydrate gels that provide the binding of the cement paste. This reaction causes some of the C-S-H to dissolve.

At the end of 360 days, compressive strength results showed that the strength of the specimens in sulfate solution decreased in all cement types. It was observed that the strength increase of the specimens kept in magnesium sulfate solution stopped and even decreased. The reason for the strength decrease is that magnesium sulfate causes the formation of gypsum in the concrete and the formation of etrengite of the metastable C_4ASH_{12} products. In addition, magnesium sulfate causes some of the C-S-H gels to dissolve. The silica gel formed as a result of this reaction reacts very slowly with magnesium hydroxide and causes the formation of crystalline magnesium silicate with no binding value [23], [24]. These reactions are the main reasons for the strength decrease.

One of the most important parameters affecting the sulfate resistance of concrete to external sulfate attack is the amount of tricalcium aluminate (C_3A) in the cement. Low C_3A content can result in higher sulfate resistance by limiting the formation and transformation of ettringite [25], [26]. This research shows that SR-5 cement with the lowest C_3A content has the highest sulfate resistance. No loss of strength was observed in SR-5 cement maintained in a sulfate environment for 360 days. In general, mixtures prepared with CRM-substituted cements show improved durability performance in aggressive environments such as sulfate [27], [28]. In this study, NP blend cement showed the lowest sulfate resistance, with strength decreasing after 90 days. One of the reasons for the improved durability of CRM-substituted cements is the lower amount of C_3A in diluted clinker [29]. In this study, NP blend cement had the highest C_3A content. Therefore, the performance is usually worse than the other cements. The other types of cement have a similar C_3A content to ordinary Portland cement (CEM II/A has a higher C_3A) and showed almost similar sulfate resistance. Physical factors such as a dense matrix and low porosity due to low water/binder content can also limit sulfate penetration and improve durability [30], [31]. Limestone is known to aid in the formation of a dense matrix and limit the formation of gypsum and ettringite [32]. However, it should be noted that a high degree of limestone substitution can increase porosity. In limestone mixing systems, the formation of stable hydration products requires less sulfate compared to ordinary Portland cement, which can increase the sulfate resistance of the mix [33]. However, it is also reported in the literature that limestone substitution of 20% or more has a negative effect on sulfate resistance [32]. As a result, when fineness and content ratios are optimized, blended cements produced with less clinker can show at least as much sulfate resistance as ordinary Portland cement. Moreover, LS-blended cement can outperform NP-blended cement.

Baldermann et al. (2018) concluded that when limestone powder is substituted with cement at ratios less than 50%, it can show better sulfate resistance than ordinary Portland cement due to the reduction in total porosity and pore diameter [34]. Makhloufi et al. (2016) revealed that the substitution of limestone and natural pozzolan with cement has a positive effect on sulfate resistance [35]. In the present study, similar results were obtained to the studies reported in the literature and the performances of the additives were compared with each other.

4. CONCLUSIONS

The following conclusions were made in this research carried out with different cements of the same strength class.

Cements with different clinker contents were ground at different Bliane finenesses to provide the same strength class according to TS EN 197-1. In this way, cement containing approximately 88% clinker and cement containing approximately 77% clinker can belong to the same strength class. It is understood that the clinker difference of about 10% can be compensated by increasing the Blaine fineness.

The setting time of NP blended cement was delayed compared to other cements. However, an improvement in setting time was found when LS admixture was used together with NP. Similar situation was observed in both early and ultimate strength. When NP blended cement was compared with NP-LS blended cement, NP-LS blended cement gave better results. However, the difference in Blaine fineness should not be ignored. The pozzolanic activity of the NP used in the study was determined as 5.7 MPa and the reactive SiO2 ratio was 28.1%. Although the NP used met the requirements of TS 25, it has low reactivity. It can be concluded that finer ground inert limestone can perform better than the NP with

pozzolanic activity of 5.7 MPa.

The experimental study demonstrated the sulfate resistance of limestone and natural pozzolan blended cements. Due to its low C3A content, SR-5 cement did not lose strength for 360 days in sulfate solution.

Compared to natural pozzolan blended cement, limestone blended cement has higher sulfate resistance. NP blended cement suffered a strength loss of approximately 6% after 360 days of sulfate exposure, while LS blended cement did not show any strength difference. This may again be related to Blaine fineness. It was concluded that the dense microstructure and low void ratio of the finer grinded LS blended cement made sulfate penetration more difficult.

The results show that blended cements containing less clinker can be as durable as conventional Portland cement when appropriate fineness and content ratios are selected. This study emphasizes that limestone and natural pozzolan blended cements can contribute to environmental sustainability goals.

Credit Authorship Contribution Statement

[Ahmet Yiğit] Conceptualization, Methodology, Investigation, Resources, Formal Analysis, Writing - Original Draft; [Furkan Türk] Conceptualization, Methodology, Writing - Review & Editing, Visualization; [Ülkü Sultan Keskin] Conceptualization, Methodology, Resources, Supervision, Funding Acquisition, Project Administration, Validation, Writing - Review & Editing.

Data Availability

The data presented in this study are fully contained in the figures and tables of this article.

Declaration of Ethical Standards

The authors declare that the study complies with all applicable laws and regulations and meets ethical standards.

Declaration of Competing Interest

One of the authors of this study works in the cement factory where the production takes place. Authors declare that there is no conflict of interest that this affects the results of the study.

REFERENCES

[1]   W. L. Baloch, H. Siad, M. Lachemi, and M. Sahmaran, "The role of supplementary cementitious materials and fiber reinforcements in enhancing the sulfate attack resistance of SCC/ECC composite systems," Constr Build Mater, vol. 423, p. 135821, 2024, doi: https://doi.org/10.1016/j.conbuildmat.2024.135821.

[2]   X. Lv, L. Yang, J. Li, and F. Wang, "Roles of fly ash, granulated blast-furnace slag, and silica fume in long-term resistance to external sulfate attacks at atmospheric temperature," Cem Concr Compos, vol. 133, p. 104696, 2022, doi: https://doi.org/10.1016/j.cemconcomp.2022.104696.

[3]   A. L. M. V. Rodrigues, Á. Á. F. Mendes, V. Gomes, A. F. Battagin, M. R. M. Saade, and M. G. Da Silva, "Environmental and mechanical evaluation of blended cements with high mineral admixture content," Front Mater, vol. 9, p. 880986, 2022, doi: 10.3389/fmats.2022.880986.

[4]   A. Skaropoulou, K. Sotiriadis, G. Kakali, and S. Tsivilis, "Use of mineral admixtures to improve the resistance of limestone cement concrete against thaumasite form of sulfate attack," Cem Concr Compos, vol. 37, pp. 267–275, 2013, doi: https://doi.org/10.1016/j.cemconcomp.2013.01.007.

[5]   A. M. Diab, H. E. Elyamany, A. E. M. Abd Elmoaty, and M. M. Sreh, "Effect of nanomaterials additives on performance of concrete resistance against magnesium sulfate and acids," Constr Build Mater, vol. 210, pp. 210–231, 2019, doi: https://doi.org/10.1016/j.conbuildmat.2019.03.099.

[6]   S. Sathe, M. Zain Kangda, and G. A. Amaranatha, "Resistance against sulphate attack in concrete by addition of nano alumina," Mater Today Proc, vol. 60, pp. 294–298, 2022, doi: https://doi.org/10.1016/j.matpr.2022.01.124.

[7]   S. A. H and E.-G. M. M, "Long-Term Sulfate Resistance of Blended Cement Concrete with Waste Glass Powder," Practice Periodical on Structural Design and Construction, vol. 27, no. 4, p. 04022047, Nov. 2022, doi: 10.1061/(ASCE)SC.1943-5576.0000731.

[8]   S. A. Yildizel, M. Uzun, M. A. Arslan, and T. Ozbakkaloglu, "The prediction and evaluation of recycled polypropylene fiber and aggregate incorporated foam concrete using Artificial Neural Networks," Constr Build Mater, vol. 411, p. 134646, 2024, doi: https://doi.org/10.1016/j.conbuildmat.2023.134646.

[9]   H. Hafez, R. Kurda, W. M. Cheung, and B. Nagaratnam, "Comparative life cycle assessment between imported and recovered fly ash for blended cement concrete in the UK," J Clean Prod, vol. 244, p. 118722, 2020, doi: https://doi.org/10.1016/j.jclepro.2019.118722.

[10]   D. A. Salas, A. D. Ramirez, N. Ulloa, H. Baykara, and A. J. Boero, "Life cycle assessment of geopolymer concrete," Constr Build Mater, vol. 190, pp. 170–177, 2018, doi: https://doi.org/10.1016/j.conbuildmat.2018.09.123.

[11]   X. Huang, Z. Jiao, F. Xing, L. Sui, B. Hu, and Y. Zhou, "Performance assessment of LC3 concrete structures considering life-cycle cost and environmental impacts," J Clean Prod, vol. 436, p. 140380, 2024, doi: https://doi.org/10.1016/j.jclepro.2023.140380.

[12]   K. Scrivener, F. Martirena, S. Bishnoi, and S. Maity, "Calcined clay limestone cements (LC3)," Cem Concr Res, vol. 114, pp. 49–56, Dec. 2018, doi: 10.1016/J.CEMCONRES.2017.08.017.

[13]   M. Dener, U. Altunhan, and A. Benli, "A green binder for cold weather applications: enhancing mechanical performance of alkali-activated slag through modulus, alkali dosage, and Portland cement substitution," Archives of Civil and Mechanical Engineering, vol. 24, no. 3, p. 176, 2024, doi: 10.1007/s43452-024-00991-w.

[14]   M. Ben Haha, P. Termkhajornkit, A. Ouzia, S. Uppalapati, and B. Huet, "Low clinker systems - Towards a rational use of SCMs for optimal performance," Cem Concr Res, vol. 174, p. 107312, 2023, doi: https://doi.org/10.1016/j.cemconres.2023.107312.

[15]   A. S. Basavaraj, H. Hafez, A. Bell, M. Drewniok, and P. Purnell, "Transition Towards Low Carbon Concrete – Persuading Parameters," in Smart & Sustainable Infrastructure: Building a Greener Tomorrow, N. Banthia, S. Soleimani-Dashtaki, and S. Mindess, Eds., Cham: Springer Nature Switzerland, 2024, pp. 296–303.

[16]   Z. Xia, A. Bergmann, and L. Sanchez, "Assessment of Alkali-Silica Reaction Development in High Limestone Replacement Portland-Limestone Mortar and Concrete," in Proceedings of the 17th International Conference on Alkali-Aggregate Reaction in Concrete, L. F. M. Sanchez and C. Trottier, Eds., Cham: Springer Nature Switzerland, 2024, pp. 710–717.

[17]   R. A. dos Santos et al., "Durability and mechanical properties of concretes with limestone filler with particle packing," Materiales de Construcción, vol. 74, no. 355, p. e348, Oct. 2024, doi: 10.3989/mc.2024.366423.

[18]   E. Hosseinzadehfard and B. Mobaraki, "Investigating concrete durability: The impact of natural pozzolan as a partial substitute for microsilica in concrete mixtures," Constr Build Mater, vol. 419, p. 135491, 2024, doi: https://doi.org/10.1016/j.conbuildmat.2024.135491.

[19]   H. Kaplan and H. Binici, "TRAS VE TRASLI ÇİMENTOLAR," Pamukkale Üniversitesi Mühendislik Bilimleri Dergisi, vol. 1, no. 2, pp. 121–127, 1995, [Online]. Available: https://dergipark.org.tr/en/pub/pajes/issue/20554/219072

[20]   X. Pu, "Investigation on pozzolanic effect of mineral additives in cement and concrete by specific strength index," Cem Concr Res, vol. 29, no. 6, pp. 951–955, 1999, doi: https://doi.org/10.1016/S0008-8846(99)00012-5.

[21]   H. J. Li, L. Yang, and Y. J. Xie, "Effect of Fineness on the Properties of Cement Paste," Key Eng Mater, vol. 629–630, pp. 366–370, 2015, doi: 10.4028/www.scientific.net/KEM.629-630.366.

[22]   M. Öner, K. Erdoğdu, and A. Günlü, "Effect of components fineness on strength of blast furnace slag cement," Cem Concr Res, vol. 33, no. 4, pp. 463–469, 2003, doi: https://doi.org/10.1016/S0008-8846(02)00713-5.

[23]   X. J. Li, "Study on the mechanism of magnesium sulfate to cement and CSH gel," Adv Mat Res, vol. 243, pp. 4687–4690, 2011, doi: 10.4028/www.scientific.net/AMR.243-249.4687.

[24]   R. Vedalakshmi, A. S. Raj, S. Srinivasan, and K. G. Babu, "Effect of magnesium and sulphate ions on the sulphate resistance of blended cements in low and medium-strength concretes," Advances in Cement Research, vol. 17, no. 2, pp. 47–55, 2005, doi: 10.1680/adcr.2005.17.2.47.

[25]   A. Neville, "The confused world of sulfate attack on concrete," Cem Concr Res, vol. 34, no. 8, pp. 1275–1296, 2004, doi: https://doi.org/10.1016/j.cemconres.2004.04.004.

[26]   M. Maes and N. De Belie, "Resistance of concrete and mortar against combined attack of chloride and sodium sulphate," Cem Concr Compos, vol. 53, pp. 59–72, 2014, doi: https://doi.org/10.1016/j.cemconcomp.2014.06.013.

[27]   E. F. Irassar, A. Di Maio, and O. R. Batic, "Sulfate attack on concrete with mineral admixtures," Cem Concr Res, vol. 26, no. 1, pp. 113–123, 1996, doi: https://doi.org/10.1016/0008-8846(95)00195-6.

[28]   R. I. Martínez-Rosales, J. M. Miranda-Vidales, L. Narváez-Hernández, and J. M. Lozano de Poo, "Strength and Corrosion Studies of Mortars Added with Pozzolan in Sulphate Ions Environment," KSCE Journal of Civil Engineering, vol. 24, no. 12, pp. 3810–3819, 2020, doi: 10.1007/s12205-020-0183-2.

[29]   K. Tosun-Felekoğlu, "The effect of C3A content on sulfate durability of Portland limestone cement mortars," Constr Build Mater, vol. 36, pp. 437–447, 2012, doi: https://doi.org/10.1016/j.conbuildmat.2012.04.091.

[30]   A. M. Tahwia, R. M. Fouda, M. Abd Elrahman, and O. Youssf, "Long-Term Performance of Concrete Made with Different Types of Cement under Severe Sulfate Exposure," Materials, vol. 16, no. 1, p. 240, Dec. 2022, doi: 10.3390/ma16010240.

[31]   X. Lv, L. Yang, J. Li, and F. Wang, "Roles of fly ash, granulated blast-furnace slag, and silica fume in long-term resistance to external sulfate attacks at atmospheric temperature," Cem Concr Compos, vol. 133, p. 104696, 2022, doi: https://doi.org/10.1016/j.cemconcomp.2022.104696.

[32]   A. Rossetti, T. Ikumi, I. Segura, and E. F. Irassar, "Performance of Blended Cements with Limestone Filler and Illitic Calcined Clay Immediately Exposed to Sulfate Environment," in Calcined Clays for Sustainable Concrete, S. Bishnoi, Ed., Singapore: Springer Singapore, 2020, pp. 655–664.

[33]   H. Zhu, D. Mapa, B. Lorentz, K. Riding, and A. Zayed, "Sulfate Optimization for CCIL Blended Systems," in Calcined Clays for Sustainable Concrete, S. Bishnoi, Ed., Singapore: Springer Singapore, 2020, pp. 323–330.

[34]   A. Baldermann et al., "Effect of very high limestone content and quality on the sulfate resistance of blended cements," Constr Build Mater, vol. 188, pp. 1065–1076, 2018, doi: https://doi.org/10.1016/j.conbuildmat.2018.08.169.

[35]   Z. Makhloufi, S. Aggoun, B. Benabed, E. H. Kadri, and M.Bederina, "Effect of magnesium sulfate on the durability of limestone mortars based on quaternary blended cements," Cem Concr Compos, vol. 65, pp. 186–199, 2016, doi: https://doi.org/10.1016/j.cemconcomp.2015.10.020.

IMPACT OF HEATING ON OLIVE OIL: OXIDATIVE CHANGES AND PHYSICOCHEMICAL PROPERTIES

[1] * **Mansoor Ali KANDHRO** (ID) , [2] **Sarfaraz Ahmed MAHESAR** (ID) , [3] **Syed Tufail Hussain SHERAZI** (ID) , [4] **Mustafa TOPKAFA** (ID) , [5] **Ilyas DEVECİ** (ID)

[1,2] *National Centre of Excellence in Analytical Chemistry, University of Sindh, Jamshoro, PAKISTAN*
[3] *Sindh University, Jamshoro, PAKISTAN*
[4,5] *Konya Technical University, Institute of Graduate Education, Chemical Engineering, Konya, TÜRKİYE*
[1] mansooralikandhro121@gmail.com, [2] mahesar_sarfaraz@yahoo.com, [3] tufail.sherazi@u sindh.edu.pk, [4] mtopkafa@ktun.edu.tr, [5] ideveci@ktun.edu.tr

Highlights

- Unraveling the Impact of Heating on Olive Oil.

- Experimenting with Olive Oils Chlorophyll and β-carotene Dynamics.

- Investigating the Transformation of Olive Oils Nutrients.

*Corresponding Author: Mansoor Ali KANDHRO, mansooralikandhro121@gmail.com

IMPACT OF HEATING ON OLIVE OIL: OXIDATIVE CHANGES AND PHYSICOCHEMICAL PROPERTIES

[1], *Mansoor Ali KANDHRO , [2] Sarfaraz Ahmed MAHESAR , [3] Syed Tufail Hussain SHERAZI , [4] Mustafa TOPKAFA , [5] Ilyas DEVECİ

[1, 2, 3] National Centre of Excellence in Analytical Chemistry, University of Sindh, Jamshoro, PAKISTAN
[4, 5] Konya Technical University, Institute of Graduate Education, Chemical Engineering, Konya, TÜRKİYE
[1] mansooralikandhro121@gmail.com, [2] sarfaraz.mahesar@usindh.edu.pk, [3] tufail.sherazi@usindh.edu.pk,
[4] mtopkafa@ktun.edu.tr, [5] ideveci@ktun.edu.tr

ABSTRACT: This study aimed to analyze the physicochemical parameters of various brands of olive oil (OO) available in the local markets of Hyderabad, Pakistan. The parameters studied include concentrations of chlorophyll, β-carotene, free fatty acid (FFA), conjugated diene (CD), conjugated triene (CT), and oxidative stability. The results showed that none of the analyzed (OO) is recommended for cooking due to high FFA levels, but all except one could be used as salad oil. Through a systematic analysis, we also examined the impact of heating on chlorophyll and β-carotene levels in commercial OO brands. Our findings elucidate the varying responses of OO brands to heating, with distinct alterations observed in chlorophyll, and β-carotene levels. Furthermore, the FTIR analysis provided valuable insights into the molecular changes and oxidative stability of the oils under different heating conditions. These findings have significant implications for both consumers and the OO industry, as they provide valuable insights into the selection of high-quality OO brands that maintain their nutritional integrity and flavor profiles during cooking.

Keywords: *Extra Virgin Olive Oil, Bioactive Compounds, Heating Effects, Oxidative Stability, Quality Control*

1. INTRODUCTION

Refined Olive Oil (ROO) is obtained by refining methods from virgin olive oil (VOO) that do not modify the original composition of triacylglycerol in the oil [1]. Pure olive oil (OO) with a lighter color, more neutral taste, and oleic acid ranging from 55-83%, is a lower quality oil than extra virgin olive oil (EVOO) or VOO. Pure OO is known as an all-purpose cooking oil. Usually, this oil is a combination of VOO and refined OO [2]. A significant first step would be to improve the production of useful EVOO by classifying olives based on their FFA content prior to processing [3]. In this way, during the extraction process, mixing of high and poor quality oils could be avoided [4]. Heating OO can lead to the oxidation of the oil and the formation of harmful compounds [5]. The quality of OO deteriorates as it is exposed to high temperatures, such as during cooking or frying [6]. The oxidative stability of OO which indicates its resistance to oxidation and degradation, decreases with increasing temperature and exposure time [7]. Therefore, it is recommended to use OO for cooking at lower temperatures and for shorter periods. EVOO has a lower smoke point than other oils, making it less suitable for high-temperature cooking [8]. Overall, the heating effect of OO should be considered when using it for cooking or frying, and it is important to use proper cooking techniques to minimize the production of harmful compounds [9]. The aim of the present investigation was to evaluate the physicochemical characteristics of OO commercially available in the market according to the standard AOCS methods. In addition, oxidative stability of OO at various temperatures and FTIR characterization were also done. Prior research on OO quality has typically examined individual parameters in isolation, often with methodological limitations. Our study

provides a more comprehensive assessment by simultaneously evaluating oxidative stability, color, FFA, chlorophyll, and β-carotene - key quality markers that interact during heating. Unlike previous approaches, we establish meaningful correlations between these parameters while employing rigorous analytical protocols. This integrated analysis offers practical insights for quality control, addressing gaps in current understanding.

2. MATERIAL AND METHODS

2.1. Chemicals

The reagents and chemicals used in this research such as sodium hydroxide, n-hexane, potassium iodide, sodium thiosulfate, potassium hydroxide, methyl alcohol, carbon tetrachloride, potassium bromide, hydrochloric acid, sulfuric acid, ethyl alcohol, and sodium sulfate anhydrous were bought from E-Merck (Darmstadt, Germany).

2.2 Sample collection

Samples of OO were obtained from local markets and stored at 4°C for further chemical analysis. Samples were coded as O-1 Ripe and Sweet Extra Virgin Olive Oil (RS EVOO), O-2 Natural Olive Oil, O-3 Borges Olive Oil, O-4 Sasso Olive Oil, O-5 Al- Amir Olive Oil, O-6 Refined and Sweet-Ripe Premium Olive Oil (RS- RPOO), O-7 Mondial Olive Oil, O-8 Marhaba Olive Oil, O-9 Al- Rachid, O-10 Consul Olive Oil, O-11 Olio Olive Oil, and O-12 Signature Cold Press Olive Oil.

2.3. Physicochemical parameters of OO

The physicochemical properties of OO, including Free Fatty Acid (FFA) content, conjugated diene (CD) and conjugated triene (CT) levels, β-carotene concentration, chlorophyll content, color, and oxidative stability were assessed in this study. The analysis was carried out using standard methods and protocols.

2.3.1. Determination of free fatty acid

The official procedure of AOCS Ca 5a-40 was used to quantify the amount of FFA in OO samples. In the conical flask (250 mL) added hot neutralized alcohol of exactly 50 mL and an indicator of 2 mL. The conical flask content was titrated with sodium hydroxide solution (0.1 M) until the pink color appeared. Approximately 56 g of OO sample was added into alcohol (neutralized) and titrated again, the solution constantly shaken until a permanent pink color seemed to be of a similar quality prior to sample addition [10]. The following formula was used for the calculation of FFA in OO samples.

$$FFA\% = \frac{28.2 \times V(mLNaOH) \times N\,(NaOH)}{W}$$

Where,
N= Normality of NaOH solution
V= Volume, mL of NaOH used in titrating the sample
W= mass, grams of test portion

2.3.2. Determination of conjugated diene and triene

CD and CT values were calculated as explained in the IUPAC II.D.233 analytical method (IUPAC, 1979) [11]. Around 250 mg of OO was weighed and transferred into a 25 mL volumetric flask and added isooctane. The properly homogenized sample was placed into a quartz cuvette. In

a spectrophotometer, absorbance at 232 and 270 nm was measured using isooctane as the blank solvent.

2.3.3. β-Carotene

β-carotene of OO samples was determined according to Brahmi et al., [12]. Firstly, the OO sample (1 g) was taken in a Falcon tube and diluted up to 20 mL with petroleum ether. A Perkin Elmer Lambda 25 UV-visible spectrophotometer was used to measure the carotenoid fraction at wavelengths between 440 and 480 nm.

$$\beta - Carotene = A\,\lambda_{max}\,\frac{10^5}{2650}$$

2.3.4. Chlorophyll

Chlorophyll content in OO samples was determined as reported by Kiritsakis*et al.,* [13] using air as a reference and noted the absorbance at 630, 670, and 710 nm, respectively.

The overall chlorophyll content calculation was as follows:

$$Chlorophyll\ (mg/kg) = [\ A670 - \frac{(A630 - A710)}{2}\ ]/\ (0.901 * L)$$

L is the cell thickness (cm), and A is the absorbance of the oil at the respective wavelengths.

2.3.5. Color

The official AOCS method Cc 13b-45 was used to verify the color of OO samples. In this procedure, the assessment of the oil color was done by comparing it with glasses of proven color properties. The refined and crude OO was kept in 1 and 5 inches (25.4 mm and 127 mm) cells, respectively, and placed in a Lovibond Tintometer. By obtaining the best possible match with the standard color slide, the OO sample color was decided [10].

2.3.6. Oxidative stability

The Rapidoxy instrument was used to measure the oxidative stability of OO. To know the stability of the oil, weighed around 5 g samples kept them in the test chamber, and applied 700 kPa (O_2) pressure at a fixed temperature (120 ᵒC) to accelerate the oxidation process. The test was completed when the pressure fell below the 10% p_{max} value.

2.3.7. Effect of heating on the β- carotene and chlorophyll content

To check the effect of heating on the β-carotene and chlorophyll content, the OO samples were heated for 8 h according to traditional methods of frying. The oils were subjected to varying temperatures (110, 120, 130, and 140 ᵒC) to expedite the oxidation process. This was achieved by heating the oils in a stainless steel shallow pan, measuring 20-30 cm in diameter, over a gas flame. No food was added during this experiment, as the focus was solely on examining the impact of heating on the oils. After the heating process, the β-carotene and chlorophyll content in the OO samples was measured to determine how the different temperatures affected these components.

2.3.8 FTIR characterization of Olive oil

Infrared (IR) spectra were collected using the FT-IR spectrometer(Thermo Nicolet iS10) with DTGS as the detector to track the consistency and oxidative degradation of OO. FTIR set to 4 cm^{-1} resolution, 4000-650 cm^{-1} range, scans 16, and SB-ATR diamond crystal accessory. Before the study of samples, a background spectrum was collected. For capturing the spectra, approximately 50 μL of the oil sample was placed on the diamond crystal. To collect the FTIR data and instrumental control OMINIC software (Version 9) was used.

2.3.9. Statistical analysis

The data was subjected to statistical analysis using Minitab16 USA software. The analysis involved performing a variance analysis (ANOVA) followed by the Tukey test with a significance level of p ≤ 0.05. The reported results for each data point consist of the mean value along with its corresponding standard deviation (mean ± SD), and three replicates were considered in the analysis.

3.   Results and Discussion

Typically, at first glance, buyers judge the consistency of foods from their appearance, such as (shape, texture, and color), so this appraisal affects the decision of whether or not to buy it. This is partially linked to food color, which usually shows the stage of ripeness, the conditions of industrial processing/ agricultural production, and other variables. In contrast, color is synonymous with food consistency, which plays a vital role in buying oil by customers.

3.1 Color

The OO color is much related to its apparent feature and consequently to its acceptability. In current research work, the yellow, blue, and red color in commercial OO samples was determined by Tintometer and found in the range from 40.65 to 3.05, 1.0 to 7.0, and 2.0 to 5.35, respectively. The summarized results of the yellow, blue, and red color index of commercial OO are shown in Table 1. Such color evaluations are essential as they influence the perceived quality and acceptability of the product among consumers.

Table 1. Color index of commercial OO

Samples	YELLOW (Y)	BLUE (B)	RED (R)
O-1	31.0±0.51e	1.5±0.01h	5.05±0.34b
O-2	26.0±0.61	6.5±0.31b	5.35±0.91a
O-3	42.0±0.41b	6.0±0.41c	4.0±0.06d
O-4	11.2±0.70i	1.95±0.21g	3.25±0.13f
O-5	22.0±0.43h	4.0±0.12e	3.65±0.06e
O-6	43.0±0.47a	7.0±0.59a	5.2±0.07ab
O-7	30.1±0.61f	1.0±0.40j	2.0±0.41h
O-8	31.1±0.67e	1.4±0.04h	5.2±0.84ab
O-9	32.1±0.56d	1.2±0.03i	4.1±0.41cd
O-10	40.7±0.06c	1.4±0.02h	4.35±0.91c
O-11	40.65±0.33c	5.5±0.21d	3.75±0.77e
O-12	3.05±0.34j	2.4±0.02f	2.65±0.06g
P-value	7963.87***	3605.25***	141.12***

3.2 Free fatty acid (FFA)

The acidity level significantly influences the quality of VOO. Furthermore, it is commonly employed as a conventional criterion for the classification of OO grades. The quality of the VOO is inversely proportional to the value of this factor. The rise in acidity can be primarily attributed to enzymatic activity resulting from the damage to olive tissue. FFA is the key parameter used to scrutinize the various types of OO. In our results, FFA was found to range from 1.22 to 1.65% (Table 2). The higher FFA content was noted in O-5. On the other hand, a lower value of FFA was determined in O-12.

3.3. Conjugated diene (CD) and triene (CT)

The lower quality of OO has a higher quantity of CD formed due to oxidative processes in the oil. A lower absorption value in the spectrum region from 200 to 300 nm indicates better quality of OO and a higher absorption value describes the lower quality of oils. In our results, CD was found to range from 0.40 to 1.31 (Table 2). The highest value suggests a greater oxidation rate. On the other hand, initially, the rate of CD formation was smaller but increased with storage time or heating. In our results, CT was found in the range of 0.42 to 3.05 (Table 2).

3.3. β-carotene

Pigments are responsible for the color of OO and are an important constituent that is directly related to the quality of oil. OO contains a relatively rich variety of carotenoids (i.e., β-carotene). Our research findings revealed that the β-carotene content in the analyzed OO samples varied between 1.70 to 8.46 mg/kg. Particularly, O-12 exhibited a notably higher amount of β-carotene compared to other samples, while O-3 showed a relatively lower value of β-carotene content (Table 2). These results highlight the significance of β-carotene in determining the color and quality differences among various types of OO.

3.4. Chlorophyll

The color of OO is mainly due to the presence of pheophytins a & b in fresh oils. The level of chlorophyll (and carotenoids) depends on many factors such as genetics, degree of fruit ripening, and extraction technology. The chlorophyll content decreases as the fruit ripens. In this study, chlorophyll content was found in the range of 3.2 to 166.7 mg/kg (Table 2).

3.5. Oxidative stability

The oxidative stability of VOO is heavily influenced by the cultivar and is impacted by various factors, including the composition of fatty acids, phenolic compounds, and tocopherols. The sample with the highest oxidative stability (29.3 h) was found to be O-1, while the sample with the lowest oxidative stability (11.8 h) was O-11. In contrast, O-12 exhibits an intermediate level of oxidative stability, as indicated by a value of 19.2 h (Table 2). The enhanced resistance to oxidation observed in O-1 can be attributed to its elevated concentration of phenolic compounds, reduced linolenic acid content, and elevated levels of monounsaturated fatty acids. Contrarily, O-11 exhibits lower stability compared to O-1 and O-12 due to its high linolenic acid content, which makes it highly susceptible to oxidation, and its relatively lower amount of monounsaturated fatty acids.

Table 2. Physicochemical parameters of commercial Olive oil samples.

Sample	FFA (%)	CD	CT	β-carotene (mg/kg)	Chlorophyll (mg/kg)	Oxidative stability (h)
O-1	1.60±0.42d	0.40±0.11j	1.69±0.45g	7.19±0.15c	107.2±0.36ab	29.3±0.21a
O-2	1.26±0.34h	0.56±0.37i	3.05±0.34a	5.45±0.78f	24.4±0.33c	15.2±0.13e
O-3	1.37±0.47f	0.73±0.20f	1.90±0.28f	1.70±0.59l	3.20±0.12c	13.0±0.48h
O-4	1.33±0.38g	0.72±0.13f	1.18±0.31h	7.02±0.97d	28.7±0.82bc	12.9±0.27h
O-5	1.65±0.35b	0.90±0.52d	2.47±0.75b	5.21±0.12g	38.0±0.58bc	14.2±0.13f
O-6	1.34±0.37g	0.86±0.11d	2.39±0.86c	2.49±0.72k	59.5±0.78bc	14.0±0.41g
O-7	1.40±0.43e	0.83±0.11e	2.24±0.22d	6.39±0.87e	37.1±0.28bc	23.7±0.84b
O-8	1.62±0.40c	0.69±0.07g	2.50±0.71b	7.90±0.56b	56.0±0.58bc	18.0±0.48d
O-9	1.38±0.32ef	0.73±0.09f	2.17±0.35e	4.21±0.12i	63.6±0.01abc	12.0±0.41j
O-10	1.39±0.30ef	0.64±0.01h	1.69±0.44g	3.47±0.75j	58.8±0.70bc	12.2±0.14i
O-11	3.31±0.98a	1.16±0.27b	2.47±0.76b	4.25±0.06h	17.30±0.12c	11.8±0.70k
O-12	1.22±0.40i	1.31±0.47a	0.42±0.22i	8.46±0.76a	166.7±0.98a	19.2±0.70c
P-value	6683.83***	1959.49***	1592.58***	131715.06***	1.85**	10193.44***

Table 3. Pearson correlation of physicochemical properties of Olive oil.

Parameters	FFA	CD	CT	β-carotene	Chlorophyll	OSI
FFA	1					
CD	0.199	1				
CT	0.344	0.392	1			
β- carotene	-0.119	-0.492	-0.522	1		
Chlorophyll	-0.29	-0.565	-0.675	0.573	1	
OSI	-0.196	-0.519	-0.407	0.673	0.479	1

Table 3 shows the correlation of studied parameters such as FFA, CD, CT, β-carotene, chlorophyll and oxidative stability of commercial OO samples. It was observed that FFA showed a negative correlation with β-carotene, chlorophyll, and OSI, while a positive relationship with CD and CT. A strong negative correlation was noted between CD toβ-carotene, chlorophyll, and OSI, while a positive correlation of CD was observed with CT and FFA. On the other hand, β-carotene showed a strong positive correlation with chlorophyll and OSI. A strong negative correlation was noted with CD and CT, while a least positive correlation was observed with FFA. A strong positive correlation was observed between chlorophyll to β-carotene and OSI, whereas a negative relationship was noted between FFA, CD, and CT. In contrast, OSI showed a strong positive relationship with β-carotene and chlorophyll, while a strong negative correlation was noted with CD and CT and the least with FFA.

3.6. β-carotene and chlorophyll content in olive oil after heating

Recent studies have shown that heating olive oil can alter its levels of chlorophyll and beta-carotene. The degradation and alterations of chlorophyll and β-carotene, which are sensitive to temperature and oxidation, can occur when they are subjected to heat. These changes have the potential to impact their concentrations and the potential health benefits they offer.

Scholarly investigations have been conducted to examine the influence of heating on the phytochemical composition of olive oil. An investigation conducted by [14] explored the degradation process of chlorophyll and carotenoids in VOO under the influence of eating. The findings of the study demonstrated a decline in the concentrations of these compounds as the temperature of heating escalated. A similar trend was also observed in the present study when OO was subjected to heat at different temperatures. The β-carotene and chlorophyll content of OO before and after heating are shown in Tables 4A and 4B

Table 4a β-carotene content in OO before and after heating

Sample	β-carotene (mg/kg)	Temperature (°C)			
		110	120	130	140
O-1	7.19±0.30d	6.89±0.34a	4.73±0.26b	4.11±0.58a	2.48±0.05bc
O-2	5.95±0.23j	4.94±0.21g	3.93±0.17d	2.03±0.38h	0.33±0.07h
O-3	6.23±0.28f	5.78± 0.23d	4.74±0.78b	3.20±0.13c	2.43±0.09c
O-4	7.22±0.34c	6.50±0.32c	4.96±0.47a	3.22±0.81c	2.00±0.42e
O-5	5.21±0.20k	3.79±0.34k	2.94±0.50g	1.56±0.05i	0.24±0.08i
O-6	2.99±0.14l	1.78±0.08l	2.58±0.31h	2.30±0.60e	2.28±0.03d
O-7	6.79±0.33e	5.17±0.25f	3.06±0.34f	2.03±0.38h	2.00±0.25e
O-8	7.90±0.39b	5.26±0.27e	3.94±0.50d	2.16±0.47g	2.50±0.35b
O-9	6.12±0.30g	4.21±0.21j	4.09±0.29c	3.89±0.58b	2.82±0.67a
O-10	5.99±0.29i	4.61±0.23i	3.75±0.77e	2.69±0.86d	1.89±0.58f
O-11	6.06±0.24h	4.84±0.22h	3.94±0.50d	2.24±0.07f	1.59±0.30g
O-12	8.96±0.44a	6.61±0.27b	4.74±0.79b	2.06±0.34h	0.04±0.13j
P-value	68962.71***	59934.25***	19134.13***	2103.76***	3000.45***

Table 4b Chlorophyll content in OO before and after heating

Samples	Chlorophyll (mg/kg)	Temperature (°C)			
		110	120	130	140
O-1	105.05±0.48b	94.90±0.06b	88.0±0.48b	79.90±0.63a	25.90±0.63b
O-2	24.20±0.13l	22.30±0.63i	19.90±0.63j	12.90±0.56l	3.10±0.07h
O-3	26.30±0.05k	24.10±0.34h	18.30±0.06l	14.50±0.41j	4.0±0.62f
O-4	28.40±0.34i	23.0±0.12i	19.20±0.20k	19.0±0.43g	16.90±0.63d
O-5	37.80±0.41g	31.20±0.28e	25.10±0.34h	19.30±0.06f	4.90±0.12e
O-6	59.10±0.27d	47.30±0.70d	36.90±0.56d	17.90±0.56h	3.10±0.41h
O-7	36.90±0.06h	26.60±0.41f	20.10±0.34d	14.0±0.48k	3.30±0.22g
O-8	53.80±0.41f	25.10±0.48g	35.10±0.27e	21.30±0.99e	3.10±0.22h
O-9	64.80±0.70c	48.0±0.13d	30.0±0.48f	16.90±0.63i	3.0±0.42i
O-10	58.80±0.63e	49.80±0.03c	42.20±0.20c	34.20±0.13c	27.0±0.56a
O-11	27.60±0.77j	26.90±0.56	26.10±0.27g	25.10±0.34d	25.0±0.84c
O-12	164.50±0.13a	136.0±0.41a	96.10±0.34a	54.10±0.34b	2.20±0.14j
P-value	24155541.96***	18704.04***	1648484.90***	641379.09***	225284.42***

3.7. FT-IR Characterization

IR spectroscopy is useful for determining molecular structures because of the abundance of data it provides and the ability to attribute certain absorption bands to functional groups. The majority of the peaks and shoulders observed in the spectrum of fats and oils can be attributed to the distinctive functional groups present. This is evident in the typical spectra of O-12, as depicted in Figure 1A. The observable peaks attributed to the stretching mode of C–H bonds occur within the wavenumber range of 2800–3100 cm^{-1}. Similarly, the stretching of C=O bonds can be observed within the range of 1700–1800 cm^{-1}. Additionally, the stretching of C–O–C bonds and the bending of C–H bonds can be easily observed within the range of 900–1400 cm^{-1}. The spectra of oils exhibited a nearly indistinguishable range, with only subtle differences discernible upon close examination. The observed phenomenon can be attributed to the comparable chemical composition of the oils under consideration. It has been reported that IR analysis relies heavily on data from the wave number ranges 3100-2800 cm^{-1} and 1800-900 cm^{-1} [15]. Figure 1B illustrates the group spectra of OO in the wavenumber range of 4000-650c m^{-1}.To check the possible effect on the intensity of various functional groups during heating, one representative sample

was selected. Table 5 shows FT–IR spectral changes in the functional groups present in OO before and after heating. It was observed that negligible change appeared in the intensities of various functional groups during heating.
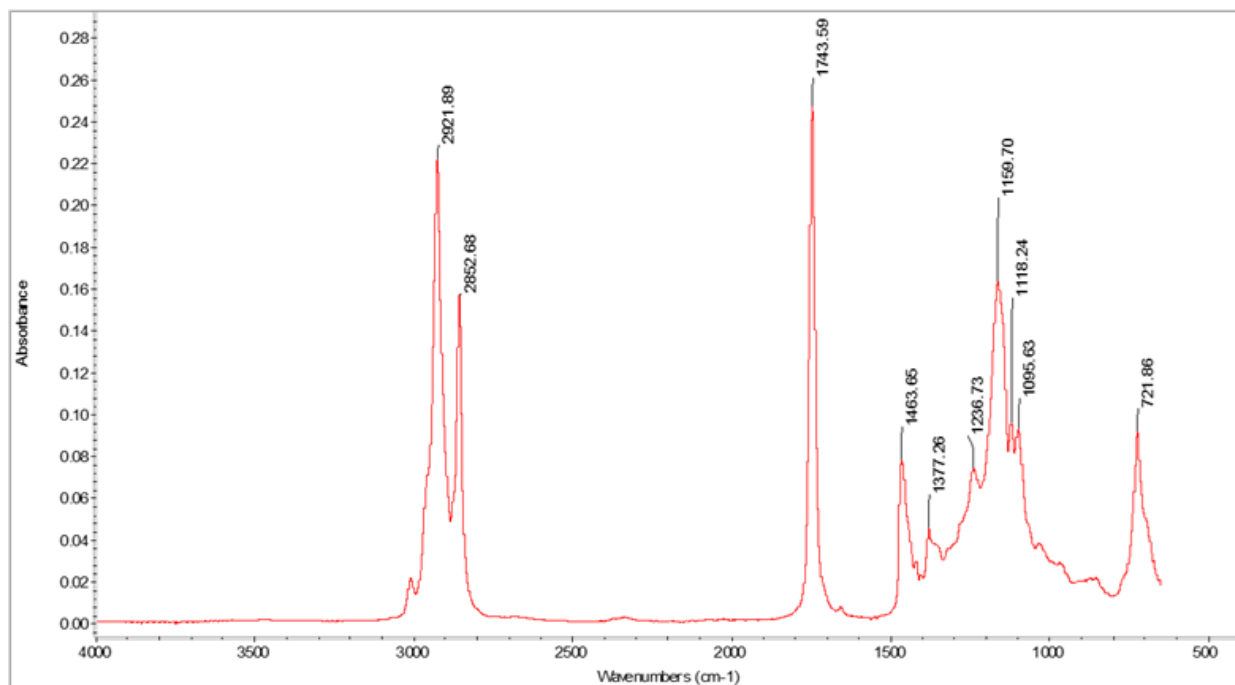
Figure 1A. Representative FT- IR spectrum of O-12
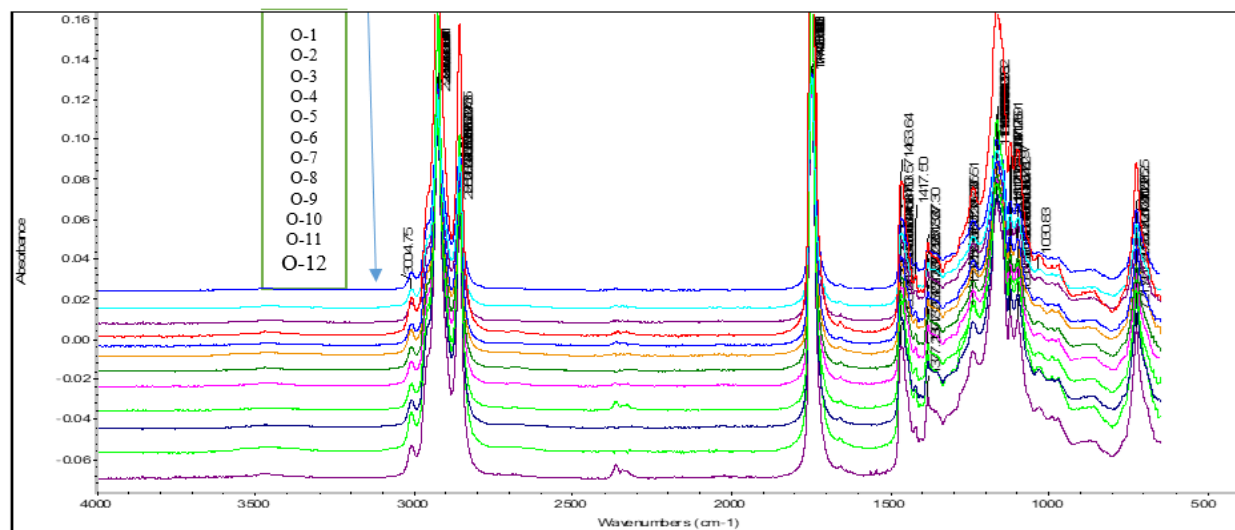
Figure 1B. FT- IR group spectra of commercial Olive oil

Table 5. Shows FT–IR spectral changes in the functional groups present in OO Samples

Sample	Functional group	=C–H (cis)	–C–H (CH3)	–C–H (CH2)	–C–H (CH2)	–C=O (ester)	–C–H (CH2)	–C–H (CH3)	–C–O –CH2–	–C–O –CH2–	–C–O	C-C-O	CH	CH
	Nominal Frequency cm^{-1}	3004	2929	2921	2852	1743	1463	1377	1236	1160	1117	1095	965	721
Intensity O-1	Before Heating	0.03	0.04	0.21	0.15	0.23	0.07	0.04	0.07	0.16	0.09	0.09	0.08	0.03
	After Heating	0.02	0.03	0.22	0.15	0.23	0.07	0.04	0.07	0.16	0.09	0.09	0.08	0.03
Intensity O-2	Before Heating	0.03	0.04	0.21	0.15	0.23	0.07	0.04	0.07	0.15	0.09	0.09	0.08	0.03
	After Heating	0.02	0.03	0.21	0.15	0.23	0.07	0.04	0.07	0.16	0.09	0.09	0.08	0.03
Intensity O-3	Before Heating	0.03	0.04	0.21	0.15	0.23	0.07	0.04	0.07	0.15	0.09			
	After Heating	0.02	0.03	0.21	0.15	0.23	0.07	0.04	0.07	0.16	0.09	0.09	0.08	0.03
Intensity O-4	Before Heating	0.03	0.04	0.21	0.15	0.23	0.07	0.04	0.07	0.16	0.09			
	After Heating	0.02	0.22	0.21	0.15	0.23	0.07	0.04	0.07	0.16	0.09	0.09	0.08	0.03
Intensity O-5	Before Heating	0.03	0.02	0.21	0.15	0.23	0.07	0.04	0.07	0.158	0.09			
	After Heating	0.02	0.22	0.21	0.15	0.23	0.07	0.04	0.07	0.16	0.09	0.09	0.08	0.03
Intensity O-6	Before Heating	0.03	0.02	0.21	0.15	0.24	0.07	0.04	0.07	0.161	0.09			
	After Heating	0.02	0.22	0.22	0.15	0.23	0.07	0.04	0.07	0.16	0.09	0.09	0.08	0.03
Intensity O-7	Before Heating	0.03	0.02	0.21	0.15	0.24	0.07	0.04	0.07	0.161	0.09			
	After Heating	0.02	0.22	0.22	0.15	0.23	0.07	0.04	0.07	0.16	0.09	0.09	0.08	0.03
Intensity O-8	Before Heating	0.03	0.02	0.22	0.15	0.24	0.07	0.04	0.07	0.16	0.09			
	After Heating	0.02	0.22	0.22	0.15	0.23	0.07	0.04	0.07	0.16	0.09	0.09	0.08	0.03
Intensity O-9	Before Heating	0.03	0.02	0.22	0.15	0.25	0.07	0.04	0.07	0.16	0.09			
	After Heating	0.02	0.22	0.22	0.15	0.24	0.07	0.04	0.07	0.16	0.09	0.09	0.08	0.03
Intensity O-10	Before Heating	0.03	0.02	0.21	0.15	0.23	0.07	0.04	0.07	0.15	0.08			
	After Heating	0.02	0.22	0.22	0.15	0.23	0.07	0.04	0.04	0.16	0.09	0.09	0.08	0.03
Intensity O-11	Before Heating	0.03	0.02	0.21	0.15	0.24	0.07	0.04	0.07	0.16	0.09			
	After Heating	0.02	0.22	0.22	0.15	0.24	0.07	0.04	0.04	0.16	0.09	0.09	0.08	0.03
Intensity O-12	Before Heating	0.03	0.04	0.018	0.16	0.24	0.08	0.05	0.06	0.16	0.1			
	After Heating	0.02	0.03	0.22	0.16	0.24	0.08	0.05	0.16	0.16	0.09	0.09	0.08	0.03

4. CONCLUSIONS

In conclusion, our research conducted a comprehensive analysis of important factors such as chlorophyll, β-carotene, FFA, CD, CT, and oxidative stability in various commercially available OO products. The findings suggest that the utilization of analyzed oils for culinary purposes should be discouraged due to the presence of elevated levels of FFA. Furthermore, our study on the impact of heating on chlorophyll and β-carotene revealed distinct responses based on the brand of the samples. These findings were further supported by the analysis of molecular changes and oxidative stability using FTIR. The aforementioned findings are of great importance, as they provide valuable guidance to consumers and the olive oil industry in choosing high-quality olive oil brands that maintain their nutritional value and flavour profiles, even when subjected to the demands of cooking.

Declaration of Ethical Standards

I hereby declare that this paper adheres to the highest ethical standards. It is based on honest research and original work. All sources are properly cited, and no data has been falsified. I have avoided any form of plagiarism and have given appropriate credit to all contributors

Credit Authorship Contribution Statement

All authors made substantial contributions to this paper. Each person was involved in the research, writing, and final approval of the manuscript. We all take responsibility for the work and its accuracy.

Declaration of Competing Interest

I have no competing interests to disclose. This research was conducted without any financial or personal conflicts that could influence the results.

Funding / Acknowledgements

Data Availability

Feel free to modify the contact information as needed!

REFERENCES

[1]   L. Cecchi *et al.*, "Co-milling of sound olives with fresh chili peppers improves the volatile compound, capsaicinoid and sensory profiles of flavoured olive oil with respect to the typical infusion," vol. 404, p. 134696, 2023.

[2]   S. Ropciuc, F. Dranca, M. A. Oroian, A. Leahu, G. G. Codină, and A. E. J. G. Prisacaru, "Structuring of Cold Pressed Oils: Evaluation of the Physicochemical Characteristics and Microstructure of White Beeswax Oleogels," vol. 9, no. 3, p. 216, 2023.

[3]   B. Castells, A. Varela, F. J. Castillo-Ruiz, L. F. Calvo, L. Medic, and A. J. P. T. Tascón, "Ignition

and explosion characteristics of olive-derived biomasses," vol. 420, p. 118386, 2023.

[4] M. D. Ferro, M. J. Cabrita, J. M. Herrera, and M. F. J. F. Duarte, "A New Laboratory Scale Olive Oil Extraction Method with Comparative Characterization of Phenolic and Fatty Acid Composition," vol. 12, no. 2, p. 380, 2023.

[5] D. Kaniewski *et al.*, "Climate change threatens olive oil production in the Levant," vol. 9, no. 2, pp. 219-227, 2023.

[6] G. Indrayanto and A. J. F. Q. A. Rohman, "Chromatographic methods for the analysis of oils and fats," pp. 119-147, 2023.

[7] D. Malavi, A. Nikkhah, K. Raes, and S. J. F. Van Haute, "Hyperspectral Imaging and Chemometrics for Authentication of Extra Virgin Olive Oil: A Comparative Approach with FTIR, UV-VIS, Raman, and GC-MS," vol. 12, no. 3, p. 429, 2023.

[8] Y. Wang *et al.*, "Comparative study on quality characteristics of Bischofia polycarpa seed oil by different solvents: Lipid composition, phytochemicals, and antioxidant activity," vol. 17, p. 100588, 2023.

[9] T. F. V. Bôas *et al.*, "Energy potential from the generation of biogas from anaerobic digestion of olive oil extraction wastes in Brazil," vol. 4, p. 100083, 2023.

[10] D. Firestone, *Official methods and recommended practices of the AOCS*. AOCS, 2009.

[11] M. M. Mossoba, R. E. McDonald, D. J. Armstrong, and S. W. J. J. o. c. s. Page, "Identification of minor C18 triene and conjugated diene isomers in hydrogenated soybean oil and margarine by GC-MI-FT-IR spectroscopy," vol. 29, no. 8, pp. 324-330, 1991.

[12] F. Brahmi, B. Mechri, M. Dhibi, and M. J. A. P. P. Hammami, "Variation in antioxidant activity and phenolic content in different organs of two Tunisian cultivars of Olea europaea L," vol. 36, pp. 169-178, 2014.

[13] A. K. Kiritsakis, *Olive oil: from the tree to the table*. Food & Nutrition Press, 1998.

[14] S. Gómez-Alonso, M. D. Salvador, G. J. J. o. a. Fregapane, and f. chemistry, "Phenolic compounds profile of Cornicabra virgin olive oil," vol. 50, no. 23, pp. 6812-6817, 2002.

[15] T. R. Gonçalves *et al.*, "Evaluation of Brazilian monovarietal extra virgin olive oils using digital images and independent component analysis," vol. 31, pp. 1955-1963, 2020.

CRAMER-RAO LOWER BOUND ANALYSIS FOR MAGNETIC LOCALIZATION OF A ROBOTIC CAPSULE ENDOSCOPE

[1, *]**Muzaffer KANAAN** (iD) , [2]**Muhammed CİL** (iD), [3]**Memduh SUVEREN** (iD)

[1, 3] *Erciyes University, Mechatronics Engineering Department, Kayseri, TÜRKİYE*
[2] *Kafkas University, Mechanical Engineering Department, Kars, TÜRKİYE*
[1]mkanaan@erciyes.edu.tr , [2]muhammed.cil@kafkas.edu.tr, [3]msuveren@erciyes.edu.tr

Highlights

- A performance analysis is presented for magnetic wireless capsule localization.
- The analysis is based on the Cramer-Rao Lower Bound.
- Performance dependency on a number of system parameters is explored.
- The capsule can be localized inside the body with sub-millimeter accuracy.

Graphical Abstract
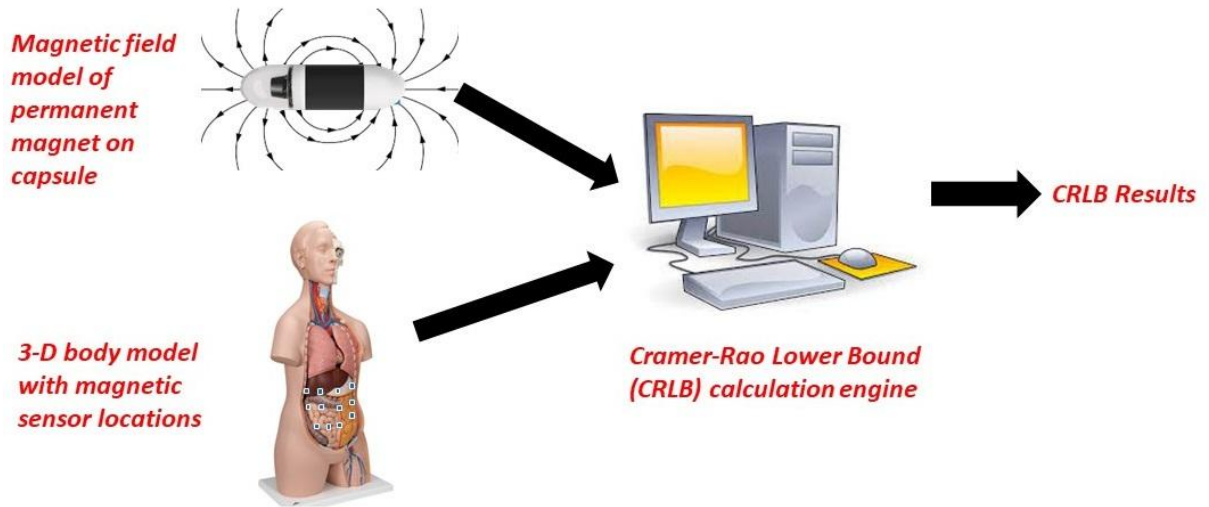
*Corresponding Author: Muzaffer KANAAN, mkanaan@erciyes.edu.tr

CRAMER-RAO LOWER BOUND ANALYSIS FOR MAGNETIC LOCALIZATION OF A ROBOTIC CAPSULE ENDOSCOPE

[1, *]**Muzaffer KANAAN** [ID] , [2]**Muhammed CİL** [ID] , [3]**Memduh SUVEREN** [ID]

[1, 3] *Erciyes University, Mechatronics Engineering Department, Kayseri, TÜRKİYE*
[2] *Kafkas University, Mechanical Engineering Department, Kars, TÜRKİYE*
[1]mkanaan@erciyes.edu.tr , [2]muhammed.cil@kafkas.edu.tr, [3]msuveren@erciyes.edu.tr

ABSTRACT: In robotic capsule endoscopy, highly accurate localization of the capsule device inside the human body is a critical problem for disease diagnosis and treatment. Quantitative analysis of lower bounds, such as the Cramer-Rao Lower Bound, is practically important for localization systems, as they inform system designers of the best achievable performance under a given set of conditions. This paper presents a comprehensive, systematic analysis of the Cramer-Rao Lower Bound for the scenario of magnetic localization of a robotic wireless capsule endoscope inside the human body. The specific contributions of the study are threefold. First, we undertake a systematic analysis of the bound in the presence of a realistic 3D body model. Second, we present a detailed analysis of the effects of capsule motion as well as other system parameters (such as magnet type and magnet dimensions) inside the body on the bound values. Finally, we interpret the findings to come up with recommendations on system parameters to guarantee optimal performance.

Keywords: *Cramer-Rao Lower Bound, Magnetic Localization, Robotic Capsule Endoscopy*

1. INTRODUCTION

Wireless capsule endoscopy (WCE) technology is rapidly becoming a very popular medical imaging technique, especially for the diseases of the gastrointestinal (GI) tract[1-3]. This is because WCE technology is minimally invasive (the patient only has to swallow a capsule) and painless for the patient in contrast to conventional endoscopy, where the patient typically has to be sedated. As a result, clinical use of WCE has been extended to imaging other parts of the GI tract, such as the stomach, esophagus, duodenum and the colonic mucosa[4, 5]. Current generation of WCE systems used in clinical settings are commonly classified as *passive* devices, in the sense that external control of the capsule inside the GI tract is not possible; the capsule moves through the GI tract via standard muscle contractions and is naturally excreted out of the body.

In recent years, WCE technology started to evolve towards *active*, or *robotic* capsule endoscopy (RCE) [6-8]. In contrast to WCE systems, an RCE capsule now becomes a small-size robot, whose motion can be externally controlled. This expands the functionality of the endoscopy capsule, in that the medical specialist can now maneuver the expanse of the GI tract at will, bypassing regions that are not of interest, and focusing more on areas deemed worthy of detailed examination (such as a suspicious tumor, or a lesion, for example). Furthermore, an RCE capsule fitted with adequate sensors and actuators can even carry out other tasks (such as collection of biopsy samples from a tumor, or even ablation of the tumor in a minimally invasive manner). The specific focus of this paper is on RCE systems.

Ever since WCE systems first appeared in clinical settings, the problem of localizing the capsule inside the GI tract has been of interest, since WCE images without corresponding location data are clinically meaningless for diagnosis and treatment purposes. This *localization problem* has previously been studied in considerable detail [9-11]. Much of this research has focused on passive WCE systems. Accurate solution to the localization problem becomes even more critical in an RCE setting, where the user (i.e. the medical

---

*Corresponding Author: Muzaffer KANAAN, mkanaan@erciyes.edu.tr

specialist) has to know precisely where the capsule is, on a real-time basis, in order to guide the capsule inside the GI tract for an efficient and thorough medical examination.

There are several methods proposed in the literature for localizing a capsule endoscope device inside the GI tract. These methods include RF localization (i.e. using the RF signal emitted by the capsule to relay images for localization purposes) [12], MR and ultrasound [13], X-ray and Gamma-ray imaging [14], hybrid methods (such as those that leverage RF localization with image processing)[15, 16], and magnetic localization [17]. RF localization, while a very attractive option in principle, has serious accuracy issues when used on its own. This is due to the severe way the RF signal is distorted by the human body tissues (as body tissues have different electrical characteristics, which are also frequency-dependent) [3]. The use of MR and ultrasound techniques may require additional components inside the capsule itself, which is already constrained in terms of size[18, 19]. The use of X-rays and Gamma-rays, while technically an option, are not advisable, as they expose the patient to potentially dangerous amounts of ionizing radiation[20]. Hybrid methods, such as those that use RF localization in conjunction with the processing of received capsule images, are another option; however, this may result in increased computational load, which goes against the real-time localization requirements for RCE systems. This leaves magnetic localization as the most promising alternative option for accurate, real-time localization [21]. As such, this paper focuses on magnetic localization of an RCE capsule inside the GI tract.

In a magnetic localization system, the location-dependent magnetic field from a magnet is sensed by magnetic field sensors and used to come up with a location estimate. Thus, a small permanent magnet located on the capsule can be used to localize the capsule inside the GI tract. Magnetic localization is the most accurate for WCE and future RCE systems, due to the fact that human body tissues have the same magnetic characteristics as free space; therefore, the magnetic field emitted by the permanent magnet is not affected by the body tissues, thus reducing the localization problem to that of localizing a magnetic field source in free space.

For any localization system, the main performance indicator is the localization accuracy, defined as the error between the actual location of the capsule and the location determined by a localization algorithm. This brings up another important question: for a given system scenario and system parameter set, what is the best achievable localization accuracy? Answering this question is of paramount importance for design and performance optimization of localization algorithms. Statistical lower bounds, such as the Cramer-Rao Lower Bound (CRLB), can be used to address this question. In this paper, we present a systematic analysis of the CRLB for magnetic localization of an endoscopy capsule in an RCE scenario.

Although an initial analysis of the CRLB for magnetic localization of an endoscopy capsule was presented in [22], we believe that the analysis needed to be considerably extended, in order to be valid for our RCE scenario. This forms the main motivation of the current paper. The results reported in [22] focused, for the most part, on a planar arrangement of sensors. In a practical scenario, where the sensors are typically on the body surface, this is not realistic. In addition, for magnetic localization, there are other system-related parameters which affect performance, such as magnet size, and magnetic materials. The dependence of the CRLB on such system-related parameters is missing in [22], and could be extremely useful to system designers.

The specific contributions of this paper can be summarized as follows. First, we undertake the CRLB analysis using a realistic 3-D human body model. Second, we present a detailed analysis of the effects of capsule motion inside this body model on the CRLB. Third, we explore the dependence of the CRLB on system-related parameters, such as magnet size and magnetic materials. Finally, we interpret the findings to come up with fundamental recommendations on system parameters to guarantee optimal performance.

The rest of this paper is organized into three sections. Section 2 ("Material and Methods") gives a general overview of magnetic localization techniques, the Cramer-Rao Lower Bound and presents the theoretical framework for the performance evaluation in subsequent sections. Section 3, titled "Results and Discussion", presents the results of the CRLB analysis, based on different practical system scenarios of interest. The paper ends with concluding remarks in Section 4.

2.   MATERIAL AND METHODS

2.1 Magnetic Localization Techniques

The magnetic localization technique is based on a small magnet placed on the capsule, which does not require a power supply and connection cable. The magnet attached to the capsule creates a static magnetic field around the human body as it moves with the capsule. This magnetic field can be measured by N magnetic sensors placed on the surface of the patient's body, where N is the number of sensors. Since the magnetic field measured by the sensors depends on the 3-dimensional coordinates and orientation angles in the magnetic field distribution, the capsule position and orientation can be determined by solving an inverse problem.

In order to determine the mathematical expression of the magnetic field distribution in free space, various models can be used[23]. One such model is the magnetic dipole model, preferred in many studies due to its simplicity[24]. The dipole model is based on the equations of magnetic field strength and magnetic flux density emitted by the magnet. The dipole model created for the capsule is based on a cylindrical permanent magnet, as shown in Fig. 1. The capsule diameter is expressed as R1, while the diameter of the magnet surrounding the capsule is expressed as R2
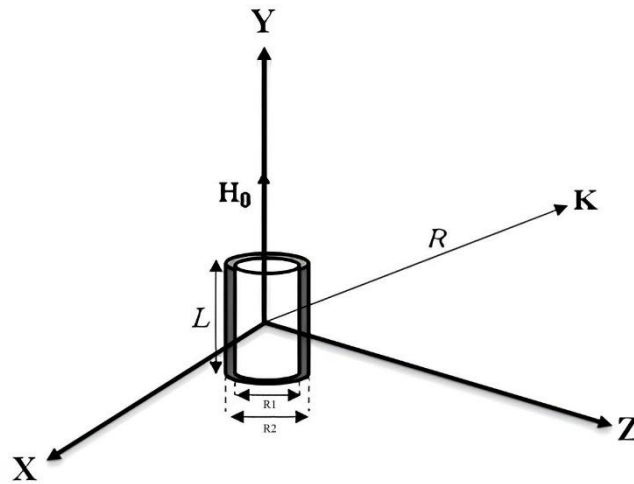
Figure 1. Magnetic field produced by a cylindrical magnet

In this study, a cylindrical magnet geometry, hollow in the inside, is assumed (see Fig. 2), such that the magnet is wrapped over the actual capsule. This ensures that the overall physical size of the capsule does not increase noticeably, thereby allowing the capsule to move more easily through the body and preserving the usability of the device.
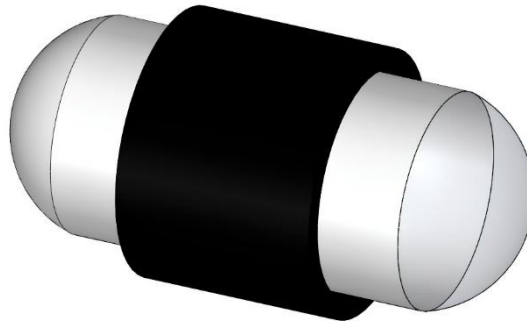
Figure 2. Structure of the capsule including the cylindrical permanent magnet

The dipole model to characterize the magnetic flux density is given by

$$\mathbf{B} = B_T \left(\frac{3(\mathbf{H_0} \cdot \mathbf{K})\mathbf{K}}{R^5} - \frac{\mathbf{H_0}}{R^3} \right) \tag{1}$$

where r_1 and r_2 represent the inner and outer radius of the magnet, respectively. The parameter L represents the length of the magnet and $\mathbf{K} = (x_i, y_i, z_i)^T$ is a spatial point in the Cartesian coordinate system of the magnet, where the magnetic field strength is observed. In addition, R shows the distance between the magnet and $\mathbf{K}$, while $\mathbf{H}_0$ shows the orientation vector of the magnet. The parameter B_T is expressed as $B_T = \frac{\mu_r \mu_0 M_T}{4\pi}$ and $M_T = \pi(r_2^2 - r_1^2) L M_0$, where M_0 is the uniform magnetization (A/m). Relative permeability is represented by μ_r, and $\mu_0 = 4\pi \times 10^{-7}$ (H/m) is the magnetic permeability of free space.

The magnetic flux density measured by the i-th sensor is given by

$$\boldsymbol{B}_i = B_{x,i}\hat{\boldsymbol{x}} + B_{y,i}\hat{\boldsymbol{y}} + B_{z,i}\hat{\boldsymbol{z}} \quad (i = 1, \dots, N) \tag{2}$$

Axial magnetic flux density expressions can be written as

$$B_{x,i} = B_T \left\{ \frac{3\left[m(x_i - a) + n(y_i - b) + p(z_i - c) \right](x_i - a)}{R_i^5} - \frac{m}{R_i^3} \right\} \tag{3}$$

$$B_{y,i} = B_T \left\{ \frac{3\left[m(x_i - a) + n(y_i - b) + p(z_i - c) \right](y_i - b)}{R_i^5} - \frac{n}{R_i^3} \right\} \tag{4}$$

$$B_{z,i} = B_T \left\{ \frac{3\left[m(x_i - a) + n(y_i - b) + p(z_i - c) \right](z_i - c)}{R_i^5} - \frac{p}{R_i^3} \right\} \tag{5}$$

where (x_i, y_i, z_i) are the known coordinates of the i-th sensor and $R_i = \sqrt{(x_i - a)^2 + (y_i - b)^2 + (z_i - c)^2}$. Equations (3)-(5) form the basis for the calculation of the CRLB, as discussed in the next section.

2.2. Analysis Of The Magnetic Localization Technique Using The CRLB

The Cramer-Rao Lower Bound (CRLB) represents a lower bound on the error covariance of an unbiased estimator, of some unknown parameter vector $\varepsilon = [\varepsilon_1, \varepsilon_2, \cdots \varepsilon_k]^T$ based on a set of observations[25-30]. The bound is based on the probability density function, $p(x/\varepsilon)$, of the observation vector $\mathbf{x}$, conditioned on the *deterministic*, unknown parameter vector, $\boldsymbol{\varepsilon}$. Let the vector $\tilde{\boldsymbol{\varepsilon}}$ represent the vector of estimated parameters. The CRLB can then be expressed as

$$cov_\varepsilon(\tilde{\boldsymbol{\varepsilon}}) \geq \boldsymbol{J}_\varepsilon^{-1} \tag{6}$$

where $cov_\varepsilon(\tilde{\boldsymbol{\varepsilon}}) = E\{(\tilde{\boldsymbol{\varepsilon}} - \boldsymbol{\varepsilon})(\tilde{\boldsymbol{\varepsilon}} - \boldsymbol{\varepsilon})^T\}$ is the $K \times K$ covariance matrix of the estimation error and $\mathbf{J}_\varepsilon$ is the $K \times K$ Fisher information matrix. For the purposes of the capsule localization problem, $\mathbf{x} = \hat{\mathbf{B}}(\varepsilon)$, where $\hat{\mathbf{B}}$ is the vector of observed magnetic flux density values, that is a function of the unknown location and orientation parameters, $\boldsymbol{\varepsilon} = [a,b,c,m,n,p]^T$, and thus $K = 6$. The (j,k) element of the Fisher information matrix is defined as

$$\left[\mathbf{J}_\varepsilon\right]_{jk} = E_\varepsilon\left\{\frac{\partial}{\partial\varepsilon_j}\log p\left(\hat{\mathbf{B}}\middle|\varepsilon\right)\cdot\frac{\partial}{\partial\varepsilon_k}\log p\left(\hat{\mathbf{B}}\middle|\varepsilon\right)\right\} \tag{7}$$

The starting point for the calculation of the CRLB is an observation model, which expresses the noisy measurements of the components of the magnetic flux density from the capsule. This model is given by

$$\hat{B}_{x,i} = B_{x,i}\left(a,b,c,m,n,p\right)+n_{x,i}$$
$$\hat{B}_{y,i} = B_{y,i}\left(a,b,c,m,n,p\right)+n_{y,i} \tag{8}$$
$$\hat{B}_{z,i} = B_{z,i}\left(a,b,c,m,n,p\right)+n_{z,i}$$

where $\left(\hat{B}_{x,i},\hat{B}_{y,i},\hat{B}_{z,i}\right)$ is the set of magnetic flux density values measured by sensor i ($i = 1,\dots,N$), $\left(B_{x,i},B_{y,i},B_{z,i}\right)$ is the set of real magnetic flux density values (as expressed by (3)-(5) above) and $\left(n_{x,i},n_{y,i},n_{z,i}\right)$ are the set of independent, identically distributed (i.i.d) zero-mean Gaussian random variables with standard deviation σ, which model the measurement noise associated with sensor i. The i.i.d. assumption is one that is usually used in order to come up with results that are analytically tractable. It is certainly possible that in the case of wearable sensors, the sensor noise could be correlated Gaussian (a scenario briefly considered in Appendix B), or even non-Gaussian. For the case of non-Gaussian noise, other distributions, such as Gaussian Mixture Models (GMMs), could be used[31].

Equation (8) can be succinctly written in vector notation as

$$\hat{\mathbf{B}}\left(\varepsilon\right)=\mathbf{B}\left(\varepsilon\right)+\mathbf{n} \tag{9}$$

Therefore, the conditional distribution of the observation vector, $\hat{\mathbf{B}}$, conditioned on the unknown parameter set can be written as

$$p\left(\hat{\mathbf{B}}\middle|\varepsilon\right)= p_n\left(\hat{\mathbf{B}}-\mathbf{B}\right) \tag{10}$$

where $p_n\left(\mathbf{x}\right)$ is the multivariate normal distribution, with mean $\boldsymbol{\mu}$ and covariance $\boldsymbol{\Sigma}$ given by

$$p_n\left(\mathbf{x}\right)=\frac{1}{\left[\left(2\pi\right)^K\det\left(\boldsymbol{\Sigma}\right)\right]^{1/2}}\exp\left[-\frac{1}{2}\left(\mathbf{x}-\boldsymbol{\mu}\right)^T\boldsymbol{\Sigma}^{-1}\left(\mathbf{x}-\boldsymbol{\mu}\right)\right] \tag{11}$$

With the above framework in place, the $\left(j,k\right)$ element of the Fisher information matrix can be expressed as (see Appendix A for the derivation)

$$\left[\mathbf{J}_\varepsilon\right]_{jk} = \frac{1}{\sigma^2}\sum_{i=1}^{N}V_{jk}^{(i)} \tag{12}$$

where

$$V_{jk}^{(i)} = \frac{\partial B_{x,i}}{\partial\varepsilon_j}\frac{\partial B_{x,i}}{\partial\varepsilon_k}+\frac{\partial B_{y,i}}{\partial\varepsilon_j}\frac{\partial B_{y,i}}{\partial\varepsilon_k}+\frac{\partial B_{z,i}}{\partial\varepsilon_j}\frac{\partial B_{z,i}}{\partial\varepsilon_k} \tag{13}$$

The Fisher matrix is symmetric and can be expressed as a 2×2 block matrix of the form

$$\mathbf{J}_\varepsilon = \begin{bmatrix} \mathbf{J}_L & \mathbf{C}_{LO} \\ \mathbf{C}_{LO}^T & \mathbf{J}_O \end{bmatrix} \tag{14}$$

where $\mathbf{J}_L$ and $\mathbf{J}_O$ are 3×3 matrices consisting only of the terms pertaining to the location parameters, (a,b,c), and the orientation parameters, (m,n,p), respectively, as given by

$$\mathbf{J}_L = \begin{bmatrix} J_{aa} & J_{ab} & J_{ac} \\ J_{ba} & J_{bb} & J_{bc} \\ J_{ca} & J_{cb} & J_{cc} \end{bmatrix} \tag{15}$$

$$\mathbf{J}_O = \begin{bmatrix} J_{mm} & J_{mn} & J_{mp} \\ J_{nm} & J_{nn} & J_{np} \\ J_{pm} & J_{pn} & J_{pp} \end{bmatrix} \tag{16}$$

and $\mathbf{C}_{LO}$ is another 3×3 matrix that contains cross-terms between the location and orientation parameters:

$$\mathbf{C}_{LO} = \begin{bmatrix} J_{am} & J_{an} & J_{ap} \\ J_{bm} & J_{bn} & J_{bp} \\ J_{cm} & J_{cn} & J_{cp} \end{bmatrix} \tag{17}$$

Since $\mathbf{J}_\varepsilon$ can be written as a block matrix in the form of (11), its inverse will also be a symmetric matrix of the form (for details, see, for example[32])

$$\mathbf{J}_\varepsilon^{-1} = \begin{bmatrix} \mathbf{M}_{11} & \mathbf{M}_{12} \\ \mathbf{M}_{12}^T & \mathbf{M}_{22} \end{bmatrix} \tag{18}$$

and since $\mathbf{J}_\varepsilon \mathbf{J}_\varepsilon^{-1} = \mathbf{I}$, it can be shown that

$$\mathbf{M}_{11} = \left[\mathbf{J}_L - \mathbf{C}_{LO}\mathbf{J}_O^{-1}\mathbf{C}_{LO}^T \right]^{-1} \tag{19}$$

$$\mathbf{M}_{12} = -\mathbf{J}_L^{-1}\mathbf{C}_{LO}\left[\mathbf{J}_O - \mathbf{C}_{LO}^T\mathbf{J}_L^{-1}\mathbf{C}_{LO} \right]^{-1} \tag{20}$$

$$\mathbf{M}_{12}^T = -\mathbf{J}_O^{-1}\mathbf{C}_{LO}^T\left[\mathbf{J}_L - \mathbf{C}_{LO}\mathbf{J}_O^{-1}\mathbf{C}_{LO}^T \right]^{-1} \tag{21}$$

$$\mathbf{M}_{22} = \left[\mathbf{J}_O - \mathbf{C}_{LO}^T\mathbf{J}_L^{-1}\mathbf{C}_{LO} \right]^{-1} \tag{22}$$

Thus, the CRLB is defined only under the assumption that the associated inverses in (19) - (22) are defined.

A close examination of (18) - (22) offers several points of insight. First, the $\mathbf{M}_{11}$ block on the right-hand side of (18) gives the lower bound on error covariance associated with estimation of the *location parameters only*. However, a closer examination of the right-hand side of (19) reveals that this block is affected by the unknown orientation parameters, as evidenced by the presence of terms involving $\mathbf{J}_O$ and $\mathbf{C}_{LO}$. If the orientation parameters, (m,n,p), were somehow known, and the only unknown parameters being

estimated were the location parameters (a,b,c), then we would have $\mathbf{M}_{11} = \mathbf{J}_L^{-1}$. Thus, the term $\mathbf{C}_{LO}\mathbf{J}_O^{-1}\mathbf{C}_{LO}^T$ in (19) can be viewed as an objective measure of the "penalty" we have to pay for estimating the location and orientation parameters at the same time. A similar argument can be made regarding the $\mathbf{M}_{22}$ block in (18), which concerns the lower bound associated with estimation of *orientation parameters only*; thus the term $\mathbf{C}_{LO}^T\mathbf{J}_L^{-1}\mathbf{C}_{LO}$ in (22) can be viewed as a measure of the penalty in this case.

A well-known and commonly used metric for evaluating the performance of localization systems is the *Root Mean Square Error* (*RMSE*) which is defined as the square-root of the mean-square error between the estimated and actual location (or orientation) parameters. Thus, a lower-bound on this metric would be of practical interest. Upon examination of (18) – (22), it is clear that the diagonal elements of the $\mathbf{M}_{11}$ block in (18) are the lower-bounds on the error covariance associated with the estimation of location parameters, (a,b,c). Thus a lower-bound on the RMSE for location estimation, denoted by $RMSE_L$, can be calculated based on the sum of the diagonal elements of $\mathbf{M}_{11}$:

$$RMSE_L = \sqrt{sum\left(diag\left(\mathbf{M}_{11}\right)\right)} \tag{23}$$

Similarly, a lower bound on the RMSE for estimation of orientation parameters, denoted by $RMSE_O$, can be determined based on the sum of the diagonal elements of $\mathbf{M}_{22}$:

$$RMSE_O = \sqrt{sum\left(diag\left(\mathbf{M}_{22}\right)\right)} \tag{24}$$

3.   RESULTS AND DISCUSSION

In this section, we present and analyze the CRLB results for the magnetic localization technique with real position and orientation values based on a 3-D human body model. We begin with a discussion of the general assumptions underlying the results in the following subsections.

The magnetic localization technique consists of a magnetic source and the sensor plane in which the magnetic sensors are placed. It is assumed that the magnetic source is hollow cylindrical in such a way that it wraps around the outside of the capsule, as shown in Fig. 2. The magnet material is assumed to be NdFeB (Neodymium-Iron-Boron), since this is the material combination with the highest amount of magnetic flux per unit volume. For the purposes of the current study, the geometrical parameters of the magnet are: outer diameter R2=15 mm, inner diameter R1= 11mm, and length L=20 mm with a uniform magnetization value of $M_0 = 750x10^3$ (Amp/meter). The magnetic sensor model is based on Honeywell's (HMC1043) tri-axial magnetic field sensors. For the purposes of this analysis, the sensor array on the body surface was created by taking into the account 3-dimensional human body dimensioning the model. Fig. 3 (a), (b) and (c) show the body model where the sensors are placed, the tissue state of the intestine in this body, the shape of the intestine transformed into a digital solid model to obtain the capsule positions, respectively. Solidworks™ CAD software was used to obtain the digital 3-D model of the intestinal region and an interpolation relationship was defined between known real intestinal positions. The goal here is to create a framework for performance evaluation which would allow for numerical evaluation of the CRLB at an arbitrary number of positions in the large as well as the small intestine.
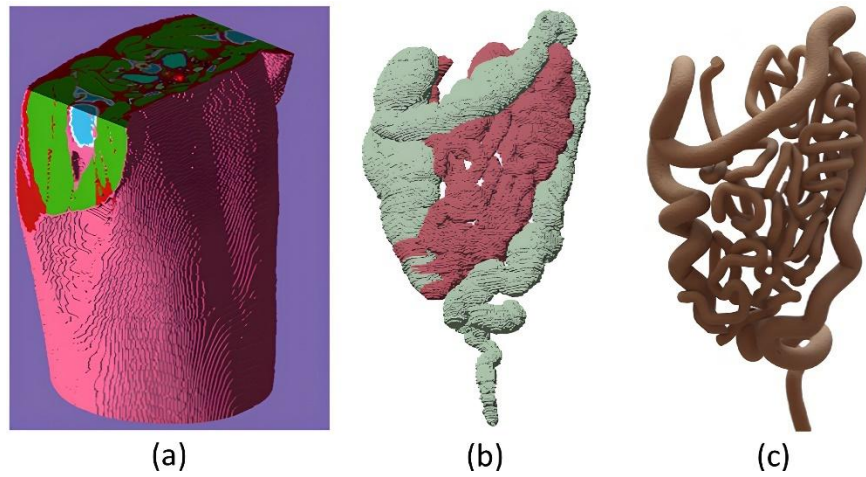
Figure 3. (a) Human torso model, (b) Intestine tissue model, (c) Numerical intestine model

A total of 256 magnetic sensors in contact with the skin are used on the body model. In addition, simulation data were obtained for 375 locations in which the magnetic capsule was positioned in the intestine model. The entire 3D working space, where the sensor and capsule positions can be seen together, is given in Fig. 4.
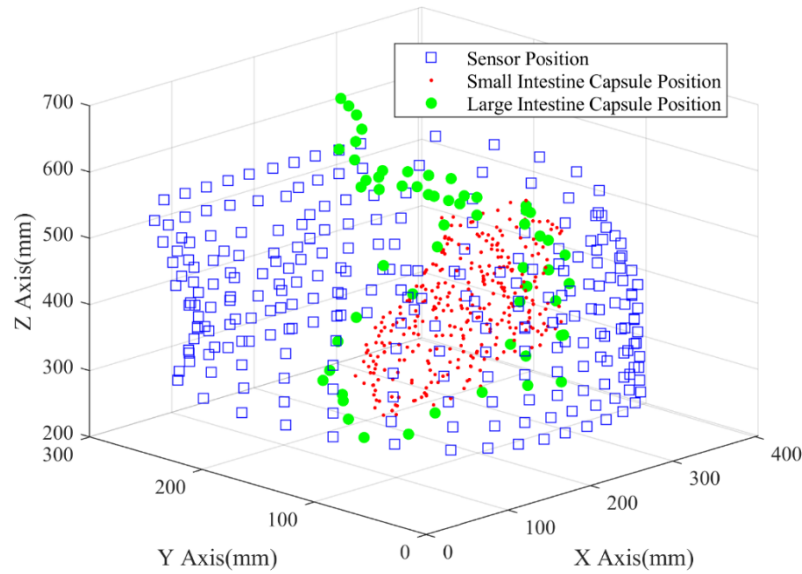
Figure 4. Sensor and capsule locations

3.1 CRLB for Capsule Position and Orientation Parameters

CRLB values are shown in Fig. 5 and Fig. 6 according to the increase in the number of sensors for each position in the capsule movement. The results reported here are based on 375 positions of the capsule covering the small intestine and large intestine. These results are a function of the number of sensors, which was increased to a maximum of 256. Fig. 5 shows the CRLB values for the capsule's position parameters, while Fig. 6 shows CRLB values for the capsule's orientation parameters. CRLB values above average are observed in capsule positions in the large intestine (318-375) and in the small intestine (1-317). When examining Fig. 5 and Fig.6 for each position during the capsule's movement, it is observed that the maximum CRLB values occur in the 4-sensor configuration, while the CRLB values progressively decrease

in the 8 and 16 sensor configurations. Although the CRLB values between these three sensor configurations are noticeable, the difference decreases and CRLB values are minimized when the effects of 32 and 64 sensor configurations are analyzed. In the subsequent 128 and 256 sensor configurations, no substantial change in CRLB values is observed.
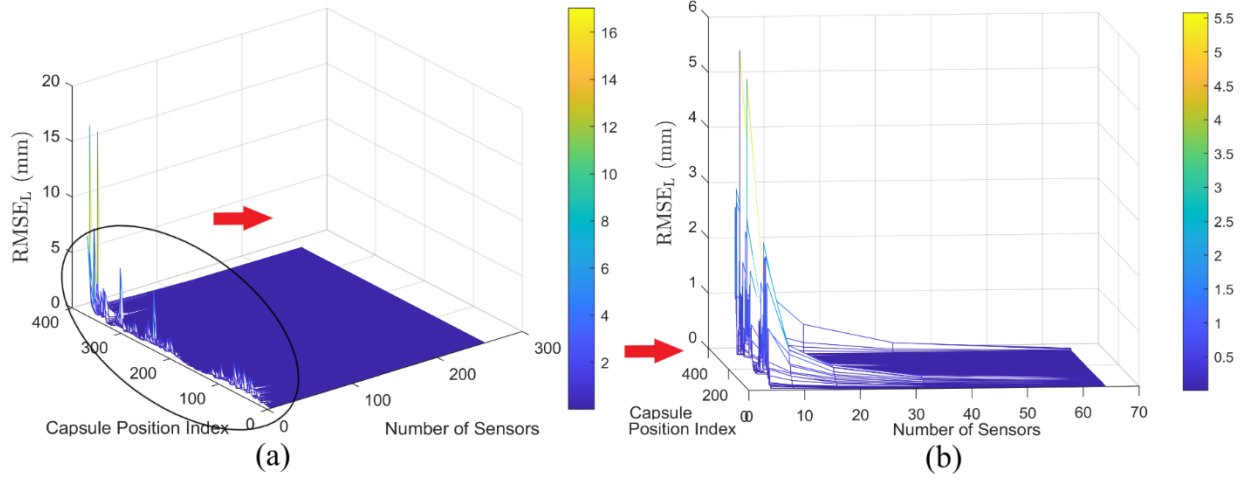
Figure 5. (a) RMSE$_L$ for capsule position parameters (b) zoomed region
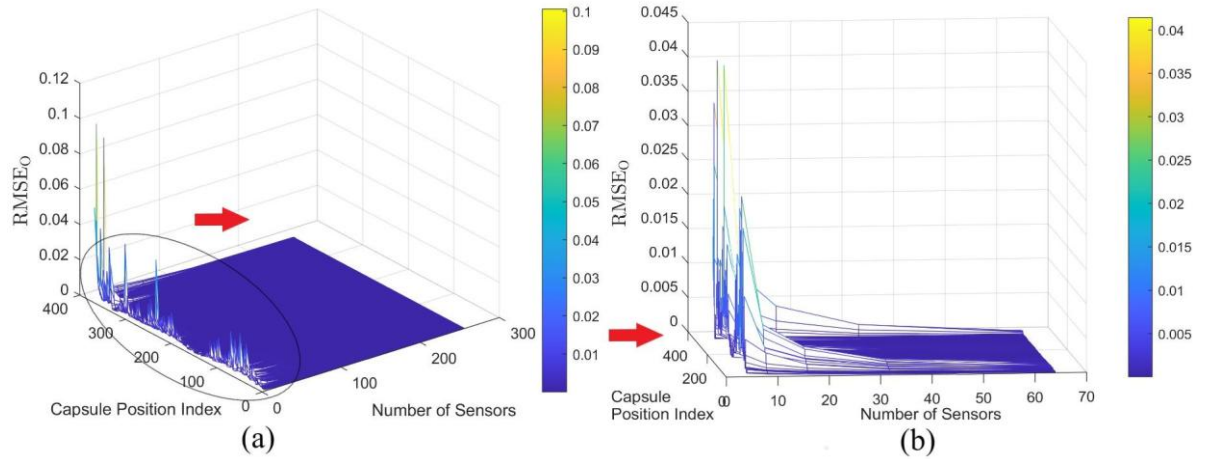
Figure 6. (a) RMSE$_O$ for capsule orientation parameters (b) zoomed region

By averaging the values across each capsule position, Fig. 7 is generated. This figure illustrates how increasing the sensor count leads to a reduction in the average RMSE values. Specifically, when the sensor configuration is increased from 4 to 8 sensors, the average RMSE value decreases by 82.79%. This reduction further improves to 91.43% when the sensor count is raised to 16. Similarly, a 32-sensor array achieves a 96.53% decrease in total error compared to a 4-sensor configuration, while a 64-sensor array shows a reduction of 98.98%. This ratio decreases to a minimum in arrays with 128 and 256 sensors. Fig. 7(b) presents data for sensor arrays ranging from 32 to 64 sensors. When evaluating the RMSE reduction for every 8-sensor increase, a 31.63% improvement is observed between 32 and 40 sensors, which further increases to 50.87% at 48 sensors. In contrast, further additions to 56 and 64 sensors yield only an approximate 10% reduction. Based on these results, it can be concluded that a 48-sensor array achieves an optimal balance between the sensor count and RMSE error reduction.
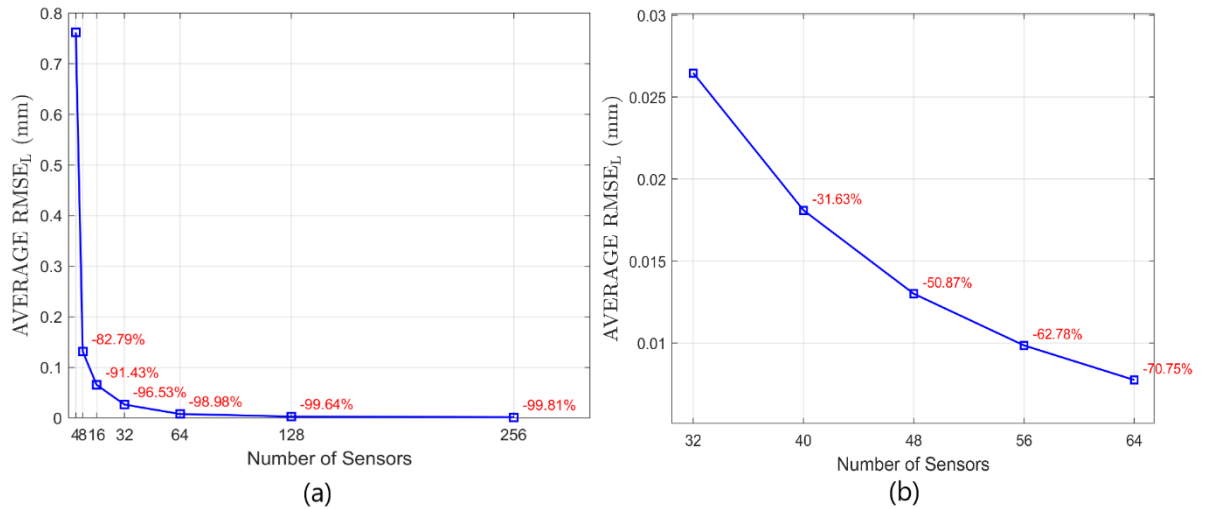
Figure 7. (a) Average RMSE$_L$ for capsule position parameters (b) between 32 and 64 sensors

3.2   *Effect of Magnet Size on CRLB*

In this section, we examine the effect of the size of the magnet wrapped outside the capsule on the CRLB. An attempt has been made to find out how the thickness and length of the magnet affect the CRLB. Fig. 8 shows CRLB values according to the increase in the number of sensors for different magnet sizes and thicknesses. The CRLB values presented here are average values, based on CRLB values obtained at all capsule locations (375 in total). The graph is based on an estimate of the capsule's position parameters. The number of sensors is again gradually increased up to a maximum of 256 sensors. In the results, it is seen that increasing the size of the magnet reduces CRLB values by the same rate. This, in turn, can be explained by the fact that the increase in the size of the magnet is directly proportional to the increase in the magnetic field.
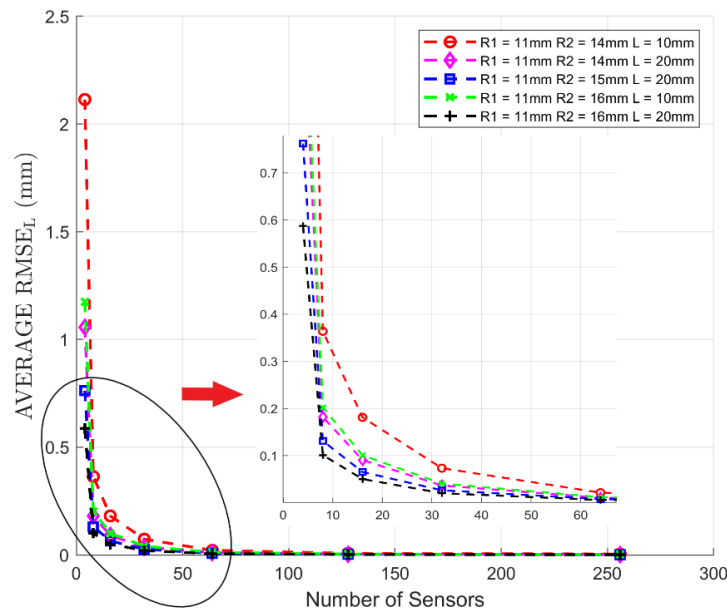
Figure 8. RMSE by magnet size

Increasing the size of the magnet can create practical limitations, as it increases the overall dimensions of the capsule. Difficulty swallowing, limitations based on bowel size, and discomfort to the patient, are

all factors that should be considered when determining the size of the magnet. A review of the medical literature compares the dimensions of some of the most widely used capsule endoscope devices [33]. Based on this information, the average length of the device appears (end-to-end, including the dome-shaped cameras, potentially at both ends) to be approximately 25.5 mm and the average diameter is approximately 11 mm. Considering the cylindrical structure of the magnet as shown in Fig. 2, it is obvious that the length of the magnet needs to be less than 25.5 mm (since the field-of-view of the camera should not be obstructed). Therefore, a length of L = 20 mm is reasonable. The CRLB values for two different values of L, and different thickness values (i.e. different values of R2) are shown in Fig. 8. Of particular interest from this perspective, is the case where L = 20 mm and R2 = 14 mm (see purple curve on Fig. 8). This particular scenario translates to a magnet thickness of only 1.5 mm and thus can be considered practically feasible. Thus, the results of Fig. 8 clearly show that highly accurate localization is possible at practically feasible magnet dimensions.

3.3   Effect of the Magnetic Material on the CRLB

The size of the magnet, as well as the type of magnetic material, affects the magnetic field of the magnet, and thus the CRLB. In this study, the effect of different types of magnets with different uniform magnetism values on CRLB was examined.   The goal here is to determine which type of magnet will give better localization performance. The magnet types considered are FeCoCr, Alnico, Ferrite, SmCo and NdFeB. These magnets are the main hard magnetic materials[34]. The graph in Fig. 9 is obtained when magnets are compared according to uniform magnetism values. The graph is based on estimate of the capsule's position parameters, and CRLB is an average of the capsule positions. As can be seen from the graph, the increase in uniform magnetism gives lower CRLB values. NdFeB and SmCo magnets appear to give the smallest CRLB values with the highest uniform magnetism values, indicating that these are the best magnetic materials for optimal positioning performance. The results of Fig. 9 also clearly illustrate that after a certain number of sensors (approximately 50), the graph becomes flat, indicating that it really does not matter which magnetic material is used. This observation can be explained by the notion that if the system employs a relatively large number of magnetic sensors, a certain subset will be able to provide measurements of high enough quality (enough to compensate for those sensors with lower-quality measurements) so that the overall localization performance will not be impacted noticeably.
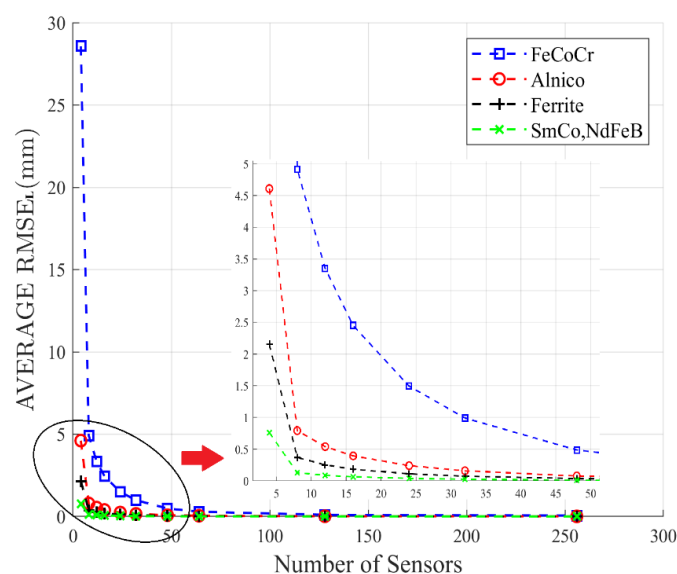
Figure 9. RMSE by uniform magnetism value

3.4 Effect of Sensor Location on CRLB

It is to be expected that the localization performance (and thus the CRLB) will be affected by the location of the sensors on the body surface. With this in mind, , localization performance is compared on the basis of the CRLB according to the body region where the sensors are employed. 48 sensors were selected for the four separate regions of the body surface (denoted as "left", "right", "front" and "back" in the results that follow), as shown in Figure 10.
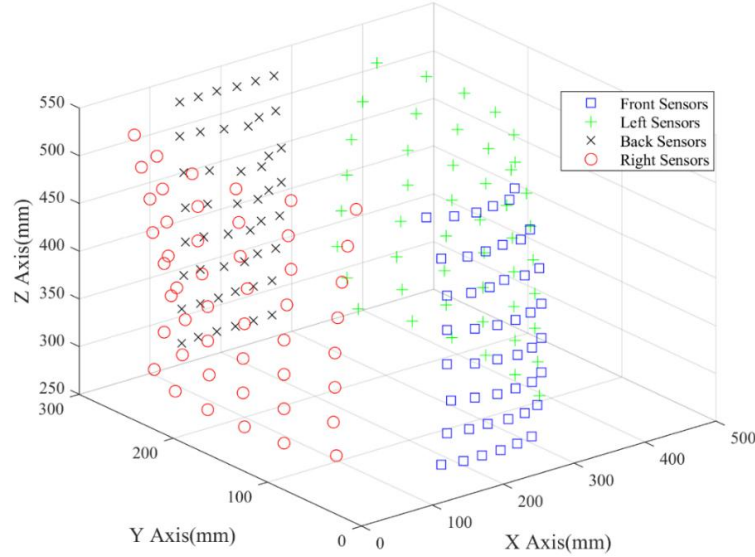
Figure 10. 48 sensor locations selected for each body part

The question here is: which of these four regions of the body would give rise to better localization performance (i.e. lower localization and orientation error)? show CRLB values for position and orientation parameters (based on the region where the sensors are employed) relative to actual capsule positions in the GI tract.
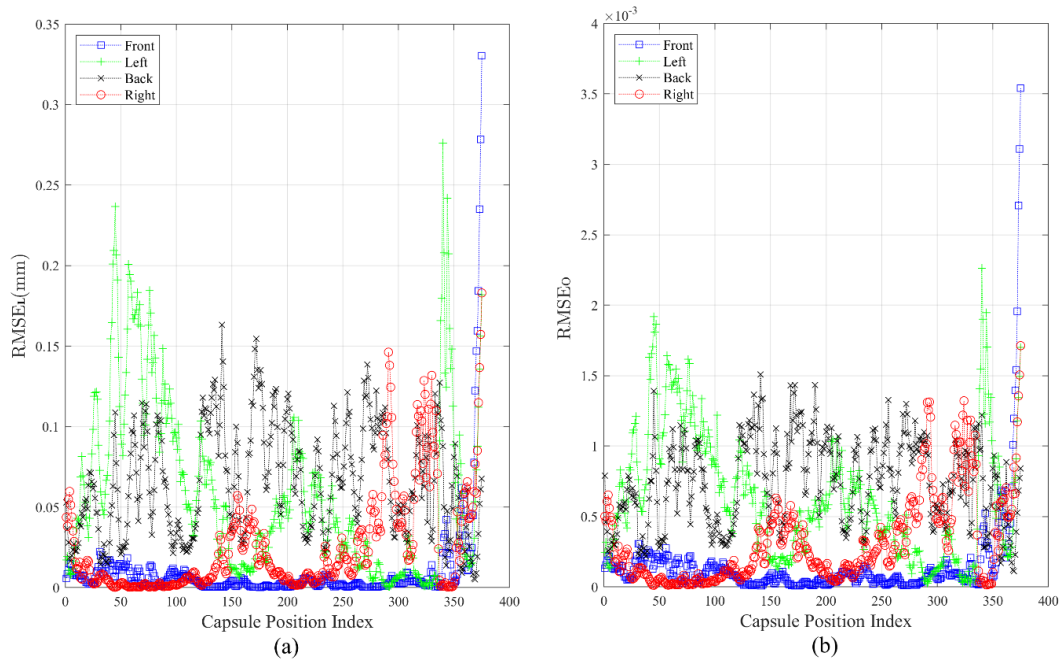
Figure 11. (a) RMSE$_L$ for position parameters by body region, (b) RMSE$_O$ for orientation parameters by body region

In order to give a more simplified view of the above results, Table I gives CRLB values averaged over all capsule positions for the four separate regions. Based on these results, it is seen that the smallest estimation error can be achieved with sensors placed on the front region of the body (covering the torso), indicating that that is the region of the body surface for optimal localization performance. This might well have to do with the fact that the intestinal region, in general, is closer to the front surface of the body (i.e. the torso) as opposed to the back of the body, thus allowing higher-quality magnetic sensor data. The right part of the body resulted in the second lowest prediction error, while the left and back part gave an equal prediction error. To illustrate this point another way, a 3-D intestinal "heat map" of the CRLB values is shown for the four sensor regions in Fig. 12.

Table 1 Average RMSE by Capsule Location

RMSE	Front	Back	Left	Right
Position (mm)	0.0098	0.0656	0.0593	0.0246
Orientation (10^{-4})	1.4791	7.3919	6.3185	3.1047
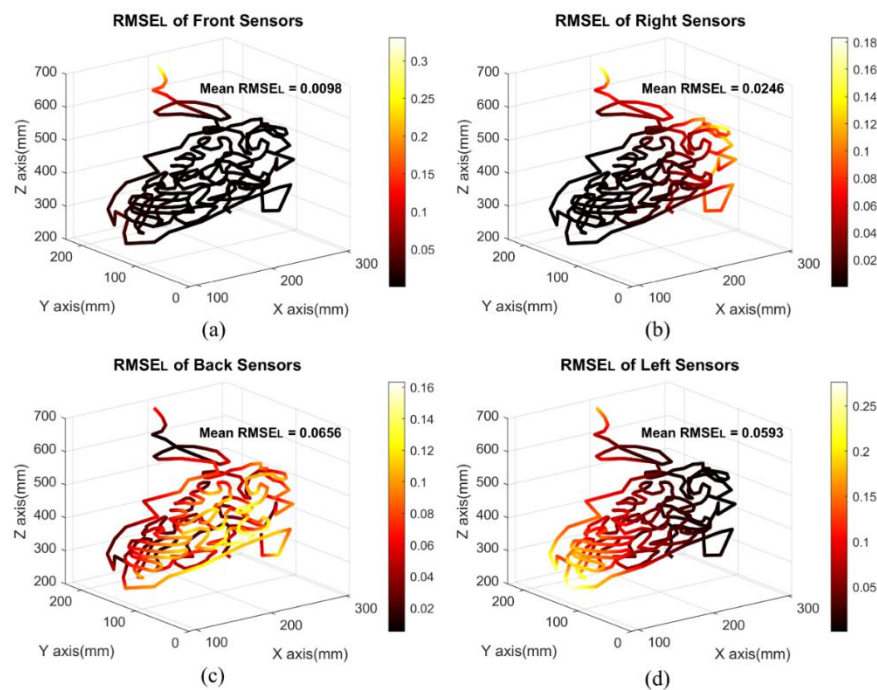
Figure 12. Intestinal heat map of RMSE$_L$ values according to sensor position on the body
(a)Front Sensors (b) Right Sensors (c) Back Sensors (d)Left Sensors

The results, as given in Fig. 12, show that localization performance with the front placement of sensors, while satisfactory in some parts of the intestine, is not quite as good in other parts. This raises yet another question: is it possible to enhance performance by providing spatial diversity among sensors? In other words, is it possible to enhance localization performance by augmenting the sensors placed on the front with sensors placed on the left and the right? The next set of results attempt to answer these questions. The sensor locations on the body surface for this study are shown in Fig. 13. In order to facilitate an effective comparison with the previous set of results, the total number of sensors is kept fixed at 48; however, 24 of these are located on the front of the torso, and the rest are located either on the right or the left. Note that the case of sensors on the back of the torso was not incorporated into this particular set of results, since the results of Fig. 14 clearly indicate poorer localization performance in this case.
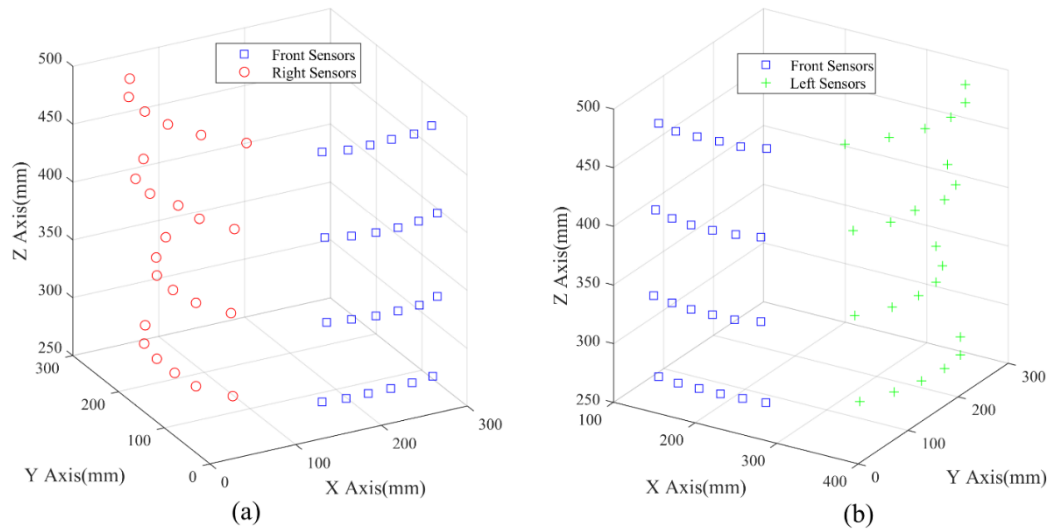
Figure 13. (a) Front and Right sensors locations (b) Front and Left sensors locations
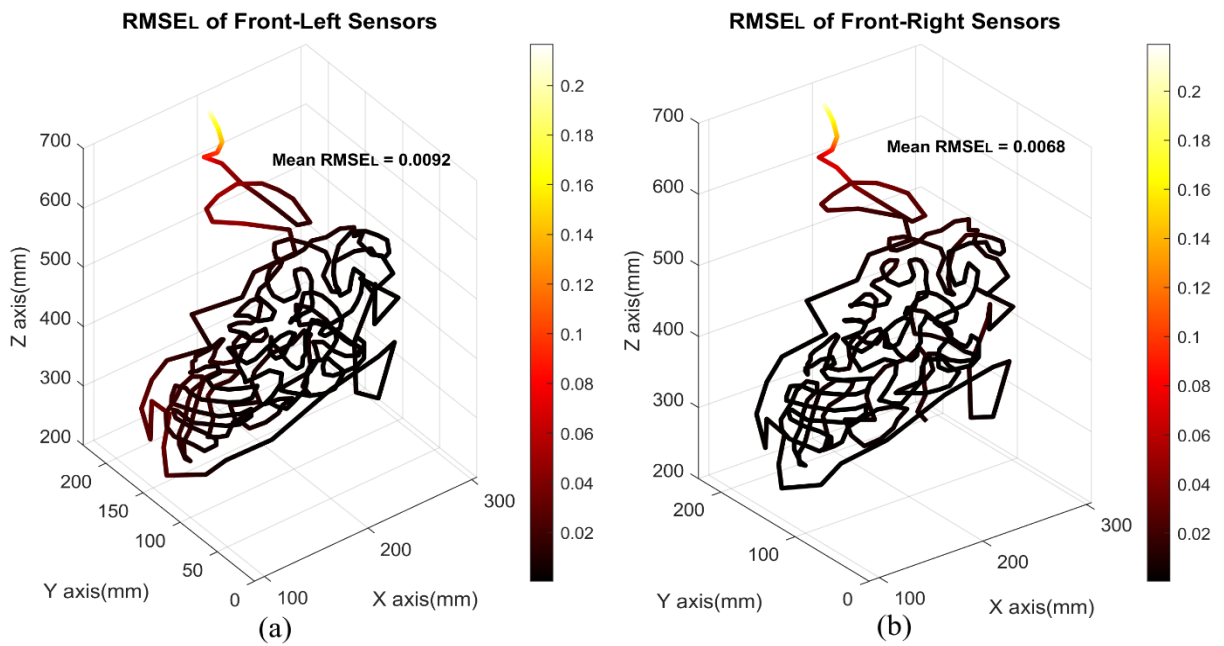
Figure 14. The impact of spatial diversity among sensors: Intestinal heat map of localization RMSE values based on the location of sensors: (a) Front-Left (b) Front-Right

Once again, in order to convey a more simplified perspective on the above results, the average RMSE over all the capsule locations considered in Fig. 14 has been computed and tabulated in Table II. These results show that, on average, both the positioning and orientation RMSE figures for the front-right case are approximately 26% better than the corresponding figures for the front-left case. To interpret these results in another way, we can compare the average RMSE figures for the *front-right* case to the results for the *front* case in Table I. This comparison indicates that the average positioning RMSE for the front-right case is approximately 31% better than the figure for the front case. A similar comparison for the average orientation RMSE indicates that the front-right case results in a performance improvement of approximately 30%. These results indicate that spatial diversity among sensors can have a positive impact on performance.

Table 2 Average RMSE by Capsule Location (Spatial Diversity Case)

RMSE	Front-Left	Front-Right
Position (mm)	0,0092	0,0068
Orientation (10⁻⁴)	1,3986	1,0405

3.5 General Discussion

Some general points pertaining to the above results are worthy of further discussion. The first such point involves the 3D body model used to derive the results.

The results reported in this paper are based on one 3D body model, the details of which are publicly available. It is a fact that no two human bodies are exactly alike. There are differences in body mass index, patient size and body composition (e.g. the amount of muscle versus fat). In addition, there are dynamic factors, such as bowel movements, which can cause subtle changes in the position of the organs in the GI tract. All of these factors can affect the magnetic field distribution, and thus the CRLB, and cannot necessarily be accounted for in a static 3-D model. The ideal way to address this issue would be to compute the CRLB for a number of different body models of adequate resolution; unfortunately, at the time of writing, the authors only had access to a single body model which satisfied this criterion.

In lieu of computing the CRLB for a range of body models, a small-scale sensitivity analysis is attempted, and the results are depicted in Fig. 15. This analysis is based on the 48 sensors located on the torso region. In this analysis, we have attempted to assess how the CRLB changes as a function of patient size in the torso region (as might be the case, for example, for a patient with a greater or lesser amount of body fat in the torso, compared to the original body model). This was simulated by adding or subtracting an offset value (20 mm) from the y-coordinate of all the sensors, and the resulting change in the CRLB values are shown in Fig. 15. It is observed that when the offset value is added, meaning the sensors are positioned farther from the body, the RMSE values increase; whereas when the offset value is subtracted, meaning the sensors are positioned closer to the body, the RMSE values decrease. In part (b) of Figure 15, a zoomed-in view is presented, and the mentioned differences can be clearly observed. These results show, at least at a basic level, that increases in patient size in the torso region could increase CRLB values.
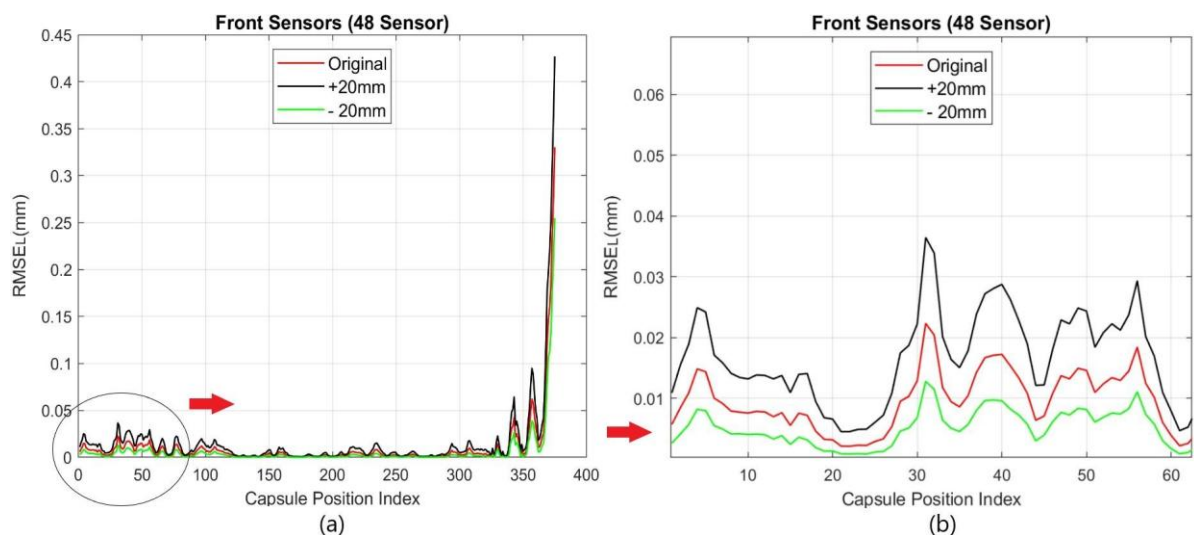
Figure 15. (a) RMSE by sensor distance (b) zoomed region

The second point worthy of discussion involves real-time localization of the capsule for RCE applications. Since CRLB represents a lower bound on the accuracy of a location estimator, it does not specify how real-time localization might be implemented. Nevertheless, the ability to accurately localize the capsule inside the body in a short timeframe is critical for RCE applications. The basic idea behind the localization algorithms is to leverage an analytical model for the magnetic field distribution (such as the

dipole model of equation (1)) to solve an inverse problem, i.e. to find the location coordinates (a,b,c) and the orientation parameters (m,n,p). Since the analytical models are inherently nonlinear functions of the location and orientation parameters, optimization methods are generally used to solve the problem. One very commonly used algorithm is the Levenberg-Marquardt (L-M) algorithm [35]. This algorithm, however, is generally very sensitive to the starting point for the calculations, and can take a long time to converge. To speed up the convergence, the L-M algorithm is generally used in conjunction with a metaheuristics algorithm, which can both provide a good starting point, thus speeding up convergence [16].

4 CONCLUSION

In this paper, we focused on the problem of magnetic localization for wireless capsule endoscopy, and specifically attempted to address the question of optimal performance through the use of the Cramer-Rao Lower Bound (CRLB). In order to obtain results of practical significance, a realistic 3-D human body model is used. Various scenarios have been considered with different sensor configurations and other system-related parameters, such as magnet size and magnetic materials. Based on the results obtained, we conclude that there is an optimal number of sensors (which appears to be 48), beyond which no appreciable improvement in the performance is obtained and that sensors should be positioned on the front of the body for optimal performance. The results also indicate that there are tradeoffs that need to be made in terms of magnetic materials and magnet size and their impact on performance. We believe the results should be of interest to all scientists and engineers interested in advancing wireless capsule endoscopy. Future work will focus on different cases for measurement noise and comparison of the results with other localization methods and practical testbed scenarios.

Declaration of Ethical Standards

The authors declare that the study complies with all applicable laws and regulations and meets ethical standards.

Credit Authorship Contribution Statement

Author 1: Methodology, Supervision, Validation, Formal analysis, Writing – review & editing
Author 2: Conceptualization, Formal analysis, Investigation, Methodology, Resources, Software, Writing – original draft, Writing – review & editing,
Author 3: Formal analysis, Investigation, Resources, Visualization, Writing – review & editing,

Declaration of Competing Interest

The authors declare that they have no known competing financial interests or personal relationships that could have appeared to influence the work reported in this paper.

Funding / Acknowledgements

The authors acknowledge that no funding support has been sought for the work reported in this paper, and thank the anonymous reviewers for their help and thoughtful comments.

Data Availability

The data that support the findings of this study are available from the corresponding author upon reasonable request.

REFERENCES

[1] G. Iddan, G. Meron, and A. Glukhovsky, "Wireless capsule endoscopy. Nature," *vol,* vol. 405, p. 25, 2000.

[2] G. J. Iddan and C. P. Swain, "History and development of capsule endoscopy," *Gastrointestinal Endoscopy Clinics,* vol. 14, no. 1, pp. 1-9, 2004.

[3] M. Kanaan and H. Farhadi, "Advances in wireless video capsule endoscopy," *International Journal of Wireless Information Networks,* vol. 24, pp. 166-167, 2017.

[4] B. S. Lewis and P. Swain, "Capsule endoscopy in the evaluation of patients with suspected small intestinal bleeding: results of a pilot study," *Gastrointestinal endoscopy,* vol. 56, no. 3, pp. 349-353, 2002.

[5] O. H. Maghsoudi, M. Alizadeh, and M. Mirmomen, "A computer aided method to detect bleeding, tumor, and disease regions in Wireless Capsule Endoscopy," in *2016 IEEE Signal Processing in Medicine and Biology Symposium (SPMB),* 2016: IEEE, pp. 1-6.

[6] X. Wang, *Study on magnetic localization and actuation of active capsule endoscope* (no. 03). 2006.

[7] T. D. Than, G. Alici, H. Zhou, and W. Li, "A review of localization systems for robotic endoscopic capsules," *IEEE transactions on biomedical engineering,* vol. 59, no. 9, pp. 2387-2399, 2012.

[8] A. Moglia, A. Menciassi, M. O. Schurr, and P. Dario, "Wireless capsule endoscopy: from diagnostic devices to multipurpose robotic systems," *Biomedical microdevices,* vol. 9, no. 2, pp. 235-243, 2007.

[9] G. Ciuti, A. Menciassi, and P. Dario, "Capsule endoscopy: from current achievements to open challenges," *IEEE reviews in biomedical engineering,* vol. 4, pp. 59-72, 2011.

[10] D. Fischer, R. Schreiber, D. Levi, and R. Eliakim, "Capsule endoscopy: the localization system," *Gastrointestinal Endoscopy Clinics,* vol. 14, no. 1, pp. 25-31, 2004.

[11] C. Hu, M. Q.-H. Meng, and M. Mandal, "Efficient magnetic localization and orientation technique for capsule endoscopy," *International Journal of Information Acquisition,* vol. 2, no. 01, pp. 23-36, 2005.

[12] C. Xiao, Z. Liang, and J. Yang, "Radiation characteristic analysis of antenna deeply implanted in human body and localization sensor array," *IEEE Transactions on Instrumentation and Measurement,* vol. 71, pp. 1-12, 2022.

[13] K. Diamantis, T. Anderson, J. A. Jensen, P. A. Dalgarno, and V. Sboros, "Development of super-resolution sharpness-based axial localization for Ultrasound Imaging," *IEEE Access,* vol. 7, pp. 6297-6309, 2018.

[14] J. Boese, N. Rahn, and B. Sandkamp, "Method for determining the position and orientation of an object, especially of a catheter, from two-dimensional X-ray images," ed: Google Patents, 2010.

[15] P. Muruganantham and S. M. Balakrishnan, "Attention aware deep learning model for wireless capsule endoscopy lesion classification and localization," *Journal of Medical and Biological Engineering,* vol. 42, no. 2, pp. 157-168, 2022.

[16] M. Suveren, R. Akay, M. Y. Yildirim, and M. Kanaan, "Application of hybrid metaheuristic with Levenberg-Marquardt algorithm for 6-dimensional magnetic localization," *Evolving Systems,* vol. 13, no. 6, pp. 849-867, 2022.

[17] I. Castro, J. W. de Wit, J. van Vooren, T. Van Quaethem, W. Huang, and T. Torfs, "Magnetic localization of wireless ingestible capsules using a belt-shaped array transmitter," *Electronics,* vol. 12, no. 10, p. 2217, 2023.

[18] A. C. Moldovan, M. V. Turcanu, S. Mitra, and S. Cochran, "Ultrasound technology for capsule endoscopy," in *Endorobotics*: Elsevier, 2022, pp. 215-240.

[19] N. Pagoulatos, W. S. Edwards, D. R. Haynor, and Y. Kim, "Interactive 3D registration of ultrasound and magnetic resonance images based on a magnetic position sensor," *IEEE Transactions on Information Technology in Biomedicine,* vol. 3, no. 4, pp. 278-288, 1999.

[20] T. D. Than *et al.*, "An effective localization method for robotic endoscopic capsules using multiple positron emission markers," *IEEE Transactions on Robotics,* vol. 30, no. 5, pp. 1174-1186, 2014.

[21] F. Bianchi *et al.*, "Localization strategies for robotic endoscopic capsules: a review," *Expert review of medical devices,* vol. 16, no. 5, pp. 381-403, 2019.

[22] B. Moussakhani, T. Ramstad, J. T. Flåm, and I. Balasingham, "On localizing a capsule endoscope using magnetic sensors," in *2012 Annual International Conference of the IEEE Engineering in Medicine and Biology Society*, 2012: IEEE, pp. 4058-4062.

[23] M. N. Sadiku *et al.*, *Fundamentals of engineering electromagnetics*. CRC press, 2018.

[24] F. T. Ulaby and U. Ravaioli, *Fundamentals of applied electromagnetics*. Pearson Upper Saddle River, NJ, 2015.

[25] H. L. Van Trees, *Detection, estimation, and modulation theory, part I: detection, estimation, and linear modulation theory*. John Wiley & Sons, 2004.

[26] A. Eshkevari and S. M. S. Sadough, "On the Cramer-Rao Lower Bound Based Analysis of Direct Position Determination and DOA Position Finding for Co-Channel Emitter Localization," *Journal of Applied Research in Electrical Engineering,* vol. 1, no. 2, pp. 131-138, 2022.

[27] D. Dmitrieva, D. Anzai, J. Kirchner, G. Fischer, and J. Wang, "Cost-Efficient Real-Time Adaptive Location Tracking With Interacting Multiple Transition Model for Implantable Medical Device," *IEEE Journal of Electromagnetics, RF and Microwaves in Medicine and Biology,* vol. 7, no. 2, pp. 102-109, 2022.

[28] A. Eshkevari and S. M. S. Sadough, "An improved method for localization of wireless capsule endoscope using direct position determination," *IEEE Access,* vol. 9, pp. 154563-154577, 2021.

[29] M. Kanaan and M. Cil, "Cramer-Rao Lower Bounds for Magnetic Localization of a Wireless Capsule Endoscope based on the Magnetic Dipole Model," in *2019 IEEE 30th International Symposium on Personal, Indoor and Mobile Radio Communications (PIMRC Workshops)*, 2019: IEEE, pp. 1-5.

[30] A. Dammann, B. Siebler, and S. Sand, "Cramér–Rao Lower Bound for Magnetic Field Localization around Elementary Structures," *Sensors,* vol. 24, no. 8, p. 2402, 2024.

[31] T. Costa, G. Boccignone, and M. Ferraro, "Gaussian mixture model of heart rate variability," *PloS one,* vol. 7, no. 5, p. e37731, 2012.

[32] T.-T. Lu and S.-H. Shiou, "Inverses of 2× 2 block matrices," *Computers & Mathematics with Applications,* vol. 43, no. 1-2, pp. 119-129, 2002.

[33] N. Hosoe, K. Takabayashi, H. Ogata, and T. Kanai, "Capsule endoscopy for small-intestinal disorders: current status," *Digestive Endoscopy,* vol. 31, no. 5, pp. 498-507, 2019.

[34] S. Tumanski, *Handbook of magnetic measurements*. CRC press, 2016.

[35] M. Chi, S. Chang, Z. Guo, Q. Zhao, G. Zhang, and F. Meng, "Research on localization control of magneto-controlled capsule endoscopy based on sensor array," *Robotic Intelligence and Automation,* 2025.

[36] S. M. Kay, "Fundamentals of Statistical Signal Processing: Estimation Theory," ed: Prentice Hall, 1993.

[37] A. Verbyla, "A NOTE ON THE INVERSE COVARIANCE MATRIX OF THE AUTOREGRESSIVE PROCESS 1," *Australian Journal of Statistics,* vol. 27, no. 2, pp. 221-224, 1985.

APPENDIX A – CALCULATION OF THE FISHER MATRIX

The derivation proceeds from equation (10). Since the noise samples are assumed to be zero-mean, i.i.d. with the same variance σ^2, it is clear that $\boldsymbol{\Sigma} = \sigma^2 \mathbf{I}$, where $\mathbf{I}$ is the identity matrix. Using the identities for inverse and determinant of a diagonal matrix, we can write

$$p\left(\hat{\mathbf{B}}\big|\boldsymbol{\varepsilon}\right) = \frac{1}{\left[2\pi\sigma^2\right]^{K/2}} \cdot \exp\left[-\frac{1}{2}\left(\hat{\mathbf{B}} - \mathbf{B}\right)^{T} \boldsymbol{\Sigma}^{-1}\left(\hat{\mathbf{B}} - \mathbf{B}\right)\right] \tag{A.1}$$

Taking the logarithm of both sides of (A.1) yields

$$\log p\left(\hat{\mathbf{B}}\big|\boldsymbol{\varepsilon}\right) = \log \frac{1}{\left[2\pi\sigma^2\right]^{K/2}} - \frac{1}{2}\left(\hat{\mathbf{B}} - \mathbf{B}\right)^T \boldsymbol{\Sigma}^{-1}\left(\hat{\mathbf{B}} - \mathbf{B}\right)$$

$$= \log \frac{1}{\left[2\pi\sigma^2\right]^{K/2}} - \frac{1}{2\sigma^2}\sum_{i=1}^{N}\left[\left(\hat{B}_{x,i} - B_{x,i}\right)^2 + \left(\hat{B}_{y,i} - B_{y,i}\right)^2 + \left(\hat{B}_{z,i} - B_{z,i}\right)^2\right] \quad \text{(A.2)}$$

Taking the partial derivative of both sides of (A.2), the *jk*-element of the Fisher matrix can be succinctly written as shown in equation (9) above (see[36]). To come up with more succinct expressions below, we let

$$x = x_i - a \quad \text{(A.3)}$$

$$y = y_i - b \quad \text{(A.4)}$$

$$z = z_i - c \quad \text{(A.5)}$$

$$q = mx + ny + pz \quad \text{(A.6)}$$

$$R_i = \sqrt{(x_i - a)^2 + (y_i - b)^2 + (z_i - c)^2} \quad \text{(A.7)}$$

As such, the expressions for the specific elements of the matrix are based on $V_{jk}^{(i)}$ and can be written as

$$V_{aa}^{(i)} = \frac{9m^2}{R_i^8} + \frac{9q^2 + 9x^2 - 36mqx}{R_i^{10}} + \frac{45q^2x^2}{R_i^{12}} \quad \text{(A.8)}$$

$$V_{bb}^{(i)} = \frac{9n^2}{R_i^8} + \frac{9q^2 + 9y^2 - 36nqy}{R_i^{10}} + \frac{45q^2y^2}{R_i^{12}} \quad \text{(A.9)}$$

$$V_{cc}^{(i)} = \frac{9p^2}{R_i^8} + \frac{9q^2 + 9z^2 - 36pqz}{R_i^{10}} + \frac{45q^2z^2}{R_i^{12}} \quad \text{(A.10)}$$

$$V_{ab}^{(i)} = V_{ba}^{(i)} = \frac{9mn}{R_i^8} + \frac{9xy - 18q(my + nx)}{R_i^{10}} + \frac{45xyq^2}{R_i^{12}} \quad \text{(A.11)}$$

$$V_{ac}^{(i)} = V_{ca}^{(i)} = \frac{9mp}{R_i^8} + \frac{9xz - 18q(mz + px)}{R_i^{10}} + \frac{45xzq^2}{R_i^{12}} \quad \text{(A.12)}$$

$$V_{bc}^{(i)} = V_{cb}^{(i)} = \frac{9np}{R_i^8} + \frac{9zy - 18q(nz + py)}{R_i^{10}} + \frac{45yzq^2}{R_i^{12}} \quad \text{(A.13)}$$

$$V_{mm}^{(i)} = \frac{3x^2}{R_i^8} + \frac{1}{R_i^6} \quad \text{(A.14)}$$

$$V_{nn}^{(i)} = \frac{3y^2}{R_i^8} + \frac{1}{R_i^6} \quad \text{(A.15)}$$

$$V_{pp}^{(i)} = \frac{3z^2}{R_i^8} + \frac{1}{R_i^6} \quad \text{(A.16)}$$

$$V_{mn}^{(i)} = V_{nm}^{(i)} = \frac{3xy}{R_i^8} \quad \text{(A.17)}$$

$$V_{mp}^{(i)} = V_{pm}^{(i)} = \frac{3xz}{R_i^8} \tag{A.18}$$

$$V_{np}^{(i)} = V_{pn}^{(i)} = \frac{3yz}{R_i^8} \tag{A.19}$$

$$V_{am}^{(i)} = V_{ma}^{(i)} = \frac{3(q-mx)}{R_i^8} + \frac{12x^2q}{R_i^{10}} \tag{A.20}$$

$$V_{an}^{(i)} = V_{na}^{(i)} = \frac{3(nx-2my)}{R_i^8} + \frac{12xyq}{R_i^{10}} \tag{A.21}$$

$$V_{ap}^{(i)} = V_{pa}^{(i)} = \frac{3(px-2mz)}{R_i^8} + \frac{12xzq}{R_i^{10}} \tag{A.22}$$

$$V_{bm}^{(i)} = V_{mb}^{(i)} = \frac{3(my-2nz)}{R_i^8} + \frac{12xyq}{R_i^{10}} \tag{A.23}$$

$$V_{bn}^{(i)} = V_{nb}^{(i)} = \frac{3(q-ny)}{R_i^8} + \frac{12y^2q}{R_i^{10}} \tag{A.24}$$

$$V_{bp}^{(i)} = V_{pb}^{(i)} = \frac{3(py-2nz)}{R_i^8} + \frac{12zyq}{R_i^{10}} \tag{A.25}$$

$$V_{cm}^{(i)} = V_{mc}^{(i)} = \frac{3(mz-2px)}{R_i^8} + \frac{12xzq}{R_i^{10}} \tag{A.26}$$

$$V_{cn}^{(i)} = V_{nc}^{(i)} = \frac{3(nz-2py)}{R_i^8} + \frac{12yzq}{R_i^{10}} \tag{A.27}$$

$$V_{cp}^{(i)} = V_{pc}^{(i)} = \frac{3(q-pz)}{R_i^8} + \frac{12z^2q}{R_i^{10}} \tag{A.28}$$

APPENDIX B – CORRELATED GAUSSIAN NOISE SCENARIO

The correlated Gaussian noise scenario corresponds to the case where the covariance matrix, Σ, is not necessarily diagonal, i.e. $\Sigma \neq \sigma^2 \mathbf{I}$. Suppose that the N sensor measurements are spatially correlated, i.e. the magnetic flux density components for the i-th sensor measurement ($i=1,\ldots,N$) are modeled as an AR(1) random process (first-order autoregressive process), as follows

$$\begin{aligned} \hat{B}_{x,i} &= \alpha \hat{B}_{x,i-1} + n_{x,i} \\ \hat{B}_{y,i} &= \alpha \hat{B}_{y,i-1} + n_{y,i} \\ \hat{B}_{z,i} &= \alpha \hat{B}_{z,i-1} + n_{z,i} \end{aligned} \tag{B.1}$$

where the dependence on the location and orientation parameters, (a,b,c,m,n,p), is omitted for brevity. The parameter α denotes the degree of correlation between sensor measurements, and is generally selected as $|\alpha| < 1$ in order to ensure weak-sense stationarity of the random process. $\left(n_{x,i}, n_{y,i}, n_{z,i}\right)$ are assumed to be zero-mean Gaussian random variables with variance σ^2.

The inverse of the covariance matrix for this AR(1) process is a special case of the general scenario of an AR(p) process (i.e. an autoregressive process of order p) (see [37], equation (3)):

$$\mathbf{\Sigma}^{-1} = \frac{1}{\sigma^2}\left(\mathbf{I}_N + \alpha^2 \mathbf{F} - \alpha \mathbf{G}\right) \tag{B.2}$$

where $\mathbf{I}_N$ is an $3N \times 3N$ identity matrix, $\mathbf{F}$ is an $3N \times 3N$ identity matrix with the first and last ones set to zero, and $\mathbf{G}$ is an $3N \times 3N$ matrix with ones along the first minor diagonals and zero elsewhere. Note that for the case of spatially uncorrelated sensor measurements (i.e. $\alpha = 0$), equation (B.2) reduces to $\mathbf{\Sigma}^{-1} = \frac{1}{\sigma^2}\mathbf{I}_N$ in line with the i.i.d. Gaussian scenario assumed earlier.

With the above definitions in place, it can be shown that the inverse of the covariance matrix has a tridiagonal, or Toeplitz structure. For the sake of clarity, we give a small example of this matrix for N=4:

$$\mathbf{\Sigma}^{-1} = \frac{1}{\sigma^2}\begin{bmatrix} 1 & -\alpha & 0 & 0 \\ -\alpha & 1+\alpha^2 & -\alpha & 0 \\ 0 & -\alpha & 1+\alpha^2 & -\alpha \\ 0 & 0 & -\alpha & 1 \end{bmatrix} \tag{B.3}$$

Substituting (B.2) into the right-hand side of equation (A.2), we can write

$$
\begin{aligned}
\log p\left(\hat{\mathbf{B}}\big|\mathbf{\varepsilon}\right) &= \log\frac{1}{\left[2\pi\sigma^2\right]^{K/2}} - \frac{1}{2}\left(\hat{\mathbf{B}} - \mathbf{B}\right)^T \mathbf{\Sigma}^{-1}\left(\hat{\mathbf{B}} - \mathbf{B}\right) \\
&= \log\frac{1}{\left[2\pi\sigma^2\right]^{K/2}} - \frac{1}{2\sigma^2}\left(\hat{\mathbf{B}} - \mathbf{B}\right)^T \left(\mathbf{I}_N + \alpha^2\mathbf{F} - \alpha\mathbf{G}\right)\left(\hat{\mathbf{B}} - \mathbf{B}\right) \\
&= \log\frac{1}{\left[2\pi\sigma^2\right]^{K/2}} - \frac{1}{2\sigma^2}\left(\hat{\mathbf{B}} - \mathbf{B}\right)^T \mathbf{I}_N\left(\hat{\mathbf{B}} - \mathbf{B}\right) \\
&\quad - \frac{\alpha^2}{2\sigma^2}\left(\hat{\mathbf{B}} - \mathbf{B}\right)^T \mathbf{F}\left(\hat{\mathbf{B}} - \mathbf{B}\right) + \frac{\alpha}{2\sigma^2}\left(\hat{\mathbf{B}} - \mathbf{B}\right)^T \mathbf{G}\left(\hat{\mathbf{B}} - \mathbf{B}\right)
\end{aligned}
\tag{B.4}
$$

For convenience and clarity, we introduce the following shorthand notation

$$
\begin{aligned}
\Delta B_{x,i} &= \hat{B}_{x,i} - B_{x,i} \\
\Delta B_{y,i} &= \hat{B}_{y,i} - B_{y,i} \\
\Delta B_{z,i} &= \hat{B}_{z,i} - B_{z,i}
\end{aligned}
\tag{B.5}
$$

Assuming both $\hat{\mathbf{B}}$ and $\mathbf{B}$ to be $3N \times 1$ vectors (3 spatial magnetic field components for each sensor measurement), and exploiting the special structures of matrices $\mathbf{F}$ and $\mathbf{G}$, the right-hand side of (B.4) can be rewritten as

$$
\begin{aligned}
\log p\left(\hat{\mathbf{B}}\big|\mathbf{\varepsilon}\right) &= \log\frac{1}{\left[2\pi\sigma^2\right]^{K/2}} - \frac{1}{2\sigma^2}\sum_{i=1}^{N}\left[\left(\Delta B_{x,i}\right)^2 + \left(\Delta B_{y,i}\right)^2 + \left(\Delta B_{z,i}\right)^2\right] \\
&\quad - \frac{\alpha^2}{2\sigma^2}\left[\left(\Delta B_{y,1}\right)^2 + \left(\Delta B_{z,1}\right)^2 + \sum_{i=2}^{N-1}\left[\left(\Delta B_{x,i}\right)^2 + \left(\Delta B_{y,i}\right)^2 + \left(\Delta B_{z,i}\right)^2\right] + \left(\Delta B_{x,N}\right)^2 + \left(\Delta B_{y,N}\right)^2\right] \\
&\quad + \frac{\alpha}{\sigma^2}\left[\sum_{i=1}^{N-1}\Delta B_{x,i}\Delta B_{x,i+1} + \sum_{i=1}^{N-1}\Delta B_{y,i}\Delta B_{y,i+1} + \sum_{i=1}^{N-1}\Delta B_{z,i}\Delta B_{z,i+1} + \Delta B_{y,1}\Delta B_{x,N} + \Delta B_{z,1}\Delta B_{y,N}\right]
\end{aligned}
\tag{B.6}
$$

To compute the jk-element of the Fisher matrix, we take the partial derivatives of both sides of (B.6) with respect to ε_j and ε_k and substitute into equation (7). In order to facilitate this, the following relations can be obtained by using the chain rule for partial derivatives:

$$\frac{\partial}{\partial \varepsilon_j} \left(\Delta B_{x,i} \right)^2 = -2\Delta B_{x,i} \frac{\partial B_{x,i}}{\partial \varepsilon_j}$$

$$\frac{\partial}{\partial \varepsilon_j} \left(\Delta B_{y,i} \right)^2 = -2\Delta B_{y,i} \frac{\partial B_{y,i}}{\partial \varepsilon_j} \qquad (B.7)$$

$$\frac{\partial}{\partial \varepsilon_j} \left(\Delta B_{z,i} \right)^2 = -2\Delta B_{z,i} \frac{\partial B_{z,i}}{\partial \varepsilon_j}$$

where the partial derivatives $\dfrac{\partial B_{x,i}}{\partial \varepsilon_j}$, $\dfrac{\partial B_{y,i}}{\partial \varepsilon_j}$ and $\dfrac{\partial B_{z,i}}{\partial \varepsilon_j}$ can be readily obtained by differentiating both sides

of (3), (4) and (5) with respect to ε_j.

The third term on the right-hand side of (B.6) includes some product terms. The partial derivatives of these terms can be computed using the product rule:

$$\frac{\partial}{\partial \varepsilon_j} \left(\Delta B_{x,i} \Delta B_{x,i+1} \right) = -\Delta B_{x,i} \frac{\partial B_{x,i+1}}{\partial \varepsilon_j} - \Delta B_{x,i+1} \frac{\partial B_{x,i}}{\partial \varepsilon_j}$$

$$\frac{\partial}{\partial \varepsilon_j} \left(\Delta B_{y,i} \Delta B_{y,i+1} \right) = -\Delta B_{y,i} \frac{\partial B_{y,i+1}}{\partial \varepsilon_j} - \Delta B_{y,i+1} \frac{\partial B_{y,i}}{\partial \varepsilon_j}$$

$$\frac{\partial}{\partial \varepsilon_j} \left(\Delta B_{z,i} \Delta B_{z,i+1} \right) = -\Delta B_{z,i} \frac{\partial B_{z,i+1}}{\partial \varepsilon_j} - \Delta B_{z,i+1} \frac{\partial B_{z,i}}{\partial \varepsilon_j} \qquad (B.8)$$

$$\frac{\partial}{\partial \varepsilon_j} \left(\Delta B_{y,1} \Delta B_{x,N} \right) = -\Delta B_{y,1} \frac{\partial B_{x,N}}{\partial \varepsilon_j} - \Delta B_{x,N} \frac{\partial B_{y,1}}{\partial \varepsilon_j}$$

$$\frac{\partial}{\partial \varepsilon_j} \left(\Delta B_{z,1} \Delta B_{y,N} \right) = -\Delta B_{z,1} \frac{\partial B_{y,N}}{\partial \varepsilon_j} - \Delta B_{y,N} \frac{\partial B_{z,1}}{\partial \varepsilon_j}$$

Taking the partial derivative of both sides of (B.6) and substituting the relations from (B.7) and (B.8), the partial derivative of $\log p\left(\hat{\mathbf{B}} | \boldsymbol{\varepsilon} \right)$ with respect to ε_j can be obtained. The same relations in (B.7) and (B.8) can be used to obtain the partial derivative $\log p\left(\hat{\mathbf{B}} | \boldsymbol{\varepsilon} \right)$ with respect to ε_k, by simply replacing ε_j with ε_k. With these two partial derivatives in hand, the *jk*-element of the Fisher matrix, $\mathbf{J}_\varepsilon$, can be readily obtained using equation (7). The exact form of the different elements of the Fisher matrix is complex (largely due to the more complicated nature of the covariance matrix and its inverse as given in equation (B.2)) and is therefore omitted in the interests of brevity.

REAL-TIME TRAJECTORY TRACKING OF ROBOTIC MANIPULATOR BASED ON COMPUTED TORQUE CONTROL

1, *Tuğçe YAREN (ID) **, ²Selçuk KİZİR** (ID)

¹ *Balikesir University, Electrical and Electronic Engineering Department, Balikesir, TÜRKİYE*
² *Kocaeli University, Mechatronic Engineering Department, Kocaeli, TÜRKİYE*
¹ tugce.yaren@balikesir.edu.tr, ² selcuk.kizir@kocaeli.edu.tr

Highlights

- Developed a 3-DOF manipulator model using the SOA framework, reducing complexity.

- Designed and implemented real-time Computed Torque Control for precise tracking.

- Demonstrated controller's robustness through static and dynamic trajectory tracking

Graphical Abstract

Flowchart of the proposed method

*Corresponding Author: Tuğçe YAREN, tugce.yaren@balikesir.edu.tr

REAL-TIME TRAJECTORY TRACKING OF ROBOTIC MANIPULATOR BASED ON COMPUTED TORQUE CONTROL

1, *Tuğçe YAREN [ID], 2Selçuk KİZİR [ID]

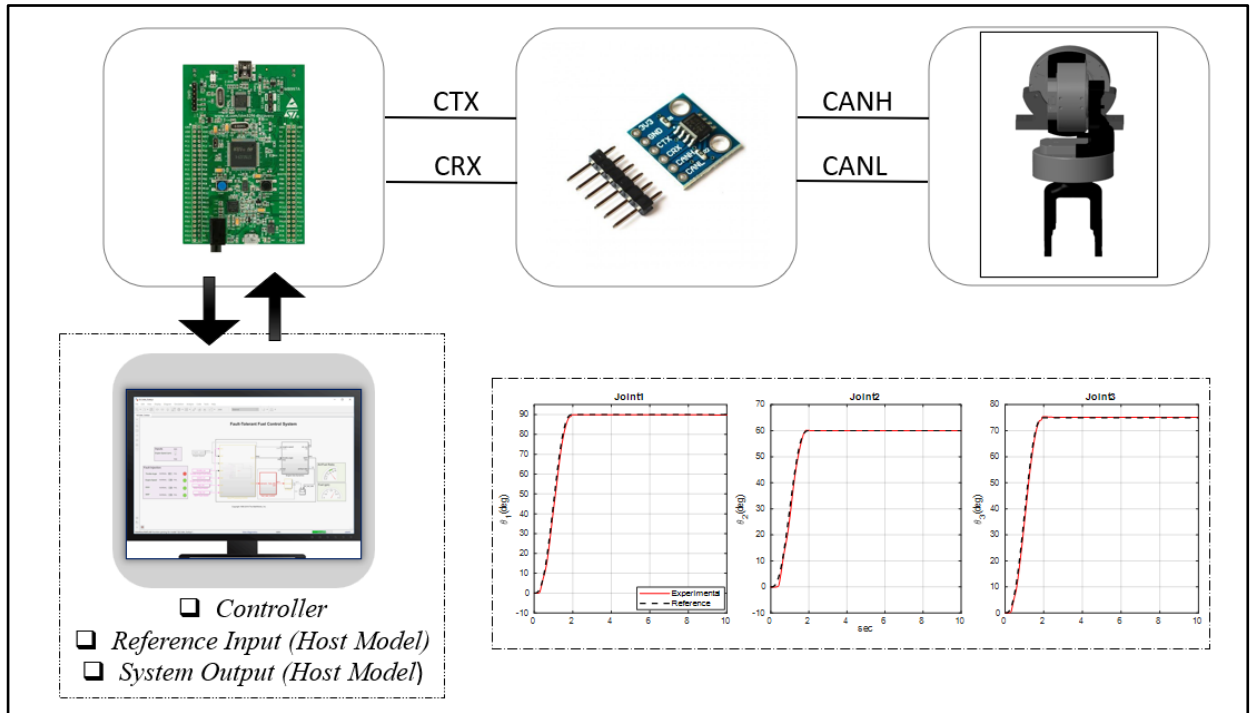*1 Balikesir University, Electrical and Electronic Engineering Department, Balikesir, TÜRKİYE*
2 Kocaeli University, Mechatronic Engineering Department, Kocaeli, TÜRKİYE
1 tugce.yaren@balikesir.edu.tr, 2 selcuk.kizir@kocaeli.edu.tr

ABSTRACT: This study presents obtaining the mathematical model of a three-degree-of-freedom robotic manipulator using spatial operator algebra (SOA), designing a controller based on the obtained model, and implementing the designed controller in real time. SOA is a technique that provides a mathematical foundation for reducing the complexity of robotic systems, analyzing, and optimizing them. The control of the robotic arm is achieved using the computed torque control method calculated based on mathematical model derived from SOA. The performance of the controller is rigorously evaluated through real-time trajectory tracking experiments, where it consistently achieved high precision in following predefined trajectories, maintaining tracking errors below 2.5 degrees. The effectiveness of the controller is further validated in disturbance rejection tests, where it effectively maintained trajectory accuracy despite manual external perturbations. These tests demonstrate the controller's capability to handle dynamic tasks and disturbances, showcasing the practical applicability and robustness of the SOA-based computed torque control scheme.

Keywords: Computed Torque Control, Modelling, Robotics, Spatial Operator Algebra, Trajectory Tracking

1. INTRODUCTION

Since the 1960s, the emergence of robotics in various application areas has led to the need to design nonlinear controllers instead of linear control. Currently, numerous nonlinear controllers are employed in robots. While there are various studies on nonlinear controllers in the literature, computed torque control, adaptive control, and robust control, which are specialized applications of feedback linearization for mechanical systems such as robots, are preferred.

One of the most popular approaches used in the control of robotic manipulators is the computed torque control method. This method provides the necessary torques to successfully track the desired joint-space trajectories. This approach is also referred to in the literature as "inverse dynamics control". This is because this approach relies on the use of the inverse dynamic model to linearize and decompose the nonlinear dynamics of the robot. In cases where all parameters are known with high accuracy, the computed torque control (CTC) method demonstrates high performance. However, the effectiveness of CTC may decrease due to parameter uncertainties such as incorrect inertia matrix and unmodeled dynamics such as joint flexibility [1].

CTC method integrates a PD control term with a feedback dynamic compensation term, which is determined using the system's actual velocity and desired acceleration signals. This structure functions as a PD controller enhanced with a feedback inner loop, allowing the CTC controller to provide improved trajectory tracking and resistance to disturbances. Despite its advantages, the method has two primary limitations [2]. Firstly, the dynamic compensation relies on a model with constant parameters, while the system's parameters typically change during trajectory execution. As a result, the controller's ability to achieve effective dynamic balancing is compromised. To enhance dynamic compensation, adaptive control strategies are often recommended. Such approaches are particularly effective in mitigating external disturbances by leveraging adaptive or robust control frameworks.

Secondly, in the CTC approach, linear PD controllers with fixed proportional and derivative constants

*Corresponding Author: Tuğçe YAREN, tugce.yaren@balikesir.edu.tr

are utilized to minimize tracking errors. However, when nonlinear factors such as modeling inaccuracies and friction are present in the manipulator's dynamics, the CTC controller may struggle to deliver the desired level of tracking precision. To address this, alternative strategies have been developed to dynamically tune the PD gains of the CTC controller. For instance, Yang et al. [3] proposed the use of intelligent optimization techniques to enhance the PD gain coefficients, thereby improving trajectory tracking performance. Despite these improvements, the practical implementation of such controllers remains challenging due to their intricate design and significant computational demands. A simpler and more effective alternative involves the use of nonlinear PD controllers. These controllers are capable of mitigating uncertainties and demonstrate superior performance compared to traditional PD controllers, all while maintaining a relatively straightforward structure [4].

CTC has been applied to different types of robots, including serial, parallel, humanoid, and collaborative robots. Due to its ability to provide high dynamic performance, this control method has been extensively investigated in the literature, particularly in serial robots. Shang and Cong [2] developed a nonlinear computed torque controller and applied it to a high-speed planar parallel manipulator. The stability of the parallel manipulator system was proven using the Lyapunov theorem, and it was demonstrated that the developed controller guarantees both the asymptotic convergence of tracking error and the error rate to zero. Hayat et al. [5] proposed a model-independent robust-adaptive controller for Euler-Lagrange systems with a quantitative performance analysis in terms of state errors. The proposed controller structure operates as an adaptive computed torque control method. Real-time control of 3-DOF and 7-DOF serial robots was successfully achieved. Lee et al. [6] developed a computed torque control method combined with H∞ control, which demonstrates successful tracking performance even in fast tracking control where full dynamics computation is not easy. Real-time control of the Stewart platform was successfully implemented using the developed method. Due to the high computational load, applying this control method can be challenging even on very high-speed DSPs (Digital Signal Processors). The proposed method addresses this issue. Polydoros et al. [7] proposed a machine learning approach for modeling inverse dynamics and provided information about its application to a physical robotic system. In their study, a collaborative robot was real-time controlled using the computed torque control method. The controller was designed based on the inverse dynamic model obtained using the proposed approach. They obtained an advantage in the computed torque method by obtaining the dynamic model using machine learning due to the problems in obtaining the dynamic model analytically. In general, it is concluded in the literature that the computed torque control method is preferred in robot control applications, but updates are made to its structure to eliminate its disadvantages.

In the CTC, the inverse dynamic model of the system is the most important building block, and the methods commonly used for dynamic modeling of systems are the Lagrange-Euler, Newton-Euler, and Hamilton equations. These methods are fundamental techniques used to model and analyze the motion and behavior of mechanical systems. Each method has its advantages, disadvantages, and application areas, so selecting the right method depends on the system characteristics and analysis requirements. However, obtaining a dynamic model may not be straightforward for every system. As system complexity increases, the difficulty of obtaining the model also increases. The kinematic and dynamic analysis of high-degree-of-freedom hybrid systems, which use serial and parallel robots together on a fixed or mobile platform, is a highly challenging, complex, and time-consuming problem [8]. Considering these structures, classical methods can be both inadequate and costly in terms of computational power.

Obtaining the kinematic and dynamic models of complex and high-degree-of-freedom robots using recursive methods instead of classical methods both simplifies the modeling process and reduces computation time by eliminating unnecessary calculations. Spatial operator algebra (SOA) is one of the prominent structures in this field. Spatial operators can be easily applied to multi-manipulator systems thanks to their recursive structure. It is a more systematic and easily programmable high-performance computing algorithm compared to other kinematic and dynamic analysis methods [9].

SOA is a method based on coordinate-free vector representation, which provides great convenience for the designer as it allows the designer to choose a set of free axes in the configuration. Since this

algorithm does not use gradient-based derivatives, discontinuities and sharp changes in trajectory functions are not a problem. Therefore, systems analyzed using this method are very suitable for real-time programming and control. The Jacobian matrix can be numerically obtained using a systematic and easily programmable method with SOA. It also provides the designer with an analytical expression for the inverse of the mass matrix. The SOA algorithm can provide shorter cycle times. With shorter cycle times, robot arms and robotic systems can be controlled more effectively and powerfully. Thus, the use of the SOA method in robot control enables both robustness and speed to be achieved simultaneously. In summary, SOA is a highly efficient calculation algorithm that is more systematic and easily programmable compared to other kinematic and dynamic analysis methods [10, 11].

Jain [12] described a computational modeling architecture developed to meet a wide range of robot modeling needs, including analysis, simulation, and embedded modeling for robotic systems. The architecture is based on the theoretical framework of UOC for computational dynamics, with calculations performed by fast, structure-based algorithms. The work was conducted at the JPL Laboratory (in collaboration with NASA). Wensing et al. [13] introduced an algorithm based on spatial vector algebra that enables operational space control of sliding-base systems to be performed at higher speeds. The algorithm reduced the computational load $O(n^3 + m^3)$ from to (nd), where n is the system's degrees of freedom, m is the number of constraints, and d is the depth of the kinematic connectivity tree. The accuracy of the algorithm was demonstrated through simulation at a speed of 3.6 m/s, controlling a quadrupedal robot model. They emphasized the ease of creating control structures with SOA modeling. Nakanishi et al. [14] conducted the control of a 16-DOF bipedal robot using inverse dynamics and PD control methods in a simulation environment. Their primary focus in this study was to develop a general and computationally efficient inverse dynamics algorithm for a robot with a free-floating base and constraints. Additionally, effective access to the parameters required for the controller can be achieved through a SOA-based dynamic formulation.

In this paper, the aim was to obtain a dynamic model using the SOA method, design a nonlinear controller based on the obtained model, and implement the designed controller in real-time. To provide a systematic approach in real-time robot control, it was planned to leverage the advantages of the SOA method. A 3-DOF robotic manipulator was utilized to validate the designed controllers in real-time. The real-time application of CTC based on SOA was implemented on a 3-DOF structure, and the applicability of the SOA algorithm in real-time control structures was observed. The equations of motion are derived using SOA in Section 2. The SOA-based CTC are designed in Section 3. In Section 4, the performance of the designed controller is tested.

2. MATERIAL AND METHODS

2.1. Dynamic Modelling of the 3-DOF Manipulator

The right and left views of the manipulator, along with a frame assignment diagram, are presented in Fig. 1. The design of the manipulator emulates the human shoulder, which can be modeled as having three degrees of freedom: flexion/extension, abduction/adduction, and internal/external rotation. Each joint of the manipulator is motor-driven: the first joint facilitates rotation around the z-axis, the second joint around the y-axis, and the third joint around the x-axis. These movements are all coordinated in relation to a fixed frame, mirroring the complex interactions found in human shoulder movements.

The mathematical model of this structure was derived using the SOA algorithm. Consequently, the frame assignment adheres to the conventions used in SOA, facilitating the analysis and simplification of the manipulator's dynamics. The fixed frame serves as a reference point from which all measurements and movements are defined, ensuring consistency in the model's mathematical formulation.

Table 1 details the system parameters, including the mass, link lengths, and inertia properties of the manipulator's links. The inertia matrices are derived from the SolidWorks CAD model.

The link length vectors of the manipulator are given in Eq. (1).

$$\vec{l_1} = \begin{bmatrix} 0 \\ -l_2 \\ l_1 \end{bmatrix} \qquad \vec{l_2} = \begin{bmatrix} -l_4 \\ -l_3 \\ 0 \end{bmatrix} \qquad \vec{l_3} = \begin{bmatrix} -l_5 \\ 0 \\ 0 \end{bmatrix} \tag{1}$$

The skew-symmetric form of the link length vectors is arranged in Eq. (2).

$$\widehat{l_1} = \begin{bmatrix} 0 & -l_1 & -l_2 \\ l_1 & 0 & 0 \\ l_2 & 0 & 0 \end{bmatrix} \qquad \widehat{l_2} = \begin{bmatrix} 0 & 0 & -l_3 \\ 0 & 0 & l_4 \\ l_3 & -l_4 & 0 \end{bmatrix} \qquad \widehat{l_3} = \begin{bmatrix} 0 & 0 & 0 \\ 0 & 0 & l_5 \\ 0 & -l_5 & 0 \end{bmatrix} \tag{2}$$
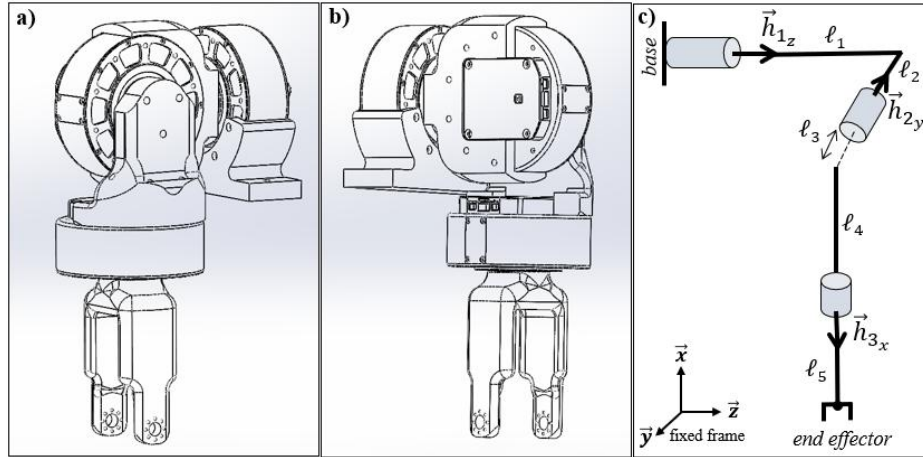
Figure 1. a) Right view of the manipulator, b) left view of the manipulator, c) frame assignment.

Table 1. System parameters

Parameter	Value	Unit
$[m_1 \ m_2 \ m_3]$	[0.850 0.805 0.250]	kg
$[l_1 \ l_2 \ l_3 \ l_4 \ l_5]$	[0.0625 0.0235 0.0195 0.11365 0.1105]	m
$[I_{xx}^1 \ I_{yy}^1 \ I_{zz}^1]$	[837,720.17 1,252,091.31 809,756.36]	gmm²
$[I_{xx}^2 \ I_{yy}^2 \ I_{zz}^2]$	[1,087,199.53 1,087,199.53 1,129,158.39]	gmm²
$[I_{xx}^3 \ I_{yy}^3 \ I_{zz}^3]$	[62,771.32 81,874.85 122,408.01]	gmm²

The link velocity propagation operators can be seen in Eq. (3).

$$\emptyset_{1,0} = \begin{bmatrix} I_3 & 0_3 \\ 0_3 & I_3 \end{bmatrix} \quad \emptyset_{2,1} = \begin{bmatrix} I_3 & 0_3 \\ -\widehat{l_1} & I_3 \end{bmatrix} \quad \emptyset_{3,2} = \begin{bmatrix} I_3 & 0_3 \\ -\widehat{l_2} & I_3 \end{bmatrix} \quad \emptyset_{t,3} = \begin{bmatrix} I_3 & 0_3 \\ -\widehat{l_3} & I_3 \end{bmatrix} \tag{3}$$

The axes of rotation vectors are given in Eq. (4).

$$\vec{h_1} = \begin{bmatrix} 0 \\ 0 \\ 1 \end{bmatrix} \quad \vec{h_2} = \begin{bmatrix} 0 \\ -1 \\ 0 \end{bmatrix} \quad \vec{h_3} = \begin{bmatrix} -1 \\ 0 \\ 0 \end{bmatrix} \tag{4}$$

The axes of rotation matrices are given in Eq. (5).

$$\overrightarrow{H_1} = \begin{bmatrix} \vec{h_1} \\ \vec{0} \end{bmatrix} \quad \overrightarrow{H_2} = \begin{bmatrix} \vec{h_2} \\ \vec{0} \end{bmatrix} \quad \overrightarrow{H_3} = \begin{bmatrix} \vec{h_3} \\ \vec{0} \end{bmatrix} \tag{5}$$

Manipulator rotation axis matrix is given in Eq. (6).

$$H = \begin{bmatrix} \overrightarrow{H_1} & \vec{0} & \vec{0} \\ \vec{0} & \overrightarrow{H_2} & \overrightarrow{0} \\ \vec{0} & \vec{0} & \overrightarrow{H_3} \end{bmatrix} \quad H \in R^{18x3} \tag{6}$$

The manipulator propagation matrix can be seen in Eq. (7). I and 0 is the 6x6 identity and zero matrix, respectively.

$$\emptyset = \begin{bmatrix} I & 0 & 0 \\ \emptyset_{2,1} & I & 0 \\ \emptyset_{3,1} & \emptyset_{3,2} & I \end{bmatrix} \quad \emptyset \in R^{18x18} \tag{7}$$

Tip point propagation matrix is given in Eq. (8).

$$\emptyset_t = [0_{6x6} \quad \emptyset_{t,3}] \tag{8}$$

The Jacobian matrix of the manipulator can be obtained from Eq. (9).

$$J = \emptyset_t \emptyset H \tag{9}$$

The forward kinematic equation of the manipulator can be obtained from Eq. (10).

$$\overrightarrow{V_t} = J\underline{\dot{\theta}} \tag{10}$$

where V_t is the velocity vector of the tip point and $\underline{\dot{\theta}}$ is the stacked link spatial velocities of the manipulator. The inverse kinematic equation of the manipulator can be obtained from Eq. (11).

$$\underline{\dot{\theta}} = J^{-1}\overrightarrow{V_t} \tag{11}$$

The mass matrices of the links are given in Eq. (12).

$$M_1 = \begin{bmatrix} I_1 & m_1\hat{l}_1 \\ -m_1\hat{l}_1 & I_3 m_1 \end{bmatrix} \quad M_2 = \begin{bmatrix} I_2 & m_2\hat{l}_2 \\ -m_2\hat{l}_2 & I_3 m_2 \end{bmatrix} \quad M_3 = \begin{bmatrix} I_3 & m_3\hat{l}_3 \\ -m_3\hat{l}_3 & I_3 m_3 \end{bmatrix} \tag{12}$$

where I_x is the inertia matrix of link x, m_x is the mass vector of link x, and I_3 is the 3x3 identity matrix. The inertia matrix of the joints is assumed to be the identity matrix. The manipulator mass matrix is given in Eq. (13).

$$M = \begin{bmatrix} M_1 & 0 & 0 \\ 0 & M_2 & 0 \\ 0 & 0 & M_3 \end{bmatrix} \tag{13}$$

The generalized mass matrix of the manipulator can be derived from Eq. (14).

$$\boldsymbol{M} = H^T \emptyset^T M \emptyset H \tag{14}$$

Bias terms of the manipulator are given in Eq. (15) (including Coriolis and gravity).

$$\underline{C} = H^T \emptyset^T (M \emptyset \underline{a} + \underline{b}) \tag{15}$$

where $\underline{a}$ is the bias spatial accelerations of the manipulator, $\underline{b}$ is the bias spatial forces of the manipulator. The inverse dynamic equation of the manipulator can be obtained from Eq. (16).

$$\underline{\tau} = M \underline{\ddot{\theta}} + \underline{C} + J^T \vec{F}_t \tag{16}$$

where F_t is spatial forces at the tip point of the manipulator. The inverse dynamics model obtained in Eq. (16) is used in controller design.

2.2. Controller Design

The computed torque control approach is based on the use of inverse dynamics model, as can be seen from Fig. 2. Since it is a model-based approach, obtaining the dynamic model precisely is of critical importance.

The CTC consists of two loops: feedback inner loop and PD control outer loop. CTC control equation obtained according to the block diagram is given in Eq. (17).

$$u = M(\theta)\left[\ddot{\theta}_d + K_v \dot{e} + K_p e\right] + C\left(\theta, \dot{\theta}\right) + G(\theta) \tag{17}$$

where e is joint position error and $\dot{e}$ is joint velocity error, are shown in Eq. (18). CTC has two gain parameters, proportional (K_p) and derivative (K_v).

$$e = \theta_d - \theta \qquad \dot{e} = \dot{\theta}_d - \dot{\theta} \tag{18}$$

where $\theta_d, \dot{\theta}_d, \ddot{\theta}_d$ is the desired position, velocity and acceleration, respectively. Two separate matrix, C and G, appearing in Eq. (17), are included in the $\underline{C}$ matrix in the SOA model. The gains K_p and K_v are obtained through trial-and-error method as 100 and 70, respectively.
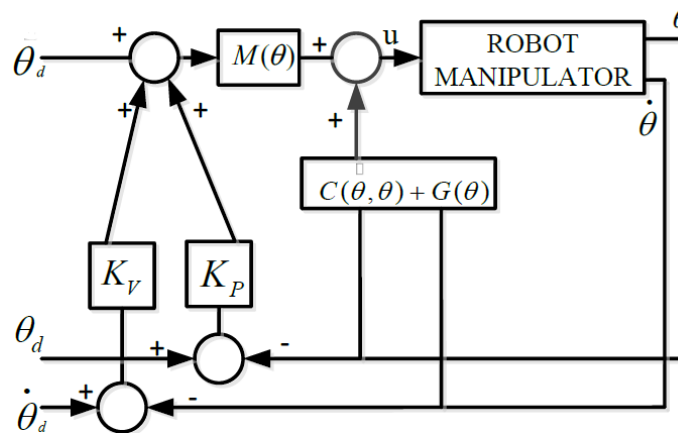
Figure 2. Computed torque control block diagram [15]

3. RESULTS AND DISCUSSION

3.1. Simulation Model

Fig. 3 illustrates the Simulink simulation model constructed based on the CTC strategy as Fig. 2. The dynamic model in the CTC was obtained with the SOA algorithm. A Simmechanics model of a 3-DOF manipulator was used to test the controller's effectiveness on the system.

Inputs to the system include desired joint angles, velocities, and accelerations, derived from predefined reference trajectories. The model integrates feedback of joint angles and velocities, calculating position and velocity errors to adjust the control inputs effectively. These inputs are processed through the SOA algorithm, which computes the necessary torque commands to achieve precise joint positioning and movement, ensuring robust control performance across various operational scenarios.
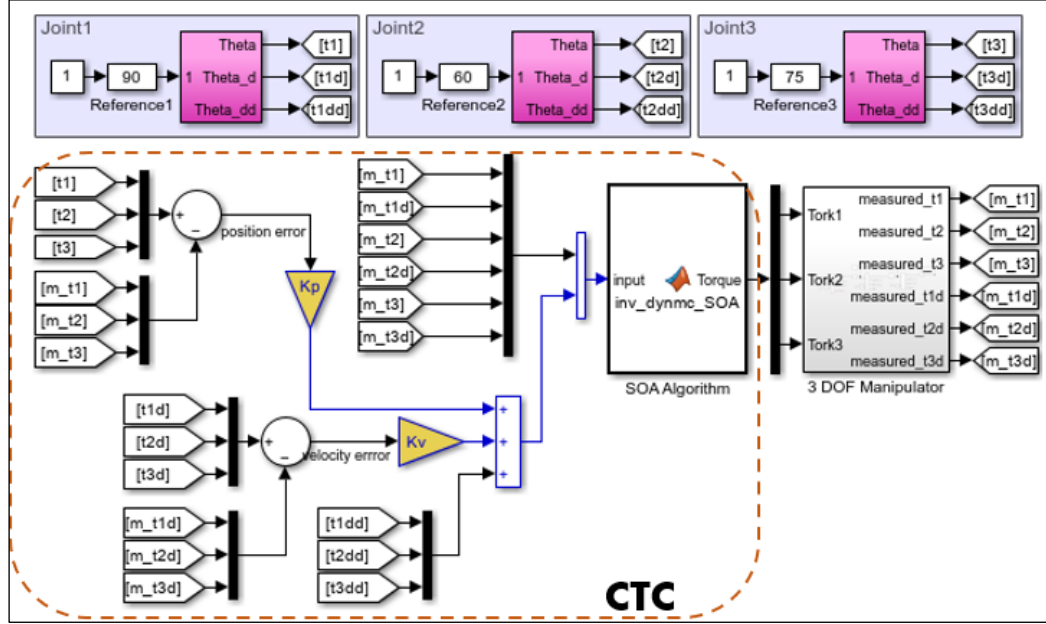
Figure 3. Computed torque control simulation model

The controller performance was tested by applying a trajectory reference signal in simulation. In this test, the robot's trajectory, which meets the initial and final conditions and provides a continuous change over time, is modeled by the 5th-degree polynomial seen in Eq. (19). This polynomial allows the robot to make a smooth and continuous transition from the starting point (t_0) to the endpoint (t_f) within a specific time interval.
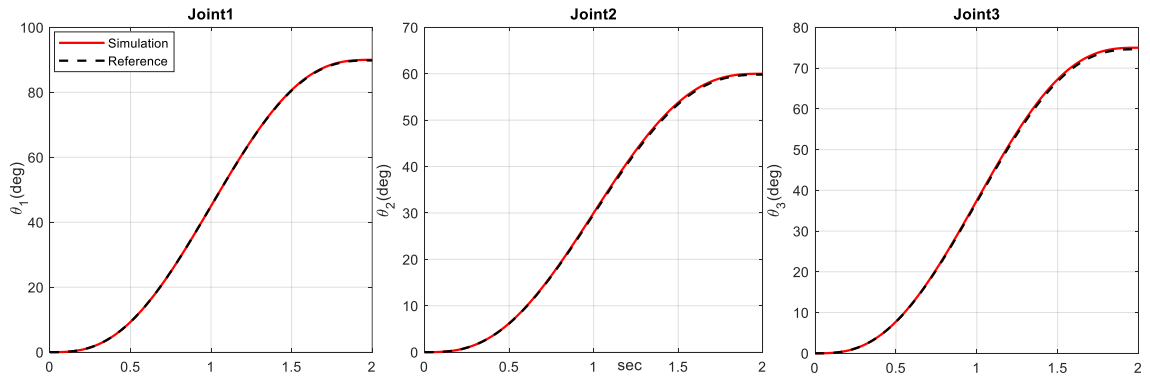
Figure 4. CTC simulation results

$$\theta(t) = a_0 + a_1 t + a_2 t^2 + a_3 t^3 + a_4 t^4 + a_5 t^5 \tag{19}$$

where the coefficients are: $a_0 = \theta_0$, $a_1 = \dot{\theta}_0 = 0$, $a_2 = \frac{1}{2}\ddot{\theta}_0 = 0$, $a_3 = \frac{1}{2t_f^3}(20)(\theta_f - \theta_0)$, $a_4 = \frac{1}{2t_f^4}(30)(\theta_0 - \theta_f)$, $a_5 = \frac{1}{2t_f^5}(12)(\theta_f - \theta_0)$. θ_0 represents the robot's starting position, while θ_f represents the final position.

Initially, the robot's velocity and acceleration were considered to be zero (a_1, a_2). Based on this polynomial, the desired trajectories are defined as follows: $\theta_{1d}(t_0) = 0°, \theta_{1d}(t_f) = 90°, \theta_{2d}(t_0) = 0°, \theta_{2d}(t_f) = 60°, \theta_{3d}(t_0) = 0°, \theta_{3d}(t_f) = 75°$ with $t_0 = 0\ s, t_f = 2\ s$. The trajectory tracking results of the simulation are shown in Fig. 4. The simulation results indicate that all joints successfully achieved their desired positions with minimal tracking errors.

3.2. Experimental Results

The STM32F4 discovery board was used as the microcontroller. The code was generated using the Waijung Blockset by Aimagin [16] in MATLAB Simulink.

The motor used in the system is the MyActuator RMD-X8 Pro intelligent actuator. This actuator integrates a high-torque BLDC motor, an internal motor controller, an absolute encoder, and a 6:1 planetary reduction gear into a single compact unit. It supports control via the CAN bus interface, enabling users to specify target position, velocity, or torque for seamless operation [17]. The key specifications of the RMD-X8 Pro are provided in Table 2.

RMD X8-PRO communication is carried out using the CAN bus protocol. To enable communication with any processor, a CAN module is required. In this paper, an STM32F4 development kit and an SN65HVD230 CAN module were used for communication with the motors. The communication structure established between the computer and the motor is depicted in Fig. 5. With this structure, commands can be sent from the computer to the motor, and data can be collected from the motor. The motor has three operating modes: position, velocity, and torque. In this study, the control applications were implemented in the torque mode.

Table 2. RMD-X8 Pro parameters

Parameter	Value
Weight (g)	750
Gear ratio	6:1
Nominal Torque (Nm)	12
Peak Torque (Nm)	35
Torque density (Nm/kg)	46.7
Joint Velocity (rad/s)	23.6
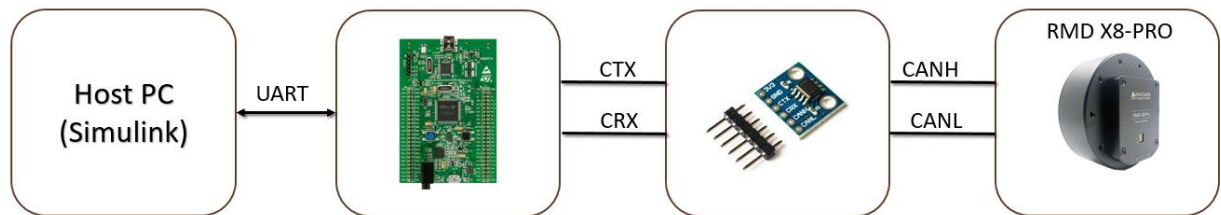
Figure 5. Communication structure

Controller performance was tested by applying different reference signals. In the first real-time test, the reference signal applied in the simulation study was applied to the manipulator ($\theta_{1d}(t_0) = 0°, \theta_{1d}(t_f) = 90°, \theta_{2d}(t_0) = 0°, \theta_{2d}(t_f) = 60°, \theta_{3d}(t_0) = 0°, \theta_{3d}(t_f) = 75°$ with $t_0 = 0\ s, t_f = 2\ s$).

The trajectory tracking experimental results of the first test are shown in Fig. 6. The experimental results indicate that all joints successfully achieved their desired positions with minimal tracking errors. This demonstrates the high accuracy and stability of the controller under steady-state conditions.
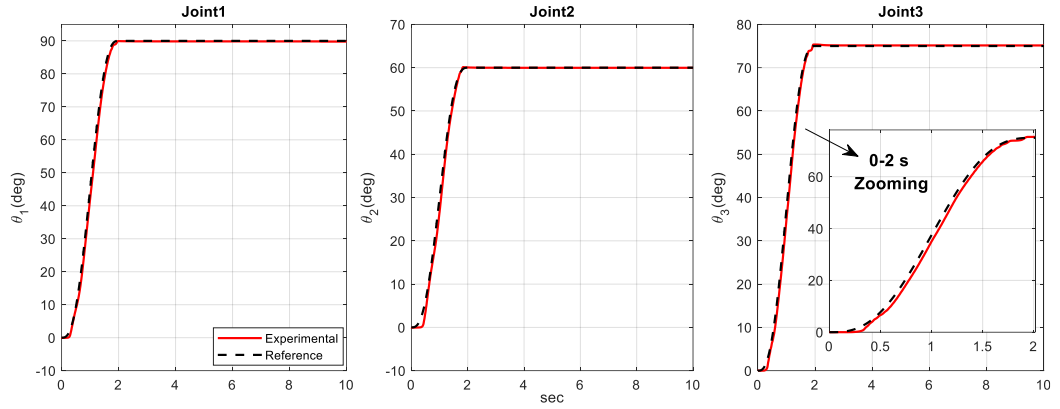
Figure 6. First test results **-** the joint positions.

The corresponding torque responses in Fig. 7 show smooth and efficient control efforts, with no significant oscillations, indicating energy-efficient actuation. These results highlight the controller's capability for stable and precise joint motion under static reference conditions.
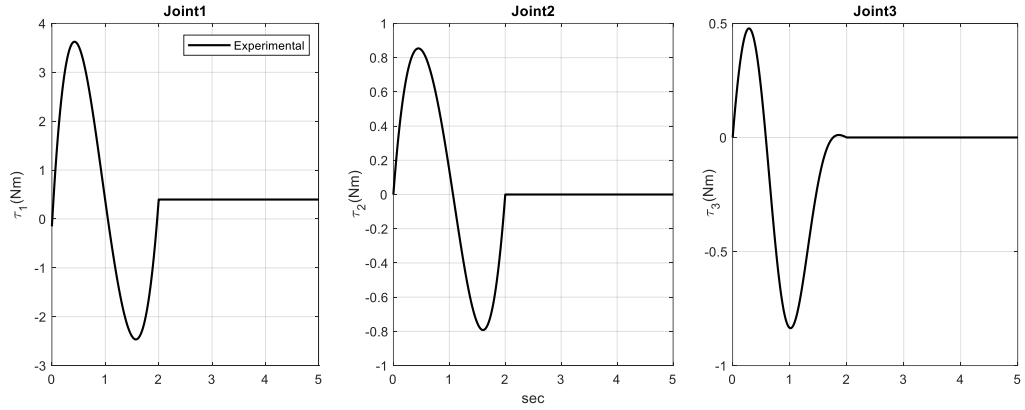
Figure 7. First test results **-** the joint torques.

In the second test, a sinusoidal reference signal with varying amplitudes for each joint. The desired signal amplitudes are 90° at the first joint, 30° at the second, and 60° at the third. The results confirm that the controller can accurately follow dynamic trajectories, even with continuous changes in the reference (see Fig. 8). The smooth sinusoidal tracking demonstrates the system's adaptability and robustness in handling varying control demands. This highlights the controller's potential for applications requiring periodic or repetitive motions, such as industrial pick-and-place tasks or dynamic path following.
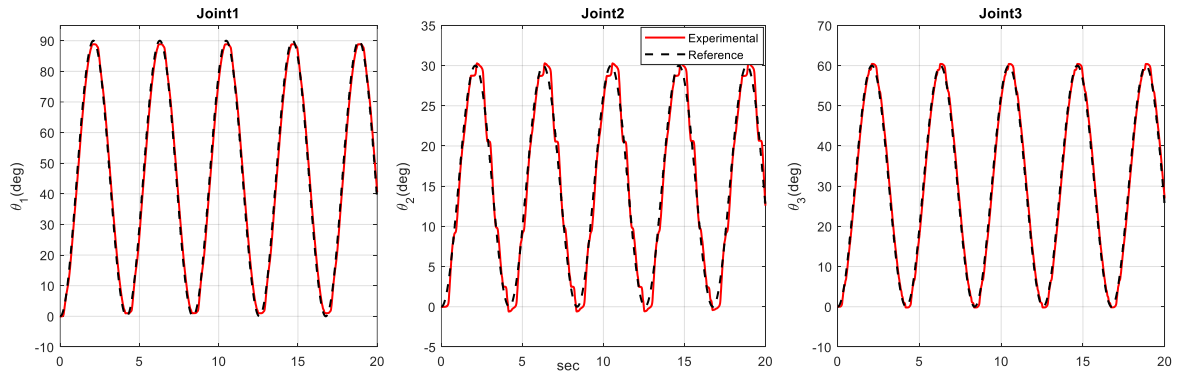
Figure 8. Second test results **-** the joint positions.

Fig. 9 presents a detailed analysis of the tracking errors for each joint during the second test. The maximum tracking error observed was approximately 2.5° for the second joint while the tracking errors mostly within ±2.5 degrees for all joints. The tracking errors averaged within ±1.25°, indicating the system's ability to track alignment with the desired trajectories.
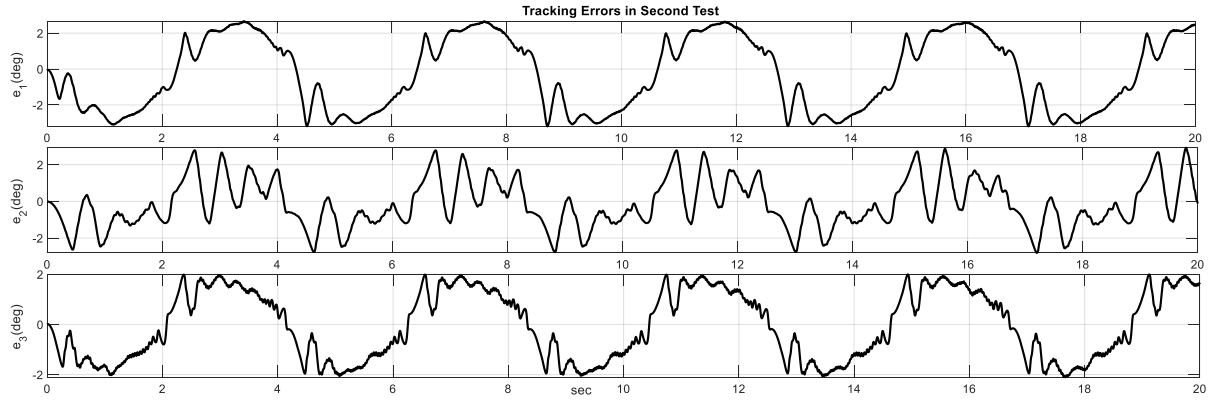
Figure 9. Second test results – tracking errors.
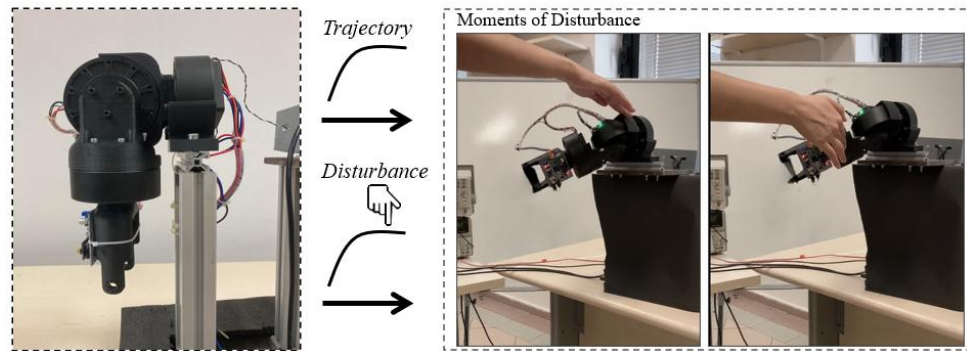
Figure 10. Demonstration of disturbance application in third test

The third test was designed to evaluate the controller's ability to reject disturbances by applying physical obstructions to the joints during trajectory tracking, as illustrated in Fig. 10. During this test, manual forces were intermittently applied to each joint to simulate unexpected physical interferences, challenging the controller's ability to maintain the predefined trajectory.
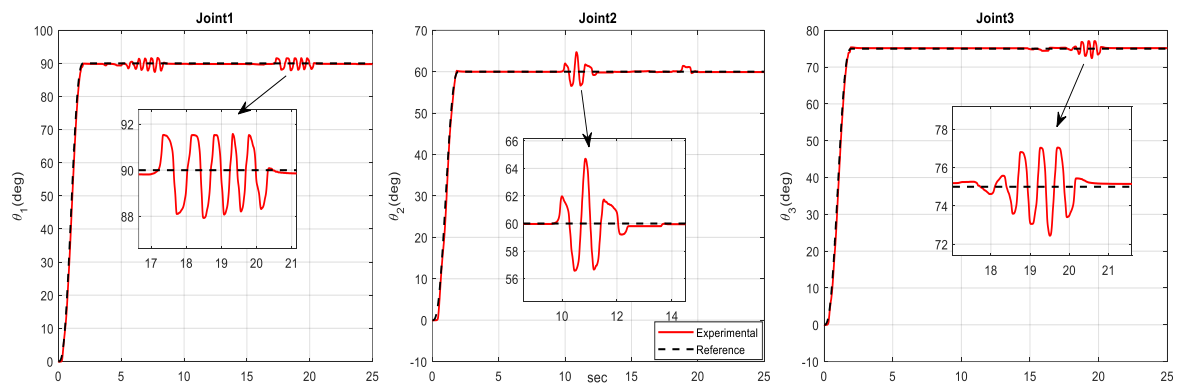
Figure 11. Third test results - the joint positions.

The system exhibited maximum overshoots of 1.78% for joint-1, 7.33% for joint-2, and 2.67% for joint-3 in response to disturbances, as shown in Fig. 11. The settling times to return to the reference band were

3.5 seconds for joint-1, 2.6 seconds for joint-2, and 2.9 seconds for joint-3, respectively. Although the disturbance caused temporary deviations of approximately 2-3 degrees, the controller successfully restored the joints to their reference positions. This response demonstrates the resilience of the controller under external perturbations and its ability to maintain stability and accuracy, even in non-ideal conditions. Such robustness is crucial for real-world applications where external disturbances are inevitable.

4. CONCLUSIONS

In this study, the 3-DOF robotic manipulator was mathematically modeled, and the system's equations of motion were derived using the Spatial Operator Algebra (SOA) framework. Leveraging the complete and verified SOA dynamic model, a Computed Torque Control (CTC) strategy was designed and successfully implemented on a microcontroller. To evaluate the controller's performance, three distinct tests were conducted: parabolic and sinusoidal trajectory tracking, as well as disturbance rejection.

The experimental results demonstrated the controller's high precision in tracking both static and dynamic reference signals. Furthermore, its robust performance under external disturbances validated its reliability for real-world applications. These findings underscore the CTC controller's effectiveness as a practical and robust solution for advanced robotic systems.

An important conclusion from this study is the successful real-time integration of the SOA algorithm into control applications. The feasibility of combining SOA with CTC was verified experimentally, opening up new possibilities for real-time applications in robotics. Future research could explore enhancing the control strategy to improve energy efficiency or extending the methodology to manipulators with higher degrees of freedom. Additionally, integrating advanced control techniques, such as Nonlinear Model Predictive Control (NMPC), with the SOA framework could further enhance the system's performance and adaptability.

Declaration of Ethical Standards

The authors declare that all ethical guidelines including authorship, citation, data reporting, and publishing original research.

Credit Authorship Contribution Statement

Autor 1: Design, experiments, result analysis, writing, editing; Autor 2: Design, editing, supervision.

Declaration of Competing Interest

The authors declare that they have no known competing financial interests or personal relationships that could have appeared to influence the work reported in this paper.

Funding / Acknowledgements

Data Availability

Research data has not been made available in a repository.

REFERENCES

[1]   T. Yaren and S. Kizir, "Efficiency assessment of SOA-based computed torque control: A

comparative analysis with NE-based approach", *Proceedings of the Institution of Mechanical Engineers, Part I: Journal of Systems and Control Engineering*, vol. 238, no. 8, pp. 1410-1424, 2024.

[2] W. Shang and S. Cong, "Nonlinear computed torque control for a high-speed planar parallel manipulator", *Mechatronics*, vol. 19, no. 6, pp. 987–992, 2009.

[3] Z. Yang, J. Wu and J. Mei, "Motor-mechanism dynamic model based neural network optimized computed torque control of a high speed parallel manipulator", *Mechatronics*, vol. 17, no. 7, pp. 381–390, 2007.

[4] Y. Xu, J. M. Hollerbach and D. Ma, "A nonlinear PD controller for force and contact transient control", *IEEE Control Systems Magazine*, vol. 15, no. 1, pp. 15–21, 1995.

[5] R. Hayat, M. Leibold and M. Buss, "Robust-Adaptive Controller Design for Robot Manipulators Using the H∞ Approach", *IEEE Access*, vol. 6, pp. 51626–51639, 2018.

[6] S. H. Lee, J. B. Song, W. C. Choi and D. Hong, "Position control of a Stewart platform using inverse dynamics control with approximate dynamics", *Mechatronics*, vol. 13, no. 6, pp. 605–619, 2003.

[7] A. S. Polydoros, E. Boukas and L. Nalpantidis, "Online multi-target learning of inverse dynamics models for computed-torque control of compliant manipulators", In IEEE Int Conf Intell Robot Syst, 2017, pp. 4716-4722.

[8] H. Ozakyol, C. Karaman and Z. Bingul, "Kinematic and Dynamic Analysis and Design Toolbox of High-DOF Hybrid Multibody Systems", In IECON 44th Annu. Conf. IEEE Ind. Electron. Soc., IEEE, 2018, pp. 2558–63.

[9] G. Yıldız, "Nonlinear Control Methods Of Industrial Serial Robots", Master Thesis, Istanbul Technical University, Istanbul, Türkiye, 2014.

[10] A. Jain, "Structure-Based Computational Modeling Architecture for Robotics", In IEEE International Conference on Robotics and Automation, 2013.

[11] T. Yaren and S. Kizir, "Real-Time Nonlinear Model Predictive Control of a Robotic Arm Using Spatial Operator Algebra Theory", *Journal of Field Robotics*, 2025. DOI: 10.1002/rob.22514

[12] T. Yaren and S. Kizir, "Advanced SOA-NMPC Controller Design Minimising Real-Time Computational Burden for Dynamic Obstacle Avoidance in Robotic Manipulators", *International Journal of Systems Science*, 2025. DOI: 10.1080/00207721.2025.2479769

[13] P. M. Wensing, L. R. Palmer and D. E. Orin, "Efficient recursive dynamics algorithms for operational-space control with application to legged locomotion", *Auton Robots*, vol. 38, pp. 363–81, 2015.

[14] J. Nakanishi, M. Mistry and S. Schaal, "Inverse Dynamics Control with Floating Base and Constraints", In Proc. 2007 IEEE Int. Conf. Robot. Autom., 2007, pp. 1942–7.

[15] A. Elşavi, "Fractional-order impedance control of 2-DOF seri robot", Master Thesis, Kocaeli University, Kocaeli, Türkiye, 2019.

[16] S. Kizir, T. Yaren and E. Kelekçi, "Matlab Simulink Destekli Gerçek Zamanlı Kontrol: Teori ve Mühendislik Uygulamaları", Ankara, Türkiye: Seçkin Yayıncılık; 2019.

[17] T. Kang, J. Kim, D. Song, T. Kim and S. J. Yi, "Design and Control of a Service Robot with Modular Cargo Spaces", In 18th Int. Conf. Ubiquitous Robot, 2021, pp. 595–600.

RURAL VS. URBAN TRAVEL BEHAVIOR: A COMPARATIVE ANALYSIS OF MOBILITY PATTERNS IN THE IZMIR URBAN RAIL MASS TRANSIT SYSTEM (IZBAN)

[1]**Ahmet KARAKURT** (iD)

[1] *University of Delaware, Department of Civil & Environmental Engineering, Newark, DE, USA*
[1] karakurt@udel.edu

Highlights

- Travel Behavior
- Public Transportation
- Urban rail transit
- Rural-urban disparities
- Transportation equity
- Socio-economic factors
- Sustainable mobility

*Corresponding Author: Ahmet KARAKURT, karakurt@udel.edu

RURAL VS. URBAN TRAVEL BEHAVIOR: A COMPARATIVE ANALYSIS OF MOBILITY PATTERNS IN THE IZMIR URBAN RAIL MASS TRANSIT SYSTEM (IZBAN)

¹ Ahmet KARAKURT ID

¹ University of Delaware, Department of Civil & Environmental Engineering, Newark, DE, USA
¹ karakurt@udel.edu

ABSTRACT: Understanding travel behavior is critical for designing equitable and sustainable transportation systems, particularly in the context of rapid urbanization and rural-urban disparities. This study examines the differences in travel behavior between rural and urban areas, with a focus on the Izmir Urban Rail Mass Transit System (IZBAN) in Turkey. By analyzing data from 606 face-to-face surveys, the research explores key factors such as mode choice, trip purpose, travel distance, socio-economic influences, and user costs. Descriptive statistics, correlation analysis, chi-square tests, and hypothesis testing were applied using SPSS to identify patterns and significant differences in travel behavior between rural and urban respondents. The study highlights the distinct challenges faced by rural and urban travelers, including limited transportation options in rural areas and issues of congestion, high rents, and inequality in urban centers. The findings reveal that urban travelers benefit from shorter travel times, greater access to public transportation, and proximity to transit hubs, while rural travelers rely more on private vehicles and face longer travel distances. The study also emphasizes the role of socio-economic factors, such as income and household structure, in shaping travel behavior, as well as the environmental and policy implications of these patterns. By providing a comprehensive analysis of rural and urban travel behavior, this research aims to inform transportation policies that promote accessibility, affordability, and sustainability. The study's insights are particularly relevant for addressing the mobility challenges of underserved populations and optimizing public transportation systems in rapidly growing cities. Ultimately, this research contributes to the broader discourse on sustainable urban development and equitable access to transportation, offering valuable lessons for policymakers and urban planners in Izmir and beyond.

Keywords: *Travel Behavior, Public Transportation, Urban Rail Transit, Rural-Urban Disparities, Transportation Equity, Socio-Economic Factors, Sustainable Mobility*

1. INTRODUCTION

Travel behavior is a cornerstone of transportation research, influencing urban planning, environmental sustainability, and the overall quality of life for individuals and communities. As cities expand and rural areas face unique challenges, understanding the nuances of travel behavior in different geographic contexts becomes increasingly important. This study delves into the differences and similarities in travel behavior between rural and urban areas, with a particular focus on the Izmir Urban Rail Mass Transit System (IZBAN), a critical component of public transportation in Izmir, Turkey. By examining how people in these distinct environments choose to travel, this research aims to provide insights that can inform more effective transportation policies and infrastructure development. Unlike previous studies that often focus exclusively on either urban or rural contexts, this research provides a comparative analysis of both within the same transit system, allowing for a direct and contextualized understanding of spatial disparities in travel behavior. The key contribution of this study is the integration of socio-economic and spatial data to highlight how differences in access, affordability, and mobility manifest between rural and urban IZBAN passengers.

The rapid urbanization of the 21st century has led to significant changes in how people move within and between cities. Increasing migration from rural areas to modern cities has resulted in excessive urban growth, which, while fostering economic opportunities, has also introduced challenges such as increased travel distances, higher transportation costs, and social inequalities [1]. Urban areas, characterized by high population density and mixed land-use patterns, offer a wide array of transportation options, including public transit, cycling, walking, and ride-sharing services. These options are often supported by well-developed infrastructure, such as dedicated bike lanes, extensive public transit networks, and pedestrian-friendly streets [2]. However, urban expansion often exacerbates issues such as traffic congestion, air pollution, and energy consumption, while also contributing to social disparities. For instance, high rents in city centers force lower-income households to relocate to suburban or peri-urban areas, where housing is more affordable, but transportation costs and travel times are significantly higher [3]. This dynamic creates a paradox where households seeking to avoid high rents face increased transportation burdens, further perpetuating inequality and discrimination in access to urban amenities and opportunities.

In contrast, rural areas often face challenges such as limited public transportation options, longer travel distances, and a greater reliance on private vehicles. These disparities in transportation infrastructure and accessibility have profound implications for travel behavior, influencing mode choice, trip purpose, travel distance, and socio-economic factors [1]. Rural residents, particularly those with lower incomes or limited access to private vehicles, often face mobility challenges that restrict their access to essential services such as healthcare, education, and employment [4]. Addressing these challenges requires tailored policies that improve rural transportation infrastructure, promote carpooling, and support demand-responsive transit systems [5].

Understanding these differences is crucial for designing transportation systems that are both efficient and equitable. Urban areas, with their dense populations and diverse transportation options, often experience issues such as traffic congestion, air pollution, and high energy consumption. Policies promoting public transportation, active mobility, and compact urban development are commonly implemented to mitigate these challenges [6]. On the other hand, rural areas, with their dispersed populations and limited infrastructure, face different challenges, such as higher per capita emissions due to reliance on private vehicles and limited access to essential services like healthcare and education [4]. Addressing these challenges requires tailored policies that improve rural transportation infrastructure, promote carpooling, and support demand-responsive transit systems [1].

This study aims to explore these differences by examining the travel behavior of IZBAN passengers in both rural and urban contexts. By analyzing data collected through a comprehensive survey, the research seeks to identify patterns and trends that can inform transportation policies and infrastructure development. The study also considers the impact of socio-economic factors, environmental sustainability, and emerging technologies on travel behavior, providing a holistic view of the challenges and opportunities in rural and urban transportation systems. For instance, socio-economic factors such as income, age, and household structure play a significant role in shaping travel behavior. In urban areas, lower-income groups are more likely to rely on public transportation, while higher-income groups may prefer private vehicles or ride-sharing services [3]. In rural areas, socio-economic factors similarly influence travel behavior, but the lack of transportation alternatives often limits choices, particularly for older adults and low-income households [4].

The significance of this research lies in its potential to contribute to the development of more equitable and sustainable transportation systems. By understanding the distinct travel behavior patterns in rural and urban areas, policymakers and urban planners can design targeted interventions that address the unique needs of each context. For instance, improving public transportation options in rural areas could reduce reliance on private vehicles, thereby lowering greenhouse gas emissions and enhancing mobility for underserved populations. Similarly,

*Corresponding Author: Ahmet KARAKURT, karakurt@udel.edu

optimizing urban transportation systems could alleviate traffic congestion, improve air quality, and enhance the overall quality of life for city dwellers.

In summary, this research seeks to bridge the gap in understanding travel behavior differences between rural and urban areas, with a focus on the IZBAN system. By doing so, it aims to provide valuable insights that can inform transportation policies, enhance sustainability, and improve the quality of life for both rural and urban residents. The findings of this study have the potential to influence not only Izmir but also other cities facing similar transportation challenges, contributing to the broader discourse on sustainable urban development and equitable access to transportation. As cities continue to grow and evolve, understanding the complexities of travel behavior will be essential for creating transportation systems that are not only efficient but also inclusive and sustainable.

2. LITERATURE REVIEW

Travel behavior is a critical area of study in transportation research, as it directly influences infrastructure development, environmental sustainability, and quality of life. Understanding the differences and similarities in travel behavior between rural and urban areas is essential for designing effective transportation policies and systems. This review synthesizes existing research on travel behavior in rural and urban contexts, focusing on mode choice, trip purpose, travel distance, socio-economic influences, environmental and policy implications, and emerging trends.

Mode choice is shaped by the availability of transportation options, infrastructure, and socio-economic factors. In urban areas, residents have access to a wide range of transportation modes, including public transit, walking, cycling, and ride-sharing services. High population density and mixed land-use patterns in cities encourage the use of non-motorized and public transportation [2]. The proliferation of bike-sharing programs and app-based ride-hailing services has further diversified urban mobility options [7]. However, private car use remains prevalent in many cities, often leading to traffic congestion and environmental challenges [8]. In rural areas, public transportation options are limited, and there is a greater reliance on private vehicles. The dispersed nature of rural settlements and longer travel distances make car ownership a necessity for most residents [1]. Walking and cycling are less common due to inadequate infrastructure and safety concerns [4]. Carpooling and demand-responsive transit systems have been explored as alternatives, but their adoption remains limited [5].

Trip purpose varies significantly between rural and urban areas, reflecting differences in land use, accessibility, and lifestyle. Urban trips are often shorter and more frequent, with common purposes including commuting, shopping, and leisure activities [9]. The proximity of residential, commercial, and recreational areas in cities facilitates multi-purpose trips, reducing the need for long-distance travel [6]. Rural trips, on the other hand, are typically longer and less frequent, with a focus on essential activities such as work, education, and healthcare [10]. Limited access to services and amenities in rural areas often necessitates longer travel distances, making trip chaining less feasible [11].

Travel distance and time are key determinants of travel behavior, influenced by geographic and infrastructural factors. In urban areas, residents generally experience shorter travel distances due to the compact nature of cities. However, traffic congestion can lead to longer travel times despite shorter distances [12]. Efficient public transportation systems and active mobility options help mitigate these challenges in well-planned urban areas. In rural areas, residents face longer travel distances due to the dispersed nature of settlements and limited infrastructure. While congestion is less of an issue, the lack of efficient transportation options often results in significant travel times [1].

Socio-economic factors such as income, age, and household structure play a significant role in shaping travel behavior. In urban areas, income levels and employment type strongly influence mode choice. Lower-income groups are more likely to rely on public transportation, while higher-

income groups may prefer private vehicles or ride-sharing services [3]. Age and household structure also affect travel patterns, with younger adults and smaller households more likely to use active transportation modes [13]. In rural areas, socio-economic factors similarly influence travel behavior, but the lack of transportation alternatives often limits choices. Older adults and low-income households in rural areas are particularly vulnerable to mobility challenges, as they may lack access to private vehicles or affordable transportation options [4].

Travel behavior has significant implications for environmental sustainability and transportation policy. In urban areas, travel behavior contributes to air pollution, greenhouse gas emissions, and energy consumption. Policies promoting public transportation, active mobility, and compact urban development are commonly implemented to reduce these impacts [6]. Smart city initiatives and digital technologies are increasingly being used to optimize urban transportation systems [7]. In rural areas, the reliance on private vehicles results in higher per capita emissions and energy use. Addressing these challenges requires policies that improve rural transportation infrastructure, promote carpooling, and support demand-responsive transit systems [1].

Recent developments in technology and societal changes are reshaping travel behavior in both rural and urban areas. In urban areas, the rise of smart cities and digital technologies has transformed urban travel behavior, with increased use of apps for trip planning and real-time information [7]. The COVID-19 pandemic has also led to significant shifts, including increased remote work and reduced public transportation use [14]. These innovations have the potential to improve accessibility and reduce reliance on private vehicles.

In conclusion, travel behavior in rural and urban areas is influenced by distinct geographical, socio-economic, and infrastructural factors. While urban areas benefit from greater transportation options and shorter travel distances, rural areas face challenges related to limited infrastructure and longer travel needs. Addressing these disparities requires tailored policies and innovative solutions to promote sustainable and equitable mobility for all. Future research should focus on the impacts of emerging technologies and societal changes on travel behavior, particularly in rural contexts.

3. METHODOLOGY

This study aims to observe the differences in travel behavior between rural and urban areas. To this end, a comprehensive survey research methodology was employed, incorporating data set. The data set was collected through face-to-face questionnaires administered to 606 participants. This survey examines travel behavior through metrics such as travel frequency, journey days, travel time, travel distance, public transportation modes, access types to IZBAN, travel costs, and times of departure and arrival. Additionally, user cost aspects including access time, in-vehicle time, and waiting times were assessed, alongside demographic characteristics of the respondents including age, gender, education, occupation, household income, and household size.

SPSS (Statistical Package for the Social Sciences) was selected for the statistical analysis in this study on travel behavior differences between rural and urban areas due to its user-friendly interface, extensive statistical capabilities, and widespread use in social sciences research. SPSS is known for its ability to handle large datasets efficiently and perform complex analyses with relative ease [15]. Its wide range of statistical tools, including descriptive statistics, correlation analysis, and hypothesis testing, makes it ideal for exploring patterns and differences in travel behavior between rural and urban contexts [16]. Additionally, SPSS's ability to produce clear and interpretable output, along with its flexibility in data manipulation, ensures that the analysis is both accurate and comprehensible [17]. The software's robustness in handling various data types and its compatibility with multiple data formats made it a suitable choice for analyzing the diverse variables involved in the study of travel behavior across different geographic regions.

*Corresponding Author: Ahmet KARAKURT, <u>karakurt@udel.edu</u>

3.1. Izmir Urban Rail Mass Transit System (IZBAN)

The public transportation pricing system in Izmir exhibits considerable variability. A flat fare structure is employed for services such as buses, the metro, and trams. Conversely, a distance-based fare system is applied on certain long-distance bus lines and suburban trains [18]. IZBAN, a prominent component of Izmir's public transit network, has been operational since 2010, linking Aliağa and Selçuk. It represents one of Turkey's largest urban rail mass transit systems connected to the airport [19].
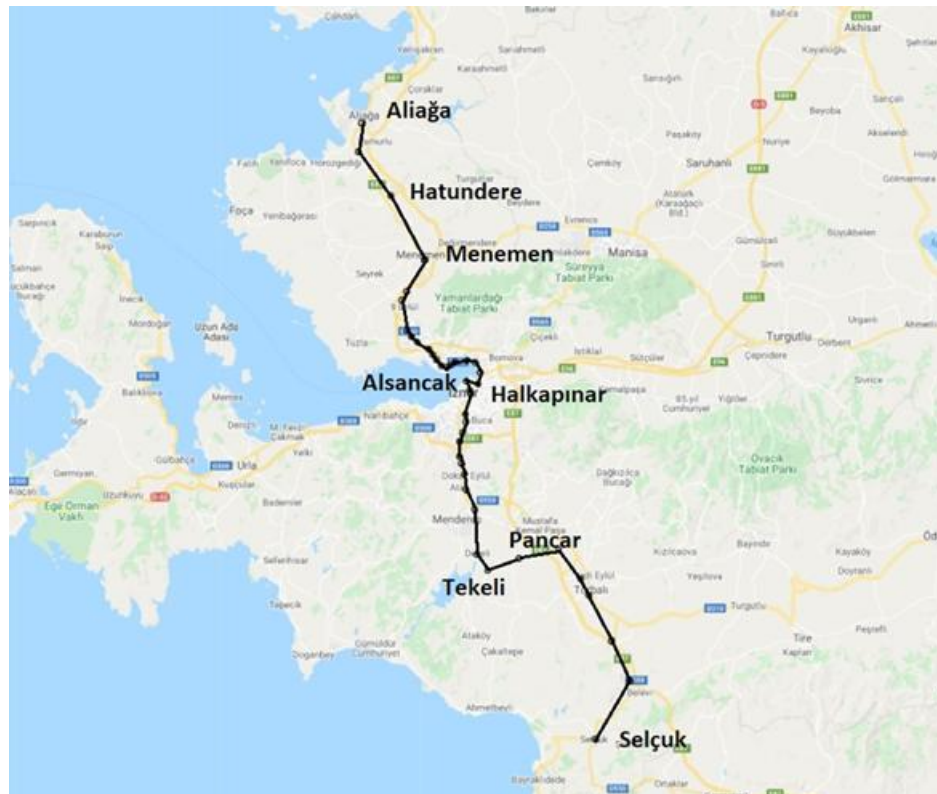
Figure 1. IZBAN stations (Google Maps).

Initially, IZBAN operated with 31 stations. This number increased to 32 with the addition of the Hilal station, and further expanded to 38 following the inauguration of the Torbalı line. The network grew to 40 stations with the opening of Saglık and Selcuk stations in 2019. Notably, the Hilal and Halkapınar stations serve as key interchange points between Izmir Metro and IZBAN [20].

IZBAN serves approximately 650,000 passengers daily, with the current line extending 136 kilometers. Upon completion of the expansion project, the total length of the line will reach 185 kilometers, extending to Bergama [19]. Initially, IZBAN operated on a flat fare system; however, in 2018, it transitioned to a distance-based pricing model. Under this system, passengers are initially charged based on the maximum distance from their departure station. At their arrival station, any fare corresponding to the distance not traveled is subsequently refunded.

All transportation fares and rent cost data referenced in this study correspond to the year 2019, which reflects the period during which the survey was conducted and aligns with the most recent available IZBAN and housing market data. The IZBAN ticket tariff is structured as follows: 2.86 TL for full fare passengers, 1.65 TL for students, 2.20 TL for teachers, and 1 credit for staff when traveling within the flat fare distance limit of 25 kilometers. Despite this, the distance-based pricing system presents several challenges for passengers.

Passengers are required to preload their transportation cards with varying amounts of money depending on their departure station. For instance, a passenger departing from Aliağa must maintain a minimum balance of 10.60 TL on their card, calculated based on the fare to the farthest station, such as Selçuk. This requirement is often perceived as costly by passengers. Additionally, there is the issue of passengers potentially forgetting to claim refunds for unused fare at arrival stations. These factors may deter passengers from using IZBAN, prompting them to seek alternative public transportation options.

3.2. Data Collection

As part of the data collection process, the following information has been gathered from the Izmir Metropolitan Municipality Suburban and Rail System Investments Department:

- IZBAN's station information and line length

- Distance between stations

- Travel time between stations

- Annual passenger numbers for each stop

- Ticket tariffs under the flat rate system (from IZBAN's inception until the transition to the distance-based pricing system)

- Travel prices between each stop under the distance-based pricing system

Based on the data collected, a preliminary survey was conducted to assess the relevance and effectiveness of the questions for a more comprehensive questionnaire. Following this evaluation, a detailed survey was administered to IZBAN passengers.

The interviewer-assisted method is frequently employed by researchers for data collection and is typically categorized into two types: personal interviews and telephone interviews. While telephone interviews can be efficient, they present several drawbacks, including potential misunderstandings of questions, a higher risk of incomplete responses, and constraints related to time. Additionally, given that the target group for this study consists of IZBAN passengers, reaching them via telephone interviews poses significant challenges. Consequently, personal interviews are deemed the most effective approach for this research, ensuring clearer communication and better engagement with participants.

To enhance the statistical efficiency of the survey, the number of surveys conducted at each train station is determined based on ridership data. The formulation used for this calculation is provided as follows [21]:

$$n_i = n \left(\frac{N_i}{\sum_{i=1}^{L} N_i} \right) = n \left(\frac{N_i}{N} \right) \qquad (1)$$

where n is the total number of sample units, n_i is the number of sample units to allocate to stratum i, L is the number of strata, N_i is the number of sample units within stratum i, N is the number of sample units in the population.

3.3. Survey Design

The questionnaire is structured into two distinct sections. The first part focuses on capturing information related to participants' travel behavior, user costs, and demographic characteristics. The

*Corresponding Author: Ahmet KARAKURT, karakurt@udel.edu

second part aims to identify passengers' priorities regarding public transportation and assess their perceived importance of rental prices and travel distances. To achieve comprehensive insights, both revealed preference and stated preference methods are utilized within the questionnaire.

The revealed preference section of the questionnaire includes detailed inquiries into demographic information, travel behavior characteristics, and user costs, with responses providing quantitative data. In the pre-questionnaire phase, the rent-distance relationship is evaluated without considering immediate travel behavior conditions. Consequently, the questions are designed to gather information on the following aspects:

Card Type: Type of transportation card used
Travel Frequency: How often the participant travels
Mean Travel Time: Average duration of travel
Travel Days: Days of the week the participant travels
Journey Hours: Time of day for outward and return journeys
Access Type to IZBAN: Method of reaching the IZBAN station
Departure and Arrival Stations: Stations used for the journeys
Travel Purpose: Reasons for travel
Preferred Public Transportation Mode: Most frequently used mode of public transport
The demographic section addresses:
Gender, Age, Education, Occupation, Monthly Household Income,
Closest IZBAN Stop: Nearest station to the participant's location
Car Ownership: Whether the participant owns a car
Rental Status: Housing situation (own or rent)
Rental Price: Cost of current housing
Additionally, the third part of the questionnaire seeks to gather information on:
In-Vehicle Travel Time: Duration spent traveling within the vehicle
Waiting Time: Time spent waiting for the vehicle

Access Time: Time required to access IZBAN, including the journey from home to the station and from the turnstile to the platform.

In the stated preference method applied to the section addressing passenger expectations from public transportation, the following factors are evaluated: Ticket Price, Travel Time, Waiting Time and Comfort.

Each factor is compared against the others to assess its relative importance to users. This approach is designed to gauge how passengers prioritize these aspects of public transportation and to understand their preferences in terms of value and service quality. The insights gained from this analysis will help in identifying which factors are most critical to passengers and how they influence their overall satisfaction with public transportation.

Based on the 2018 IZBAN data, which reports a total of 84,450,567 passengers annually and a daily ridership of 231,371, the sample size for the survey is determined using Yamane [22]'s formula. For a 95% confidence level and assuming a proportion P=0.5, the required sample size is calculated as follows:

$$ n = \frac{N}{1 + N(e^2)} \tag{2} $$

where n is the sample size, N is the population size, e is the level of precision.

A total of 606 questionnaires were administered, with the distribution of participants across stations based on annual ridership data. The number of participants for each station is calculated by applying the percentage distribution of annual ridership to the total number of surveys. For example:

Şirinyer Station: With an annual ridership of 7,848,161, the station has 72 participants.
Ciğli Station: With an annual ridership of 3,478,991, the station has 32 participants.

The survey does have certain limitations:

Passengers Under Age 18: This group is excluded from the survey because they may lack the financial independence required to answer questions about rent and other economic factors, as they often rely on family support.

University Students in Dormitories: These individuals are also excluded from the survey due to the relevance of rent prices to the study. University students residing in dormitories are not typically responsible for rental expenses, which makes their input less applicable to the research focus on rent prices and related financial considerations.

4. ANALYSIS AND RESULTS

4.1. Analysis of Travel Behavior Patterns

The results of the IZBAN passenger survey align with several findings in the literature regarding public transportation usage patterns and factors affecting commuter behavior. Table 1 represents descriptive statistics of the survey.

Ticket Types and Usage Patterns: The predominance of full fare cards (67%) and the substantial use of student cards (24.8%). This reflects a broader trend where standard fare systems dominate public transportation usage, particularly in environments with substantial student populations.

Journey Frequency and Peak Hours: The finding that 27.90% of passengers use IZBAN five days a week mirrors trends observed in other urban transit systems where daily commuters frequently utilize public transport during peak hours [23]. The peak travel period between 06:00 and 10:00, and the low usage between 20:00 and 24:00, correspond with findings that peak hours are characterized by higher ridership due to work-related travel [24].

Travel Time Perceptions: The perception of journey time as short by 34.70% of passengers and very long by 0.70%. Short journey times are often perceived positively, while long journey times can significantly impact passenger satisfaction.

Return Trip Patterns: The predominance of return trips between 16:00 and 20:00 (47.40%) reflects a common pattern in commuter behavior, where significant travel activity occurs during the late afternoon and early evening due to work-related returns. The low return trip frequency between 06:00 and 10:00 highlights the difference in travel behavior patterns compared to outward journeys.

Travel Purposes: The high proportion of trips for school and work (48.10%) and visiting (41.30%). The minimal use for emergencies (1.20%) corroborates findings that emergency trips are less frequent compared to regular commuting and social activities.

Access Modes: The finding that 49.80% of passengers walk to IZBAN stations and 45.20% use other public transportation modes is supported by studies on multimodal access to transit systems, where walking and transfers from other public modes are common [25]. The low usage of cars (3.60%) aligns with the preference for non-motorized access to reduce parking and congestion issues around transit hubs.

Mode Preferences: The high utilization rate of IZBAN (44.20%) compared to other public transportation modes, particularly ferries (1.80%), highlights the importance of proximity to major transit routes.

These results reflect broader trends observed in the field of urban transportation and provide valuable insights into the usage patterns and preferences of IZBAN passengers.

*Corresponding Author: Ahmet KARAKURT, karakurt@udel.edu

Table 1. Descriptive statistics of the survey

Questions		Frequency	Percent (%)
Rental Status	Yes	237	39.1
	No	369	60.9
Card Type	full fare	406	67.0
	student	150	24.8
	teacher	8	1.3
	60 years	19	3.1
	staff card	14	2.3
	Over 65 free card	9	1.5
Journey Frequency	5 or more times a week	169	27.9
	3-4 times in a week	103	17.0
	1-2 times in a week	154	25.4
	1-3 times in a month	118	19.5
	Less than once a month	62	10.2
Mean Travel Time	very short	79	13.0
	short	210	34.7
	short middle	132	21.8
	middle	94	15.5
	long middle	68	11.2
	long	19	3.1
	very long	4	.7
Journey Days	In-week	261	43.1
	Weekend	174	28.7
	Both	171	28.2
Outward Journey Time	06:00-10:00	236	38.9
	10:00-13:00	134	22.1
	13:00-16:00	142	23.4
	16:00-20:00	83	13.7
	20:00-24:00	11	1.8
Return Journey Time	06:00-10:00	4	.7
	10:00-13:00	8	1.3
	13:00-16:00	51	8.4
	16:00-20:00	287	47.4
	20:00-24:00	256	42.2
Access to IZBAN	foot	302	49.8
	other pt modes	274	45.2
	taxi	6	1.0
	own car	22	3.6
	bicycle	2	.3
Journey Purpose	work	201	33.2
	school	90	14.9
	visiting	250	41.3
	shopping, bank and other	58	9.6
	hospital	7	1.2
Public Transportation Type	bus	212	35.0
	railway	268	44.2
	ferry	11	1.8
	tramway	37	6.1
	metro	14	2.3
	dolmuş	64	10.6

Ridership Patterns and Station Characteristics: The highest ridership is observed at the Şirinyer stop, located in Buca, a district with significant population density and proximity to major commercial and residential avenues. Şirinyer benefits from its location in Izmir's most populous county, which has a population of 507,773 [26]. This high population density contributes to elevated ridership levels at this station. Table 2. shows descriptive statistics for departure and arrival stations.

The Halkapınar stop, an important transfer hub connecting the metro, bus, and tram networks, also experiences substantial ridership. Its strategic location near densely populated districts such as Bornova and Konak, where many metro passengers transfer from, further enhances its usage. This

finding aligns with literature indicating that transfer stations, especially those integrating multiple modes of transport, tend to attract higher passenger volumes due to increased connectivity [27].

Table 2. Descriptive statistics for departure and arrival stations.

	Station	Departure Frequency	Departure Percent (%)	Arrival Frequency	Arrival Percent (%)
North Axix	Aliağa	16	2.6	25	4.1
	Biçerova	3	.5	1	.2
	Hatundere	5	.8	1	.2
	Menemen	27	4.5	26	4.3
	Egekent 2	17	2.8	12	2.0
	Ulukent	8	1.3	3	.5
	Egekent	21	3.5	15	2.5
	Ata Sanayi	17	2.8	3	.5
	Çiğli	39	6.4	26	4.3
	Mavişehir	18	3.0	14	2.3
	Şemikler	18	3.0	8	1.3
	Demirköprü	9	1.5	8	1.3
	Nergiz	13	2.1	14	2.3
	Karşıyaka	23	3.8	61	10.1
	Alaybey	8	1.3	3	.5
	Naldöken	4	.7		
	Turan	2	.3	9	1.5
Central Axis	Bayraklı	19	3.1	14	2.3
	Salhane	3	.5	11	1.8
	Halkapınar	62	10.2	55	9.1
	Alsancak	20	3.3	103	17.0
	Hilal	34	5.6	39	6.4
	Kemer	9	1.5	7	1.2
	Şirinyer	97	16.0	30	5.0
	Koşu	33	5.4	2	.3
	Inkılap	15	2.5	2	.3
	Semt Garajı	17	2.8	14	2.3
	Esbaş	9	1.5	45	7.4
	Gaziemir	10	1.7	19	3.1
	Sarnıç	9	1.5	9	1.5
	Havalimanı			15	2.5
	Cumaovası	5	.8	2	.3
	Develi				
	Tekeli			2	.3
	Pancar	1	.2		
	Kuşçuburun	1	.2		
South Axis	Torbalı	9	1.5	5	.8
	Tepeköy	5	.8	1	.2
	Sağlık				
	Belevi				
	Selçuk			2	.3

Similarly, the Hilal stop, which is connected solely to the metro, exhibits high ridership. This is consistent with the observation that stations with metro connections, particularly in areas with significant commuter traffic, generally have higher patronage.

In contrast, the Kuşçuburun, Hatundere, and Biçerova stops exhibit lower ridership levels. These stations are situated in rural areas, distant from the city center, which typically results in reduced usage [24]. The low ridership at these stops corroborates findings that stations located in less urbanized areas or farther from central commercial zones attract fewer passengers [28].

Furthermore, Develi, Tekeli, Sağlık, and Belevi stations also report minimal usage, likely due to their remote locations and lack of significant residential or commercial development. The Havalanı

*Corresponding Author: Ahmet KARAKURT, karakurt@udel.edu

station, built primarily to serve the airport, and the recently constructed Selçuk station, along with Sağlık and Belevi stations in 2019, currently show no departures, reflecting their recent addition to the network and limited time for passenger establishment.

Arrival Station Ridership Patterns: The distribution of ridership across arrival stations exhibits notable patterns influenced by geographic and investment factors. Alsancak, a highly attractive area in Izmir known for its appeal to businesses, students, and tourists, shows the highest ridership. This aligns with findings that stations located in vibrant commercial and cultural hubs tend to attract more passengers [24].

Similarly, Karşıyaka, situated in the northern part of the city near popular bazaars, avenues, and the coast, also experiences high ridership. The station's proximity to these amenities contributes to its attractiveness and high passenger volume.

In contrast, Esbaş station, while also experiencing significant passenger traffic, shows a considerable disparity between arrival and departure ridership. Located near a major industrial free zone and Izmir's largest shopping mall, Esbaş serves primarily employees and shoppers, highlighting how commercial investments can influence station usage patterns [28].

Conversely, Hatundere and Biçerova are among the least preferred stations for arrival, reflecting their location in more rural and less accessible areas. The lack of ridership at these stations confirms previous research indicating that stations situated in less urbanized areas or with limited amenities attract fewer passengers [24].

Additionally, stations such as Naldöken, Develi, Pancar, Kuşçuburun, Sağlık, and Belevi are not selected as arrival stations, suggesting limited appeal or accessibility. The new Selçuk station, despite its status as a tourist destination, shows low ridership, which may be attributed to its novelty and the relatively low frequency of visits.

User Cost Components in the Passenger Survey:

The second part of the survey focuses on estimating various user cost components, including access time, platform access time, waiting time, and in-vehicle time. Table 3. indicates descriptive statistics of user cost components.

Access Time: A significant majority of passengers, 48.34%, reported an access time to IZBAN of 10 minutes or less, indicating efficient proximity for most users. In contrast, 3.30% of passengers experience an access time exceeding 30 minutes. The mean access time from home to the IZBAN station is 14.1980 minutes. These findings suggest that while most passengers have relatively short access times, a small segment experiences notably longer commutes, reflecting the variability in access times across different residential areas.

Platform Access Time: Regarding the time required to access the platform from the turnstile, 49.83% of passengers reported it takes 1 minute or less, which suggests efficient station design and minimal congestion. Conversely, 0.82% reported a platform access time exceeding 5 minutes. The average platform access time is 1.7163 minutes. These results indicate that most passengers face minimal delays when transitioning from the turnstile to the platform.

Waiting Time: The survey results show that 63.86% of passengers wait between 5 and 10 minutes at stations. A smaller percentage, 4.29%, report waiting times exceeding 15 minutes. The mean waiting time is 9.2855 minutes. These findings highlight that while most passengers experience moderate waiting times, a minority faces longer waits, potentially affecting overall travel satisfaction.

In-Vehicle Time: In-vehicle time, defined as the duration from entering to exiting the train, shows that 36.96% of passengers spend between 10 and 20 minutes on the train. However, 1.98% of passengers report an in-vehicle time exceeding 60 minutes. The average in-vehicle time is 25.9620 minutes. This data reflects a diverse range of journey lengths, with a substantial portion of passengers experiencing relatively short trips, while a small segment endures longer travel durations.

These components provide a comprehensive view of the typical travel experience for IZBAN passengers and underscore areas for potential improvement in service efficiency and user satisfaction.

Table 3. Descriptive statistics of user cost components.

Variable	Minimum	Maximum	Mean	Std. Deviation	Variance
Access time (home to IZBAN)	2.00	100.00	14.1980	10.61523	112.683
Access (to platform)	.16	12.50	1.7163	1.25045	1.564
Waiting time	1.00	30.00	9.2855	3.80683	14.492
In-vehicle time	3.00	105.00	25.9620	16.65601	277.423

Travel Distance and Pricing Patterns:

Most passengers, specifically 82.84%, travel 26 kilometers or less and thus are not subject to the distance-based pricing system. In contrast, only 0.17% of passengers travel distances exceeding 75 kilometers. For those traveling beyond 26 kilometers, the travel price is determined based on the distance traveled. Table 4. explains descriptive statistics of travel distance and travel price.

Regarding ticket tariffs, 55.94% of participants pay the standard fare of 2.86 TL, while 20.13% benefit from the discounted student tariff of 1.65 TL. Additionally, 16.34% of passengers are subject to the distance-based pricing rules. The mean travel distance reported is 15.8231 kilometers, and the average travel price is 2.5852 TL.

Table 4. Descriptive statistics of travel distance and travel price.

Variable	Minimum	Maximum	Mean	Std. Deviation	Variance
Travel distance	1.00	75.47	15.8231	13.65743	186.525
Travel price	0.00	6.39	2.5852	0.92979	0.865

These results are influenced by the availability of free or discounted tickets, such as those provided to individuals aged 65 and over, teachers, and staff. The presence of these discount schemes affects the overall distribution of travel costs among passengers, highlighting the impact of ticket tariff structures on travel expenditure.

Stated Preference Analysis:

In the stated preference section of the survey, passenger expectations for IZBAN were evaluated. The results indicate that passengers prioritize factors in the following order: travel time, travel price, waiting time, and travel comfort. Table 5. summarizes comparisons between travel time, price, comfort and waiting time.

This prioritization suggests that while comfort is a less critical factor for shorter trips, it becomes more significant for longer journeys.

The emphasis on travel time and price reflects the broader trend where efficiency and cost are primary determinants of travel behavior. The lower emphasis on comfort for short trips aligns with the expectation that shorter journeys are less likely to impact overall passenger satisfaction compared to longer trips.

Table 5. Comparisons between travel time, price, comfort and waiting time.

Criteria	Frequency	Percent (%)		Frequency	Criteria
Travel time	410	67.7	32.3	196	Price
Comfort	223	36.8	63.2	383	Price
Comfort	148	24.4	75.6	458	Travel time
Waiting time	47	7.8	92.2	559	Travel time
Waiting time	412	68.0	32.0	194	Comfort

*Corresponding Author: Ahmet KARAKURT, karakurt@udel.edu

Demographic Information of Survey Participants:

The final section of the survey provides a detailed demographic profile of the respondents. Table 6. shows demographic results of the survey. Of the participants, 62.9% are male, while 37.1% are female. In terms of housing arrangements, 39.1% of respondents pay rent, whereas 60.9% own their homes.

Educational attainment among participants varies, with 48.3% holding a high school diploma, and only 0.8% having completed a doctoral program. This distribution highlights a predominance of secondary education among most respondents.

Employment status reveals that employees constitute the largest group of IZBAN users. Private sector employees lead with a rate of 54.8%, followed by students at 22.1%, and public sector employees at 9.7%. The survey also includes housewives, retirees, and individuals not currently engaged in work, with 1.7% of participants indicating that they do not work.

These demographic insights provide a comprehensive understanding of the IZBAN user base, reflecting a predominantly male, employed population with varying levels of educational attainment.

Table 6. Demographic results of the survey.

Questions		Frequency	Percent (%)
Gender	female	225	37.1
	male	381	62.9
Education	primary school	71	11.7
	high school	293	48.3
	vocational school	64	10.6
	bachelor	154	25.4
	master	19	3.1
	Ph.D.	5	.8
Occupation	public sector	59	9.7
	private sector	332	54.8
	student	134	22.1
	housewife	33	5.4
	retired	38	6.3
	non-worker	10	1.7

Age and Household Composition of Survey Participants:

Participants under the age of 18 were excluded from the study due to their likely dependency on family units, which could affect their financial independence and rental decisions. The majority of survey respondents are employees aged between 27 and 59, comprising 49.83% of the sample. In contrast, only 1.49% of participants are over the age of 65. The mean age of the participants is 32 years. Table 7. Indicates descriptive statistics of age and household size.

Regarding household size, the number of household members among participants ranges from 1 to 12. Notably, 31.7% of the respondents come from households with four members. The average household size is between 3 and 4 individuals. This distribution highlights a predominance of moderately sized households among the survey population.

These demographic details provide valuable context for understanding the socio-economic background of IZBAN users, which may influence their travel behaviors and preferences

Household Income and Rent Preferences:

Household income is a crucial factor in evaluating housing and transportation affordability, as many individuals consider their income when making purchasing decisions [29]. Accordingly, household income data was collected for this study to understand its impact on travel and rental preferences. Table 8. explains distribution of income, rent price and car ownership. Among the survey participants, 16.8% report a household income ranging from 4000 to 5000 TL, representing the highest proportion within all income brackets. The average monthly household income of participants is between 5000 and 6000 TL.

Table 7. Descriptive statistics of age and household size.

Variable	Minimum	Maximum	Mean	Std. Deviation	Variance
Age	18.00	76.00	31.9455	12.18109	148.379
Household size	1.00	12.00	3.4752	1.39606	1.949

Table 8. Distribution of income, rent price and car ownership.

Variable		Frequency	Percent (%)
Household income	below 2000TL	25	4.1
	2000-2999TL	79	13.0
	3000-3999 TL	100	16.5
	4000-4999 TL	102	16.8
	5000-5999 TL	82	13.5
	6000-6999 TL	69	11.4
	7000-7999 TL	37	6.1
	8000-8999 TL	26	4.3
	9000-9999 TL	36	5.9
	10.000-10.999	16	2.6
	11.000-11.999	6	1.0
	12.000 TL and	28	4.6
Rent cost	Below 500 TL	22	3.6
	500-744 TL	66	10.9
	750-999 TL	162	26.7
	1000-1249 TL	125	20.6
	1250-1499 TL	83	13.7
	1500-1749 TL	54	8.9
	1750-1999 TL	33	5.4
	2000-2249 TL	28	4.6
	2250-2499 TL	11	1.8
	2500-2749 TL	14	2.3
	2750-2999 TL	3	.5
	3000 TL and	5	.8
Car ownership	yes	256	42.2
	no	350	57.8

Regarding rental preferences, all participants were asked about their potential rent payments, even those currently living in their own homes. If they did not own a house, 26.7% indicated they would be willing to pay between 750 and 1000 TL for rent, while only 0.5% would pay between 2750 and 3000 TL. The mean rent preference is between 1000 and 1250 TL.

*Corresponding Author: Ahmet KARAKURT, karakurt@udel.edu

Car ownership is also a significant factor influencing travel behavior. The survey results show that 42.2% of participants own a car, whereas 57.8% do not. This indicates that a substantial proportion of respondents prefer using IZBAN over personal vehicles, underscoring the role of public transportation in their travel choices.

Distribution of Closest IZBAN Stops:

The distribution of the closest IZBAN stops among participants mirrors the patterns observed for departure stations. Table 9. indicates closest IZBAN stations to participants. The Şirinyer stop, with its high population density, accounts for the largest share of 16.2% of respondents. This is followed by the Halkapınar and Ciğli stops, which also show relatively high representation.

In contrast, stops such as Kuşçuburun, Pancar, and Tekeli have the lowest representation, each comprising only 0.2% of the total. Additionally, certain stops—including Havalimanı, Develi, Sağlık, Belevi, and Selçuk—were not selected by any respondents as their closest stop. This lack of selection for these stations likely reflects their lower accessibility or the limited residential areas surrounding them.

These findings highlight the influence of demographic factors and stop accessibility on the selection of IZBAN stations by passengers.

Table 9. Closest IZBAN stations to participants.

Station	Frequency	Percent (%)	Station	Frequency	Percent (%)
Aliağa	16	2.6	Salhane	4	.7
Biçerova	3	.5	Halkapınar	57	9.4
Hatundere	5	.8	Alsancak	15	2.5
Menemen	30	5.0	Hilal	30	5.0
Egekent 2	18	3.0	Kemer	10	1.7
Ulukent	8	1.3	Şirinyer	98	16.2
Egekent	20	3.3	Koşu	34	5.6
Ata Sanayi	16	2.6	Inkılap	18	3.0
Çiğli	36	5.9	Semt Garajı	16	2.6
Mavişehir	20	3.3	Esbaş	9	1.5
Şemikler	18	3.0	Gaziemir	9	1.5
Demirköprü	9	1.5	Sarnıç	7	1.2
Nergiz	16	2.6	Cumaovası	6	1.0
Karşıyaka	27	4.5	Tekeli	1	.2
Alaybey	9	1.5	Pancar	1	.2
Naldöken	4	.7	Kuşçuburun	1	.2
Turan	2	.3	Torbalı	7	1.2
Bayraklı	19	3.1	Tepeköy	7	1.2

The results of the t-test, as shown in Figure 2, indicate a significant difference between rural and non-rural station passenger counts, with a p-value of 0.0147, which is below the 0.05 threshold for statistical significance. The t-statistic of -2.5849 indicates that the rural group has a lower mean passenger count than the non-rural group. The degrees of freedom for the test are 31, reflecting the number of independent observations in the data. Cohen's d value of -1.0103 suggests a large effect size, meaning that the difference between the two groups is substantial in terms of standard deviations. Overall, the findings indicate that rural stations have fewer passengers than non-rural stations, and this difference is both statistically significant and practically meaningful.

The results presented in Table 10 highlight significant differences in travel behavior and preferences between urban and rural travelers. Urban commuters generally have shorter travel times (-0.234, p < .001), including reduced access time to the platform (-0.097, p = .016), waiting time (-0.088, p = .031), and in-vehicle time (-0.283, p < .001). They also live closer to IZBAN stations (-0.084, p = .038) and pay significantly higher rent (-0.454, p < .001). In terms of preferences, urban travelers prioritize comfort over waiting time (-0.117, p = .004) and are less willing to wait longer for cheaper tickets (-0.124, p = .002). Their commutes are typically shorter (-0.186, p < .001), and they mostly access IZBAN by walking or using public transport.
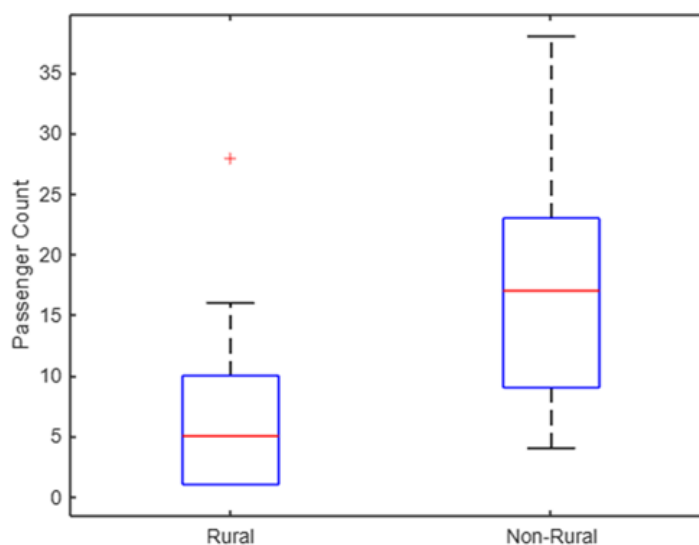
Figure 2. Comparison of passenger counts between rural and urban stations

Table 10. Correlation and Interpretation of Travel Variables Between Urban and Rural Travelers

Variable	Correlation	p-value	Interpretation
Mean travel time	-0.234	<.001	Urban travelers have shorter travel times compared to rural travelers.
Access time to platform	-0.097	0.016	Urban travelers take slightly less time to reach the platform.
Waiting time for train	-0.088	0.031	Urban travelers experience slightly shorter wait times.
In vehicle time	-0.283	<.001	Urban travelers spend significantly less time inside the vehicle.
Waiting time or ticket price	-0.124	0.002	Urban travelers are less willing to tolerate longer waiting times for cheaper tickets.
Comfort or waiting time	-0.117	0.004	Urban travelers value comfort more over waiting time.
Distance to IZBAN stop	-0.084	0.038	Urban travelers live closer to an IZBAN station.
Rent price	-0.454	<.001	Urban areas have significantly higher rental prices.
Travel distance	-0.186	<.001	Urban travelers commute shorter distances.
Access to IZBAN	0.082	0.043	Rural travelers are slightly more likely to access IZBAN using taxis or their own cars. Urban travelers are slightly more likely to access IZBAN by foot or public transportation.
Arrival station	0.142	<.001	Rural travelers are more likely to arrive at rural stations.
Comfort or travel time	0.281	<.001	Rural travelers are more willing to sacrifice travel time for comfort.

*Corresponding Author: Ahmet KARAKURT, karakurt@udel.edu

On the other hand, rural travelers depend more on taxis or private cars to reach IZBAN (0.082, p = .043). Their journeys frequently begin or end at rural stations (0.142, p < .001), and they demonstrate a stronger preference for comfort over shorter travel times (0.281, p < .001).

5. CONCLUSION AND DISCUSSIONS

This study aimed to investigate the differences in travel behavior between urban and rural passengers using the IZBAN public transportation system in Izmir. The scope of the research included an analysis of commuter patterns, access methods, and preferences across different geographic contexts. A quantitative methodology was employed, using survey data and statistical analyses (including t-tests and effect size measures) to identify significant behavioral differences between the two groups.

The results highlight a clear distinction in both commuter patterns and preferences, as urban travelers demonstrate shorter travel times, reduced access and waiting times, and closer proximity to IZBAN stations, contributing to their higher rental prices. These findings are statistically significant, with p-values consistently below 0.05 and Cohen's d values indicating large effect sizes, particularly for the differences between rural and non-rural stations (t-statistic of -2.5849, p = 0.0147). Urban travelers' tendency to prioritize comfort over waiting time and their general reliance on walking or public transportation further emphasize the ease of access and efficiency in urban environments. Conversely, rural travelers experience longer commutes, with more reliance on private cars and taxis for access to IZBAN, and they demonstrate a stronger preference for comfort over shorter travel times.

The study's analysis reveals that the proximity to public transportation and the quality of the commute influence residential choices, with urban dwellers facing higher rents due to the benefits of accessibility and convenience (p-value < 0.001). Rural commuters, on the other hand, are more likely to use private transport modes and are more willing to sacrifice travel time for comfort. These findings underline the crucial role that transit systems, such as IZBAN, play in shaping travel behavior and residential patterns, contributing to both commuter satisfaction and urban housing market dynamics.

By providing statistical evidence of the significant differences in travel behavior between rural and urban passengers, this research not only deepens our understanding of commuter preferences but also informs urban planners and policymakers seeking to optimize transportation systems and address housing affordability. The implications of these findings extend beyond Izmir, offering valuable lessons for other cities with similar characteristics, such as Paris, Istanbul, and Berlin, where the dynamics of public transportation are similarly intertwined with residential choices and urban development. The study paves the way for future research exploring how public transportation systems can be further integrated with urban planning to promote accessibility, affordability, and sustainability across diverse regions.

REFERENCES

[1]   J. Pucher and J. L. Renne, "Rural mobility and mode choice: Evidence from the 2001 National Household Travel Survey," *Transportation*, vol. 32, no. 2, pp. 165–186, 2005.

[2]   R. Cervero, "Built environments and mode choice: Toward a normative framework," *Transportation Research Part D: Transport and Environment*, vol. 7, no. 4, pp. 265–284, 2002.

[3]   D. G. Chatman, "Does TOD need the T?" *Journal of the American Planning Association*, vol. 79, no. 1, pp. 17–31, 2013.

[4]   I. Shergold and G. Parkhurst, "Transport-related social exclusion amongst older people in rural Southwest England and Wales," *Journal of Rural Studies*, vol. 28, no. 4, pp. 412–421, 2012.

[5]   E. Ferguson, "The rise and fall of the American carpool: 1970–1990," *Transportation*, vol. 24, no. 4, pp. 349–376, 1997.

[6]   R. Ewing and R. Cervero, "Travel and the built environment: A meta-analysis," *Journal of the American Planning Association*, vol. 76, no. 3, pp. 265–294, 2010.

[7]   S. Shaheen, A. Cohen, and I. Zohdy, *Shared mobility: Current practices and guiding principles*. Federal Highway Administration, 2015.

[8]   T. Litman, "Evaluating transportation equity," *World Transport Policy & Practice*, vol. 26, no. 2, pp. 10–25, 2020.

[9]   P. L. Mokhtarian and C. Chen, "TTB or not TTB, that is the question: A review and analysis of the empirical literature on travel time (and money) budgets," *Transportation Research Part A: Policy and Practice*, vol. 38, no. 9–10, pp. 643–675, 2004.

[10]   S. Nutley, "Monitoring rural travel behavior: A longitudinal study in Northern Ireland 1979–2001," *Journal of Transport Geography*, vol. 13, no. 3, pp. 247–263, 2005.

[11]   J. Hine and F. Mitchell, "Better for everyone? Travel experiences and transport exclusion," *Urban Studies*, vol. 38, no. 2, pp. 319–332, 2001.

[12]   D. Schrank, B. Eisele, T. Lomax and J. Bak, *Urban Mobility Scorecard*. Texas A&M Transportation Institute, 2015.

[13]   E. Blumenberg and A. E. Evans, "Planning for demographic diversity: The case of immigrants and public transit," *Journal of Public Transportation*, vol. 13, no. 2, pp. 1–19, 2010.

[14]   J. Molloy, T. Schatzmann, B. Schoeman, C. Tchervenkov, B. Hintermann, and K. W. Axhausen, "Observed impacts of the COVID-19 pandemic on travel behavior in Switzerland," *Transp. Res. Part A Policy Pract.*, vol. 145, pp. 1–14, 2021.

[15]   A. Field, *Discovering statistics using IBM SPSS statistics*, 4th ed. Sage, 2013.

[16]   J. Pallant, *SPSS survival manual: A step-by-step guide to data analysis using IBM SPSS*, 7th ed. McGraw-Hill Education, 2020.

[17]   IBM, *IBM SPSS Statistics 27 documentation*. IBM, 2021. [Online]. Available: https://www.ibm.com/support/knowledgecenter/SSLVMB_27.0.0

[18]   İzmir Büyükşehir Belediyesi, *İzmir Ulaşım Rehberi*. İzmir Büyükşehir Belediyesi Yayınları, 2020.

[19]   İzmir Banliyö Sistemi, *İzmir Banliyö Sistemi: Tarihçe ve Gelişim*, 2019. [Online]. Available: [URL]

[20]   İzmir Ulaşım A.Ş., *2019 Yılı İstatistik Raporu*. İzmir Ulaşım A.Ş., 2021.

[21]   P. G. Vries, *Sampling Theory for Forest Inventory: A teach-yourself course*, Berlin: Springer, 1986.

[22]   T. Yamane, *Statistics: An Introductory Analysis*, 2nd ed. New York: Harper and Row, 1967.

[23]   P. Newman and J. Kenworthy, *Sustainability and Cities: Overcoming Automobile Dependence*. Island Press, 1999.

[24]   R. Cervero and M. Duncan, "Which Reduces Vehicle Travel More: Jobs-Housing Balance or Retail-Housing Mixing?" *Journal of the American Planning Association*, vol. 72, no. 4, pp. 475–490, 2006.

[25]   L. Bertolini, *Planning for Sustainable Transport*. Routledge, 2013.

*Corresponding Author: Ahmet KARAKURT, karakurt@udel.edu

[26]   TUIK, *Turkish Statistical Institute: Population Statistics*, 2020. [Online]. Available: [TUIK website]

[27]   R. Cervero, The Transit Metropolis: A Global Inquiry, Washington, DC: Island Press, 1998.

[28]   R. Vickerman, "High-speed rail and regional development: the case of intermediate stations," *Journal of Transport Geography*, vol. 42, pp. 157-165, 2015.

[29]   CNT (Center for Neighborhood Technology), *The Housing and Transportation Affordability Index*, 2012. [Online]. Available: [CNT website]

DESIGN AND PERFORMANCE ANALYSIS OF AN X-BAND MMIC HPA WITH USING GAN-ON-SIC TECHNOLOGIES

* Mert KARAHAN [ID]

National Defence University, Turkish Military Academy, Electronics and Communication Engineering Department, Ankara, TÜRKİYE
mert.karahan@msu.edu.tr

Highlights

- Designed X-band MMIC HPA with 4 parallel HEMTs (8×125 μm) for 7.6–10.3 GHz.

- Achieved max small-signal gain of 11.7 dB with 0.59 dB/GHz gain flatness.

- CPW structure with GaN-on-SiC tech improves matching and eliminates via-holes.

- Simulated saturated power of 41.21 dBm and peak PAE of 39.81%.

- Unconditional stability verified for satellite, radar, and EW applications.

Graphical Abstract

(a)   (b)

(a) The layout of the X-band MMIC HPA and (b) Detailed Photography of the Fabricated X-band MMIC HPA

*Corresponding Author: Mert KARAHAN, mert.karahan@msu.edu.tr

DESIGN AND PERFORMANCE ANALYSIS OF AN X-BAND MMIC HPA WITH USING GAN-ON-SIC TECHNOLOGIES
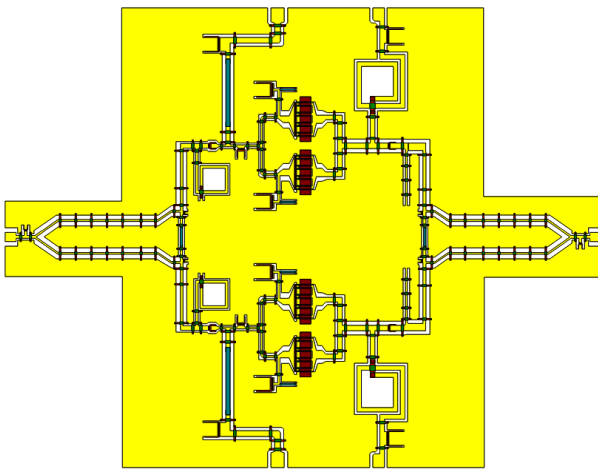
* Mert KARAHAN ⓘD

National Defence University, Turkish Military Academy, Electronics and Communication Engineering Department, Ankara, TÜRKİYE
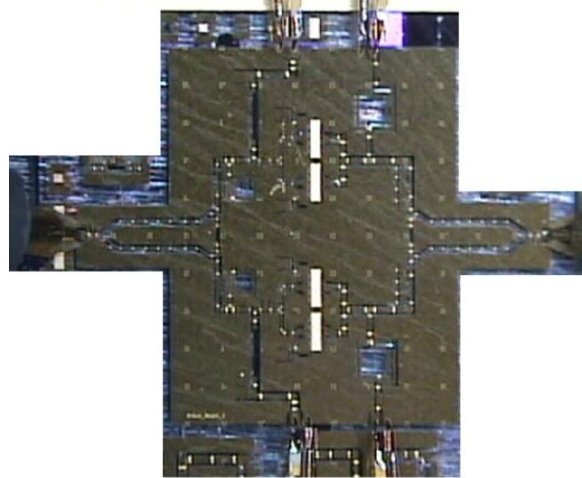mert.karahan@msu.edu.tr

ABSTRACT: This paper presents the design and performance analysis of an X-band monolithic microwave integrated circuit (MMIC) high-power amplifier (HPA) using four parallel high-electron-mobility transistors (HEMTs) with dimensions of 8×125 μm^2. Operating in the frequency range of 7.6–10.3 GHz, the proposed amplifier achieves a maximum small-signal gain of 11.7 dB with a gain flatness of 0.59 dB/GHz, ensuring consistent performance across the operating band. The coplanar waveguide (CPW) structure, implemented using Gallium Nitride (GaN) on a Silicon Carbide (SiC) process, eliminates the need for via-holes, reducing manufacturing complexity while improving impedance matching and compactness. Stability analyses confirm unconditional stability, with the K-factor and μ-factor exceeding 1 and Delta remaining below 1 across the entire operating frequency range. Power simulations demonstrate a saturated output power of 41.21 dBm and a peak power-added efficiency (PAE) of 39.81%, highlighting the amplifier's high efficiency and robust performance. The measurement results exhibit a remarkable consistency with the simulated data. These results demonstrate the suitability of the amplifier for demanding X-band applications including satellite communications, radar systems, and electronic warfare.

Keywords: X-band, High-Electron-Mobility Transistors (HEMTs), Monolithic Microwave Integrated Circuit (MMIC), High-Power Amplifier (HPA), Gallium Nitride (GaN) on a Silicon Carbide (SiC), Coplanar Waveguide (CPW)

1. INTRODUCTION

The frequency bands above 8 GHz include X, Ku, K, and Ka bands. The various applications where these bands are used to include radar systems, satellite communication, and electronic warfare. Excellent propagation characteristics with the ability to support high-resolution, long-range operations make these bands suitable for these applications. Significant growth has been witnessed in the field of satellite communication technologies using X-Band, especially in military applications [1]. This has driven great demand for high-power amplifiers in recent years, hence the development of devices such as MMIC technologies that meet this demand. There is a high affinity for MMICs especially for their compact size and easy integration, as well as superior performance. These integrated circuits are designed to operate particularly within microwave frequencies between 300 MHz and 300 GHz. In other words, such circuits can find wide use in some fields like microwave mixers, power amplifiers, low-noise amplifiers, and high-frequency switching. Moreover, the input and output ports are always matched to the standard impedance levels. In this respect, they have considerable ease of integration into the different systems [2].

A major breakthrough in technology related to MMICs for high-frequency amplifiers is brought about by the use of a high-electron-mobility transistor (HEMTs). Normally, this kind of transistor is famous for its high mobility of electrons, which promises faster operations and higher efficiency compared with conventional ones [3]. In other words, this means they are almost idealistic for improving further the efficiencies and output powers of HPA. Recent works also showed astonishing improvements in performance, particularly in aspects of output power and PAE [4]-[6]. For example, one such GaN-based HEMT amplifier achieved an output power of 40.06 dBm with a better PAE than 44.53% in the frequency

*Corresponding Author: Mert KARAHAN, mert.karahan@msu.edu.tr

range from 8.5 to 10.5 GHz [7], while another design was able to provide 47.5-48.7 dBm with a PAE of 40-45% over the frequency band from 8 to 12 GHz [8]. This indeed reflects the very outstanding performance of HEMTs, in particular when used in compact configurations. The use of Gallium Nitride on Silicon Carbide substrates will further enhance the performance of HPA. Major advantages related to GaN-on-SiC technology are high efficiency, wide bandgap material, high power density, very wide frequency range, and excellent integration capabilities; hence, it is preferred for modern high-frequency applications. Some designs achieve a 3-stage X-band GaN MMIC power amplifier using Qorvo's 150 nm GaN-on-SiC technology [9] and wideband millimeter-wave power amplifiers using the GaN-on-SiC technology, specifically for frequencies of 24.5-29 GHz [10].

The other technique employed to enhance performance and manufacturability is the CPW structure. In contrast to microstrip designs, CPW eliminates the need for through-holes, thus minimizing fabrication processes and costs. The design using CPW also helps improve impedance matching due to reduced parasitic effects. These, in turn, permit easy integration and compact layouts. Such as: [11] focuses a two-stage CPW based E/W-band amplifier MMICs fabricated in a 60 nm GaN-on-Si process with a maximum gain of 16 dB. In the two-stage X-band MMIC amplifier, CPW was used to align the optimum noise matching and input matching of each element; in the three-stage W-band amplifier, because CPW can be used, each stage is able to be put close to each other for increasing the bandwidth [12]. Along this line, a compact Wilkinson power divider was designed in [13], using gallium-nitride-based CPW integrated passive device technology. It thus follows that the employment of CPW technology can be employed to advance both the functionality and manufacturability of microwave-integrated circuits [14]-[16].

In this paper, a novel design for the X-band MMIC HPA is presented; this includes four parallel HEMTs, each $8×125$ μm^2 in size, to realize greater output power without detuning in operational frequency. A CPW structure is utilized that simplifies the manufacturing process, as it eliminates the need for via-holes, thereby enhancing the impedance matching. This HPA achieves a maximum small-signal gain of 11.7 dB with a flatness of 0.59 dB/GHz. Power simulations reveal a saturated output power of 41.21 dBm and peak PAE of 39.81%. The stability analysis confirms that the design is unconditionally stable across the entire frequency range, with both the K-factor and μ-factor exceeding 1 ($K > 1$, $\mu > 1$) and Delta remaining below 1. These results demonstrate the high efficiency and reliability of the amplifier. It aims to support advances in MMIC technology by presenting a study on the design of HPA for X-band applications.

(a)   (b)
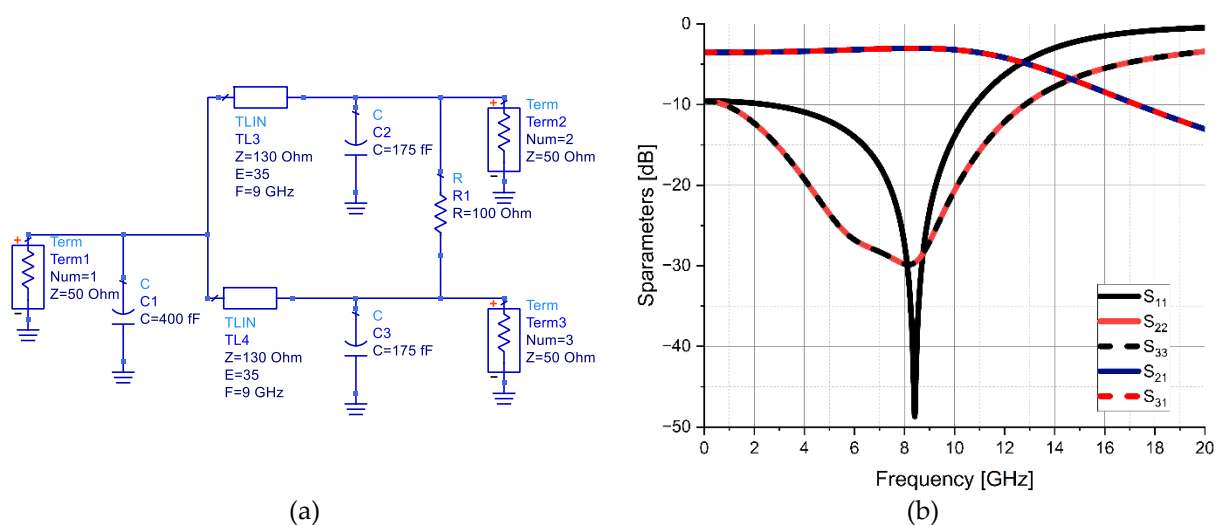
Figure 1. (a) Schematic and (b) S-parameter simulation results of the proposed compact WPD

2. DESIGN

In the design, commercially available Keysight's Advanced Design System (ADS) Momentum is employed, performing numerical analysis of electromagnetic problems using the Method of Moments (MoM). At the beginning of the design process, direct current (DC) and radio frequency (RF) analyses of HEMTs of different sizes are performed. The simulation results indicate that an HEMT with 8 fingers and a gate width of 125 μm is selected, operating under a bias condition of 28 V_{ds} and 240 mA for a single transistor. To increase the output power, the single MMIC HPA comprises two parallel HEMTs. Additionally, two identical Wilkinson power dividers are used for combining the two MMIC HPAs in proposed design.

The traditional WPD design consists of two $\lambda/4$ transmission lines and an isolation resistor (100 Ω) between output ports. However, $\lambda/4$ transmission lines become longer at lower frequencies. To minimize the traditional WPD, $\lambda/4$ transmission lines are replaced with a shunt capacitor, a series inductor, and another shunt capacitor, known as the π-type equivalent circuit method. As shown in Figure 1(a), the proposed Wilkinson power divider is designed using a shunt capacitor of 400 fF, a serially connected transmission line with a characteristic impedance of 130 Ω and an electrical length of 35°, and shunt capacitors of 175 fF. The TLIN impedance (130 Ω) was selected to match the even-mode impedance requirements of the divider, while the 35° electrical length (corresponding to ~$\lambda/8$ at 8.95 GHz) minimizes phase distortion. Shunt capacitors (400 fF/175 fF) were optimized via harmonic balance simulations in ADS Momentum to compensate for parasitic inductances and achieve broadband matching. Additionally, an isolation resistor of 100 Ω is placed between the output ports to maintain isolation and ensure proper power division.

In the S-parameter simulation results of the miniaturized WPD, it is observed that the input return loss (S_{11}) is better than -12 dB within the frequency range of 7.6-10.3 GHz. Additionally, the output return losses (S_{22} and S_{33}) are better than -19 dB in the same frequency range. The transmission coefficients (S_{21} and S_{31}) are less than -3.2 dB throughout the 7.6-10.3 GHz bandwidth. Figure 1(b) illustrates these results.
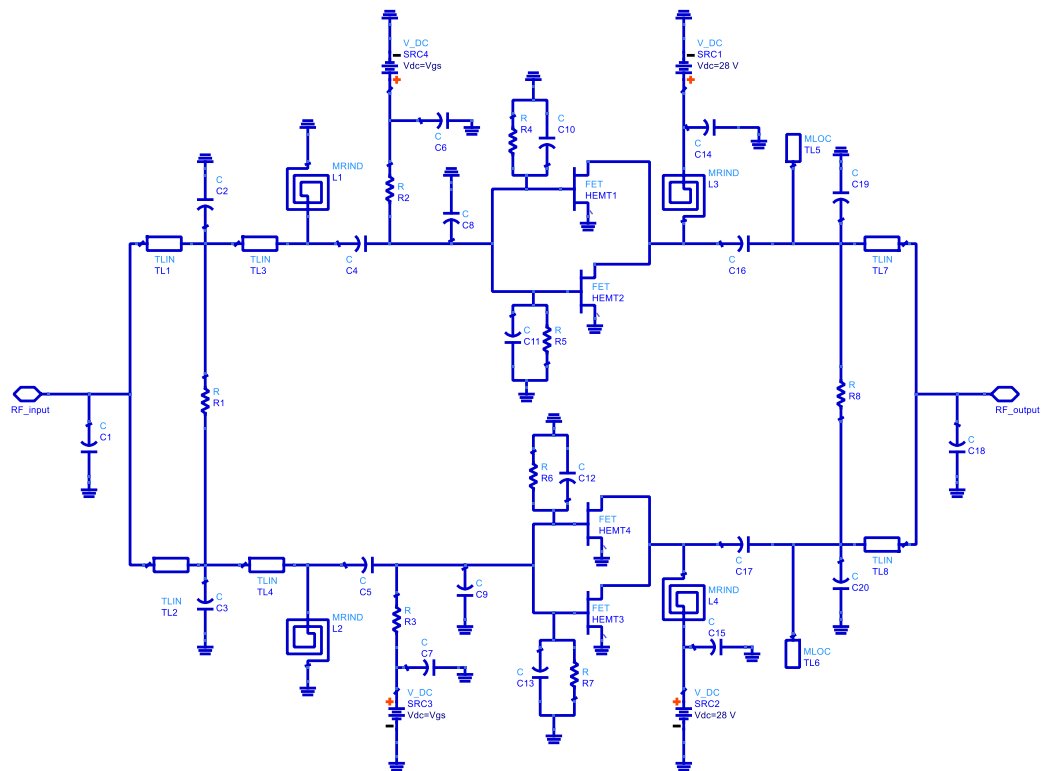
Figure 2. The Schematic of the X-band MMIC HPA

In the schematic depicted in Figure 2, ideal lumped elements are used in the design. Two WPDs are positioned at the input and output ports of the MMIC HPA to split and combine the RF signals without any phase difference. The design includes two parallel MMIC HPAs, each consisting of two 8×125 μm^2 HEMTs, resulting in a total of four 8×125 μm^2 HEMTs. To prevent DC flow through the RF input and output ports, serially connected DC block capacitors (C_4, C_5, C_{16}, and C_{17}) are included. The drain bias line incorporates serially connected resistors (R_2, R_3) to improve stability, while shunt capacitors (C_6, C_7) are added to the gate bias line to prevent undesired DC oscillations. Spiral inductors (L_3, L_4) are used in the drain bias line as choke inductors to block the RF signal flow into the DC supplies. Furthermore, parallel RC networks (R_4C_{10}, R_6C_{12}) are shunt-connected at the RF input ports of the transistors to enhance circuit stability. This configuration ensures the reliable and efficient operation of the amplifier.
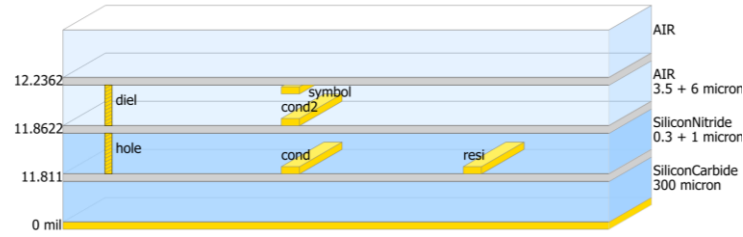
Figure 3. GaN on SiC MMIC technology

After the initial schematic design, the lumped elements are implemented using the GaN-on-SiC process, which features a dielectric constant of 9.6 and a thickness of 300 μm. CPW technology is employed to avoid the expensive and complex via-hole processes. The design includes four metallization layers: underpass (cond), second metal layer (cond2), Nickel Chrome (NiCr) resistor (resi), and airbridge metals (symbol), as illustrated in Figure 3. In the layout design, 2nd metal layer is utilized to carry both RF and DC signals. On the other hand, airbridge structure is utilized cross over the 2nd metal layer for electrical conductivity. To ensure the electrical conductivity of the ground planes, they are connected using an underpass metal at intervals of less than $\lambda/24$, where λ is the guided wavelength at the center frequency (8.95 GHz). This spacing ($\lambda/24 \approx 0.6$ mm for $\varepsilon_{eff} \approx 6.7$) was chosen to suppress parasitic resonances while maintaining a compact layout. The value derives from $\lambda = c / (f \sqrt{\varepsilon_{eff}})$, where c is the speed of light and ε_{eff} is the effective dielectric constant of the GaN-on-SiC CPW structure.

| (a) | (b) |
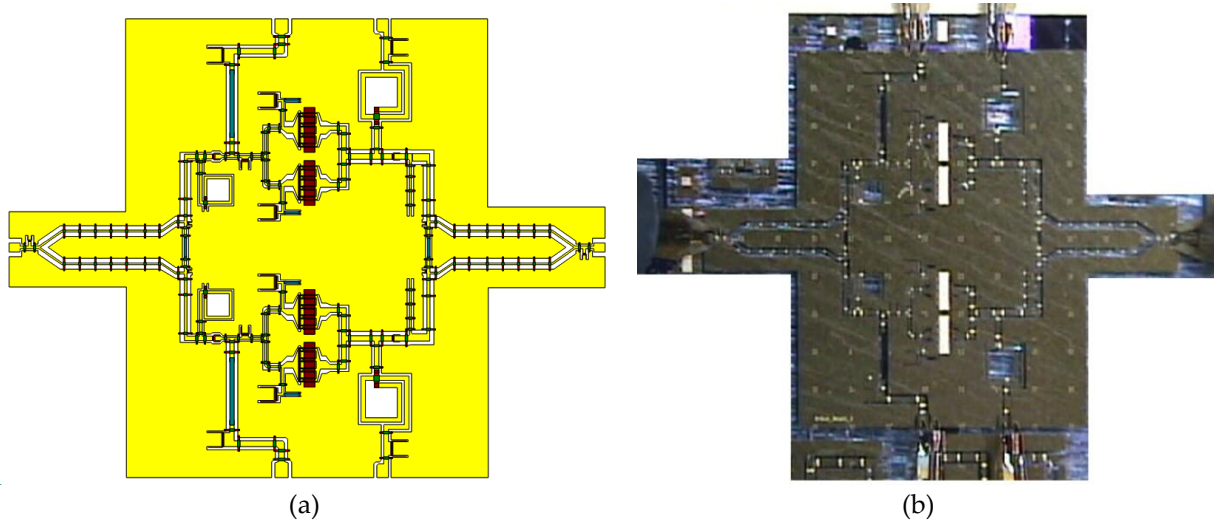
Figure 4. (a) The Layout of the X-band MMIC HPA and (b) Detailed Photography of the Fabricated X-Band MMIC HPA

The final design of the X-band MMIC HPA incorporates four parallel HEMTs, each with dimensions of 8×125 μm^2. These transistors operate with a 28 V_{ds} bias, resulting in a total drain current of 960 mA and

a DC power dissipation of 26.88 W. The HEMTs are chosen because of their high efficiency and performance at microwave frequencies. The design uses coplanar waveguide (CPW) technology, avoiding the need for costly via holes by placing the signal line and ground plane on the same layer. This approach results in a compact layout. To enhance circuit stability, the gate bias is fed through serially connected Nickel Chrome (NiCr) resistors, while shunt capacitors are used in both the gate and drain bias lines to suppress unwanted oscillations. Spiral inductors are employed in the drain bias line as choke inductors to block RF signals from reaching the DC supply. Additionally, serially connected DC block capacitors are placed at the input and output of each MMIC HPA to prevent DC flow through the RF paths. Small-value shunt capacitors are implemented using short stubs for compactness. The layout of the X-band MMIC HPA, showing these design elements, is presented in Figure 4(a).

(a)

(b)

(c)
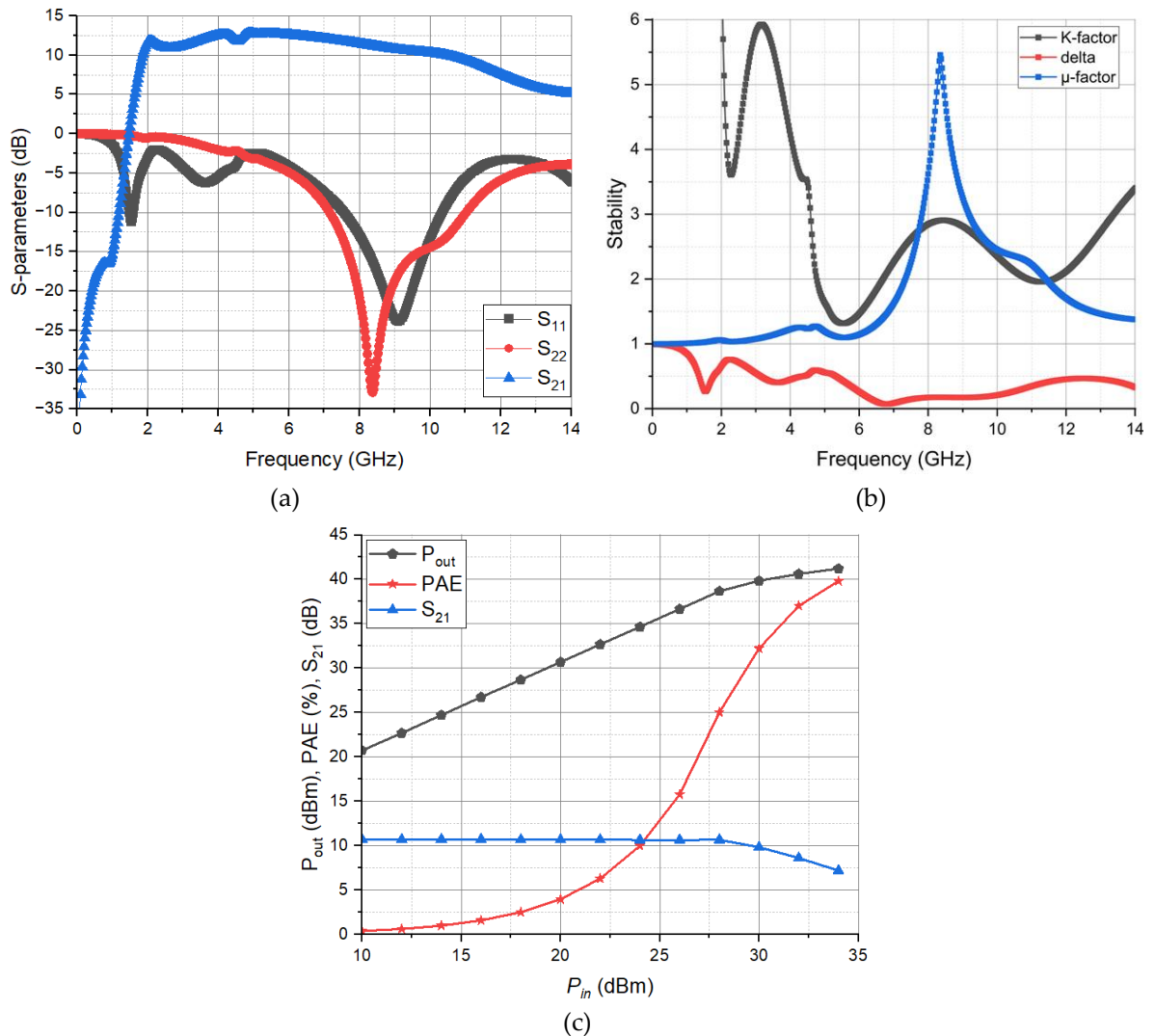
Figure 5. Simulation Results of the Proposed X-band MMIC HPA (a) S-parameter, (b) Stability, and (c) Power Simulation

3. ANALYSES AND DISCUSSION

As Figure 5(a) is analyzed, the following conclusions are drawn. The forward gain (S_{21}) shows that the amplifier achieves a maximum small-signal gain of 11.7 dB and a minimum gain of 10.1 dB, resulting in a gain flatness of 0.59 dB/GHz within operating frequency range 7.6 - 10.3 GHz. This flatness indicates minimal gain variation across the operating frequency range, ensuring consistent performance for broadband applications. The input reflection coefficient (S_{11}) reaches a minimum value of -23.5 dB near

the center of the operating frequency 7.6 - 10.3 GHz, indicating good impedance matching and minimal signal reflection at the input port. As to the output reflection coefficient (S_{22}), a similar trend to S_{11} is observed, with a minimum value approaching -20 dB near the center of the operating band. This signifies effective output matching, which is critical for maintaining high power transfer efficiency and minimizing signal distortion. Moreover, in Figure 5(b), it is observed that for both K-stability and μ-stability analyses, the proposed MMIC HPA is unconditionally stable. Furthermore, CPW structure contributes to the observed impedance matching by eliminating parasitic effects typically associated with via-holes, thus improving matching performance and reduces manufacturing costs by eliminating the need for costly via-holes to connect the ground plane to the substrate.

Table 1. Summary of Key Performance Metrics

Parameter	Value	Remarks
Frequency Bandwidth	7.6–10.3 GHz	Wideband X-band operation
Input Power	-10 dBm	Linear operation at low input power
Forward Gain	11.7 dB (max), 10.1 dB (min)	Stable gain with 0.59 dB/GHz flatness
Input Reflection Coefficient	-10 dB	Good input matching
Output Reflection Coefficient	-14 dB	Superior output matching
Power-Added Efficiency (PAE)	39.81%	High efficiency near saturation
Saturated Output Power, P_3dB	41.21 dBm	High output power for X-band applications
Power Dissipation, P_{dis}	26.88 W	Consistent with high-power operation
Stability	Unconditionally stable	Stable across all conditions and frequencies

The Figure 5(c) presents the relationships between input power (P_{in}), output power (P_{out}), power-added efficiency (PAE), and forward gain (S_{21}). P_{out} demonstrates a linear increase with P_{in} until approximately 25 dBm, then starts to saturate and reaches a value of about 41.21 dBm, indicating the maximum output power capability of the amplifier. PAE increases rapidly with input power, peaking at approximately 39.81% near the saturation point. This high PAE value highlights the efficiency of the proposed design. At lower input power levels ($P_{in} <$ 20 dBm), the PAE is relatively low, which is typical for amplifiers as they operate with reduced efficiency in the linear region. S_{21} represents the amplifier's small-signal gain, remaining relatively constant at approximately 10 dB for input power levels below P_{in} ≈ 28 dBm. Beyond this point, S_{21} begins to degrade and the amplifier enters the non-linear region, characterized by gain compression and power saturation. The parameters and analysis results for the X-Band MMIC High Power Amplifier (HPA) design are summarized in Table-1.

The amplifier was fabricated via standard GaN-on-SiC processing: optical lithography defined the CPW (Ti/Al/Ni/Au metallization), followed by HEMT formation (mesa isolation, ohmic contacts, T-gates). NiCr resistors, MIM capacitors, and airbridges were integrated before final dicing. The electrical performance of the proposed structure was thoroughly evaluated using an Agilent Technologies E8364B PNA Network Analyzer (covering a frequency range of 10 MHz to 50 GHz) and a Cascade MPS150 RF probe station. RF signals were delivered through GGB RF probes, while DC biases were applied using multi-contact DC probes. The prototype, depicted in Figure 4(b), was tested to validate its operational capabilities over the intended frequency range. The results of the measurements, illustrated in Figures 6, demonstrate a high level of agreement with the simulated data, affirming the accuracy and robustness of the design methodology. Specifically, the measured small-signal gain, gain flatness, P_{out}, and PAE closely match the simulation results. The consistency between simulation and experimental outcomes confirms the reliability of the proposed design, emphasizing its potential for practical X-band applications within operating frequency range 7.6 - 10.3 GHz.
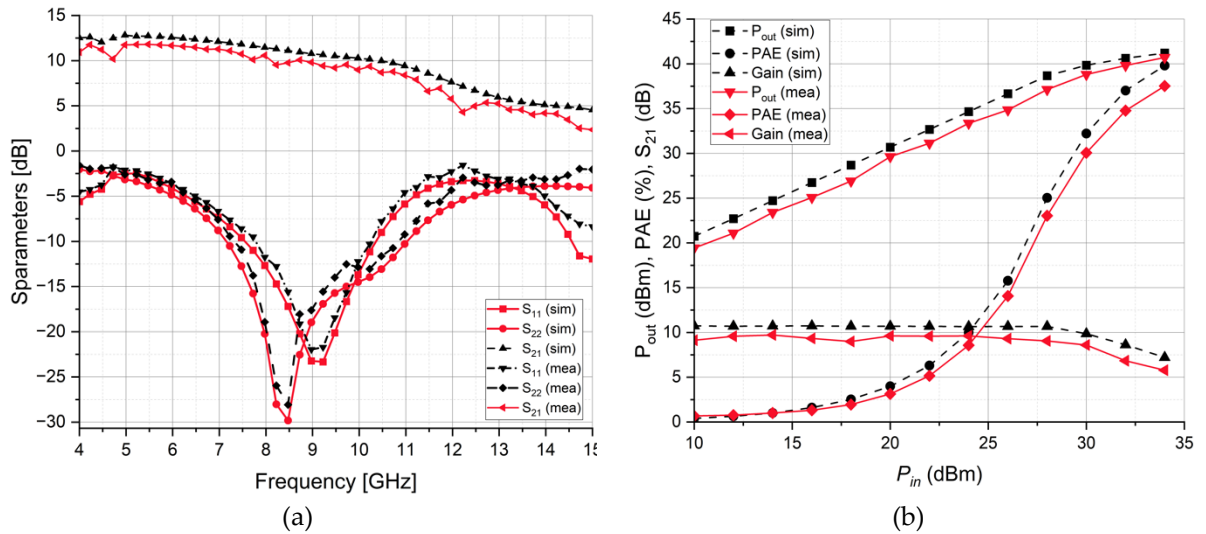
Figure 6. Simulation vs. Measurement Results For (a) S-Parameters and (b) Power Characteristics

4. CONCLUSIONS

The proposed X-band MMIC HPA, designed using GaN-on-SiC technology, incorporates four parallel HEMTs with dimensions of 8×125 μm^2. Operating over the 7.6–10.3 GHz frequency range, the amplifier achieves unconditional stability, as confirmed by K-factor and μ-factor values exceeding 1 and Delta remaining below 1 across the entire band. Utilizing the GaN-on-SiC process enables the implementation of a coplanar waveguide (CPW) structure, eliminating the need for via-holes, thus simplifying the manufacturing process and enhancing both impedance matching and compactness. Power simulations reveal that the amplifier delivers a saturated output power of 41.21 dBm and achieves a peak power-added efficiency (PAE) of 39.81%, along with a small-signal gain of 11.7 dB with a flatness of 0.59 dB/GHz. The measurement results are in agreement with the simulation results. It is observed that this amplifier design shows a well-balanced optimization in terms of linearity, power handling, and efficiency, as demonstrated by its gain compression characteristics and the efficiency peak observed near saturation. These features position the design as a robust solution for challenging X-band applications including radar, satellite communications, and electronic warfare systems.

Declaration of Ethical Standards

The author confirms adherence to all ethical standards, including those related to authorship, proper citation, accurate data reporting, and the publication of original research.

Declaration of Competing Interest

The author states that there are no financial or personal relationships that could have influenced the findings presented in this paper.

Funding / Acknowledgements

The author confirms that no funding or research grants were received during the preparation, research, or writing process of this article.

Data Availability

The data supporting the findings of this study will be provided upon request.

REFERENCES

[1]   G. O. Arican and N. Akçam, "Design of a Low Cost X-Band LNA with Sub-1-dB NF for SATCOM Applications," *Gazi University Journal of Science*, vol. 36, no. 1, pp. 208–218, Mar. 2023.

[2]   H. Hausman, *Microwave power amplifier design with MMIC modules*. Artech House microwave library. Boston London: Artech House, 2018.

[3]   G. O. Arican, N. Akcam, and E. Yazgan, "Ku-band GaAs mHEMT MMIC and RF front-end module for space applications," *Micro & Optical Tech Letters*, vol. 63, no. 2, pp. 417–425, Feb. 2021.

[4]   H. Jin, F. Yang, H. Tao, W. Xiao, Y. Zhou, and L. Cai, "A *Ku* -Band 100-W High-Power Amplifier MMIC Using 0.2-μm GaN Technology," *IEEE Microw. Wireless Tech. Lett.*, vol. 34, no. 1, pp. 80–83, Jan. 2024.

[5]   J. Kamioka, Y. Tarui, Y. Kamo, and S. Shinjo, "54% PAE, 70-W *X* -Band GaN MMIC Power Amplifier With Individual Source via Structure," *IEEE Microw. Wireless Compon. Lett.*, vol. 30, no. 12, pp. 1149–1152, Dec. 2020.

[6]   Y. S. Noh and I. B. Yom, "A Linear GaN High Power Amplifier MMIC for Ka-Band Satellite Communications," *IEEE Microw. Wireless Compon. Lett.*, vol. 26, no. 8, pp. 619–621, Aug. 2016.

[7]   G. O. Arıcan and B. A. Yılmaz, "A 10-W GaN on SiC CPW MMIC High-Power Amplifier With 44.53% PAE for X-Band AESA Radar Applications," *ELECTRICA*, vol. 24, no. 3, pp. 780–788, Nov. 2024.

[8]   H.-Q. Tao, W. Hong, B. Zhang, and X.-M. Yu, "A Compact 60W X-Band GaN HEMT Power Amplifier MMIC," *IEEE Microw. Wireless Compon. Lett.*, vol. 27, no. 1, pp. 73–75, Jan. 2017.

[9]   B. Zhao, "A 3-Stage, 51% PAE, High Linearity, 70W X-Band GaN MMIC Power Amplifier," in *2024 IEEE Texas Symposium on Wireless and Microwave Circuits and Systems (WMCS)*, Waco, TX, USA: IEEE, Apr. 2024, pp. 1–5.

[10] M. van Heijningen *et al.*, "Ka-band AlGaN/GaN HEMT high power and driver amplifier MMICs," presented at the European Gallium Arsenide and Other Semiconductor Application Symposium, Paris, France: GAAS 2005, pp. 237–240.

[11] B. Cimbili, C. Friesicke, F. V. Raay, S. Wagner, M. Bao, and R. Quay, "2.6- and 4-W *E* -Band GaN Power Amplifiers With a Peak Efficiency of 22% and 15.3%," *IEEE Microw. Wireless Tech. Lett.*, vol. 33, no. 6, pp. 847–850, Jun. 2023.

[12] W. Deal, "Coplanar waveguide basics for MMIC and PCB design," *IEEE Microwave*, vol. 9, no. 4, pp. 120–133, Aug. 2008.

[13] G. O. Arıcan, "Design and fabrication of compact Wilkinson power divider on gallium nitride coplanar technology", *NOHU J. Eng. Sci.*, vol. 12, no. 1, pp. 113–118, Nov. 2022.

[14] B. Dökmetaş and M. Karahan, "Miniaturized GaN-Based Wilkinson Power Divider for X-Band Communication Systems", *Osmaniye Korkut Ata University Journal of The Institute of Science and Techno*, vol. 8, no. 1, pp. 432–444, Jan. 2025.

[15] J. Jeong et al., "X-band quasi class-F HPA MMIC using DynaFET GaN HEMT modelling," Electronics Letters, vol. 60, no. 10, p. e13221, May 2024.

[16] S.-H. Han and D.-W. Kim, "Robust Ku-Band GaN Low-Noise Amplifier MMIC," *J. Electromagn. Eng. Sci*, vol. 24, no. 2, pp. 170–177, Mar. 2024.

DEVELOPMENT OF A TERNARY LEVELS EMOTION CLASSIFICATION MODEL UTILIZING ELECTROENCEPHALOGRAPHY DATA SET

[1, *] **Hatice OKUMUS** [iD], [2] **Ebru ERGUN** [iD]

[1] *Karadeniz Technical University, Electrical and Electronics Engineering Department, Trabzon, TÜRKİYE*
[2] *Recep Tayyip Erdogan University, Electrical and Electronics Engineering Department, Rize, TÜRKİYE*
[1] haticeokumus@ktu.edu.tr, [2] ebru.yavuz@erdogan.edu.tr

Highlights

- This study segments EEG data and extracts features via Hilbert transform for classification.

- Feed-forward neural networks classify valence and arousal levels with high accuracy.

- EEG feature sets achieve 99.70% arousal and 98.60% valence accuracy in emotion recognition.

Graphical Abstract

Flowchart of the proposed method

*Corresponding Author: Hatice OKUMUS, haticeokumus@ktu.edu.tr

DEVELOPMENT OF A TERNARY LEVELS EMOTION CLASSIFICATION MODEL UTILIZING ELECTROENCEPHALOGRAPHY DATA SET

1, * Hatice OKUMUS [ID], **2 Ebru ERGUN** [ID]

1 Karadeniz Technical University, Electrical and Electronics Engineering Department, Trabzon, TÜRKİYE
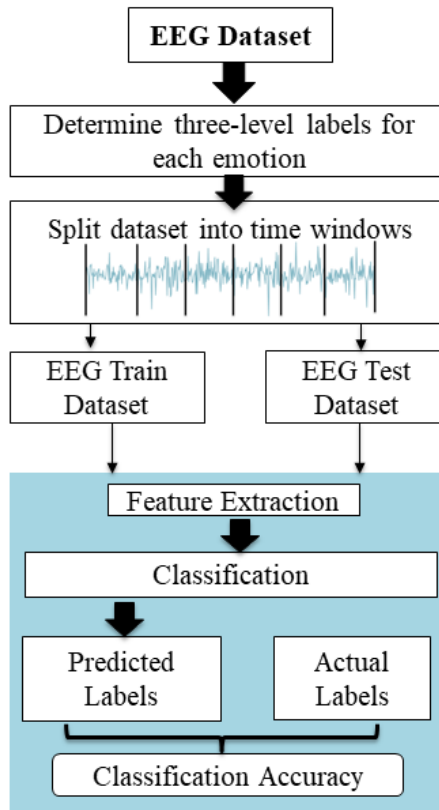*2 Recep Tayyip Erdogan University, Electrical and Electronics Engineering Department, Rize, TÜRKİYE*
1 haticeokumus@ktu.edu.tr, 2 ebru.yavuz@erdogan.edu.tr

ABSTRACT: Electroencephalogram (EEG)-based emotion recognition has gained increasing attention due to its potential in objectively assessing affective states. However, many existing studies rely on limited datasets and focus on binary classification or narrow feature sets, limiting the granularity and generalizability of their findings. To address these challenges, this study explores a ternary classification framework for both valence and arousal dimensions—dividing each into low, medium, and high levels—to capture a broader spectrum of emotional responses. EEG recordings from ten randomly selected participants in the DEAP dataset were used. Each 60-second EEG segment was divided into six non-overlapping windows of 10 seconds to preserve temporal stability and extract reliable features. The Hilbert Transform was applied to compute instantaneous amplitude and phase information, enabling the detection of subtle variations in emotional states. These features were then classified using a feed-forward neural network. The proposed approach achieved impressive classification accuracies of 99.13% for arousal and 99.50% for valence, demonstrating its effectiveness in recognizing multi-level emotional states. By moving beyond binary labels and leveraging time-frequency domain features, this study contributes to the development of more refined and responsive emotion recognition systems. These findings offer promising insights for real-world applications in affective computing, mental health monitoring, and adaptive human-computer interaction, where precise emotion modeling plays a critical role.

Keywords: Electroencephalography, Emotion, Feature Extraction, Hilbert Transform, Multi-Classification, Signal Processing

1. INTRODUCTION

Emotion refers to the internal affective state, mood, or subjective experience of an individual [1]. These emotional states emerge as responses to external stimuli such as events, social interactions, or personal thoughts, and are typically accompanied by physiological, cognitive, and behavioral reactions. A wide variety of emotions—ranging from happiness, sadness, fear, anger, and surprise to love, hatred, curiosity, and disappointment—constitute essential components of human nature. These emotional responses play a significant role in daily life, influencing interpersonal relationships, decision-making processes, learning, memory, and overall behavior. In recent years, there has been a growing interest in recognizing and analyzing these emotional states, particularly for applications in human-machine interfaces, which aim to create seamless interaction channels between humans and intelligent systems [2]. Conventional emotion recognition methods often rely on external cues such as voice intonation, facial expressions, or posture. However, such approaches are vulnerable to intentional suppression or masking of emotions, potentially leading to inaccurate interpretations. To overcome this limitation, researchers have turned to physiological signals, including electrooculogram, respiration patterns, galvanic skin response, and especially electroencephalography (EEG), which captures the brain's electrical activity in real time [3]. EEG signals, which reflect neural communication via fluctuations in voltage across the scalp, are particularly promising for emotion recognition, as they originate directly from the central nervous system—the primary control center of the body [4]. These signals provide a high temporal resolution,

*Corresponding Author: Hatice OKUMUS, haticeokumus@ktu.edu.tr

enabling fine-grained analysis of dynamic emotional processes.

The growing interest in EEG-based emotion recognition has led to the development and use of various publicly available EEG datasets. One of the most widely used is the SEED dataset [5,6], which has served as the foundation for numerous studies. Li et al., for instance, proposed a hierarchical convolutional neural network (HCNN) using differential entropy features arranged in 2D maps to maintain spatial electrode topology, achieving a classification accuracy of 86.20% [7]. Asghar et al. adopted a deep neural network based on the AlexNet architecture and spectrogram preprocessing, obtaining 93.80% accuracy with an SVM classifier [8]. Similarly, Cheah et al. applied ResNet18 to raw EEG signals, yielding a 93.42% accuracy in classifying emotions into three categories [9]. Building on these approaches, Xiao et al. developed a four-dimensional attention-based neural network (4D-aNN) that dynamically weighted brain regions and frequency bands, achieving 95.39% accuracy [10]. In another study, Jin et al. examined both power spectral density (PSD) and differential entropy (DE) features, reporting accuracies of 85.24% and 94.72%, respectively, using the SEED dataset [11].

In addition to SEED, the DREAMER [12] and DEAP [13] datasets have been widely adopted. Song et al. reported average recognition accuracies of 90.4% in subject-dependent and 79.95% in subject-independent settings on SEED, while achieving 86.23%, 84.54%, and 85.02% for valence, arousal, and dominance respectively on DREAMER [14]. Zhang et al. proposed a Graph Convolutional Backbone (GCB) network with a Broad Learning System (BLS), which achieved 94.24% accuracy using DE features on SEED [15]. Li et al. introduced a spatiotemporal demographic network model employing adaptive time windows and GRU layers, achieving 68.28% and 71.48% accuracy for valence and arousal on the DEAP dataset [16]. Lin et al. developed a Dual-Scale EEG Mixer (DSE-Mixer) combining brain region and electrode mixing mechanisms, achieving over 95% accuracy in binary classifications, and between 89.77% and 93.35% in four-class tasks [17]. Furthermore, Gao et al. employed a CNN architecture optimized using a novel GPSO algorithm for hyperparameter tuning, achieving an average accuracy of 92.00% [18].

Despite the notable progress in the field, most existing studies have focused on binary or quadrant-based emotional categorizations, limiting their sensitivity to intermediate affective states. To address this, the current study proposes a ternary-level classification approach for both valence and arousal dimensions, offering a more granular understanding of emotion dynamics. EEG data from ten randomly selected participants in the DEAP dataset were analyzed. The recordings were segmented into time windows, and features were extracted using the Hilbert Transform (HT), which captures instantaneous signal characteristics such as amplitude and phase. These features were then input into a feed-forward neural network (FNN) for classification. To provide a comprehensive performance comparison, additional classifiers—k-nearest neighbors (k-NN) and random forest (RF)—were also employed. All experimental procedures were conducted using MATLAB 2023.

The proposed framework achieved impressive results, with mean classification accuracies of 99.13% for arousal and 99.50% for valence, significantly outperforming many existing approaches. These findings underscore the potential of ternary-level EEG-based emotion recognition systems to enhance affective computing and enable more adaptive, responsive human-machine interactions.

The rest of this paper is organized as follows: Section 2 outlines the experimental design, methodology, and data preprocessing steps. Section 3 presents the experimental results. Section 4 provides a detailed comparison with existing classification methods and discusses the implications of the findings. Finally, Section 5 offers concluding remarks and directions for future research.

2. MATERIAL AND METHODS

2.1. Data Description

Sander Koelstra et al. [13] developed a multimodal dataset called DEAP, which includes EEG and physiological signals. This dataset, derived from recordings of 32 participants aged between 19 and 37 years, maintained a balanced male-female ratio. In this study, a subset of ten participants was randomly selected from the original pool of 32 individuals included in the DEAP dataset. The primary objective of

this selection was to conduct a controlled yet representative investigation into multi-level emotion classification. By narrowing the focus to ten subjects, a balanced trade-off was achieved between computational feasibility and data variability. Furthermore, the emotion ratings provided by each participant were used to label their responses into three discrete classes—low, medium, and high—based on their individual valence and arousal scores. This ternary classification strategy was chosen to reflect the complexity of human emotional states beyond binary schemes and to enable more nuanced modeling of affective patterns in EEG signals.

Each participant was exposed to 40 videos with emotional content, selected manually from a pool of 120 music videos with affective tags obtained from last.fm. The videos were selected using a web-based subjective emotion rating interface. All videos were 1 minute in length and contained music content. EEG data were recorded at a sampling rate of 512 Hz using 32 active AgCl electrodes according to the international 10-20 system shown in Figure 1. In addition, 13 peripheral physiological signals were recorded, including GSR, respiratory amplitude, skin temperature, electrocardiogram, blood volume by plethysmograph, electromyograms of the zygomatic and trapezius muscles, and electrooculography (EOG). The synchronization of EEG with emotion data began with the display of a fixation cross on the screen, with the participant being instructed to relax for 2 minutes. Each participant was then presented with 40 one-minute videos on a trial-by-trial basis, preceded by a 2-second progress screen and a 5-second fixation cross for relaxation. Due to the highly subjective nature of emotional transition states, participant ratings were used to mark induced emotions.

The processed EEG recordings in the DEAP dataset were down-sampled to 128 Hz, and eye blink artefacts were removed using blind source separation. A band-pass frequency filter from 4.0 to 45.0 Hz was applied, and the data were averaged to the common reference before being segmented into 60-second trials with a 3-second pre-trial baseline (from the 5-second baseline recording). Participants' ratings were provided separately for valence, arousal, and dominance. DEAP and SEED are the two most widely used publicly available EEG emotion datasets, both of which use audiovisual stimuli to elicit emotion. While the DEAP dataset has a larger number of EEG recordings and physiological signals, the SEED dataset has a higher spatial resolution of EEG recordings due to a larger number of electrodes. The SEED dataset used 15 different video clips with a maximum duration of 4 minutes, in contrast to the DEAP dataset which used 40 different 1-minute video clips. Furthermore, the SEED dataset used a categorical emotion model, while the DEAP dataset used a dimensional emotion model. The proposed method was only tested on the DEAP datasets.
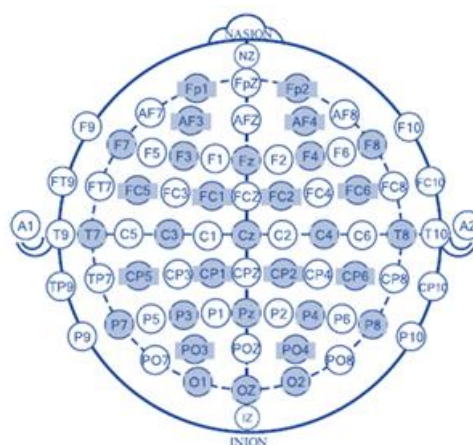

Figure 1. EEG electrode positions [19]

2.2. Methods

The proposed methodology comprises four distinct stages, each of which is integral to the comprehensive analysis of emotional responses. The general flowchart illustrating the relationship

between these stages is shown in Figure 2. First, a critical aspect is the establishment of three-level labels for each emotion, strategically segmenting the emotional spectrum into low, moderate and high intensity. This segmentation is crucial for the subsequent stages of the analysis process [20]. Following the careful categorization of emotions, the second step is to segment the data by applying a time window. This temporal segmentation of EEG signals is essential to capture nuanced fluctuations in emotional states over specific intervals. Temporal segmentation facilitates a granular examination of emotional dynamics, allowing for more detailed analysis. An example of temporal segmentation is shown in Figure 3.
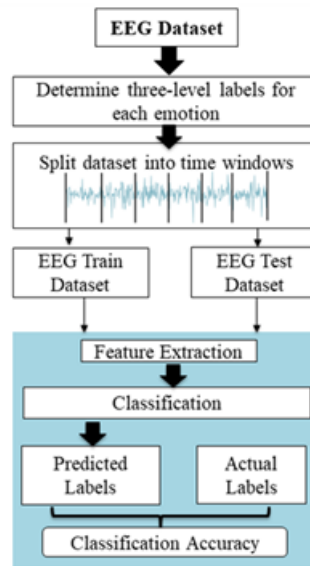
Figure 2. General flow chart of the methodology proposal

In this study, each 60-second EEG segment was divided into six non-overlapping windows of 10 seconds. The rationale behind selecting a 10-second window was to maintain a meaningful balance between signal stability and temporal resolution. Very short windows tend to reflect transient artifacts or momentary fluctuations that may not correspond to stable emotional states. Conversely, significantly longer windows may smooth out essential temporal variations, potentially diminishing the discriminative power of the extracted features. Therefore, a 10-second window was deemed optimal for preserving the integrity of emotional patterns while providing a sufficient number of samples for robust feature extraction and classification. This decision also ensured consistency across all participants and trials, which is essential for reliable performance evaluation.

Figure 3. Temporal segmentation of EEG signals

The third stage of the proposed method involves extracting relevant features from the segmented data. This step is crucial for identifying distinctive patterns and characteristics within the EEG signals that are indicative of different emotional intensities. Feature extraction acts as a bridge between the raw data and the subsequent classification process, ensuring that relevant information is used effectively. The final step is to classify the pre-processed data into discrete emotional classes. Specifically, EEG signals related to arousal and valence emotions are stratified into three distinct levels corresponding to low, moderate and high emotional intensity. The assignment of labels is derived from participants' ratings, in which each emotion is systematically evaluated. A meticulous approach is taken, whereby if individuals give a rating

within the range of 0-3, the label is designated as low; if the rating falls between 3-6, the label is classified as moderate; and if the rating extends from 6-9, the label is designated as high. It is important to emphasize that this categorization methodology is closely linked to the subjective ratings provided by the participants, reflecting the diverse range of emotional experiences and responses within the population studied. Through this multifaceted approach, the proposed method seeks to provide a nuanced and comprehensive understanding of emotional dynamics as manifested in EEG signals.

The EEG data under consideration were acquired from 32 channels, recorded at a sampling rate of 128 Hz, and each data segment had a duration of 60 seconds, resulting in a total of 1 trial. Expressing the data format as trial × number of channels × samples, the data size for the 60 second interval is 1×32×7680. For temporal analysis, the EEG data were then divided into 10 second windows. This temporal segmentation resulted in a total of 6 trials, with each trial having a data size of 6×32×1280. In the analysis pipeline, features essential for the subsequent classification process were extracted from the EEG signals using the HT method. The extracted features were then subjected to classification using three different algorithms, FNN, k-NN and RF. The use of multiple classification algorithms contributes to the robustness and reliability of the test results. In order to assess the performance of the classification models, all results were calculated by averaging the results after a 10-fold cross-validation. This approach ensures a comprehensive evaluation, taking into account variations in the dataset through multiple rounds of cross-validation. It is worth noting that the computational infrastructure used for these processes was a computer with a configuration of 16 GB RAM and a 2.92 GHz Intel Core i7 processor. This hardware configuration is essential to meet the computational demands of the feature extraction, classification and cross-validation processes, thus contributing to the accuracy and efficiency of the analyses performed in this study.

Furthermore, the continuous self-assessment scores for valence and arousal were discretized into three ordinal levels—low, medium, and high—using participant-specific thresholds. After this labeling process, the distribution of samples across the ternary classes was examined. While the resulting class frequencies were not perfectly balanced, no extreme skew was observed. To address potential bias caused by moderate class imbalance, a 10-fold cross-validation strategy was adopted, ensuring that each fold retained a representative distribution of class labels. This procedure enhances the model's robustness by exposing it to diverse subsets of the data and mitigating the risk of overfitting to overrepresented classes.

2.2.1. Feature Extraction Using Hilbert Transform

Data mining and machine learning rely heavily on feature extraction, a technique that is integral to discovering and extracting attributes from data sets to improve their relevance and usability [21]. Essentially, the aim is to transform complex or high-dimensional data into low-dimensional, meaningful and unambiguous features. In the context of this study, feature extraction was performed using HT. In the field of EEG signal processing, the extraction of significant features is of paramount importance in revealing underlying patterns and information essential for subsequent analysis [22]. The HT proves to be a crucial tool in this regard. Particularly being adept at analyzing time-varying signals, the HT facilitates the extraction of amplitude and phase information from complex signals such as EEG data. By applying the HT to EEG recordings, researchers can capture dynamic changes in brain activity and identify temporal patterns associated with specific cognitive or emotional states. Incorporating the HT into feature extraction improves our understanding of the temporal dynamics inherent in EEG signals. This in turn facilitates the development of robust models for various tasks, including but not limited to emotion recognition, cognitive state classification, and diagnosis of neurological disorders.

The HT, introduced by David Hilbert in the early 20th century, has proven to be a versatile mathematical operation with applications spanning diverse fields such as telecommunications, physics, and biomedical signal processing [23]. Its efficacy is particularly notable in the analysis of time-varying signals, where the representation of frequency as a rate of change in phase over time facilitates the investigation of non-stationary signals [22]. In the context of raw data, which inherently encompasses a multitude of frequencies evolving over time, the HT simplifies the representation of these frequencies in

the frequency domain. Notably, it introduces a $\pm90°$ phase shift based on the sign of each frequency component within a function. In the case of this study, the EEG signal, denoted as $k(l)$, undergoes HT processing. This involves convolving the signal with $h(t) = 1/\pi l$, as outlined in Equation 1. The impulse response of $h(l)$ is detailed in Equation 2.

$$H\{k(t)\} = \hat{k}(l) = k(l) * \frac{1}{\pi l} = \frac{1}{\pi} \int_{-\infty}^{\infty} \frac{k(\tau)}{l-\tau} d\tau \tag{1}$$

$$H(\omega) = F[h(l)] = -i * sign(\omega) \tag{2}$$

In Equation 2, the impulse response of the signal exhibits a phase shift of $+i$ for $\omega < 0$ and $-i$ for $\omega > 0$. This indicates that the HT introduces a $+90$ degree shift for negative frequency components of the signal $k(l)$ and a -90 degree shift for positive frequency components. Adhering to the principle of causality, the HT of a signal $k(l)$ is associated with both its real and imaginary parts, as elucidated in Equation 3. The averaging of the real parts of $\hat{k}(l)$, denoted as (HT_{feat}), is mathematically expressed in Equation 4. Here, n represents the length of $\hat{k}(l)$. In the present study, the values of (HT_{feat}) are employed as features, effectively representing EEG trials. This utilization of (HT_{feat}) as features in the context of EEG trials serves to encapsulate the temporal dynamics revealed through the HT.

$$\widehat{kn}(l) = r(\widehat{kn}(l)) + i(\widehat{kn}(l)) \tag{3}$$

$$HT_{feat} = \frac{\sum_{i=1}^{n} r(\widehat{kn}_i(l))}{n} \tag{4}$$

In this study, the HT was utilized to extract features from EEG signals, owing to its effectiveness in capturing both the instantaneous amplitude and phase components of neural activity. These characteristics are essential for decoding the temporal dynamics of emotional states, which often manifest in subtle changes in neural oscillations. Unlike Fourier Transform, which is constrained by the assumption of signal stationarity and lacks temporal resolution, HT provides an analytic signal representation that maintains the non-stationary and nonlinear properties of EEG. Compared to Wavelet Transform, HT also offers a simpler implementation framework without the requirement for predefined basis functions, and with more direct access to phase-related features that are known to be informative in affective computing contexts.

2.2.2. Classification Procedure

Both data mining and machine learning require classification techniques [24]. Classification is essentially the process of assigning components in a data collection to a particular class or category. This process assigns components to specific classes based on characteristics in the existing data collection. Classification algorithms discover patterns throughout the learning process and accurately categories subsequent cases. The error matrix (or confusion matrix) is a table used to evaluate the performance of a classification model. This matrix shows the relationship between the actual and expected classes of the model. A three-class error matrix is often divided into four categories: true positive (yP), true negative (yN), false positive (hP) and false negative (hN). yP, a true positive occurs when the model correctly predicts a sample to be positive, yN, a true negative occurs when the model correctly predicts a sample to be negative, hP, a false positive occurs when the model incorrectly classifies a sample as positive, and hN, a false negative occurs when a model incorrectly predicts a sample to be negative [25]. The three-class confusion matrix is shown in Table 1. These metrics allow us to evaluate the performance of a classification model from different perspectives. CA is the overall accuracy rate, sensitivity (SeN) is how well one class is recognized, and specificity (SeP) is how well other classes are recognized. CA, SeN and SeP are also given in equations 5, 6 and 7, respectively.

To evaluate the robustness of the proposed model, 10-fold cross-validation was employed. This technique ensures that each segment of the data is used in both training and validation phases, minimizing bias and improving the model's generalizability. This method provides a balanced compromise between training size and evaluation reliability.

Table 1. Class labels

Confusion Matrix		Predicted Classes		
		$Class_1$	$Class_2$	$Class_3$
Actual Classes	$Class_1$	yP	hP_1	hP_2
	$Class_2$	hN_1	yP	hP_3
	$Class_3$	hN_2	hN_3	yP

$$CA = \frac{yP}{yP+hP_1+hP_2+hP_3+hN_1+hN_2+hN_3} x100 \qquad (5)$$

$$SeN = \frac{yP}{yP+hN_1+hN_2+hN_3} x100 \qquad (6)$$

$$SeP = \frac{yP}{yP+hP_1+hP_2+hP_3} x100 \qquad (7)$$

2.2.2.1. Feedforward Neural Network

FNN is a neural network model commonly used in artificial intelligence and machine learning. This paradigm features a forward flow in the information processing process, meaning that information starts in an input layer and progresses through subsequent layers to the output layer [26]. FNN consists of three basic layers, each of which consists of many neurons (or nodes): the input layer, the hidden layer(s), and the output layer. The input layer contains the data that the model receives from the outside world. Hidden layers are used to extract features from this input and improve the model's learning capabilities. The output layer is responsible for the final prediction or classification results of the model. Each neuron generates an output by multiplying its inputs with weights and sending them through an activation function. This is done using backward learning algorithms, which change the parameters of the model as it learns. FNNs have a wide range of applications. They have been used effectively in a wide range of applications, including classification, regression, pattern recognition and prediction [27]. When discussing FNNs in academic articles, aspects such as activation functions, number of layers, number of neurons, learning methods and performance evaluation measures are often highlighted. In addition, analyses of the model's effectiveness and learning capabilities in a given application provide valuable academic information.

In this study, the FNN model was developed using MATLAB's feedforwardnet function, which is part of the Deep Learning Toolbox (formerly known as Neural Network Toolbox). The model was configured with default parameters, except that the maximum number of training epochs was set to 100. All experiments were conducted with 10-fold cross-validation, and the reported metrics represent the averaged results over the folds.

2.2.2.2. k-Nearest Neighbors

The k-NN algorithm is a supervised machine learning approach utilized for classification tasks. Its operation involves assigning a label to a test trial based on the classification of its nearest neighbor(s) within the training set. The algorithm strives to assess the distance or similarity between instances in the training and test datasets. This study employed various distance measures, including Euclidean, Cosine, City Block, and Correlation [28], to determine the proximity between trials. Notably, the Euclidean distance yielded the most favorable outcomes among these measures. The Euclidean distance (EUC)

between two trials is quantified using Equation 8, where b and v represent n points, and EUC denotes the Euclidean distance. The selection of an appropriate distance measure is crucial in influencing the algorithm's performance, and in this case, the study found the Euclidean distance to be the most effective [29]. Another key consideration in the k-NN method is determining the value of the k parameter. This parameter indicates the number of the nearest neighbors to be considered in the classification process. In the present study, the optimal value of k was systematically determined for each modality and subject in each run, using the cross-validation method. This meticulous approach ensured the robustness of the k-NN model, and subsequent test classifications were performed accordingly. The systematic calculation of optimal k-values contributes to the adaptability and effectiveness of the model across different datasets and scenarios.

$$EUC(b, v) = \sqrt{\sum_{i=1}^{n} (y_{bi} - y_{vi})^2} \tag{8}$$

2.2.2.3. Random Forest Algorithm

The RF is a powerful and popular ensemble learning approach in machine learning [30]. An ensemble learning technique combines many separate models to make predictions, and RF is known for its adaptability and resilience. The algorithm is a member of the decision tree family of techniques and is characterized by its ability to generate a large number of decision trees during training. The RF generates a forest of decision trees, each of which is created using a portion of the training data and features. Randomization in the selection of both data instances and features increases the diversity among the constituent trees, which helps the model resist overfitting and improves generalization performance on previously unknown data. In a RF, predictions are made by aggregating the outputs of individual trees. For classification tasks, the method uses a majority voting mechanism, but for regression tasks it takes the average of the predictions. This ensemble-based technique allows RF to capture complicated correlations within the data, providing a robust solution to a wide range of machine learning problems. One of the main advantages of the RF is its ability to handle large, high-dimensional datasets containing both categorical and numerical variables. In addition, its inherent resistance to overfitting, ease of implementation, and adaptability to different domains contribute to its prominence in academic research and practical applications [31]. The versatility and effectiveness of the algorithm make it a useful tool for solving complicated problems in a wide range of disciplines, including finance, healthcare and image identification.

3. DEPICTION OF EXPERIMENTAL RESULTS

In this study, an illustrative graph is used to convey the research results, as exemplified by the subject-specific bar graphs shown in Figure 4. Each graph shows the 10-fold cross-validation results for three classification algorithms: k-NN, RF and FNN, applied to 10 different subjects. The individual columns within the bar graph correspond to the CA, SeP and SeN achieved for each subject, labelled $S_1, S_2, S_3, S_4, S_5, S_6, S_7, S_8, S_9$ and S_{10}, representing subject 1 to subject 10 respectively. The demarcation lines between the bar columns act as boundary indicators, with values of 20, 40, 60, 80 and 100 delineating the CA, SeP and SeN scale. In the figure, Subject 10 achieves a value of 88.68% according to the SeP metric, whereas a separate calculation reveals a value of 75.82% for Subject 6 based on the SeN metric. Notably, given that the experiment involved 10 different subjects, the totality of the experimental results, including the subject-specific test CA, SeP and SeN results for each classifier, is systematically presented using these graphical representations to enhance the visual clarity and comprehension of the study results.
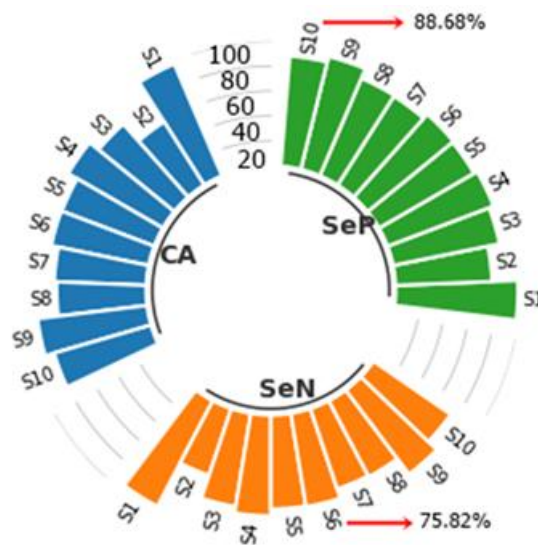
Figure 4. General presentation of topic-specific bar graphs

4. RESULTS

The primary aim of the current investigation was to overcome this limitation by assessing the classification accuracy and efficacy of different EEG feature sets in discriminating emotional states, with a particular focus on valence and arousal. Initially, a crucial aspect was the curation of a 3-class EEG dataset, where the establishment of three-level labels for each emotion played a pivotal role in strategically segmenting the emotional spectrum into low, moderate and high intensities. The dataset was then segmented into 6-second intervals. Features based on the HT were then extracted from the segmented signals, and the resulting features underwent classification using FNN, with subsequent labelling of unknown test trials. The proposed methodology for the ternary-level emotion dataset, comprising 10 randomly selected subjects, was applied independently to each subject, targeting valence and arousal emotions within 6 second time segments. The entirety of the EEG channels was used in all classification processes, and the resulting classification results were computed for metrics such as CA, SeN, and SeP. The subject-specific bar chart in Figure 5 shows the classification results for each metric using FNN.
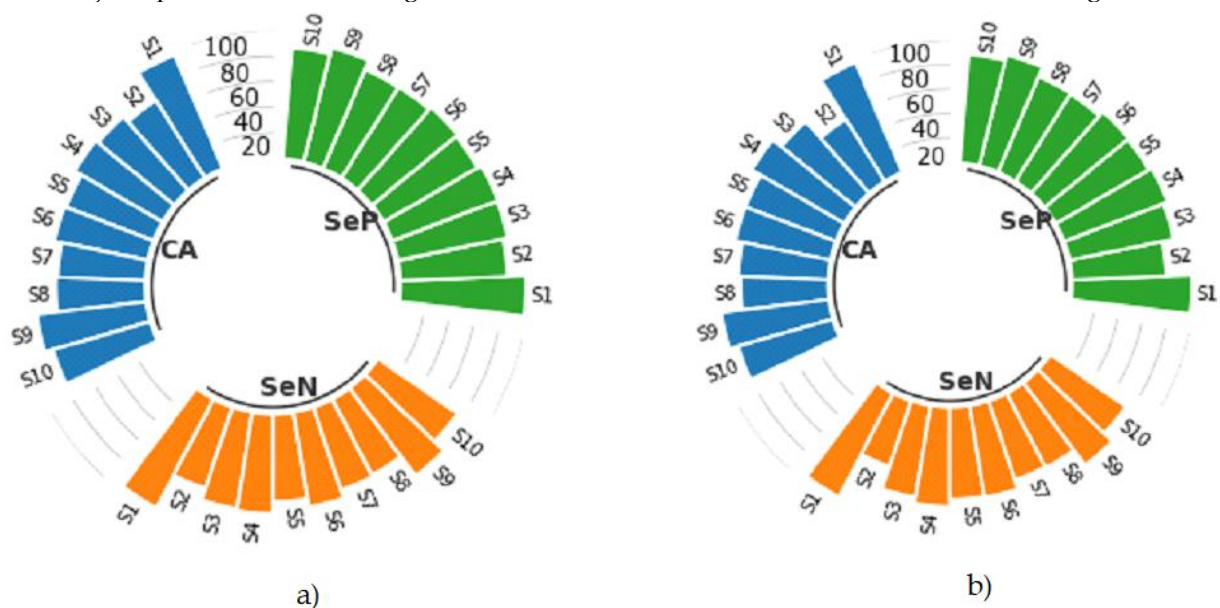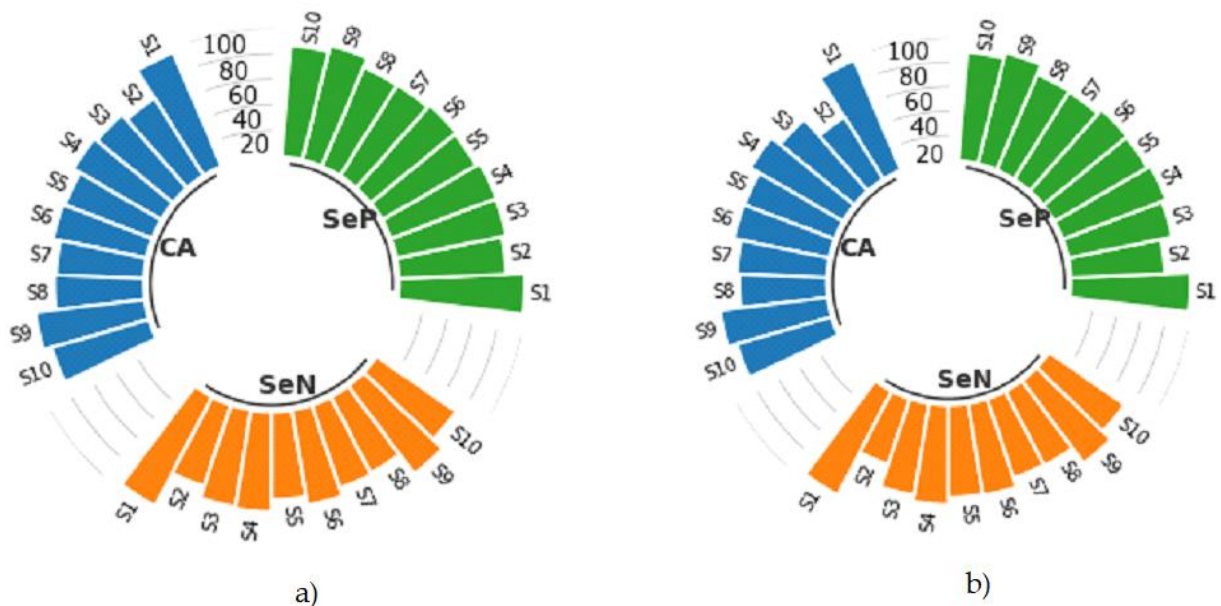

Figure 5. Classification results for a) valence and b) arousal emotion with FNN

As shown in the figure, the optimal test CA values for valence were found to be 100.00% for subjects S1, S3 and S10 respectively. In contrast, the lowest test CA of 98.75% was observed for subject S6 and S7. Furthermore, the highest test CAs for arousal were calculated as 100.00% for subjects S5 and S6 while the least favorable test CAs were documented as 97.50% for subjects S10. In order to provide a comprehensive comparison of the classification results, we also used k-NN and RF algorithms to compute classification results for valence and arousal emotions. The results for k-NN are shown in Figure 6, while those for RF are shown in Figure 7. As can be seen in Figure 6, the best CA was computed at 97.08% for S1, while the worst CA was determined at 69.16% for S7 for valence. Conversely, in Figure 6, the highest CA was calculated at 97.50% for S1, while the lowest CA was recorded at 60.00% for S2 for arousal. In Figure 7, the CA was calculated at 95.83% for S1, while the least favorable CAs were determined at 77.91% for both S2 and S7 in the context of valence classification. Conversely, within the same figure, the highest CAs were calculated at 94.58% for S1 and S4, while the lowest CA was recorded at 74.16% for S2 in the context of arousal classification. In addition, to highlight the effectiveness of using the FNN classifier to classify valence and arousal emotions, we present the mean classification results in Table 2. For valence emotion, the average values for k-NN were calculated as 77.91%, 76.08% and 87.97% for CA, SeN and SeP, respectively. In contrast, the corresponding averages for RF were 85.75%, 82.87% and 91.89%. Similarly, for arousal emotion, the means for k-NN were 79.66%, 75.68% and 88.18%, while for RF they were 85.79%, 81.53% and 91.27%. In particular, when examining the results in the table, it becomes clear that the most favorable average classification results are obtained with FNN. Specifically, for valence the averages were 99.50%, 99.52% and 99.73% for CA, SeN and SeP, respectively, whereas the averages were 99.13%, 98.96% and 99.47% for arousal emotion. These results highlight the effectiveness of the FNN in discriminating signals within the proposed experimental paradigm of this study.

Table 2. Result of classifying mean CA, SeN and SeP metrics for valence and arousal

Classifier	Valence			Arousal		
	CA	SeN	SeP	CA	SeN	SeP
k-NN	77.91	76.08	87.97	79.66	75.68	88.18
RF	85.75	82.87	91.89	85.79	81.53	91.27
FNN	**99.50**	99.52	99.73	**99.13**	98.96	99.47

Figure 6. Classification results for a) valence and b) arousal emotion with k-NN
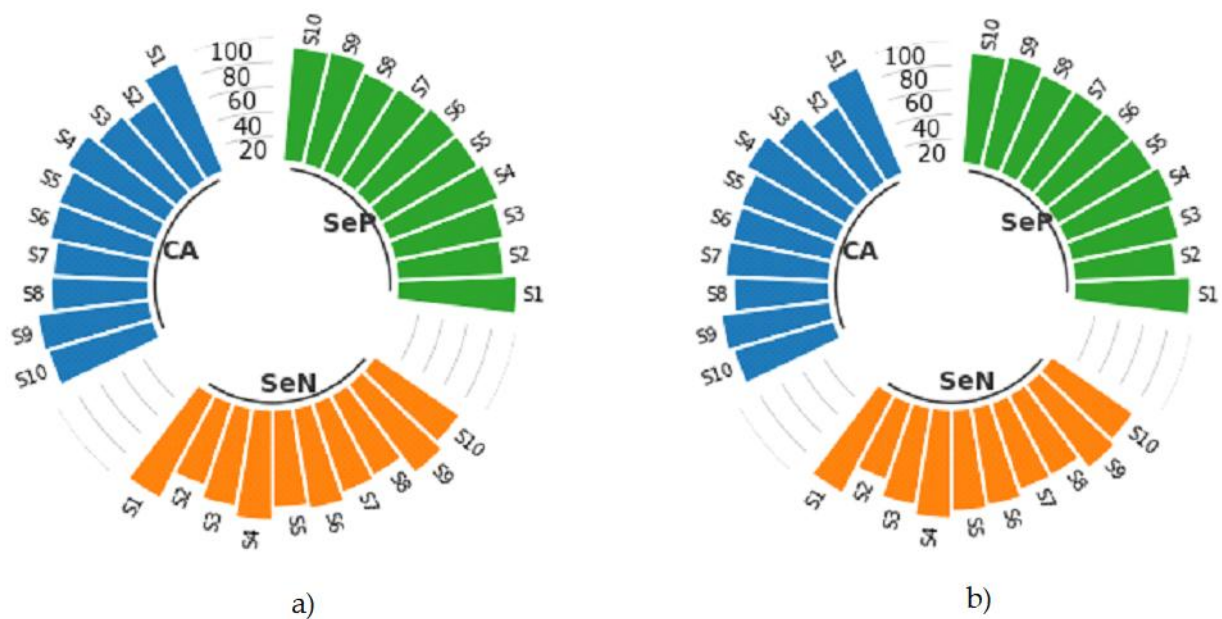
Figure 7. Classification results for a) valence and b) arousal emotion with RF

As shown in Table 3, the subject-wise and average confusion matrix results for valence classification with FNN indicate that the model performed particularly well in distinguishing high valence levels. For instance, the number of correctly classified high-valence instances was consistently high across most subjects. This trend suggests that the features extracted for high valence states were more distinguishable, possibly due to higher signal-to-noise ratio or stronger EEG activation patterns associated with high arousal-affective states.

In contrast, low valence samples showed more variability across subjects. For example, S10 had only 1.80 correctly classified low-valence samples, while S6 achieved 8.80. Some misclassifications were observed between low and adjacent medium valence classes, particularly in S9 and S6, where 0.1 and 0.2 samples were misclassified, respectively. This may be attributed to overlapping feature representations between low and medium emotional states, which are often less separable in EEG-based studies.

Medium valence classes generally showed high accuracy, with almost no confusion across categories. However, Subjects 2 and 7 had 0.1 misclassifications from medium to low, indicating a subject-dependent variability in class separability.

Similarly, in Table 4, arousal classification with FNN yielded highly accurate results for high arousal across multiple subjects. For instance, S1 (14.3), S3 (7.1), S5 (10.8), S6 (12.0), and S10 (12.5) showed nearly perfect or perfect classification in the high arousal category. Misclassifications primarily occurred in medium arousal samples, such as in S1 and S2, where 0.1–0.2 samples were misclassified into the high class. This is expected due to the gradual transition in physiological patterns between medium and high arousal states. Interestingly, the medium arousal class showed the highest variation in classification accuracy. For example, S4 had the highest correct classification count for medium arousal (15.9), while S9 and S10 had lower accuracy due to confusion with low and high classes. The low arousal class was generally well classified across subjects, with particularly strong performance in S8 (7.8), S9 (6.4), and S3 (4.2), but some instances in S10 and S6 were misclassified into the medium or high classes. In both valence and arousal confusion matrices, a clear trend is observed where extreme classes (low and high) tend to be classified more accurately than the intermediate (medium) class. This can be attributed to the relatively blurred emotional boundaries.

Table 3. Subject-wise and average confusion matrix results for valence classification with FNN

S1		Predicted Classes			S2		Predicted Classes		
		low	medium	high			low	medium	high
Actual Classes	low	7.20	0.00	0.00	Actual Classes	low	3.60	0.00	0.00
	medium	0.00	6.00	0.00		medium	0.10	8.30	0.00
	high	0.00	0.00	10.80		high	0.00	0.00	12.00

S3		Predicted Classes			S4		Predicted Classes		
		low	medium	high			low	medium	high
Actual Classes	low	5.40	0.00	0.00	Actual Classes	low	3.00	0.00	0.00
	medium	0.00	11.40	0.00		medium	0.00	10.8	0.00
	high	0.00	0.00	7.20		high	0.00	0.10	10.10

S5		Predicted Classes			S6		Predicted Classes		
		low	medium	high			low	medium	high
Actual Classes	low	3.00	0.00	0.00	Actual Classes	low	8.80	0.00	0.20
	medium	0.00	11.30	0.10		medium	0.00	6.00	0.00
	high	0.00	0.00	9.60		high	0.10	0.00	8.90

S7		Predicted Classes			S8		Predicted Classes		
		low	medium	high			low	medium	high
Actual Classes	low	6.50	0.10	0.00	Actual Classes	low	6.60	0.00	0.00
	medium	0.10	8.30	0.00		medium	0.00	4.80	0.00
	high	0.10	0.00	8.90		high	0.00	0.10	12.50

S9		Predicted Classes			S10		Predicted Classes		
		low	medium	high			low	medium	high
Actual Classes	low	4.70	0.00	0.10	Actual Classes	low	1.80	0.00	0.00
	medium	0.00	7.10	0.10		medium	0.00	12.00	0.00
	high	0.00	0.00	12.00		high	0.00	0.00	10.20

We also conducted a comparison with studies in the literature that used the same dataset. The methods and results of these studies are presented in Table 5. Looking at the results in the table, it is clear that previous research efforts have opted to create a common dataset with four classes combining valence and arousal, rather than clearly classifying valence and arousal emotions. In contrast, the current study classified valence and arousal emotions into three distinct levels. A review of the literature shows that the best result, with a score of 96.90%, was achieved by classifying deep learning architectures with features based on continuous wavelet transform (CWT). Conversely, in [38], the least favorable result was calculated at 69.67%, using Graph Regularized Extreme Learning. Comparing the results obtained, it is clear that the ternary classification proposed in this study makes a significant contribution to the literature, achieving test accuracies of 99.50% and 99.13%.

Furthermore, Although the class structures differ among studies, we report the comparison to demonstrate the robustness of our model under a more fine-grained ternary classification setting, which is inherently more complex than binary class divisions.

4. CONCLUSIONS

This study implemented and evaluated a methodological framework to fulfil its primary objective to assess the classification accuracy and efficacy of different EEG feature sets in discriminating emotional

states, with a particular focus on valence and arousal. The research began with the curation of a 3-class EEG dataset, strategically incorporating three-level labels indicative of emotional intensity. This was followed by temporal segmentation into 10-second intervals, which facilitated the extraction of HT-based features for subsequent classification using FNN. Application of the ternary-level emotion dataset to 10 subjects produced subject-specific bar charts depicting FNN classification results. In addition, a comparative analysis with related studies using the same dataset revealed a departure from the conventional approach of creating a common dataset with four classes combining valence and arousal emotions. Instead, our study adopted a more refined structure by distinctly categorizing valence and arousal emotions into three levels each. This enhanced labeling scheme improved the granularity and interpretability of emotion classification results.

Table 4. Subject-wise and average confusion matrix results for arousal classification with FNN

S1		Predicted Classes		
		low	medium	high
Actual Classes	low	4.20	0.00	0.00
	medium	0.00	5.30	0.10
	high	0.10	0.00	14.30

S2		Predicted Classes		
		low	medium	high
Actual Classes	low	3.00	0.00	0.00
	medium	0.00	11.80	0.20
	high	0.00	0.00	9.00

S3		Predicted Classes		
		low	medium	high
Actual Classes	low	4.20	0.00	0.00
	medium	0.00	12.60	0.00
	high	0.00	0.10	7.10

S4		Predicted Classes		
		low	medium	high
Actual Classes	low	2.40	0.00	v
	medium	0.00	15.90	0.30
	high	0.00	0.10	5.30

S5		Predicted Classes		
		low	medium	high
Actual Classes	low	3.00	0.00	0.00
	medium	0.00	10.20	0.00
	high	0.00	0.00	10.80

S6		Predicted Classes		
		low	medium	high
Actual Classes	low	3.60	0.00	0.00
	medium	0.00	8.40	0.00
	high	0.00	0.00	12.00

S7		Predicted Classes		
		low	medium	high
Actual Classes	low	3.60	0.00	0.00
	medium	0.00	5.400	0.00
	high	0.00	0.2	14.80

S8		Predicted Classes		
		low	medium	high
Actual Classes	low	7.80	0.00	0.00
	medium	0.10	5.30	0.00
	high	0.00	0.00	10.80

S9		Predicted Classes		
		low	medium	high
Actual Classes	low	6.40	0.00	0.20
	medium	0.00	4.20	0.00
	high	0.10	0.00	13.10

S10		Predicted Classes		
		low	medium	high
Actual Classes	low	1.60	0.10	0.10
	medium	0.00	9.30	0.30
	high	0.00	0.10	12.50

Table 5. Comparison of classification accuracy with prior studies

References	Procedure			
	Features Method	**Classifier Method**	**Classes**	**CA (%)**
[19]	Time domain features	CNN	4	76.77
[32]	Empirical mode decomposition	LSTM	4	88.42
[33]	CWT	AlexNet, ResNet-18, Vgg-19, Inception-v1, Inception-v3	4	96.90
[34]	Frequency temporal spatial	CNN-FcaNet	4	88.46
[35]	Information Potential	RF	4	71.43
[36]	Pearson correlation coefficient	CNN	4	73.10
[37]	Power spectral density, differential entropy, differential asymmetry, rational asymmetry, asymmetry and differential causality	Graph regularized Extreme Learning	4	69.67
[38]	Phase space dynamics and poincare sections	Multi-class SVM	4	81.67
[39]	Spectrograms	CNN	4	75.00
Proposed Method	HT	FNN	3	Valence:99.50 Arousal: 99.13

The model achieved exceptionally high classification accuracies—99.50% for valence and 99.13% for arousal—driven by the synergy of carefully designed methodological components. Specifically, the segmentation strategy increased training data while maintaining temporal integrity; the use of Hilbert Transform-based features enabled the extraction of rich instantaneous signal characteristics; and the neural network architecture captured relevant discriminative patterns. Together, these elements contributed to the robust performance of the proposed approach.

The presented methodology offers a solid foundation for future research into emotional state detection using advanced signal processing and classification techniques. The proposed three-level emotion classification framework has promising implications across various real-life domains. In healthcare, such models can be integrated into neurofeedback systems for emotion regulation therapies, particularly in managing anxiety, depression, or post-traumatic stress disorder (PTSD). In education, emotion-aware intelligent tutoring systems can adapt instructional content based on a learner's emotional state, enhancing engagement and learning outcomes. In the field of human-computer interaction, particularly in affective computing and virtual reality environments, real-time emotion detection can improve system responsiveness and user experience. Furthermore, the model's capacity to distinguish between low, moderate, and high emotional intensities allows for a more nuanced understanding of affective states, which is critical in continuous monitoring applications. These insights demonstrate that the model is not only technically robust but also applicable in diverse interdisciplinary settings where emotional intelligence is increasingly vital.

Despite the promising performance of the proposed model, several limitations must be acknowledged. EEG signals are prone to noise arising from muscular artifacts, environmental interference, and hardware limitations. The controlled laboratory setting may not fully reflect real-world emotional dynamics, potentially affecting ecological validity. Moreover, the use of a feed-forward neural network, although effective in static classification tasks, does not leverage temporal relationships that may exist within EEG time series. These aspects may introduce variability in classification performance and will be

systematically addressed in future investigations.

Declaration of Ethical Standards

The authors declare that all ethical guidelines including authorship, citation, data reporting, and publishing original research are followed.

Credit Authorship Contribution Statement

All authors contributed equally. Author1 contributed to the preparation of the methodology and description of the dataset, while Author2 analyzed the results and formulated the conclusions. In addition, Author1 and Author2 collaborated on data validation prior to manuscript preparation. They also contributed to drafting the manuscript.

Declaration of Competing Interest

The authors declare that there is no conflict of interest.

Funding / Acknowledgements

Data Availability

No data available.

REFERENCES

[1]   M. G. Huddar, S. S. Sannakki, and V. S. Rajpurohit, "Attention-based multi-modal sentiment analysis and emotion detection in conversation using RNN," *Int. J. Interact. Multimedia Artif. Intell*, vol. 6, no. 6, June 2021, doi: 10.9781/ijimai.2020.07.004.

[2]   W. Rahmouni, G. Bachir, and M. Aillerie, "A new control strategy for harmonic reduction in photovoltaic inverters inspired by the autonomous nervous system," *J. Electr. Eng.*, vol. 73, no. 5, pp. 310–317, September 2022, doi: 10.2478/jee-2022-0041.

[3]   L. George and H. Hadi, "User identification and verification from a pair of simultaneous EEG channels using transform-based features," *Int. J. Interact. Multimedia Artif. Intell.*, vol. 5, no. 5, pp. 54-62, June 2019, doi: 10.9781/ijimai.2018.12.008.

[4]   J. Wang and M. Wang, "Review of the emotional feature extraction and classification using EEG signals," *Cogn. Robot.*, vol. 1, pp. 29–40, April 2021, doi: 10.1016/j.cogr.2021.04.001.

[5]   W. L. Zheng and B. L. Lu, "Investigating critical frequency bands and channels for EEG-based emotion recognition with deep neural networks," *IEEE Trans. Auton. Ment. Dev.*, vol. 7, no. 3, pp. 162–175, May 2015, doi: 10.1109/TAMD.2015.2431497.

[6]   R. N. Duan, J. Y. Zhu, and B. L. Lu, "Differential entropy feature for EEG-based emotion classification," in Proc. 6th Int. IEEE/EMBS Conf. Neural Eng. (NER), San Diego, CA, USA, November 2013, pp. 81–84, doi: 10.1109/NER.2013.6695889.

[7]   J. Li, Z. Zhang, and H. He, "Hierarchical convolutional neural networks for EEG-based emotion recognition," *Cogn. Comput.*, vol. 10, pp. 368–380, April 2018, doi: 10.1007/s12559-017-9533-x.

[8]   M. A. Asghar et al., "EEG-based multi-modal emotion recognition using bag of deep features: An optimal feature selection approach," *Sensors*, vol. 19, no. 23, p. 5218, November 2019, doi: 10.3390/s19235218.

[9]   K. H. Cheah, H. Nisar, V. V. Yap, C. Y. Lee, and G. R. Sinha, "Optimizing residual networks and VGG for classification of EEG signals: Identifying ideal channels for emotion recognition," *J. Healthcare Eng.*, vol. 1, pp. 1–10, March 2021, doi: 10.1155/2021/5599615.

[10]   G. Xiao et al., "4D attention-based neural network for EEG emotion recognition," *Cogn. Neurodynamics*, vol. 16, pp. 1–14, January 2022, doi: 10.1007/s11571-021-09751-5.

[11]   M. Jin, H. Chen, Z. Li, and J. Li, "EEG-based emotion recognition using graph convolutional network with learnable electrode relations," in Proc. 43rd Annu. Int. Conf. IEEE Eng. Med. Biol. Soc. (EMBC), Mexico, November 2021, pp. 5953–5957, doi: 10.1109/EMBC46164.2021.9630062.

[12]   S. Katsigiannis and N. Ramzan, "DREAMER: A database for emotion recognition through EEG and ECG signals from wireless low-cost off-the-shelf devices," *IEEE J. Biomed. Health Inform.*, vol. 22, no. 1, pp. 98–107, March 2017, doi: 10.1109/JBHI.2017.2688239.

[13]   S. Koelstra et al., "DEAP: A database for emotion analysis using physiological signals," *IEEE Trans. Affect. Comput.*, vol. 3, no. 1, pp. 18–31, December 2011, doi: 10.1109/T-AFFC.2011.15.

[14]   T. Song, W. Zheng, P. Song, and Z. Cui, "EEG emotion recognition using dynamical graph convolutional neural networks," *IEEE Trans. Affect. Comput.*, vol. 11, no. 3, pp. 532–541, March 2018, doi: 10.1109/TAFFC.2018.2817622.

[15]   T. Zhang, X. Wang, X. Xu, and C. P. Chen, "GCB-Net: Graph convolutional broad network and its application in emotion recognition," *IEEE Trans. Affect. Comput.*, vol. 13, no. 1, pp. 379–388, August 2019, doi: 10.1109/TAFFC.2019.2937768.

[16]   R. Li et al., "SSTD: A novel spatio-temporal demographic network for EEG-based emotion recognition," *IEEE Trans. Comput. Soc. Syst.*, vol. 10, no. 1, pp. 376–387, January 2022, doi: 10.1109/TCSS.2022.3188891.

[17]   K. Lin, L. Zhang, J. Cai, J. Sun, W. Cui, and G. Liu, "DSE-Mixer: A pure multilayer perceptron network for emotion recognition from EEG feature maps," *J. Neurosci. Methods*, vol. 401, January 2024, doi: 10.1016/j.jneumeth.2023.110008.

[18]   Z. Gao, Y. Li, Y. Yang, X. Wang, N. Dong, and H. D. Chiang, "A GPSO-optimized convolutional neural networks for EEG-based emotion recognition," *Neurocomputing*, vol. 380, pp. 225–235, March 2020, doi: 10.1016/j.neucom.2019.10.096.

[19]   H. Chao and L. Dong, "Emotion recognition using three-dimensional feature and convolutional neural network from multichannel EEG signals," *IEEE Sensors J.*, vol. 21, no. 2, pp. 2024–2034, September 2020, doi: 10.1109/JSEN.2020.3020828.

[20]   K. Martín-Chinea, J. Ortega, J. F. Gómez-González, E. Pereda, J. Toledo, & L. Acosta, "Effect of time windows in LSTM networks for EEG-based BCIs. Cognitive Neurodynamics", vol. 17, no.2, 385-398, April 2023. doi: 10.1007/s11571-022-09832-z.

[21]   S. Zhou, B. Chen, Y. Zhang, H. Liu, Y. Xiao, and X. Pan, "A feature extraction method based on feature fusion and its application in the text-driven failure diagnosis field," *Int. J. Interact. Multimedia Artif. Intell.*, vol. 6, no. 4, pp. 121-130, December 2020, doi: 10.9781/ijimai.2020.11.006.

[22]   E. Ergün and O. Aydemir, "A Hybrid BCI Using Singular Value Decomposition Values of the Fast Walsh–Hadamard Transform Coefficients," *IEEE Trans. Cogn. Dev. Syst.*, vol. 15, no. 2, pp. 454–463, October 2020, doi: 10.1109/TCDS.2020.3028785.

[23]   H. M. Emara et al., "Hilbert transform and statistical analysis for channel selection and epileptic seizure prediction," *Wireless Pers. Commun.*, vol. 116, pp. 3371–3395, January 2021, doi: 10.1007/s11277-020-07857-3.

[24]   E. Ergün, "Artificial Intelligence Approaches for Accurate Assessment of Insulator Cleanliness in High-Voltage Electrical Systems," *Electr. Eng.*, pp. 1–16, August 2024, doi: 10.1007/s00202-024-02691-.

[25]   E. Yavuz, and Ö. Aydemir, "Classification of EEG based BCI signals imagined hand closing and opening". In IEEE 40th International Conference on Telecommunications and Signal Processing (TSP), pp. 425-428, July 2017, doi: 10.1109/TSP.2017.8076020.

[26] D. Svozil, V. Kvasnicka, and J. Pospichal, "Introduction to multi-layer feed-forward neural networks," *Chemom. Intell. Lab. Syst.*, vol. 39, no. 1, pp. 43–62, November 1997, doi: 10.1016/S0169-7439(97)00061-0.

[27] H. Choubey and A. Pandey, "A combination of statistical parameters for the detection of epilepsy and EEG classification using ANN and KNN classifier," *Signal Image Video Process.*, vol. 15, no. 3, pp. 475–483, April 2021, doi: 10.1007/s11760-020-01767-4.

[28] E. Ergün, "Deep learning-based multiclass classification for citrus anomaly detection in Agriculture". *Signal Image Video Process*, vol. 18, pp. 8077–8088, July 2024. doi: 10.1007/s11760-024-03452-2.

[29] E. Yavuz, and Ö. Aydemir, "Olfaction recognition by EEG analysis using wavelet transform features". In IEEE International Symposium on Innovations in Intelligent Systems and Applications (INISTA), pp. 1-4, August 2016, doi: 10.1109/INISTA.2016.7571827.

[30] G. Mary, S. Chitti, R. B. Vallabhaneni, and N. Renuka, "EEG Signal Classification Automation using Novel Modified Random Forest Approach," *J. Sci. Ind. Res.*, vol. 82, no. 1, pp. 101–108, January 2023, doi: 10.56042/jsir.v82i1.70213.

[31] A. Sakalle, P. Tomar, H. Bhardwaj, D. Acharya, and A. Bhardwaj, "A LSTM based deep learning network for recognizing emotions using wireless brainwave driven system," *Expert Syst. Appl.*, vol. 173, no.1, p. 114516, July 2021, doi: 10.1016/j.eswa.2020.114516.

[32] S. Bagherzadeh, K. Maghooli, A. Shalbaf, and A. Maghsoudi, "Emotion recognition using continuous wavelet transform and ensemble of convolutional neural networks through transfer learning from electroencephalogram signal," *Front. Biomed. Technol.*, vol. 10, no. 1, pp. 47–56, January 2023, doi: 10.18502/fbt.v10i1.11512.

[33] Y. Luo, C. Wu, and C. Lv, "Cascaded Convolutional Recurrent Neural Networks for EEG Emotion Recognition Based on Temporal–Frequency–Spatial Features," *Appl. Sci.*, vol. 13, no. 11, p. 6761, June 2023, doi: 10.3390/app13116761.

[34] J. Kim, J. Oh, and T. Y. Heo, "Acoustic classification of mosquitoes using convolutional neural networks combined with activity circadian rhythm information," *Int. J. Interact. Multimedia Artif. Intell.*, vol. 7, no. 2, pp. 59-65, December 2021, doi: 10.9781/ijimai.2021.08.009.

[35] V. Gupta, M. D. Chopda, and R. B. Pachori, "Cross-subject emotion recognition using flexible analytic wavelet transform from EEG signals," *IEEE Sensors J.*, vol. 19, no. 6, pp. 2266–2274, March 2019, doi: 10.1109/JSEN.2018.2883497.

[36] H. Mei and X. Xu, "EEG-based emotion classification using convolutional neural network," *in* Proc. Int. Conf. Security, Pattern Anal., Cybern. (SPAC), Shenzhen, China, December 2017, pp. 130–135, doi: 10.1109/SPAC.2017.8304301.

[37] W. L. Zheng, J. Y. Zhu, and B. L. Lu, "Identifying stable patterns over time for emotion recognition from EEG," *IEEE Trans. Affect. Comput.*, vol. 10, no. 3, pp. 417–429, June 2017, doi: 10.1109/TAFFC.2017.2712143.

[38] M. Zangeneh Soroush, K. Maghooli, S. K. Setarehdan, and A. M. Nasrabadi, "A novel EEG-based approach to classify emotions through phase space dynamics," *Signal Image Video Process.*, vol. 13, pp. 1149–1156, March 2019, doi: 10.1007/s11760-019-01455-y.

[39] Y. H. Kwon, S. B. Shin, and S. D. Kim, "Electroencephalography based fusion two-dimensional (2D)-convolution neural networks (CNN) model for emotion recognition system," *Sensors*, vol. 18, no. 5, p. 1383, April 2018, doi: 10.3390/s18051383.

COMPARATIVE ANALYSIS OF EAST-WEST AND SOUTH-NORTH SINGLE-AXIS SOLAR TRACKING SYSTEMS

* Kutbay SEZEN [ID]

Alanya Alaaddin Keykubat University, ALTSO Vocational School of Higher Education, Antalya TÜRKİYE
kutbay.sezen@alanya.edu.tr

Highlights

- Solar radiation gain
- Single-axis tracking
- East-west orientation
- South-north orientation
- Konya region tracking angles

*Corresponding Author: Kutbay SEZEN, kutbay.sezen@alanya.edu.tr

COMPARATIVE ANALYSIS OF EAST-WEST AND SOUTH-NORTH SINGLE-AXIS SOLAR TRACKING SYSTEMS

* Kutbay SEZEN ⓘD

Alanya Alaaddin Keykubat University, ALTSO Vocational School of Higher Education, Antalya TÜRKİYE
kutbay.sezen@alanya.edu.tr

ABSTRACT: As global energy demand continues to grow, maximizing the efficiency of solar energy as a renewable resource is increasingly critical. Solar tracking systems offer an effective solution by optimizing panel orientation to capture more solar radiation. This study evaluates the annual and seasonal solar radiation gains of single-axis tracking systems, comparing east-west and south-north orientations with fixed-tilt and horizontal surfaces. Daily, monthly, and annual radiation values were calculated based on the average day of each month, and hourly radiation variations were analyzed for June and December. Annually, the east-west tracking system increased radiation capture by approximately 30% compared to a horizontal surface and 19% compared to a fixed-tilt surface, while the south-north system achieved gains of 16% and 6%, respectively. In June, the east-west system outperformed the south-north setup by 2.02 kWh/m² daily (a 29% increase), whereas in December, the south-north system collected 0.43 kWh/m² more per day (a 25% increase) due to better alignment with the sun's lower southern path. The method used in this study is based on manual, equation-driven modeling, aiming to enhance transparency and provide a cost-effective, software-independent tool. The calculated hourly tracking angles can be applied to future systems in the same region, while the overall procedure can be easily adapted to other locations by incorporating region-specific input parameters.

Keywords: Solar Radiation Gain, Single-Axis Tracking, East-West Orientation, South-North Orientation, Konya Region Tracking Angles

1. INTRODUCTION

The global demand for energy continues to rise sharply due to rapid industrialization, urban expansion, and population growth. Traditionally, fossil fuels have dominated the global energy mix, but their environmental consequences—including greenhouse gas emissions and air pollution—have intensified the need for sustainable alternatives. Among renewable energy sources, solar energy is particularly attractive due to its abundance, accessibility, and environmental friendliness.

Solar energy can be harnessed through various technologies, the most common of which are photovoltaic (PV) systems. PV systems are widely adopted due to their modularity, scalability, and relatively low maintenance requirements. Improving the efficiency of photovoltaic (PV) systems has become a key research area in the transition to clean energy [1].

Enhancing the power output of photovoltaic (PV) systems remains a central focus in renewable energy research, with numerous strategies proposed to improve efficiency. One widely studied approach involves concentrated photovoltaic systems (CPVS), which utilize reflective mirrors to direct and intensify solar radiation onto a smaller PV surface. In this context, low-concentration PV systems (LCPVS) have gained attention due to their simplicity and cost-effectiveness. Studies by Kolamroudi et al. [2, 3] showed that LCPVS using mirrors combined with water-based cooling systems can increase power output by up to three times compared to standard flat-panel systems, while also reducing the required PV surface area. Additionally, their review study [4] provided a comprehensive comparison of LCPVS with other systems, emphasizing the benefits of using mirrors and passive cooling to improve system efficiency and reduce installation costs.

In parallel, cooling techniques have been extensively investigated to mitigate thermal losses in PV

*Corresponding Author: Kutbay SEZEN, kutbay.sezen@alanya.edu.tr

panels. A recent review by Utomo et al. [5] classified cooling strategies into conductive, convective, and radiative methods, highlighting the effectiveness of nanofluids and phase change materials (PCMs) in reducing panel temperatures by up to 40°C and enhancing energy output by approximately 1.67%.

Beyond system design, material innovations also play a crucial role in efficiency improvement. Emerging photovoltaic technologies such as organic, dye-sensitized, perovskite, and quantum dot solar cells offer advantages like lightweight construction and lower production costs. However, as noted by Gressler et al. [6], these advanced systems require careful life cycle assessment due to environmental and material sustainability concerns. In addition to material advances, bifacial PV panels have demonstrated performance gains by harvesting both direct sunlight and reflected radiation from the ground. According to Aksoy and Çalık [7], bifacial systems installed over white or sandy surfaces generated up to 6.4% more energy annually than monofacial panels under identical conditions, proving especially effective in high-reflectance environments.

Cleaning systems have also shown measurable effects on efficiency. Park et al. [8] developed a low-cost robotic cleaning solution that increased panel voltage and current by 8.02% and 18.78%, respectively, emphasizing the role of maintenance in long-term performance. Optimal panel tilt is another factor influencing solar gains. Kabul et al. [9] analyzed exergy potential across varying tilt angles in Turkey and found that a 30° tilt yielded the best year-round efficiency, which aligns with typical design practices for fixed and tracking systems.

One of the most effective strategies for improving PV system performance is solar tracking, which enhances energy harvest by adjusting panel orientation to follow the sun's movement. Solar tracking systems can be either single-axis or dual-axis. Single-axis systems have a simpler structure, allowing panels to move along only one axis. These systems track the sun's daily movement in either the east-west or south-north direction to enhance energy gains. Dual-axis systems, on the other hand, can track both the azimuth and elevation angles of the sun, enabling them to collect more solar radiation than single-axis systems. Although dual-axis systems come with higher costs and complexity, they offer a greater capacity for solar energy collection.

Experimental studies have consistently demonstrated that tracking systems outperform fixed configurations. Akpinar et al. [10] observed that solar tracking improved energy output of thermal and photovoltaic panels by up to 75.2% and 26.3%, respectively, depending on panel type. Similarly, Singh et al. [11] and Kabilan et al. [12] developed low-cost automatic tracking systems using LDRs and microcontrollers, both reporting significant improvements in current, voltage, and power output over fixed setups.

Review studies that provide a comprehensive examination of the technical and economic aspects of solar tracking systems, along with tracking control methods in light of current researches, offer valuable insights on the subject. Kumba et al. [13] compiled studies on solar tracking systems, evaluating the performance and energy efficiency of passive, active, single-axis, dual-axis, and hybrid systems under various environmental conditions. This study summarizes the energy production increases achieved by different tracking systems and highlights potential areas for future technological advancement. Kazem et al. [14] gathered studies focusing on the design, cost, and efficiency of solar tracking systems, providing critical information on how advanced technologies—particularly artificial intelligence and machine learning—can be used to optimize these systems. Kuttybay et al. [15] assessed studies examining the geographic, climatic, and design factors affecting the efficiency of solar tracking systems, summarizing the efficiency gains of single and dual-axis systems compared to fixed systems. Bahrami et al. [16] conducted a technical and economic comparison of fixed, single-axis, and dual-axis tracking systems in Nigeria, highlighting variations in annual energy yield and levelized cost of electricity. Their results offer practical guidelines for selecting the most cost-effective tracking options in diverse geographical contexts. Together, these studies offer a holistic perspective on the technical and economic parameters that should be considered in the development and implementation of solar tracking systems.

In the literature, studies on solar tracking systems often focus on either the control methods used to operate these systems or the radiation gains achieved by tracking surfaces compared to fixed or

horizontal surfaces in specific regions. This study, however, examines radiation gains based on the hourly maximum power angle, analyzing both east-west and south-north tracking directions rather than the specific control elements managing the tracking system. As a result, solar radiation gains provided by one axis tracking systems in different orientations are explored in detail on an annual, monthly, and hourly basis.

Some studies focused on solar tracking control methods include the following. Kumba et al. [17] proposed a novel single-axis solar tracking system based on the second-class lever principle, eliminating the need for an external motor by balancing the PV panel's mass with that of water and analyzing the resulting power output increase compared to traditional systems. Alshaabani [18] developed a low-cost, real-time single-axis solar tracking system that monitors the sun's angle using four photodiodes. Er and Balcı [19] designed a dual-axis solar tracking system without using any sensors, programming it via a PLC to move based on the sun's angle and observing an increase in efficiency. Toylan [20] designed a dual-axis solar tracking system using a fuzzy logic controller optimized by a genetic algorithm, reporting that this system outperformed fixed PV panels. Attou et al. [21] proposed a control system aimed at enhancing energy efficiency in PV systems through maximum power point tracking (MPPT) using the Perturb & Observe algorithm. Khan and Tacer [22] developed an MPPT controller based on a microinverter, improving PV system performance in terms of dynamic response and efficiency. Arpacı et al. [23] compared a fuzzy logic controller and the Perturb & Observe algorithm for MPPT, analyzing their effectiveness in tracking the maximum power point in PV systems. Başoğlu et al. [24] developed an Arduino-based dual-axis solar tracking system for a 45W PV panel, achieving higher efficiency than static PV systems. Alhaj Omar et al. [25] conducted a comparative analysis of three commonly used MPPT algorithms—Perturb & Observe, Incremental Conductance, and Fuzzy Logic—under varying weather conditions, finding that the Fuzzy Logic algorithm showed best performance with its fast response.

Dual-axis tracking systems have been extensively researched due to their ability to offer the highest efficiency in solar energy harvest. Sungur [26] reported that a dual-axis solar tracking system controlled by a PLC in Turkey produced 42.6% more energy compared to a fixed system. Yılmaz et al. (2015) indicated that a dual-axis tracking system used in a 4.6 kW PV system achieved a 34% increase in energy harvest over a fixed system. Üçgül and Şenol (2016) observed that microcontroller-controlled dual-axis systems yielded 28% more power daily than fixed panels. Şenol et al. (2021) reported a 9% efficiency gain with their dual-axis solar tracking system, which employed a fuzzy logic control algorithm. Garip (2021) demonstrated that dual-axis systems provided 25–35% higher energy harvest compared to static systems, while Bilhan and Etci (2021) found that dual-axis systems in the Konya region produced 16.7% more energy than fixed systems.

However, some studies have noted that the benefits of tracking systems may be limited in certain conditions. Kelly and Gibson [27] developed an algorithm that captured 50% more energy in a horizontal position compared to dual-axis tracking on cloudy days. Quesada et al. [28] showed that, particularly at higher latitudes, a horizontal position captured more radiation than a fixed angle on cloudy days, suggesting that solar tracking strategies should be optimized for such conditions.

Single-axis solar tracking systems are widely studied due to their ability to increase efficiency with lower costs and less complexity compared to dual-axis tracking. Öztürk et al. [29] reported that a single-axis solar tracking system with bifacial PV modules in Konya achieved 75.5% energy efficiency and a maximum electrical efficiency of 36.42%, with a sustainability index of 1.29. Kayri [30] developed a single-axis solar tracking system designed to improve the long-term durability of modules against atmospheric conditions, demonstrating a 30.84% increase in efficiency on an annual basis. Arslanoğlu and Yiğit [31] highlighted that placing parabolic trough-type single-axis solar collectors in a south-north orientation can enhance thermal energy production efficiency, making this system ideal for high-temperature energy generation. Alomar et al. [32] compared the performance of fixed, single-axis, and dual-axis systems, noting that single-axis systems produced 16.5% more electricity than fixed systems and reduced CO_2 emissions by approximately 4,000 tons annually. Azam et al. [33] examined a single-

axis system that employed an intermittent tracking algorithm rather than continuous tracking, finding that it provided 1.12% less radiation gain than a fixed system but reduced its own energy consumption by 34%. Celen et al. [34] conducted an energy and exergy analysis of solar collectors at varying tilt angles in Erzincan, finding that optimal tilt angles significantly impact radiation capture and efficiencies, with maximum energy and exergy efficiencies of 74.2% and 9.7%, respectively.

Distinctively in this study, a single-axis tracking system is analyzed in both east-west and south-north orientations, comparing these two configurations to fixed-angle and horizontal surfaces within the Konya province of Turkey. The selected region was chosen based on its high solar energy potential and favorable geographical characteristics, as highlighted by Doğan and Karakılçık [35]. Unlike many existing works that emphasize control mechanisms or sensor systems, this study focuses on the radiation gains achieved by each orientation on annual, monthly, and hourly scales. The analysis was conducted using the monthly average day method, with daily tracking divided into hourly intervals to establish a more holistic and simplified modeling framework. Inspired by the emphasis on simple and easy-to-maintain tracking designs discussed by Kuttybay et al. [15], this study proposes a semi-tracking approach that reduces system complexity and energy consumption while maintaining significant radiation gains.

The instantaneous and daily radiation values on inclined surfaces were calculated based on published theoretical and empirical formulas. Mathematical models for east-west tracking, south-north tracking, fixed-tilt, and horizontal surfaces were developed in MS-Excel. Using the iterative solution provided by the Solver add-in, the optimal angle values that yield the highest hourly radiation gain were determined for each month's average day for the study location. The annual total solar radiation gain of the four surfaces was compared, and the monthly average daily radiation values were calculated. Additionally, the hourly instantaneous radiation values for June and December, representing the summer and winter solstices, were compared. The resulting hourly tracking angle change table for each month's average day in Konya provides valuable data for future single-axis solar tracking systems in the region. Furthermore, the calculation method presented in this study can be easily adapted to other geographical locations worldwide to generate site-specific angle tables for optimized tracking performance.

In the literature, studies on solar tracking systems often emphasize either the control methods used to operate these systems or the radiation gains achieved by tracking surfaces relative to fixed or horizontal configurations in specific regions. This study, however, focuses on radiation gains calculated based on the hourly maximum power angle, analyzing both east-west and south-north tracking directions independently of the specific control mechanisms. Accordingly, the radiation gains of one-axis tracking systems in different orientations are explored in detail on an annual, monthly, and hourly basis.

While many commercial solar simulators can produce comparable results using built-in empirical models, this study deliberately employs a manual, equation-based approach to promote transparency and scientific clarity. By explicitly applying and visualizing the underlying solar geometry and radiation equations, the method offers deeper insight into the core principles driving solar tracking performance. Moreover, this approach is cost-effective, independent of proprietary software, and easily adaptable to other locations through region-specific input adjustments or empirical model selection.

2. MATERIAL AND METHODS

In this study, solar radiation gains were compared across four configurations: a single-axis tracking system oriented east-west, a single-axis tracking system oriented south-north, a south-facing surface with an annual fixed optimal tilt angle, and a horizontal surface. First, the theoretical calculation method for daily solar radiation on inclined and horizontal surfaces is explained, followed by a detailed calculation of instantaneous solar radiation on an inclined surface to guide the calculation of daily solar radiation for the single-axis tracking system. The mathematical models developed by Liu and Jordan [36, 37] and the empirical equations compiled by Yiğit and Atmaca [38] were used in the calculations.

2.1. Calculation of Total Daily Solar Radiation on Horizontal and Inclined Surfaces

The total solar radiation falling on a horizontal surface, H, can be determined using Equation 1:

$$H = K_T . H_o \tag{1}$$

Where K_T is the clearness index, and H_o represents the total solar radiation falling on a horizontal surface outside the atmosphere, calculated with Equation 2:

$$H_o = \frac{24 x 3600 G_{sc}}{\pi}\left[1 + 0.033 cos(\frac{360d}{365})\right].\left[cos\phi cos\delta sin\omega_s + \frac{2\pi\omega_s}{360} sin\phi sin\delta\right] \tag{2}$$

Here, ϕ is the latitude angle, d is the day of the year, δ is the declination angle, and ω_s is the sunset hour angle. The solar constant G_{sc} is the solar radiation intensity falling on the horizontal plane outside the atmosphere and can be taken as 1367 W/m².

The declination angle δ, which is the angle between the sun's rays and the equatorial plane, is calculated based on the day of the year d using Equation 3:

$$\delta = 23{,}45 sin(360 \frac{284+d}{365}) \tag{3}$$

For monthly average daily total solar radiation calculations, the average day value (d) for each month, as listed in Table 1, can be used.

Table 1. Average day value (d) of each month [38]

Month	Jan	Feb	Mar	Apr	May	Jun	Jul	Aug	Sep	Oct	Nov	Dec
Avg. Day	17	47	75	105	135	162	198	228	258	288	318	344

The sunset hour angle ω_s is defined by Equation 4:

$$\omega_s = cos^{-1}(-tan\phi tan\delta) \tag{4}$$

After calculating the solar radiation on a horizontal surface H_o, the clearness index K_T, given by Equation 5, can be used to find the total daily solar radiation on an inclined surface:

$$K_T = \left(a + b\frac{n}{N}\right) \tag{5}$$

Where N is the day length, n is the actual sunshine duration, and a and b are regional constants defined by Equation 6 and Equation 7, respectively:

$$a = 0{,}103 + 0{,}000017Z + 0{,}198 cos(\phi - \delta) \tag{6}$$

$$b = 0{,}533 - 0{,}165 cos(\phi - \delta) \tag{7}$$

Here, Z represents the altitude (in meters). The day length N can be calculated using Equation 8:

$$N = \frac{2}{15}\omega_s \tag{8}$$

The actual sunshine duration (n) for a given region is based on observational data and, for Turkish provinces, is published by Güneş Enerji Potansiyeli Atlası (GEPA) [39]. Table 2 provides the average monthly sunshine duration for studied province.

Table 2. Monthly sunshine duration (n) for Konya (hour) [39]

Month	Jan	Feb	Mar	Apr	May	Jun	Jul	Aug	Sep	Oct	Nov	Dec
Konya	4,19	5,51	6,88	8,03	9,46	11,28	11,97	11,36	9,79	7,35	5,53	3,93

The total daily solar radiation on a horizontal surface, H, consists of direct H_b and diffuse H_d components:

$$H = H_d + H_b \tag{9}$$

The relationship between diffuse radiation H_d and total radiation H is defined by Equation 10:

$$H_d = H(1 - 1{,}13K_T) \tag{10}$$

The total daily solar radiation H_T on an inclined surface can be calculated using Equation 11:

$$H_T = H_b \bar{R}_b + H_d \left(\frac{1+cos\beta}{2}\right) + H \rho \left(\frac{1-cos\beta}{2}\right) \tag{11}$$

Where β is the tilt angle of the surface, and ρ is the reflection coefficient, which can be taken as 0.7 on snowy days and 0.2 on other days [38]. For Konya, December, January, and February are typically snowy months, according to Meteroloji Genel Müdürlüğü (MGM) data [40].

The ratio of daily direct radiation on an inclined surface to daily direct radiation on a horizontal surface $\bar{R}_b$ is defined by Equation 12:

$$\bar{R}_b = \frac{cos(\phi-\beta)cos\delta sin\omega_s' + (\pi/180)\omega_s' sin(\phi-\beta)sin\delta}{cos\phi cos\delta cos\omega_s + (\pi/180)\omega_s sin\phi sin\delta} \tag{12}$$

Here, ω_s' is the hour angle when the sun first strikes the inclined surface, calculated by Equation 13:

$$\omega_s' = \min \begin{bmatrix} cos^{-1}(-tan\phi tan\delta) \\ cos^{-1}(-\tan(\phi-\beta)\tan\delta) \end{bmatrix} \tag{13}$$

2.2. Calculation of Instantaneous Solar Radiation on an Inclined Surface

The instantaneous solar radiation incident on a horizontal surface outside the atmosphere I_o can be calculated using Equation 14:

$$I_o = \frac{12 x 3600 G_{sc}}{\pi} \left[1 + 0.033 cos\left(\frac{360d}{365}\right)\right] . \left[cos\phi cos\delta(sin\omega_2 - sin\omega_1) + \frac{2\pi(\omega_2 - \omega_1)}{360} sin\phi sin\delta\right] \tag{14}$$

Where ω is the hour angle, which can be calculated based on solar time (ST) using Equation 15. ω_2 and ω_1 are the hour angles corresponding to the time interval in which the instantaneous value is calculated.

$$\omega = 15(ST - 12) \tag{15}$$

The ratio (r_d) of the diffuse instantaneous radiation on a horizontal surface I_d to the total daily diffuse radiation H_d is equal to the ratio of instantaneous extraterrestrial solar radiation I_0 to daily total extraterrestrial radiation H_0, as defined in Equation 16:

$$r_d = \frac{I_d}{H_d} = \frac{I_0}{H_0} \tag{16}$$

The instantaneous solar radiation on a horizontal surface can be calculated using the ratio r_t defined in Equation 17 and applied in Equation 18:

$$r_t = \frac{\pi}{4N} \left\{ cos\left(\frac{180}{2}\frac{\omega}{\omega_s}\right) + \frac{2}{\sqrt{\pi}}(1 - \psi) \right\} \tag{17}$$

$$r_t = \frac{I}{H} \tag{18}$$

Here, ω represents the hour angle at the midpoint between two solar time (ST) intervals.

Ψ is defined as below:

$$\psi = exp\left\{ -4\left(1 - \frac{|\omega|}{\omega_s}\right)^2 \right\} \tag{19}$$

The instantaneous solar radiation on a horizontal surface I consists of both diffuse I_d and direct I_b components:

$$I = I_d + I_b \tag{20}$$

Using the value of I obtained from Equation 18 and I_d from Equation 16, I_b can be calculated with Equation 20.

The instantaneous solar radiation incident on an inclined surface, I_T, comprises direct I_{bT}, diffuse I_{dT}, and reflected I_{refT} radiation components:

$$I_T = I_{bT} + I_{dT} + I_{refT} \tag{21}$$

The diffuse component of the instantaneous solar radiation on an inclined surface I_{dT} can be calculated using Equation 22:

$$I_{dT} = I_d \frac{1 + cos\beta}{2} \tag{22}$$

The direct component of the instantaneous solar radiation on an inclined surface I_{bT} can be calculated using Equation 23:

$$I_{bT} = R_b . I_b \tag{23}$$

Where R_b is the geometric factor, defined in Equation 24:

$$R_b = \frac{cos\theta}{cos\theta_z} \tag{24}$$

θ is the solar incidence angle, calculated with Equation 25:

$$cos\theta = sin\delta sin\phi cos\beta - sin\delta cos\phi sin\beta cos\gamma + cos\delta cos\phi cos\beta cos\omega + cos\delta sin\phi sin\beta cos\gamma cos\omega + \tag{25}$$
$$cos\delta sin\beta sin\gamma sin\omega$$

Here, γ is the surface azimuth angle, which is 0° for south-facing, 180° for north-facing, 270° for east-facing, and 90° for west-facing surfaces.

θ_z is the zenith angle, representing the solar incidence angle on a horizontal surface ($\beta = 0$), as defined in Equation 26:

$$cos\theta_z = cos\delta cos\phi cos\beta cos\omega + sin\delta sin\phi \tag{26}$$

Instantaneous reflected radiation I_{refT} on an inclined surface is defined in Equation 27:

$$I_{refT} = I\rho \left(\frac{1-cos\beta}{2}\right) \tag{27}$$

2.3. Solution Procedure

This section presents the core methodology developed for this study, based on theoretical radiation models and numerical optimization techniques, to calculate and compare solar gains across four surface configurations.

Using the theoretical calculations for daily and instantaneous solar radiation defined in Sections 2.1 and 2.2, mathematical models were developed in MS Excel for four surface types: a horizontal surface, a fixed south-facing inclined surface, an east-west tracking surface, and a south-north tracking surface. The Konya province in Turkey, which has high solar energy potential and favorable economic and topographic conditions for solar power plant installations, was selected as the study area. The study area is located at 37.97°N latitude and 32.57°E longitude, with an altitude of 1031 meters above sea level.

The input parameters used in the mathematical model are summarized in Table 3.

**Table 3.** Input parameters for the mathematical model

Parameter Description	Symbol	Value / Source
The latitude angle (°)	ϕ	37.97
The altitude (m)	Z	1031
The average day value of month	d	(Table 1) [38]
Actual sunshine duration (h) of month	n	(Table 2) [39]
Tilt angle of the surface (°)	β	Iteratively optimized via Solver add-in.
Reflection coefficient	ρ	0.7 (Dec, Jan, Feb), 0.2 (others) [40]
Solar time (h)	ST	Examined time
Surface azimuth angle (°)	γ	0° for south-facing, 180° for north-facing, 270° for east-facing, and 90° for west-facing surfaces
The solar constant (W/m²)	G_{sc}	1367

The daily solar radiation on the horizontal surface was calculated using the average day of each month, and the resulting monthly values were summed to determine the annual total. Figure 1 illustrates the step-by-step procedure for calculating daily solar radiation on a horizontal surface.
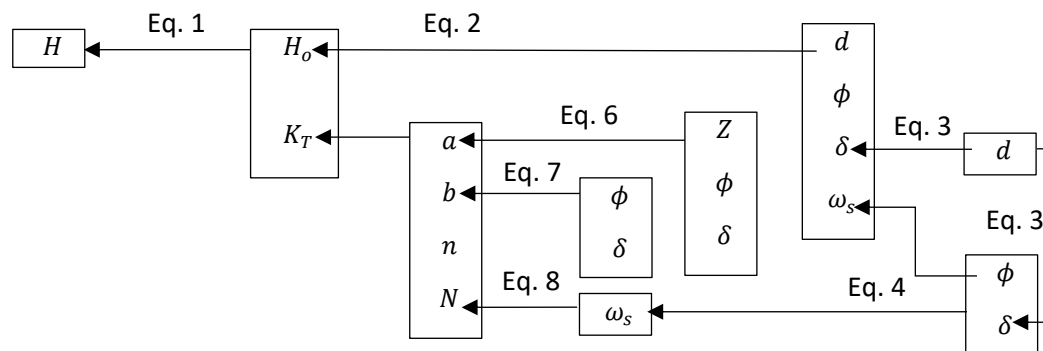
Figure 1. Calculation procedure for daily solar radiation on a horizontal surface

For the fixed south-facing inclined surface, the tilt angle that yields the maximum annual total solar radiation was determined through iterative optimization using Excel's Solver add-in. This tool adjusts input cell values to maximize (or minimize) a target cell, enabling the model to identify the optimal tilt angle. The calculation process is based on monthly average days and is repeated for each month to compute monthly values, which are then summed to obtain the annual total. The procedure is illustrated in Figure 2.
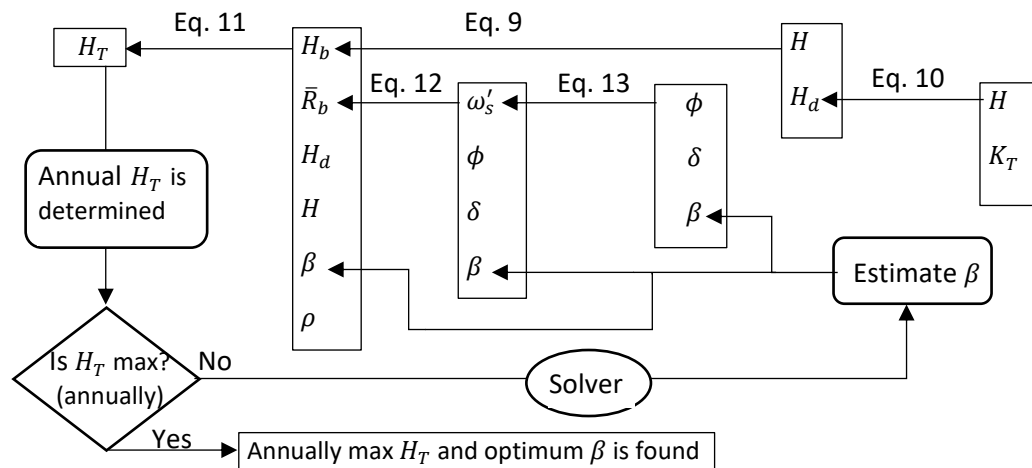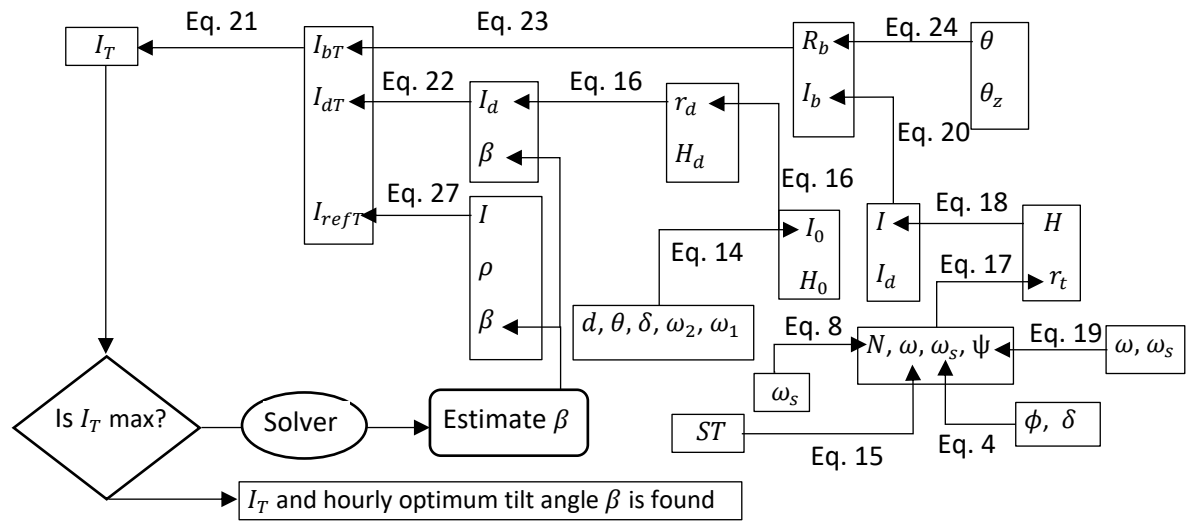
Figure 2. Procedure for determining the optimal tilt angle β for maximum annual solar radiation on a fixed inclined surface

For the tracking surfaces, instantaneous solar radiation was computed at hourly intervals throughout the day. At each hour, the tracking angle that provides the maximum radiation was determined iteratively using the Solver add-in. The resulting hourly values were then aggregated to compute daily total radiation, which in turn was used to obtain monthly and annual totals. The model used the monthly average day method for these calculations. The calculation procedure for instantaneous radiation on inclined tracking surfaces is shown in Figure 3.

In this context, negative tilt angle β values indicate that the surface is oriented from east to west or from south to north.

This method is applicable to any global location as it is based on general solar geometry and empirical equations. While the current study uses data specific to the selected region, the same procedure can be repeated elsewhere using local inputs. For greater accuracy, region-specific empirical formulas can be used.

Figure 3. Procedure for determining optimal tilt angles for maximum instantaneous radiation in inclined tracking surface

3. RESULTS AND DISCUSSION

In this study, the solar radiation gains of four surface configurations were compared specifically for the Konya province in Turkey: an east-west tracking surface, a south-north tracking surface, a fixed south-facing inclined surface optimized for maximum annual solar radiation gain, and a horizontal surface. The Konya region, selected as the study area due to its geographical and economic suitability for solar power plant installations in Turkey, provides favorable conditions for solar energy generation.

3.1. Monthly And Hourly Variation of Tilt Angles for Tracking Surfaces

On the representative (average) day of each month, the tilt angles that yield the maximum instantaneous solar radiation for each hour were determined for both east-west and south-north tracking surfaces. These calculations were conducted for the study region using the mathematical modeling and Solver-based optimization approach detailed in Section 2.3. The resulting hourly optimum tilt angles are summarized in Table 4 and Table 5, respectively.

Table 4. Calculated monthly and hourly tilt angles for the east-west solar tracking system in the selected region

Solar Time	Jan	Feb	Mar	Apr	May	Jun	Jul	Aug	Sep	Oct	Nov	Dec
5:30					81,4°	78,9°	80,7°	86,6°				
6:30			81,4°	74,2°	69,0°	67,3°	69,0°	73,9°	80,6°			
7:30		80,4°	68,1°	62,0°	57,5°	56,2°	57,8°	62,1°	68,0°	73,7°	77,5°	
8:30	63,6°	70,8°	55,1°	49,5°	45,6°	44,6°	46,0°	49,9°	55,1°	60,4°	64,9°	75,2°
9:30	49,0°	58,2°	40,7°	36,1°	33,1°	32,4°	33,6°	36,6°	40,9°	45,4°	49,7°	63,5°
10:30	30,7°	40,2°	24,9°	21,9°	20,0°	19,6°	20,4°	22,4°	25,3°	28,3°	31,3°	45,4°
11:30	10,5°	14,8°	8,4°	7,3°	6,7°	6,6°	6,9°	7,6°	8,6°	9,6°	10,7°	17,3°
12:30	-10,5°	-14,8°	-8,4°	-7,3°	-6,7°	-6,6°	-6,9°	-7,6°	-8,6°	-9,6°	-10,7°	-17,3°
13:30	-30,7°	-40,2°	-24,9°	-21,9°	-20,0°	-19,6°	-20,4°	-22,4°	-25,3°	-28,3°	-31,3°	-45,4°
14:30	-49,0°	-58,2°	-40,7°	-36,1°	-33,1°	-32,4°	-33,6°	-36,6°	-40,9°	-45,4°	-49,7°	-63,5°
15:30	-63,6°	-70,8°	-55,1°	-49,5°	-45,6°	-44,6°	-46,0°	-49,9°	-55,1°	-60,4°	-64,9°	-75,2°
16:30		-80,4°	-68,1°	-62,0°	-57,5°	-56,2°	-57,8°	-62,1°	-68,0°	-73,7°	-77,5°	
17:30			-81,4°	-74,2°	-69,0°	-67,3°	-69,0°	-73,9°	-80,6°			
18:30					-81,4°	-78,9°	-80,7°	-86,6°				

Table 5. Calculated monthly and hourly tilt angles for the south-north solar tracking system in the selected region

Solar Time	Jan	Feb	Mar	Apr	May	Jun	Jul	Aug	Sep	Oct	Nov	Dec
5:30					-66,8°	-64,9°	-67,1°	-77,8°				
6:30			37,2°	-10,2°	-26,3°	-31,7°	-30,6°	-20,7°	16,9°			
7:30	70,2°	69,5°	35,9°	12,0°	-3,2°	-9,2°	-6,9°	5,5°	28,8°	53,8°	68,0°	
8:30	71,7°	63,6°	36,4°	19,8°	7,8°	2,7°	5,2°	15,5°	31,9°	48,4°	60,1°	73,6°
9:30	67,9°	60,6°	36,4°	23,1°	13,2°	9,0°	11,3°	20,1°	33,1°	46,0°	55,7°	69,8°
10:30	65,6°	58,9°	36,2°	24,7°	16,0°	12,2°	14,4°	22,3°	33,6°	44,6°	53,2°	67,3°
11:30	64,4°	58,1°	36,0°	25,3°	17,1°	13,6°	15,7°	23,2°	33,7°	44,0°	51,9°	66,1°
12:30	64,4°	58,1°	36,0°	25,3°	17,1°	13,6°	15,7°	23,2°	33,7°	44,0°	51,9°	66,1°
13:30	65,6°	58,9°	36,2°	24,7°	16,0°	12,2°	14,4°	22,3°	33,6°	44,6°	53,2°	67,3°
14:30	67,9°	60,6°	36,4°	23,1°	13,2°	9,0°	11,3°	20,1°	33,1°	46,0°	55,7°	69,8°
15:30	71,7°	63,6°	36,4°	19,8°	7,8°	2,7°	5,2°	15,5°	31,9°	48,4°	60,1°	73,6°
16:30	70,2°	69,5°	35,9°	12,0°	-3,2°	-9,2°	-6,9°	5,5°	28,8°	53,8°	68,0°	
17:30			37,2°	-10,2°	-26,3°	-31,7°	-30,6°	-20,7°	16,9°			
18:30					-66,8°	-64,9°	-67,1°	-77,8°				

The east-west tracking system follows the sun's path from sunrise to sunset along the same axis. As the summer solstice approaches and the days lengthen, the start and end times of solar tracking shift to earlier and later hours. At solar noon, 12:00, when the sun is at its highest position, a horizontal orientation provides the maximum radiation gain.

The south-north tracking system does not exhibit a similar directional pattern throughout the year as the east-west tracking system does. This difference is primarily due to the sun's varying path across the sky throughout the year, as illustrated in Figure 4. During the spring and autumn equinoxes, the sun rises and sets exactly in the east and west, respectively; in summer, it shifts northward, rising and setting in more northerly directions, while in winter, it remains in the southern hemisphere throughout the day. As the sun's rising and setting directions deviate from the east-west line, the start and end angles of the south-north tracking system become increasingly steep. In December, the starting and ending angle of the system faces south at 73.6°, whereas in June, due to the sun rising from the north, this angle shifts to -64.9°, pointing northward. In April and September, the surface starts the day at a near-horizontal angle of -10.2° and 16.9°, respectively.
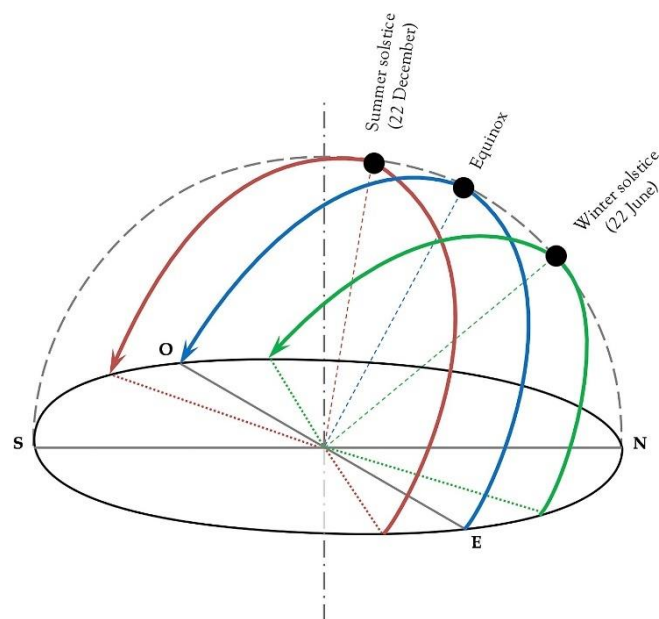
Figure 4. The path of the sun in the sky throughout the year in the southern hemisphere [41]

3.2. Monthly and Annual Total Solar Radiation on Surfaces

Daily total radiation values were calculated for each surface configuration—east-west tracking, south-north tracking, fixed south-facing surface with optimal tilt angle, and horizontal surface—based on the average day of each month. From these calculations, monthly and annual total gain values were determined. The calculated annual total solar radiation values for each surface type are presented in Table 5. The lowest annual total solar radiation falls on the horizontal surface. The fixed south-facing surface with an optimal tilt angle of 28.58°, which provides the maximum annual gain, collects 9% more radiation than the horizontal surface. Meanwhile, the south-north tracking surface achieves a 16% higher radiation gain, and the east-west tracking surface provides a 30% higher gain than horizontal surface. Consequently, the east-west tracking system is identified as the most suitable single-axis tracking method for the Konya region in terms of annual total gain.

Table 5. Calculated annual total solar radiation on surfaces in in the selected region

Surface Type	East-West Tracking	South-North Tracking	Fixed Tilt	Horizontal
Annual Total Radiation	2074 kWh/m²/year	1845 kWh/m²/year	1738 kWh/m²/year	1597 kWh/m²/year
Gain compared to Horiz.	30%	16%	9%	-

The daily total solar radiation values for each surface, calculated using the mathematical model and Solver-based procedure described in Section 2.3, based on the average day of each month, are shown in Figure 5 for comparison. The advantage of the east-west tracking surface becomes especially evident in the summer months. For example, in June, the south-north tracking surface collects an average of 6.96 kWh/m² of radiation daily, while the east-west tracking surface receives 2.02 kWh/m² more, reaching 8.98 kWh/m². In winter, however, the east-west tracking surface receives less solar radiation than the south-north tracking surface. This is due to the sun's southward path throughout winter, which prevents the east-west tracking surface from focusing on the south. In December, for example, the south-north tracking surface collects an average of 2.12 kWh/m² of radiation daily, while the east-west tracking surface receives 1.69 kWh/m², resulting in a 0.43 kWh/m² lower gain.
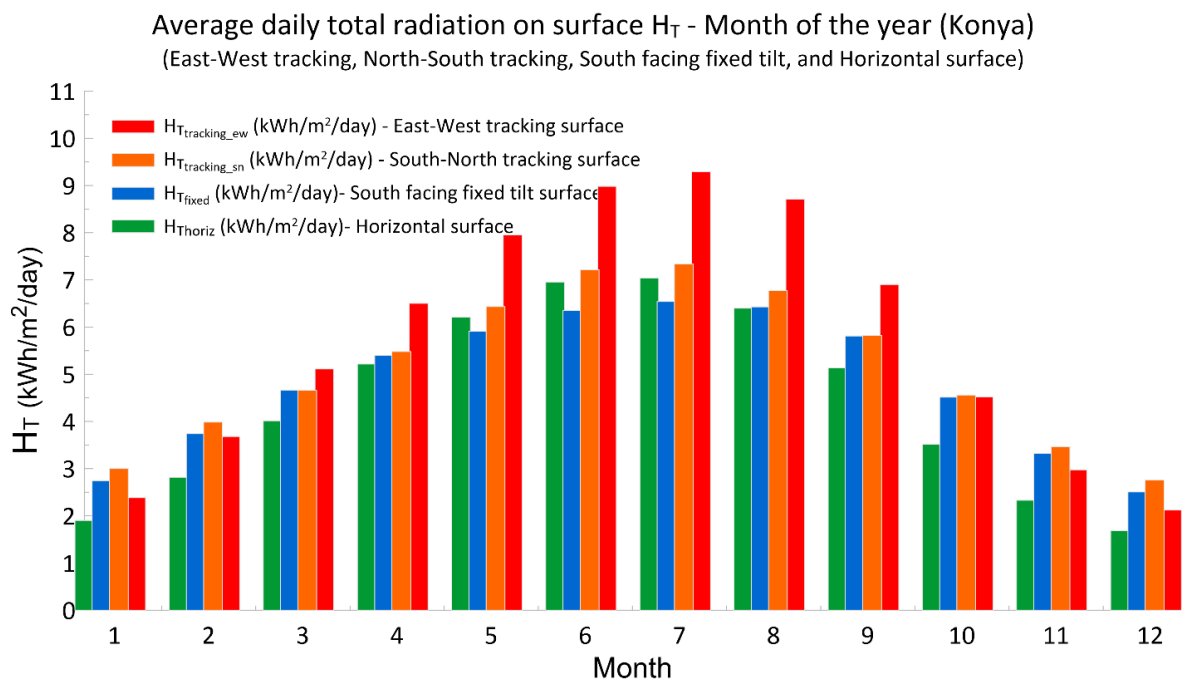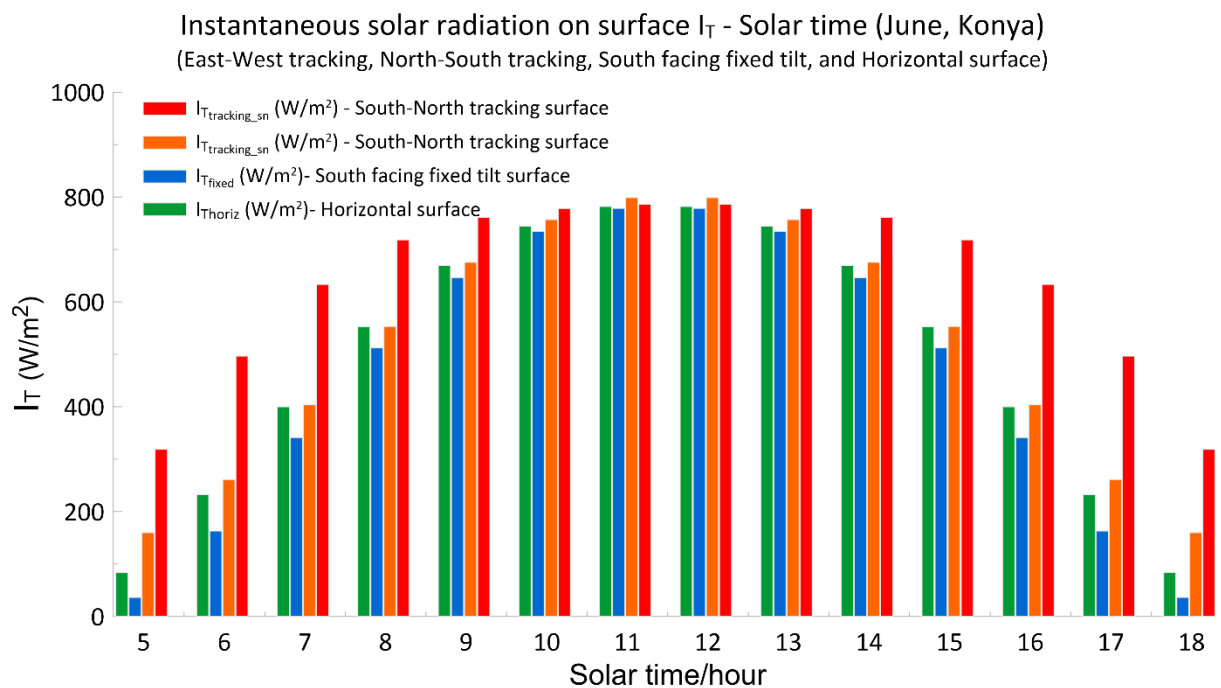

Figure 5. Monthly variation of daily total radiation on east-west tracking, south-north tracking, fixed-tilt, and horizontal surfaces in Konya

In conclusion, the east-west tracking system offers an advantage in terms of annual gain, while the south-north tracking system performs more effectively during the winter season. The fixed-tilt surface, compared to the horizontal surface, provides higher radiation gain throughout the year except in May, June, and July. The south-north tracking surface, always oriented at the optimal angle toward the south at any hour of the year, consistently collects more solar radiation than both the horizontal and fixed-tilt systems each month.

3.3. Hourly Variation of Instantaneous Solar Radiation on Surfaces in June and December

The values presented in this section were obtained using the solution procedure described in Section 2.2 and the calculation workflow shown in Figure 3, which determines both the instantaneous solar radiation and the corresponding optimal tilt angles for inclined tracking surfaces.

The calculated hourly variation of instantaneous solar radiation on east-west tracking, south-north tracking, fixed-tilt, and horizontal surfaces for the month of June is presented in Figure 6. As expected, the advantage of the east-west tracking surface becomes apparent in the morning and evening hours when the sun is positioned in the east and west. Around midday, when the sun is near its peak, both tracking systems approach a horizontal position and receive a similar amount of solar radiation. The fixed-tilt surface, set at the angle for optimal annual gain, collects lower radiation in June compared to the horizontal surface, particularly in the morning and evening. This is primarily due to the south-facing surface's reduced ability to capture sunlight from the sun's northward path, in contrast to the horizontal surface.
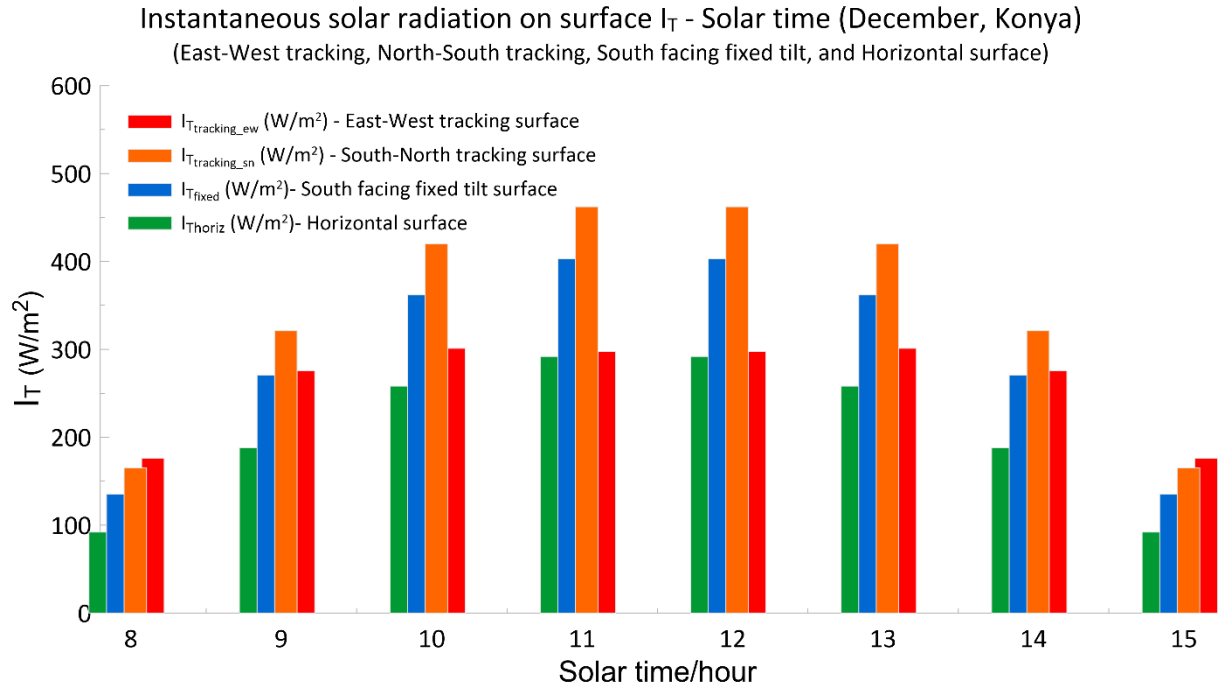

Figure 6. Hourly variation of instantaneous radiation on east-west tracking, south-north tracking, fixed-tilt, and horizontal surfaces in selected region during June

Figure 7 presents the hourly variation of instantaneous solar radiation on east-west tracking, south-north tracking, fixed-tilt, and horizontal surfaces for the month of December. In December, the sun is positioned significantly southward and reaches the earth from a tilted angle even at midday. The east-west tracking surface cannot fully utilize this southern sunlight and, therefore, collects less solar radiation during midday compared to south-facing surfaces. For instance, between 12:00 and 13:00, the instantaneous radiation on the south-north tracking surface is 462.2 W/m², whereas the east-west tracking surface receives only 297.4 W/m². The instantaneous radiation on the fixed-tilt surface,

however, reaches 402.9 W/m² during this time period, making it more advantageous than the east-west tracking system, which aligns closer to the horizontal at noon.

In the morning, as the sun rises from the east, the east-west tracking surface collects 176.2 W/m² of instantaneous radiation between 08:00 and 09:00. This value is only slightly higher than the 165.2 W/m² received by the south-north tracking surface, resulting in an insignificant gain in total radiation.

Figure 7. Hourly variation of instantaneous radiation on east-west tracking, south-north tracking, fixed-tilt, and horizontal surfaces in selected region during December

In conclusion, the east-west tracking surface provides an additional gain of up to 2 kWh/m² daily compared to the south-north tracking surface, particularly during the summer months. In winter, however, the south-north tracking system can offer a higher gain of up to 0.4 kWh/m² daily. Therefore, for applications prioritizing annual gains, such as PV electricity generation plants, the east-west tracking system would be a suitable choice. In applications focused on winter performance, the south-north tracking system presents a more advantageous option. This is especially true in conditions where environmental factors obstruct the sunrise and sunset, making the south-north tracking system even more favorable in winter. Future studies could further evaluate the annual, monthly, and instantaneous gains of dual-axis tracking systems and compare their performance with single-axis tracking systems.

4. CONCLUSIONS

In this study, the annual and seasonal solar radiation gains of single-axis solar tracking systems in two different orientations were analyzed specifically for the Konya region. For four surfaces—east-west tracking, south-north tracking, a fixed tilt angle optimized for annual gain, and a horizontal surface—the monthly average daily radiation and the annual total radiation values were calculated. The hourly variations in instantaneous solar radiation were also determined and compared for December and June. The findings reveal that solar radiation gains vary significantly by season, depending on surface orientation.

The east-west tracking system delivered the highest annual performance, capturing approximately 30% more radiation than the horizontal surface and 19% more than the fixed-tilt surface. During June, it also outperformed the south-north setup by 2.02 kWh/m² per day, a 29% increase, making it particularly

effective for applications such as photovoltaic (PV) power plants that prioritize annual energy production.

In contrast, during December, the south-north tracking system collected 0.43 kWh/m² more daily radiation than the east-west orientation—a 25% seasonal advantage due to its alignment with the sun's lower southern path. This makes the south-north orientation more favorable for winter-dominant energy needs or in regions where seasonal demand peaks in colder months.

The fixed-tilt surface, set to an optimal annual angle, achieved a 9% gain over the horizontal surface on an annual basis. While it consistently outperformed the horizontal surface throughout the year, it did not match the higher gains achieved by the tracking systems. Notably, the south-north tracking system, with its ability to maintain an optimal southward orientation year-round, provided consistently higher solar radiation than both the fixed-tilt and horizontal surfaces.

The hourly tracking angle values obtained in this study can be directly applied to tracking systems designed for the Konya region. Additionally, the solution method used in this study can be adapted for other regions, allowing for the creation of region-specific hourly angle tables.

In summary, for applications prioritizing annual yield, such as PV plants, the east-west tracking system provides the most efficient single-axis solution. However, for applications where winter performance is essential, the south-north tracking system is more effective. Future studies could build on these findings by analyzing dual-axis tracking systems, providing a more comprehensive comparison of annual, monthly, and hourly gains relative to single-axis systems. This would enable a deeper understanding of the optimal tracking configurations for diverse energy needs and seasonal variations.

Declaration of Ethical Standards

The authors declare that they have carried out this completely original study by adhering to all ethical rules including authorship, citation and data reporting.

Declaration of Competing Interest

The authors declared that they have no conflict of interest.

Funding / Acknowledgements

The author(s) received no financial support for the research.

Data Availability

Data supporting the findings of this study can be obtained from the corresponding author with reasonable requests to assist in scientific studies.

REFERENCES

[1] N. Çetinkaya, "IMPROVING OF RENEWABLE ENERGY SUPPORT POLICY AND A PERFORMANCE ANALYSIS OF A GRID-CONNECTED 1 MWP PV POWER PLANT IN KONYA," (in en), *Selçuk Üniversitesi Mühendislik, Bilim Ve Teknoloji Dergisi*, vol. 5, no. 3, pp. 251-261, September 2017, doi: 10.15317/Scitech.2017.86.

[2] M. Karimzadeh Kolamroudi, M. Ilkan, F. Egelioglu, and B. Safaei, "Maximization of the output power of low concentrating photovoltaic systems by the application of reflecting mirrors," *Renewable   Energy*,   vol.   189,   pp.   822-835,   2022/04/01/   2022,   doi: https://doi.org/10.1016/j.renene.2022.03.031.

[3] M. K. Kolamroudi, M. Ilkan, F. Egelioglu, and B. Safaei, "Feature selection by ant colony optimization and experimental assessment analysis of PV panel by reflection of mirrors

perpendicularly," *Renewable Energy,* vol. 218, p. 119238, 2023/12/01/ 2023, doi: https://doi.org/10.1016/j.renene.2023.119238.

[4]   M. Karimzadeh Kolamroudi, M. Ilkan, F. Egelioglu, and B. Safaei, "A comparative study of LCPV by mirror reflection against other systems: Recent techniques, implications, and performances," *Solar Energy,* vol. 250, pp. 70-90, 2023/01/15/ 2023, doi: https://doi.org/10.1016/j.solener.2022.12.017.

[5]   B. Utomo, J. Darkwa, D. Du, and M. Worall, "Solar photovoltaic cooling and power enhancement systems: A review," *Renewable and Sustainable Energy Reviews,* vol. 216, p. 115644, 2025/07/01/ 2025, doi: https://doi.org/10.1016/j.rser.2025.115644.

[6]   S. Gressler, F. Part, S. Scherhaufer, G. Obersteiner, and M. Huber-Humer, "Advanced materials for emerging photovoltaic systems – Environmental hotspots in the production and end-of-life phase of organic, dye-sensitized, perovskite, and quantum dots solar cells," *Sustainable Materials and Technologies,* vol. 34, p. e00501, 2022/12/01/ 2022, doi: https://doi.org/10.1016/j.susmat.2022.e00501.

[7]   M. H. Aksoy and M. K. Çalık, "PERFORMANCE INVESTIGATION OF BIFACIAL PHOTOVOLTAIC PANELS AT DIFFERENT GROUND CONDITIONS," (in en), *Konya Journal of Engineering Sciences,* vol. 10, no. 3, pp. 704-718, September 2022, doi: 10.36306/konjes.1116729.

[8]   H. Park, A. Öztürk, H. Park, and M. U. Khan, "UTILIZATION OF ROBOTICS FOR SOLAR PANEL CLEANING AND MAINTENANCE," (in en), *Konya Journal of Engineering Sciences,* vol. 7, no. 4, pp. 768-775, December 2019, doi: 10.36306/konjes.654942.

[9]   A. Kabul, F. Yiğit, and A. Duran, "ESTIMATING THE SOLAR EXERGY POTENTIAL OF SURFACES WITH DIFFERENT TILT ANGLES," (in en), *Konya Journal of Engineering Sciences,* vol. 12, no. 3, pp. 756-772, September 2024, doi: 10.36306/konjes.1473068.

[10] E. Akpinar, G. Gül Katircioglu, and M. Das, "Effects of solar tracking on different types of solar panels; experimental study for thermal and photovoltaic types," *International Journal of Hydrogen Energy,* 2025/02/17/ 2025, doi: https://doi.org/10.1016/j.ijhydene.2025.02.155.

[11] B. Singh, P. Kaur, A. K. Yadav, M. K. Awasthi, and A. Kumar, "Design and Analysis of Solar Tracking System for PV Thermal Performance Enhancement," in *Heat Transfer Enhancement Techniques*, 2025, pp. 251-267.

[12] M. Kabilan, V. Manikandan, and S. Dharshini, "Automatic Solar Tracking System: A Comprehensive Overview of an advanced Automatic Solar Tracking system using ESP8266," *Asian Journal of Applied Science and Technology (AJAST),* vol. 9, no. 1, pp. 11-20, 2025.

[13] K. Kumba, P. Upender, P. Buduma, M. Sarkar, S. P. Simon, and V. Gundu, "Solar tracking systems: Advancements, challenges, and future directions: A review," *Energy Reports,* vol. 12, pp. 3566-3583, 2024/12/01/ 2024, doi: https://doi.org/10.1016/j.egyr.2024.09.038.

[14] H. A. Kazem, M. T. Chaichan, A. H. A. Al-Waeli, and K. Sopian, "Recent advancements in solar photovoltaic tracking systems: An in-depth review of technologies, performance metrics, and future trends," *Solar Energy,* vol. 282, p. 112946, 2024/11/01/ 2024, doi: https://doi.org/10.1016/j.solener.2024.112946.

[15] N. Kuttybay *et al.,* "Assessment of solar tracking systems: A comprehensive review," *Sustainable Energy Technologies and Assessments,* vol. 68, p. 103879, 2024/08/01/ 2024, doi: https://doi.org/10.1016/j.seta.2024.103879.

[16] A. Bahrami, C. O. Okoye, and U. Atikol, "Technical and economic assessment of fixed, single and dual-axis tracking PV panels in low latitude countries," *Renewable Energy,* vol. 113, pp. 563-579, 2017/12/01/ 2017, doi: https://doi.org/10.1016/j.renene.2017.05.095.

[17] K. Kumba, S. P. Simon, K. Sundareswaran, P. S. R. Nayak, K. A. Kumar, and N. P. Padhy, "Performance Evaluation of a Second-Order Lever Single Axis Solar Tracking System," *IEEE Journal of Photovoltaics,* vol. 12, no. 5, pp. 1219-1229, 2022, doi: 10.1109/JPHOTOV.2022.3187647.

[18] A. Alshaabani, "Developing the Design of Single-Axis Sun Sensor Solar Tracking System," *Energies,* vol. 17, no. 14, doi: 10.3390/en17143442.

[19] Z. Er and E. Balcı, "Dual axis solar angle tracking system without any sensor," (in en), *Journal of Energy Systems,* vol. 2, no. 3, pp. 127-136, September 2018, doi: 10.30521/jes.456606.

[20] H. Toylan, "DESIGN AND APPLICATION OF SOLAR TRACKING SYSTEM USING OPTIMIZED FUZZY LOGIC CONTROLLER BY GENETIC ALGORITHM," (in en), *Mugla Journal of Science and Technology,* vol. 6, no. 1, pp. 136-145, June 2020, doi: 10.22531/muglajsci.641904.

[21] A. Attou, A. Massoum, and M. Saidi, "Photovoltaic Power Control Using MPPT and Boost Converter," (in en), *Balkan Journal of Electrical and Computer Engineering,* vol. 2, no. 1, pp. 23-27, March 2014. [Online]. Available: https://dergipark.org.tr/tr/pub/bajece/issue/3360/46444 https://dergipark.org.tr/tr/download/article-file/39741.

[22] M. A. Khan and M. E. Tacer, "PV Panel Based Micro Inverter Using Boost Control Topology with PWM and MPPT (Perturb and Observe) Method," (in en), *International Journal of Electronics Mechanical and Mechatronics Engineering,* vol. 10, no. 1, pp. 1785-1794, January 2020. [Online]. Available: https://dergipark.org.tr/tr/pub/ijemme/issue/65301/1005821 https://dergipark.org.tr/tr/download/article-file/2013945.

[23] G. Nazlı Arpacı, P. D. M. C. Taplamacıoğlu, and D. D. H. Gözde, "Design and Comparison of Perturb & Observe and Fuzzy Logic Controller in Maximum Power Point Tracking System for PV System by Using MATLAB/Simulink," (in en), *International Journal of Multidisciplinary Studies and Innovative Technologies,* vol. 3, no. 1, pp. 66-71, March 2019. [Online]. Available: https://dergipark.org.tr/tr/pub/ijmsit/issue/43647/569324 https://dergipark.org.tr/tr/download/article-file/732206.

[24] M. E. Başoğlu, R. Ünsal, and G. Çağşırlıoğlu, "Realization of a Dual Axis Solar Tracking System," (in en), *Bilecik Şeyh Edebali Üniversitesi Fen Bilimleri Dergisi,* vol. 9, no. 1, pp. 52-61, June 2022, doi: 10.35193/bseufbd.991613.

[25] F. Alhaj Omar, G. Gökkuş, and A. A. Kulaksız, "ŞEBEKEDEN BAĞIMSIZ FV SİSTEMDE MAKSİMUM GÜÇ NOKTASI TAKİP ALGORİTMALARININ DEĞİŞKEN HAVA ŞARTLARI ALTINDA KARŞILAŞTIRMALI ANALİZİ," (in tr), *Konya Journal of Engineering Sciences,* vol. 7, no. 3, pp. 585-594, September 2019, doi: 10.36306/konjes.613871.

[26] C. Sungur, "Multi-axes sun-tracking system with PLC control for photovoltaic panels in Turkey," *Renewable Energy,* vol. 34, no. 4, pp. 1119-1125, 2009/04/01/ 2009, doi: https://doi.org/10.1016/j.renene.2008.06.020.

[27] N. A. Kelly and T. L. Gibson, "Improved photovoltaic energy output for cloudy conditions with a solar tracking system," *Solar Energy,* vol. 83, no. 11, pp. 2092-2102, 2009/11/01/ 2009, doi: https://doi.org/10.1016/j.solener.2009.08.009.

[28] G. Quesada, L. Guillon, D. R. Rousse, M. Mehrtash, Y. Dutil, and P.-L. Paradis, "Tracking strategy for photovoltaic solar systems in high latitudes," *Energy Conversion and Management,* vol. 103, pp. 147-156, 2015/10/01/ 2015, doi: https://doi.org/10.1016/j.enconman.2015.06.041.

[29] A. ÖZTÜRK, B. DOĞAN, and M. YEŞİLYURT, "Energy, exergy, sustainability, and economic analyses of a grid-connected solar power plant consisting of bifacial PV modules with solar tracking system on a single axis," *Science and Technology for Energy Transition (STET),* vol. 78, 2023.

[30] İ. Kayri, "Fotovoltaik Uygulamalar İçin Kararlı Tek Eksenli Bir Güneş Takip Sistemi Tasarımı ve Uygulaması," (in tr), *Yüzüncü Yıl Üniversitesi Fen Bilimleri Enstitüsü Dergisi,* vol. 28, no. 2, pp. 432-450, August 2023, doi: 10.53433/yyufbed.1256765.

[31] N. Arslanoğlu and A. Yiğit, "Parabolik Oluk Güneş Toplayıcılarının Simülasyonu ve Anlık Isıl Performanslarının İncelenmesi," (in tr), *Mühendis ve Makina,* vol. 63, no. 709, pp. 709-725, December 2022, doi: 10.46399/muhendismakina.1121249.

[32] O. R. Alomar, O. M. Ali, B. M. Ali, V. S. Qader, and O. M. Ali, "Energy, exergy, economical and environmental analysis of photovoltaic solar panel for fixed, single and dual axis tracking systems: An experimental and theoretical study," *Case Studies in Thermal Engineering,* vol. 51, p. 103635, 2023/11/01/ 2023, doi: https://doi.org/10.1016/j.csite.2023.103635.

[33] M. S. Azam *et al.,* "Performance enhancement of solar PV system introducing semi-continuous tracking algorithm based solar tracker," *Energy,* vol. 289, p. 129989, 2024/02/15/ 2024, doi: https://doi.org/10.1016/j.energy.2023.129989.

[34] A. Celen, M. Y. Kaba, A. Kurnuç Seyhan, and P. Celen, "FARKLI EĞİM AÇILARINDA GÜNEŞ KOLLEKTÖRLERİNİN ENERJİ VE EKSERJİ ANALİZİ: ERZİNCAN İLİ ÖRNEĞİ," (in tr), *Konya Journal of Engineering Sciences,* vol. 10, no. 3, pp. 634-648, September 2022, doi: 10.36306/konjes.1096936.

[35] E. Doğan and Y. Karakılçık, "TÜRKİYE'DE GÜNEŞ PANELLERİNDEN ENERJİ ÜRETİMİ: KONYA İLİ ÜZERİNE BİR DEĞERLENDİRME," (in tr), *Karamanoğlu Mehmetbey Üniversitesi Sosyal Ve Ekonomik Araştırmalar Dergisi,* vol. 26, no. 46, pp. 471-485, June 2024. [Online]. Available: https://dergipark.org.tr/tr/pub/kmusekad/issue/85312/1428767
https://dergipark.org.tr/tr/download/article-file/3695682.

[36] B. Y. H. Liu and R. C. Jordan, "The interrelationship and characteristic distribution of direct, diffuse and total solar radiation," *Solar Energy,* vol. 4, no. 3, pp. 1-19, 1960/07/01/ 1960, doi: https://doi.org/10.1016/0038-092X(60)90062-1.

[37] B. Liu and R. Jordan, "Daily insolation on surfaces tilted towards equator," (in English), vol. 10, 1961-10-01 1961, doi: Journal Name: ASHRAE J.; (United States); Journal Volume: 10.

[38] A. Yiğit and İ. Atmaca, *Güneş Enerjisi.* Alfa Aktüel Yayınları, 2010.

[39] "Güneş Enerjisi Potansiyel Atlası." Enerji İşleri Genel Müdürlüğü. https://gepa.enerji.gov.tr/MyCalculator/ (accessed 25.09.2024, 2024).

[40] "Resmi İklim İstatistikleri." Meteoroloji Genel Müdürlüğü https://www.mgm.gov.tr/veridegerlendirme/il-ve-ilceler-istatistik.aspx (accessed 20.09.2024, 2024).

[41] B. Malet-Damour, S. Guichard, A. P. Jean, F. Miranville, and H. Boyer, "SHADECO: A low-cost shadow-ring for diffuse measures: State of the art, principles, design and application," *Renewable Energy,* vol. 117, pp. 71-84, 2018/03/01/ 2018, doi: https://doi.org/10.1016/j.renene.2017.09.083.